THE UNIVERSITY *of* ADELAIDE

Characterising the Performance of Vortex-Based Solar Thermal Particle Receiver-Reactors

Dominic M. W. Davis

A thesis presented for the degree of
Doctor of Philosophy

Centre for Energy Technology
School of Mechanical Engineering
The University of Adelaide
Australia

July, 2019

Abstract

This thesis investigates vortex-based solar thermal particle receivers to provide new understanding of the mechanisms controlling their performance. This new understanding is needed to optimise a receiver on a case-by-case basis for the different requirements of a range of alternative potential applications. There is growing interest in the use of solid particles as the heat transfer medium in concentrating solar thermal systems because particles are efficient absorbers of direct irradiation and have strong potential as a low-cost thermal storage medium. The vortex-based class of solar particle receiver is under development as a device for the solar heating of both inert particles, via sensible heat, and of reacting particles, via chemical (and sensible) heat. Such a receiver typically consists of a cylindrical cavity receiver, through which particles are conveyed by a vortex flow of gas so that the particles are directly irradiated by concentrated solar radiation entering the cavity through a circular aperture. This thesis supports the further development of the vortex-based solar particle receiver by characterising three different aspects of the performance of such a receiver. Firstly, the influence of key input and geometric parameters on the receiver thermal performance is presented. Next, fundamental insights into dimensionless parameters controlling particle residence time distributions within such receivers are provided. Finally, the performance of a vortex-based solar particle receiver in a common industrial thermochemical process is characterised. Key results and findings of this thesis have been published in two peer-reviewed research articles in the journals, *Solar Energy* and *Green Chemistry*, while a further two articles have been submitted to the journals *Chemical Engineering Science* and *Solar Energy*.

A one-dimensional numerical model is developed to systematically characterise the heat and mass transport processes within vortex-based solar particle receivers and provide key insights into the factors affecting the thermal performance. The model adapts the zonal method to calculate heat and mass transport within the enclosure of the receiver, incorporating radiative and convective heat transfer between the particle phase, the gas phase and the receiver wall, together with re-radiative and conductive losses. Sensitivity studies of the thermal performance reveal that a vortex-based solar

particle receiver can be configured to operate as either an air-heater or a particle-heater, depending primarily on the particle mass loading. Furthermore, assessment of the two-phase flow direction finds that a counter-flow (relative to the incident concentrated solar radiation) tends to result in a higher thermal efficiency than a co-flow direction. The first order trends of the sensitivity of the receiver's thermal performance to the particle and air mass flow rates, particle size and receiver length are also reported, predicting overall receiver thermal efficiencies of up to 88%. It is, however, expected that the thermal efficiency of the device for all operating conditions assessed will improve with an increase in scale from the laboratory to the industrial scale. The model developed in this thesis is thereby used to advance understanding of the dominant mechanisms controlling the thermal performance of vortex-based solar particle receivers.

The first direct measurement of particle residence time distributions (RTDs) within a vortex-based solar particle receiver is presented to provide new understanding of the physical mechanisms controlling the two-phase flow behaviour within the device. The tracer pulse method is extended to directly measure the residence time of the particle phase for a systematic and independent variation of particle size, gas volumetric flow rate, inlet velocity and receiver tilt angle (orientation relative to gravity). Two regimes of particle behaviour are identified, characterised by both the Stokes and the Froude numbers of the two-phase flow. In the low Froude number regime, an increase in the Stokes number increases particle residence time, so that large particles have a longer residence time than the smaller particles, as is desirable for the efficient processing of polydisperse particles. In the high Froude number regime, the Stokes number has a weaker influence on the residence time than it does in the low Froude number regime. The higher Froude numbers result in a decrease in the particle residence time. The comparison of experimentally-measured RTDs with those of ideal reactors finds that the two regimes of particle behaviour can be described by a single analytical compartment model consisting of a small plug flow reactor followed by a series of two interconnected continuously-stirred tank reactors (CSTRs). For the low Froude number regime, there is a significant degree of back-mixing between the two CSTRS, while, for the high Froude number regime, there is negligible. Finally, assessment of alternative receiver tilt angles finds that particle recirculation is enhanced and particle residence times are longer when the two-phase flow proceeds in the direction opposite to gravity. This is because the vertical orientation (corresponding to upward-facing receiver tilt angles) aligns the direction of gravity with the reverse flow direction generated by the central recirculation flow zone to augment the recirculation of particles towards the base of the cavity. However, the assessment also finds that the influence of the receiver tilt angle on the particle residence time is relatively weak for smaller particles. This implies that it is preferable to operate tower-mounted systems (i.e. with downward facing receiver tilt angles) with small particles. This study provides both new experimental data and understanding of the factors influencing the particle RTDs within vortex-based solar particle receivers.

Finally, a first-of-a-kind demonstration that alumina can be calcined with concentrated solar radiation in a small-scale vortex-based solar particle receiver is presented. In this novel application of the device, simulated concentrated solar radiation at radiative fluxes up to 2.2 MW m^{-2} is used to directly irradiate and calcine aluminium hydroxide particles at nominal receiver temperatures over the range 887 – 1277 °C. This yields chemical conversions of up to 95.8% with nominal residence times of approximately 3 s and solar energy conversion efficiencies of up to 20.4%. Potential improvements in the alumina product quality (particle pore diameter and specific surface area) are also identified, relative to the quality of alumina produced with the conventional industrial Bayer process. This suggests that concentrated solar thermal processing can be used to improve the quality of alumina over existing fossil fuel based processes through a combination of a high heating rate and avoided contamination by combustion products. Furthermore, the solar-driven process has the potential to avoid the discharge of combustion-derived 165 kg-CO_2 per tonne-alumina of emissions for the calcination stage of the conventional Bayer process, at least during those periods when the solar resource is available.

List of Papers

Davis, D, Jafarian, M, Chinnici, A, Saw, WL & Nathan, GJ 2019, 'Thermal performance of vortex-based solar particle receivers for sensible heating', *Solar Energy*, vol. 177, pp. 163–177.

Davis, D, Troiano, M, Chinnici, A, Saw, WL, Lau, T, Solimene, R, Salatino, P & Nathan, GJ 2019, 'Particle residence time distributions in a vortex-based solar particle receiver-reactor: an experimental, numerical and theoretical study', Manuscript submitted to *Chemical Engineering Science*.

Davis, D, Troiano, M, Chinnici, A, Saw, WL, Lau, T, Solimene, R, Salatino, P & Nathan, GJ 2019, 'Particle residence time distributions in a vortex-based solar particle receiver-reactor: the influence of receiver tilt angle', Manuscript submitted to *Solar Energy*.

Davis, D, Müller, F, Saw, WL, Steinfeld, A & Nathan, GJ 2017, 'Solar-driven alumina calcination for CO_2 mitigation and improved product quality', *Green Chemistry*, vol. 19, no. 13, pp. 2992–3005.

Declaration

I, Dominic Davis, certify that this work, *Characterising the Performance of Vortex-Based Solar Thermal Particle Receiver-Reactors*, contains no material which has been accepted for the award of any other degree or diploma in my name, in any university or other tertiary institution and, to the best of my knowledge and belief, contains no material previously published or written by another person, except where due reference has been made in the text. In addition, I certify that no part of this work will, in the future, be used in a submission in my name, for any other degree or diploma in any university or other tertiary institution without the prior approval of the University of Adelaide and where applicable, any partner institution responsible for the joint-award of this degree.

I acknowledge that copyright of published works contained within this thesis resides with the copyright holder(s) of those works.

I also give permission for the digital version of my thesis to be made available on the web, via the University's digital research repository, the Library Search and also through web search engines, unless permission has been granted by the University to restrict access for a period of time.

I acknowledge the support I have received for my research through the provision of an Australian Government Research Training Program Scholarship.

Dominic M. W. Davis

Acknowledgements

This work and my quite indescribable joy at its completion are the direct result of the help, guidance and support of many people. I would like to acknowledge these people here.

Firstly, I would like to thank my supervisors, Prof. Gus Nathan, Dr. Woei Saw and Dr. Alfonso Chinnici. Gus has taught me a great amount about the importance of performing scientific investigation for the primary purpose of developing new understanding. I am sincerely grateful to him for his passionate support over the course of my studies, and for always providing me with timely, thorough and critical review of my work. My writing and presentation skills have improved significantly due to his feedback. Saw has always been available to discuss any problem that needs solving, and his technical support in setting up my experiments was hugely important. It has always been a pleasure to knock on his door for a chat; his guidance has been very helpful, and for that I am very grateful. I am also very grateful to Alfonso, for his support of my work and for his very practical advice on completing this work, particularly the two residence time papers, in a timely manner. He deserves special thanks for always greeting me with a smile, no matter how many times a day I knock on his door.

Much of my work has involved collaboration with international partners. For this I count myself very lucky. I am very grateful to Prof. Aldo Steinfeld at ETH Zürich, for welcoming me into his research group to carry out the solar calcination of alumina experiments. I had a wonderful experience over the three month stay and learnt much. Thanks also go to Dr. Fabian Müller for the hard work that resulted in a high quality paper, but also for showing me Zürich and a good time. I enjoyed myself immensely during this work. My partner, among others, for the particle residence time work was Dr. Maurizio Troiano, who helped with experiments and analysing the data. Thank you, Maurizio, for being great fun to work with and also responding so very quickly under time pressure. I hope to be able to shout you that pizza in Napoli soon! I am also grateful to Dr. Roberto Solimene and Prof. Piero Salatino, for their crucial (and timely) input into the writing of our particle residence time papers.

Others who have helped me over the last four years include Dr. Mehdi Jafarian, who taught me how to develop a numerical model, and Dr. Timothy Lau, who helped me to develop particle concentration measurement devices. I am grateful to both of them for these pearls of wisdom and for their valuable contributions to my work. I would also like to express my gratitude to the School of Mechanical Engineering workshop staff, who were very helpful with designing and building the experimental apparatus required for my work.

For financial support, I would like to acknowledge both the Commonwealth of Australia for the provision of an Australian Government Research Training Program Scholarship, and the Australian Solar Thermal Research Initiative (ASTRI), a project supported by the Australian Government, through the Australian Renewable Energy Agency (ARENA). This support has meant that I could lead a very comfortable student life, abundant with good food for nourishment, beverages in those times they're just essential, and a cosy home to ride my bike home to.

To my office mates of S324b, Orddom, Ken, Shen, Frank, Esho, Amy, Sam, Dave and Hou Zhi, thank you for the industrious and always enjoyable vibe in the office. It was always a pleasure to spend a day in the office with you. I can't wait to follow the magnificent things you achieve and the beautiful figures you produce.

To my good mates, here, there and everywhere, there is nothing I love more than to spend time with you and hear about your lives. I once heard that *no man is a failure who has friends*; it's in no small part thanks to you that this work has been a success. My housemates, Mike and Olly, especially deserve my gratitude, because it has always been a pleasure to go home to their company. Thanks also to the extended Prospect crew, Tim, Matt V, Chris Mc, Matt E, Chris B, Matt D, John S, John F James, Rhea, and Lucy, for always being on hand.

And of course, to Emma, thank you for the unconditional support you've given me as this work has come to an end. I am extremely excited for whatever the future brings and I hope you'll be a big part of that. You're wonderful.

I feel very privileged to have an incredibly supportive and loving brother and sister, on whom I will always be able to rely. Thank you, Nick and Lily. I love seeing you two flourish in all that you do.

To my parents, Gabi, the sharpest mind I know, who taught me the importance of being well-rounded, and Paul, the example of a truly good man, who taught me to be sure of myself, you are models I will never stop trying to emulate. Thank you for teaching me what it means to be loved and happy. My gratitude and unconditional love are the least you deserve.

Contents

Nomenclature

Acronyms

1-D	One-dimensional.
BET	Brunauer–Emmett–Teller.
BJH	Barrett–Joyner–Halenda.
CCD	Charge-coupled device.
CFD	Computational fluid dynamics.
CSP	Concentrating solar power.
CST	Concentrated solar thermal.
CSTR	Continuously-stirred tank reactor.
IR	Infrared.
ISO	International Organization for Standardization.
PFR	Plug flow reactor.
RTD	Residence time distribution.
SEM	Scanning electron microscopy.
SEVR	Solar expanding vortex receiver-reactor.
SGA	Smelter grade alumina.
SSA	Specific surface area.
SVR	Solar vortex receiver-reactor.
TGA	Thermogravimetric analysis.
XRD	X-ray diffraction.

Latin Characters

A	Area [m].
C	Solar concentration ratio [1 sun = 1 kW m^{-2}].
c_p	Constant pressure specific heat capacity [J kg^{-1} K^{-1}].
D	Diameter (a characteristic length scale) [m].
d_p	Particle diameter [µm].
d_{pore}	Mean pore diameter [nm].
$E(t)$	The residence time (or exit age) probability distribution function [s^{-1}].

$E(\theta)$	The dimensionless residence time probability distribution function.
E_b	Blackbody emissive power [W m^{-2}].
F	Radiation shape factor; force [N].
Fr	Froude number.
g	Standard acceleration due to gravity, $g = 9.81$ m s^{-2}.
$\Delta\dot{H}$	Rate of enthalpy change of a species [W].
$\Delta\bar{h}^{\circ}$	Standard specific enthalpy of reaction [kJ mol^{-1}].
h	Coefficient of heat transfer [W m^{-2} K^{-1}]; specific enthalpy [J kg^{-1}].
$i(t)$	Inlet concentration of tracer at time, t.
J	Radiosity [W m^{-2}].
k	Thermal conductivity [W m^{-1} K^{-1}].
L	Length [m]; total length of the receiver [m].
LoI	Loss on Ignition [wt.%].
m	Mass of a species/sample [kg].
m_{1p}	Mass of one particle [kg].
$\dot{m}$	Mass flow rate [kg s^{-1}].
N	Number of CSTRs in series used to model a PFR ($N \geq 10$ representative of PFR).
N_p	Number of particles.
$\dot{N}_p$	Number flow rate of particles [s^{-1}].
n	Number of moles of a species [mol]; number of axial discretisations.
$\dot{n}$	Molar flow rate of a species.
Nu	Nusselt number.
$o(t)$	Outlet concentration of tracer at time, t.
$\dot{Q}$	Rate of heat transfer [W].
$\dot{Q}_s$	Solar radiative power input [W].
$\dot{q}$	Heat flux [W m^{-2}].
$\dot{q}_s$	Solar radiative heat flux input [W m^{-2}].
R	Radius of the receiver at a given cross-section [m].
R^2	Coefficient of determination.
r	Radial coordinate [mm].
Re	Reynolds number.
Sk	Stokes number.
T	Temperature [K].
t	Time [s].
U	Velocity (a characteristic velocity scale) [m s^{-1}].
u	Component of total velocity, U [m s^{-1}].
$u(\theta - \delta)$	Heaviside unit step function, with dimensionless time delay δ.
V	Volume [m^3].
V_{pore}	Total specific pore volume [cm^3 g^{-1}].
$\dot{V}$	Volumetric flow rate [m^3 s^{-1}, slpm].
X	Extent of chemical conversion [mol.%].

z	Axial coordinate [mm].

Greek Characters

α	Receiver cone angle [º]; absorptivity.
β	Fraction of particles taking compartment modelling CSTR branch.
δ	Dimensionless time delay, dimensionless space-time of a PFR.
ε	Volume ratio of two CSTRs in series; emissivity.
$\varepsilon_{\max}$	Maximum absolute difference between two consecutive iterations.
η_{th}	Overall thermal efficiency [%].
θ	Dimensionless time, $\theta = t/\bar{\tau}_{\text{p}}$; XRD incident angle [º].
θ_{CSTR}	Dimensionless space-time of a CSTR.
κ	Linear radiation extinction coefficient [m^{-1}].
μ	Dynamic viscosity [$\text{kg m}^{-1}\,\text{s}^{-1}$].
ρ	Density [kg m^{-3}].
σ	Stefan-Boltzmann constant, $\sigma = 5.67 \times 10^{-8}\,\text{W m}^{-2}\,\text{K}^{-4}$.
${\sigma_{\text{p}}}^2$	Normalised variance, ${\sigma_{\text{p}}}^2 = {\sigma_{\text{p},t}}^2/\bar{\tau}_{\text{p}}^2$.
${\sigma_{\text{p},t}}^2$	Calculated variance of $E(t)$ [s^2].
τ	Residence time [s].
τ_{nom}	Nominal residence time, $\tau_{\text{nom}} = V_{\text{r}}/\dot{V}_{\text{gas}}$ [s].
$\bar{\tau}_{\text{p}}$	Mean particle residence time [s].
$\tau_{\text{p,90}}$	90th percentile particle residence time [s].
ϕ	Particle to air volume fraction.
φ	Angular coordinate [º].
$\chi_{\text{air-p}}$	Energy absorption ratio.
ψ	Receiver tilt angle (downward-facing: $\psi > 0$º, upward-facing: $\psi < 0$º) [º].

Subscripts/Superscripts

573	Evaluated over the temperature range 298 – 573 K.
1273	Evaluated over the temperature range 573 – 1273 K.
ads	Adsorbed moisture, Evaluated over the temperature range 298 – 423 K.
air	Air phase.
$Al(OH)_3$	Aluminium hydroxide (gibbsite) feed particles.
Al_2O_3	Aluminium oxide (alumina) produced.
ap	Aperture.
back	The back entry configuration.
base	Receiver base.
c	Receiver internal cavity.
calcination	Calcination reaction.
cent	Centrifugal inertial.
cone	Receiver conical section.
corner	Corner at the receiver cone-cylinder intersection.

correction	Correction for distance between true inlet/outlet and measurement location.
cyl	Receiver cylindrical section.
d-b	Down-beam face of an element (relative to the direction of solar radiation input).
end	End wall.
f	Fluid.
fr	Front wall.
front	The front entry configuration.
g	Gravitational.
gas	Gas input to the device.
H_2O	Evolved water vapour.
i	A given discretised element.
$i-1$	The element up-beam of a given element, i.
$i+1$	The element down-beam of a given element, i.
in	Inlet.
j	A given discretised element.
LP	Large particles.
max	Maximum value along the radial axis.
measured	From experimental measurements.
modelled	From the present numerical model.
n	At normal conditions (273 K, 1 atm).
n	Evaluated in the nth element.
new	The value calculated in the current iteration.
nom	From the present numerical model.
old	The value calculated in the previous iteration.
out	Outlet.
p	Particle phase.
products	Calcination reaction products.
r, receiver	receiver-reactor.
r	Radial component.
rad	Radiative.
reactant	Calcination reactant.
S	Surface area.
SP	Small particles.
steam	Additional steam input.
TGA	Reference TGA temperature.
T_r	Evaluated at reactor temperature, T_r.
u-b	Up-beam face of an element (relative to direction of solar radiation input).
w, wall	Receiver internal wall.
X	Evaluted over the temperature range for determining X, 423 – 1273 K.
z	Axial component.
φ	Tangential component.
∞	Surroundings.

1

Introduction

The present thesis is aligned with the need to develop solar thermal receiver technologies that can achieve operating temperatures up to and above 1000 °C with concentrated solar thermal (CST) energy (Ho 2017). This is a contemporary need because solar receivers in current commercially available systems, which generally use liquids or gases as the heat transfer medium, are limited to ∼600 °C due to radiative flux limitations arising from the use of indirect irradiation and the temperature limitations of the heat transfer medium (Ho 2016). Temperatures in the range 700 – 1000 °C are being sought to enable the use of new advanced power cycles for higher efficiency concentrating solar power (CSP), such as Brayton cycles with recuperation and combined bottoming cycles as well as supercritical-CO_2 cycles (Besarati & Goswami 2017; Stein & Buck 2017). Operating temperatures of a similar range and even higher are also required for the application of solar energy into high temperature thermochemical processes via process heat, such as alumina and lime calcination (Flamant et al. 1980; Steinfeld et al. 1992), the gasification of carbonaceous feedstock (Z'Graggen et al. 2006; Lichty et al. 2010), metal reduction (Kräupl & Steinfeld 2001; Lapp et al. 2012) and the production of solar hydrogen (Steinfeld 2005; Kodama & Gokon 2007; Perkins & Weimer 2009; Sattler et al. 2017). As one way to achieve these higher temperatures (Ho & Iverson 2014), the present thesis considers the use of particles as the heat transfer medium in the central receiver of a CST system. However, thermal losses increase with temperature, so that achieving higher receiver temperatures with particles requires better understanding of the heat and mass transport processes in solar thermal particle receivers.

Solid particles are a heat transfer medium which, due to their high surface area per unit mass and capacity for direct irradiation, offer the potential to achieve receiver exit temperatures up to and above 1000 °C (Tan & Chen 2010; Ho & Iverson 2014; Wu et al. 2014; Ho 2016; Ho 2017). Furthermore, direct irradiation of a cloud of particles offers the significant potential benefits of

reducing the exergetic losses associated with heat transfer through a wall and improving the rate of heat transfer to the heat transfer medium due to the high effective temperature of the sun (Ho & Iverson 2014; Ho 2017). On the other hand, direct irradiation requires the development of either windowless receivers that avoid the egress of solid particles, or windowed receivers that avoid the deposition of particles onto the window. Nevertheless, additional benefits of using particles as the directly irradiated heat transfer medium within a solar receiver include the possibility of high absorptivity of solar radiation wavelengths, as well as favourable heat capacity, corrosion and sintering resistance properties (Ho & Iverson 2014). Furthermore, the thermal storage of hot particles is a relatively simple and low-cost process (Ho & Iverson 2014; Ho 2017). Solar particle receivers of a number of configurations have been proposed and tested without yet the deployment of commercial systems. Therefore, to demonstrate that solar particle receivers are a viable technology for use in CSP systems or in industrial thermochemical processes, further research into the key mechanisms controlling their performance is required.

Solar thermal particle technology has the potential to play an important role in reducing the carbon intensity, not only of the electricity generation sector, but also of the industrial sector through the direct provision of high temperature process heat. However, this application of the technology remains relatively untapped (IEA 2017). Within the industrial sector, the refining of minerals accounts for 18.5% (of 2008 levels) of global greenhouse gas emissions. Some of these emissions are inherent to the mineral process, however a significant proportion is also derived from the combustion of fuels to heat and react mineral particles (McLellan et al. 2012; Olivier et al. 2015). The production of cement is one of these processes that accounts for ∼7% of man-made CO_2 emissions (IEA 2018a) and requires a significant thermal energy input, particularly to the calcination stage. The calcination of cement uses a predominantly limestone ($CaCO_3$) feedstock and drives off CO_2 to produce lime/clinker (CaO) at a reaction temperature of ∼900 °C with a state of the art energy intensity of 3.0 – 3.4 GJ/tonne-clinker (Eglinton et al. 2013; IEA 2018a). The potential suitability of solar thermal particle technologies to such an industrial calcination process has been demonstrated with small-scale particle receiver-reactor prototypes and solar simulator research facilities that enable the required solar concentration ratios and reaction temperatures to be reached (Flamant et al. 1980; Steinfeld et al. 1992; Meier et al. 2006; Nikulshina et al. 2009a). With a global interest in reducing all carbon emissions while decoupling industrial production from its associated emissions, there is a need to investigate such innovative low-carbon process routes (IEA 2017). Replacing combustion with concentrated solar energy as a source of direct process heat to reacting particles is one potential means to reduce society's reliance on fossil fuels.

A calcination process that is also highly energy-intensive but has not previously been demonstrated with the application of CST is that of alumina production. Calcination is the last step of the Bayer process for alumina production which heats the hydrated alumina from the precipitation stage

to drive off the water of hydration and form anhydrous alumina. This alumina is a product in its own right, but is also the precursor to primary aluminium, the production of which has an energy intensity of 218 GJ/tonne-primary aluminium and is among the most energy intensive of all mineral processes (Das & Green 2010). Globally, some 132 million tonnes per annum of alumina is produced by calcination at an energy intensity of ∼11.1 GJ/tonne-alumina and a temperature of about 1000 °C (IAI 2019). This temperature is in the mid-range of many other high temperature processes and is readily achievable with CST technologies, which provide a potential alternative energy source to fossil fuels. In addition, the alumina calcination process is not typically sensitive to some ingress of air, which raises the possibility that direct irradiation of particles may be achievable without the need for a window to completely seal a solar particle receiver-reactor. However, the technical feasibility of undertaking alumina calcination with CST is yet to be evaluated.

1.1 Background on concentrating solar thermal

Of all sources of renewable energy, solar energy is the most abundant. In one year, the maximum extractable energy from solar radiation incident on Earth's surface is 2.7×10^{24} J (Szargut 2003; Hermann 2006), which is three orders of magnitude greater than human society's total primary energy demand (IEA 2011). However, this solar resource is also of very low energy density and is variable. This is a particular disadvantage compared with fossil fuels, which are concentrated and can be used continuously. Presently some 81% of society's energy demand is met by fossil fuel sources, accounting for 3.26×10^{13} kg-CO_2 eq. of climate change inducing emissions (IEA 2018b) – an economically, environmentally and socially unsustainable activity (IEA 2015). The use of concentrating solar thermal (CST) technologies to harness some of the abundant, renewable, but dilute solar resource is an important component in the least-cost future energy production mix that is required to limit climate change (IEA 2015). The low energy density and variability of solar energy represent challenges to harnessing the resource cost-effectively, but the potential advantages of a clean CST technology with inherent energy storage capabilities also represent an opportunity. That is, new understanding of CST technologies is required to develop systems that efficiently harness the solar resource and operate cost-competitively at an industrial scale.

CST systems use mirrors to concentrate solar radiation and provide a high flux, renewable heat input to a power cycle to produce electricity or to drive thermochemical reactions (Steinfeld & Palumbo 2001). However, electricity generation is the only use for CST that is currently operated commercially. Together with the advantages of a high flux renewable heat source, CST has the inherent capacity for low-cost thermal energy storage as well as suitability to fossil-fuel back up (IEA 2015), which allow for increased reliability and dispatchability of supply (Jamel et al. 2013; Nathan et al. 2017b). In CSP, these advantages allow electricity generation to be decoupled from solar

energy collection and shifted to times of peak demand, such as after sunset (IEA 2015). This also indicates that CSP can operate synergistically with solar photovoltaic technologies to provide solar electricity over daily time periods longer than sunshine hours (IEA 2015; IEA 2017). From a system perspective, the flexibility of CST technologies to incorporate thermal storage, hybridisation and synchronous power generation provide a strong advantage over alternative solar technologies, such as photovoltaics, which require additional systems for energy storage and do not inherently provide all required ancillary services (IEA 2015). From a national interest perspective, CST technologies provide additional potential to heighten energy security through exploitation of a renewable resource whose availability is import-independent (IEA 2011). These potential benefits justify research effort to develop cost-effective CST technologies that operate alongside a suite alternative renewable energies.

In a CST system the receiver plays a fundamental role as the device, located at the optical focal point of a solar concentrator, that harvests concentrated solar radiation via complex high temperature heat transfer mechanisms. The function of the receiver is to convert concentrated solar radiation into thermal or chemical energy by heating a heat transfer medium, or providing the process heat to drive a chemical reaction (Tan & Chen 2010). Solar concentrators concentrate radiation onto either a line or a point, and therefore require either linear or point receivers. Examples of linear concentrators are Parabolic troughs and Fresnel reflectors, while the point concentrators are solar dishes and the heliostat field of a solar tower (Behar et al. 2013). Figure 1.1 presents a schematic diagram of a solar tower CST system, in which a field of sun-tracking heliostats concentrates solar radiation onto a solar receiver positioned on a central tower. It should also be noted that, as well as conventional tower-mounted receivers with aperture directed towards the ground (as shown in Figure 1.1), beam-down receivers with aperture directed upwards are also under development (Yogev et al. 1998; Kodama et al. 2014). Beam-down receivers require a secondary reflector to be mounted on the central tower, which in turn reflects radiation towards the receiver located at ground level. The advantages of central receivers relative to linear receivers include the capacity for high concentration of the solar radiation (greater than 1000 suns = 1 MW m^{-2}), allowing for higher temperatures and greater overall efficiencies (Behar et al. 2013; Ho 2017). Relative to dish systems, central tower systems have lower optical efficiency, but they also have the relative advantage of a potential for larger scale. This is because in dish systems the receiver needs to be fixed in position relative to the dish so that the receiver and dish move together, which imposes physical limits on the size of the dish receiver. The capacity of central receiver systems is potentially of the order 10^2 MW, which is significantly larger than is possible for dish systems and is potentially lower cost for a given output (Behar et al. 2013). The present thesis investigates the performance of directly irradiated solar particle receivers that are relevant to solar tower CST systems.

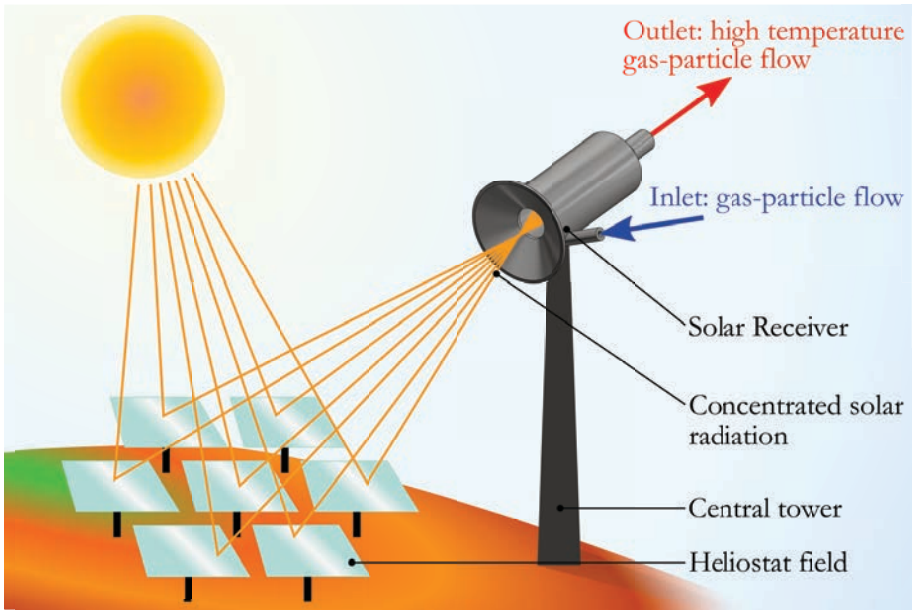

Figure 1.1: Schematic diagram of a solar tower CST system, in which a field of sun-tracking heliostats concentrates solar radiation onto a solar receiver located on a central tower.

1.2 Vortex-based solar particle receivers

One class of solar particle receiver technologies that has received significant attention is the vortex-based solar particle receiver-reactor, which typically consists of a cylindrical cavity receiver, through which particles are conveyed by a vortex flow of gas to be directly irradiated in the irradiation zone from a solar concentrator. Vortex-based solar particle receiver-reactors – often termed solar vortex receiver-reactors (SVRs) – have been used to experimentally demonstrate several solar thermochemical processes at laboratory-scale with a range of alternative receiver configurations (Imhof 1991; Steinfeld et al. 1992; Steinfeld et al. 1998; Kräupl & Steinfeld 2001; Hirsch & Steinfeld 2004b; Z'Graggen et al. 2006; Müller et al. 2017). SVRs feature highly efficient heat transfer to the particle phase due to direct irradiation within a cavity, as demonstrated by the high extents of chemical conversion reported in the thermochemical assessments above, for particle residence times on the order of seconds and reported exit temperatures of over 1000 °C. Figure 1.2 presents a simplified schematic diagram of one particular configuration of SVR showing concentrated solar radiation entering the cylindrical cavity through a circular aperture. The two-phase vortex flow of particles transported by a gas is established with two tangentially oriented inlets located at the aperture-end of the cavity. The gas-particle vortex flow then proceeds to the rear of the cavity, so that the particles and gases emerge axially. This SVR configuration (Figure 1.2) has been used to assess the solar gasification of carbonaceous particle feedstock (Z'Graggen et al. 2006; Müller et al. 2017). However, SVRs can be configured in many alternative ways, for a range of alternative applications. Together with the configuration shown in Figure 1.2, the present thesis investigates SVR configurations that introduce the two-phase vortex flow from the rear (so that the flow exits at the front near to the aperture) as well as alternative receiver geometries and outlet port orientations. This investigation builds upon previous research into vortex-based solar particle receiver-reactors by providing new understanding of the mechanisms that control their performance. This new understanding is required to enable the optimisation of SVRs on a case-by-case basis for the different requirements of a range of alternative potential applications within the areas of CSP and solar thermochemistry.

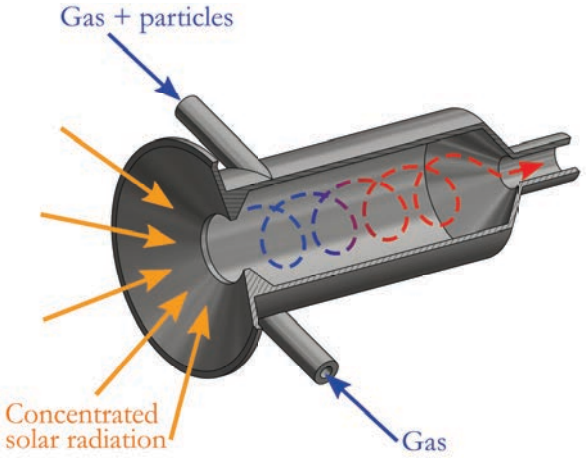

Figure 1.2: Simplified schematic diagram of a vortex-based particle receiver (SVR). This illustration is an adaptation of a particular configuration that was used for the solar gasification of carbonaceous particle feedstock (Z'Graggen et al. 2006). The diagram shows concentrated solar radiation entering the cylindrical cavity through a circular aperture, together with inlets for the two-phase gas-particle flow at the aperture-end of the cavity oriented tangentially and a single axially-oriented outlet at the rear.

1.3 Thesis

1.3.1 Thesis objective

The objective of the present thesis is to characterise the performance of vortex-based solar particle receiver-reactors[1] (SVRs) with investigations into three aspects: the thermal performance; the particle residence time performance; and the performance of the solar thermochemical process of calcining alumina particles. Specifically, the present thesis aims to provide new understanding of the influence of key receiver input and design parameters on these performance aspects, so that the device may be scaled up and optimised on a case-by-case basis for various applications.

1.3.2 Thesis outline

Chapter 2 of the present thesis provides a critical review of the literature concerning SVRs. Various research gaps are identified in this review, from which are derived the specific scientific aims of the present thesis. These aims are addressed by examining three different aspects of the performance of vortex-based solar particle receivers. The first of these aspects is addressed in Chapter 3, which develops a one-dimensional heat transfer model to assess the sensitivity of the receiver thermal per-

[1]For brevity, throughout this thesis the term 'receiver-reactor' is referred to as a 'receiver' except where the purpose of the device is clearly for the thermochemical reaction of particles.

formance to various key operating parameters. Insights into the dominant mechanisms controlling the thermal performance of SVRs are provided. Next, Chapter 4 provides a fundamental assessment of particle residence time distributions (RTDs) within SVRs. First-of-a-kind direct measurements of particle RTDs in such a device are presented. These are used to assess the influence of key dimensionless parameters on the receiver particle residence time performance, for a range of operational parameters including a range of receiver tilt angles. The final aspect of the performance addressed in the thesis is the technical feasibility of applying the receiver to an industrial thermochemical process. Chapter 5 presents a demonstration that alumina can be calcined with concentrated solar radiation in a small-scale SVR. The parameters controlling this solar process are assessed, together with the potentially improved quality of the alumina particles produced. Chapter 6 then provides a summary of the key outcomes of the work and discusses the potential future development of SVRs.

1.3.3 Thesis format

The present thesis is presented in a *thesis by publication format*, following guidelines of The University of Adelaide. As such, Chapters 3, 4 and 5 consist of work from four journal articles which have either been peer-reviewed and published, or have been submitted for peer review. The contents of the journal articles included in these chapters are identical to the original articles, published or submitted, with the following exceptions:

- only content from the methodology, results, discussion and conclusion of each article is presented to avoid repetition of information;
- the typesetting and referencing have been altered, so that the format throughout the thesis is consistent;
- the positioning and numbering of the figures, tables and equations differ from the articles to be consistent throughout the thesis and to improve legibility; and
- some terminology within the text has been altered to be consistent throughout the thesis, without altering the sense of the text.

The journal articles in their published version or their submitted manuscript version are included as appendices to the thesis.

2

Literature Review

Numerous configurations of solar thermal particle receiver-reactors have been proposed and developed to varying degrees of maturity for the purpose of the solar heating of both inert particles, via sensible heat, and of reacting particles, via chemical (and sensible) heat. Configurations that allow for the direct irradiation of particles avoid the solar radiation flux limitations associated with current commercial tubular receivers that heat a medium indirectly through walls (Tan & Chen 2010; Alonso & Romero 2015; Ho 2017; Kodama et al. 2017a). Direct irradiation of particles allows for higher rates of heat transfer to the particle phase and lower exergetic losses. However, directly irradiating particles in a solar receiver requires either: windowed receivers that avoid particle deposition onto the window and can withstand high temperature/pressure environments at large scale; or windowless receivers that avoid the loss of particles (or harmful high temperature gases) through an open aperture (Ho 2017; Kodama et al. 2017a). Examples of configurations of solar particle receivers that employ direct irradiation include: freely-falling and obstructed-falling curtains of particles (Evans et al. 1987; Hruby et al. 1988; Chen et al. 2007; Siegel et al. 2010; Khayyat et al. 2015; Ho et al. 2016; Ho et al. 2019); centrifuged films of particles within rotating-kiln type cavity receivers (Haueter et al. 1999; Schunk et al. 2008; Wu et al. 2014; Wu et al. 2015; Ebert et al. 2018); fluidised beds of particles (Kodama et al. 2008; Gokon et al. 2009; Kodama et al. 2010; Bai et al. 2014; Tregambi et al. 2016; Wang et al. 2016); and entrained (vortex) flows of particles transported in suspension (Steinfeld et al. 1992; Steinfeld et al. 1998; Hirsch & Steinfeld 2004b; Z'Graggen et al. 2006). The performance of each of these configurations of solar particle receiver is controlled by complex, non-linear, radiative and turbulent heat and mass transport processes that are too complex to predict exactly. Hence new understanding of these processes is needed to advance the development of solar particle receivers toward deployment at larger scale.

The vortex-based class of solar particle receiver technologies – in which a vortex gas flow transports particles through the direct irradiation zone from a solar concentrator within a cylindrical cavity – is an aerodynamic device, which offers the potential of a particle heating atmosphere that can be controlled. Such an aerodynamic particulate device shares similarities with industrial gas suspension flash calciners (Jenkins & Bertrand 2001; Williams & Schmidt 2012) and blast furnaces (Eglinton et al. 2013), and so benefits from the inherent low-cost reliability of aerodynamic devices and robust construction of the refractory-lined steel vessel. Previous experimental demonstrations of vortex-based solar particle receivers (solar vortex receivers, SVRs) reported that energy conversion efficiencies are significantly greater (often by a factor greater than 2) when heat is recovered from the transporting gas phase or the device is employed in a system that can make use of the transport gas (Steinfeld et al. 1992; Hirsch & Steinfeld 2004b; Z'Graggen et al. 2006). This is attributed to the high rates of convective heat transfer within the cylindrical cavity due to the turbulent swirling process (Szekely & Carr 1966). In contrast, both falling curtain and centrifugal particle receiver configurations seek to heat only the particles in an air atmosphere, which is desirable where the target output is sensible heating of particles alone. However, this approach does not offer the potential to control the gaseous atmosphere. SVRs, together with fluidised bed configurations, necessarily heat both the particle and gas phases, offering potential advantages for processes with reacting particles, such as calcination processes, where the gas atmosphere influences the reaction. Fluidised beds, however, are necessarily vertical. Hence direct irradiation of the particle bed requires either transparent walls, which are susceptible to particle deposition, or a beam-down solar concentrating system to directly irradiate the bed from the top. However, beam-down systems are yet to be employed commercially and have a number of limitations. SVRs have the potential to be configured for operation with tower-mounted orientations (as well as beam-down orientations) and are unique in offering potential for direct irradiation into a particle system that can benefit from a controlled atmosphere, but can tolerate some small ingress. They also have potential for heating the gas phase. However, there is a need to further investigate the parameters that control the heat and mass transport characteristics of SVRs to provide new understanding of operation in particle or gas heating regimes, together with thermochemical process performance in controlled gaseous atmospheres.

2.1 Vortex-based solar particle receivers (SVRs)

Previous studies of SVRs have primarily focussed on the technical demonstration of various gas-particle solar thermochemical reactions, including: the calcination of limestone (Imhof 1991; Steinfeld et al. 1992); the combined reduction of zinc and production of syngas (Steinfeld et al. 1998; Kräupl & Steinfeld 2001); the decomposition of natural gas (Hirsch & Steinfeld 2004b; Maag et al.

2009b); and the gasification of carbonaceous feedstock (Z'Graggen et al. 2006; Z'Graggen et al. 2007; Müller et al. 2017). These studies reported that an increase in both reactor temperature and particle residence time results in an increase in the extent of chemical conversion of the respective processes. However, despite the controlling influence of particle residence time on the performance of SVRs, no direct measurements of the particle residence time have been reported. Rather, the particle residence times are calculated as mean or nominal values from volumetric flow rates and reactor volumes ($\tau_{\mathrm{nom}} = V_{\mathrm{r}}/\dot{V}_{\mathrm{gas}}$), so that the actual particle residence time is unknown. Furthermore, in these studies a SVR of a single configuration was oriented either horizontally or vertically for testing in laboratory conditions with a solar simulator or laboratory-scale solar testing facilities, so that no general information is available of the influence of a range of alternative receiver geometries and orientations on the performance of the device. Good potential for the technology has been shown with these studies, however, there is a need for further systematic study of the influence of key controlling parameters on the performance of the device – including angle of receiver orientation and the parameters that influence the particle residence time.

An alternative configuration of SVR – termed the Solar Expanding Vortex Receiver-Reactor (SEVR) – has recently been developed, with a view to capitalising on the high energy conversion efficiencies of the previous SVR configurations whilst also addressing some of their limitations. It has been found that SVRs typically have a particle residence time distribution that is approximately independent of the particle size (Chinnici et al. 2015), which is an inefficiency for processing polydisperse particles, as is common in current industrial processes. A tendency of particles to egress through the aperture and deposit onto the sealing window or be lost to the environment has also been identified for SVRs, which requires a high auxiliary gas flow to mitigate. Figure 2.1 presents a schematic diagram of the SEVR configuration proposed by Chinnici et al. (2015), which injects the two-phase gas-particle flow at the opposite end of the receiver to the aperture, and introduces a conical expansion so that the flow expands as it proceeds to the outlet located near to the aperture plane. These modifications serve to decrease the swirl intensity of the vortex at the aperture plane to such an extent that the particle egress through the aperture is reduced by an order of magnitude (Chinnici et al. 2015; Chinnici et al. 2016). Furthermore, altering the outlet so that it is oriented radially – which differs from the orientation of the vortex flow near the outlet (tangential) – is important to inhibit the exit of large particle from the chamber due to their greater inertia, relative to smaller particles. This enables the SEVR to aerodynamically classify the particles; larger particles are retained within the receiver for much longer than small particles, so that efficient heating/processing of the particles is achieved (Chinnici et al. 2015). These mechanisms have been partially validated by an experimental investigation into the flow field (Chinnici et al. 2016; Chinnici et al. 2017). However, no direct assessments of particle residence times are presently available for the SEVR (or any configuration of SVR) and there is a need to assess the influence of these geometric and

configurational modifications (for example, the direction of the two-phase gas-particle flow) on the performance of the device. Therefore, new data are needed to assess the validity of previous hypotheses and to develop refinements of various SVR configurations.

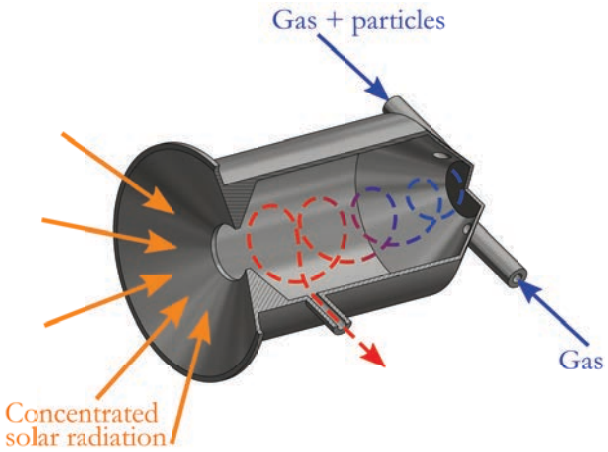

Figure 2.1: Schematic diagram of the Solar Expanding Vortex Receiver-Reactor (SEVR), showing: tangential inlets to the two-phase gas-particle flow located at the opposite end of the receiver to the aperture, conical expansion section and radially-oriented receiver outlet.

2.1.1 Residence time control in solar particle receivers

Both mechanical and aerodynamic means to control particle residence time within solar receivers are under development. Residence time control is important for achieving the required extents of particle heating or reaction within a solar receiver and, therefore, for efficient heating/processing of particles. For the case of falling particle receivers, characterisation of the curtain behaviour has found that the larger the particle size the shorter the residence time of the particle within the receiver due to faster falling velocities (Evans et al. 1987; Hruby et al. 1988; Chen et al. 2007; Siegel et al. 2007; Ho et al. 2017). Furthermore, greater mass flow rates of falling particles entrain greater amounts of air in the downward direction, which serves to reduce the drag on the particles and reduce their residence time further (Evans et al. 1987; Hruby et al. 1988; Chen et al. 2007). To address this adverse relationship between particle size/flow rate and residence time, various mechanical means of increasing residence time have been proposed. Mechanical obstructions to falling, in the form of chevron-shaped mesh structures, have shown strong potential to reduce the velocity of particles falling through the receiver, allowing longer residence time for heating and more efficient operation, together with the additional benefit of stabilising the falling particle curtain (Ho et al. 2014; Khayyat et al. 2015; Lee et al. 2015; Ho et al. 2019). Alternatively it has demonstrated with heat transfer modelling that increasing falling particle residence time by recycling the particles over

multiple passes has the potential to enhance the thermal efficiency of the falling particle receiver, particularly in responding to variations in the solar thermal input throughout the day (Röger et al. 2011). However, a technical challenge arises with the handling of particles at high temperature. For a centrifugal (rotating-kiln) type particle receiver, particle residence time is controlled mechanically by adjusting the tilt angle and rotational velocity of the cavity, which presents challenges associated with the requirement of large mechanical moving parts for the rotation of the cavity (Wu et al. 2014; Wu et al. 2015; Amsbeck et al. 2018; Ebert et al. 2018). Overcoming reliability challenges associated with moving parts and the potential over-heating/deterioration of obstructions will potentially allow for significant improvement of residence time control in solar particle receivers and result in improvements in the efficiency of their operation. Therefore, there is a need to develop new understanding of mechanisms that allow for the reliable recirculation of particles through a solar particle receiver to control the particle residence time.

Aerodynamic means to control particle residence time within solar particle receivers offer an inherent reliability without the need for additional moving parts. Devices that use such aerodynamic mechanisms generate a pressure field within the receiver that allows for controlled rates of particle circulation. This has been demonstrated for circulating fluidised bed solar particle receivers, in which the rate of circulation through an irradiation zone is controlled with pressure differences within the bed (Flamant et al. 2013; Flamant et al. 2014; Benoit et al. 2015). However, these receivers are necessarily vertical and require indirect heat transfer to the particle bed through the walls of the receiver. In entrained flow solar particle receivers, mechanisms for controlling the internal recirculation and, therefore, residence time of the gas-particle flow are well-established in the field of combustion. For example, swirling jets are often applied to flames as an effective means of controlling the mixing of reactants and of recirculating flow (Beér & Chigier 1972). For a swirling flow proceeding through a cylindrical cavity, at sufficiently high degrees of swirl (characteristic swirl number, $S > 0.6$) a central reversed flow zone is established (Chigier & Beér 1964; Beér & Chigier 1972). Chinnici et al. (2015) asserted that, for the SEVR configuration, in which the swirl number is sufficiently high, the central reversed flow zone could serve to augment particle recirculation and increase particle residence time within the receiver (Chinnici et al. 2015). Furthermore, it was proposed that aerodynamically inhibiting larger particles (with characteristic Stokes number, $Sk \gg 1$) from leaving the radially-oriented outlet allowed for the preferential retention of large particles relative to small particles, as is desired for efficient processing of polydisperse particles. Since many current industrial processes use polydisperse particles, it is desirable that the residence time of particles within the receiver is dependent on particle size. That is, larger particles that require longer for heating to a desired temperature, should have longer residence times within the receiver. Aerodynamic mechanisms for controlling residence time potentially offer robust and reliable means of achieving this within an entrained flow solar particle receiver. However, new data and systematic

assessment of the controlling parameters are required to confirm any potential benefits to particle residence time control.

2.1.2 Thermal performance modelling of SVRs

Several models of the heat transfer within entrained flow solar particle receiver-reactors have been developed, spanning simple one-dimensional models to more complex three-dimensional computational fluid dynamics (CFD) models. These are complementary because CFD models are generally too computationally expensive to be used to assess a large number of receiver configurations and operating cases. In contrast, a one-dimensional model of the particle receiver operation can provide powerful insights into the dominant mechanisms influencing the thermal performance, before narrowing down to a limited number of configurations that justify the use of more detailed and computationally-expensive CFD models. Previous examples of first order models include the assessment by van Eyk et al. (2016) of an entrained flow solar reactor for the gasification of coal. They adapted a long furnace model (Kasule et al. 2012) to incorporate high-flux solar radiation in a reactor with a one-dimensional axial flow of gas and coal particles. Such lower dimension models (Kasule et al. 2012; van Eyk et al. 2016) have proven useful for sensitivity studies of a large number of configurations but are not well suited to assess the influence of geometry on heat transfer in a relatively short reactor. In contrast, the zonal method has been used to assess relatively short devices in which radiative heat transfer is important. The method has been used to predict gas and refractory wall temperature profiles in a furnace (Hottel & Cohen 1958) a rotating-kiln (Jenkins & Moles 1981) and, in a modified form, to investigate radiation exchange associated with the solid particle phase in the furnace of a coal boiler (Cañadas et al. 1990). In each of these cases, radiation is treated as non-directional, as is typical of combustion. Solar concentrators, however, provide highly directional concentrated solar radiation to the receiver-reactor. Therefore, to model the heat transfer within a solar receiver for a systematic assessment of a wide range of operating conditions, the zonal method of analysis needs to be modified to incorporate high-flux directional solar radiation as the heat input to the enclosure, so that its influence on the two-phase gas-particle flow within the receiver and the receiver's enclosure walls can be assessed.

The directionality of concentrated solar radiation can alternatively be modelled with the use of advanced Monte Carlo and finite volume modelling techniques, as has been developed for the steam gasification reaction of carbonaceous particles in a SVR (Z'Graggen & Steinfeld 2008a; Z'Graggen & Steinfeld 2008b; Z'Graggen & Steinfeld 2009). These models have been validated at 5 kW laboratory-scale and have been used to conduct extensive sensitivity analyses of molar extent of reaction and thermal efficiency to key input parameters, such as solar thermal input, feedstock feed rates and particle size. Despite significant modelling efforts characterising the solar steam-

gasification thermochemical reaction in a SVR, there is a need for less computationally-intensive models of SVRs for application to the sensible heating of particles with a range of sizes, together with a range of receiver geometries and flow configurations. Therefore, there is a need to develop simplified models of the operation of SVRs for the sensible heating of inert particles.

The SVR can be configured in a wide range of alternative ways for the heating and thermochemical reaction of particles with CST. Also, the optimal configuration of a solar thermal particle receiver cannot be determined in isolation from other components of the CST system, but must be calculated together with that of the pneumatic conveying system, thermal storage system and hybridisation system, for example (Nathan et al. 2017a; Nathan et al. 2017b). In addition, little is known of the thermal performance of SVRs during transient operation over long periods. Hence, determining the transient performance of the SVR within a system of complex components requires a model that is: sufficiently simple to be solved for half-hour time-steps for multiple years (Saw et al. 2017) without excessive computational expense; and sufficiently accurate to account for the dominant physical processes within them. However, no first order model of a SVR is presently available.

2.2 Key dimensionless parameters

Dimensionless parameters are used to provide reliable understanding of the heat and mass transport processes of an industrial-scale SVR device from experimental data gathered at a smaller scale. This is because experimental investigation and model development/validation are undertaken predominantly at smaller scale than the practical large scale system, so that experimental data needs to be obtained with dimensionless parameters at a comparable scale to those of the larger scale system. Without this, the heat and mass transport processes occurring at significantly different scales (e.g. laboratory and industrial scales) can exhibit significantly different behaviour (Nathan et al. 2012). Hence, experiments should be designed so that the dimensionless parameters with the greatest influence on the performance of the device are analogous to real conditions.

The performance of each physical system is usually only characterised by a few key dimensionless parameters. Furthermore, each dimensionless parameter scales in different ways and is typically asymptotic. For example, for operation entirely in the fully turbulent regime, changes in Reynolds number will not have a large influence on the heat and mass transport processes. Therefore, to gain new understanding of the device and its potential operation at larger scale, it is necessary to identify the most important dimensionless parameters in a given situation and determine their controlling influence. This section presents the key dimensionless parameters that have previously been identified as important to understanding the operation of SVRs.

The Reynolds number is defined as the ratio of inertial to viscous forces within a fluid and characterises whether the fluid flow is laminar or turbulent. The Reynolds number is evaluated as:

$$Re = \frac{\rho_\mathrm{f} U_\mathrm{f} D_\mathrm{f}}{\mu_\mathrm{f}}, \tag{2.1}$$

where U_f and D_f are characteristic velocity and length scales of the fluid, respectively, ρ_f is the fluid density and μ_f is the fluid dynamic viscosity. This can be evaluated for given flow regions within a SVR. Industrial-scale particulate processing devices, such as flash calciners, operate with fully turbulent flow conditions, e.g. with inlet Reynolds number, $Re_\mathrm{in} = \rho_\mathrm{f} U_\mathrm{in} D_\mathrm{in}/\mu_\mathrm{f} > 8000$ (Jenkins & Bertrand 2001; Mikulcic et al. 2012). This implies that experimental investigation of SVRs should be conducted in fully turbulent regimes, to ensure relevance of experimental findings to scaled up operation.

The Stokes number is defined as the ratio of the characteristic time-scale of a particle to the characteristic time-scale of a fluid eddy. In the case of a SVR, the Stokes number characterises how closely a particle will follow the gas streamlines through the receiver. The Stokes number is evaluated as:

$$Sk = \frac{\rho_\mathrm{p} d_\mathrm{p}^2 U_\mathrm{f}}{18 \mu_\mathrm{f} D_\mathrm{f}}, \tag{2.2}$$

where U_f and D_f are characteristic velocity and length scales of the fluid, respectively, ρ_p is the particle density, d_p is the particle diameter and μ_f is the fluid dynamic viscosity. For $Sk \ll 1$ the particle motion closely follows the transport fluid streamlines within a receiver, while for $Sk \gg 1$ the particle motion is inertia dominated and weakly influenced by the fluid motion. Chinnici et al. (2015) proposed that, for the SEVR, a radially-oriented outlet results in large particles having large $Sk > 1$, as evaluated at the outlet. This implies that large particles with greater inertia will be less likely to follow the flow gradient at the outlet, but will be preferentially retained within the vortex flow of the receiver and have relatively longer residence time than smaller particles. This is the primary mechanism, by which it has been proposed that the SEVR is able to increase the residence time of large particles relative to small particles (Chinnici et al. 2015).

The Froude number, for a fluid or particle within a vortex flow, is defined as the ratio of the centrifugal inertial force acting on the fluid/particle due to their circular (vortex) motion, to that of the external gravitational field. The Froude number is evaluated as:

$$Fr = \frac{U_\varphi^2}{gR}, \tag{2.3}$$

where U_φ is the characteristic tangential velocity of the fluid/particle, R is the characteristic radius of circular motion and g is the standard acceleration due to gravity. This definition of Fr is analogous

to the definition of the separation factor of a particle cyclone separator. The primary purpose of cyclone separators is to centrifuge particles to the wall of the cyclone, so that the design *Fr* for cyclones is typically greater than 5, for large low velocity cyclones, and often greater than 1000, for small high pressure cyclones (Cortés & Gil 2007; Hoffmann & Stein 2007). In contrast, SVRs do not seek to centrifuge particles to the walls of the receiver, so that the influence of the Froude number on particle trajectories within SVRs needs to be assessed.

The swirl number of a flow is defined as the axial flux of angular momentum to the axial flux of linear momentum (Beér & Chigier 1972; Gupta et al. 1984) and characterises the vortex intensity of a flow. The swirl number at a given cross-sectional plane within a cylindrical chamber is evaluated as:

$$S = \frac{\int_0^R u_z u_\varphi r^2 dr}{R \int_0^R u_z^2 r dr}, \tag{2.4}$$

where, u_z and u_φ are the axial and tangential components of fluid velocity at a given radius within the cross-sectional plane, r, and R is the radius of the cylindrical chamber. For a swirl burner, the swirl number characterises whether or not the swirl is sufficiently intense to establish a recirculation flow zone (Beér & Chigier 1972). Typically, values of $S > 0.6$ are characterised as strongly swirling flows that generate recirculation (Beér & Chigier 1972). Similarly, in a SVR the swirl number characterises whether or not a central reversed flow recirculation zone will be established. When evaluated at the aperture plane of a SVR, Chinnici et al. (2015) found that *S* is the primary indicator of the propensity for particles to exit the receiver through the aperture; the bigger the value of *S* the greater the mass flux of particles through the aperture.

The Biot number, as evaluated for a directly irradiated particle, characterises the relative significance of internal heat transfer resistance within the particle, to the external heat transfer resistance at the particle surface. For the case of an opaque particle with temperature, T_p, suspended in a gas flow with temperature, $T_\mathrm{g} < T_\mathrm{p}$, surrounded by cold walls and irradiated by an external flux, $\dot{q}_\mathrm{rad}$, the Biot number can be evaluated, following Maag et al. (2009a), as:

$$Bi = \frac{d_\mathrm{p} \left\{ \varepsilon_\mathrm{p} \left[\frac{\dot{q}_\mathrm{rad}}{T_\mathrm{p} - T_\mathrm{g}} - \sigma (T_\mathrm{p} + T_\mathrm{g})(T_\mathrm{p}^2 + T_\mathrm{g}^2) \right] - h_\mathrm{conv} \right\}}{k_\mathrm{p}}, \tag{2.5}$$

where d_p is the particle diameter, ε_p is the particle emissivity, σ is the Stefan-Boltzmann constant, h_conv is the external convective heat transfer coefficient and k_p is the thermal conductivity of the particle. In this formulation of *Bi* the external irradiation term is incorporated with positive sign, while the external radiative and convective heat transfer terms have negative sign. This is because as the external irradiation increases, the internal particle temperature gradient will be greater and so *Bi* increases. Conversely, as the rates of radiative and convective heat transfer from the particle

to the external fluid increase, the internal particle temperature gradient will decrease, and so Bi decreases. For a particle directly irradiated within a SVR with $Bi \ll 1$, the particle can be assumed to have negligible internal temperature gradient. That is, the particle is isothermal (Maag et al. 2009a).

The apparent absorptivity of a solar cavity receiver is defined as the fraction of radiation incident on the aperture that is absorbed by the internal cavity walls (Holman 2010). The apparent absorptivity is evaluated as:

$$\alpha_{\text{cavity}} = \frac{\varepsilon_{\text{w}} A_{\text{w}}}{A_{\text{ap}} + \varepsilon_{\text{w}}(A_{\text{w}} - A_{\text{ap}})}, \tag{2.6}$$

where A_{ap} is the aperture area, A_{w} is the internal cavity wall surface area and ε_{w} is the emissivity of the cavity walls. This formulation of α_{cavity} assumes that the internal walls of the cavity are diffusely radiating grey surfaces with uniform temperature and emissive properties. It can be seen that as $A_{\text{ap}}/A_{\text{w}} \to 0$ and $\varepsilon_{\text{w}} \to 1$, $\alpha_{\text{cavity}} \to 1$, so that the aperture to internal wall area ratio should be minimised and wall emissivity should be maximised for a solar cavity receiver to approach a black body absorber. For a SVR, the calculation of α_{cavity} does not account for internal heat transfer to the two-phase gas-particle flow and is subject to limitations of the above-mentioned assumptions for the internal wall properties. However, α_{cavity} provides a useful indicator of the radiation absorption performance of the SVR cavity geometry.

2.3 Particle residence time distributions (RTDs)

The residence time distribution (RTD) of particles is widely used to characterise the performance of thermochemical particle reactors. The particle RTD describes the probability distribution of residence times a particles spends within a vessel for a given set of operating conditions, which is difficult to predict a priori without experimental data due to the complexity of two-phase gas-particle flows. This is particularly the case in strongly recirculating flows such as those in swirling turbulent systems, owing to their non-linear behaviour (Lede et al. 1987; Allal et al. 1998; Li et al. 2008). Knowledge of the particle RTD within a vessel is needed because most particulate vessels do not conform well to the classical idealisation of either a well-stirred reactor, with uniform properties through the vessel, or a plug-flow reactor, in which all fluid and particles have the same residence time (Danckwerts 1953; Nauman 2008). Furthermore, the behaviour of particles is likely to be different from that of the transporting gas (Lede et al. 1987), particularly for cases where the Stokes number of the gas-particle flow is greater than unity (Chinnici et al. 2015). The SVR is one swirling particulate device, of which the residence time behaviour is imperfectly understood. Therefore, to support the development of SVRs, new experimental data together with new understanding of the particle RTD within them are required.

2.3.1 Particle residence time in SVRs

No previous direct measurements of particle residence time within SVRs have been reported. In the absence of measured data, previous assessments have relied on the nominal particle residence time, based on the ratio of receiver internal volume to gas volumetric flow rate ($\tau_{\mathrm{nom}} = V_{\mathrm{r}}/\dot{V}_{\mathrm{gas}}$). This value can be corrected for the dependence of gas density on temperature, and for the influence of chemical reactions on temperature and species. However, both the gas and particle phase residence times in a vortex flow configuration can differ significantly from this nominal residence time. Shilapuram et al. (2011) found that, for a solar cyclone reactor, the mean residence times of both particle and gas phases is significantly greater than the nominal value. Moreover, the particles exhibit a wide distribution of residence times that depend on the operating conditions. In characterising this distribution, the normalised variance, ${\sigma_{\mathrm{p}}}^2 = {\sigma_{\mathrm{p},t}}^2/\bar{\tau}_{\mathrm{p}}$, of the distribution has been recommended by Buffham & Mason (1993) to be the single best measure of the extent of spreading of the RTD and has been adopted elsewhere (Gao et al. 2011). Various thresholds have also been adopted to characterise the particle RTD, such as the time required for a given fraction of particles (e.g. 90% of the inlet stream) to exit the vessel. Therefore, new understanding of the influence of input and geometric operating parameters on the particle residence time within SVRs is required, together with characterisation not only of the mean residence time value, $\bar{\tau}_{\mathrm{p}}$, but also the full function of the RTD.

The alternative vortex-based solar particle receiver-reactor configuration – the SEVR – has been proposed to generate a RTD that increases with the particle size for particles larger than a critical value, characterised by the Stokes number (Chinnici et al. 2015). The SEVR has a conical inlet section at the opposite end of the cylindrical cavity to the aperture and a radial outlet at the aperture end of the cavity (Chinnici et al. 2015), so that the different orientation of the outlet to that of the vortex flow (tangential) inhibits the exit of larger particles from the chamber due to their greater inertia. These proposed mechanisms have been partially validated by an experimental investigation into the flow field (Chinnici et al. 2016), but no direct assessments of particle RTD are available for the SEVR configuration (or indeed any configuration of SVR). Hence, investigation into the influence of the controlling parameters of particle size, gas flow rate and inlet velocity on the particle RTD within the SEVR is required.

2.3.2 Influence of receiver tilt angle

Understanding the influence of the tilt angle on the performance of solar cavity receivers is a necessary component in the development of optimal concentrating solar thermal (CST) systems. This is because the receiver tilt angle relative to gravity has a bearing, not only on the heat and mass

transport within the receiver itself, but also on the layout of the heliostat field and the height of the tower on which the receiver is mounted. That is, the angle at which a solar cavity receiver is mounted on the tower of a CST system has a direct influence on the thermal performance of the receiver, the optical performance of the concentrator and the techno-economics of the system (Behar et al. 2013; Ho & Iverson 2014; Kodama et al. 2017b). Solar cavity receivers generally require polar heliostat fields, so that the receiver is either north or south facing, depending on the hemisphere (Li et al. 2016). As a result, the tower is required to be taller, and therefore more expensive, than for surround fields for a given solar power input (Kodama et al. 2017b). Significant research effort has been directed towards the optimisation of the optical design of solar cavity receivers with polar heliostat fields (Schmitz et al. 2006; Behar et al. 2013). However, to fully optimise the CST system, information is also required as to the influence of receiver tilt angle on the heat and mass transport within the receiver and, therefore, on the thermal performance of the receiver. Furthermore, the design of the field, tower and receiver tilt angle will be dependent on geographic location of the CST system, which further implies that information is required as to how a receiver performs with various tilt angles. As an alternative to the tower-mounted systems, beam-down receivers are also under development (Yogev et al. 1998; Kodama et al. 2014), for which the receiver will be oriented upwards, together with many variations between the two extremes of beam-up and beam-down. There is therefore a need to characterise the heat and mass transport performance of solar cavity receivers with a wide range of receiver tilt angles.

While many investigations of the influence of receiver tilt angle on the thermal performance have been performed for single-phase cavity receivers, particularly with respect to their convective losses (Clausing 1983; Leibfried & Ortjohann 1995; Wu et al. 2010), this is not true for two phase devices that employ a gas-particle suspensions flow within the cavity. Convection heat loss from the cavity of a single phase device is particularly dependent on the Richardson number (Lee et al. 2018), with the natural convective losses being associated with the relative significance of stagnant and convective zones of gas flow, which is strongly correlated with internal cavity geometry and receiver tilt angle. For a simple cubical cavity it was found that natural convective heat loss (i.e. without any significant wind) is greatest for receiver tilt angles approximately 30º to 60º above the horizontal, without considering the presence of wind (Leibfried & Ortjohann 1995; Lee et al. 2018). Wu et al. (2010) presents a review of research investigating convective heat loss from cavity receivers. However, the influence of the receiver tilt angle on the performance of two-phase solar particle receivers, in which the particle mass transport has potential to be strongly influenced by the direction of gravity, has not previously been assessed. One measure of this particle mass transport performance of a solar particle receiver is the particle RTD within the receiver (Danckwerts 1953; Levenspiel 1999; Fogler 2006). However, no data is presently available as to the influence of the tilt angle of the cavity of a solar particle receiver on its particle RTD.

For a SVR, the alignment of gravity relative to the direction of particle mass transport is potentially important. However, all previous thermochemical assessments of SVRs have been performed with the cylindrical cavity oriented horizontally or vertically so that gravity acts normal to the central axis (Steinfeld et al. 1992; Steinfeld et al. 1998; Kräupl & Steinfeld 2001; Hirsch & Steinfeld 2004b; Z'Graggen et al. 2006; Müller et al. 2017). This introduces some potential differences to tower-mounted cavities in which the axis of the receiver is likely to be directed with a downward tilt to align it with the heliostat field. In addition, Chinnici et al. (2015) identified some potential advantages of a vertical orientation of the alternative SEVR configuration in augmenting the retention of large particles within the receiver to increase their residence time relative to small particles. However, no experimental measurements of the influence of the orientation on residence time have been reported previously for any configuration of SVR. Hence there is a need to investigate the effect of tilt angle (alignment relative to gravity) on particle RTD in SVRs.

2.3.3 Measurement of the particle residence time distribution

Methods with which to measure particle residence time within a vessel have advanced from those measuring only a mean value (Szekely & Carr 1966; Lede et al. 1987; Li et al. 2008) to those measuring the full distribution of residence times in micro-detail and their sensitivity to a wide range of operating conditions. Particle RTDs are typically measured by detecting the concentration with time of tracer particles using techniques such as phosphorescence (Harris et al. 2002), colour (Kieviet & Kerkhof 1995), ferromagnetism (Guío-Pérez et al. 2013), chemically-doping (Kang et al. 1989), difference in electrical permittivity (Cai et al. 2014) and size (Mitsutani et al. 2005). For some methods of tracer detection, the offline detection of tracer particles is required. Examples of this include the measurement of potassium chloride coated tracer particles in samples taken periodically from the exit flow of a cyclone separator (Kang et al. 1989), the counting of specially marked particles exiting a circulating fluidised bed system (Kehlenbeck et al. 2002), and the concentration measurement of coloured particles in samples collected every two seconds from a spray drier (Kieviet & Kerkhof 1995). Additionally, to assess the particle RTD of different sized particles, a pulse of particles with a wide size distribution can be used and the system response determined by calculating the size fractions of samples collected at regular time intervals, as was done for a continuous liquid-solid classifier (Mitsutani et al. 2005). These methods of offline detection of tracer particles have temporal resolution on the orders of 10^{-2} – 10^{0} Hz, which is insufficient for a device such as the SVR, whose residence time is on the order of seconds (at laboratory-scale). Therefore, there is a need for experimental methods that characterise the specific detail of an RTD with high temporal resolution.

Optical measurement of particles offers a fast response, inline and non-intrusive method of tracer detection that can be based on light emission, scattering or extinction (Amaral et al. 2015). To measure the particle RTD in the riser of a circulating fluidised bed, Harris et al. (2002) used phosphorescent pigment coated particles as a tracer located within the bulk particle phase. The tracer particles were activated at the inlet of the riser with a high intensity pulse of light, rather than a physical pulse injection of tracer, and were then detected with a photomultiplier at the riser exit. This fast-response method avoids measurement bias associated with a physical pulse injection to the steady-state internal flow, but requires correction for the time-decay of phosphorescence. Lede et al. (1987) and Allal et al. (1998) used a combination of a light source and a photoelectric sensor to measure the outlet pulse-response of particles injected into a cyclone reactor and a vertical tube reactor, respectively, by measuring the extinction of light due to particles passing an illuminated zone at the reactor outlet. Such a method is suitable for operation in dilute particle volume fraction regimes so that the injection of particles has negligible impact on the steady-state gas flow (Elghobashi 1994). The assessment by Lede et al. (1987) measured single particles and thus only reported mean residence times, while Allal et al. (1998) measured particle RTDs with particles whose properties were not monodisperse, making it impossible to isolate the effect of particle diameter from that of turbulence on the RTD. However, specialised particles with monodisperse properties are now available (Lau & Nathan 2016), which offers the possibility of developing the light extinction method to isolate the influence of particle size on the particle RTD within a vessel. To measure particle RTDs in a SVR at laboratory-scale a technique is required with fast response time, due to residence times on the order of seconds and the importance of capturing micro-scale detail of the distributions. Methods of particle concentration measurement with a well-characterised light source and a fast-response optical sensor together with the use of specialised monodisperse particles are now sufficiently advanced to provide this new particle RTD information (particularly the influence of particle size). Therefore, the optical method of measuring the RTD of monodisperse particles was chosen in the present thesis.

2.3.4 The compartment modelling approach

The compartment modelling approach seeks to decompose the residence time behaviour of real reactors into a combination of idealised classes of reactors, which is useful for understanding the real reactors and allowing analysis to be performed with little computational effort. These analytical models typically consist of plug flow reactors (PFRs) that assume a uniform residence time or continuously-stirred tank reactors (CSTRs) that assume perfect mixing of the flow. This analytical approach advances understanding of the flow mixing behaviour within the device and provides a useful design tool to incorporate residence time phenomena into component or system performance models (Gao et al. 2012). In addition to fitting ideal flow reactors to measured

RTDs, compartment models are important in diagnosing pathological flow phenomena, including stagnancy and bypassing (Nauman 2008). Stagnancy is associated with a region of the flow with a much longer residence time than average and can be identified by a long tail in the measured RTD, while bypassing is associated with a region of much shorter residence time and can be identified by a sharp peak much shorter than the mean (Levenspiel 1999; Nauman 2008). As examples of the application of the compartment modelling approach to describe particle phase residence times, Kehlenbeck et al. (2002) and Guío-Pérez et al. (2013) used the well-known model of a PFR in series with a CSTR to describe the residence time behaviour of circulating fluidised beds (Levenspiel 1999). This model was used to predict mean particle residence time within the fluidised bed as a function of dimensionless mass turnover, as well as to characterise the extent of particle mixing. For the case of a liquid-solid classifier, Mitsutani et al. (2005) applied the tanks-in-series model to describe the particle residence time (Levenspiel 1999; Fogler 2006). It was found that the number of tanks-in-series required to model the measured particle residence times was in the range 1 – 4, implying an intermediate mixing behaviour between well-stirred and plug flow. The compartment modelling approach to describing the particle residence time behaviour of SVRs has not previously been assessed. This is an aim of the present thesis.

2.4 Solar calcination of alumina

Solar thermochemistry makes use of concentrated solar radiation as the source of high-temperature heat to drive energy-intensive processes towards the production of fuels and material commodities (Steinfeld & Palumbo 2001; Alonso & Romero 2015; Kodama et al. 2017a). Advantages of solar particle receivers in thermochemical applications include the possibility of higher operating temperatures that favour faster reaction rates and the removal of the need for combustion to provide process heat, which in turn reduces emission of greenhouse gases and avoids the contamination of the reaction products (Alonso & Romero 2015). The thermochemical process of interest to the present investigation is the calcination of alumina, which is an energy-intensive process that shares similarities with the calcination of limestone and is potentially well-suited to SVRs.

2.4.1 The industrial alumina calcination process

Alumina is an intermediate product in the production of aluminium and is also a product in its own right. Alumina refining accounts for approximately 27% of the primary energy used in aluminium production, over 90% of which is provided by the combustion of fossil fuels (Kermeli et al. 2015). Calcination is the last step of the Bayer process, which heats the hydrated alumina (aluminium hydroxide or gibbsite, $Al(OH)_3$) from the precipitation stage, to drive off the water of hydration

and form anhydrous alumina (aluminium oxide, Al_2O_3). It is an energy-intensive process, which has historically been conducted with the use of fossil fuels and a rotary-kiln (Williams & Schmidt 2012). However, since the oil crisis of the 1970s and the consequential increase in the cost of fuels, stationary calciners (circulating fluidised bed, gas suspension and fluid-flash calciners) have been favoured over rotary-kilns due to their significantly reduced fuel consumption (Perander et al. 2009; Raahauge 2015). The process heat requirements of modern industrial calciners and estimated resulting CO_2 emissions (calculated from the combustion of methane) are now approximately 3 GJ/tonne-alumina and 165 kg-CO_2/tonne-alumina product, respectively, for which the predominant fuel is natural gas (Jenkins & Bertrand 2001; Lovegrove et al. 2015). Today, the increasing cost of fuels continues to be a driver for technological development of more fuel efficient alumina calciner technology (Klett & Perander 2015). With the price of natural gas forecast to increase in some locations such as Australia (Lovegrove et al. 2015), and with the global need to reduce greenhouse gas emissions, there is strong incentive to seek alternative energy sources such as CST for process heat (Eglinton et al. 2013).

Calcination reactions are thermal decomposition reactions that require the application of high temperature process heat to a solid reactant, resulting in the chemical change of the solid and the evolution of a gaseous product. The calcination of alumina proceeds endothermically according to the following reaction:

$$2Al(OH)_3 \longrightarrow \alpha\text{-}Al_2O_3 + 3H_2O, \qquad \Delta\bar{h}^{\circ}_{\text{calcination}} = +185.2\,\text{kJ mol}^{-1}. \tag{2.7}$$

Modern plants typically process alumina (generally in the gibbsite form) within flash calciners using particles of $\sim$100 µm in diameter transported in a gas suspension through the reactor with residence times on the order of a few seconds. The SVR is a solar reactor that has been used to process powders of similar size to a flash calciner. Furthermore, the temperature at which alumina calcination takes place in the Bayer process, 1273 – 1373 K, is readily achievable in current commercially available solar tower concentrators (Eglinton et al. 2013) and is significantly less than the 1750 K that has been achieved previously in a laboratory-scale SVR used for solar gasification (Z'Graggen et al. 2006). The potential for alumina to be calcined with CST has been assessed with a packed bed of boehmite (an aluminium oxyhydroxide) in a crucible positioned at the focal plane of a Fresnel concentrator by Padilla et al. (2014). They reported 75% conversion after 10 minutes of exposure to solar radiation concentrated to 2644 suns and full conversion with exposure time of 90 minutes (Padilla et al. 2014). However to date, no assessments have been reported for the calcination of gibbsite in a practical reactor such as the SVR under conditions relevant to flash calcination.

The industrial gibbsite calcination process shares similarities with the calcination of limestone ($CaCO_3 \rightarrow CaO + CO_2$, part of the cement production process), which takes place at $\sim$1150 K and has previously been demonstrated with the application of CST. Various configurations of continuous

solar particle reactor have been used for this process, including the modified cyclone gas-particle separator (Imhof 1991; Steinfeld et al. 1992), fluidised beds (Flamant et al. 1980) and continuously fed rotary kilns (Meier et al. 2004; Meier et al. 2006). In each of these laboratory-scale solar particle reactors, the direct irradiation of calcium carbonate particles resulted in chemical conversions to calcium oxide of over 80%, with the important observation that 100% conversion could be achieved with sufficient particle residence time. This not only provides a potential pathway to decarbonise the lime production industry, but also suggests that similar reactors may be suitable for alumina calcination. It is also noteworthy that the alumina calcination process is sensitive to the gas-phase composition, which is one reason that natural gas is a preferred fuel for alumina production (Wefers & Misra 1987; Wang et al. 2006). The application of CST to the calcination process has the potential to further improve product quality by eliminating the possibility of contamination with combustion products and by reducing the significance of back-reactions from the presence of H_2O, which is a product of combustion. While this indicates that the alumina calcination process has good potential for solar processing, its technical feasibility cannot be predicted by implication. Due to the complex, coupled nature of the process, there is a need to experimentally demonstrate – not only that the calcination process can be carried out under solar simulated conditions – but also the extent to which alumina can be calcined, which has not previously been reported.

2.4.2 Details of the alumina calcination chemistry

When gibbsite (the most commonly refined form of aluminium hydroxide) is calcined, the solid reactant evolves through various intermediate materials, including the monohydrated aluminium oxyhydroxide and several transition phases of alumina before the final, thermodynamically stable α-alumina is formed at temperatures in the range 1375 – 1450 K (Wefers & Misra 1987; Whittington & Ilievski 2004). Both the type of intermediate transition aluminas that are formed and their relative presence in the alumina product depend particularly on the heating rate, particle size and the presence of water vapour in the reaction atmosphere (Gan et al. 2009). Studies have previously proposed the gibbsite reaction pathways according to these parameters (Wefers & Misra 1987; Ingram-Jones et al. 1996; Whittington & Ilievski 2004), the consensus of which is as follows:

(a) fine gibbsite particles ($< 10\,\mu m$) decompose via χ-Al_2O_3, an amorphous alumina, followed by κ-Al_2O_3 before reaching the final α-Al_2O_3 phase;

(b) coarse gibbsite particles ($> 100\,\mu m$) decompose via the intermediate aluminium oxyhydroxide, boehmite (AlO(OH)). Upon further heating this progressively decomposes to γ-, δ-, and θ-Al_2O_3, before reaching the α-Al_2O_3 phase; and

(c) gibbsite which undergoes the high heating rates of flash calcination (4700 – 15 000 K s^{-1}) thermally decomposes initially to the amorphous χ-Al_2O_3 as in pathway (a) before crossing over to pathway (b) and progressively forming γ-, δ-, and θ-Al_2O_3, and finally the α-Al_2O_3 phase.

The formation of the intermediate species, boehmite, occurs in the range 380 – 575 K and is favoured by rapid heating of coarse gibbsite particles, such that there is a high local water vapour pressure within the large gibbsite particles (Wefers & Misra 1987). For the case where the gibbsite particles are small enough for the water of hydration to be released without the increase of internal pressure, boehmite does not evolve (Wefers & Misra 1987). Its formation is also favoured by high water vapour pressures in the transport air, as is typical of combustion gases in alumina refinery calciners (Rouquerol et al. 1975; Whittington & Ilievski 2004). On the basis that the use of CST will avoid the presence of H_2O as a combustion product, it can be deduced that the substitution of combustion with CST will inhibit the formation of boehmite. This would be beneficial because boehmite contains structural hydroxyls that degrade product quality for alumina smelting. The transition aluminas are characterised by their large internal porosity and resulting large surface area. They are thus useful for smelting and as catalysts. In contrast, the highly ordered and stable crystalline structure of the α-alumina phase makes it suitable for use in abrasives, refractories and ceramics (Ingram-Jones et al. 1996). The present thesis focusses on the refining of alumina for the purpose of smelting to produce primary aluminium. A study conducted by Whittington & Ilievski (2004) suggests that the majority of refinery-prepared smelter grade alumina (SGA) reacts via χ-Al_2O_3 (pathway c) to feature large proportions of the γ-Al_2O_3 phase. The phase composition of numerous SGAs has previously been determined with quantitative X-ray diffraction (XRD) analysis to reveal that the product from stationary calciners comprises 60 – 90% γ-Al_2O_3 content while that from rotary-kiln calciners comprises 60 – 70% γ-Al_2O_3 content (Whittington & Ilievski 2004). This was corroborated by Wind & Raahauge (2013), who reported that in an industrial gas suspension calcination system only 3 – 8% boehmite content was found in the pre-calcination stages, and by (Perander et al. 2007) who found that refinery-produced SGA was dominated by the γ-Al_2O_3 phase. On this basis, it can be anticipated that the high heating rates inherent with solar processing will favour reaction pathway (c) to form predominantly γ-Al_2O_3. However, there is a need to assess the validity of this deduction by experiment.

The fraction of residual water in the alumina product is another important measure of product quality. This is because residual water has the propensity to drive the adverse formation of hydrogen fluoride gas during the downstream aluminium smelting process (Sommerseth et al. 2012). It is important that alumina is calcined to a sufficient extent for the residual water content to be in the range 0.69 – 0.95 wt.% (Wind et al. 2010). Alumina water content can be present in both a chemically-bound state (as in the case of aluminium hydroxides, $Al(OH)_3$ and AlO(OH)) and in a

physically-adsorbed state. It has been found that both types of moisture in alumina contribute to hydrogen fluoride formation in the downstream smelting process although the physically-adsorbed moisture is more easily removed from alumina at low temperatures below 473 K, while chemically-bound moisture requires higher temperatures. The present investigation at laboratory-scale features a single pass of gibbsite particles through the solar reactor. There is thus a need to determine the maximum extent of conversion (minimum moisture content) that can be achieved with a single pass. There is also a further need to assess the partitioning of any residual water within the alumina product into these two types.

Two crucial measures of alumina product quality are its mean pore size and specific surface area (SSA). This is because, for the subsequent smelting process, the alumina serves not only as the feedstock but also as the material with which hydrogen fluoride (and other fluorine compounds) from smelter gases are removed (via a dry-scrubbing process) (Wind & Raahauge 2013). The SSA and mean pore size are the primary indicators of the adsorption capacity of alumina, so that product quality is enhanced both by a larger SSA and a larger mean pore size (Perander 2010). Specifically, the subsequent process of aluminium smelting requires that the characteristic pore diameter of the alumina be an order of magnitude larger than the hydrogen fluoride molecule, which has a van der Waals diameter of 0.36 nm (Perander 2010). This is to ensure high adsorption of the hydrogen fluoride in the dry-scrubbing process used in aluminium production. Previous investigations have determined that, during the calcination of gibbsite through the transition alumina, the SSA of the material increases rapidly to a maximum ($> 300\ m^2\ g^{-1}$) at about 673 K, due to its microporous structure (average pore size < 2 nm). With higher temperatures, the extent of calcination increases, causing the average pore size to increase and the SSA to decrease and generate a mesoporous structure. Hence the final α-alumina has the lowest SSA of the various alumina phases (Wefers & Misra 1987; Metson et al. 2006; Perander et al. 2009; Raahauge 2015) and there is a trade-off between the desire to obtain both a low residual water content and a high SSA (Perander et al. 2007; Perander et al. 2011). It has been proposed, however, that under rapid heating, such as tends to occur with flash calcination, the structural rearrangement of the gibbsite calcination sequence can be decoupled from the water removal (Metson et al. 2006). The high heating rates possible with directly irradiated CST therefore offer the potential to produce alumina with both favourable residual moisture content and favourable microstructural properties. There is thus a need to confirm whether or not this potential benefit can be realised in practice through testing with a small scale solar reactor.

2.5 Gaps in the literature

The performance of SVRs is controlled by non-linear radiative and turbulent heat and mass transport processes that are too complex to predict a priori. Hence, experimental data of their performance is needed to better understand the processes and allow the development of validated simplified models. The specific gaps in the understanding of SVR performance that are addressed in the present investigation can be summarised as follows.

- No previous systematic assessment of how different input and geometric parameters influence the performance of SVRs is available, even though numerous important technical demonstrations of solar thermochemical processes with SVRs have been performed. Although these previous assessments have demonstrated good potential for the technology, they have been undertaken with a single configuration, so that these are not optimised. There is therefore a need for a systematic study of the performance of SVRs, for a wide range of input and geometric parameters.
- Simplified heat transfer models are required to enable systematic comparison of the thermal performance of many different cases without excessive computational expense. Furthermore, the thermal performance of a receiver can not be determined in isolation from other components in the CST system. There is therefore a need for simplified receiver models accounting for the dominant heat transfer mechanisms with sufficient numerical simplicity to allow a model to be solved for half-hour time-steps and multiple years within CST system models. No first order heat transfer model of the thermal performance of SVRs is presently available.
- No systematic study of the parameters that control the particle residence time within SVRs is presently available. In the absence of measured data, previous assessments have relied either on the nominal particle residence time, based on the ratio of receiver internal volume to gas volumetric flow rate ($\tau_{\text{nom}} = V_{\text{r}}/\dot{V}_{\text{gas}}$). However, both the gas and particle phase residence times in a vortex flow configuration can differ significantly from this nominal residence time as well as differ from each other. New experimental data and understanding of the influence of key operational parameters on the particle residence time within SVRs is therefore required.
- No experimental measurements of the influence of receiver tilt angle (orientation relative to the gravity) on particle residence time are available for any configuration of SVR. There is thus a need to characterise the residence time performance of vortex-based solar particle receivers with a wide range of receiver tilt angles.
- The mechanisms by which the SEVR configuration is able to achieve a residence time distribution that increases with particle size have been proposed and partially validated by an

experimental investigation into the flow field (Chinnici et al. 2016), but no direct assessments of particle RTD are available for the SEVR (or indeed any SVR).

- Previous studies that measure the particle RTD within particulate devices have used particles whose properties were not monodisperse, making it impossible to isolate the effect of particle diameter from that of turbulence on the RTD. Specialised particles with monodisperse properties are now available (Lau & Nathan 2016), which offers the possibility of developing fast response inline optical methods of RTD measurement that isolate the influence of particle size on the RTD.
- The technical feasibility of calcining alumina with concentrated solar radiation cannot be determined by implication, despite the process being highly endothermic and proceeding at ∼1273 K, which is readily achievable with solar tower technology. Due to the complex, coupled nature of the process, it is necessary to assess this experimentally with a prototype solar reactor.
- There is a need to confirm the potential benefits of the solar calcination process to the alumina product quality (as compared to conventional industrial processing with the combustion of natural gas). This is because the influence of the high heating rates inherent to CST energy and the effect of removing combustion products from the solar thermochemical reaction site have not been assessed.

2.6 Objective & scientific aims

The objective of the present thesis is to characterise the performance of vortex-based solar particle receiver-reactors with investigations into three aspects: the thermal performance; the particle residence time performance; and the performance of the solar thermochemical process of calcining alumina particles. Specifically, the present thesis aims to provide new understanding of the influence of key receiver input and design parameters on these performance aspects, so that the device may be scaled up and optimised on a case-by-case basis for various applications.

Three groups of specific scientific aims within the three performance aspects are derived from the gaps in the literature that were identified above. The investigation into thermal performance of SVRs (Chapter 3) aims:

- to further develop simplified modelling tools that allow the systematic assessment of a wide range of input variables with sufficient accuracy to account for the dominant physical processes within the receiver and sufficient numerical simplicity to allow for a timely comparison of many different cases without excessive computational expense; and

- to characterise with first order accuracy the influence of the particle/gas flow rates, particle loading and size, receiver geometry and flow direction on the overall thermal efficiency of the receiver, together with the partitioning of solar energy absorption between the particle and air phases, and the air and particle temperature rise through the receiver.

The investigation into particle residence time characteristics of SVRs (Chapter 4) aims:

- to develop a fast-response, non-intrusive, inline optical method of measuring particle residence time distribution within a particulate vessel that captures the micro-scale detail and allows for the isolation of particle size effects;
- to determine the influence of key dimensionless parameters on the particle behaviour within a SVR and the resulting influence on measured particle residence time, with a systematic and independent variation of particle size, inlet velocity and gas volumetric flow rate;
- to experimentally characterise the influence of receiver tilt angle (i.e. alignment relative to gravity) on the particle residence time distributions within a SVR; and
- to develop a model describing the measured particle residence time behaviour of a SVR using ideal reactor theory (i.e. a compartment model consisting of ideal flow reactors, PFRs and CSTRs).

The investigation into the solar calcination of alumina particles within an SVR (Chapter 5) aims:

- to obtain detailed understanding of the influence of key experimental parameters (particle residence time and reactor temperature) on the extent to which alumina may be calcined with concentrated solar radiation in a laboratory-scale vortex-based solar particle reactor;
- to develop a preliminary understanding of the viability of the solar-driven calcination process at a much larger scale, by relating the performance of the laboratory scale reactor to an industrial scale device; and
- to assess the impact of processing alumina in the SVR with direct solar radiation on the alumina moisture content and the alumina microstructure (mean pore size and specific surface area), which are primary measures of product quality, and to deduce the transition alumina reaction pathway.

3

Thermal Performance

The thermal performance of vortex-based solar particle receivers is the first performance aspect considered in the present thesis. In this chapter, a one-dimensional numerical model is developed to calculate the heat and mass transport processes within the enclosure of a vortex-based solar particle receiver. The model adapts the zonal method and incorporates radiative and convective heat transfer between the particle phase, the gas phase and the receiver wall, together with re-radiative and conductive loss from the receiver.

This simplified one-dimensional model is then used for a first-order assessment of the sensitivity of receiver thermal performance to the following key operating parameters:

- the particle and air mass flow rates;
- the axial direction of the two-phase flow;
- the particle size; and
- the receiver length.

The reference case geometry that is assessed in this chapter consists of a cylindrical cavity with conical section, corresponding to the SVR developed by Z'Graggen et al. (2006), for which data for model validation was collected. To ensure relevance to both this configuration of SVR and the SEVR configuration the analysis that follows provides assessment of the influence of the direction of the two-phase. That is, a front entry from the aperture end of the cavity is relevant to the SVR configuration, while a back entry from the base end of the receiver is relevant to the SEVR. In summary, the systematic assessment with first order accuracy of the influence of key input parameters is used here to advance understanding of the dominant mechanisms controlling thermal performance of SVRs.

The material in this chapter has been published in the journal article:

Davis, D, Jafarian, M, Chinnici, A, Saw, WL & Nathan, GJ 2019, 'Thermal performance of vortex-based solar particle receivers for sensible heating', *Solar Energy*, vol. 177, pp. 163–177.

The article in its published format is available at: https://doi.org/10.1016/j.solener.2018.10.086

Statement of Authorship

Title of Paper	Thermal performance of vortex-based solar particle receivers for sensible heating
Publication Status	☑ Published ☐ Accepted for Publication ☐ Submitted for Publication ☐ Unpublished and Unsubmitted w ork w ritten in manuscript style
Publication Details	Davis, D, Jafarian, M, Chinnici, A, Saw, WL & Nathan, GJ 2019, 'Thermal performance of vortex-based solar particle receivers for sensible heating', *Solar Energy*, vol. 177, pp. 163-177.

Principal Author

Name of Principal Author (Candidate)	Dominic Davis
Contribution to the Paper	Conducted lit. review into vortex-based solar particle receivers and previous modelling of their thermal performance. Developed the numerical heat transfer model used for all analysis in the paper. Collected experimental data used for validation of the model. Implemented the model for all assessments presented in the paper. Interpreted the results of modelling. Wrote and edited the paper. Produced all figures.
Overall percentage (%)	70%
Certification:	This paper reports on original research I conducted during the period of my Higher Degree by Research candidature and is not subject to any obligations or contractual agreements with a third party that would constrain its inclusion in this thesis. I am the primary author of this paper.
Signature	Date 26/2/2019

Co-Author Contributions

By signing the Statement of Authorship, each author certifies that:

i. the candidate's stated contribution to the publication is accurate (as detailed above);

ii. permission is granted for the candidate to include the publication in the thesis; and

iii. the sum of all co-author contributions is equal to 100% less the candidate's stated contribution.

Name of Co-Author	Mehdi Jafarian		
Contribution to the Paper	Helped to develop the numerical model. Advised on the numerical method of solving the fundamental energy balance equations. Helped to develop the cases to be assessed with the model. Helped with interpretation of the results. Advised on the development of the structure of the paper. Edited the manuscript.		
Signature		Date	23,02,2019.

Name of Co-Author	Alfonso Chinnici		
Contribution to the Paper	Advised on the development of the model. Helped to identify the key assumptions required to develop the model. Provided feedback on the interpretation of the data. Edited the manuscript.		
Signature		Date	25/02/19

Name of Co-Author	Woei Saw		
Contribution to the Paper	Supervised the development of the model. This included input into the specific heat transfer terms included in the model. Provided feedback on the interpretation of the data. Edited the manuscript.		
Signature		Date	25/02/2019

Name of Co-Author	Graham 'Gus' Nathan		
Contribution to the Paper	Supervised the development of the work, including the initial collection of experimental data for model validation, as well as the specific cases to be assessed with the model. Provided important feedback for the development of the model, including identification of the key assumptions, and reviewing the specific heat transfer components of the model. Helped to develop the structure of the paper and interpret the data. Provided feedback on the analysis within the paper. Edited the whole manuscript.		
Signature		Date	25/2/2019

3.1 Numerical heat transfer model development

3.1.1 Model description & assumptions

The one-dimensional heat transfer model presented here adapts the zonal method of Hottel & Cohen (1958) and Hottel & Sarofim (1967) for application to SVRs. This method requires that a simple one-dimensional flow pattern and particle distribution within the receiver cavity be known or assumed. The enclosure is then discretised into a number of volume zones (containing gas and particle phases) and surface zones that are small enough to be considered isothermal. A consideration of the energy balance for each of the zones (or elements) results in a set of simultaneous equations that can be solved to determine a one-dimensional distribution of particle, gas and wall temperatures within the receiver.

Figure 3.1a presents a simplified schematic representation of the SVR employed for the solar gasification of carbonaceous feedstock (Z'Graggen et al. 2006). This shows that concentrated solar radiation enters the cylindrical receiver cavity through a circular aperture. The two-phase vortex flow of particles and air is established with two tangentially-oriented inlets located at the front of the receiver and the vortex flow proceeds to the rear, axially-oriented exit.

Figure 3.1b presents the simplified SVR internal geometry and the discretisation regime for the present numerical model, considering only the internal volume of the cylindrical cavity. The receiver internal volume is discretised into n elements along the axial coordinate of the receiver, z, where each element, i, comprises a cylindrical or conical disk of air and particles in a two-phase combination. Each disk element, i, is bounded by a cylindrical or conical wall element. For an element, i, the width of the volume and surface zones is equal to L/n, while their diameter is equal to D_{c} for those in the cylindrical section of the receiver and $2(L-z)\tan\alpha + D_{\mathrm{end}}$ in the conical section of the receiver. Within an element i, the particle phase is of a uniform temperature, $T_{\mathrm{p},i}$, as shown in Figure 3.1b. Similarly, the air phase is $T_{\mathrm{air},i}$ and the wall is treated as isothermal at temperature $T_{\mathrm{w},i}$. The additional aperture, front and end surfaces are treated also as isothermal surfaces and included in the energy balance equations. While the receiver pictured in Figure 3.1a has two tangential inlets, the one dimensional discretisation of the receiver (Figure 3.1b) does not take into account the inlet conditions or distinguish between the two inlets. That is, the mass flowrate of particles and gas into the first discretised element ($i = 1$) models the total mass flow rate from the two tangential inlets of the practical receiver.

To incorporate the influence of the three-dimensional receiver geometry on the one-dimensional axial distribution of radiative heat transfer within the receiver, the present model calculates the radiative shape factors for the internal walls of the SVR as a function of the receiver geometry – D_{ap},

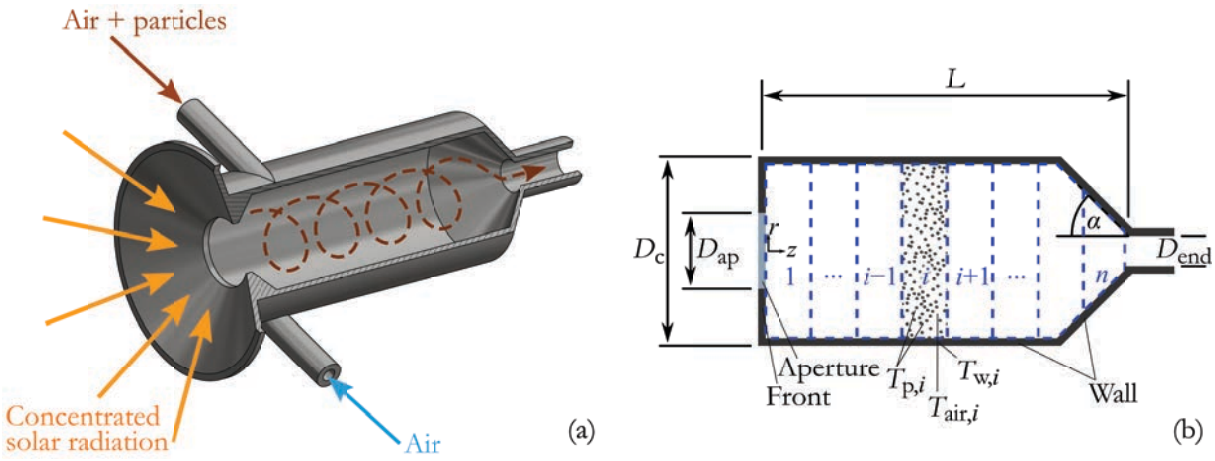

Figure 3.1: Schematic diagrams of **(a)** the solar vortex receiver (SVR) showing concentrated solar radiation entering the receiver through the aperture, together with two tangential inlets for air and particles; and **(b)** the simplified model, showing the discretisation regime used in the present numerical model. The n cylindrical and conical volume elements are enclosed by n cylindrical and conical wall surface elements as well as by the additional surfaces of the aperture and the front wall. The temperature of the particle and air phases as well as the wall temperature of a given element, i, are also shown.

D_c, L, α and D_{end} shown in Figure 3.1b. In addition to the n discretised cylindrical or conical wall surface elements, three additional surfaces are required to enclose the receiver cavity: the aperture surface (a disk), the front wall (an annulus surrounding the aperture disk) and the end wall (a disk). The shape factors between all discretised receiver walls, w_i, and the aperture, front and end walls are then calculated assuming diffuse radiation and using the reciprocity relation, to be:

$$\boldsymbol{F} = \begin{bmatrix} F_{w_1-w_1} & F_{w_1-w_2} & \cdots & F_{w_1-ap} & F_{w_1-fr} & F_{w_1-end} \\ F_{w_2-w_1} & F_{w_2-w_2} & \cdots & F_{w_2-ap} & F_{w_2-fr} & F_{w_2-end} \\ \vdots & \vdots & \ddots & \vdots & \vdots & \vdots \\ F_{ap-w_1} & F_{ap-w_2} & \cdots & F_{ap-ap} & F_{ap-fr} & F_{ap-end} \\ F_{fr-w_1} & F_{fr-w_2} & \cdots & F_{fr-ap} & F_{fr-fr} & F_{fr-end} \\ F_{end-w_1} & F_{end-w_2} & \cdots & F_{end-ap} & F_{end-fr} & F_{end-end} \end{bmatrix}, \tag{3.1}$$

where, $\sum_j^n F_{i-j} = 1$ for all i. For $i = w_1, \ldots w_n, fr, end$, the radiation shape factors F_{i-j} were calculated according to analytical equations for the equivalent geometry (Buschman & Pittman 1961; Feingold 1978; Hamilton & Morgan 1952; Leuenberger & Person 1954; Sparrow & Jonsson 1963). Details of these calculations are provided in the supplementary material (Appendix B).

The model is based on the following assumptions:

1. The gas-particle flow proceeds in one direction only, along paths parallel to the receiver's central axis (z-axis) with constant mass flow rates (plug flow). The residence time of particles, τ_p, in the receiver is therefore considered to be equal to the nominal air residence time, i.e. $\tau_\mathrm{p} = \tau_\mathrm{nom} = V_\mathrm{r}/\dot{V}_\mathrm{air}$ (where V_r is the total internal volume of the receiver and $\dot{V}_\mathrm{air}$ is the volumetric flow rate of air corrected for temperature). The number of particles within the receiver at a given instant, N_p, is then calculated as follows:

$$N_\mathrm{p} = \dot{N}_\mathrm{p}\tau_\mathrm{p} = \frac{\dot{m}_\mathrm{p}}{m_\mathrm{1p}}\tau_\mathrm{p}, \tag{3.2}$$

   where $\dot{N}_\mathrm{p}$ is the number flow rate of particles into the receiver, $\dot{m}_\mathrm{p}$ is the mass flow rate of the particle phase and m_1p is the mass of a single particle. Since the actual flow within the SVR is swirling, an alternative interpretation of this assumption is that the residence time is controlled by the axial component of the flow, or that the influence of the characteristic recirculation zone (Chinnici et al. 2017) is small. This assumption is expected to be reasonable for configurations with relatively low Swirl number, but the model will under-estimate both the residence time and the number density of particles within the receiver at larger Swirl numbers and will also assume the wrong axial flow direction within sub-volumes (such as along the axis), although the bulk flow direction remains correct. This limitation could be addressed in future versions of the model by adjusting the residence time and number density based on other input parameters, such as geometry and Stokes number. To modify the flow in the axial direction due to the recirculation zone would require a recirculation model to be developed. However, any of these additional improvements would also require additional data that is not yet available, so that they are not incorporated here.

2. The particles assessed here are limited to $d_\mathrm{p} < 100\,\mu\mathrm{m}$, which is small enough to be transported in suspension and to follow closely the gas streamlines within the SVR. That is, the characteristic Stokes number of the two-phase flow is less than unity and the particles approach being flow tracers, providing justification to the assumption that $\tau_\mathrm{p} = \tau_\mathrm{nom}$. Such particle sizes are typical of suspension flow devices such as entrained flow gasifiers and flash calciners in the cement and alumina industry for which particles are conveyed pneumatically (Jenkins & Bertrand 2001; Kasule et al. 2012). It can therefore additionally be assumed that the role of particle deposition onto the walls of the receiver is small. The particles are assumed to be spherical with a monodisperse size distribution for any given case.

3. Particles are assumed to be uniformly distributed within each discretised volume element. Each volume element has an equal number of particles, such that $N_{\mathrm{p},i} = N_\mathrm{p}/n$, where $N_{\mathrm{p},i}$ is the number of particles in a given element, i, and n is the number of volume elements into which the receiver internal volume is discretised. This one-dimensional simplification equates to an assumption that the dominant gradient in energy flux is axial, which is consistent with

knowledge that the radiation is absorbed by the particles as it penetrates axially into the device. This could readily be extended in the future to account for radial gradients, but would require additional data that are not yet available. This assumption of a one-dimensional distribution of particles is expected to be reasonable for cases in which the two-phase flow is maintained in one- and two-way coupling regimes (Elghobashi 1994), which corresponds to a particle to gas mass ratio, $\dot{m}_{\mathrm{p}}/\dot{m}_{\mathrm{air}} < 2$ for the present conditions. To make this distinction, the boundaries between the regimes is shown on the figures, where data in the four-way coupling regime is shown in dashed lines to provide insight into likely trends in this regime.

4. The aperture was modelled as an opaque fictive surface of known radiosity, J_{ap}, that is equal in flux magnitude and direction to the incident concentrated solar radiative flux, following the modelling method of Tescari et al. (2013). The directional distribution of radiosity from the fictive aperture surface was weighted according to available experimental data for concentrated solar radiation entering a cylindrical cavity through a circular aperture, based on a 7 lamp solar simulator focussed at the aperture plane of the SVR. That is, for each geometrical receiver configuration assessed in this investigation, $F_{\mathrm{ap}-j}$ was calculated with the use of a Monte Carlo ray tracer, *CUtrace*, which is freely available online at MATLAB Central (Rowe et al. 2015). It is further assumed that no mass transfer occurs through the aperture (no convective heat loss through the aperture) and that any thermal effects of the secondary concentrator are negligible. The method of treating the aperture as a fictive surface is justified by Tescari et al. (2013), who found no significant difference in the predicted temperature distributions of a laboratory-scale solar rotary kiln compared with those from a more computationally-intensive discrete ordinates method of radiation modelling. Note that the difference between the assumption of directional radiation from the fictive aperture surface and diffuse radiation (as with the internal discretised surface elements) is presented in Figure 3.5 for the model validation. The assumption of directional radiation provides better validation of the model.

5. Concentrated solar radiation emitted by the fictive aperture surface is absorbed either by the particles in suspension or by the receiver walls. The linear radiation extinction coefficient κ, is also used to model the rate at which the concentrated solar radiation intensity decreases along the axial coordinate of the receiver due to this absorption by the particle phase and the receiver walls. This is calculated as follows:

$$\kappa = \frac{\pi}{4} d_{\mathrm{p}}^2 \varepsilon_{\mathrm{p}} \frac{N_{\mathrm{p}}}{V_{\mathrm{r}}}. \tag{3.3}$$

where, d_{p} is the particle size, and ε_{p} is the emissivity of the particle. The linear radiation extinction coefficient is used, due to the one-dimensional discretisation of the receiver volume, so that the difference in solar radiative intensity between two axial locations is equal to the

solar radiation absorbed by the particles and wall surface between the two locations, following van Eyk et al. (2016).

6. Thermal radiation interchange between particles both within a given discretised volume and between volumes is assumed to be small relative to the incident concentrated solar radiation (Haugen & Mitchell 2015). This is because for the present conditions the two-way coupling regime applies, that is, the SVR operates with particle mass loadings of $\dot{m}_{\mathrm{p}}/\dot{m}_{\mathrm{air}} < 2$, corresponding to particle-to-air volumetric loadings of $\dot{V}_{\mathrm{p}}/\dot{V}_{\mathrm{air}} < 2 \times 10^{-4}$, according to $\dot{m}_{\mathrm{p}}/\dot{m}_{\mathrm{air}} = (\dot{V}_p/\dot{V}_{\mathrm{air}})(\rho_p/\rho_{\mathrm{air}})$. Further support for this assumption can be found in the study by Jafarian et al. (2012) who found that convective cooling dominates over radiation heat transfer with a wall for individual particles of $d_{\mathrm{p}} < 100\,\mu\mathrm{m}$ within conditions relevant to the SVR. For these reasons and for the purpose of a simplified heat transfer model, inter-particle radiation is neglected in the present model, as was similarly assumed in the development of a one-dimensional model of an entrained-flow solar reactor for the gasification of coal (van Eyk et al. 2016).

7. Thermal radiation heat transfer between the wall elements is calculated in one dimension using the radiosity method. The three-dimensional shape factors calculated for a given receiver geometry are used to determine the radiative heat transfer between the internal wall surfaces of the receiver using the radiosity method, which is then implemented into the one-dimensional heat and mass transfer model with a one-dimensional receiver discretisation. The fictive aperture surface is considered as a black body absorber, whose radiosity matches the concentrated solar radiation input into the receiver. Its incident radiation from all other cavity wall elements is equal to the re-radiation losses of the receiver. The particle phase is assumed not to participate in the thermal radiation heat transfer between the internal walls because of the low values of mass loading $\dot{m}_{\mathrm{p}}/\dot{m}_{\mathrm{air}} < 2$ (corresponding to volumetric loading, $\dot{V}_{\mathrm{p}}/\dot{V}_{\mathrm{air}} < 2 \times 10^{-4}$) in the two-way coupling regime and because the intensity of thermal radiation from the walls is much lower than that entering through the aperture.

8. Particle-to-wall radiative heat transfer is limited to within each element. The surface area of this emission is equal to the total surface area of particles within the element and all of this emission is intercepted by the wall surface of the element. This is an overestimate of the rate of radiative heat transfer between the particles and the wall of the element.

9. Radiation emission and absorption by the particle phase, the receiver wall and the aperture are considered to be equal over all radiation wavelengths. Furthermore, both the particles and receiver walls are treated as grey bodies, for which Kirchhoff's identity holds, i.e. $\varepsilon = \alpha$. Their emissivities and absorptivities are here assumed to be constant and independent of temperature.

10. The gas phase is transparent, so that it does not participate in radiative heat transfer, as has similarly been assumed in alternative heat transfer models of solar receivers (Klein et al. 2007; Jafarian et al. 2013; Tescari et al. 2013; van Eyk et al. 2016).
11. Each particle has a uniform temperature (i.e. there is no temperature gradient within any particle) as justified by the calculation of the Biot number for the particles directly irradiated by a concentrated source of thermal radiation following previous work (Jafarian et al. 2013; Maag et al. 2009a). This calculation was made for the case of largest particle size and greatest radiative intensity of the present investigation.
12. Although the simple flow field proceeding in one direction only does not consider the inlet conditions of a practical SVR, it is assumed that the SVR operates in a fully-turbulent regime, as was the case for the validation experiments (Z'Graggen et al. 2006). Reynolds number will increase further with scale up.

It should be noted that these assumptions allow for the development of a simplified one-dimensional heat transfer model of the SVR for the identification of first order trends of mass and energy balance. Nevertheless, limitations to these assumptions exist particularly those of uniform distribution of particles and the neglect of inter-particle radiation, for cases of large volumetric loading. For this reason, modelling results presented for cases of mass loading, $\dot{m}_{\mathrm{p}}/\dot{m}_{\mathrm{air}} \geq 2$ (approximately corresponding to volumetric loading $\phi \geq 2 \times 10^{-4}$), are shown with dashed lines, indicating a higher degree of uncertainty. The trends presented nevertheless provide a valuable insight into the thermal performance of the SVR.

3.1.2 Energy conservation equations

The energy conservation equation for the receiver cavity walls is formulated using the radiosity method, in which the net radiant energy absorbed by the wall of an element i, is balanced by heat lost to the air through convection and to the surroundings by conduction through the receiver walls. This equation can be written as follows:

$$\dot{Q}_{\mathrm{ap-w},i} + \dot{Q}_{\mathrm{w-w},i} + \dot{Q}_{\mathrm{p-w},i} + \dot{Q}_{\mathrm{w-air},i} - \dot{Q}_{\mathrm{w-}\infty,i} = 0 \tag{3.4}$$

The energy conservation equations for the air and particle phases are formulated by accounting for the enthalpy change of mass transported across an element, i, due to various heat transfer mechanisms within the element, i. For the particle and air phases respectively, the energy balance can be written as follows:

$$\Delta\dot{H}_{\mathrm{p},i} = \dot{Q}_{\mathrm{ap-p},i} + \dot{Q}_{\mathrm{p-p},i} - \dot{Q}_{\mathrm{p-air},i} - \dot{Q}_{\mathrm{p-w},i}, \text{ and} \tag{3.5}$$

$$\Delta \dot{H}_{\mathrm{air},i} = \dot{Q}_{\mathrm{p-air},i} + \dot{Q}_{\mathrm{w-air},i}. \tag{3.6}$$

Figure 3.2a presents the flow configuration for the case in which the two-phase air-particle flow proceeds from the front to the rear of the receiver (front entry). For this case, the enthalpy change across element i (with datum state, $h = 0$, at ambient temperature, T_∞) is quantified for the particle phase as follows:

$$\begin{aligned} \Delta \dot{H}_{\mathrm{p},i} &= \dot{H}_{\mathrm{p},i} - \dot{H}_{\mathrm{p},i-1} \\ &= \dot{m}_{\mathrm{p}} c_{p,\mathrm{p},i} (T_{\mathrm{p},i} - T_\infty) - \dot{m}_{\mathrm{p}} c_{p,\mathrm{p},i-1} (T_{\mathrm{p},i-1} - T_\infty), \end{aligned} \tag{3.7}$$

and for the air phase as follows:

$$\begin{aligned} \Delta \dot{H}_{\mathrm{air},i} &= \dot{H}_{\mathrm{air},i} - \dot{H}_{\mathrm{air},i-1} \\ &= \dot{m}_{\mathrm{air}} c_{p,\mathrm{air},i} (T_{\mathrm{air},i} - T_\infty) - \dot{m}_{\mathrm{air}} c_{p,\mathrm{air},i-1} (T_{\mathrm{air},i-1} - T_\infty). \end{aligned} \tag{3.8}$$

Figure 3.2b presents the alternative case for which the two-phase air-particle flow proceeds from the rear to the front of the receiver (back entry). The enthalpy change across element i in this case is the difference in enthalpies from $i + 1$ to i.

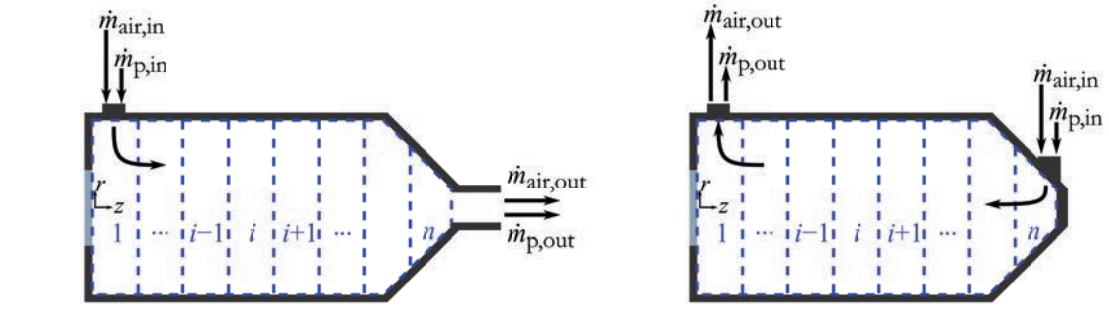

Figure 3.2: Schematic diagram of the two one-dimensional flow configurations assessed with the present model, with **(a)** a front entry, in which the flow proceeds from the front to the rear of the receiver (elements 1 to n); and **(b)** a back entry configuration, in which the flow proceeds from the rear to the front of the receiver (elements n to 1).

The specific formulation of the heat transfer terms in Equations (3.4), (3.5) and (3.6) can be explained as follows. The equation

$$\dot{Q}_{\mathrm{ap-w},i} = A_{\mathrm{ap}} F_{\mathrm{ap-w}_i} J_{\mathrm{ap}} e^{-\kappa_i z_i} \tag{3.9}$$

accounts for the solar radiative power emitted from the fictive aperture surface (which in reality enters through the aperture from the optical concentrator) that reaches the wall surface of element i. The imposed radiosity of the aperture surface, J_{ap}, is equivalent in flux magnitude and direction to concentrated solar radiation, such that $\dot{Q}_{\mathrm{s}} = A_{\mathrm{ap}} J_{\mathrm{ap}}$ where, $\dot{Q}_{\mathrm{s}}$ is the input solar energy to be modelled and A_{ap} is the receiver aperture area. The shape factor, $F_{\mathrm{ap-w}_i}$, incorporates the directivity of the radiosity from the aperture along the one-dimensional discretisation of surface and volume elements (following assumption 4), while the exponential term accounts for the reduction in solar radiation intensity due to absorption up-beam of element i along the one-dimensional discretisation of the receiver. The radial component of the radiation path length in the exponential term of Equation (3.9) was considered in the development of the model, however, it was found to have negligible impact on the temperature distributions calculated through the receiver, and therefore negligible impact on the trends presented here. To maintain the one-dimensionality of the present heat transfer model, the radial component is not included here.

The equation

$$\dot{Q}_{\mathrm{w-w},i} = \left[\sum_{j \neq i,\mathrm{ap}}^{n} A_{\mathrm{w}_i} F_{i-j} J_j - A_{\mathrm{w}_i} J_i (1 - F_{i-i}) \right] \tag{3.10}$$

accounts for the net thermal radiation exchange between all wall elements, j, and the wall surface of element i, including the wall element itself and the end and front surfaces of the cavity, but not including the aperture radiosity (which is defined in Equation (3.9)). Following assumption 7 the re-radiation losses of the receiver are calculated as $\dot{Q}_{\mathrm{w-ap}} = \sum_i^n A_{\mathrm{w}_i} F_{\mathrm{w}_i-\mathrm{ap}} J_i$.

The equation

$$\dot{Q}_{\mathrm{p-w},i} = N_{\mathrm{p},i} \pi {d_{\mathrm{p}}}^2 h_{\mathrm{p-w},i} \left(T_{\mathrm{p},i} - T_{\mathrm{w},i} \right) \tag{3.11}$$

accounts for the thermal radiation interaction between the particles in element i and the wall surface of element i, following assumption 8, where the radiative heat transfer coefficient is defined as $h_{\mathrm{p-w},i} = \sigma \varepsilon_{\mathrm{p}} ({T_{\mathrm{p},i}}^2 + {T_{\mathrm{w},i}}^2)(T_{\mathrm{p},i} + T_{\mathrm{w},i})$.

The equation

$$\dot{Q}_{\mathrm{w-air},i} = h_{\mathrm{w-air}} A_{\mathrm{w},i} (T_{\mathrm{w},i} - T_{\mathrm{air},i}) \tag{3.12}$$

describes the heat lost from the cavity walls by forced convection to the vortex flow of air, where the convective heat transfer coefficient is calculated using the heat transfer correlation for cyclones: $Nu_{D_{\mathrm{in}}} = 0.042 {Re_{D_{\mathrm{in}}}}^{0.8}$ (Szekely & Carr 1966). Such a correlation was similarly used by Hirsch &

Steinfeld (2004a) in their radiative transfer model of a vortex flow of methane in a cylindrical cavity and applies for vortex flow in the fully turbulent regime. Although the receiver inlet conditions are not directly considered in the model, the dimensions of the inlet are accounted for through the Nusselt and Reynolds numbers in the heat transfer correlations. These are calculated with an effective diameter, D_{in}, that gives an inlet velocity, $U_{\text{in}} = 20\,\text{m}\,\text{s}^{-1}$, from each of two circular jets according to the explicit relationship: $D_{\text{in}} = [(2/\pi) \times (\dot{V}_{\text{air,in}}/U_{\text{in}})]^{1/2}$.

The equation

$$\dot{Q}_{\text{w}-\infty,i} = h_{\text{w}-\infty} A_{\text{w},i} (T_{\text{w},i} - T_{\infty}) \tag{3.13}$$

accounts for the heat lost from the cavity walls by conduction through the wall to the surroundings. The overall heat transfer coefficient for heat lost to the surroundings is assumed to be uniform along the receiver, $h_{\text{w}-\infty} = 20\,\text{W}\,\text{m}^{-2}\,\text{K}^{-1}$. While this is reasonable for the small-scale laboratory receiver chosen for validation, the conduction heat losses can be minimised by sufficient insulation and by upscaling toward commercial devices. Furthermore, conductive heat losses will not be uniform over the receiver, as surface sections near the focal plane of the concentrated solar radiation such as a secondary concentrator may require active cooling. It is expected that lower values of $h_{\text{w}-\infty}$ could be achieved with larger scale of SVR, resulting in relatively higher overall efficiency of the device. The sensitivity of thermal performance to the value of $h_{\text{w}-\infty}$ is provided in the supplementary material (Appendix B).

The equation

$$\begin{aligned}\dot{Q}_{\text{ap}-\text{p},i} = {} & A_{\text{ap}} F_{\text{ap}-i_{\text{u-b}}} J_{\text{ap}} e^{-\kappa_i z_{i_{\text{u-b}}}} - A_{\text{ap}} F_{\text{ap}-i_{\text{d-b}}} J_{\text{ap}} e^{-\kappa_i z_{i_{\text{d-b}}}} \\ & - A_{\text{ap}} F_{\text{ap}-\text{w}_i} J_{\text{ap}} e^{-\kappa_i z_i}\end{aligned} \tag{3.14}$$

describes the amount of solar radiation absorbed by the particles in element, i. This is equal to the amount of radiation entering the up-beam face of the element, $i_{\text{u-b}}$, less the radiation absorbed by the wall of the element i and the radiation exiting the down-beam face of the element, $i_{\text{d-b}}$, as shown in Figure 3.3. Radiation intensity from the aperture decreases along the axial direction of the receiver at a rate determined by the extinction coefficient, κ, which is a function of the number of particles in the elements up-beam of a given element and the total volume of the elements up-beam of a given element, i. Following the assumption that each element has an equal number of particles, $N_{\text{p},i} = N_{\text{p}}/n$, the radiation intensity at any axial location, z_i, in the discretised receiver can be determined. This is used in Equations (3.9) and (3.14) to determine the rate of solar energy absorption by the receiver wall and the particle phase, and the spatial distribution of this absorption.

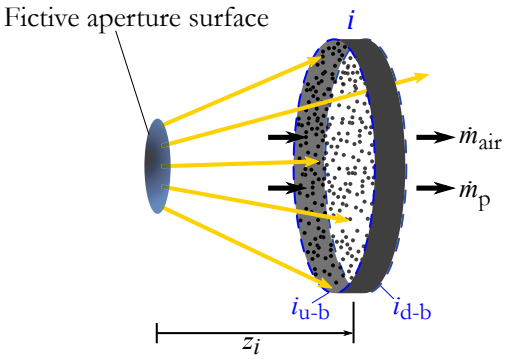

Figure 3.3: Schematic representation of concentrated solar radiation emitted from the fictive aperture surface and either absorbed by the particles or the wall of a given element, i, or passing through to down-beam elements. Shown are the boundaries for the up-beam ($i_{u\text{-}b}$) and down-beam ($i_{d\text{-}b}$) faces of element i.

The equation

$$\dot{Q}_{p-air,i} = N_{p,i}\pi {d_p}^2 h_{p-air,i}(T_{p,i} - T_{air,i}) \tag{3.15}$$

accounts for the heat transferred to the air phase in each element by convection from the particle phase. It is assumed that convection heat transfer between particles and air occurs as forced convection over a sphere, where $h_{p-air,i} = (Nu \times k_{air,i})/d_p$, and $Nu = 2$ according to the empirical relation for no-slip velocity between the particle and the air (Jafarian et al. 2013). The area, over which the convective heat transfer occurs is equal to the sum of the particle surface area of the total number of particles in the element, i.

It should be noted that the heat transfer term for inter-particle radiation, $\dot{Q}_{p-p,i}$ in Equation (3.5), is ignored here, following assumption 6.

3.1.3 Particle and air properties

The particles assessed in the present investigation are assumed to have similar properties to CARBO-HSP, a high temperature ceramic material that has been used previously in investigations of solar particle receivers (Siegel et al. 2014; Siegel et al. 2015). The particle density and emissivity, $\rho_p = 2000\,\mathrm{kg\,m^{-3}}$ and $\varepsilon_p = 0.93$, are based on those of CARBO-HSP (Siegel et al. 2014). The temperature-dependent relation for the specific heat capacity, $c_{p,p}$, used here is based on that of aluminium oxide due to the wider range of temperatures for which $c_{p,p}$ data are available (Chase 1998). These values of $c_{p,p}$ are nevertheless close to those of CARBO-HSP for the data that are available (Ho et al. 2017; Siegel et al. 2015). Following the assumption that the particle sizes investigated here are small enough to closely follow gas streamlines and thus $\tau_p = \tau_{nom}$, the particle sizes under consideration are

limited to under 100 µm (Z'Graggen & Steinfeld 2008b). For the present study, air was used as the transport gas conveying particles in suspension through the receiver. All thermophysical properties of the air phase and their temperature dependencies were provided by Hilsenrath (1955).

3.1.4 Solution technique

Figure 3.4 presents a flow chart describing the solution algorithm used in the present numerical model to attain a steady-state solution to a given set of input parameters. The energy conservation Equations (3.4), (3.5) and (3.6) were rearranged to obtain explicit equations for J_i, $T_{\mathrm{p},i}$ and $T_{\mathrm{air},i}$, for all discretised elements, $i = 1 \ldots n$ (as well as for J_{ap}, J_{fr}, J_{end}). The resulting equations were then solved iteratively for each element and all cavity wall surfaces using a Gauss-Seidel technique with the use of MATLAB. With each iteration new values for $T_{\mathrm{p},i}$ and $T_{\mathrm{air},i}$ were calculated as well as new $T_{\mathrm{w},i}$ from J_i according to:

$$E_{b_i} = J_i + \frac{1-\varepsilon_{\mathrm{w}}}{\varepsilon_{\mathrm{w}} A_{\mathrm{w},i}} \left(\dot{Q}_{\mathrm{p-w},i} - \dot{Q}_{\mathrm{w-air},i} - \dot{Q}_{\mathrm{w-}\infty,i} \right) \text{ and} \tag{3.16}$$

$$T_{\mathrm{w},i} = \sqrt[4]{\frac{E_{b_i}}{\sigma}}. \tag{3.17}$$

To ensure adequate convergence, iterations were terminated when the maximum absolute difference between two consecutive temperature values, $\varepsilon_{\max}$, was $< 10^{-6}$. It was found that the solution of the energy balance equations and resulting temperature distributions was independent of the number of axial elements for $n = 500$ discretisations. This number was used for each case assessed here.

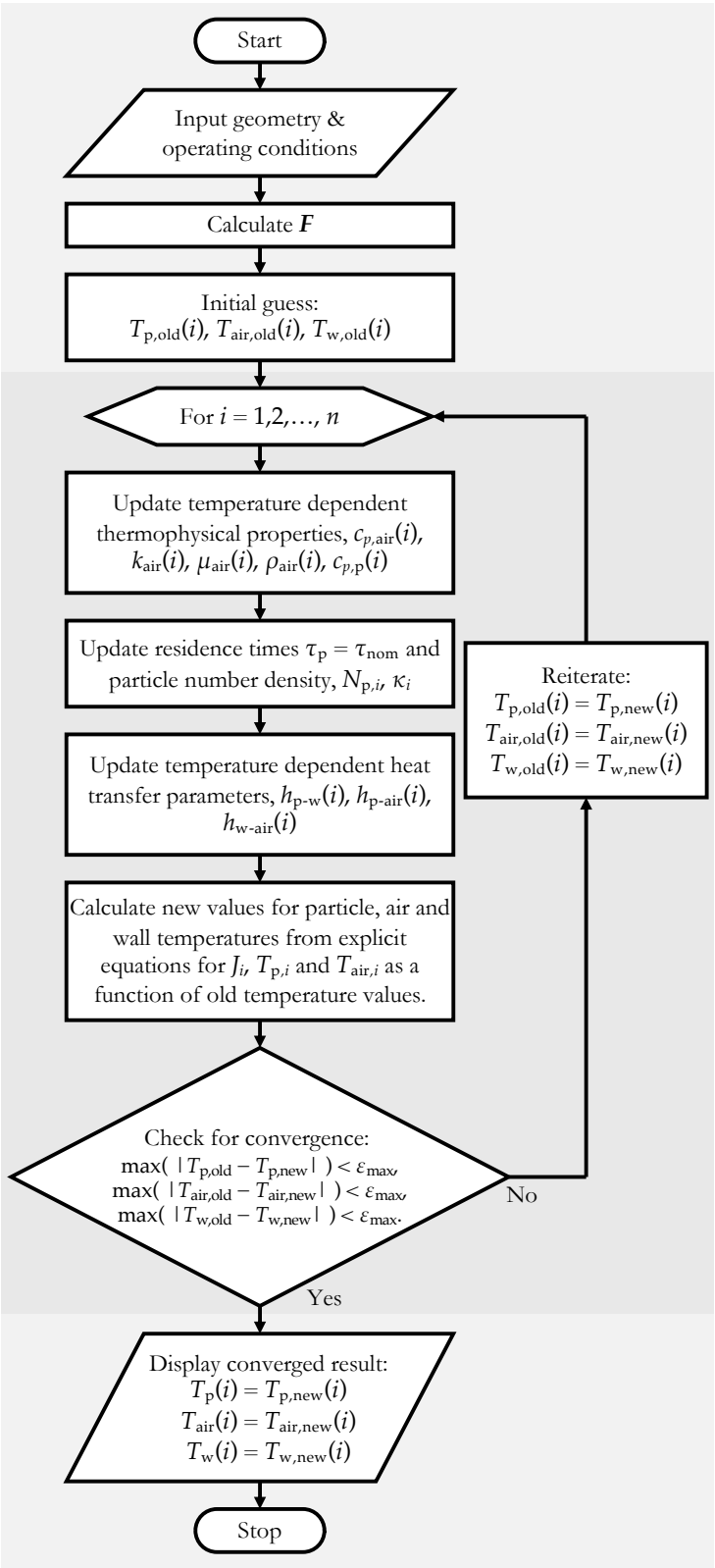

Figure 3.4: Solution algorithm flow chart for the present numerical heat transfer model.

3.1.5 Performance parameters

The thermal performance indicators of the SVR are the overall thermal efficiency, η_{th}, the energy absorption ratio, $\chi_{\text{air-p}}$, and the particle and air phase outlet temperatures, $T_{\text{p,out}}$ and $T_{\text{air,out}}$. These performance parameters are defined as follows:

- The overall thermal efficiency of the receiver accounts for the heat absorbed by both the particle and the air phase, which are both considered to be useful. The efficiency of downstream components of the system would need to be incorporated in a system model, which lies outside the scope of the present investigation. Hence the efficiency of the receiver only is defined as follows:

$$\eta_{\text{th}} = \frac{\Delta\dot{H}_{\text{p}} + \Delta\dot{H}_{\text{air}}}{\dot{Q}_{\text{s}}} = \frac{\dot{m}_{\text{p}} \int c_{p,\text{p}} dT + \dot{m}_{\text{air}} \int c_{p,\text{air}} dT}{\dot{Q}_{\text{s}}}. \tag{3.18}$$

- The energy absorption ratio is the ratio of heat absorbed in the air phase through the receiver to the heat absorbed by the particle phase, defined as:

$$\chi_{\text{air-p}} = \frac{\Delta\dot{H}_{\text{air}}}{\Delta\dot{H}_{\text{p}}}. \tag{3.19}$$

- The particle and air outlet temperatures are defined as the steady state particle and air phase temperatures resulting from the steady-state solution in the last discretised receiver element ($i = n$), which is:

$$T_{\text{p,out}} = T_{\text{p},n}, \tag{3.20}$$

$$T_{\text{air,out}} = T_{\text{air},n}. \tag{3.21}$$

  Note that for the case of the back entry flow direction (Figure 3.2b) the outlet temperatures are the steady state solution temperature in the first receiver element ($i = 1$).

3.2 Model validation & reference case

The accuracy of the model was validated by comparison with experimental measurements for 16 separate cases of the solar sensible heating of air in the SVR. Table 3.1 lists the geometric and operational conditions of the experimental measurements, which were used as the input parameters to the present heat transfer model. The overall conduction heat loss coefficient for the SVR used in the present validation cases, $h_{w-\infty}$, was previously reported to be variable along the receiver axial direction (Z'Graggen 2008). Table 3.1 also presents the reference case geometric and operational conditions for the following sensitivity study, together with the range over which these values were varied from those of the reference case.

Table 3.1: Geometric and operational input parameters to the present model, for the 16 validation cases, the reference case of the present sensitivity study, and the variation of these parameters in the following sensitivity study.

Input parameter	Validation case values	Reference case values	Sensitivity study variation
Geometric			
D_{ap} [m]	0.050	0.050	-
D_{ap}/D_c [-]	0.516	0.516	-
L/D_c [-]	2.547	2.55	1.00 – 4.00
α [°]	45	45	-
Operational			
Flow direction	Front entry	Front entry	Front/back entry
$\dot{q}_s$ [kW m^{-2}]	1086 – 2151	2000	-
$\dot{m}_{air}$ [kg s^{-1}]	1.95 – 4.32 × 10^{-4}	4.00 × 10^{-4}	1.41 – 11.31 × 10^{-4}
$\dot{m}_p/\dot{m}_{air}$ [-]	-	1	0.354 – 1.414 (and 2.000 – 5.657)
d_p [µm]	-	40	10 – 80
T_{in} [K]	290	300	-
$h_{w-\infty}$ [W m^{-2} K^{-1}]	12 – 142	20	-
ε_w [-]	0.8	0.8	-

The model results for the validation cases are compared with temperature measurements taken in 8 locations: two air measurements with Al_2O_3-shielded thermocouples 20 mm inside (towards the central axis) from the inner wall of the SVR at axial locations $z = 52$ mm and 162 mm, and 6 wall measurements at axial locations $z = 50$ mm, 115 mm (with three angular locations) and 190 mm (with two angular locations). For the comparison, the wall temperature measurement at each axial location, z, was calculated as the average of all wall thermocouple readings at that axial location and corrected for the temperature gradient through the Inconel wall, such that the measurements represented internal wall temperatures. It should also be noted that the internal thermocouples were shielded from direct irradiation but open at one end to the vortex flow, so that the temperature

measurement can be assumed to closely match the temperature of vortex gas flow at the specific axial location.

Figure 3.5 compares measurements taken with the SVR for one experimental validation case and the prediction of the present numerical model with the two different assumptions of directional and diffuse radiation emitted by the fictive aperture surface (as outlined in assumption 4 in section §3.1.1). The model calculations with these two different assumptions are provided here as justification for choosing the directional radiation assumption to model input solar radiation from the fictive aperture surface. It can be seen that the model with directional radiation assumption predicts a wall temperature over the range 459 – 1408 K with maximum temperature at $z = 97$ mm. It can also be seen that the model overestimates the measured wall temperature at measurement locations, $z = 115$ mm, and 190 mm, however the hottest part of the predicted wall temperature distribution is located near the middle of the receiver, as was similarly measured with the wall thermocouple measurements. Good agreement between air temperature measurements and those predicted with the directional radiation assumption can also be seen at $z = 52$ mm and 162 mm. In this validation case (and each other validation case) the rear air thermocouple measurement was higher than the front measurement, which provides justification for the use of the directional radiation assumption. On the other hand, it can be seen for the diffuse radiation assumption that the model predicts the air to be of lower temperature at the rear measurement location compared with the front. Similarly, the hottest part of the wall temperature distribution is predicted to occur at the front of the receiver, which is not borne out in the temperature measurements made for each validation case.

A summary of the mean absolute relative error in the present model compared to 16 cases of experimental measurement of the solar sensible heating of air in the SVR is listed in Table 3.2. It can be seen that the standard deviation of the absolute relative errors between the model and experimental measurement varies over the range 4.5 – 10.9 % for the data that are available. This is deemed to be sufficient for the present purposes. It should be noted that the mean errors presented in Table 3.2 are lower than those resulting from the model with the assumption of diffuse radiation from the aperture. No experimental measurements of particle temperatures within the SVR are available for the present validation.

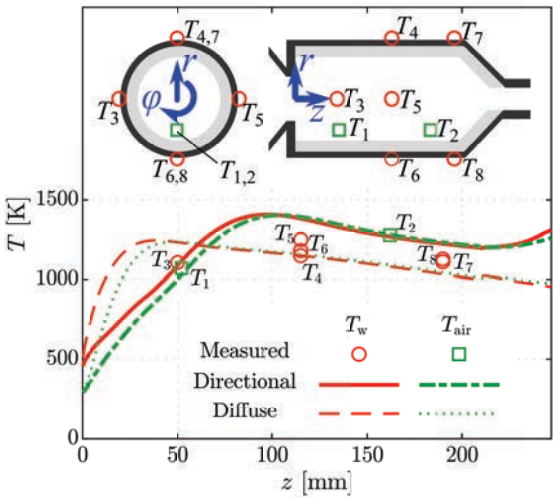

Figure 3.5: A typical comparison between the measurements taken with the SVR and the numerical model calculated with the assumption of either directional or diffuse radiation from the fictive aperture surface. For this case, the solar radiative power input, $\dot{Q}_s = 2315.8\,\mathrm{kW}$, and mass flow rate of air, $\dot{m}_{air} = 2.59 \times 10^{-4}\,\mathrm{kg\,s^{-1}}$. Errors from all cases are shown in Table 3.2.

Table 3.2: Model comparison with experimental measurements of the 16 validation cases for the solar sensible heating of air in the SVR.

Measurement	$T_{w,z=50mm}$	$T_{w,z=115mm}$	$T_{w,z=190mm}$	$T_{air,z=52mm}$	$T_{air,z=162mm}$
Mean absolute relative error[a]	9.0%	25.9%	17.0%	17.0%	5.4%
Minimum absolute relative error[a]	0.4%	14.8%	6.6%	2.0%	0.2%
Maximum absolute relative error[a]	16.5%	48.2%	27.4%	37.2%	14.1%
Standard deviation of absolute relative errors[a]	4.6%	8.9%	6.7%	10.9%	4.5%

[a] Absolute relative error is defined as: $|T_{modelled} - T_{measured}|\,/T_{measured}$.

3.3 Results & discussion

3.3.1 Reference case configuration performance

Figure 3.6 presents the calculated dependence of the thermal performance of the SVR on the mass flow rate of air for a series of values of particle mass loading, as obtained from the present numerical model. Here, the reference case geometry is assessed ($D_{ap} = 0.050$ m, $D_{ap}/D_c = 0.516$, $L/D_c = 2.55$, $\alpha = 45°$) with front entry flow direction and a constant solar thermal input $\dot{q}_s = 2000\,\mathrm{kW\,m^{-2}}$ ($\dot{Q}_s = 3.927$ kW), particle size $d_p = 40\,\mu$m, and inlet temperature $T_{in} = 300$ K. Figure 3.6a presents the dependence of η_{th} on $\dot{m}_{air}$ for nine different values of particle mass loading, $\dot{m}_p/\dot{m}_{air}$. For each value of $\dot{m}_{air}$ assessed here in the range $1.414 - 11.31 \times 10^{-4}\,\mathrm{kg\,s^{-1}}$, $\dot{m}_p$ is varied to assess the particle mass loading, $\dot{m}_p/\dot{m}_{air}$, in the range $0.354 - 1.414$ (together with $\dot{m}_p/\dot{m}_{air} = 2.000 - 5.657$ presented with dashed lines to represent a higher level of uncertainty as discussed in assumption 3 in section §3.1.1). Lines of constant thermal input to total heat capacity of the two-phase flow, $\dot{Q}_s/\left(\dot{m}_p c_{p,p} + \dot{m}_{air} c_{p,air}\right)$, are also plotted on Figure 3.6a. It can be seen that a decrease in this ratio, $\dot{Q}_s/\left(\dot{m}_p c_{p,p} + \dot{m}_{air} c_{p,air}\right)$, has the effect of increasing η_{th}, which is consistent with expectation because increasing mass flow rates at a constant energy input will decrease the temperature rise of the two-phase flow by an energy balance. This in turn results in lower thermal losses and a higher efficiency. Furthermore, for a given $\dot{Q}_s/\left(\dot{m}_p c_{p,p} + \dot{m}_{air} c_{p,air}\right)$, there is a negligible change in η_{th}, for the range of mass loading values considered here. This indicates that, although the particle and air phases undergo heating by different mechanisms at different rates, heat transfer to and between the particle and air phases is fast enough for the performance of the SVR to be most strongly correlated with the total heat capacity of the particle and air throughput rather than the relative mass of each stream. It can also be seen that η_{th} increases both with $\dot{m}_p/\dot{m}_{air}$ for all values of $\dot{m}_{air}$ and with $\dot{m}_{air}$ for all values of $\dot{m}_p/\dot{m}_{air}$. This is because in both cases the input heat is absorbed by a greater mass flow rate of either particles or air, resulting in lower temperatures through the receiver and, in turn, lower thermal losses. It should also be noted that the modest values of thermal efficiency reported here are consistent with the small thermal scale of the device (Z'Graggen et al. 2006) and that an increase in this efficiency is expected with an increase in thermal scale.

Figure 3.6b presents the dependence of $\chi_{air\text{-}p}$ on $\dot{m}_{air}$ for nine different values of $\dot{m}_p/\dot{m}_{air}$. Lines of constant thermal input to total heat capacity of the two-phase flow, $\dot{Q}_s/\left(\dot{m}_p c_{p,p} + \dot{m}_{air} c_{p,air}\right)$, are also plotted. It can be seen that the dominant variable influencing $\chi_{air\text{-}p}$ is the particle mass loading, with the fraction of absorbed solar energy that is partitioned with the particle phase increasing with $\dot{m}_p/\dot{m}_{air}$ for constant $\dot{Q}_s/\left(\dot{m}_p c_{p,p} + \dot{m}_{air} c_{p,air}\right)$. It is significant that for a mass loading of $\dot{m}_p/\dot{m}_{air} = 1$, $\chi_{air\text{-}p}$ is approximately equal to 1 for the cases considered here. This means that the incident solar energy is transferred in approximately equal proportions to the two phases. That is,

for $\dot{m}_{\mathrm{p}}/\dot{m}_{\mathrm{air}} \leq 1$, the receiver acts as an air heater, while for $\dot{m}_{\mathrm{p}}/\dot{m}_{\mathrm{air}} > 1$, it acts as a particle heater. In addition, to achieve efficient operation, the recovery of energy from both streams needs to be considered.

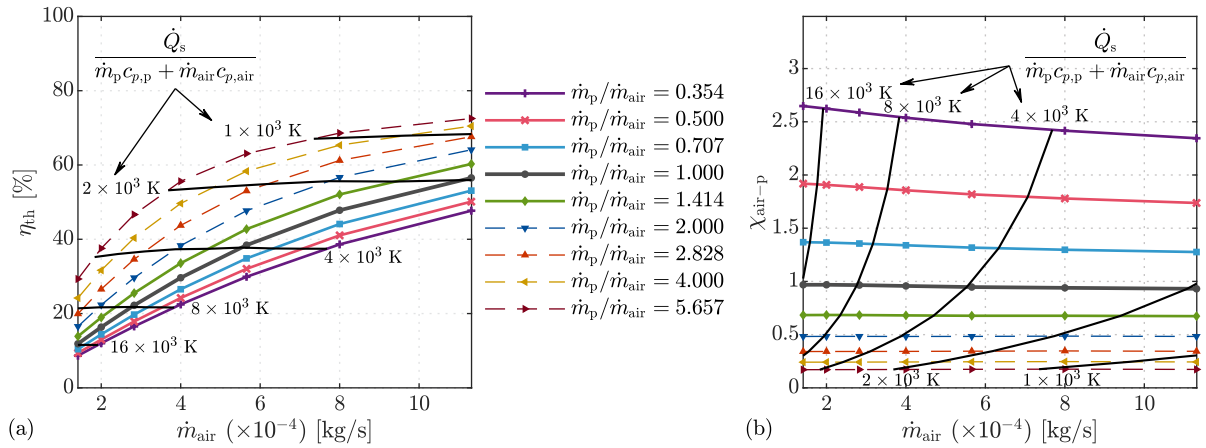

Figure 3.6: Assessment of the operation of the SVR with reference case geometry ($D_{ap} = 0.050$ m, $D_{ap}/D_c = 0.516$, $L/D_c = 2.55$, $\alpha = 45°$), and for a constant solar thermal input, $\dot{q}_s = 2000$ kW m^{-2} ($\dot{Q}_s = 3.927$ kW), $d_p = 40$ µm, $T_{in} = 300$ K, for varying mass flow rates of the particle and air phases. Presented are **(a)** the receiver thermal efficiency, η_{th}, with lines of constant ratio of thermal input to total heat capacity of the two-phase flow, $\dot{Q}_s / \left(\dot{m}_p c_{p,p} + \dot{m}_{air} c_{p,air}\right)$; and **(b)** the energy absorption ratio, $\chi_{air\text{-}p}$, also with lines of constant ratio of thermal input to total heat capacity of the two-phase flow; as a function of mass flow rate of air, $\dot{m}_{air}$, for nine different values of mass loading, $\dot{m}_p/\dot{m}_{air}$. The trends for $\dot{m}_p/\dot{m}_{air} \geq 2$, are presented with dashed lines due to higher levels of uncertainty as noted in assumption 3.

Further insight into the trends presented above can be gained by assessing the temperature distributions within the SVR for certain cases. Figure 3.7 presents the calculated axial temperature distributions of the receiver wall, T_w, the particle phase, T_p, and the air phase, T_{air}, for a constant solar thermal input, $\dot{q}_s = 2000\,\text{kW m}^{-2}$ ($\dot{Q}_s = 3.927\,\text{kW}$), a mass loading $\dot{m}_p/\dot{m}_{air} = 1$, and three different ratios of thermal input to total heat capacity of the two-phase flow, $\dot{Q}_s/\left(\dot{m}_p c_{p,p} + \dot{m}_{air} c_{p,air}\right)$. These three values of $\dot{Q}_s/\left(\dot{m}_p c_{p,p} + \dot{m}_{air} c_{p,air}\right) = 15.7$, 5.54 and 1.96×10^3 K, correspond to particle and air mass flow rates of $\dot{m}_p = \dot{m}_{air} = 1.414$, 4.000 and $11.31 \times 10^{-4}\,\text{kg s}^{-1}$, respectively. It can be seen that the temperatures within the receiver decrease at each axial location with a decrease in $\dot{Q}_s/\left(\dot{m}_p c_{p,p} + \dot{m}_{air} c_{p,air}\right)$, consistent with the trend presented in Figure 3.6a of increasing η_{th} with a reduction in temperature. The model predicts nominal residence time for these cases of $\tau_{nom} = 2.42$, 1.00 and 0.55 s, respectively (calculated as $\tau_{nom} = V_r/\dot{V}_{air}$, where $\dot{V}_{air}$ is evaluated at mean air phase temperature). The reduction in τ_{nom} with an increase in $\dot{m}_{air}$ corresponds to a decrease in the temperatures of the particles, air and walls. It can be seen for the highest case of $\dot{Q}_s/\left(\dot{m}_p c_{p,p} + \dot{m}_{air} c_{p,air}\right)$ both the particle and air phases undergo the majority of their temperature rise within the front 25 mm of the receiver. The two phases reach maximum temperatures of $T_p = 1909$ K and $T_{air} = 1862$ K at axial coordinate $z = 81$ mm and 89 mm, respectively, and then cool with further distance to reach $T_{p,out} = 1714$ K and $T_{air,out} = 1725$ K. The cooling is attributed to heat loss through the walls. In contrast, the rate of heating is lower for the cases of lower $\dot{Q}_s/\left(\dot{m}_p c_{p,p} + \dot{m}_{air} c_{p,air}\right)$, so that the peak temperatures occur further toward the rear of the receiver. It is also evident that for each case, the particle phase is heated at a faster rate than the air phase in the front sections of the receiver and also reaches a higher peak temperature. This indicates that heat is absorbed by the particle phase and then transferred to the air phase. However, in the rear section of the receiver the particle and air phases approach equilibrium, tending towards the same temperature. The overall thermal efficiency for the conditions presented in Figure 3.7 with $\dot{Q}_s/\left(\dot{m}_p c_{p,p} + \dot{m}_{air} c_{p,air}\right) = 15.7$, 5.54 and 1.96×10^3 K are $\eta_{th} = 11.9\%$, 29.6% and 56.5%, respectively. This trend is consistent with that of the wall temperature. A lower wall temperature reduces both the re-radiation losses from the wall through the aperture and the rate of conduction heat loss through the receiver wall. It should be noted, that the small rise in temperature at $z > 210$ mm for each of the temperature distributions is caused by the change in shape of the receiver. The conical section receives a larger proportion of radiation from the aperture than the adjacent cylindrical section due to the directional nature of the radiation and the comparatively larger radiative shape factors. In addition, the calculated particle number density increases in the conical section due to the smaller cross-sectional area. This results in a relatively greater proportion of solar radiation absorption in the conical section, leading to a higher particle temperature.

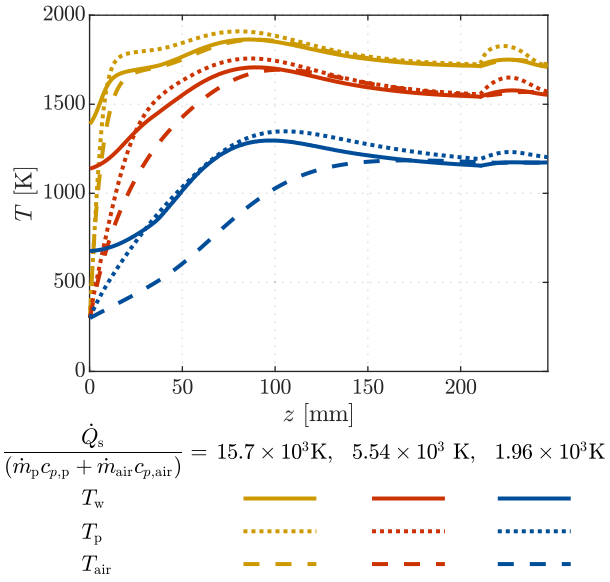

Figure 3.7: Calculated axial temperature distributions of the receiver wall, T_w, the particle phase, T_p, and the air phase, T_{air}, for a constant solar thermal input, $\dot{q}_s = 2000\,\mathrm{kW\,m^{-2}}$ ($\dot{Q}_s = 3.927\,\mathrm{kW}$), a mass loading $\dot{m}_p/\dot{m}_{air} = 1$, and three different ratios of thermal input to total heat capacity of the two-phase flow, $\dot{Q}_s/\left(\dot{m}_p c_{p,p} + \dot{m}_{air} c_{p,air}\right)$. Geometry and operational conditions of the reference case were used: front entry configuration with $D_{ap} = 0.050$ m, $D_{ap}/D_c = 0.516$, $L/D_c = 2.55$, $\alpha = 45°$, $d_p = 40\,\mu\mathrm{m}$, $T_{in} = 300$ K. These distributions are generated from the solution of the energy balance equations for each of the 500 discretised elements along the receiver's axial coordinate, z.

3.3.2 Influence of flow direction

Figure 3.8a presents the calculated axial distributions of the temperatures of the receiver wall, the particle phase and the air phase for the front entry and back entry flow directions (shown in Figure 3.2) with the reference conditions (Table 3.1). For the front entry flow direction, the two-phase flow enters at $z = 0$ mm and exits at $z = 247$ mm; and vice versa for the back entry flow direction. It can be seen that, for the front entry flow direction, the particle phase undergoes rapid heating to a maximum temperature, $T_{\mathrm{p}} = 1757$ K at $z = 87$ mm, which then decreases slightly to an exit value of $T_{\mathrm{p,out}} = 1571$ K. The air phase undergoes less rapid heating than the particle phase to reach a maximum temperature, $T_{\mathrm{air}} = 1694$ K at $z = 104$ mm, which then also decreases slightly to an exit value of $T_{\mathrm{air,out}} = 1566$ K. The difference in temperature between the air and particle phases in the front half of the chamber, $z = 0 - 140$ mm, is due to the greater rate of radiative heating to the particle phase, than that of cooling by convection to the air phase. However, for $z > 140$ mm, the temperatures of both phases approach that of the wall, indicating low rates of heat transfer due to near equilibrium.

It can be also seen from Figure 3.8a that, in contrast to the front entry case, for the back entry flow direction, the particle and air phases are heated at similar rates from $z = 247 - 210$ m. The particle phase reaches a maximum temperature, $T_{\mathrm{p}} = 1749$ K at $z = 61$ mm and exits with $T_{\mathrm{p,out}} = 1717$ K, while the air phase reaches a maximum temperature, $T_{\mathrm{air}} = 1664$ K at $z = 61$ mm and exits with $T_{\mathrm{air,out}} = 1588$ K. While the peak temperatures of the respective phases are similar for the two configurations, the exit temperatures are higher for the back entry than the front entry. In addition, the two phases are not in equilibrium at the exit for the rear entry case, while they are for the front entry case. The η_{th} for the front and back entry flow configurations are 29.6% and 31.9%, respectively. This increase in efficiency for the back entry flow configuration can be attributed to the higher particle exit temperature because the particle phase undergoes greater heating in the front sections of the receiver than the air phase, and thus has higher temperature at the exit. It should be noted that while the back entry flow case may have favourable efficiency, it can also be seen that the particle phase has a shorter residence time at elevated temperature (above 1500 K, say). For the back entry case, the particle phase has temperature greater than 1500 K only at axial locations $z = 0 - 121$ mm, whereas, for the front entry case the particle phase has temperature greater than 1500 K at axial locations $z = 34 - 247$ mm. The greater residence time at a given elevated temperature for the front entry configuration may be beneficial for the application of the SVR to reacting particles, which require minimum residence time at a given temperature for adequate chemical conversion. However, it is not an advantage for the heating of inert particles.

Figure 3.8b presents the calculated axial distributions of the thermal losses via conduction through the wall, $\dot{q}_{\mathrm{w}-\infty}$, and re-radiation through the aperture, $\dot{q}_{\mathrm{w}-\mathrm{ap}}$, for the front entry and back entry flow

directions. It can be seen that the biggest component of heat loss for both the front and back entry configurations is by conduction through the receiver wall. The calculated values for conduction heat loss integrated over the internal surface area of the receiver are 51% and 47% of the solar thermal input for the front and back entry configurations, respectively. The distributions of these heat losses in Figure 3.8b show that conduction heat loss is greater at the back of the receiver for the front entry configuration, while it is greater at the front of the receiver for the back entry flow configuration, as is expected from the axial distributions of receiver wall temperature presented in Figure 3.8a. It can also be seen that the majority of re-radiation losses from the receiver wall through the aperture originate from the front sections of the receiver wall, due to the radiative shape factors, while most of the re-radiation from the back sections of the receiver wall intersect with the internal surface of the receiver rather than the aperture. As a consequence, it can be seen that re-radiation losses calculated with the present model are controlled by wall temperatures in the front section of the receiver. Here, the front entry configuration has reduced re-radiation losses compared with the back entry configuration, calculated to be 15% and 18% of the solar thermal input, respectively. The extent of thermal loss by re-radiation is significantly lower than that by conduction for the present case, which is consistent with the small size of the reactor. However, the present model assumes a constant, conservative conduction heat loss coefficient value ($h_{w-\infty} = 20\,\mathrm{W\,m^{-2}\,K^{-1}}$), which could be minimised with the application of sufficient insulation and also with an increase in thermal scale, in which case re-radiation heat loss would become relatively more important.

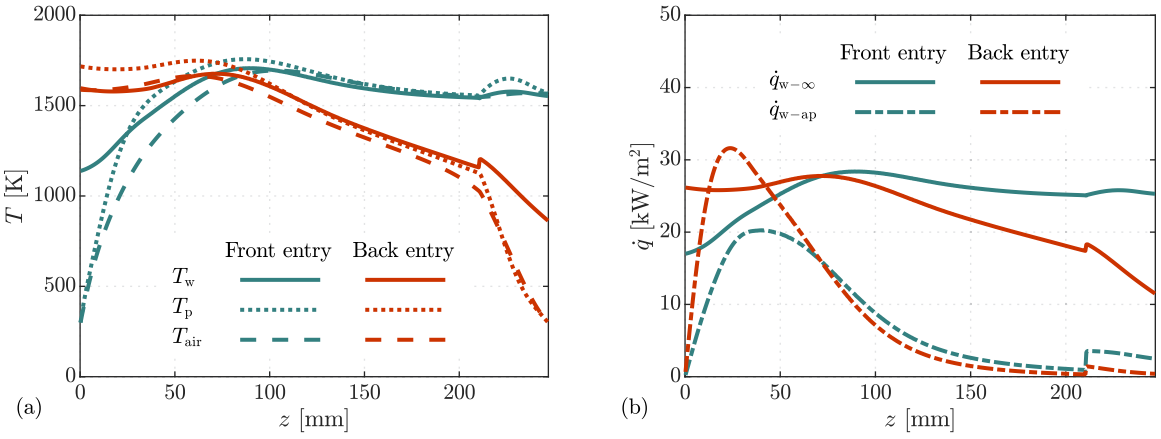

Figure 3.8: Calculated axial distributions of **(a)** the temperatures of the receiver wall, T_w, the particle phase, T_p, and the air phase, T_{air}; and **(b)** the thermal losses via conduction through the wall, $\dot{q}_{w-\infty}$, and re-radiation through the aperture, $\dot{q}_{w-ap}$; for the front entry and back entry flow configurations with reference case geometry and operational conditions: $D_{ap} = 0.050\,\mathrm{m}$, $D_{ap}/D_c = 0.516$, $L/D_c = 2.55$, $\alpha = 45°$, $\dot{q}_s = 2000\,\mathrm{kW\,m^{-2}}$ ($\dot{Q}_s = 3.927\,\mathrm{kW}$), $\dot{m}_p/\dot{m}_{air} = 1$, $\dot{m}_p = \dot{m}_{air} = 4.000 \times 10^{-4}\,\mathrm{kg\,s^{-1}}$, $d_p = 40\,\mu\mathrm{m}$, $T_{in} = 300\,\mathrm{K}$.

Figure 3.9 presents the dependence on particle and air phase mass flow rates of thermal efficiency of the SVR with the back entry flow configuration as calculated with the present numerical model. Here, the reference case geometry is assessed ($D_{ap} = 0.050\,\text{m}$, $D_{ap}/D_c = 0.516$, $L/D_c = 2.55$, $\alpha = 45^o$) with a constant solar thermal input $\dot{q}_s = 2000\,\text{kW m}^{-2}$ ($\dot{Q}_s = 3.927\,\text{kW}$), particle size $d_p = 40\,\mu\text{m}$, and inlet temperature $T_{in} = 300\,\text{K}$. It can be seen that, as for the front entry flow configuration (Figure 3.6a), η_{th} increases asymptotically with increasing $\dot{m}_{air}$, for all values of $\dot{m}_p/\dot{m}_{air}$ (noting that trends for $\dot{m}_p/\dot{m}_{air} \geq 2$ are presented with dashed lines due to the higher level of uncertainty as discussed in assumption 3 in section §3.1.1). The thermal efficiency tends towards a maximum of 88% for the highest particle loading considered here, $\dot{m}_p/\dot{m}_{air} = 5.657$. In addition, the efficiency increases with $\dot{m}_p/\dot{m}_{air}$, so that the device is most efficient with high particle loadings. It can also be seen that, similar to the front entry flow configuration, a decrease in the ratio $\dot{Q}_s/\left(\dot{m}_p c_{p,p} + \dot{m}_{air} c_{p,air}\right)$ has the effect of increasing η_{th}. However, Figure 3.9a shows here that at constant $\dot{Q}_s/\left(\dot{m}_p c_{p,p} + \dot{m}_{air} c_{p,air}\right)$ it is beneficial to the thermal efficiency for the SVR to be operated with higher particle loading. This implies that efficiency is dominated by the heat transfer between the incoming concentrated solar radiation and the particles, which directly absorb the radiation before leaving from the front section of the receiver where the concentrated solar radiation is most intense.

Figure 3.10 presents the ratio of the receiver thermal efficiency for the back entry configuration relative to the front entry case, $\eta_{th,back}/\eta_{th,front}$, as a function of $\dot{m}_{air}$ for nine different values of $\dot{m}_p/\dot{m}_{air}$ (noting that trends for $\dot{m}_p/\dot{m}_{air} \geq 2$ are presented with dashed lines due to the higher level of uncertainty). It can be seen that the back entry flow configuration has a higher thermal efficiency for the majority of cases, although it has a lower thermal efficiency for the cases with sufficiently low particle loading $\dot{m}_p/\dot{m}_{air} = 0.354$ and $\dot{m}_{air} \leq 8.000 \times 10^{-4}\,\text{kg s}^{-1}$, and for $\dot{m}_p/\dot{m}_{air} = 0.500$ and $\dot{m}_{air} \leq 5.657 \times 10^{-4}\,\text{kg s}^{-1}$. This is consistent with general understanding of the difference between co-flow and counter-flow heat exchangers. The counter-flow arrangement achieves a higher outlet temperature, resulting in a greater thermal efficiency, despite the trade-off between an increase in radiation losses through the aperture. In contrast, for the low mass loading cases, the heat exchange is dominated by heat transfer from the walls to the air, so that the front entry configuration results in a counter-flow arrangement relative to the high temperature rear section of the chamber (Figure 3.8). It can be seen that, for the cases of $\dot{m}_{air} \leq 2.828 \times 10^{-4}\,\text{kg s}^{-1}$ considered here, $\eta_{th,back}/\eta_{th,front}$ increases with particle loading, such that a maximum value of $\eta_{th,back}/\eta_{th,front} = 1.72$ occurs for $\dot{m}_p/\dot{m}_{air} = 5.657$, with $\dot{m}_{air} = 2.000 \times 10^{-4}\,\text{kg s}^{-1}$. However, for higher $\dot{m}_{air}$ it can be seen that there is a critical mass loading, above which $\eta_{th,back}/\eta_{th,front}$ decreases. For $\dot{m}_{air} = 4.000 \times 10^{-4}\,\text{kg s}^{-1}$ this value is $\dot{m}_p/\dot{m}_{air} = 4.000$, and for $\dot{m}_{air} = 5.657 \times 10^{-4}\,\text{kg s}^{-1}$ this value is $\dot{m}_p/\dot{m}_{air} = 2.828$.

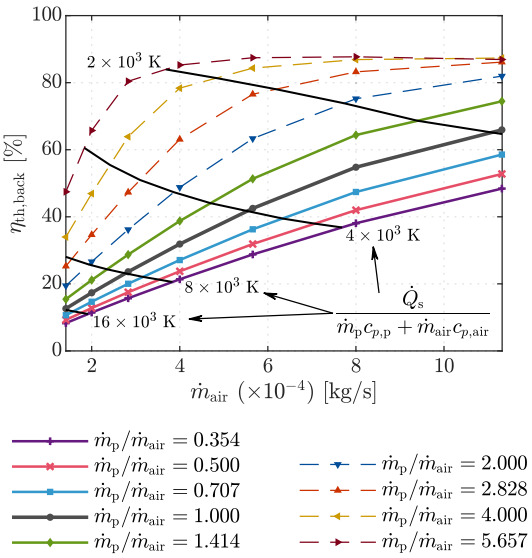

Figure 3.9: The thermal efficiency of the SVR with back entry flow configuration, $\eta_{\text{th,back}}$, with lines of constant ratio of thermal input to total heat capacity of the two-phase flow, $\dot{Q}_s / \left(\dot{m}_p c_{p,p} + \dot{m}_{air} c_{p,air}\right)$, as a function of mass flow rate of air, $\dot{m}_{air}$, for nine different values of mass loading, $\dot{m}_p/\dot{m}_{air}$. Assessments are made for the reference case geometry and operational conditions (Table 3.1), for varying mass flow rates of the particle and air phases. The trends for $\dot{m}_p/\dot{m}_{air} \geq 2$, are presented with dashed lines due to higher levels of uncertainty as noted in assumption 3.

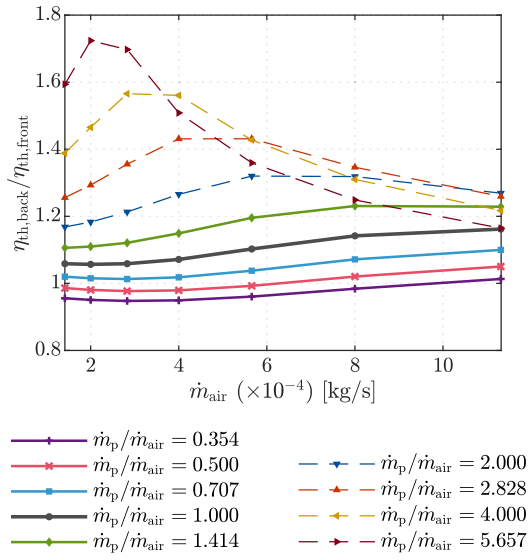

Figure 3.10: The ratio of the thermal efficiency of the SVR with back entry configuration relative to the front entry configuration, $\eta_{\text{th,back}}/\eta_{\text{th,front}}$, as a function of mass flow rate of air, $\dot{m}_{air}$, for nine different values of mass loading, $\dot{m}_p/\dot{m}_{air}$. Assessments are made for the reference case geometry and operating conditions (Table 3.1), for varying mass flow rates of the particle and air phases. The trends for $\dot{m}_p/\dot{m}_{air} \geq 2$, are presented with dashed lines due to higher levels of uncertainty as noted in assumption 3.

3.3.3 Influence of particle size

Figure 3.11 presents the calculated axial distributions of the temperatures of the receiver wall, the particle phase and the air phase for two particle sizes, $d_p = 40$ and 80 µm, with reference case geometry, front entry configuration and $\dot{m}_p = \dot{m}_{air} = 4.000 \times 10^{-4}$ kg s^{-1}. It can be seen that a decrease in the particle size increases the rate at which the particle phase absorbs concentrated solar radiation in the front section of the receiver, as expected. For example, within the first 50 mm of the receiver the 80 µm sized particle phase heats to 1446 K, while the 40 µm size particle phase heats to 1633 K. This is consistent with the proportionality relationship between radiation extinction coefficient and particle size for a given mass of particles, which can be described as: $\kappa \propto {d_p}^{-1}$. The greater attenuation of concentrated solar radiation in the front part of the receiver by the smaller particles results in higher temperature and resulting higher wall temperature. However, the influence is small as the two-phase flow proceeds to the rear of the receiver, where the temperature of the particle and air phases approach equilibrium. For $z > 211$ mm the particle phase (and the air to a lesser extent) undergoes heating for both $d_p = 40$ and 80 µm. This is due to relatively larger radiation shape factors from the aperture to the conical section of the receiver as well as increased concentration of particles. In addition, the 80 µm particles undergo greater heating and thus leave with higher temperature than the 40 µm particles. This is because the solar radiation penetrates further into the receiver for the larger particles, such that its intensity is greater in the conical section of the receiver than for the smaller particle size. However, the net effect of increasing the particle size is to translate the temperature distribution toward the back of the cavity, which will lower radiative losses through the aperture.

Figure 3.12 presents the influence of particle sizes in the range 10 to 80 µm on the thermal performance of the front entry configuration of the SVR, for the reference geometry and operating conditions (Table 3.1). Figure 3.12a presents the dependence of η_{th} on d_p for four different values of $\dot{m}_p/\dot{m}_{air}$ spanning 0.500 to 4.000 (noting that trends for $\dot{m}_p/\dot{m}_{air} \geq 2$ are presented with dashed lines due to the higher level of uncertainty). It can be seen that increasing the particle size causes a significant increase in the overall thermal efficiency of the process. Specifically, for $\dot{m}_p/\dot{m}_{air} = 1.000$ an increase in particle size from 10 µm to 80 µm results in a 18.2% improvement in thermal efficiency from 26.4% to 31.2%. This is consistent with the temperature distributions presented in Figure 3.11, which imply a lower radiation loss through the aperture for the larger particles, whose temperatures peak further from the aperture.

Figure 3.12b presents the dependence of the relative thermal losses by conduction, $\dot{Q}_{w-\infty}/\dot{Q}_s$, and re-radiation, $\dot{Q}_{w-ap}/\dot{Q}_s$, on d_p for four different values of $\dot{m}_p/\dot{m}_{air}$. It can be seen that, for the four particle mass loadings considered here, the particle size has the most significant influence on the re-radiation loss, $\dot{Q}_{w-ap}/\dot{Q}_s$, which reduces with increasing d_p as identified previously. This is due

to the slower initial temperature rise as larger particles are introduced into the receiver and the resulting shift of the temperature profiles downstream to the rear of the receiver, where the receiver wall has smaller radiation shape factor with the aperture. It can also be seen that particle size has less of an influence on $\dot{Q}_{w-\infty}/\dot{Q}_s$.

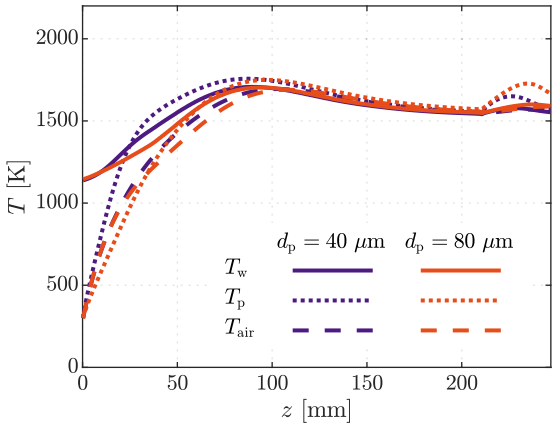

Figure 3.11: Calculated axial temperature distributions of the receiver wall, T_w, the particle phase, T_p, and the air phase, T_{air}, for the SVR with front entry flow configuration and two different values of particle size, $d_p = 40$ and $80\ \mu m$. Geometry and operational conditions of the reference case were used: $D_{ap} = 0.050$ m, $D_{ap}/D_c = 0.516$, $L/D_c = 2.55$, $\alpha = 45°$, $\dot{q}_s = 2000\ kW\ m^{-2}$ ($\dot{Q}_s = 3.927$ kW), $\dot{m}_p/\dot{m}_{air} = 1$, $\dot{m}_p = \dot{m}_{air} = 4.000 \times 10^{-4}\ kg\ s^{-1}$, $T_{in} = 300$ K.

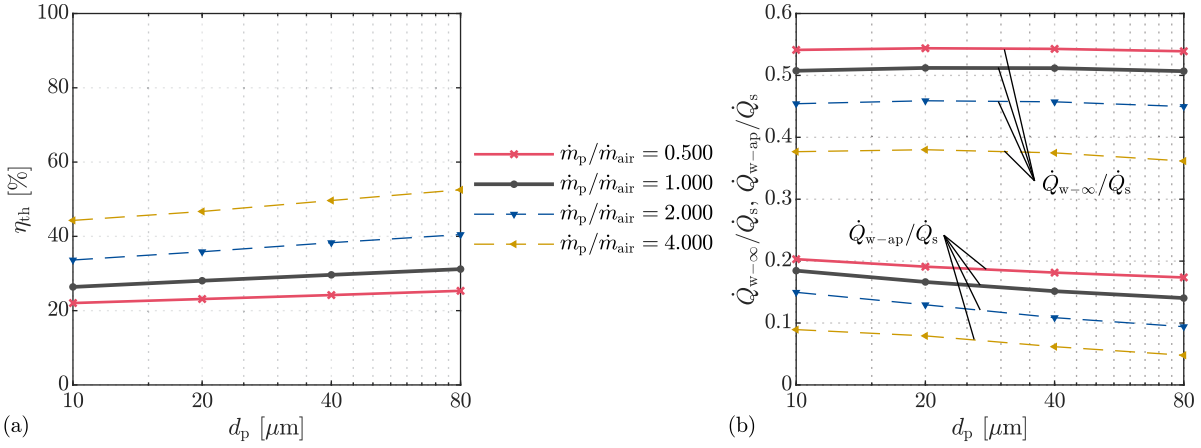

Figure 3.12: The dependence on particle diameter, d_p, of the performance of the SVR with reference case geometry ($D_{ap} = 0.050$ m, $D_{ap}/D_c = 0.516$, $L/D_c = 2.55$, $\alpha = 45°$), for a constant solar thermal input, $\dot{q}_s = 2000\ kW\ m^{-2}$ ($\dot{Q}_s = 3.927$ kW), $\dot{m}_{air} = 4.000 \times 10^{-4}\ kg\ s^{-1}$ and for four different values of mass loading, $\dot{m}_p/\dot{m}_{air}$, with $T_{in} = 300$ K. Presented are **(a)** the receiver thermal efficiency, η_{th}; and **(b)** the relative thermal losses, $\dot{Q}_{w-\infty}/\dot{Q}_s$ and $\dot{Q}_{w-ap}/\dot{Q}_s$. The trends for $\dot{m}_p/\dot{m}_{air} \geq 2$, are presented with dashed lines due to higher levels of uncertainty as noted in assumption 3.

3.3.4 Influence of receiver length

Figure 3.13 presents the axial distributions of temperature of the particle and air phases, together with that of the receiver wall for three receivers of varying length, $L/D_c = 1.0$, 2.5 and 4.0 (where the front entry flow configuration is used and other geometries are those of the reference case). It can be seen that, for each case, the particle phase is heated rapidly in the front sections of the receiver where the incident concentrated solar radiation is most intense. This, in turn, causes the air phase to also heat rapidly. The rate of heating reduces with axial distance. For the case of shortest length, $L/D_c = 1.0$, it can be seen that the particle and air phases reach maximum temperatures towards the rear of the receiver; $T_{p,max} = 2191$ K at $z/L = 0.77$ and $T_{air,max} = 1955$ K at $z/L = 0.85$. Further down-beam (relative to the direction of the concentrated solar radiation input) their temperatures decrease only slightly before exiting with temperatures, $T_{p,out} = 1944$ K and $T_{air,out} = 1936$ K. The corresponding thermal efficiency is, $\eta_{th} = 39.5\%$. In comparison, the position of peak temperature is relatively further upstream for receivers with a greater length, $L/D_c = 2.5$ and 4.0, providing more distance for cooling to a progressively lower exit temperature ($T_{p,max} = 1764$ K at $z/L = 0.36$ for $L/D_c = 2.5$ and $T_{p,max} = 1681$ K at $z/L = 0.22$ for $L/D_c = 4.0$). This means that increasing the cavity length above an optimal has a net effect of increasing heat losses. It can also be observed that, for both $L/D_c = 2.5$ and 4.0, the particle and air phase tend towards equilibrium with the wall in the rear half of the cavity, which is a source of heat loss via conduction and re-radiation. The extent of this heat loss increases with length of the receiver. This is borne out by the values of overall thermal efficiency for the processes: $\eta_{th} = 30.1\%$ and 20.0% for the receivers with $L/D_c = 2.5$ and 4.0, respectively. However, it should be noted that the residence time of the two-phase flow at elevated temperature increases with the length of the SVR. The model therefore provides a means to optimise residence time and conduction heat losses to suit the process. Additional assessments (in the supplementary information, Appendix B) confirm that $T_{p,out}$ and $T_{air,out}$ decrease with increasing receiver length for all values of $\dot{m}_p/\dot{m}_{air}$ considered here. This has the effect of a concurrent decrease in η_{th} with increasing receiver length.

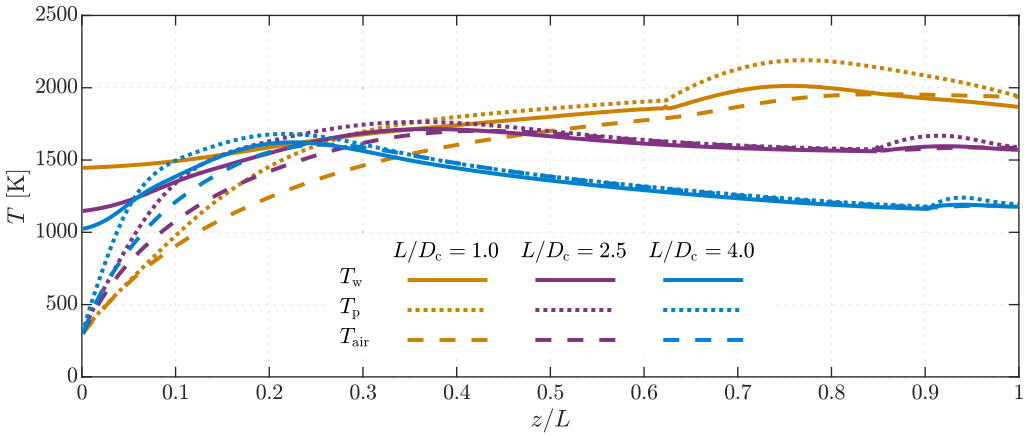

Figure 3.13: Calculated axial temperature distributions of the receiver wall, T_w, the particle phase, T_p, and the air phase, T_{air}, in the SVR with front entry configuration and three different values of length to diameter ratio, L/D_c. Other geometry and operational conditions of the reference case were used: $D_{ap} = 0.050$ m, $D_{ap}/D_c = 0.516$, $\alpha = 45^o$, $\dot{q}_s = 2000\,\mathrm{kW\,m^{-2}}$ ($\dot{Q}_s = 3.927$ kW), $\dot{m}_p/\dot{m}_{air} = 1$, $\dot{m}_p = \dot{m}_{air} = 4.000 \times 10^{-4}\,\mathrm{kg\,s^{-1}}$, $d_p = 40\,\mu$m, $T_{in} = 300$ K.

3.4 Key findings

The first order numerical model developed here to assess the fundamental aspects of heat transfer within a vortex-based solar particle receiver has been found to yield good qualitative and reasonable quantitative agreement with the available experimental data of operation of the device at laboratory-scale under solar simulated conditions. The first order assessment of the sensitivity of thermal performance of the SVR to key geometric and operational parameters revealed the following:

- The particle mass loading of the two-phase flow was found to be important in defining whether the receiver acts primarily as an air-heater or a particle heater. For the case analysed here in which there is no particle recirculation, a critical value of $\dot{m}_{\mathrm{p}}/\dot{m}_{\mathrm{air}} \sim 1$ was found to define the boundary, above which the device acts as a particle heater, and below which it acts as an air heater. However, the critical value may increase for configurations with significant flow recirculation. To maximise the overall efficiency of a system, it will be necessary to consider the recovery of enthalpy from both the particle and air streams.
- The direction of the flow of particles relative to that of the concentrated solar radiation was found to have an important influence on the efficiency. A counter-flow direction tends to increase the efficiency relative to the co-flow direction for high mass loadings, consistent with known trends in other counter-flow heat exchangers. This configuration leads to higher exit temperature, primarily due to reduced conduction losses and particle heating directly before leaving from the front section of the receiver, where the concentrated solar radiation is most intense.
- The ratio of receiver thermal input to heat capacity of the two-phase flow controls the thermal efficiency of the SVR with front entry configuration. This is because the incident solar energy is absorbed by greater mass flow rates, resulting in lower temperatures and reduced thermal losses. However, for the back entry flow configuration and a given ratio of thermal input to total heat capacity of the two-phase flow, efficiency increases with the mass loadings because efficiency is dominated by the heat transfer between the incoming concentrated solar radiation and the particles in the counter-flow arrangement.
- The distribution of temperatures of the particles and walls within the device was found to have an important secondary influence on the radiation losses. A translation of the peak wall temperature toward the back was found to reduce radiation losses through the aperture and so, increase thermal efficiency. This explains why operation with larger particles, which absorb radiation less efficiently and allow the incident concentrated solar radiation to penetrate further into the receiver, thereby shifting peak temperatures towards the rear of the receiver, results in higher efficiency.

- The optimal cavity length is controlled by the balance between increased solar energy absorption and increased conductive losses through the wall. Hence, modelling is needed to optimise the configuration on a case-by-case basis.

4

Particle Residence Time Performance

Typically, analyses of the performance of solar particle receivers assume ideal flow patterns, such as well-stirred or plug flow conditions. Indeed the model developed in the previous chapter of this thesis assumes plug flow, so that the particle residence time is equal to the nominal gas residence time. This is because detailed knowledge of particle residence times within solar particle receivers is unavailable. Therefore, the next performance aspect of vortex-based solar particle receivers presented in detail in this chapter is that of the residence time distributions (RTDs) of particles within such a receiver.

Firstly, this chapter outlines a method that has been developed to measure particle RTDs within an isothermal, laboratory-scale vortex-based solar particle receiver. Also outlined are the details of additional methods, by which the particle RTD is assessed.

Next a joint experimental, numerical and theoretical study of particle residence times in a vortex-based particulate vessel of SEVR configuration is presented. The operating parameters of particle size, gas volumetric flow rate and inlet velocity are systematically varied to assess their influence on the particle RTD and to determine the mechanisms controlling the behaviour of the two-phase flow in the SEVR. This fundamental study is performed with the SEVR oriented with a single receiver tilt angle relevant to beam-down solar concentrating optics.

The material in this study has been submitted to a journal as the following research article:

Davis, D, Troiano, M, Chinnici, A, Saw, WL, Lau, T, Solimene, R, Salatino, P & Nathan, GJ 2019, 'Particle residence time distributions in a vortex-based solar particle receiver-reactor: an experimental, numerical and theoretical study', submitted to *Chemical Engineering Science*.

4. Particle Residence Time Performance

The next part of this chapter presents a systematic assessment of the influence of the receiver tilt angle on the particle RTD within a SEVR of the same configuration. Receiver tilt angles spanning vertically-upward facing to vertically-downward facing are assessed, with two particle sizes and two receiver inlet velocities. This systematic variation enables the identification of the key parameters controlling the particle RTD within the receiver for various receiver tilt angles.

The material in this study has been submitted to a journal as the following research article:

Davis, D, Troiano, M, Chinnici, A, Saw, WL, Lau, T, Solimene, R, Salatino, P & Nathan, GJ 2019, 'Particle residence time distributions in a vortex-based solar particle receiver-reactor: the influence of receiver tilt angle', submitted to *Solar Energy*.

Statement of Authorship

Title of Paper	Particle residence time distributions in a vortex-based solar particle receiver-reactor: an experimental, numerical and theoretical study
Publication Status	☐ Published ☐ Accepted for Publication ☑ Submitted for Publication ☐ Unpublished and Unsubmitted w ork w ritten in manuscript style
Publication Details	Davis, D, Troiano, M, Chinnici, A, Saw, WL, Lau, TCW, Solimene, R, Salatino, P & Nathan, GJ 2019, 'Particle residence time distributions in a vortex-based solar particle receiver-reactor: an experimental, numerical and theoretical study', Manuscript submitted to *Chemical Engineering Science*.

Principal Author

Name of Principal Author (Candidate)	Dominic Davis
Contribution to the Paper	Conducted lit. review into particle RTD measurement techniques. Developed particle RTD measurement techniques used in the investigation. This included procurement of lasers and sensors, as well as construction of the receiver rig and associated tubing. Designed experiments. Identified key parameters to assess. Set up and performed all of the experiments. Interpreted experimental data and incorporated CFD data into the paper's analysis. Incorporated compartment modelling results into the paper's analysis. Wrote and edited the paper. Produced all figures.
Overall percentage (%)	65%
Certification:	This paper reports on original research I conducted during the period of my Higher Degree by Research candidature and is not subject to any obligations or contractual agreements with a third party that would constrain its inclusion in this thesis. I am the primary author of this paper.
Signature	Date 26/2/2019

Co-Author Contributions

By signing the Statement of Authorship, each author certifies that:

i. the candidate's stated contribution to the publication is accurate (as detailed above);

ii. permission is granted for the candidate to include the publication in the thesis; and

iii. the sum of all co-author contributions is equal to 100% less the candidate's stated contribution.

Name of Co-Author	Maurizio Troiano
Contribution to the Paper	Helped to perform experiments. Helped to interpret the experimental data. Processed the experimentally-measured RTDs into dimensionless RTDs and proposed the compartment model to describe the measured RTDs. Provided feedback on analysis of experimental data and provided key input into the compartment modelling analysis of the paper. Edited the manuscript.
Signature	Date: 21/02/2019

Name of Co-Author	Alfonso Chinnici
Contribution to the Paper	Advised on the development of the experimental technique. Developed the CFD model that was used to complement experimental analysis. Provided flow field data used to calculate key dimensionless parameters. Helped to interpret the data and develop the analysis within the paper. Helped to develop the particle trajectory analysis. Provided feedback on the development of the paper Edited the manuscript.
Signature	Date: 25/02/19

Name of Co-Author	Woei Saw
Contribution to the Paper	Supervised the development of the work, particularly the development of the experimental technique. Supervised the construction of the experimental rig and procurement of apparatus. Helped with the interpretation of experimental data. Provided feedback on development of the paper. Edited the manuscript.
Signature	Date: 25/02/2019

Name of Co-Author	Timothy Lau
Contribution to the Paper	Advised on the development of the experimental technique. This included identification of required apparatus and advice on data collection methods. Helped to interpret the experimental data and advised on dimensionless analysis. Provided feedback on development of the paper. Edited the manuscript.
Signature	Date: 25/02/2019

Name of Co-Author	Roberto Solimene
Contribution to the Paper	Provided key input into the compartment modelling analysis of the paper. Provided critical input into the interpretation of data. Provided feedback on the development of the paper.
Signature	Date: 21/02/2019

Name of Co-Author	Piero Salatino
Contribution to the Paper	Provided key input into the compartment modelling analysis of the paper and the proposal of the compartment model configuration. Provided feedback on the analysis of the paper.
Signature	Date: 21/02/2019

Name of Co-Author	Graham 'Gus' Nathan
Contribution to the Paper	Supervised the development of work, including the identification of the need for residence time measurements. Advised on the development of the experimental technique. Helped to develop the dimensionless analysis of controlling parameters. Helped to structure the paper and provided significant feedback on the development of the paper. Edited the whole manuscript.
Signature	Date: 25/2/2019

Statement of Authorship

Title of Paper	Particle residence time distributions in a vortex-based solar particle receiver-reactor: the influence of receiver tilt angle
Publication Status	☐ Published ☐ Accepted for Publication ☑ Submitted for Publication ☐ Unpublished and Unsubmitted w ork w ritten in manuscript style
Publication Details	Davis, D, Troiano, M, Chinnici, A, Saw, WL, Lau, TCW, Solimene, R, Salatino, P & Nathan, GJ 2019, 'Particle residence time distributions in a vortex-based solar particle receiver-reactor: the influence of receiver tilt angle', Manuscript submitted to *Solar Energy*.

Principal Author

Name of Principal Author (Candidate)	Dominic Davis
Contribution to the Paper	Conducted lit. review into influence of receiver tilt angle on particle RTDs. Developed particle RTD measurement technique further to enable the assessment of the influence of receiver orientation. Constructed additional apparatus to change the orientation of the rig. Designed experiments and identified key parameters to assess. Set up and performed all of the experiments. Interpreted experimental data. Incorporated compartment modelling results into the paper's analysis. Developed scale-up analysis. Wrote and edited the paper. Produced all figures.
Overall percentage (%)	65%
Certification:	This paper reports on original research I conducted during the period of my Higher Degree by Research candidature and is not subject to any obligations or contractual agreements with a third party that would constrain its inclusion in this thesis. I am the primary author of this paper.
Signature	Date 26/2/2019

Co-Author Contributions

By signing the Statement of Authorship, each author certifies that:

i. the candidate's stated contribution to the publication is accurate (as detailed above);

ii. permission is granted for the candidate to include the publication in the thesis; and

iii. the sum of all co-author contributions is equal to 100% less the candidate's stated contribution.

Name of Co-Author	Maurizio Troiano
Contribution to the Paper	Performed all experiments with Dominic. Helped to interpret the experimental data. Processed the experimentally-measured RTDs into dimensionless RTDs and proposed modifications to the previous compartment model to describe the influence of receiver orientation. Provided feedback on analysis of experimental data and provided key input into the compartment modelling analysis of the paper. Edited the manuscript.
Signature	Date: 21/02/2019

Name of Co-Author	Alfonso Chinnici
Contribution to the Paper	Supervised the experiment design. This included identifying the parameters/cases to be assessed. Helped to interpret the data and develop the analysis within the paper. Provided feedback on the development of the paper. Edited the manuscript.
Signature	Date: 25/02/19

Name of Co-Author	Woei Saw
Contribution to the Paper	Supervised the development of the work, particularly identification of parameters/cases to assess. Supervised the construction of the experimental rig and procurement of apparatus. Helped with the interpretation of experimental data. Provided feedback on development of the paper. Edited the manuscript.
Signature	Date: 25/02/2019.

Name of Co-Author	Timothy Lau
Contribution to the Paper	Helped to interpret the experimental data and advised on dimensionless analysis. Provided feedback on development of the paper, particularly the written explanation of the dimensionless analysis. Edited the manuscript.
Signature	Date: 25/02/2019

Name of Co-Author	Roberto Solimene
Contribution to the Paper	Provided key input into the compartment modelling analysis of the paper. Provided input into the interpretation of data. Provided feedback on the development of the paper.
Signature	Date 21/02/2019

Name of Co-Author	Piero Salatino
Contribution to the Paper	Provided key input into the compartment modelling analysis of the paper and the proposal of the compartment model configuration. Provided feedback on the analysis of the paper.
Signature	Date 21/02/2019

Name of Co-Author	Graham 'Gus' Nathan
Contribution to the Paper	Supervised the development of work, including the need for assessment of the influence of tilt angle on particle residence time. Helped to develop analysis of experimental results. Advised on the scale-up analysis. Helped to structure the paper and provided significant feedback on the development of the paper. Edited the whole manuscript.
Signature	Date 25/2/2019

4.1 Residence time distribution measurement

The particle residence time distribution within the vortex-based solar particle receiver – of Solar Expanding Vortex Receiver (SEVR) configuration – was measured by injecting a short pulse of particles, the concentration of which was directly measured at the inlet to and outlet from the SEVR cavity following the well-established tracer pulse response method described by Levenspiel (1999) and Fogler (2006). Here, the particle phase acts both as the tracer and the medium being traced, as the pulse of particles is injected into an empty vessel. This is considered valid because the SEVR operates with a very small particle inventory inside the vessel. That is, the particle-to-air volume fraction is $< 10^{-4}$, so that the particle phase has negligible effect on the flow field of the gas phase, as has been the case in previous assessments of vortex-based solar particle receiver operation. The recorded concentration of the pulse of particles can therefore be considered to be representative of the particle behaviour for steady state operation of the SEVR with small particle hold-up and limited two-way coupling between particle and gas phases (Elghobashi 1994).

The inlet and outlet concentration of particles was measured with time-resolved laser extinction measurements. This is a non-disruptive tracer measurement technique, based on the attenuation of a monochromatic electromagnetic wave transmitted through the particulate medium and is applicable to the measurement of dilute phase gas-solid flows (Yong 1996). Furthermore, the SEVR cavity had well-defined, closed boundary conditions, as the flow in the inlet and outlet tubes was fast compared to mean flow velocities within the chamber and could therefore be assumed to be plug flow.

For a particulate system operating at steady state, the outlet concentration of particles is said to be the convolution of the inlet concentration with the residence time distribution (RTD). The convolution integral introduced by Danckwerts (1953) is:

$$o(t) = i(t) * E(t) = \int_0^t i(t - t')E(t')dt', \tag{4.1}$$

where $i(t)$ and $o(t)$ are the inlet and outlet particle concentration measurements with time, and $E(t)$ is the residence time distribution of particles within the receiver, or the exit age distribution, following Danckwerts (1953). For the case in which the injection pulse approaches a perfect Dirac delta function, the recorded outlet concentration of particles is a direct measure of the particle RTD, $E(t)$. However, since the injection pulse is rarely a true delta function, it is necessary to deconvolve Equation (4.1) to determine $E(t)$ (Gao et al. 2012), as has been done previously (Trachsel et al. 2005; Essadki et al. 2011). For the present investigation, this was accomplished by converting the recorded signals to the Fourier domain with a fast Fourier transform (Viitanen 1997), and using a regularisation factor to solve the ill-posed problem in the frequency domain (Mills & Dudukoviḱ 1989). The present analysis of RTD ignores any influence of particle deposition onto the walls of

the vessel. This was justified on the basis of observations that any deposition onto the walls was small.

Due to the stochastic distribution of particles as a discrete phase within the two-phase gas-particle flow, the extinction signal fluctuates with time. These fluctuations were reduced by averaging the $E(t)$ calculated from 12 repeated measurements, each normalised by the area bounded by the distribution, giving $\int_0^\infty E(t)dt = 1$. This number was found to result in a profile that converged closely to that from 40 repeated measurements, particularly for the measurement of mean particle residence time, which was found to be independent of the number of averaged repetitions for 12 or more repetitions. In calculating the statistical particle residence time parameters (mean, 90th percentile and normalised variance) from the RTDs averaged from an increasing number of repetitions between 12 and 40, it was found that the values deviated from the average by a maximum of 1.2%. It can therefore be said that the statistical parameters characterising the particle RTDs presented here have an approximate relative error of 1.2%.

These experiments were conducted with isothermal flow conditions and with particles and gas at room temperature.

4.1.1 Experimental arrangement

Figure 4.1 presents the experimental arrangement used to determine the particle RTD within the SEVR cavity.

The particle feeding subsystem consisted of two air lines connected in parallel. Prior to each measurement, 0.3 g of particles was loaded into the particle basket connected to the secondary feeder air line with the valve closed. Steady state vortex flow conditions within the cavity were then established by introducing equal amounts of compressed air (with flow rate controlled by electronic mass flow controllers) to the two tangential inlets, through the primary feeder air line and the second tangential inlet. To inject a pulse of particles, the valve connected to the particle basket was opened such that air flowed through both feeder air lines without disrupting the total amount of air injected into the receiver cavity. The increase in total inlet mass flow rate due to the injection of a pulse of particles is estimated to be a maximum of 22% for the maximum duration of 0.5 s. It can therefore be assumed that the vortex flow closely approximates a steady state condition for the duration of measurement (60 s).

Extinction measurements were carried out with the use of a 4.5 mW, 635 nm collimated laser diode (*Thorlabs* CPS635S) and a photodetector (*Thorlabs* DET36A/M). The laser and photodetector were mounted perpendicular to the centre axis of the inlet and outlet tubes, as shown in Figure 4.1, so that the translation of particles through the beam causes an attenuation in the signal. Laser light levels

were recorded with the photodetector with a sampling frequency of 10 kHz and for a total time of 60 seconds for each measurement repetition. The inlet/outlet concentration measurements were corrected for the flow time, $t_{\text{correction}}$, between the true inlet/outlet and the measurement position, $L_{\text{correction}}$, by assuming plug flow ($t_{\text{correction}} = L_{\text{correction}} A_{\text{in/out}} / \dot{V}_{\text{air}}$).

For the experiments reported in Section §4.2, the receiver cavity of SEVR configuration was oriented vertically, as shown in Figure 4.1, with the inlet and conical section at the bottom, such that the axis of the cavity is aligned with gravity. This corresponds to the simplest flow configuration, since it avoids a gravity bias that may cause particles to settle on the wall, whilst also being relevant to the 'beam down' configuration. Other orientations are considered in Section §4.3.

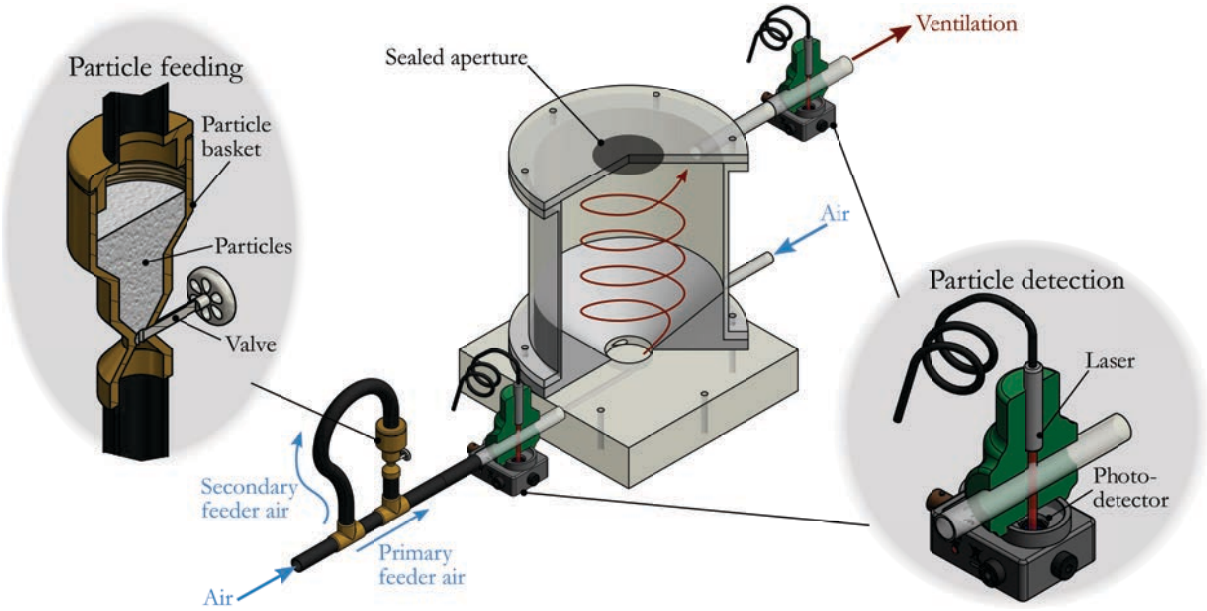

Figure 4.1: Experimental arrangement used to determine the residence time distribution of particles within a vortex-based solar particle receiver vessel. Shown are the particle feeding and detection subsystems, as well as the receiver cavity which features two tangentially-oriented inlets and a single radially-oriented outlet.

Figure 4.2, together with Table 4.1a, presents the geometry of the receiver, which was fabricated from acrylic and ABS plastics. This configuration maintains geometric similarity with that used in previous investigations of the SEVR (Chinnici et al. 2015; Chinnici et al. 2016). The following analysis refers to a cylindrical coordinate system as shown in Figure 4.2 with an origin at the centre of the base disc so that gravity acts in the negative z direction. Also shown are the zones in the receiver, at which key dimensionless parameters are evaluated.

Table 4.1b presents the range of operational parameters that were varied in the present work, namely the air volumetric flow rate, air inlet velocity and particle size. To isolate the influence of particle size on the RTD, spherical polymer particles ($\rho_p = 1200\,\mathrm{kg/m^3}$) with a narrow size distribution were used, following Lau & Nathan (2016). Figure 4.3 presents the particle size distributions, whose mean values are $\bar{d}_p = 80$, 40 and 20 µm. Although these polymer particles are not suitable for use in on-sun operation of a solar receiver, the measured residence time characteristics of the present particles can be related to those of particles that are commonly used in solar receivers (e.g. ceramic particles of alternative sizes) by matching the relevant dimensionless parameters.

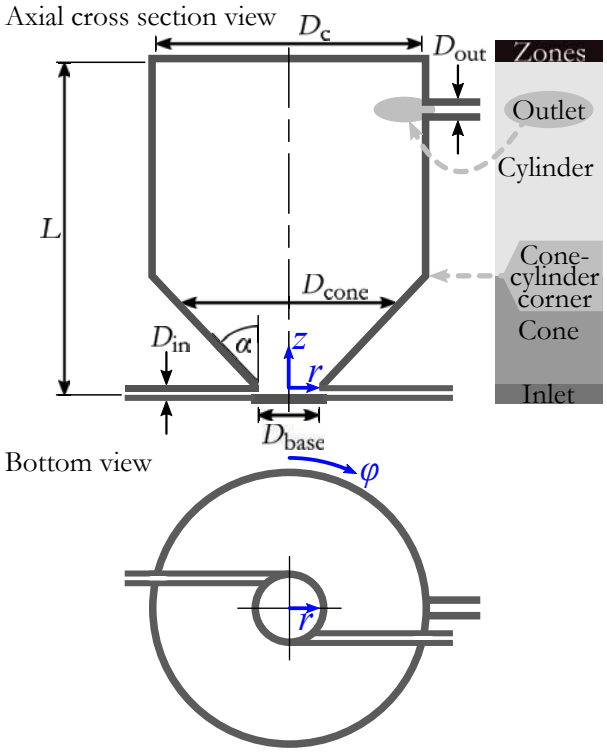

Figure 4.2: Schematic diagram of the SEVR showing the cylindrical coordinate system (r,φ,z) with origin at the centre of the base disc, together with key geometric dimensions, two inlets and one outlet. Also shown are the zones in the receiver, at which key dimensionless parameters are evaluated.

Table 4.1: (a) Values of the key dimensions of the SEVR; and **(b)** the range of input parameters systematically varied in the experiments reported in Section §4.2

(a)		(b)	
D_c	190 mm	d_p	20, 40, 80 µm
L	237.5 mm	$\dot{V}_{air}$	60 – 150 slpm
D_{base}	47.5 mm	U_{in}	16.2 – 51.8 m s^{-1}
D_{cone}	47.5 – 190 mm		
α	50°		
D_{in}	5, 6 and 7.5 mm		
D_{out}	11 mm		

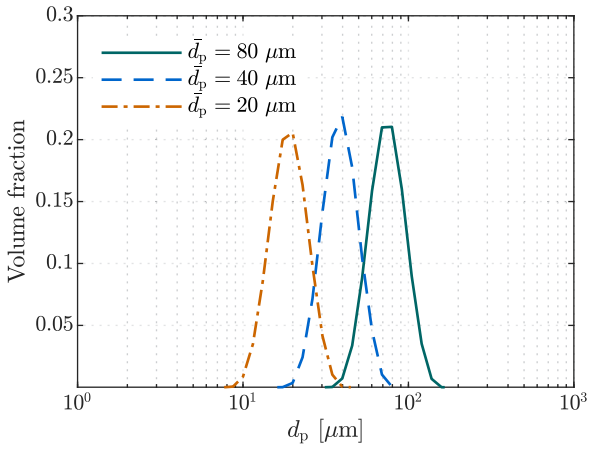

Figure 4.3: Particle size distributions of the spherical polymer particles used to measure the particle RTD in the SEVR.

4.1.2 Characterisation of the residence time distribution

The particle RTDs measured here, $E(t)$, are reported in terms of probability density functions, which can be characterised by the mean particle residence time, $\bar{\tau}_{\mathrm{p}}$, the 90th percentile particle residence time, $\tau_{\mathrm{p},90}$, and the normalised variance, ${\sigma_{\mathrm{p}}}^2 = {\sigma_{\mathrm{p},t}}^2/{\bar{\tau}_{\mathrm{p}}}^2$. These parameters are calculated as follows:

$$\bar{\tau}_{\mathrm{p}} = \int_0^{\infty} tE(t)dt, \tag{4.2}$$

$$\int_0^{\tau_{\mathrm{p},90}} E(t)dt = 0.90, \tag{4.3}$$

$${\sigma_{\mathrm{p},t}}^2 = \int_0^{\infty} \left(t - \bar{\tau}_{\mathrm{p}}\right)^2 E(t)dt. \tag{4.4}$$

The statistical parameters in Equations (4.2), (4.3) and (4.4) were calculated from curves fitted to the experimental $E(t)$ curves, with coefficient of determination values, $R^2 > 0.97$, following Buffham & Mason (1993), to mitigate the effect of measurement noise at large t.

To compare experimental RTD curves with theoretical models, it is useful to derive the normalised expression of $E(t)$ as:

$$E(\theta) = \bar{\tau}_{\mathrm{p}} E(t), \tag{4.5}$$

where $\theta = t/\bar{\tau}_{\mathrm{p}}$ is the dimensionless time term. These dimensionless terms are used in the application of generalised ideal reactor compartment models (PFRs and CSTRs) to the experimentally measured RTDs of the present investigation.

4.1.3 CFD modelling of the vortex-based solar particle receiver operation

To complement the analysis of the experimental measurements of particle RTDs in the SEVR a three-dimensional computational fluid dynamics (CFD) model was used to calculate numerical estimates of key velocity and length scales of the two-phase vortex flow within the SEVR. The model builds on previous work in which the model was validated against measurements of the gas flow field and particle deposition onto a window through the aperture (Chinnici et al. 2016; Chinnici et al. 2017). Further validation of the CFD model is provided here because of slight differences to the geometric configuration and inflow conditions of the present investigation.

The commercial CFD code ANSYS/FLUENT 17.2 was again used to simulate the turbulent fluid flows and to track the particles in the SEVR, using the Reynolds-Averaged Navier-Stokes (RANS) approach. The operating conditions, working fluid and receiver geometry were the same as those of the experimental procedure. The 3-D geometry was built in Gambit and a non-uniform unstructured (tetrahedral) grid was generated with ANSYS/Meshing 17.2. A total of ∼2.5 million cells were employed for all configurations tested. The mesh independence was checked on a coarser mesh (1 million cells) and a finer mesh (4 million cells). The mesh quality was checked to ensure suitability based on aspect ratio, orthogonality, skewness, and expansion factor, according to Tian et al. (2015).

The RNG k-ε model (with swirl factor) was selected as the turbulence closure model, this being a validated model for the prediction of the vortex structure within SEVR configurations similar to those investigated here (Chinnici et al. 2015; Chinnici et al. 2016; Chinnici et al. 2017), while also being a preferred closure model for the flows within a vortex device (Syred 2006). The Discrete Phase Model (DPM) was implemented to calculate the fluid flow fields, particle trajectories and residence time distributions, following previous work (Shilapuram et al. 2011; Chinnici et al. 2015; Chinnici et al. 2016).

For each operational case being simulated, the surface injection option in Fluent was used to inject monodisperse spherical particles with diameters $d_p = 20$, 40 or 80 µm into the modelled domain with a constant volume fraction of 2×10^{-5} corresponding to an inlet particle mass loading of 0.033. The circular tangential inlet was used as the injection surface that has a constant mesh density, which lead to a constant number of particle parcel injection points. The dispersion of the particles due to turbulence in the continuous gas phase was calculated using a stochastic tracking model with a discrete random walk that includes the effects of instantaneous turbulent velocity fluctuations on particle trajectories. Each injected particle parcel was tracked by the solver 20 times. The values of the Integral Time Scale parameter of the particle dispersion model used here, which is proportional to the particle dispersion rate (Marchioli et al. 2006), were calculated based on the average calculated values of k and ε within the receiver (ANSYS Inc. 2012). The effect of gravity (acting in the negative

z-direction) was included in the simulations. All the simulations were performed with 32 cores on the Phoenix supercomputer facilities of the University of Adelaide. The CPU-time required to achieve the desired convergence (when all the residuals reached 1×10^{-6}) was ∼100 CPU-hr.

The model was validated previously against measurements of the gas flow field for similar configurations (Chinnici et al. 2016; Chinnici et al. 2017), while additional validation from the present measurements is reported below. Table 4.2 presents a comparison between the experimentally-measured and numerically-predicted particle RTDs in terms of the mean and 90th percentile particle residence times, $\bar{\tau}_{\mathrm{p}}$ and $\tau_{\mathrm{p},90}$, for four validation cases. The operational details of these validation cases include air volumetric flow rates $\dot{V}_{\mathrm{air}} = 104$ and 140 slpm and two particle sizes $d_{\mathrm{p}} = 20$ and 80 µm. These values of $\dot{V}_{\mathrm{air}}$ generate inlet velocities $U_{\mathrm{in}} = 30.7$ and 41.3 m s^{-1} and nominal residence times $\tau_{\mathrm{nom}} = V_{\mathrm{r}} / \dot{V}_{\mathrm{air}} = 3.2$ and 2.4 s (with constant inlet diameter, $D_{\mathrm{in}} = 6$ mm). The model yields an average error of 12% for $\bar{\tau}_{\mathrm{p}}$ and 14% for $\tau_{\mathrm{p},90}$, when compared with the equivalent experimental measurements. This validation of the particle residence time characteristics of the CFD model, together with previous validation of the gas flow field predictions of the CFD model, imply that it is reasonable for the CFD model to be used in the present investigation to estimate key length and velocity scales used in calculating the Stokes and Froude numbers. Although there are limitations in the accuracy of the CFD model and the dimensionless parameter estimations (in Section §4.1.4) based on the flow field predictions, the residence time trends presented in this chapter as a function of the key dimensionless parameters are expected to be reliable. Additionally, the validation of the CFD model is reasonable enough for it to be used for qualitative assessments of particle trajectories within the SEVR, to complement analysis of the experimental results and compartment modelling.

Figure 4.4 presents the axial, u_z, tangential, u_φ, and radial, u_r, components of the calculated mean air velocity profiles, normalised by the inlet velocity, U_{in}, at four axial cross-sections through the receiver for a value of $\dot{V}_{\mathrm{air}} = 104$ slpm and $D_{\mathrm{in}} = 6$ mm, as calculated with the CFD model. It can be seen that the SEVR generates a well-defined vortex structure, as has been reported for the SEVR device previously (Chinnici et al. 2015; Chinnici et al. 2016). Key features of the vortex flow are that the vortex intensity is inversely proportional to the distance from the inlet. That is, there is a high swirl intensity in the conical section of the receiver, which transitions to a relatively low swirl intensity in the upper cylindrical part of the receiver. Furthermore, it should be noted that a reversed flow is generated in the core region of the vortex. Further details of the gas flow field generated within the SEVR can be found in previous publications (Chinnici et al. 2015; Chinnici et al. 2016; Chinnici et al. 2017).

Table 4.2: Comparison of the experimentally measured and numerically simulated values of $\bar{\tau}_p$ and $\tau_{p,90}$, for four different operational cases and for a fixed inlet jet diameter ($D_{in} = 6$ mm).

Validation case	Operational details		Experimental result		Numerical result		Relative difference[a]	
	τ_{nom} [s]	d_p [µm]	$\bar{\tau}_p$ [s]	$\tau_{p,90}$ [s]	$\bar{\tau}_p$ [s]	$\tau_{p,90}$ [s]	$\bar{\tau}_p$ [s]	$\tau_{p,90}$ [s]
1	2.4	80	2.23	4.35	2.40	4.93	7.6%	13.3%
2	3.2	80	5.83	13.34	7.00	16.10	20.1%	20.7%
3	2.4	20	1.72	3.56	2.00	4.15	16.3%	16.6%
4	3.2	20	3.19	6.77	3.05	6.41	4.4%	5.3%

[a] Calculated as the absolute relative difference: $\left|\tau_{p,numerical} - \tau_{p,experimental}\right| / \tau_{p,experimental}$.

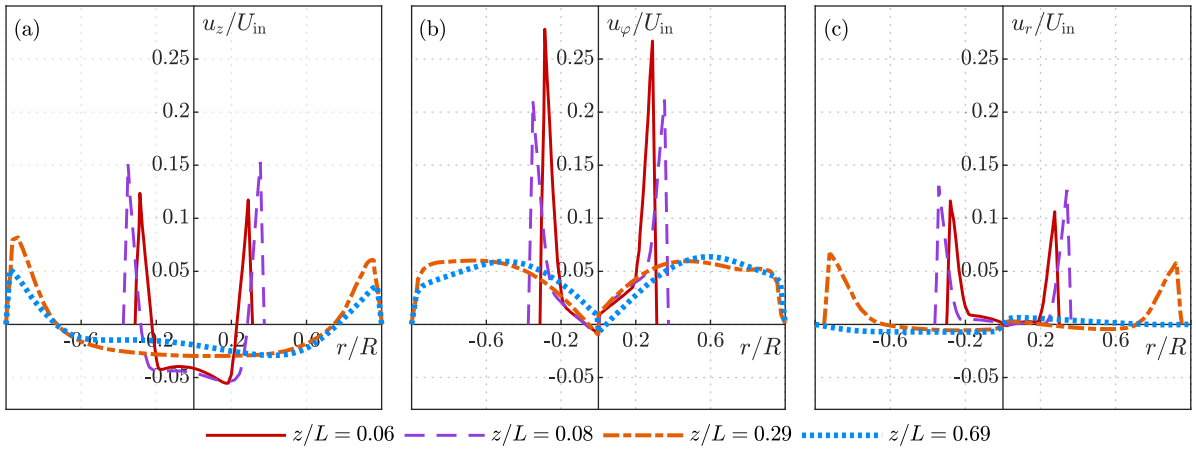

Figure 4.4: Mean air velocity profiles, as calculated with CFD, of the **(a)** axial, u_z, **(b)** tangential, u_ϕ, and **(c)** radial, u_r, components, normalised by the inlet velocity, U_{in}, at four axial cross-sections through the receiver for a value of $\dot{V}_{air} = 104$ slpm and $D_{in} = 6$ mm.

4.1.4 Key dimensionless parameters

The key dimensionless parameters influencing the isothermal multi-phase flow within the SVR are the Reynolds number, *Re*, the Stokes number, *Sk*, and the Froude number, *Fr*. The air flow rates have been chosen to ensure that the inlet jet (with constant inlet jet diameter) is always in the turbulent regime ($Re_{\text{in}} = \rho_{\text{air}} U_{\text{in}} D_{\text{in}} / \mu_{\text{air}} > 8000$). This ensures relevance to industrial scale operation of the device. However, the Stokes and Froude numbers are systematically varied.

The Stokes number, which characterises how closely a particle will follow the gas streamlines through the receiver, is calculated for a given particle size at a given zone in the chamber as follows:

$$Sk = \frac{\rho_{\text{p}} d_{\text{p}}^2 U_{\text{f}}}{18 \mu_{\text{air}} D_{\text{f}}}, \tag{4.6}$$

where ρ_{p} is the particle density, d_{p} is the particle diameter, μ_{air} is the air dynamic viscosity, U_{f} is the characteristic fluid velocity scale of the flow at a given zone in the chamber and D_{f}, is the characteristic fluid length scale of the flow at a given zone in the chamber. These zones (shown in Figure 4.2) are the inlet flow, the conical and the cylindrical sections of the receiver, the corner at the cone-cylinder intersection, and the outlet flow, of which the corresponding U_f and D_f, values are presented in Table 4.3. The characteristic velocities within the receiver are taken to be the maximum tangential velocity of the air flow field, $u_{\varphi,\text{max}}$ in the z/L plane, as calculated with CFD (and shown in Figure 4.4), while the characteristic length scales are taken to be the receiver diameter at the relevant z/L plane. For the Stokes number evaluated at the receiver outlet, the nominal outlet velocity was used, while the characteristic length scale was taken to be two times the outlet diameter. The outlet flow, at which point the vortex flow contracts to exit the receiver, features a range of velocity and length scales. However, for simplicity an average length scale of $2D_{\text{out}}$ is used to evaluate the Stokes number at the outlet, based on estimates of the gas flow field with the CFD model. Likewise, the flow tends towards the nominal outlet velocity, $U_{\text{out}} = \dot{V}_{\text{air}} / A_{\text{out}}$, so this is the single value used to evaluate Sk_{out}. Although the exact calculated values of Sk_{out} will differ from those of the actual flow, the residence time trends presented as a function of Sk_{out} are expected to be reliable.

The Froude number characterises the relative importance of the inertial centrifugal force ($F_{\text{cent}} = m_{\text{p}} U_{\varphi}^2 / R$) acting on a particle due to the circular motion of the two-phase vortex flow compared with that of the external gravitational field ($F_g = m_{\text{p}} g$). The Froude number is calculated at a given zone in the chamber as the ratio of these two forces, according to:

$$Fr = \frac{U_{\varphi}^2}{gR} \tag{4.7}$$

where g is the standard acceleration due to gravity, U_{φ} is the characteristic tangential velocity of the flow at a given zone in the chamber and R is the characteristic radius of the circular motion of

the two-phase flow at a given zone in the chamber. The zones (shown in Figure 4.2), for which the Froude number is evaluated, are the conical and the cylindrical sections of the receiver, together with the corner at the cone-cylinder intersection. The values of U_φ and R used in each of these zones are presented in Table 4.3. For simplicity, the Froude numbers presented here are considered to be independent of particle size. This is because U_φ is estimated from the air flow field only without accounting for the slip between the particles and the air phase. This implies that the Froude numbers overestimate slightly the influence of inertial forces because the tangential velocity of the particles will be less than that of the air phase. This overestimate is greatest for larger particles, due to their greater amount of slip, and is estimated from CFD to be approximately $u_{p,\varphi} \sim 0.8u_\varphi$. That is, *Fr* is over-estimated by up to 36% by ignoring the slip velocity in Equation (4.7). Nevertheless, the relative trends in *Fr* are expected to be reliable.

Table 4.3: The characteristic velocity and length scales used to evaluate the Stokes and Froude numbers in various zones of the receiver in the present study. The location of these zones within the receiver are shown in Figure 4.2.

Zone	*Sk*		*Fr*	
	Velocity, U_f	Length, D_f	Velocity, U_φ	Length, R
Inlet ($z/L = 0$ – 0.04)	$U_\mathrm{in} = \dot{V}_\mathrm{air}\,/2A_\mathrm{in}$	D_base	-	-
Cone ($z/L = 0.04$ – 0.29)	$u_{\varphi,\mathrm{max}}$ in z/L plane (estimated with CFD)	D_cone	$u_{\varphi,\mathrm{max}}$ in z/L plane (estimated with CFD)	$D_\mathrm{cone}\,/2$
Cone-cylinder corner ($z/L = 0.29$)	$u_{\varphi,\mathrm{max}}$ in z/L plane (estimated with CFD)	D_c	$u_{\varphi,\mathrm{max}}$ in z/L plane (estimated with CFD)	$D_\mathrm{c}\,/2$
Cylinder ($z/L = 0.29$ – 1)	$u_{\varphi,\mathrm{max}}$ in z/L plane (estimated with CFD)	D_c	$u_{\varphi,\mathrm{max}}$ in z/L plane (estimated with CFD)	$D_\mathrm{c}\,/2$
Outlet ($z/L = 0.85$)	$U_\mathrm{out} = \dot{V}_\mathrm{air}\,/A_\mathrm{out}$	$2D_\mathrm{out}$	-	-

4.2 Fundamental study of SEVR in beam-down orientation

4.2.1 Measurements of the particle RTD

Figure 4.5 presents four measured particle RTDs within the SEVR for particle diameter $d_p = 80\,\mu m$ and inlet velocities in the range $U_{in} = 25.4 - 41.3\,m\,s^{-1}$ with constant inlet diameter, $D_{in} = 6\,mm$, so that $U_{in} = \dot{V}_{air} / \left[2 \times (\pi/4) \times {D_{in}}^2\right]$. The corresponding nominal air residence times are in the range $\tau_{nom} = V_r / \dot{V}_{air} = 2.4 - 3.9\,s$. The distributions have been smoothed for clarity with a moving point average spanning 0.125 s of measured data. Each RTD curve can be described qualitatively to rise quickly to a maximum within 2 seconds of residence time and then to decrease more slowly. For each case also, a significant proportion of particles have a residence time much longer than the peak value. That is, the distributions are positively skewed. The slope of the initial increase to a maximum $E(t)$ value increases with U_{in} (and lower τ_{nom}), while the length of the tail of the distribution increases with lower U_{in} (and higher τ_{nom}), suggesting significant particle recirculation within the SEVR, particularly for lower flow rates and inlet velocities. It can additionally be noted that the U_{in} has a similar influence on the particle RTD in the SEVR to that of the superficial gas velocity in the riser of a square cross-section fluidised bed, whose particle RTDs bear a resemblance to those of the SEVR (Harris et al. 2003).

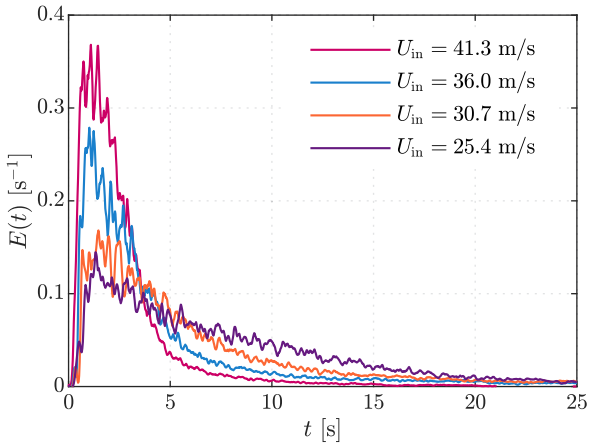

Figure 4.5: Measured particle RTDs in the SEVR for particle diameter $d_p = 80\,\mu m$ and inlet velocities in the range $U_{in} = 25.4 - 41.3\,m\,s^{-1}$ with constant inlet diameter, $D_{in} = 6\,mm$, so that $U_{in} = \dot{V}_{air} / \left[2 \times (\pi/4) \times {D_{in}}^2\right]$. The corresponding nominal air residence times are in the range $\tau_{nom} = V_r / \dot{V}_{air} = 2.4 - 3.9\,s$. The distributions have been smoothed for clarity with a moving point average spanning 0.125 s of measured data.

Figure 4.6 presents the measured particle RTDs in the SEVR for three values of outlet Stokes number, Sk_{out}, and two values of inlet velocity $U_{in} = 30.7$ and 41.3 m s^{-1}, each for the case of a constant inlet diameter, $D_{in} = 6$ mm. It can be seen that, for a given inlet velocity, the values of Sk_{out} scale with $d_p{}^2$ (here, $d_p = 20$, 40 and 80 µm), while, for a given particle size, Sk_{out} scales with U_{in}, according to Equation (4.6) and Table 4.3. For $U_{in} = 30.7$ m s^{-1} (Figure 4.6a) it can be seen that an increase in Sk_{out} causes both a shift in the RTD to longer residence times and a broadening of the distribution. Quantitatively, the increase in Sk_{out} from 1.21 to 19.44 results in an increase in $\bar{\tau}_p$ from 2.59 to 6.46 s and an increase in $\tau_{p,90}$ from 5.50 to 15.17 s.

Figure 4.6b presents the case with higher inlet velocity ($U_{in} = 41.3$ m s^{-1}). It can be seen that the particle residence times are, on average, shorter than the lower velocity case (Figure 4.6a) and also that Sk_{out} has a weaker effect on the RTD. That is, the RTDs measured with the three values of d_p are more similar to each other for $U_{in} = 41.3$ m s^{-1} than is the case for $U_{in} = 30.7$ m s^{-1}. More specifically, an increase in Sk_{out} from 1.64 to 26.16 only increases $\bar{\tau}_p$ from 1.75 to 2.21 s and $\tau_{p,90}$ from 3.52 to 4.21 s.

Table 4.4 presents the Stokes and Froude numbers of the two-phase flow within the SEVR, as calculated with the length and velocity scales presented in Table 4.3, for three particle diameters, $d_p = 20$, 40 and 80 µm, and the two values of inlet velocity presented in Figure 4.6, $U_{in} = 30.7$ and 41.3 m s^{-1}. These are all evaluated in the five zones of the receiver: the inlet, the cone, the corner at the cone-cylinder intersection, the cylinder section and the receiver outlet (shown in Figure 4.2). It can be seen for $U_{in} = 30.7$ m s^{-1} (Table 4.4a), that the Stokes numbers for $d_p = 20$ µm are < 1 through the conical and cylindrical sections of the receiver, indicating that the particles approach being flow-tracers. In contrast, for $d_p = 80$ µm, $Sk_{cone} > 1$ in the lower regions of the cone but $Sk_{cyl} < 1$ in the cylindrical section. This implies that the larger particles will be preferentially distributed toward the wall in the cone but will become more uniformly distributed in the cylindrical section. At the receiver outlet, the larger particles have $Sk_{out} \gg 1$ so that they tend not to follow the fluid through the strong gradients associated with the radial exit, but rather to be preferentially retained within the receiver. In contrast, the small particles with lower Sk_{out} will be more likely to leave with the fluid. This highlights the importance of the outlet Stokes number in controlling the particle residence time, as is shown in Figure 4.6a and has previously been hypothesised by Chinnici et al. (2015).

It can also be seen, for the case of $U_{in} = 30.7$ m s^{-1} (Table 4.4a), that the Froude number of the vortex flow decreases from $Fr_{cone} = 299.5$ in the conical section of the receiver to $Fr_{corner} = 3.6$ and $Fr_{cyl} = 3.8$ at the cone-cylinder corner and in the cylindrical section of the receiver, respectively. This indicates that the flow transitions from being highly dominated by the inertial centrifugal force as the vortex is introduced at the bottom of the cone to a flow regime in which the external gravitational field plays a more significant role as the flow undergoes an expansion through the cone. This expansion

causes the air tangential velocity at the cone-cylinder corner and in the cylindrical section to be relatively low ($\sim$2 m s^{-1}) and implies that the SEVR operates with relatively low swirl compared with other swirl devices such as a cyclone particle separator (Hoffmann & Stein 2007).

Table 4.4b shows that, for $U_{in} = 41.3$ m s^{-1}, particles exhibit higher Stokes numbers than those of the lower velocity case. However, despite the increase in Stokes numbers through the receiver for each of the particle sizes, the increase in U_{in} from 30.7 to 41.3 m s^{-1} causes each of the RTDs presented in Figure 4.6b to be shifted to shorter residence times, as compared with those presented in Figure 4.6a. Furthermore, for constant $U_{in} = 41.3$ m s^{-1}, the increase in Sk_{out} from 1.64 to 26.16 – an increase by the same factor as that shown in Figure 4.6a – has a significantly weaker influence on the residence time than that of the lower velocity case. This case of higher inlet velocity corresponds to increased Froude numbers at the cone-cylinder corner and in the cylinder, $Fr_{corner} = 6.6$ and $Fr_{cyl} = 6.9$. The increase by a factor of 1.8 relative to the lower velocity case indicates a significantly increased importance of the centrifugal inertial force in the cylindrical section of the receiver relative to that of external gravitational field. These results show that residence time depends in a complex way not only on Stokes number, which scales non-linearly with d_p^2, but also on Froude number, which scales non-linearly with U_{in}^2.

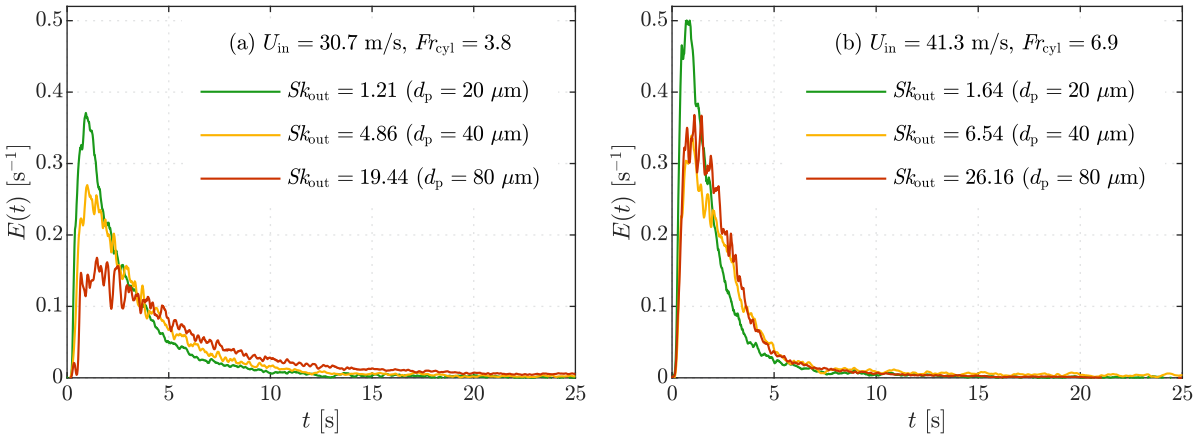

Figure 4.6: Measured particle RTDs in the SEVR for three values of Sk_{out} (three particle diameters, d_p = 20, 40 and 80 µm), with constant inlet diameter, $D_{in} = 6$ mm, and two values of inlet velocity and Froude number: **(a)** $U_{in} = 30.7$ m s^{-1}, $Fr_{cyl} = 3.8$; and **(b)** $U_{in} = 41.3$ m s^{-1}, $Fr_{cyl} = 6.9$. The values of Sk_{out} and Fr_{cyl} scale with U_{in} and $U_{in}{}^2$, respectively, according to Equations (4.6) and (4.7) and Table 4.3. The distributions have been smoothed for clarity with a moving point average spanning 0.125 s of measured data.

Table 4.4: The Stokes and Froude numbers of the two-phase flow evaluated at various zones within the SEVR for three particle diameters, d_p = 20, 40 and 80 µm and two values of inlet velocity: **(a)** $U_{in} = 30.7$ m s^{-1}; and **(b)** $U_{in} = 41.3$ m s^{-1}.

		Zone	*Sk*			*Fr*
			$d_p = 20$ µm	$d_p = 40$ µm	$d_p = 80$ µm	
(a)	$U_{in} = 30.7$ m s^{-1}	Inlet (at $z/L = 0.02$)	0.95	3.78	15.13	-
		Cone (at $z/L = 0.06$)	0.21	0.85	3.40	299.5
		Corner (at $z/L = 0.29$)	0.01	0.06	0.23	3.6
		Cylinder (at $z/L = 0.69$)	0.01	0.06	0.23	3.8
		Outlet (at $z/L = 0.85$)	1.21	4.86	19.44	-
(b)	$U_{in} = 41.3$ m s^{-1}	Inlet (at $z/L = 0.02$)	1.27	5.09	20.36	-
		Cone (at $z/L = 0.06$)	0.29	1.14	4.58	542.8
		Corner (at $z/L = 0.29$)	0.02	0.08	0.30	6.6
		Cylinder (at $z/L = 0.69$)	0.02	0.08	0.31	6.9
		Outlet (at $z/L = 0.85$)	1.64	6.54	26.16	-

Figure 4.7 presents three statistical measures of the particle RTDs for each of the conditions shown in Table 4.1b with a constant inlet diameter, $D_{in} = 6$ mm. It can be seen from Figure 4.7a, which presents $\bar{\tau}_p$ as a function of Fr_{cyl} and U_{in}, that increasing Fr_{cyl} causes a monotonic decrease in $\bar{\tau}_p$ for all d_p. For $U_{in} \leq 30.7\ m\ s^{-1}$, it can be seen that the 80 µm sized particles have mean residence time significantly longer than that of the 40 µm sized particles, $\bar{\tau}_{p,80\mu m}/\bar{\tau}_{p,40\mu m} \sim 2$. However, as Fr_{cyl} increases, the values of $\bar{\tau}_p$ for all d_p converge to a value $\bar{\tau}_p \sim 2$ s with $Fr_{cyl} = 6.9$ and $U_{in} = 41.3\ m\ s^{-1}$. This shows that there are two regimes of two-phase flow present in the SEVR, as mentioned previously. In one regime, the particle residence time of larger particles is significantly longer than that of smaller particles, while in the other, particle size has less of an influence on particle residence time.

More insight into the explanation of the two regimes of operation can be found from Figure 4.7b, which presents $\bar{\tau}_p$ as a function of Sk_{out}, with lines of constant Fr_{cyl}. It can be seen that, for $Fr_{cyl} < 4$, an increase in Sk_{out} causes an increase in $\bar{\tau}_p$. This effect has been discussed previously and is attributed to the greater inertia of large particles with high Sk_{out} having a greater likelihood of being retained within the chamber and not exiting through the radially-oriented outlet. However, an additional mechanism is apparent here, such that, as the Froude number of the vortex flow increases, the influence of Sk_{out} on $\bar{\tau}_p$ becomes weaker. This highlights the importance of the external gravitational field in influencing the particle residence time for the selected orientation.

In the low Froude number regime ($Fr_{cyl} < 4$), the significantly longer $\bar{\tau}_p$ of larger particles (high Sk_{out}) can be explained by the expansion of the vortex flow through the cone of the SEVR, which results in the particles losing a significant fraction of their kinetic energy as they reach the cone-cylinder corner and the cylindrical section of the receiver. The relatively low Froude number of the flow also implies that particles are not entirely distributed close to the wall of the receiver, but that they can also be entrained into the central reversed flow zone and recirculated to the bottom of the cone. That is, for the receiver orientation considered here, gravity serves to recirculate larger particles into the most intense part of the vortex flow. This recirculation mechanism augments the trend for larger particles to be preferentially retained within the receiver and have longer residence time than smaller particles, which follow gas streamlines more closely. This is termed here the *Froude-Stokes* regime of SEVR operation, characterised by low Froude numbers and a strong influence of Sk_{out} on particle residence time.

As Fr_{cyl} increases, it is apparent from Figure 4.7b that the influence of Sk_{out} in increasing $\bar{\tau}_p$ becomes weaker. This can be explained by the increasing importance of the inertial centrifugal force (both at the cone-cylinder corner and in the cylindrical section) acting to maintain particles in vortex suspension flow preferentially distributed near to the walls of the cylindrical chamber. In this case, Fr_{cyl} scales with ${U_{in}}^2$, such that an increase in U_{in} from 20.0 to 41.3 m s^{-1} causes an increase in the strength of the centrifugal inertial force relative to that of gravity by a factor of 4.2. Therefore,

although the larger particles are less likely to exit the radial outlet than the smaller particles due to their higher Sk_{out}, they are also less likely to enter the central reversed flow zone. This serves to decrease the mean residence time of all particle sizes within the receiver as a relatively smaller amount of particle recirculation is observed, with particles (of all sizes considered here) being retained near to the walls, and thus near to the SEVR outlet. This regime of SEVR operation, characterised by high Froude numbers and a weak influence of Sk_{out} on particle residence time, is termed here the *cyclonic* regime because particles tend to be centrifuged near to the wall of the receiver, as is the case in particle cyclones.

Figure 4.7c presents $\tau_{p,90}$ as a function of Fr_{cyl} and U_{in}, from which it can be seen that $\tau_{p,90}$ follows a similar trend to that of $\bar{\tau}_p$. It can be seen that, in the *Froude-Stokes* regime with $Fr_{cyl} < 4$, $\tau_{p,90}$ is greater for larger particle sizes, with a maximum of $\tau_{p,90} = 20.8$ s (compared with $\bar{\tau}_p = 9.7$ s) for $d_p = 80\,\mu m$ and $Fr_{cyl} = 1.6$. That 10% of particles have residence more than twice as long as the mean residence time highlights the significant recirculation of large particles in this low Froude number regime of operation. With increasing Fr_{cyl}, the values of $\tau_{p,90}$ for each d_p converge to ~4 s, corroborating the finding that in the *cyclonic* regime of operation, Sk_{out} has a weaker influence on the behaviour of particles within the SEVR.

Figure 4.7d presents the dependence of ${\sigma_p}^2$ on Fr_{cyl} and U_{in}. For $d_p = 80\,\mu m$, the ${\sigma_p}^2$ values are relatively consistent in the range $0.43 - 0.62$. These values indicate that the mixing pattern of larger particles within the SEVR is intermediate between those of an ideal continuously-stirred tank reactor (CSTR), for which ${\sigma_p}^2 = 1$, and an ideal plug flow reactor (PFR), for which ${\sigma_p}^2 = 0$ (Levenspiel 1999; Fogler 2006). In addition, over the range of values of Fr_{cyl} presented, there is a slight decrease in ${\sigma_p}^2$ with increasing Fr_{cyl}, which can be described as a slight trend towards more uniform plug flow with increasing Fr_{cyl}. The larger values of ${\sigma_p}^2$ in the range $0.77 - 0.90$, for $d_p = 80\,\mu m$ and $3.8 \leq Fr_{cyl} \leq 5.2$, can be attributed to the longer tails of the measured RTD for these cases (relatively longer $\tau_{p,90}$ in Figure 4.7c), which increase the variance of the distribution relative to the mean. For $d_p = 40\,\mu m$ a more significant decrease in ${\sigma_p}^2$ with increasing Fr_{cyl} is visible, indicating that the mixing pattern shifts from close to perfectly mixed with $Fr_{cyl} = 1.63$ and ${\sigma_p}^2 = 0.86$ to a more uniform flow with $Fr_{cyl} = 6.9$ and ${\sigma_p}^2 = 0.46$. A similar reduction in the extent of mixing is visible for $d_p = 20\,\mu m$. Therefore, it can be said that, as the operation of the device moves from the *Froude-Stokes* regime towards the *cyclonic* regime with increasing Fr_{cyl}, there is a reduction in ${\sigma_p}^2$ and, hence, a reduction in the extent of mixing in the SEVR. This is consistent with findings that the *Froude-Stokes* regime is characterised by large-scale particle recirculation within the receiver, while the *cyclonic* regime features less particle recirculation limited to the cylindrical section of the receiver.

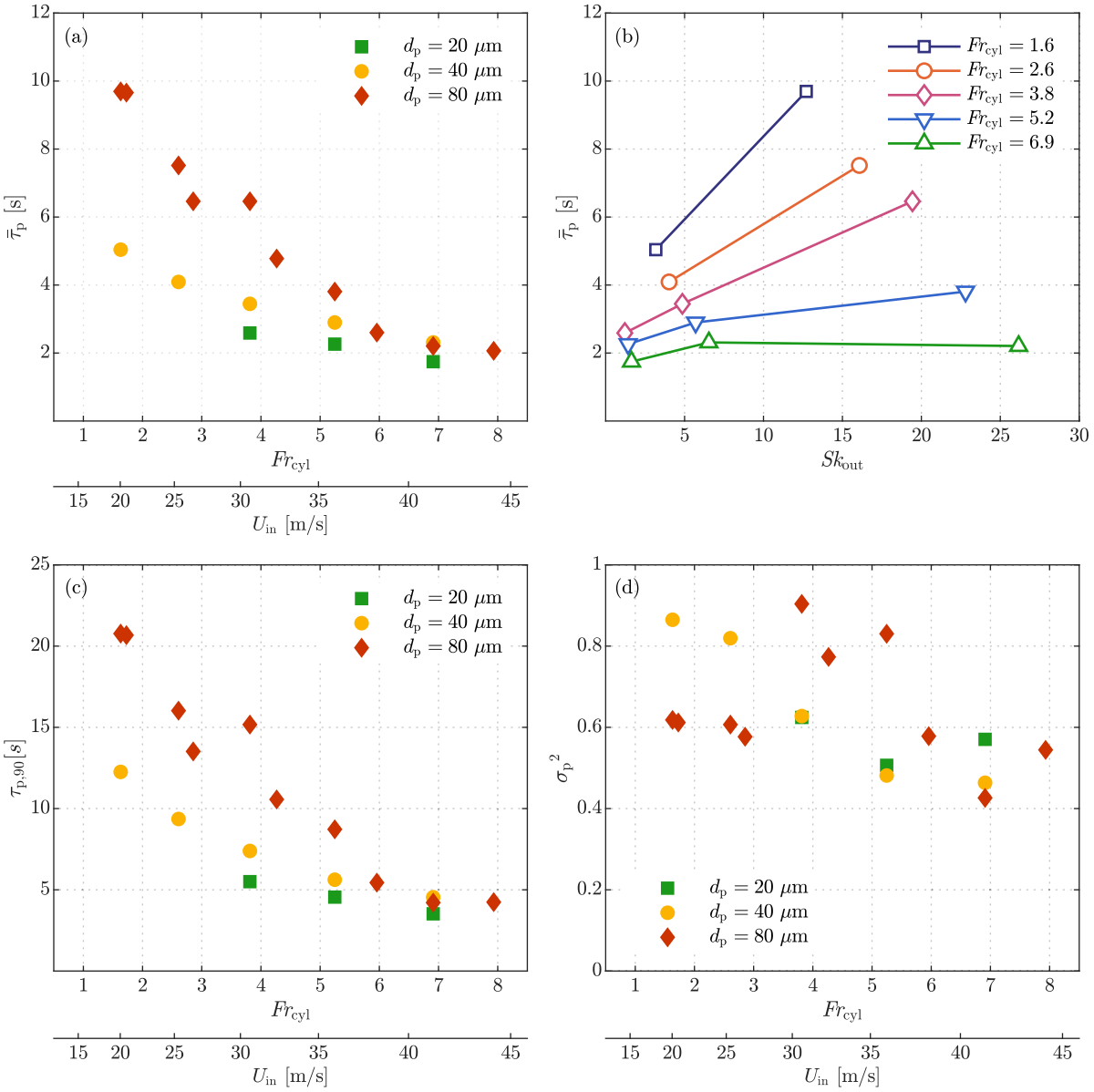

Figure 4.7: The statistical measures of the particle RTDs for three different particle diameters, $d_p = 20$, 40 and 80 µm, and inlet velocities in the range $U_{in} = 20.0 - 44.2\ m\ s^{-1}$ with constant inlet diameter, $D_{in} = 6$ mm, so that $U_{in} = \dot{V}_{air} / \left[2 \times (\pi/4) \times {D_{in}}^2\right]$. Presented are: **(a)** the mean particle residence time, $\bar{\tau}_p$, as a function of Fr_{cyl} and U_{in}; **(b)** the mean particle residence time, $\bar{\tau}_p$, as a function of Stokes numbers evaluated at the outlet, Sk_{out}, with lines of constant Fr_{cyl}; **(c)** the 90th percentile particle residence time, $\tau_{p,90}$, as a function of Fr_{cyl} and U_{in}; and **(d)** the normalised variance, ${\sigma_p}^2$, as a function of Fr_{cyl} and U_{in}.

Figure 4.8 presents $\bar{\tau}_p$ as a function of Fr_{cyl}, for one particle diameter, $d_p = 80\,\mu m$, and three different values of inlet diameter, $D_{in} = 5$, 6 and 7.5 mm. It can be seen that, similarly to the trend for $D_{in} = 6$ mm, $\bar{\tau}_p$ decreases monotonically with increasing Fr_{cyl} for both $D_{in} = 5$ and 7.5 mm. This is consistent with the previous deduction that, as Fr_{cyl} increases, the two-phase flow within the SEVR moves toward a *cyclonic* regime of operation with shorter residence times. It can also be seen that, for a given value of Fr_{cyl}, an increase in D_{in} causes a decrease in $\bar{\tau}_p$. This is attributed to the higher air volumetric flow rate required to generate a given value of Fr_{cyl} with the larger D_{in}. That is, as D_{in} increases, velocities within the receiver decrease. The effect of increasing volumetric flow rate of air to decrease the nominal residence time is well known, according to $\tau_{nom} = V_r / \dot{V}_{air}$. Indeed, in this case, the higher volumetric flow rates of air, which transports particles through the receiver, serves also to decrease the measured particle residence time, as well as the nominal value.

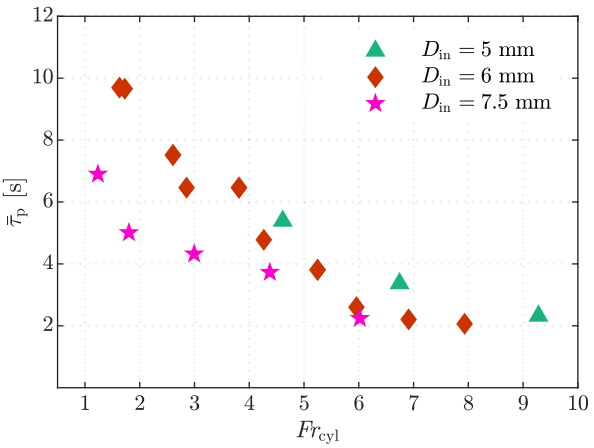

Figure 4.8: The mean particle residence time, $\bar{\tau}_p$, as a function of Fr_{cyl}, for one particle diameter, $d_p = 80\,\mu m$, and three different values of inlet diameter, $D_{in} = 5$, 6 and 7.5 mm.

4.2.2 Compartment model analysis

Figure 4.9 presents the dimensionless particle RTDs, $E(\theta)$, measured for two different particle sizes, $d_p = 20$ and 80 µm, and two inlet velocities (with constant $D_{in} = 6$ mm). These are chosen because they represent the *Froude-Stokes* and the *cyclonic* regimes identified above (the low and high Froude number regimes, respectively). Also shown in Figure 4.9 are the analytical RTDs derived from the compartment modelling approach of Levenspiel (1999) to describe the experimental RTDs. In each of the experimental distributions, $E(\theta)$ remains at zero for short dimensionless times, δ, defined as the ratio of the time for which the pulse response is zero to the mean particle residence time. After this delay time, $E(\theta)$ increases rapidly to a maximum value, and then decreases at a slower rate to zero, as described above.

Figure 4.9a and b present the dimensionless particle RTDs for $d_p = 80$ µm and $Fr_{cyl} = 2.6$ and 6.9, corresponding to the two different particle behaviour regimes. For the *Froude-Stokes* regime ($Fr_{cyl} = 2.6$), $E(\theta)$ is well described by a step increase to a maximum after a short delay, δ, followed by an exponential decay. This corresponds to the RTD of two ideal reactors in series, in which the first is a small PFR of residence time δ and the second is a CSTR. The corresponding analytical equation of $E(\theta)$ for this compartment model configuration describing operation in the *Froude-Stokes* regime can be expressed as:

$$E(\theta)|_{Froude\text{-}Stokes} = \frac{1}{1-\delta} \exp\left(-\frac{\theta-\delta}{1-\delta}\right) u(\theta-\delta), \tag{4.8}$$

where $u(\theta-\delta)$ is the Heaviside function. This function, $E(\theta)|_{Froude\text{-}Stokes}$, is presented in Figure 4.9a.

Conversely, for the cyclonic regime ($Fr_{cyl} = 6.9$, Figure 4.9b), the rate of increase that follows the similar initial dimensionless delay δ is slower, with a less prominent peak and a broader non-symmetrical dimensionless RTD. The tanks-in-series model can be used to describe this behaviour (Levenspiel 1999), where the experimental curves are modelled with two tanks of different volume connected in series following an initial delay. The $E(\theta)$ for the *cyclonic* regime can be expressed as:

$$E(\theta)|_{Cyclonic} = \frac{1+\varepsilon}{(\varepsilon-1)(1-\delta)} \left[\exp\left(-\frac{(\theta-\delta)(1+\varepsilon)}{\varepsilon(1-\delta)}\right) - \exp\left(-\frac{(\theta-\delta)(1+\varepsilon)}{(1-\delta)}\right)\right] u(\theta-\delta), \tag{4.9}$$

where ε represents the ratio of the space-times of the two tanks and $u(\theta-\delta)$ is the Heaviside function. This function, $E(\theta)|_{Cyclonic}$, is presented in Figure 4.9b. It is noteworthy that, as $\varepsilon \to 0$, Equation (4.9) collapses to Equation (4.8), demonstrating that the two regimes of operation are

closely related and have potential to be combined into a unified compartment model to describe both regimes. As a whole, the particle RTDs in the SEVR deviate slightly from the perfectly-mixed flow pattern, as also confirmed by the values of ${\sigma_p}^2$ plotted in Figure 4.7d.

Figure 4.9c and d present the dimensionless particle RTDs for $d_p = 20\,\mu m$ and $Fr_{cyl} = 3.8$ and 6.9, also corresponding to the *Froude-Stokes* and *cyclonic* particle behaviour regimes, respectively. As for the larger particles, the experimental RTDs for the *Froude-Stokes* regime ($Fr_{cyl} = 3.8$) can be described by a small PFR (represented by the delay δ) connected in series with a CSTR, as described by Equation (4.8) and illustrated in Figure 4.9c. For the *cyclonic* regime (Fr_{cyl} = 6.9) the reactor can be schematised similarly to the case with larger particle size, as two CSTRs in series with a delay, as described by Equation (4.9) and illustrated in Figure 4.9d. Altogether, Figure 4.9 highlights that the same analytical compartment model can be used to describe $E(\theta)$ for both particle sizes, suggesting that for a given particle behaviour regime, the same mixing pattern characterises the particle RTD behaviour of particles of all sizes. Further to this result, the ideal reactor schemes applied here to the two regimes of operation and described by Equations (4.8) and (4.9) were also found to hold for the experimentally measured particle RTDs with alternative inlet diameters, $D_{in} = 5$ and 7.5 mm, and the fixed particle size $d_p = 80\,\mu m$, as presented in Figure 4.8.

Figure 4.10 presents the schematic representation of the unified compartment model describing the particle RTD behaviour of the SEVR in both the *Froude-Stokes* and the *cyclonic* regimes of operation (the low and high Froude number regimes, respectively). This compartment model is composed of a PFR followed by two CSTRs in series with a degree of back-mixing between them. For the *Froude-Stokes* regime, after the short delay (represented by the PFR), the back-mixing between the two CSTRs is active, so that the particle mixing behaviour of the two CSTRs can be considered the same as a single CSTR (Fogler 2006), as is consistent with Equation (4.8). For the *cyclonic* regime, the same schematic is used to represent the SEVR. However, in this case only a small or negligible extent of back-mixing occurs between the two CSTRs, so that two independent mixing volumes are established. The volumetric ratio of the two CSTRs establishes the relative proportioning of residence time spent in each zone, as is consistent with Equation (4.9).

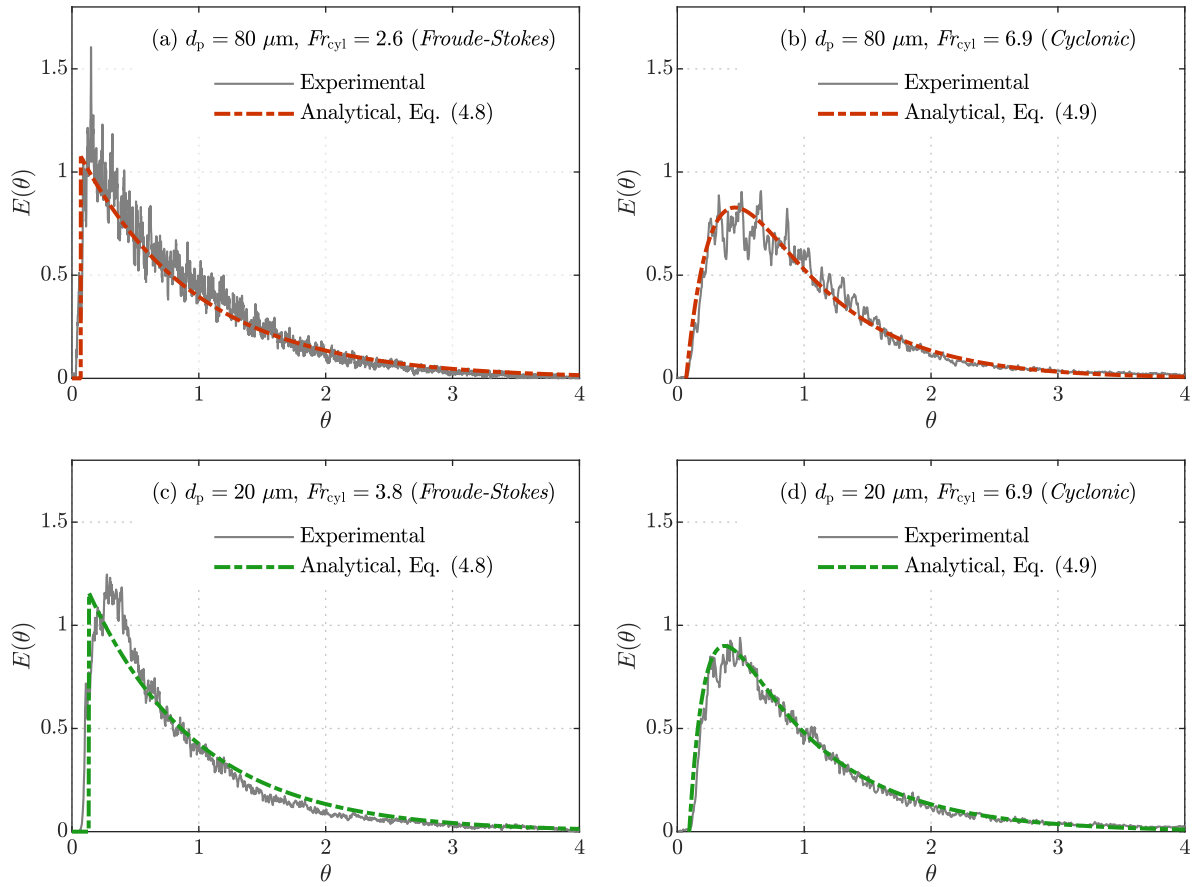

Figure 4.9: The experimentally measured dimensionless particle RTDs and functions of their corresponding analytical compartment models. Presented are distributions representing the *Froude-Stokes* and the *cyclonic* regimes (the low and high Froude number regimes, respectively) for particle sizes **(a, b)** $d_p = 80\ \mu m$; and **(c, d)** $d_p = 20\ \mu m$. The functions of the analytical distributions shown here are given in Equations (4.8) and (4.9), respectively.

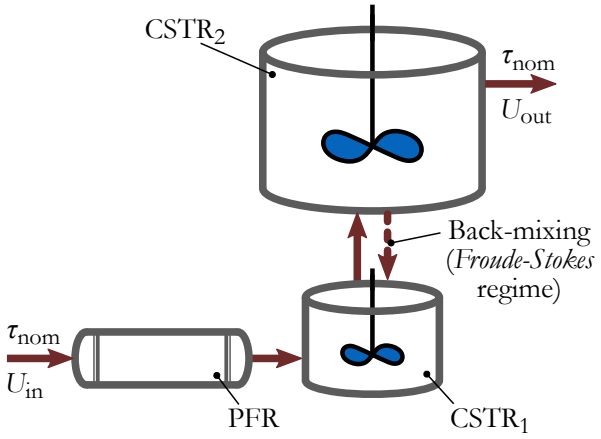

Figure 4.10: Schematic representation of the unified compartment model describing the particle RTD behaviour of the SEVR in both the *Froude-Stokes* and the *cyclonic* regimes (the low and high Froude number regimes, respectively) as a combination of an ideal plug flow reactor (PFR) and continuously-stirred tank reactors (CSTRs).

Table 4.5 presents 15 cases for which the particle RTDs were measured, together with the corresponding values of the parameters δ and ε used in Equations (4.8) and (4.9) for the compartment modelling of the two identified regimes of operation. Also shown is the coefficient of determination, R^2, between the experimental and analytical RTDs. It can be seen that δ varies between 0.055 and 0.13, which means that the ratio between the space-time of the PFR component and the total reactor space-time ranges between 5.5% and 13%. This small delay is likely due to the time needed for the particles to fulfil the reactor inventory. It is likely that in a practical reactor vessel, even in mixed flow conditions, some dispersion will occur also, resulting in a delay in the pulse response. Furthermore, for a given D_{in}, δ decreases with an increase in U_{in}, indicating that with higher inlet velocities the time to fulfil the reactor inventory reduces. On the other hand, the value of ε is equal to zero for all D_{in} and d_p in the *Froude-Stokes* (low Froude number) regime and then increases with U_{in} in the *cyclonic* (high Froude number) regime. Given that the SEVR comprises a conical and a cylindrical section, the finding that $\varepsilon = 0$ for the *Froude-Stokes* regime indicates that the two sub-volumes behave as a single mixing volume in this regime. This is consistent with the deduction that, in the *Froude-Stokes* regime, particles (particularly those with large Sk_{out}) are recirculated via the central reversed flow zone that spans both the cylindrical and conical sections of the device. The transition to the *cyclonic* regime, and higher values of ε is analogous to a reduction in the extent of particle recirculation through the entire SEVR device. Values of ε up to and above 5 highlight that particles spend less time in the conical zone of the SEVR, being quickly entrained into the cylindrical zone, where the majority of the particles' residence time is spent.

The values presented in Table 4.5 were determined by fitting the analytical RTDs to the experimentally measured RTDs with R^2 values always greater than 0.95.The coefficient of determination values in the range $R^2 = 0.95 - 0.99$ demonstrate good agreement between the experimental and analytical dimensionless RTDs. The lowest values of R^2 are predominantly for the cases with lower U_{in} and can be attributed to the presence of small peaks before the primary peak. This could be related to wall-related interactions, such as adhesion/re-entrainment. However, the area bounded by these peaks is always less than 1% of the total area bounded by the RTD curve, so that these effects are small here.

Table 4.5: The operational details and corresponding parameters used in Equations (4.8) and (4.9) to describe the measured particle RTDs with analytical compartment models, together with the coefficient of determination between experimental and analytical RTDs.

D_{in} [mm]	d_p [µm]	Fr_{cyl}	U_{in} [m s^{-1}]	Particle behaviour regime	δ	ε	R^2
6	80	2.6	25.4	*Froude-Stokes*	0.085	0	0.96
		5.2	36.0	Transitional	0.080	0.1	0.96
		6.9	41.3	*Cyclonic*	0.070	3	0.98
		7.9	44.2	*Cyclonic*	0.070	5.5	0.98
6	20	3.8	30.7	*Froude-Stokes*	0.13	0	0.95
		5.2	36.0	*Cyclonic*	0.094	6	0.99
		6.9	41.3	*Cyclonic*	0.094	6	0.99
5	80	3.2	30.6	*Froude-Stokes*	0.076	0	0.96
		4.4	35.7	Transitional	0.071	0.01	0.95
		6.0	41.6	Transitional	0.070	0.12	0.96
		6.7	44.1	*Cyclonic*	0.070	6.5	0.96
7.5	80	3.0	25.3	*Froude-Stokes*	0.11	0	0.95
		4.4	30.6	Transitional	0.10	0	0.95
		6.0	35.8	Transitional	0.080	0.02	0.96
		8.1	41.5	*Cyclonic*	0.055	6.5	0.96

4.2.3 Key features of the two regimes of particle behaviour: *Froude-Stokes* and *cyclonic*

Table 4.6 summarises the key features of the two regimes of particle behaviour identified in the present investigation, incorporating the experimental, numerical and compartment modelling analyses. Additionally, Figure 4.11 presents simplified representations of the behaviour of the SEVR deduced from the experimental and numerical analyses, including the three-dimensional flow-field within the SEVR (Figure 4.11a) and the predominant particle trajectories for operation in the *Froude-Stokes* and *cyclonic* regimes (Figure 4.11b and Figure 4.11c, respectively). It can be seen from Figure 4.11a that a key feature of the air flow field other than the main outer vortex flow is the central reversed flow zone. The response of the particles to the flow depends on their Stokes number, while the Froude number has an additional influence on the trajectories of particles within the SEVR device.

It can be seen from Table 4.6 that the boundary of the *Froude-Stokes* regime identified here is $Fr_{cyl} < 4$. In this behaviour regime small particles are preferentially distributed in regions of maximum tangential velocity through the receiver. As larger particles enter the receiver, they are directed toward the wall by their inertia, but then also become more uniformly distributed through the cylindrical section of the receiver. At the radial outlet, the larger particles are less likely than smaller particles to follow the strong flow gradients and, as a result, have longer residence time than small particles ($\bar{\tau}_{p,LP} > \bar{\tau}_{p,SP}$). It has however also been deduced that due to the low Froude number at the cone-cylinder corner and in the cylindrical section of the receiver, particles have a significant likelihood of entering the central reverse flow zone of the SEVR to be recirculated in the direction augmented by gravity into the most intense part of the vortex flow. For this reason, experiments show that the lower the Froude number, Fr_{cyl}, the greater the influence of the Stokes number, Sk_{out}, in increasing the particle residence time, τ_p. These predominant particle trajectories of small particles following gas streamlines and large particles undergoing recirculation via the central reversed flow zone are illustrated in Figure 4.11b. It is worth noting that this mechanism provides validation to that proposed by Chinnici et al. (2015) in a previous numerical investigation of a SEVR configuration similar to that investigated here. However, the role of gravity in recirculating large particles in the low Froude number regime has been identified here. In terms of compartment models, the experimental particle RTDs can be closely described by a small plug flow reactor in series with two CSTRs with back-mixing so that the mixing behaviour of the two CSTRs can be considered to be that of a single larger CSTR. This back-mixing accounts for the recirculation phenomena that is characteristic of the low Froude number particle behaviour regime and occurs predominantly with larger particles.

The higher Froude number regime has not been identified previously for this device, for which $Fr_{cyl} > 4$ (Table 4.6). This regime is characterised by a higher centrifugal inertial force acting on the

particles (relative to the gravitational force) that distributes particles of all sizes near to the wall and prohibits particles from entering the central reversed flow zone as illustrated in Figure 4.11c. While Sk_{out} still has influence on the likelihood of particles leaving the receiver, the larger particles that are retained continue to circulate near to the wall of the receiver and therefore also near to the outlet. These large particles are more likely to exit the radially-oriented outlet than to enter the central reversed flow zone, thereby having shorter mean residence time than for the lower Froude number regime. This has the overall effect of significantly reducing the mean residence time of larger particles relative to those in the low Froude number regime, while also reducing the residence time of smaller particles to a lesser extent. The same compartment model configuration of a small plug flow reactor in series with two CSTRs applies to the experimentally measured RTDs of this high Froude number regime. Furthermore, for this case, only a small or negligible amount of back-mixing between the two CSTRs is required to closely describe the receiver operation. It should be emphasised that Figure 4.11b and c are a simplified representation of the most probable particle trajectories within the SEVR inferred from particle RTD data, CFD modelling and experimental observation, although some particles will behave differently.

Table 4.6: Summary of the key features of the two particle behaviour regimes for the SEVR in a vertical orientation, including details from experimental and theoretical analyses.

Regime	Boundary	Experimental findings	Compartment model descriptions	Key features
Froude-Stokes (low Froude number)	$Fr_{cyl} < 4$	• Particles with large Sk_{out} preferentially retained within SEVR, longer τ_p. • Lower inertial centrifugal force allows particles to enter central recirculation zone. • Gravitational field in vertical orientation augments particle recirculation mostly for larger particles, which have longer residence time.	• A small plug flow reactor in series with 2 CSTRs that have back-mixing.	• $\bar{\tau}_{p,LP} > \bar{\tau}_{p,SP}$ • $\tau_{p,90,LP} > \tau_{p,90,SP}$
Cyclonic (high Froude number)	$Fr_{cyl} > 4$	• Sk_{out} has weak influence on τ_p. • Particles less likely to enter central recirculation zone due to large centrifugal inertial force.	• A small plug flow reactor in series with 2 CSTRs that have negligible back-mixing.	• $\bar{\tau}_{p,LP} \sim \bar{\tau}_{p,SP}$ • $\tau_{p,90,LP} \sim \tau_{p,90,SP}$

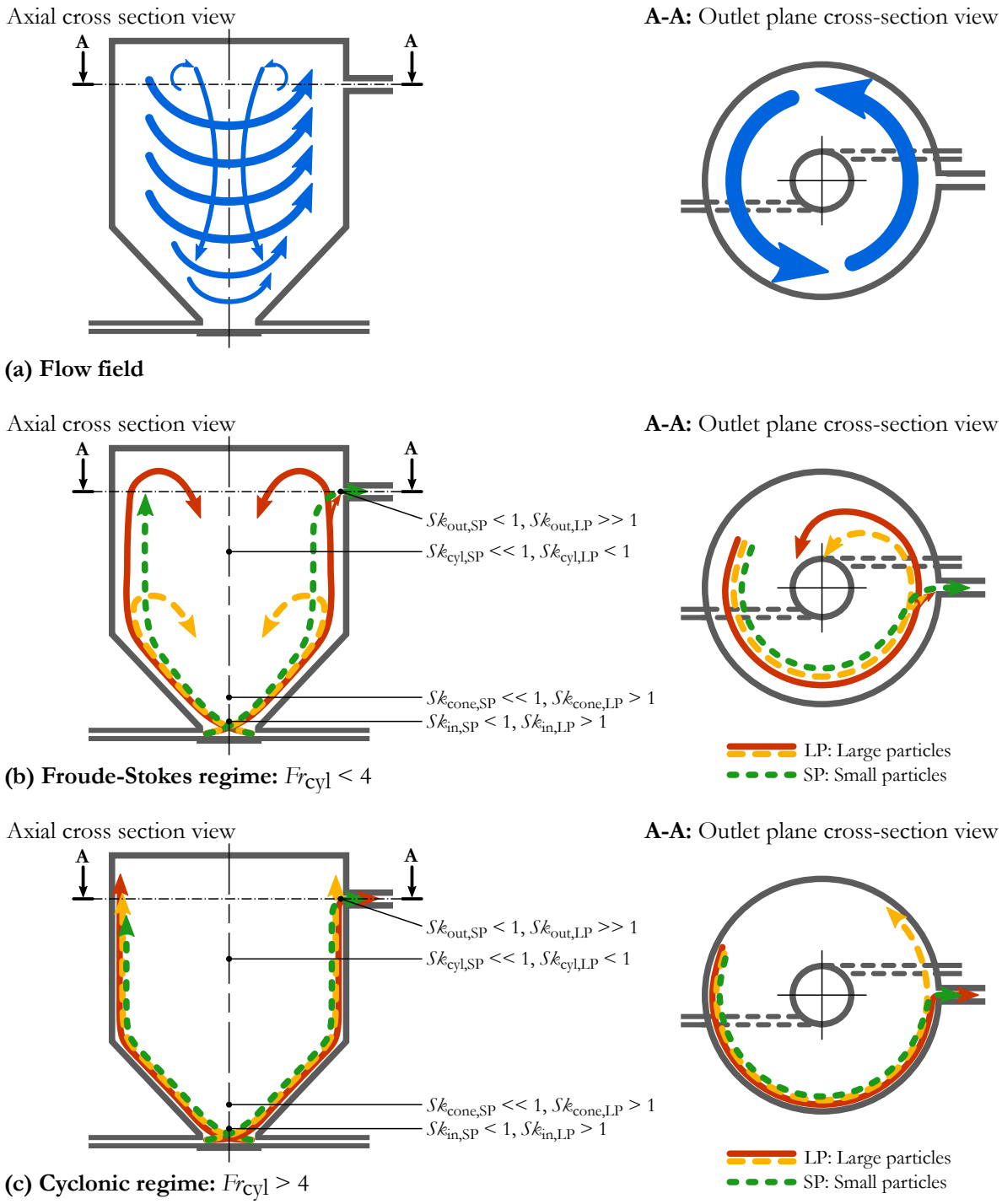

Figure 4.11: Simplified representations of the SEVR behaviour deduced from the experimental and numerical analyses, including **(a)** the three-dimensional flow-field within the SEVR; **(b)** the predominant particle trajectories of the *Froude-Stokes* regime; and **(c)** the predominant particle trajectories of the *cyclonic* regime. The trajectories of large (LP, red/yellow) and small (SP, green) particles are shown in axial/radial components through the receiver (left), and tangential/radial components at the exit plane $z/L = 0.85$ (right).

It is also instructive to compare the present device with a cyclone particle separator, for which the *Stokes-Froude* regime is typically not observed. The separation factor of a cyclone, which is analogous to the present definition of the Froude number, is typically greater than 5 and often greater than 1000 (Cortés & Gil 2007; Hoffmann & Stein 2007). This gives further support for the deduction that the critical value separating the two regimes is $Fr_{\mathrm{cyl}} \sim 4$. Nevertheless, it should be noted that the transition between the two regimes occurs over a range of Froude numbers around this critical value. Furthermore, the magnitude of the deduced critical value will be sensitive to the magnitude of the characteristic length and velocity scales, which have been estimated with a CFD model.

The wide variation in particle RTD characteristics across the two regimes of operation, as influenced by inlet velocity, air volumetric flow rate and particle size, suggests a high level of flexibility of operation of the SEVR technology. Typically, the time required to thermally process a particle will depend on its size. Therefore, the *Froude-Stokes* regime of operation, in which $\bar{\tau}_{\mathrm{p,LP}} > \bar{\tau}_{\mathrm{p,SP}}$, has potential for use in processing polydisperse groups of particles. The *Froude-Stokes* regime is also potentially advantageous to reactions in which the solid particles are destroyed (e.g. the solar gasification of solid fuel). This is because it is desirable that a large particle is preferentially retained within the reactor until it has completely reacted. As the particle reacts its size/density will reduce so that the particle becomes more likely to exit the reactor. Alternatively, for processes that require a uniform product quality (e.g. the calcination of alumina), particles should be processed with uniform residence time. The more uniform particle RTDs that were identified to be characteristic of the *cyclonic* regime of operation may be more suitable for such an application of the SEVR. Finally, for a SEVR operating in either particle behaviour regime, the residence time could potentially be altered by changing U_{in}, $\dot{V}_{\mathrm{air}}$, which is advantageous in facilitating control in response to the natural variability of the solar resource.

4.3 Influence of SEVR tilt angle on particle RTD

4.3.1 Measurement cases

Table 4.7a, together with Figure 4.12, presents the geometry of the SEVR configuration used in the present assessments of the influence of receiver tilt angle on the particle RTD. This configuration of SEVR maintains geometric similarity with that used above (Section §4.2). The receiver tilt angle, ψ (shown in Figure 4.12), is defined as the angle between the central axis of the receiver and the horizontal, with downward-facing angles considered as positive, following previous work (Leibfried & Ortjohann 1995; Wu et al. 2010). This implies that positive tilt angles ($\psi > 0^{o}$) are relevant to tower-mounted solar receiver configurations, while a tilt angle of $\psi = -90^{o}$ is relevant to a receiver with beam-down solar concentrating system.

Table 4.7b presents the range of operational parameters that were varied in the present investigation. The particle RTD was measured for seven receiver tilt angles in the range $\psi = -90^{o}$ to $+90^{o}$. It can be seen (Figure 4.12) that this change of receiver orientation is made with the radially-oriented outlet positioned on the side of the receiver to avoid gravity bias. For each value of ψ the particle RTD was measured for two particle sizes, $d_{p} = 20$ and $80\,\mu m$, and two values of air volumetric flow rate, $\dot{V}_{air} = 104$ and 122 slpm, generating two values of inlet velocity, $U_{in} = 30.7$ and $36.0\,m\,s^{-1}$, due to the constant inlet diameter. These values of U_{in} were chosen because they generate the two different particle behaviour regimes identified above (Section §4.2) for $\psi = -90^{o}$.

Table 4.8 presents the values of the key dimensionless parameters, Sk_{out} and Fr_{cyl}, for operation in the *Froude-Stokes* and *cyclonic* regimes. These parameters are generated with the two values of inlet velocity and two particle sizes used in the present investigation. It can be seen that the lower velocity, $U_{in} = 30.7\,m\,s^{-1}$, results in $Fr_{cyl} = 3.8 < 4$ so that the operation of the SEVR is within the *Froude-Stokes* regimes, while the higher velocity case resulting in $Fr_{cyl} = 5.2 > 4$ corresponds to the *cyclonic* regime of operation.

Table 4.7: (a) Values of the key dimensions of the SEVR; and **(b)** the range of variation of the independent parameters systematically varied for the present assessment of receiver tilt angle, ψ.

(a)		(b)	
D_c	190 mm	ψ	-90^o to $+90^o$
L	237.5 mm	d_p	20, 80 µm
D_{base}	47.5 mm	$\dot{V}_{air}$	104, 122 slpm
D_{cone}	47.5 – 190 mm	U_{in}	30.7, 36.0 m s^{-1}
α	50^o		
D_{in}	6 mm		
D_{out}	11 mm		

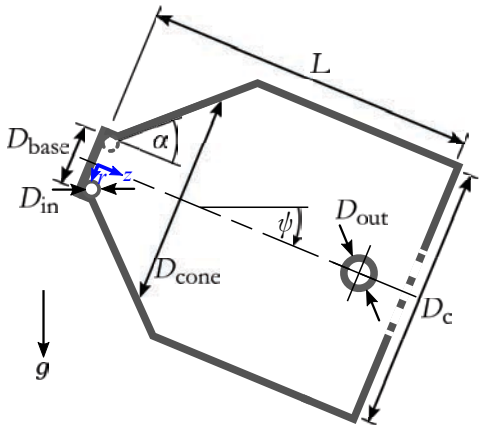

Figure 4.12: Schematic diagram of the SEVR showing the cylindrical coordinate system (r,φ,z), with origin at the centre of the base disc and the symbols that define the geometric configuration. The φ axis is defined as the right handed angle about the z axis. The values of each geometric parameter are shown in Table 4.7. Gravity acts downwards as shown by g.

Table 4.8: The operational details of the *Froude-Stokes* and *cyclonic* regimes of operation investigated here, generated with the two values of inlet velocity, U_{in}. The characteristic velocity and length scales, and values of the key dimensionless parameters, Sk_{out} and Fr_{cyl}, for each regime are also presented.

	Froude-Stokes	*Cyclonic*
U_{in} [m s^{-1}]	30.7	36.0
U_{out} [m s^{-1}][a]	18.2	21.4
$2D_{out}$ [m][b]	0.022	
$u_{\varphi,max}$ [m s^{-1}][c]	1.92	2.2
D_c /2 [m][d]	0.095	
Sk_{out} for $d_p = 20$ µm	1.2	1.4
Sk_{out} for $d_p = 80$ µm	19.4	22.8
Fr_{cyl}	3.8	5.2

[a] Characteristic velocity scale for the Sk_{out};
[b] Characteristic length scale for Sk_{out};
[c] Characteristic tangential velocity scale for Fr_{cyl};
[d] Characteristic radius of circular motion for Fr_{cyl}.

4.3.2 Measurements of the particle RTD

Figure 4.13 presents the measured particle RTDs within the SEVR for seven receiver tilt angles in the range $\psi = -90°$ to $+90°$, for two outlet Stokes numbers ($Sk_{out} = 19.4$ and 1.2), a single inlet velocity $U_{in} = 30.7$ m s^{-1} and constant inlet diameter $D_{in} = 6$ mm, generating a nominal residence time $\tau_{nom} = 3.2$ s, where $U_{in} = \dot{V}_{air} / \left[2 \times (\pi/4) \times {D_{in}}^2\right]$ and $\tau_{nom} = V_r / \dot{V}_{air}$. The distributions have been smoothed for clarity with a moving point average spanning 0.125 s of measured data.

Figure 4.13a and b present the RTDs measured for $Sk_{out} = 19.4$, and $d_p = 80$ µm. This shows that increasing ψ shifts the RTDs to shorter residence times. It can be seen that, for the negative tilt angles (Figure 4.13a) in which the two-phase flow proceeds upwards against gravity, the length of the tail of the RTD is longest for $\psi = -90°$, indicating that this orientation results in the most particle recirculation within the SEVR, as reported above Section §4.2). It can also be seen that, as the tilt angle is increased to $\psi = -60°$ and $-30°$, the peak in the RTD becomes more prominent and shifts to shorter residence times. However, the tails of the two distributions are still prominent, indicating continued particle recirculation within the SEVR for residence times up to ~10 s. Figure 4.13b presents RTDs measured for the SEVR with a horizontal orientation, as well as with positive tilt angles (noting that the scale of the abscissa in Figure 4.13b is increased relative to Figure 4.13a). Here, the peak in the RTD increases with ψ and the distributions feature small or negligible tails, such

that, for the three positive tilt angles, 90% of the particles have a residence time of less than 2.5 s. Therefore, for beam-down receiver tilt angles ($\psi < 0^{o}$), the RTDs depend strongly on the angle, while for tower-mounted receiver tilt angles ($\psi > 0^{o}$), the RTDs are less influenced by the angle. From a reactor design perspective, increasing the receiver tilt angle causes the RTD to change from that resembling a mixed flow reactor to that resembling a plug flow reactor. This in turn indicates that the broad RTDs measured for negative receiver tilt angles favour particle recirculation and potentially enhanced heat transfer in a practical solar receiver, while the positive receiver tilt angles favour reduced recirculation and uniform particle residence times.

Figure 4.13c and d present the measured RTDs for $Sk_{out} = 1.2$ and $d_p = 20\,\mu m$. This shows that the RTD is not significantly affected by the receiver orientation for the majority of tilt angles assessed, $\psi \geq -60^{o}$, and is shifted to slightly longer residence times for $\psi = -90^{o}$. It can also be seen (Figure 4.13c) that the RTD is broadest with longest residence times for $\psi = -90^{o}$. With an increase in tilt angle to $\psi = -60^{o}$ there is a reduction in residence time with a more prominent peak in the distribution. This is a similar trend to that shown for $Sk_{out} = 19.4$. However, further increases in ψ (Figure 4.13c and d) do not result in significant changes to the measured RTD. That is, the RTDs for $\psi = -60^{o}$ to $+90^{o}$ are similar to each other and do not exhibit significant differences in measured residence time. Comparing the RTDs measured with positive ψ for $Sk_{out} = 1.2$ (Figure 4.13d) with those measured for $Sk_{out} = 19.4$ (Figure 4.13b) it can be seen that, for each ψ, the RTDs are shifted to longer residence times with a reduction in Sk_{out} (e.g. by smaller particle size). This indicates that, for the tower-mounted orientation ($\psi > 0^{o}$) over the range of conditions assessed here, particle residence times decrease with an increase in Sk_{out}. Taken together, it is hypothesised from Figure 4.13 that particles with outlet Stokes number $\sim$1 are less influenced by the receiver tilt angle than are particles with an outlet Stokes number $\gg 1$.

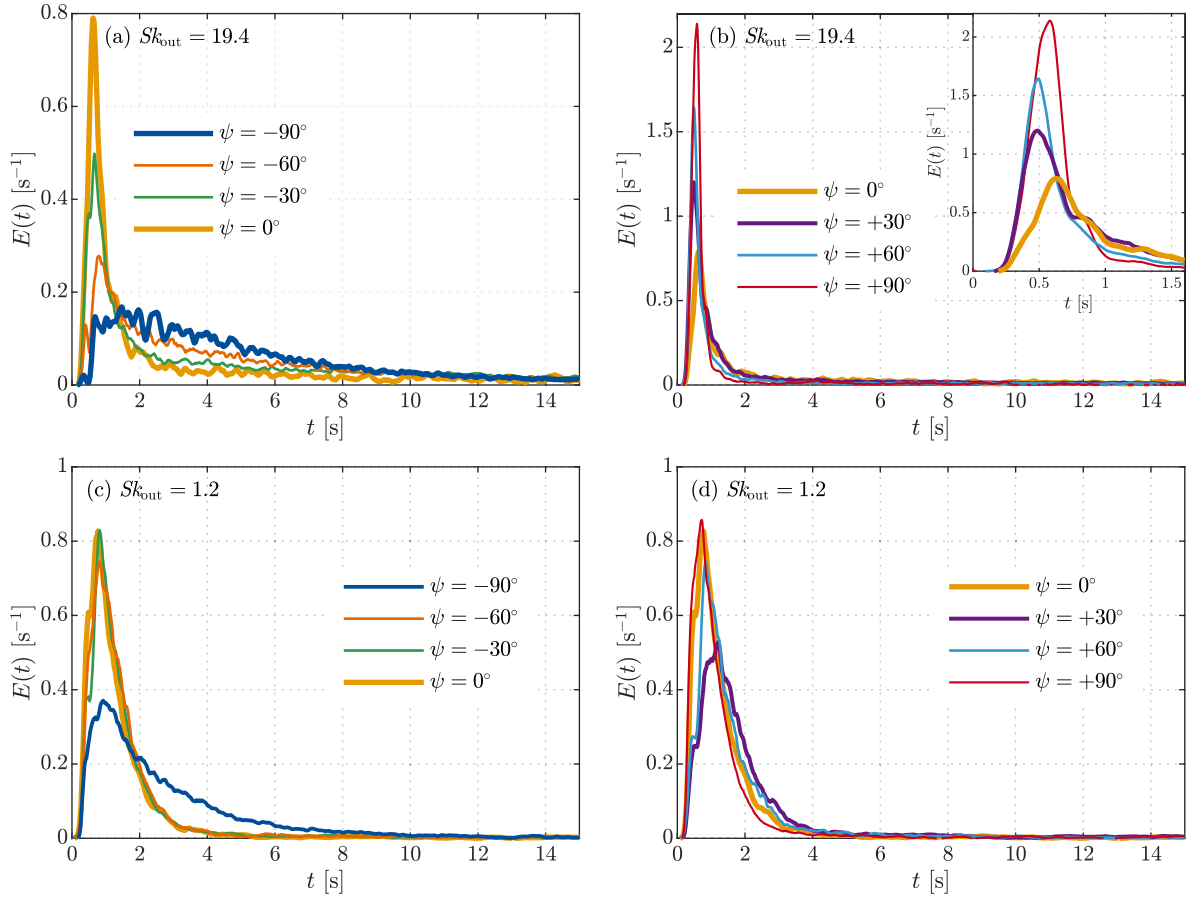

Figure 4.13: Measured particle RTDs in the SEVR for seven receiver tilt angles in the range $\psi = -90°$ to $+90°$, with inlet velocity $U_{in} = 30.7\,\mathrm{m\,s^{-1}}$ and constant inlet diameter $D_{in} = 6\,\mathrm{mm}$, generating a nominal residence time $\tau_{nom} = 3.2\,\mathrm{s}$, where $U_{in} = \dot{V}_{air} / \left[2 \times (\pi/4) \times {D_{in}}^2\right]$ and $\tau_{nom} = V_r / \dot{V}_{air}$. Presented are the distributions for two outlet Stokes numbers **(a, b)** $Sk_{out} = 19.4$ (particle diameter $d_p = 80\,\mu\mathrm{m}$); and **(c, d)** $Sk_{out} = 1.2$ (particle diameter $d_p = 20\,\mu\mathrm{m}$). The inset in (b) presents the same RTDs with time axis in the range, $t = 0$ – $1.6\,\mathrm{s}$. The distributions have been smoothed for clarity with a moving point average spanning 0.125 s of measured data.

Figure 4.14 presents three statistical measures of the particle RTDs, $\bar{\tau}_p$, $\tau_{p,90}$ and ${\sigma_p}^2$, as a function of ψ, for each of the conditions shown in Table 4.7b. It can be seen from Figure 4.14a that the dependence of $\bar{\tau}_p$ on ψ is stronger for the larger particle size, $d_p = 80\,\mu m$, than for $d_p = 20\,\mu m$. Specifically, the $\bar{\tau}_p$ for $d_p = 20\,\mu m$ decreases with an increase from $\psi = -90^o$ to -60^o, but then remains almost constant with a further increase in ψ. This implies that the alignment of gravity with the axis of the SEVR does not play a significant role for this particle size, due to their smaller inertia. That is, their residence time is controlled by their response to the vortex flow field, rather than their response to changes in the direction of gravity. In contrast, the $\bar{\tau}_p$ for $d_p = 80\,\mu m$ decreases to a significant extent with an increase from $\psi = -90^o$ to $+90^o$, indicating that the alignment of gravity does play a role for these larger particles. This can be attributed to a reduction in the component of gravitational force resisting axial motion in the positive z direction as the tilt angle increases from $\psi = -90^o$ to 0^o, and, additionally, the increase in the component of gravitational force augmenting axial motion as the tilt angle increases from $\psi = 0^o$ to $+90^o$. Importantly, for ψ greater than approximately $+30^o$, gravity augments the axial motion in the positive z direction towards the outlet to such an extent that the $\bar{\tau}_p$ is less than that of the smaller particles. That is, due to their weaker response to the vortex flow field, the change in the direction of gravity with a change in ψ has a significant influence on the residence time of $d_p = 80\,\mu m$ particles. This highlights the sensitivity of the particle residence times to the orientation of the receiver for particles of size $d_p = 80\,\mu m$, which undergo a greater reduction in mean residence time with increasing tilt angle than do the particles of size $d_p = 20\,\mu m$.

Figure 4.14a also shows that a negative receiver tilt angle ($\psi < 0^o$), i.e. when gravity resists axial motion in the positive z direction, enhances recirculation of particles by gravity towards the base of the conical section of the receiver. This trend is strong for the $d_p = 80\,\mu m$ particles and weak for the $d_p = 20\,\mu m$ particles. The smaller particles exhibit a weaker increase in $\bar{\tau}_p$ and recirculation with decreasing ψ for $U_{in} = 36.0\,m\,s^{-1}$ and only exhibit longer residence time for the vertical $\psi = -90^o$ orientation with the lower velocity case, $U_{in} = 30.7\,m\,s^{-1}$. The difference in $\bar{\tau}_p$ between the two particle sizes increases with lower U_{in}, as is characteristic of the *Froude-Stokes* regime, which was reported in Section §4.2 for the tilt angle of $\psi = -90^o$. It is noteworthy that this trend persists also for the negative tilt angles of $\psi = -60^o$ and -30^o. Although the two values of U_{in} assessed here differ by only 17%, the increase from $U_{in} = 30.7$ to $36.0\,m\,s^{-1}$ results in $\bar{\tau}_p$ decreases for $d_p = 80\,\mu m$ of 41%, 33% and 34% for $\psi = -90^o$, -60^o and -30^o, respectively. However, for $d_p = 20\,\mu m$, there is no noticeable influence of U_{in} on the $\bar{\tau}_p$ for any ψ, which can potentially be attributed to the small difference in U_{in} assessed. Overall, the SEVR configuration selected here has the potential to operate with a particle residence time that increases with particle size for a range of negative receiver tilt angles.

Figure 4.14b shows that $\tau_{p,90}$ is strongly dependent on ψ for $d_p = 80\,\mu m$, while it is almost independent of ψ for $d_p = 20\,\mu m$, which is consistent with the trend of $\bar{\tau}_p$. The greatest $\tau_{p,90}$ values were measured for $d_p = 80\,\mu m$, $U_{in} = 30.7\,m\,s^{-1}$ and $\psi = -90^o$, -60^o and -30^o ($\tau_{p,90} = 15.2$, 14.7 and 14.2 s, respectively). This indicates that, for these conditions, gravity enhances the recirculation of large particles towards the base of the conical section of the SEVR so that they are re-entrained by the most intense part of the vortex flow. The values of $\tau_{p,90}$ for $d_p = 80\,\mu m$, decrease with ψ to a minimum at $\psi = +90^o$ with values of $\tau_{p,90} = 0.85$ and 0.79 s for $U_{in} = 30.7$ and $36.0\,m\,s^{-1}$, respectively. These values are only a factor of 1.4 greater than their respective mean residence times, indicating that there is little particle recirculation of larger particles within the SEVR, for positive tilt angles. The values of $\tau_{p,90}$ for $d_p = 20\,\mu m$ are relatively consistent in the range 1.7 to 3.0 s for $\psi \geq -60^o$, indicating that the alignment of gravity relative to the axis of the receiver has no significant effect on the extent to which 20 µm particles recirculate within the SEVR, in contrast to the effect of receiver tilt angle on the larger 80 µm particles.

Figure 4.14c presents the dependence of ${\sigma_p}^2$ on ψ. It can be seen that, for the conditions assessed, the normalised variance and mixing behaviour of the SEVR varies between that of a well-stirred reactor (for which ${\sigma_p}^2 = 1$) and that of a plug flow reactor (for which ${\sigma_p}^2 = 0$), following Danckwerts (1953), Levenspiel (1999), and Fogler (2006). The normalised variance increases from ${\sigma_p}^2 = 0.90$ with $\psi = -90^o$ to a maximum of ${\sigma_p}^2 = 1.23$ with $\psi = 0^o$ for $d_p = 80\,\mu m$ and $U_{in} = 30.7\,m\,s^{-1}$, which correspond to the cases in Figure 4.14a and b featuring longest residence time and greatest extent of particle recirculation. This indicates that the large-scale recirculation for particles of this size within the SEVR with $\psi \leq 0^o$ is close to the mixing behaviour of an ideal continuously-stirred tank reactor (CSTR). It should be noted that, for $d_p = 80\,\mu m$, $U_{in} = 30.7\,m\,s^{-1}$, and the two tilt angles, $\psi = -30^o$ and 0^o, the normalised variance values are ${\sigma_p}^2 > 1$, which indicates a slight departure from an ideal reactor, as also indicated by the highly skewed RTDs for these cases (as shown in Figure 4.13a and b). For $d_p = 80\,\mu m$ and positive tilt angles, an increase in ψ causes a decrease in ${\sigma_p}^2$ to a minimum of 0.10 with $\psi = +90^o$ and both U_{in}, indicating that the flow pattern of $d_p = 80\,\mu m$ particles approaches a plug flow. This is also evident from the RTDs plotted in Figure 4.13a and b. In contrast, for the smaller particles, $d_p = 20\,\mu m$, and both U_{in}, the value of ${\sigma_p}^2$ decreases from a maximum at $\psi = -90^o$ of ${\sigma_p}^2 = 0.62$ and 0.51 for $U_{in} = 30.7$ and $36.0\,m\,s^{-1}$, respectively, but is then relatively consistent around ~0.3 for $\psi \geq -30^o$ and both U_{in}. Taken together, the trends presented in Figure 4.14c suggest that the mixing behaviour of 20 µm particles is significantly less influenced by the receiver tilt angle than are the larger 80 µm particles, which varies between the extremes of well-stirred and plug flow mixing behaviours.

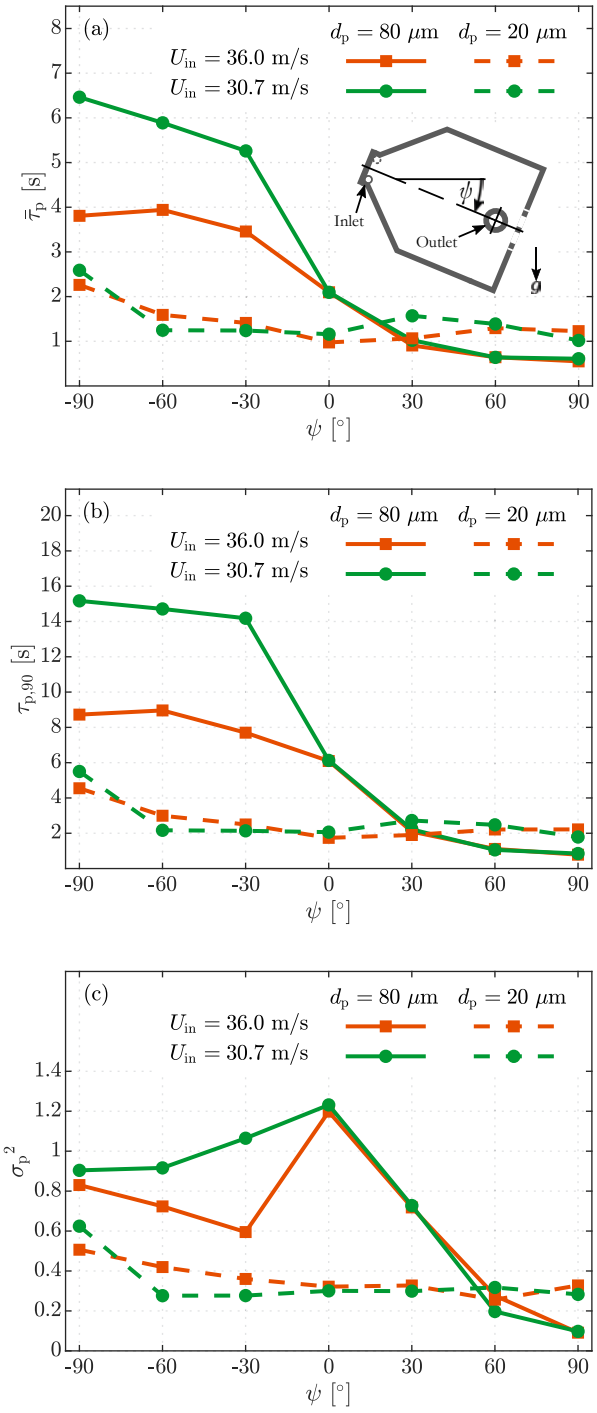

Figure 4.14: The statistical measures of the particle RTDs measured for seven receiver tilt angles in the range $\psi = -90°$ to $+90°$, and for two particle diameters, $d_p = 20$ and 80 µm, two inlet velocities $U_{in} = 30.7$ and 36.0 m s^{-1} with constant inlet diameter, $D_{in} = 6$ mm. The two inlet velocities generate nominal residence times $\tau_{nom} = 3.2$ and 2.7 s according to $\tau_{nom} = V_r / \dot{V}_{air}$ and $\dot{V}_{air} = U_{in} \times \left[2 \times (\pi/4) \times {D_{in}}^2\right]$. Presented are: **(a)** the mean particle residence time, $\bar{\tau}_p$, as a function of ψ; **(b)** the 90th percentile particle residence time, $\tau_{p,90}$, as a function of ψ; and **(c)** the normalised variance, ${\sigma_p}^2$, as a function of ψ.

Figure 4.15 presents the mean residence time of the measured particle RTDs, $\bar{\tau}_p$, as a function of Sk_{out}, for five values of receiver tilt angle in the range, $\psi = -90^o$ to $+90^o$, and for two Froude numbers evaluated in the cylindrical section of the receiver, $Fr_{cyl} = 3.8$ and 5.3 (generated with $U_{in} = 30.7$ and 36.0 m s^{-1}, respectively). These two values of Fr_{cyl} correspond to the *Froude-Stokes* and *cyclonic* regimes of particle behaviour within the SEVR.

For the negative tilt angles, $\psi = -90^o$ and -30^o, it can be seen that the particle residence time is controlled by both the particle inertia at the receiver outlet (Sk_{out}) and the influence of gravity. That is, for both $Fr_{cyl} = 3.8$ (Figure 4.15a) and $Fr_{cyl} = 5.2$ (Figure 4.15b), $\bar{\tau}_p$ increases with Sk_{out}, due to the increased inertia of a particle at the radially-oriented outlet that inhibits it from leaving the receiver. For the *Froude-Stokes* regime, this increase is more pronounced because, in addition to the effect of increased inertia, gravity plays a greater role in resisting the axial motion in the positive z direction and recirculating the particles to bottom of the receiver. This results in significantly longer residence time. For the *cyclonic* regime, the inertial centrifugal force is of greater importance in influencing particle motion and retaining particles in suspension flow near to the receiver outlet. This implies that the features of the *Froude-Stokes* and *cyclonic* regimes of operation are the same for the negative receiver tilt angles, $\psi = -60^o$ and -30^o as those reported in Section §4.2 for $\psi = -90^o$.

In contrast, for the positive receiver tilt angles $\psi \geq 0^o$, the effect of both ψ and Fr_{cyl} is relatively weak, with approximately equal values of $\bar{\tau}_p$ at the same Sk_{out} for both regimes. That is, for $\psi \geq 0^o$ and the conditions assessed in the present study, the *Froude-Stokes* and *cyclonic* regimes of operation cannot be distinguished, which may indicate that the device is inertia dominated. Furthermore, both regimes exhibit a residence time trend that decreases with Sk_{out} for $\psi > 0^o$, which is a feature not identified in Section §4.2. That is, for both $Fr_{cyl} = 3.8$ and 5.3, $\bar{\tau}_p$ decreases with increasing Sk_{out}, for the cases where the outlet is below the inlet. This is because at low Sk_{out}, particles exhibit a strong response to the flow, such that they are entrained within the vortical flow for a longer duration than particles with large Sk_{out}, which have a more direct path to the exit due to the effect of gravity. It should also be noted that for the case of a horizontal receiver tilt angle ($\psi = 0^o$), there is a weak increase in $\bar{\tau}_p$ with Sk_{out}, for both $Fr_{cyl} = 3.8$ and 5.3. For $\psi = 0^o$, there is no component of gravity acting in the axial direction, so that the increase in $\bar{\tau}_p$ can be attributed only to the increased inertia of the particles. This indicates that the particle residence time characteristics of vortex-based solar particle receivers operating in a horizontal orientation for laboratory testing with a solar simulator will potentially exhibit different residence time characteristics to those of solar particle receivers with beam-up or beam-down orientations in CST systems.

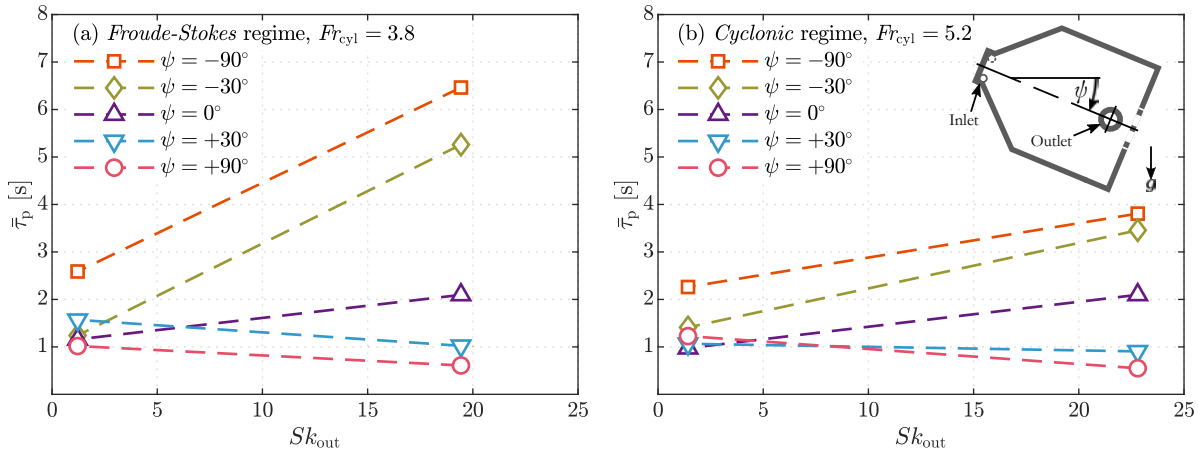

Figure 4.15: The mean particle residence time, $\bar{\tau}_p$, as a function of Sk_{out}, for five values of receiver tilt angle in the range, $\psi = -90°$ to $+90°$, and for **(a)** the *Froude-Stokes* regime of operation with $Fr_{cyl} = 3.8$ (generated with $U_{in} = 30.7\ m\ s^{-1}$); and **(b)** the *cyclonic* regime of operation with $Fr_{cyl} = 5.2$ (generated with $U_{in} = 36.0\ m\ s^{-1}$).

4.3.3 Compartment model analysis

The compartment model developed in section §4.2.2 for beam-down receiver tilt angles ($\psi = -90^{o}$) is modified here to incorporate the effect of tilt angle on the measured particle residence time behaviour. Figure 4.16 presents the dimensionless particle RTDs, $E(\theta)$, measured for the smaller particle size, $d_{p} = 20\,\mu m$, for $U_{in} = 30.7\,m\,s^{-1}$ and for the receiver tilt angles $\psi = -60^{o}$, -30^{o}, 0^{o} and $+90^{o}$. The dimensionless RTDs for the range of receiver tilt angles considered can be described similarly to those presented above for $\psi = -90^{o}$. That is, $E(\theta)$ remains at zero for short dimensionless times, δ_1, defined as the ratio of the time for which the pulse response is zero to the mean particle residence time, after which $E(\theta)$ increases rapidly to a maximum value, and then decreases at a slower rate to zero. It can also be seen that, for $\psi = -30^{o}$ and 0^{o} (Figure 4.16b and c), small peaks were detected in the RTD before the primary peak. This can be attributed to wall-related interactions, such as adhesion/re-entrainment, that are prevalent for these cases with tilt angle close to the horizontal. However, the area bounded by these peaks is always less than 5% of the total area bounded by the RTD, so that these effects are small here.

The compartment model describing the residence time behaviour presented in Figure 4.16 consists of a very small plug flow reactor (PFR) in series with two continuously-stirred tank reactors (CSTRs) as was described above. For the case of low velocities and Froude numbers (*Froude-Stokes* regime) there is back mixing between the two CSTRs causing them to behave as a single CSTR, while for higher velocities and Froude numbers (*cyclonic* regime) there is no back-mixing. Figure 4.16 presents the analytical RTDs corresponding to this configuration of compartment model as applied to the alternative values of ψ in the present study. It can be seen from the comparison between the experimental and analytical dimensionless RTDs that this same configuration of compartment model describes the residence time behaviour of the smaller particles, $d_{p} = 20\,\mu m$, and all alternative receiver tilt angles, $\psi > -90^{o}$, assessed here.

The analytical equation of the dimensionless RTDs presented in Figure 4.16 can be expressed as follows:

$$E(\theta) = \frac{1+\varepsilon}{(\varepsilon-1)(1-\delta_1)}\left[\exp\left(-\frac{(\theta-\delta_1)(1+\varepsilon)}{\varepsilon(1-\delta_1)}\right) - \exp\left(-\frac{(\theta-\delta_1)(1+\varepsilon)}{(1-\delta_1)}\right)\right] u(\theta-\delta_1), \tag{4.10}$$

where ε represents the ratio of the space-times of the two CSTRs and $u(\theta-\delta)$ is the Heaviside function. This analytical equation corresponds to the above mentioned configuration of compartment model and applies for operation in both the *Froude-Stokes* and *cyclonic* regimes. For the *Froude-Stokes* regime, $\varepsilon \to 0$ so that $E(\theta)$ tends towards that describing a PFR in series with a single CSTR, while for operation in the cyclonic regime, $E(\theta)$ describes a PFR in series with two CSTRs. The

constant compartment model configuration for all ψ and $d_p = 20\,\mu m$ implies that the behaviour of smaller particles within the SEVR is not significantly affected by the receiver tilt angle. While not pictured in Figure 4.16, the same equation and mixing patterns were found to apply for the higher inlet velocity case, $U_{in} = 36.0\,m\,s^{-1}$.

The values of the parameters used in Equation (4.10) to describe the dimensionless RTDs for $d_p = 20\,\mu m$ and all ψ are listed in Table 4.9. It can be seen that, for both U_{in}, ε is in the range 1.01 to 3, suggesting that for the present range of velocities, there is not a significant distinction in the amount of recirculation through the receiver. Also, for the smaller particle size, $d_p = 20\,\mu m$, and all tilt angles except $\psi = +60°$, the value of δ_1 decreases to a small extent with U_{in}, indicating that the higher velocity causes the particles to fill the reactor inventory more rapidly. The small increase in δ_1 for $\psi = +60°$ can be attributed to experimental error.

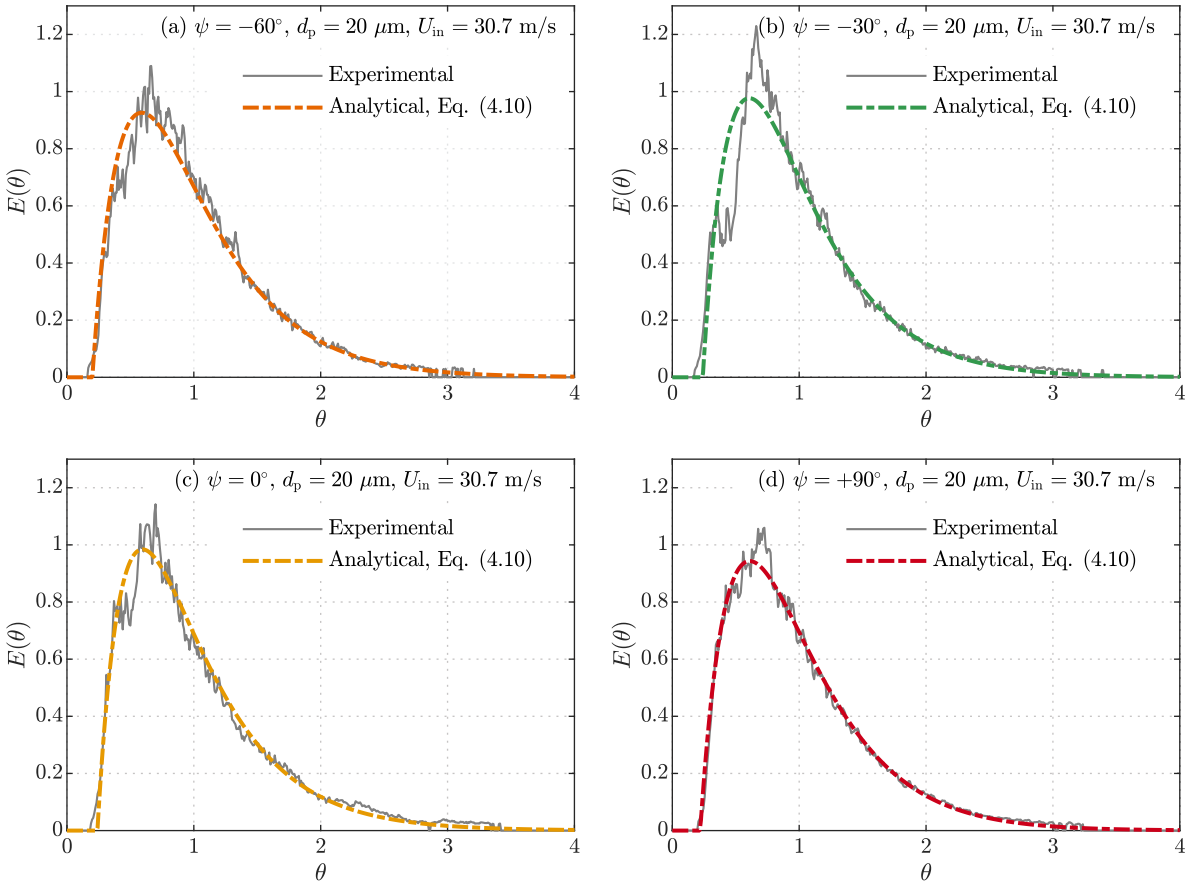

Figure 4.16: The experimentally measured dimensionless particle RTDs and functions of their corresponding analytical compartment models for $U_{in} = 30.7\,m\,s^{-1}$, $d_p = 20\,\mu m$ and the receiver tilt angles: **(a)** $\psi = -60°$; **(b)** $\psi = -30°$; **(c)** $\psi = 0°$; and **(d)** $\psi = +90°$. The function of the analytical distributions shown here is given in Equation (4.10) while the values of the equation parameters are listed in Table 4.9.

Figure 4.17 presents the dimensionless particle RTDs, $E(\theta)$, measured for the larger particle size, $d_p = 80\,\mu m$, for $U_{in} = 30.7\,m\,s^{-1}$ and for the receiver tilt angles $\psi = -60^o$, -30^o, 0^o and $+90^o$. It can be seen that the measured dimensionless RTDs deviate significantly from the previously developed compartment model described by Equation (4.10), due to the prominence of a peak in the measured distributions at dimensionless time, $\theta \approx 0.1 - 0.2$. This peak is visible for $\psi = -60^o$, -30^o and 0^o (Figure 4.17a, b and c) and appears at a significantly shorter dimensionless time than the than the peak in the dimensionless RTDs for $d_p = 20\,\mu m$ (Figure 4.16). This type of peak in the distribution is associated with a pathway through the reactor alternative to the well-mixed CSTR path identified previously. Aerodynamically, the alternative path is associated with a different flow regime, such that larger particles follow a different path to the flow, resulting in less particle recirculation and shorter mean residence times. Analytically, such an alternative path can be approximated by a PFR (Levenspiel 1999).

To account for the deviations from the compartment model described above that occur for $d_p = 80\,\mu m$ and $\psi > -90^o$, a modified compartment model configuration is proposed here. This modified compartment model consists of a small PFR (as previously) followed by two parallel branches, one containing the two CSTRs in series (as previously) and the other branch containing a PFR. The analytical equation to describe the modified compartment model of small PFR followed by a CSTR and PFR in parallel can be expressed as follows:

$$E(\theta) = \frac{\beta}{\theta_{CSTR}} \exp\left(-\frac{\theta - \delta_1}{\theta_{CSTR}}\right) u(\theta - \delta_1) + (1-\beta)\frac{1}{\delta_2}\left(\frac{\theta - \delta_1}{\delta_2}\right)^{N-1} \frac{N^N}{(N-1)!} \exp\left(-\frac{(\theta - \delta_1)N}{\delta_2}\right) u(\theta - \delta_1), \tag{4.11}$$

where β is the fraction of particles taking the path to the CSTR, $(1-\beta)$ is the fraction of particles taking the path to the PFR (with dimensionless space-time equal to δ_2) and θ_{CSTR} is the dimensionless space-time of the CSTR. It should be noted that the two CSTRs in series from the compartment model describing $d_p = 20\,\mu m$ is here modelled as a single CSTR for simplicity. Also the PFR on the parallel branch (with $(1-\beta)$ fraction of particles) is modelled as N CSTRs in series, where N is the number of CSTRs that best approximates the residence time of the parallel PFR component of the compartment model (Fogler 2006). The compartment model expressed by Equation (4.11) describes the residence time behaviour for $d_p = 80\,\mu m$, $U_{in} = 30.7\,m\,s^{-1}$ and all alternative receiver tilt angles $\psi > -90^o$, as can be seen from the analytical dimensionless RTDs also presented in Figure 4.17 (together with those for $U_{in} = 36.0\,m\,s^{-1}$, not presented here).

The values of the parameters used in Equation (4.11) to describe the dimensionless RTDs for $d_p = 80\,\mu m$ are listed in Table 4.9, from which it can be seen that β decreases so that the relative proportioning of two-phase flow to the PFR branch increases with both U_{in} and the tilt angle from $\psi = -60^o$ to $+90^o$. This implies that the fraction of large particles that bypass the recirculation (i.e.

to take the PFR branch) increases with the tilt angle. The significance of the bypass is greatest for $\psi = +90^{\circ}$ (Figure 4.17d), where all of the particles tend towards a plug flow response. This deduction is also consistent with the values of the normalised variance presented in Figure 4.14c and with the values $\beta = 0$ and $N = 17$ for $d_p = 80\,\mu m$ and $\psi = +90^{\circ}$ (Table 4.9). The analytical distribution in Figure 4.17d is almost symmetrical about $\theta = 1$ as is the case for an ideal PFR. Furthermore, for N CSTRs in series, the RTD can be assumed to be representative of a plug flow reactor for $N \geq 10$ (Levenspiel 1999). While not pictured in Figure 4.17, the modified compartment model and Equation (4.11) were also found to apply for the higher inlet velocity case, $U_{in} = 36.0\,m\,s^{-1}$ and $d_p = 80\,\mu m$ for each value of ψ.

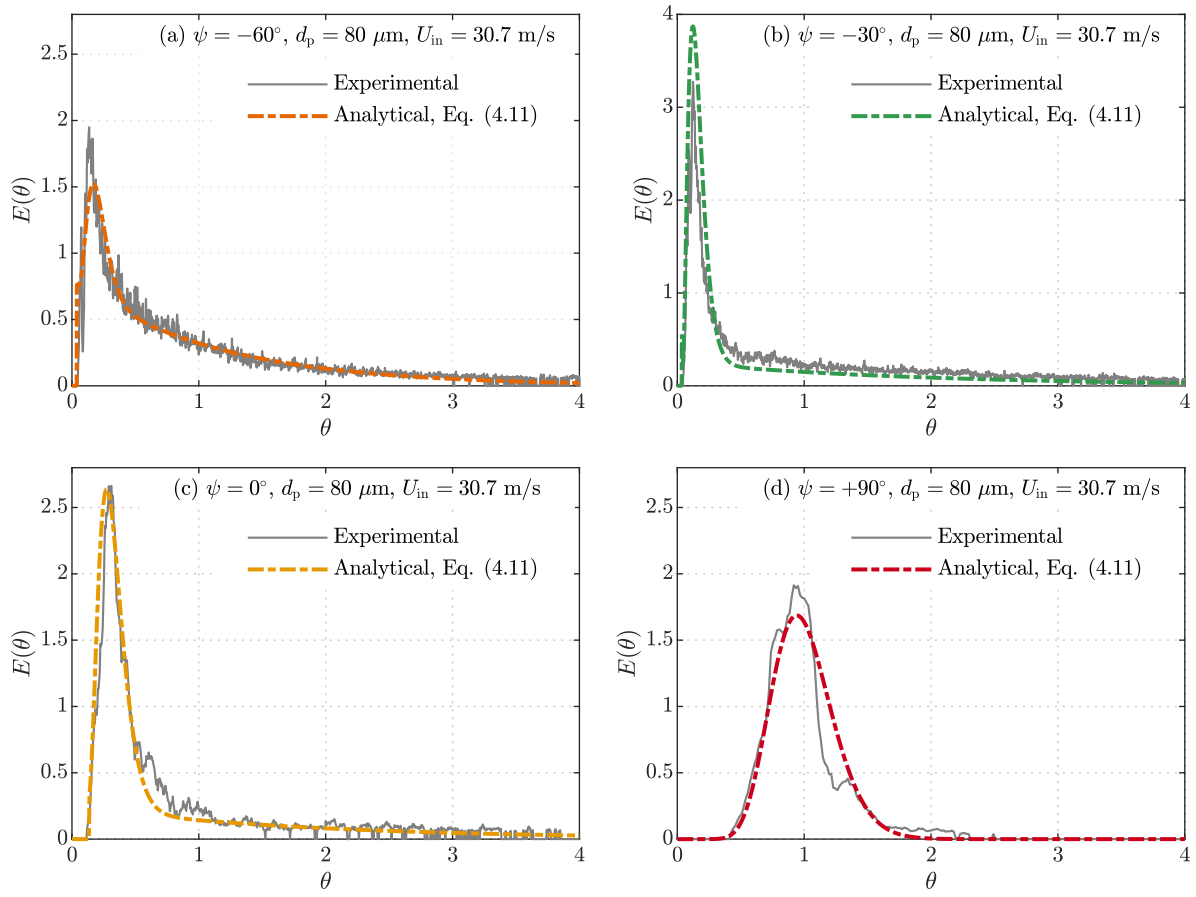

Figure 4.17: The experimentally measured dimensionless particle RTDs and functions of their corresponding analytical compartment models for $U_{in} = 30.7\,m\,s^{-1}$, $d_p = 80\,\mu m$ and the receiver tilt angles: **(a)** $\psi = -60^{\circ}$; **(b)** $\psi = -30^{\circ}$; **(c)** $\psi = 0^{\circ}$; and **(d)** $\psi = +90^{\circ}$. The function of the analytical distributions shown here is given in Equation (4.11) while the values of the equation parameters are listed in Table 4.9.

Figure 4.18 presents a schematic representation of the unified compartment model describing the particle RTD behaviour of the SEVR for the range of receiver tilt angles assessed here and for U_{in} = 30.7 and 36.0 m s^{-1}, and d_p = 20 and 80 µm. For each case, the values of the parameters used in Equations (4.10) and (4.11) are listed in Table 4.9. These values were determined by fitting the equations of the analytical dimensionless RTDs to the experimentally measured dimensionless RTDs, with a coefficient of determination R^2 always higher than 0.94.

The influence of receiver tilt angle on the residence time behaviour of the SEVR in the present study can be described as follows:

- For all ψ, d_p and U_{in} (assessed here), the flow passes through the small PFR$_1$, which represents the time taken for particles to fulfil the reactor inventory. The space-time of the PFR$_1$ component, δ_1, generally decreases with U_{in}.
- For $\psi = -90°$ and both d_p = 20 and 80 µm, $\beta = 1$, so that the residence time behaviour of particles of both sizes is represented by particles taking only the CSTR path to pass through the receiver, undergoing significant extents of particle recirculation (Equation (4.10)). In the low velocity, *Froude-Stokes* regime there is back-mixing between CSTR$_1$ and CSTR$_2$ so that they behave as a single CSTR, while for the higher velocity, *cyclonic* regime, the back-mixing is negligible.
- For all $\psi \geq -90°$ and d_p = 20 µm, $\beta = 1$, so that the residence time behaviour of smaller particles is represented by particles taking only the CSTR branch. The extent of their recirculation is not significantly influenced by the receiver tilt angle (Equation (4.10)).
- For $\psi = -60°$, $-30°$, 0°, $+30°$, $+60°$ and d_p = 80 µm, $\beta \neq 1$, so that the residence time behaviour of larger particles is represented by some fraction of particles taking the shorter parallel PFR$_2$ branch (Equation (4.11)). The fraction of particles passing the PFR$_2$ branch increases with both ψ and U_{in}. Furthermore, the behaviour of the PFR$_2$ branch tends towards that of an ideal PFR with increasing ψ, as N increases from 3 to 11 for an increase from $\psi = -60°$ to $+60°$.
- For $\psi = +90°$ and d_p = 80 µm, $\beta = 0$, so that the residence time behaviour of larger particles is represented by particles taking only take the PFR$_2$ branch and the particle RTD is representative of a purely plug flow reactor (Equation (4.11)).

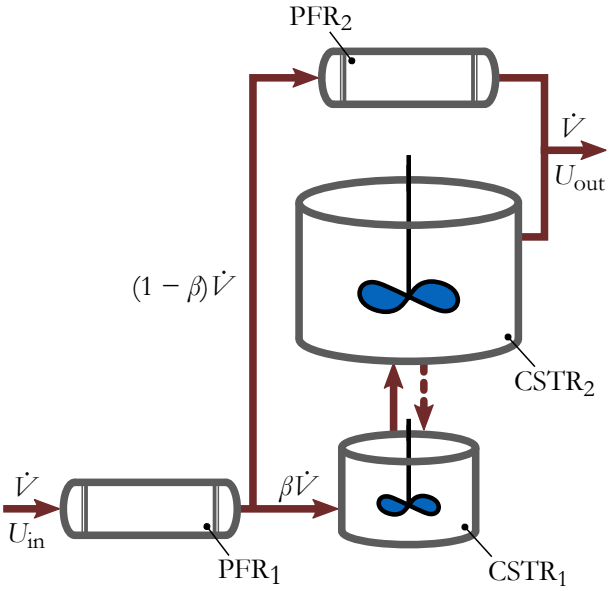

Figure 4.18: Schematic representation of the unified compartment model describing the particle RTD behaviours of the SEVR for the seven receiver tilt angles assessed here, $\psi = -90^{\circ}$, -60°, -30°, 0°, $+30^{\circ}$, $+60^{\circ}$ and $+90^{\circ}$, and for $U_{\text{in}} = 30.7$ and $36.0\,\text{m}\,\text{s}^{-1}$, and $d_{\text{p}} = 20$ and $80\,\mu\text{m}$. For each operational case, the relative proportioning, β, between the CSTR branch ($\text{CSTR}_1 + \text{CSTR}_2$) and the parallel PFR_2 branch is listed in Table 4.9, together with the values of the additional parameters used to describe the analytical dimensionless RTDs in Equations (4.10) and (4.11).

Table 4.9: The operational details and corresponding values of the parameters used in Equations (4.10) and (4.11) to describe the measured particle RTDs with analytical compartment models.

ψ [°]	d_p [µm]	Fr_{cyl}	U_{in} [m s^{-1}]	δ_1	ε	δ_2	N	β
−90	80	3.8	30.7	0.09	0	-	-	1
		5.2	36.0	0.08	0.1	-	-	1
	20	3.8	30.7	0.13	0	-	-	1
		5.2	36.0	0.094	6	-	-	1
−60	80	3.8	30.7	0.05	-	0.17	4	0.84
		5.2	36.0	0.08	-	0.18	4	0.89
	20	3.8	30.7	0.25	3	-	-	1
		5.2	36.0	0.2	1.5	-	-	1
−30	80	3.8	30.7	0.04	-	0.12	3	0.47
		5.2	36.0	0.06	-	0.17	3	0.64
	20	3.8	30.7	0.24	1.6	-	-	1
		5.2	36.0	0.21	1.6	-	-	1
0	80	3.8	30.7	0.21	-	0.21	4	0.42
		5.2	36.0	0.18	-	0.18	4	0.48
	20	3.8	30.7	0.24	1.9	-	-	1
		5.2	36.0	0.24	2	-	-	1
+30	80	3.8	30.7	0.25	-	0.35	3	0.20
		5.2	36.0	0.22	-	0.35	4	0.26
	20	3.8	30.7	0.23	1.01	-	-	1
		5.2	36.0	0.22	2.55	-	-	1
+60	80	3.8	30.7	0.26	-	0.55	10	0.18
		5.2	36.0	0.16	-	0.63	11	0.26
	20	3.8	30.7	0.24	1.1	-	-	1
		5.2	36.0	0.26	1.1	-	-	1
+90	80	3.8	30.7	0	-	1	17	0
		5.2	36.0	0	-	1	17	0
	20	3.8	30.7	0.22	1.01	-	-	1
		5.2	36.0	0.15	1.01	-	-	1

4.3.4 Preliminary scaling analysis

A preliminary scaling analysis is presented here with the goal of providing insights into the mechanisms controlling the particle residence time behaviour of a nominal industrial scale SEVR. Table 4.10 presents the nominal thermal scale of the present laboratory-scale SEVR device, $\dot{Q}_s = 5\,\text{kW}$, compared with that of a SEVR scaled up to a nominal industrial scale of $\dot{Q}_s = 50\,\text{MW}$. The preliminary sizing of the nominal industrial device has been determined by assuming constant solar thermal heat flux, so that the aperture area scales linearly with the thermal input ($A_{ap} \propto \dot{Q}_s$) and by assuming geometric similarity, so that all receiver dimensions scale with the square root of the thermal input ($D_c \propto \dot{Q}_s^{1/2}$). By further assuming that the SEVR is scaled with constant inlet velocity and constant efficiency (i.e. that mass flow rates scale linearly with thermal input, $\dot{m}_p$, $\dot{m}_{air} \propto \dot{Q}_s$), it can be seen from Table 4.10 that the nominal residence time of the scaled-up receiver is two orders of magnitude longer than that of the laboratory-scale receiver (with a four order of magnitude increase in thermal scale). The choice of constant velocity scaling is reasonable for flows with particles in suspension because the velocity cannot be reduced significantly without resulting in particle drop-out and also cannot be increased significantly without resulting in both excessive fan power requirements and excessive erosion. It should be noted that this preliminary scaling analysis is intended to provide insight into the controlling mechanisms at larger scale, rather than providing a guide to the design of a scaled-up SEVR, which is a complex process that requires data at larger scale.

It can also be seen from the preliminary scaling analysis presented in Table 4.10 that particles of the same size in the scaled industrial receiver have lower values of both Fr_{cyl} and Sk_{out} by two orders of magnitude because dimensions of the receiver scale with the square root of thermal input, D_c, $D_{out} \propto \dot{Q}_s^{1/2}$. That is, this scaled-up SEVR would operate with relatively low Froude number and therefore the *Froude-Stokes* regime of operation would be more likely. Furthermore, for this scaling, the particle size is an order of magnitude larger to achieve the equivalent *Froude-Stokes* behaviour. That is, a particle size of $d_p = 200\,\mu\text{m}$ would have the same $Sk_{out} \sim 1$ in the larger device as the $d_p = 20\,\mu\text{m}$ particles in the laboratory-scale device, although the nominal residence time is two orders of magnitude greater. This implies that the influence of the tilt angle of the scaled-up SEVR on the residence time of particles will be insignificant for particles $d_p < 200\,\mu\text{m}$, indicating that the particle residence time characteristics of a tower-mounted SEVR using particles of this size will be constant, regardless of the required tilt angle for a given heliostat field layout. This potentially provides flexibility for incorporation of the scaled-up SEVR into CST systems with a range of tilt angles and is significant because many current industrial processes operate with particles of approximately this size. It should also be noted that alternative commonly used materials for particles in solar thermal receivers (e.g. ceramic particles) will likely have different density to the polymer particles used in the present study. This implies that the dimensionless Stokes numbers of

alternative particles (with alternative size and density) will need to be compared to gain insight into the likely residence time characteristics of alternative particles in a scaled-up SEVR.

The influence of higher operating temperatures on the particle residence time characteristics of a scaled-up SEVR can be estimated by also assuming constant velocity scaling and geometric similarity. Under these assumptions, the largest impact of increasing operating temperatures would be the change in gas-phase properties, most notable, the gas density and viscosity. For example, an operating temperature of 1000 K would reduce air density, and hence mass flow rate, in the scaled-up SEVR by a factor of 3.3 relative to room temperature (300 K). Although this will decrease the gas-phase mass flow rate, the effect on the particle RTD is expected to be minimal. The particle residence time is expected to be more significantly influenced by the gas-phase velocity, which is a function of the gas volumetric flow rate, rather than the mass flow rate. However, the increase in operating temperatures will typically increase gas-phase viscosity, which in turn will decrease the characteristic Stokes number, Sk_{out} (because $Sk_{out} \propto \mu_{air}^{-1}$ with constant U_{in}, ρ_p, d_p and geometry). For instance, an increase in operating temperatures from 300 K to 1000 K will decrease Sk_{out} by a factor of 2.3. The impact of this decrease in Sk_{out} is difficult to predict in general, because the influence of Stokes number is typically non-linear, such that a factor of 2.3 is expected to influence the two-phase flow only where $Sk_{out} \sim 1$ (Lau & Nathan 2014; Lau & Nathan 2016). That is, for cases where $Sk_{out} \gg 1$ the effect of higher operating temperatures is expected to be small, while for cases where $Sk_{out} \sim 1$, the reduction in Sk_{out} with higher operating temperatures will result in the particle-phase RTD more closely matching the gas-phase residence time. In summary, a change in operating temperature is only expected to significantly influence the particle RTD characteristics for cases where $Sk_{out} \sim 1$. However, experimental data are required to truly assess the impact of temperature on the particle residence time within the SEVR.

Table 4.10: Comparison of key operational and dimensionless parameters of the Solar Expanding Vortex Receiver (SEVR) at the present laboratory-scale with the equivalent values from a preliminary scaling analysis of the receiver at a nominal industrial scale. The preliminary scaling analysis assumes constant inlet velocity, volumetric loading and heat flux through the aperture, as well as geometric similarity of the SEVR.

	SEVR at laboratory-scale		SEVR scaled to industrial-scale	
$\dot{Q}_s$ [kW]	5		50×10^3	
D_c [m][a]	0.19		19	
U_{in} [m s^{-1}][b]	30.7	36.0	30.7	36.0
τ_{nom} [s][c]	3.2	2.7	320	270
Fr_{cyl} [d]	3.8	5.3	0.038	0.053
Sk_{out} for $d_p = 20\,\mu m$[e]	1.2	1.4	0.012	0.014
Sk_{out} for $d_p = 80\,\mu m$[e]	19.4	22.8	0.194	0.228
Sk_{out} for $d_p = 200\,\mu m$[e]	∼120	∼140	∼1.2	∼1.4
Sk_{out} for $d_p = 800\,\mu m$[e]	∼1940	∼2280	∼19.4	∼22.8

[a] $D_c \propto \dot{Q}_s^{1/2}$; [b] Constant velocity scaling; [c] $(V_r/\dot{V}_{air}) \propto (\dot{Q}_s^{3/2}/\dot{Q}_s)$, $\tau_{nom} \propto \dot{Q}_s^{1/2}$;
[d] $Fr_{cyl} \propto \dot{Q}_s^{-1/2}$; [e] $Sk_{out} \propto \dot{Q}_s^{-1/2}$, ($Sk_{out} \propto d_p{}^2$).

4.4 Key findings

A method for directly measuring the residence time distribution of the particle phase has been demonstrated in a laboratory-scale vortex-based solar particle receiver-reactor. Systematic assessment of the influence of particle size, inlet velocity, and air volumetric flow rate on the particle RTD within the SEVR configuration of vortex-based solar particle receiver with a vertical orientation relevant to beam-down solar concentrating optics has revealed two regimes of particle behaviour: a low Froude number regime, where Stokes number is also important, and a high Froude number regime, dominated by centrifugal inertial forces in a similar manner to cyclonic separators.

In the low Froude number regime of operation, termed the *Froude-Stokes* regime, the characteristic Froude number of the vortex within the cylindrical section of the receiver is less than four, i.e. $Fr_{cyl} < 4$. The characteristics of this regime of operation are:

- the Stokes number of the two-phase flow at the outlet from the device, Sk_{out}, has the greatest influence on the residence time of particles. Increasing Sk_{out} increases the residence time of particles due to their greater inertia, particularly in the vicinity of the radially-oriented outlet, making them more likely to be recirculated within the vessel; and
- the low Froude number implies that gravity is also important, which, for the vertical orientation, increases the likelihood that particles will be returned to the base of the vessel with the central reversed flow zone of the vortex.

Within the above regime, for a vertical orientation, both mechanisms work synergistically to preferentially increase the residence time of larger particles, relative to smaller particles.

The high Froude number regime of operation, termed the *cyclonic* regime, occurs for $Fr_{cyl} > 4$ and is characterised by the greater centrifugal inertial force acting on the particles. The characteristics of this regime of operation are:

- the centrifugal inertial force acting on the particles due to their tangential velocity is large enough to preferentially distribute particles near to the wall of the receiver. This keeps them out of the central reversed flow zone generated by the vortex; and
- the close proximity of the particles to the outer wall means that particles are more likely to exit the receiver and have shorter residence time than if they are recirculated through the central reversed flow zone.

Systematic variation of receiver tilt angle with two inlet velocities, and two particles sizes has revealed that alignment of the central axis of the SEVR relative to gravity has a significant influence on the particle RTD for large particles ($Sk_{out} > 10$), while it is relatively weak for small particles

($Sk_{out} \sim 1$). This implies that it may be preferable to operate a tower-mounted SEVR ($\psi > 0^o$) with $Sk_{out} \sim 1$, so that the receiver's particle residence time characteristics are independent of the tilt angle and the range of possible heliostat field and central tower system configurations.

It was found that the residence time of higher Stokes number particles relative to those of order unity is increased by upward facing receiver orientations (i.e. with negative tilt angles, $\psi < 0^o$) due to their increased inertia at the radially-oriented outlet and the influence of gravity in recirculating particles to the bottom of the receiver. For these upward facing orientations and the conditions assessed here, the increase in particle residence time with higher Stokes numbers is strong for operation in the low Froude number *Froude-Stokes* regime, while the increase is weaker for operation in the higher Froude number *cyclonic* regime, due to the greater importance of the inertial centrifugal force in retaining particles in suspension flow near to the receiver outlet. It was further found that, for downward facing receiver orientation (i.e. positive tilt angles, $\psi > 0^o$), the particle residence time decreases with increasing Stokes number, which can be attributed to the weaker response to the vortex flow of particles with higher Stokes number. These higher Stokes number particles therefore, have a more direct path to the exit due to the effect of gravity, than smaller particles which are entrained within the vortical flow for a longer duration. This effect was found to occur for both Froude numbers assessed, so that for $\psi > 0^o$, the residence time trend of the high and low Froude number regimes is the same.

From a receiver-reactor design point of view, it was found that the SEVR operating in the vertical beam-down orientation ($\psi = -90^o$) can be well described with an ideal reactor compartment model consisting of a small plug flow reactor followed by a series of two interconnected CSTRs. For operation in the *Froude-Stokes* regime (low Froude number) the experimentally observed particle recirculation phenomenon is accounted for in this compartment model with back-mixing between the two CSTRs. For the *cyclonic* regime of operation (high Froude number) the back-mixing between the CSTRs is negligible.

The influence of receiver tilt angle from a receiver-reactor design point of view is such that, for the largest particles assessed ($d_p = 80\,\mu m$), increasing the tilt angle of the device switches between well-stirred mixing conditions to plug flow particle RTD characteristics. The mixing behaviour of the smallest particles assessed ($d_p = 20\,\mu m$) were found to have intermediate mixing behaviour between well-stirred and a plug flow, which is independent of the tilt angle. The modified compartment model describing this receiver tilt angle effect, incorporates an additional branch containing a PFR in parallel with the two CSTRs. In this model configuration, the proportioning of the larger particles between the two parallel branches is dependent on the tilt angle, such that negative tilt angles favour the CSTR branch and undergo significant recirculation and long residence times, while positive tilt angles favour the PFR with shorter residence times. The smaller particle residence

time behaviour is described exclusively with the first PFR and the CSTR branch of the compartment model, which is the same as that described for the beam-down tilt angle.

A preliminary scaling analysis of the present receiver configuration scaled to a nominal industrial scale of 50 MW has shown that particles of size 200 µm and smaller would have residence time behaviour similar to the smallest particles considered in the present experimental assessment with $Sk_{out} \sim 1$. That is, the influence of receiver tilt angle on the residence time of particle with $d_p < 200$ µm would be small, which indicates flexibility for incorporation of the scaled-up SEVR into CST systems. Although the design of a scaled-up receiver is a complex process requiring further data of operation at larger scale.

5

Solar Calcination of Alumina

The third aspect of the performance of vortex-based solar particle receivers investigated in this thesis is the novel application of the device to an industrial thermochemical process: the calcination of alumina. This investigation was performed in a laboratory-scale vortex-based solar particle receiver, providing the first-of-a-kind demonstration that alumina can be calcined with concentrated solar radiation.

The experimental parameters of solar radiative flux, transport air volumetric flow rate and particle mass feed rate were systematically varied to assess the influence of key controlling parameters on the extent to which alumina can be calcined in a SVR. Additionally, assessments are made, as to the influence of the solar calcination process on the quality of alumina produced in terms of moisture content and microstructure. Finally a projection of the potential performance of an industrial-scale solar reactor is made, based on the experimental performance of the laboratory-scale device.

The material in this chapter has been published in the journal article:

Davis, D, Müller, F, Saw, WL, Steinfeld, A & Nathan, GJ 2017, 'Solar-driven alumina calcination for CO_2 mitigation and improved product quality', *Green Chemistry*, vol. 19, no. 13, pp. 2992–3005.

The article in its published format is available at: https://doi.org/10.1039/c7gc00585g

Statement of Authorship

Title of Paper	Solar-driven alumina calcination for CO_2 mitigation and improved product quality
Publication Status	☑ Published ☐ Accepted for Publication ☐ Submitted for Publication ☐ Unpublished and Unsubmitted w ork w ritten in manuscript style
Publication Details	Davis, D, Müller, F, Saw, WL, Steinfeld, A & Nathan, GJ 2017, 'Solar-driven alumina calcination for CO_2 mitigation and improved product quality', *Green Chemistry*, vol. 19, no. 13, pp. 2992-3005.

Principal Author

Name of Principal Author (Candidate)	Dominic Davis
Contribution to the Paper	Conducted literature review into the calcination of alumina process, and relevant solar processes. Designed experiments, identifying the key parameters to assess and the experimental apparatus required. Developed and built the particle feeder and settling chamber apparatus. Set up and performed all of the experiments. Analysed the alumina product properties post-experiments, via thermogravimetry, SEM analysis, XRD analysis, nitrogen porosimetry. Interpreted the experimental data. Wrote and edited the paper.
Overall percentage (%)	40%
Certification:	This paper reports on original research I conducted during the period of my Higher Degree by Research candidature and is not subject to any obligations or contractual agreements with a third party that would constrain its inclusion in this thesis. I am the primary author of this paper.
Signature	Date 26/2/2019

Co-Author Contributions

By signing the Statement of Authorship, each author certifies that:

i. the candidate's stated contribution to the publication is accurate (as detailed above);

ii. permission is granted for the candidate to include the publication in the thesis; and

iii. the sum of all co-author contributions is equal to 100% less the candidate's stated contribution.

Name of Co-Author	Fabian Müller		
Contribution to the Paper	Helped to design experiments, including the identification of required apparatus and procurement of thermocouples, flow controllers, scales, tubing and gas supply. Set up and performed all of the experiments. Provided key input into the interpretation of data and the presentation of results. Wrote portions of the manuscript, particularly the reactor set up and experimental arrangement in the Methodology. Edited the manuscript with further significant input into the results section.		
Signature		Date	31.1.19

Name of Co-Author	Woei Saw		
Contribution to the Paper	Helped with the design, manufacture and testing of experimental apparatus, particularly the particle feeder, the settling chamber. Helped with interpretation of the data and planning of the paper structure. Edited the manuscript.		
Signature		Date	25/02/2019

Name of Co-Author	Aldo Steinfeld		
Contribution to the Paper	Supervised the development of work, including identifying the potential for solar calcination of alumina. Provided laboratory space and key apparatus for the experiments, which included the solar simulator, the existing solar vortex transport reactor, associated mounting and gas piping, as well as apparatus for analysing the alumina product (Thermogravimetric analyser and particle sizer). Provided comments and edited the manuscript.		
Signature		Date	30-1-2019

Name of Co-Author	Graham 'Gus' Nathan		
Contribution to the Paper	Supervised the development of work, including identifying the potential for solar calcination of alumina. Provided input into the structure and key messages of the paper. Edited the manuscript.		
Signature		Date	25/2/2019

5.1 Experimental methodology

5.1.1 Solar reactor

The vortex-based solar particle reactor (solar vortex reactor, SVR) used for the investigation of the calcination of alumina is shown schematically in Figure 5.1. This configuration was developed previously for the gasification of petroleum coke (Z'Graggen et al. 2006) and the cracking of natural gas (Maag et al. 2009a). It consists of a 200 mm-long, 100 mm-diameter ceramic lined cylindrical cavity-receiver, enclosed by a 210 mm-long, 120 mm-diameter Inconel 601 shell and a water-cooled aluminium frustum with a 3 mm-thick transparent fused quartz window. The flow of transport air and suspended $Al(OH)_3$ particles is confined to the cavity-receiver and is directly exposed to concentrated solar radiation entering through a 50 mm-diameter aperture, with an apparent absorptivity estimated to exceed 93% (Howell et al. 2011). The window is cooled and protected from particle deposition by two injected air flows: one entering radially through a circular gap directed over the internal face of the window (with flow rate $2 - 4\,L_n\,min^{-1}$), and a second through four tangential nozzles on the frustum (with flow rate $1 - 2\,L_n\,min^{-1}$). The combination of the two purge flows suppresses the migration of particles into the frustum region. The vortex transport gas flow of synthetic air was generated by two tangentially oriented nozzles at the top ($2 - 7\,L_n\,min^{-1}$ air flow) and the bottom ($2 - 7\,L_n\,min^{-1}$ air flow) of the cavity and 30 mm behind the aperture. The particles were fed to the reactor through the tangential nozzle at the top of the cavity.

5.1.2 Reactants

Aluminium hydroxide particles in the gibbsite form with a purity of 99% were used as the reactant. Figure 5.2 presents the particle size distribution of the $Al(OH)_3$, whose mean was 15.5 µm as determined with laser scattering (*HORIBA LA-950*). The SSA of the particles was found to be $1.3\,m^2\,g^{-1}$, determined with Brunauer-Emmett-Teller method (BET, *Belsorp-max*). Particles were entrained and fed using a fluidised bed feeder designed to operate over the range $1 - 2\,g\,min^{-1}$. Two streams of air were used to control the feeding of the $Al(OH)_3$ particles, one entering through a sintered plate at the bottom of the feeder to fluidise the particles, and a second flow passing through a horizontal 5 mm-diameter carrier tube, which is aligned approximately 30 mm below the top of the static particle bed. A 1 mm hole in the upper surface of the carrier tube was used to entrain particles into the carrier tube air flow. The gibbsite mass feed rate was monitored online with weight scales (*Kern FKB*).

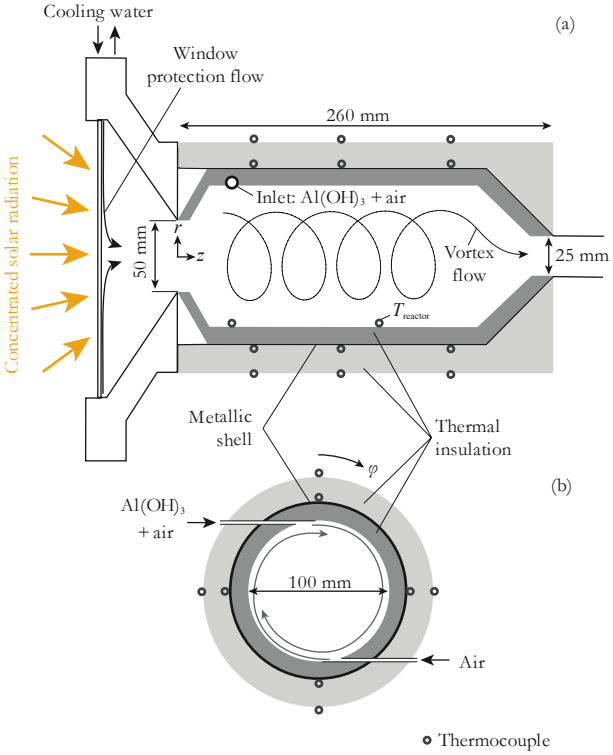

Figure 5.1: Schematic diagram of **(a)** the axial cross section; and **(b)** the front view of the solar vortex reactor.

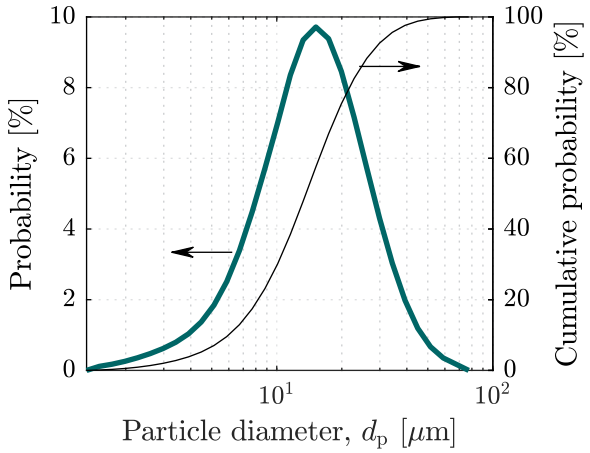

Figure 5.2: Size distribution of the reactant gibbsite particles fed to the reactor.

5.1.3 Experimental arrangement

The experimental arrangement is shown in Figure 5.3. Measurements were performed with the High-Flux Solar Simulator of ETH Zurich, which comprises an array of 7 high-pressure Xenon arcs, each close-coupled with truncated ellipsoidal specular reflectors. This provides an external source of intense thermal radiation – mostly in the visible and IR spectra – that closely approximates the heat transfer characteristics of highly concentrating solar optical systems. The solar radiative input power, $\dot{Q}_s$, was measured optically with a Lambertian target and a calibrated CCD camera. $\dot{Q}_s$ was varied over the range 2.1 – 4.3 kW, which corresponds to mean solar concentration ratios, C, through the aperture in the range 1070 – 2190 suns (1 sun = 1 kW m^{-2}). Temperatures were measured with type-K thermocouples at locations shown in Figure 5.1. A reference nominal reactor temperature, $T_{reactor}$, was measured with an Al_2O_3-shielded thermocouple located within the cavity as shown in Figure 5.1. The nominal wall temperature, T_{wall}, was calculated as the average of seven thermocouples located on the outside of the Inconel shell ($r = 61$ mm), covered with insulation, at various z-φ locations: (50 mm, 0°); (115 mm, 0°; 90°; 180°; 270°); (190 mm, 0°; 180°).

The total transport air normal flow rate, $\dot{V}_{air,n}$, was controlled with electronic flow controllers (*Bronkhorst HI-TEC*). Dry synthetic air was used as the transport air with normal flow rates, $\dot{V}_{air,n}$, in the range 12.0 – 20.0 L$_n$ min^{-1}. Additionally, for one experimental run the water vapour partial pressure in the reactor was controlled by adding steam to the air flow of the second tangential inlet with an electric steam generator (*Bronkhorst F- 201C*). The steam was injected with a mass flow rate of $\dot{m}_{steam} = 1.17$ g min^{-1} corresponding to a vapour partial pressure of 68.6 mbar.

The gibbsite particle nominal residence time, τ_{nom}, within the reactor was calculated from the cavity volume, V_r, and the total volumetric flow rate of transport air and gas product, $\dot{V}_{air}$ ($\dot{V}_{air,n}$ corrected for reactor temperature). The $\dot{V}_{air}$ input of the present investigation led to $\tau_{nom} = 1.38$ – 3.40 s. The similar value of nominal residence time in the present experimental facility to that of an industrial device despite three orders of magnitude smaller volume is attributed in part to much smaller ratio of the diameter of the inlet pipe to that of the reactor and, in part, to different methods of determining residence time. Experiments reported in Chapter 4 have shown that the actual particle residence time is unlikely to be equal to the nominal value, however, for particles that have low enough inertia that they follow the gas vortex flow closely (i.e. the Stokes number is $\ll 1$), it is reasonable to assume that the trends presented here as a function of τ_{nom} will be reliable. An average Stokes number of the particles transported through the SVR is defined, following Derksen et al. (2006), as:

$$Sk_{Derksen} = \frac{\rho_p d_p^2 U_{in}}{18 \mu D_c}, \tag{5.1}$$

which is calculated for the present investigation to be $Sk_{Derksen} \ll 1$.

The $Al(OH)_3$ particles were fed to the reactor with constant feeder conditions at ambient temperature and at mass flow rates, $\dot{m}_{Al(OH)_3}$, in the range $0.55 - 2.53\,g\,min^{-1}$. The particle to air volume fraction, ϕ, was controlled over the range $0.35 \times 10^{-5} - 1.66 \times 10^{-5}$ with changes to either $\dot{V}_{air}$ or $\dot{m}_{Al(OH)_3}$, and is defined as:

$$\phi = \frac{\dot{V}_{Al(OH)_3}}{\dot{V}_{air}}. \tag{5.2}$$

The product particles were collected in a settling chamber downstream from the reactor. The water vapor concentration in the outlet air, $\dot{m}_{H_2O}$, was measured online, downstream from the settling chamber, with a dew point sensor (*Vaisala DMT346*).

Measurements were taken at approximately steady-state and isothermal (to within 26 K) conditions, which follows a period of pre-heating to the desired temperature. Operating parameters were averaged over the duration of reactant particle feeding. A summary of the operating conditions of the 19 nominally steady-state experimental runs is provided in Table 5.1 (with additional details provided in Appendix C).

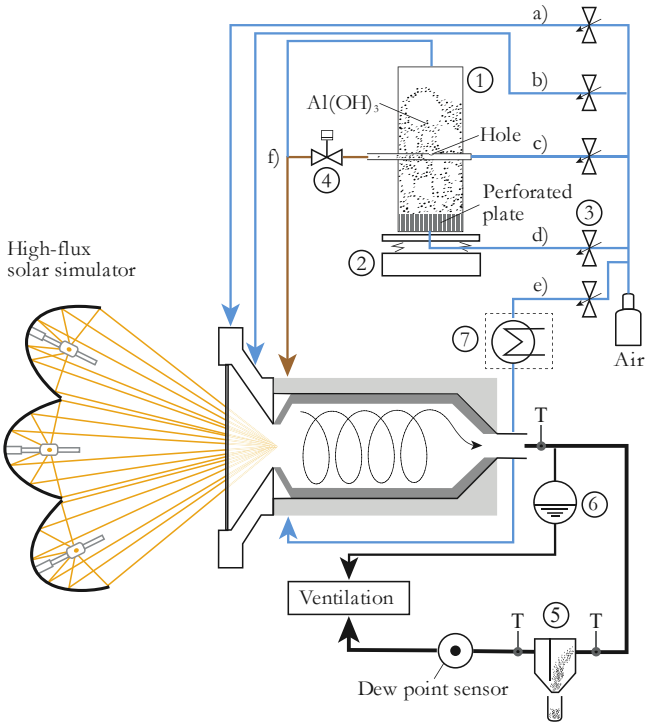

Figure 5.3: Experimental arrangement used to calcine alumina with the high-flux simulated solar radiation: (T) thermocouples, (1) fluidised bed feeder, (2) weight scales, (3) mass flow controllers, (4) piston valve, (5) settling chamber (with particle collection), (6) hydrostatic over pressure system, (7) optional steam generator unit, (a) radial window purge air, (b) tangential window purge air, (c) carrier air, (d) fluidising air, (e) 2nd tangential reactor inlet (no particles), (f) fluidising air exhaust connects to other gas flows.

Table 5.1: Summary of operational conditions for the 19 nominally steady-state experimental runs.

#	$\dot{Q}_s$ [W]	$\dot{V}_{air,n}$ [$L_n\,min^{-1}$]	$\dot{m}_{steam}$ [$g\,min^{-1}$]	$\dot{m}_{Al(OH)_3}$ [$g\,min^{-1}$]	$T_{reactor}$ [K]	T_{wall} [K]	ϕ [-]	τ_{nom} [s]
1	2285	20.03	-	1.12	1259	1114	0.57×10^{-5}	1.74
2	2108	20.03	-	0.73	1213	1020	0.40×10^{-5}	1.91
3	3642	20.03	-	0.95	1479	1246	0.43×10^{-5}	1.56
4	2132	20.03	-	0.84	1226	934	0.51×10^{-5}	2.08
5	2316	12.03	-	1.35	1258	1122	1.13×10^{-5}	2.81
6	2117	12.03	-	1.39	1161	928	1.40×10^{-5}	3.40
7	3773	12.03	-	1.45	1454	1272	1.07×10^{-5}	2.47
8	2291	20.03	-	2.07	1230	1106	1.06×10^{-5}	1.72
9	2211	20.03	-	1.33	1216	977	0.77×10^{-5}	1.97
10	4224	20.03	-	1.98	1421	1258	0.89×10^{-5}	1.51
11	3730	12.03	-	2.32	1480	1311	1.66×10^{-5}	2.33
12	3383	17.03	-	1.26	1414	1227	0.68×10^{-5}	1.84
13	3492	12.03	-	1.75	1408	1219	1.35×10^{-5}	2.55
14	4262	19.85	-	2.53	1551	1371	1.05×10^{-5}	1.38
15	3766	16.03	-	1.06	1456	1254	0.60×10^{-5}	1.92
16	2362	16.03	-	1.14	1208	1051	0.76×10^{-5}	2.29
17	2198	16.03	-	0.55	1179	943	0.41×10^{-5}	2.58
18	3965	20.03	-	1.35	1459	1284	0.59×10^{-5}	1.50
19	3832	20.03	1.17	0.85	1439	1262	0.35×10^{-5}	1.43

5.1.4 Product characterisation

Representative samples were taken from the collected particles in the settling chamber for post-experimental analyses of the following parameters: the loss on ignition (LoI) determined from the relative mass change during thermogravimetric analysis (TGA, *Netzsch STA 409 CD*); the particle morphology imaged by scanning electron microscopy (SEM, *Philips XL30*); the phases present in the sample by X-ray diffraction data (XRD, *Rigaku MiniFlex 600 diffractometer*), and the product microstructure, which was in turn evaluated by measurement of both SSA with the Brunauer-Emmett-Teller method (BET, *Belsorp-max*) and pore size distribution with the Barrett-Joyner-Halenda method (BJH, *Belsorp-max*).

Figure 5.4 presents the relative mass changes for the reactant $Al(OH)_3$ and for a representative solar-processed sample collected from the settling chamber as a function of the TGA reference temperature, T_{TGA}. This shows that the $Al(OH)_3$ begins to decompose at about 500 K, following which the mass loss increases to a maximum of 34.6 wt.% corresponding to the complete conversion of $Al(OH)_3$ to Al_2O_3. Figure 5.4 also shows that a small quantity of adsorbed moisture from the cooled, solar-processed alumina sample is released during its re-heating from ambient temperature to 423 K. The mass of this process can be quantified by the mass "Loss on Ignition" (LoI) in the temperature range: 298 – 423 K, denoted here as LoI_{ads}. The further mass loss of the solar-processed alumina from its heating to higher temperatures corresponds to the mass percentage of unreacted $Al(OH)_3$ in the solar-processed alumina. The LoI over this second range, 423 – 1273 K, is denoted as LoI_X and is used in the present investigation to calculate the overall molar conversion of $Al(OH)_3$ to Al_2O_3, X, according to:

$$X = \frac{2n_{Al_2O_3}}{n_{Al(OH)_3} + 2n_{Al_2O_3}}, \tag{5.3}$$

where, $n_{Al_2O_3}$ and $n_{Al(OH)_3}$ are the molar quantities of alumina product and unreacted $Al(OH)_3$ in the solar-processed alumina (as determined from LoI_X). The ISO standard for reporting alumina moisture content is by the LoI_{1273}, evaluated over the temperature range 573 – 1273 K (Hyland et al. 1997; Perander et al. 2011; Sommerseth et al. 2012). However, it has been shown that the reactant $Al(OH)_3$ begins to decompose at temperatures below 573 K, which means that the LoI_{1273} underestimates the amount of unreacted $Al(OH)_3$. This provides justification for the use of LoI_{ads} and LoI_X in the present investigation. Errors in the TGA measurements result from the large SSA of transition aluminas and their reactivity with moisture in the air. This error affects measurement of the LoI_{ads} most significantly, but also affects the measurement of chemical conversion, X. The relative errors in LoI_{ads} and X were determined to be $\pm$ 3.3% and $\pm$ 18.7%, respectively, based on repetitions of TGA tests and the maximum deviation from the mean result.

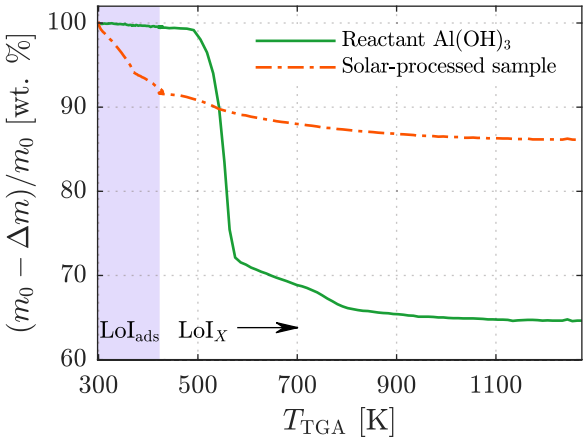

Figure 5.4: Relative mass change of the reactant $Al(OH)_3$ and a representative solar-processed alumina as a function of the reference TGA temperature, T_{TGA} during a dynamic TGA run between 298 K and 1273 K in synthetic air. The temperature ranges used in the present study for determining $\mathrm{LoI}_{\mathrm{ads}}$ and LoI_X are indicated.

5.2 Results & discussion

5.2.1 Steady-state operation

The operational conditions for the 19 nominally steady-state experimental runs listed in Table 5.1 resulted in $T_{\text{reactor}} = 1161 - 1551\,\text{K}$ and $T_{\text{wall}} = 928 - 1371\,\text{K}$[1]. The solar energy conversion efficiency, η_{th}, of the solar calcination process is defined to account for the energy required for the endothermic calcination process, as well as the sensible heating of the reaction products and the transport air, as follows:

$$\eta_{\text{th}} = \frac{\Delta \dot{H}}{\dot{Q}_{\text{s}}} = \frac{\dot{H}^{T_{\text{r}}}_{\text{products}} - \dot{H}^{\circ}_{\text{reactant}} + \Delta \dot{H}_{\text{air}}}{\dot{Q}_{\text{s}}}. \tag{5.4}$$

Here, the sensible heat of the transport air is included in the useful energy because an industrial flash calcination process recovers the majority of such sensible heat through downstream heat exchangers, which are also used to pre-heat the particles. That is, the present solar reactor needs to both heat and react the particles, while they enter an industrial reactor hot. The performance indicators, X and η_{th} were measured to be in the range $X = 84.8 - 95.8\,\%$ and $\eta_{\text{th}} = 8.8 - 20.4\,\%$, respectively. In terms of product quality parameters, the measured values of loss on ignition of adsorbed moisture were $\text{LoI}_{\text{ads}} = 5.9 - 14.1\,\%$, the measured values of SSA were found to be in the range $132.7 - 226.6\,\text{m}^2\,\text{g}^{-1}$ and the mean pore size was measured to be in the range $d_{\text{pore}} = 2.54 - 5.75\,\text{nm}$.

Figure 5.5 presents the outputs from a typical experimental run (#9). Plotted are the temporal variations of $\dot{Q}_{\text{s}}$, T_{reactor}, T_{wall}, $\dot{m}_{\text{Al(OH)}_3}$, and $\dot{m}_{\text{H}_2\text{O}}$. When the desired T_{wall} was reached and steady temperatures were measured, the particle feeding was turned on. The period, $21 - 35\,\text{min}$, is considered to be nominally steady-state.

[1] X, η_{th} and XRD results are presented as functions of T_{wall} rather than T_{reactor} due to the greater number of thermocouples contributing to the mean measurement and the lesser influence of direct irradiation on the thermocouple reading.

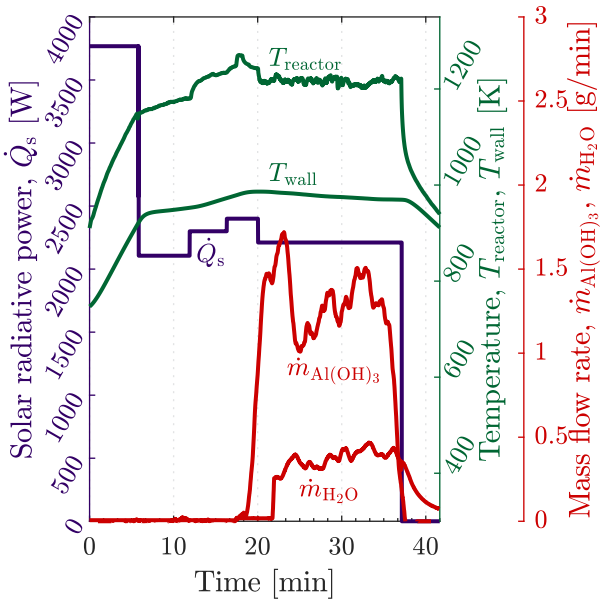

Figure 5.5: Temporal variations of solar radiative power input, $\dot{Q}_s$, reactor temperatures, $T_{reactor}$ and T_{wall}, particle mass feed rate, $\dot{m}_{Al(OH)_3}$, and mass flow rate of evolved water within the outlet stream, $\dot{m}_{H_2O}$, during a representative solar experimental run (#9).

5.2.2 Extent of calcination and efficiency

Figure 5.6a presents the dependence of X on T_{wall} for all experimental runs with four different values of $\dot{V}_{\text{air,n}}$. It is evident that the reactor temperature has a controlling influence on the extent of conversion, so that an increase in T_{wall} results in greater X. It can also be seen that a maximum chemical conversion of 95.8% was obtained for $T_{\text{wall}} = 1371$ K. Despite this temperature being within the range typical of industrial flash calciners, 1273 – 1373 K (Eglinton et al. 2013)), the conversion was below 100%. This can be attributed both to the much smaller scale of the reactor in the present study relative to industrial-scale calciners and to the additional stages in industrial calcination systems, incorporating both particle preheating stages and a holding vessel, which together reduce the temperature rise and/or residence time required for full conversion. Figure 5.6b presents the dependence of X on τ_{nom} for three T_{wall}. This shows that X is increased by an increase in τ_{nom}, although the influence is relatively weak in comparison with that of T_{wall}. The trend of increasing X with longer τ_{nom} is also consistent with well-established understanding of the alumina calcination reaction (Wefers & Misra 1987; Whittington & Ilievski 2004). The slightly stronger influence of T_{wall} than that of τ_{nom} is further evident from results of experimental run 14 with $T_{\text{wall}} = 1371$ K, which featured the greatest X despite having the shortest $\tau_{\text{nom}} = 1.38$ s.

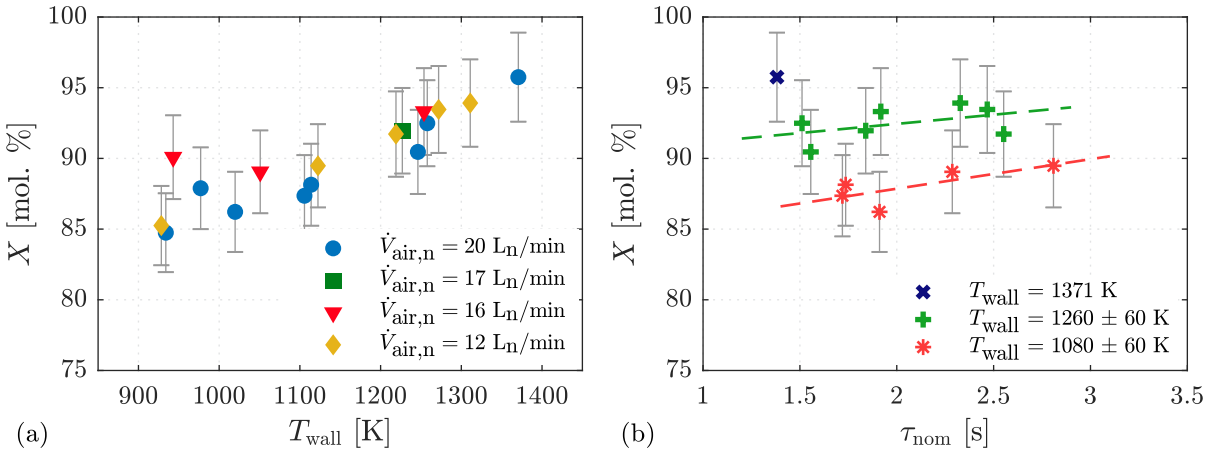

Figure 5.6: The extent of chemical conversion, X, as a function of **(a)** the average characteristic wall temperature, T_{wall}, for four different air normal flow rates, $\dot{V}_{\text{air,n}}$, and for experimental runs 1 to 17; and **(b)** the nominal particle residence time, τ_{nom}, for three different average characteristic wall temperatures, T_{wall}. Also shown are the linear lines of best fit for the data points in the two temperature ranges.

Figure 5.7 presents the dependence of η_{th} on $\dot{V}_{air}$ (corrected for reactor temperature), for four different values of T_{wall}. A maximum energy efficiency of 20.4% was achieved for this reactor. It can be seen that η_{th} increases with a reduction in T_{wall} because both the conduction and re-radiation losses depend on the reactor wall temperature. It can also be seen that, for a given value of T_{wall}, η_{th} increases with an increase in $\dot{V}_{air}$. This implies that an increase in the flow rate of air and particles causes a greater fraction of the radiation to be absorbed by the reactant and transport air than by the walls, which increases the ratio of useful heat to losses. This influence on η_{th} of T_{wall} and $\dot{V}_{air}$ is consistent with the findings reported in Chapter 3 and the values of η_{th} reported here are in a similar range to those for the equivalent experimental conditions in Chapter 3. The values of η_{th} for this reactor are low relative to industrial-scale reactors but are comparable with those from other laboratory-scale reactors (Z'Graggen et al. 2006; Nikulshina et al. 2009b). This is because the ratio of internal surface area to internal volume of the reactor decreases with an increase in scale, causing a greater fraction of energy to be absorbed by the reactants and transport air relative to the walls of the reactor, which increases efficiency consistent with the results from Figure 5.7. In addition, large scale industrial reactors are designed with heat integration and heat recovery systems to minimise heat losses and maximise efficiency.

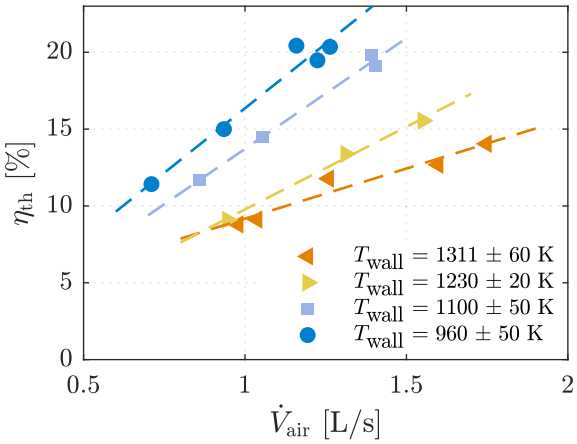

Figure 5.7: The energy efficiency, η_{th} defined in Equation (5.4), of the present solar calcination reactor as a function of the volumetric flow rate of transport air, $\dot{V}_{air}$, for four different wall temperatures, T_{wall}. See Table 5.1 for details.

5.2.3 Product quality: residual moisture

Figure 5.8 presents the $\mathrm{LoI_{ads}}$ as a function of ϕ, for four different values of T_{wall}. It can be seen that, for each value of T_{wall}, the $\mathrm{LoI_{ads}}$ increases with ϕ. This can be explained by the increase in the concentration of water vapour, the gas-phase product of the reaction, due to an increase in volumetric loading of particles. That is, an increase in the partial pressure of water vapour in the reactor increases the resistance to the release of water into the gas phase. It can also be seen that T_{wall} has a second order influence on the $\mathrm{LoI_{ads}}$, so that the highest $T_{\mathrm{wall}} = 1311 \pm 60$ K resulted in the lowest values of $\mathrm{LoI_{ads}}$.

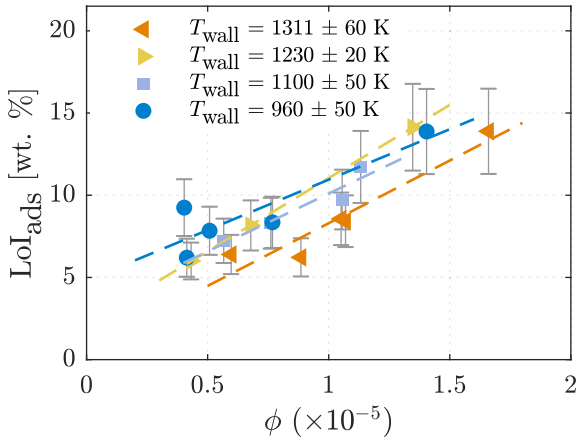

Figure 5.8: Mass percentage of adsorbed moisture, $\mathrm{LoI_{ads}}$, in the product from the solar reactor as a function of the particle to air volume fraction, ϕ defined in Equation (5.2), for four different wall temperatures, T_{wall}, and experimental runs 1 to 17.

Table 5.2 presents the influence of the addition of steam ($\dot{m}_{\mathrm{steam}} = 1.17\ \mathrm{g\,min^{-1}}$) to the transport air flow on $\mathrm{LoI_{ads}}$, X, and η_{th}, with all other operating conditions maintained nominally constant. It can be seen that the additional steam input, resulting in a water vapour partial pressure of 68.6 mbar, has a significant influence on the amount of surface moisture adsorbed by the alumina product, consistent with the trends in Figure 5.8. More specifically, the $\mathrm{LoI_{ads}}$ was found to increase from 5.91% (run #18) to 7.99% (run #19). This can be explained by the increase in the partial pressure of water vapour in the transport air, which inhibits the diffusion of chemically-released water vapour into the gas phase. It also favours an increase in the readsorption of water vapour onto the surface of the alumina particle. For reference, the partial pressure of water vapour generated by the complete combustion of methane with 10% excess air is calculated to be 176.7 mbar, which is more than twice the 68.6 mbar used in the present experiment. Because methane is the dominant component of natural gas, which is the most common fuel used for industrial flash calciners, this implies that removing H_2O from combustion by solar calcination has the potential to provide a significant benefit to product quality by reducing the partial pressure of the gas-phase moisture. It can also be

noted from Table 5.2, that the increase of the partial pressure of water vapour has no significant influence on X or η_{th} for the present conditions.

Table 5.2: The influence of addition of steam to the transport air on the mass percentage of adsorbed moisture, LoI_{ads}, extent of chemical conversion, X, and energy efficiency, η_{th}, based on experimental runs 18 and 19.

$\dot{m}_{\text{steam}}/\dot{m}_{\text{air}}$ [-]	#	LoI_{ads} [wt. %]	X [mol. %]	η_{th} [%]
0	18	5.91	94.5	14.0
0.045	19	7.99	94.0	14.2

5.2.4 Product quality: alumina microstructure

Figure 5.9 presents SEM micrographs of the solid alumina product from experimental runs #4 ($T_{\text{wall}} = 934$ K), #11 ($T_{\text{wall}} = 1311$ K), #14 ($T_{\text{wall}} = 1371$ K) and #19 ($T_{\text{wall}} = 1262$ K). It is clear that slit-shaped pores have formed in the particles, whose width increases with the value of T_{wall}. From previous work, this can be deduced to result from the calcination reaction mechanism, in which the structural hydroxyls (-OH) that hold gibbsite layers together are released rapidly as water during the calcination process, causing the gibbsite layers to split and form slit-shaped pores (Boer 1958; Perander et al. 2009).

Figure 5.10 presents the mean pore diameter, d_{pore}, and the total specific pore volume, V_{pore}, of the solar processed alumina as a function of X. It can be seen that both d_{pore} and V_{pore} increase with an increase in X, consistent with both the SEM micrographs (Figure 5.9) and the previous assessments for non-solar calcination by Perander et al. (2009). For $X = 95.8\%$, d_{pore} reaches up to 5.8 nm for run 14. It can also be seen from a comparison with reported mean pore sizes of typical smelter grade aluminas (SGAs) produced with industrial flash calciners, presented as the open symbols in Figure 5.10 (Perander 2010; Perander et al. 2011; Wind & Raahauge 2013), the solar process generates larger values of d_{pore} for a given value of X than does the conventional process. Extrapolation suggests that d_{pore} will continue to increase with X, so that solar-processed alumina has potential to achieve a larger mean pore size than the majority of conventionally-processed aluminas, noting the exception for two SGAs with pore size larger than 8 nm. It should also be recalled that the solar-processed alumina has been calcined with residence times in the order of a few seconds. This contrasts the industrial process, which also includes both a preheating stage and a holding vessel to provide additional residence time for pore growth. That is, the solar process generates a higher product quality by this measure than does the conventional processing, indicating potential to improve hydrogen fluoride adsorption capacity in the downstream dry-scrubbing process.

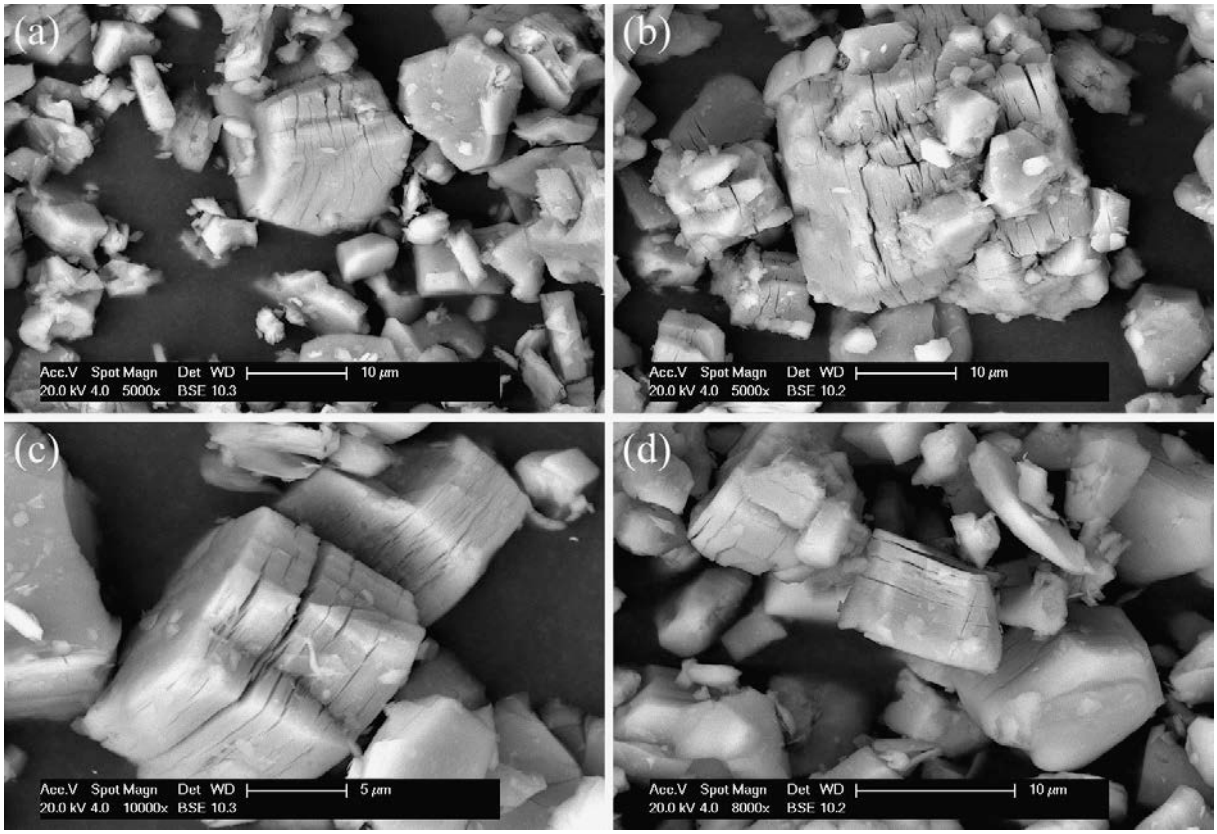

Figure 5.9: SEM micrographs of solar-processed alumina obtained from experimental runs: **(a)** #4 ($T_{\text{wall}} = 934$ K); **(b)** #11 ($T_{\text{wall}} = 1311$ K); **(c)** #14 ($T_{\text{wall}} = 1371$ K); and **(d)** #19 ($T_{\text{wall}} = 1262$ K); at 5000, 5000, 10000, and 8000 magnification, respectively.

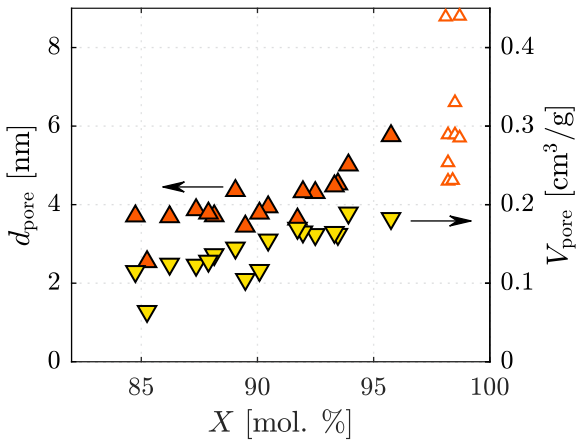

Figure 5.10: Mean pore diameter, d_{pore}, and total specific pore volume, V_{pore}, of the solar-produced aluminas as a function of the extent of chemical conversion, X, for experimental runs 1 to 17. Also shown with open symbols are the typical mean pore diameter of nine SGAs produced with industrial calciners as reported in the literature (Perander 2010; Perander et al. 2011; Wind & Raahauge 2013)

Figure 5.11 presents the measured values of SSA for the solar-produced alumina as a function of X. The figure shows that SSA is nearly constant (mostly in the range 168 – 190 $m^2 g^{-1}$) for lower values of X in the range 85 – 92 %, but then decreases with further increases in X to the minimum of 132.7 $m^2 g^{-1}$ for $X = 95.8\%$. The present values of SSA are significantly greater than previously reported values of SGA produced industrially, as shown in Figure 5.11 (Wind & Raahauge 2013). Nevertheless, more data are required before a reliable comparison with the industrial data can be made, owing to the different values of X for the experimental and industrial data, which is associated with the difference in scale of the facilities.

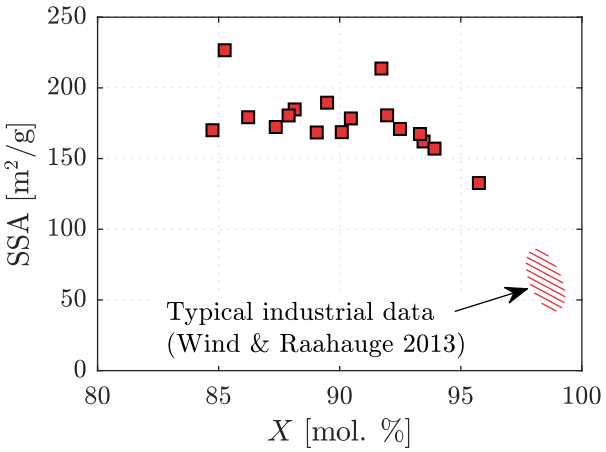

Figure 5.11: Specific surface area, SSA, of the present solar-produced aluminas as a function of the extent of chemical conversion, X, for experimental runs 1 to 17. Also shown is the typical X and SSA product quality properties of SGA calcined in an industrial gas suspension calciner (Wind & Raahauge 2013).

5.2.5 Product quality: X-ray diffraction analysis

Figure 5.12 presents a series of XRD spectra of alumina powder samples produced with different values of T_{wall}, but at constant $\dot{V}_{air,n} = 20\,L_n\,min^{-1}$ ($\phi = 0.40 \times 10^{-5}$ – 1.06×10^{-5}). For the case with $T_{wall} = 934$ K, the presence of unconverted reactant can be seen from the discrete diffraction peaks corresponding to gibbsite, notably from the two peaks of greatest intensity at $2\theta = 18.3°$ and 20.3°. For higher values of T_{wall} the discrete diffraction peaks of gibbsite reduce in intensity and are replaced by the more diffuse diffraction peaks of the transition alumina. The presence of some residual gibbsite in the alumina samples, which each combine many alumina particles, indicates that a fraction of the particles did not reach sufficient temperature for long enough to convert all of the original gibbsite. Given the wide size distribution of the particles, it is likely that the residual gibbsite is preferentially partitioned in the larger particles, which require the longest residence time for complete conversion. However, further work will be required to verify this. For $T_{wall} = 1020$ K and 1114 K a broad diffuse peak at $2\theta = 42.8°$ can be seen, which corresponds to the χ-Al_2O_3 phase

(Wefers & Misra 1987; Kogure 2004; Whittington & Ilievski 2004). For $T_{wall} = 1258$ K and 1371 K the χ-Al_2O_3 peak is not present and the dominant diffuse diffraction peaks occur at $2\theta = 19.4^o$, 31.9^o, 37.6^o, 39.3^o, 45.7^o, 60.6^o and 66.7^o corresponding to γ-Al_2O_3. This is corroborated by an additional analysis of the samples by Fourier Transform Infrared Spectroscopy (not shown), which found that the spectra from the solar-processed alumina samples are characterised by a broad distribution without sharp peaks. This is consistent with the alumina having a complex disordered structure, which is typical of χ-Al_2O_3 and γ-Al_2O_3 (Boumaza et al. 2009; Favaro et al. 2010). It should also be noted that the XRD results from the two cases with the highest T_{wall} feature small discrete peaks corresponding to α-Al_2O_3 ($2\theta = 25.6^o$, 35.1^o, 43.3^o and 57.5^o), indicating that the particles reached the temperature at which α-Al_2O_3 forms (1375 – 1450 K). Although it is difficult to quantify the relative presence of the transition aluminas due to their diffuse diffraction peaks (Perander et al. 2007; Perander et al. 2009), it is clear that γ-Al_2O_3 is the predominant phase produced during solar calcination, while small amounts of the α-Al_2O_3 phase were also observed. This is consistent with published results from refinery-produced aluminas, in which the dominant alumina phase is also γ-Al_2O_3, while α-Al_2O_3 makes up 2 – 9%; see table 5.3 (Wind et al. 2010). Taken together, these results imply that high temperature solar calcination favours the reaction pathway of χ- to γ- to α-Al_2O_3, pathway (c) as outlined in Section 2.4.2 (Wefers & Misra 1987; Ingram-Jones et al. 1996; Whittington & Ilievski 2004).

Figure 5.13 presents XRD spectra of solar-processed alumina samples produced with a range of values of T_{wall} for the lower transport air flow rate, $\dot{V}_{air,n} = 12\ L_n\ min^{-1}$ ($\phi = 1.07 \times 10^{-5}$ – 1.66×10^{-5}). As for Figure 5.12, the samples produced at lower temperatures have discrete diffraction peaks corresponding to gibbsite, which also implies the presence of unreacted gibbsite. The general trend is that the intensity of these peaks decreases with an increase in both T_{wall} and X. The exception to this is the alumina sample processed with $T_{wall} = 1219$ K, which exhibits gibbsite diffraction peaks with lower intensity than those of the two alumina samples processed with higher temperature. It should also be noted from Figure 5.13 that the only clearly visible discrete diffraction peaks of gibbsite for the cases with low T_{wall} are those at 2θ angles of 18.3^o and 20.3^o. In contrast, numerous discrete gibbsite peaks are visible for the alumina samples produced with low values of T_{wall} and larger values of $\dot{V}_{air,n}$ (Figure 5.12). The evolution of χ-Al_2O_3 at $T_{wall} = 928$ K and $T_{wall} = 1122$ K and the subsequent evolution of γ-Al_2O_3 is evident for both the lower and higher values $\dot{V}_{air,n} = 12\ L_n\ min^{-1}$ and $\dot{V}_{air,n} = 20\ L_n\ min^{-1}$. However, diffraction peaks corresponding to the intermediate aluminium oxyhydroxide, boehmite, are also visible in the XRD traces of Figure 5.13. The diffraction peaks at 2θ values of 14.5^o and 28.2^o correspond to boehmite and are particularly evident from the samples calcined with $T_{wall} = 1219$ K and 1311 K. For the sample calcined at $T_{wall} = 1311$ K, the species that can be observed are unreacted gibbsite, boehmite and, most predominantly, γ-Al_2O_3. This indicates that, under these conditions, the calcination reaction follows both the χ- to γ- to

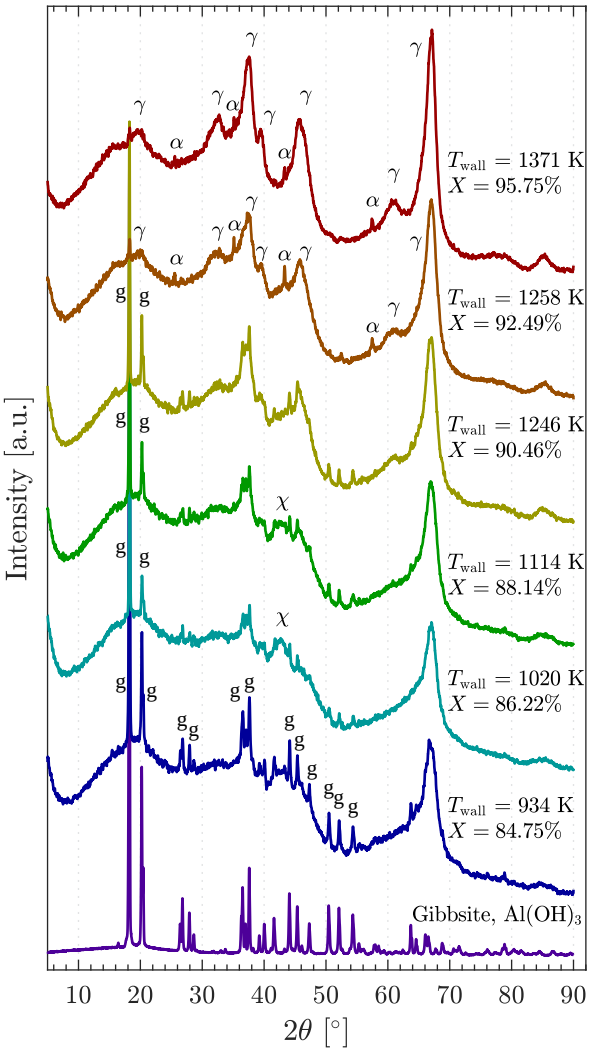

Figure 5.12: X-ray diffractograms of gibbsite and solar-processed alumina samples produced with a series of reactor temperatures (experimental runs 4, 2, 1, 3, 10 and 14) with a constant normal flow rate of transport air ($\dot{V}_{air,n} = 20\,L_n\,min^{-1}$). The reference raw gibbsite X-ray diffractogram is also shown at 1/14th the intensity. Annotations show where the diffraction peaks correspond to reported diffraction peaks of gibbsite (g), χ-Al_2O_3, γ-Al_2O_3 and α-Al_2O_3 (COD PDF Card Nos. 1011081, 2015530 & 1000017).

α-Al_2O_3 pathway (pathway (c) as in Figure 5.12 and outlined in Section 2.4.2) and the boehmite to γ- to α-Al_2O_3 pathway, pathway (b) as outlined in Section 2.4.2 (Wefers & Misra 1987; Ingram-Jones et al. 1996; Whittington & Ilievski 2004). The same particle size distribution was used throughout the present investigation, suggesting that the boehmite formation is attributable to the increased concentration of water vapour in the immediate presence of the reacting gibbsite particles due to the lower value of $\dot{V}_{air,n}$, which can be deduced to increase ϕ.

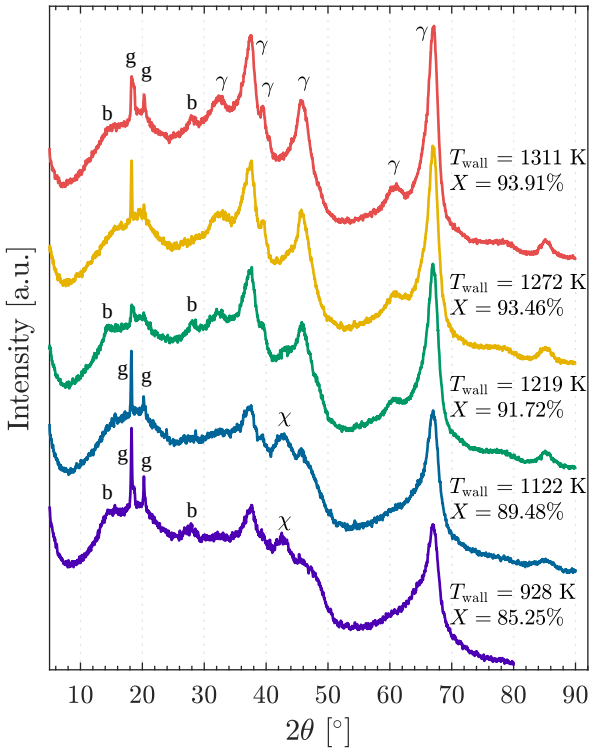

Figure 5.13: X-ray diffractograms of solar-processed alumina samples produced with a series of reactor temperatures (experimental runs 6, 5, 13, 7 and 11), with a constant normal flow rate of transport air ($\dot{V}_{\mathrm{air,n}} = 12\,\mathrm{L_n\,min^{-1}}$). Annotations show where the diffraction peaks correspond to reported diffraction peaks of gibbsite (g), boehmite (b), χ-Al_2O_3 and γ-Al_2O_3 (COD PDF Card Nos. 1011081, 9009155 & 2015530).

5.2.6 Projection to a 50 MW SVR and comparison of the product quality with the conventional process

Table 5.3a presents the ratio of internal surface area to internal volume of the reactor, A_S/V_r, the thermal input of solar radiation, $\dot{Q}_s$, and the nominal particle residence time, τ_{nom}, for the case of greatest conversion in the present investigation. Predicted values for the 50 MW industrial scale are also shown, where the scale up procedure assumes constant C, constant ϕ, constant input velocity, geometric similarity and constant η_{th} (i.e. that $\dot{m}_{Al(OH)_3}$ scales linearly with thermal input). The resulting scale up proportionality relationships are $A_S/V_r \propto \dot{Q}_s^{-1/2}$ and $\tau_{nom} \propto \dot{Q}_s^{1/2}$. The assumption of constant input velocity is reasonable because the minimum velocity is set by the need to transport particles, while higher values are undesirable to avoid erosion. The assumption of constant efficiency is conservative because the 100-fold reduction in A_S/V_r with the increase in scale will result in a significant reduction in relative heat losses (Z'Graggen & Steinfeld 2008b). Table 5.3a shows that, with these assumptions, the constant-velocity scale up results in a 100-fold increase in τ_{nom}. Even though this represents an over-estimate of the increase in residence time because the

scale-up process would also increase the relative diameter of the inlet gas stream, this is more than offset by the addition of the pre-heater and the holding vessel in the industrial process. That is, scale-up can be expected to increase X and/or reduce the value of T_{reactor} relative to the present laboratory-scale investigation. It should be noted that the scaling assumption of geometric similarity implies that the reactor aperture size will scale according to $D_{\text{ap}} \propto \dot{Q}_{\text{s}}^{-1/2}$, so that the scaled-up SVR would have an aperture diameter of 5 m. This larger size presents difficulties with the design of large-scale sealing windows or an open reactor that avoids the egress of particles. Furthermore, the larger thermal mass of the scaled-up device and the need for continuous calcination operation potentially requires the use hybrid solar-combustion technologies (Nathan et al. 2013; Nathan et al. 2017b). However, the goal of this scaling analysis is to provide insights into the mechanisms controlling the solar calcination process at larger scale, rather than providing a guide to the design of a scaled-up solar calcination reactor, which is a complex process.

Table 5.3b presents the parameters used to characterise the product quality for the present alumina product with greatest X (run #14), together with typical properties of SGA produced in industrial flash calciners as reported in the literature (Whittington & Ilievski 2004; Metson et al. 2006; Perander et al. 2007; Perander 2010; Wind & Raahauge 2013; Perander et al. 2011; Wind et al. 2010). This shows that the minimum LoI_{1273} of 1.20% achieved in the present investigation is somewhat higher than the typical value of alumina produced in industrial flash calciners. However, given that extent of conversion increases with τ_{nom}, it can be deduced that the LoI_{1273} would decrease to $<$ 1% with scale up of the solar reactor, which would comply with industrial requirements (Wind & Raahauge 2013). Furthermore, the additional incorporation of the preheating stages and holding vessels employed in current industrial processes, which provide sufficient residence time to achieve both a high conversion and a high surface area, can be expected to allow the solar reactor to be operated at lower temperature (Wind & Raahauge 2013). It can also be seen that the dominant alumina phase of the present solar product is γ-Al_2O_3 with small amounts of α-Al_2O_3, which is consistent with that found in industrial processes. However, traces of gibbsite were also found from the XRD in the present samples of calcined solar alumina, which implies a poorer quality than is required for SGA. On the other hand, the SSA of the solar-processed alumina was found to be much higher than typical for SGA, which is consistent with the small scale, since SSA is expected to decrease with an increase in conversion. Of particular note is that the mean pore size of the solar-calcined alumina is in the upper range of industrially-produced alumina. This represents a benefit from solar calcination of alumina over conventional combustion-driven calcination.

Table 5.3: (a) Comparison of key operational parameters of the solar vortex transport reactor (SVR) at present laboratory-scale and the equivalent values for a reactor at industrial scale, as scaled with constant inlet velocity and thermal efficiency. **(b)** Comparison of product quality parameters of solar-calcined alumina for the case with the highest extent of conversion (experimental run #14), together with typical properties of Smelter Grade Alumina (SGA) produced with industrial flash calciners, as reported in the literature (Whittington & Ilievski 2004; Metson et al. 2006; Perander et al. 2007; Perander 2010; Wind et al. 2010; Perander et al. 2011; Wind & Raahauge 2013).

(a) Operational parameter comparison

	SVR at laboratory-scale	SVR scaled to industrial-scale
$\dot{Q}_s$	5 kW	50 MW
A_S/V_r	31.9 m^{-1}	0.319 m^{-1}
τ_{nom}	1.38 s	138 s

(b) Product quality comparison

	Solar-processed alumina (run #14)	Refs: [a,b,c]	Ref: [d]	Ref: [e]	Ref: [f]	Ref: [g]
LoI_{1273} [wt.%]	1.20		0.7 – 0.8	0.69 – 0.95	0.3 – 1.5	0.72 – 1.05
α-Al_2O_3 content [wt.%]	Small amounts		3 – 6	2 – 9	2 – 20	3.9 – 8.1
Gibbsite content [wt.%]	Small amounts		< 0.1	< 0.1		0.56 – 2.65
Dominant alumina phase	γ-Al_2O_3	γ-Al_2O_3			γ-Al_2O_3	
SSA [m^2/g]	132.7		73 – 81	72 – 80	68 – 80	68.1 – 76.1
d_{pore} [nm]	5.8		6.6 – 8.8		4.6 – 5.8	5.7 – 11.2

[a] (Whittington & Ilievski 2004); [b] (Metson et al. 2006); [c] (Perander et al. 2007); [d] (Wind & Raahauge 2013); [e] (Wind et al. 2010); [f] (Perander 2010); [g] (Perander et al. 2011).

5.3 Key findings

The first-of-a-kind demonstration of the thermochemical calcination of alumina with concentrated solar thermal radiation has been undertaken with a laboratory-scale solar vortex reactor. This shows that it is technically possible to calcine alumina without combustion and its concomitant CO_2 emissions, at least during those periods when the solar resource is available. The experimental investigation of this solar process with a systematic variation of operating parameters revealed the following:

- The extent of chemical conversion from aluminium hydroxide to aluminium oxide increases with the solar radiative power input, and hence also with the reactor temperature, to a maximum value of 95.8% for the present investigation with a laboratory-scale reactor (4.3 kW of solar radiative power and an average reactor wall temperature of 1371 K).
- The reactor temperature is the dominant experimental variable controlling the extent of solar calcination.
- An increase in the nominal particle residence time has a secondary influence, also increasing the extent of conversion.
- Solar energy conversion efficiencies of up to 20.4% were measured for this small-scale reactor, on the basis that both the sensible and chemical heat are included as the useful heat, which is consistent with the high level of heat recovery from industrial processes. A higher reactor temperature results in a drop in efficiency, due to greater re-radiation and conduction losses.
- It is expected that the extent of calcination and energy efficiency will increase with the scale up of the SVR, allowing for lower reactor temperatures due to the longer particle residence time and relatively lower heat losses associated with larger scale reactors.

Product quality assessments of the solar-calcined alumina provide strong evidence that solar calcination can result in improved quality alumina, relative to conventional industrially-calcined alumina. This is supported by the following findings:

- The addition of steam (to a water vapour partial pressure of 68.6 mbar) to the reactor transport gas flow resulted in an increase in the amount of adsorbed moisture (from 5.91% to 7.99%). This implies that the use of solar calcination, which avoids the production of steam by combustion, can reduce the amount of surface-adsorbed moisture in the alumina product (which is deleterious to alumina smelting). Consistent with this, the amount of moisture adsorbed by the alumina surface also depends on the particle to air volume fraction. This is because an increase in the partial pressure of water vapour, resulting from an increase in

particle to air volume fraction, was found to inhibit diffusion of the water vapour into the transporting air phase.

- The solar-produced aluminas of the present investigation are characterised by a relatively large specific surface area and mesoporous structure (with large pore sizes), which is desirable for increased hydrogen fluoride adsorption required for the downstream dry-scrubbing process in aluminium smelting. The mean pore size of the solar-produced alumina was found to increase with the extent of conversion and can be expected to increase further with scale-up. The conditions producing the greatest conversion of 95.8% were associated with a specific surface area of 132.7 $m^2 g^{-1}$ and critically, a mean pore diameter of 5.8 nm.
- The X-ray diffraction analysis revealed that the alumina produced with concentrated solar thermal energy is typically characterised by a high fraction of γ-Al_2O_3 phase and a low fraction of α-Al_2O_3. This is consistent with published results from refinery-produced aluminas.

6

Summary & Outlook

In summary, the present thesis has characterised the thermal performance, particle residence time performance and alumina calcination performance of vortex-based solar particle receiver-reactors (SVRs) with systematic studies of the influence of a range of key input and design parameters on each of these performance aspects. This investigation has identified that the use of a gas-particle vortex flow within a solar thermal particle receiver allows the device to be configured in alternate ways and to operate in a range of alternate regimes; including particle or air heating; highly recirculating or plug flow conditions; sensible heating of inert particles; and thermochemical reaction of particles. The conclusions presented below outline the new understanding that has been derived from the investigation. This contributes to the development of SVR technology and its potential scale up and case-by-case optimisation for different applications, including the supply of high temperature renewable process heat and the thermochemical processing of particles, in the interest of displacing the use of CO_2 emitting fuels.

6.1 Conclusions

A one-dimensional numerical model of the heat and mass transport processes within a SVR has been developed and validated, allowing for the systematic assessment of a range of operating parameters and geometric configurations. It has been identified that SVRs have the potential to operate primarily within particle or gas heating regimes, which is attributed to the efficient absorption of direct irradiation by the particle phase and high rates of turbulent heat transfer between the gas phase, the particle phase and the receiver wall. This presents an opportunity for the combined solar processing of particles and provision of high temperature solar process heat, via a gaseous stream, to additional subsystems within a CST system. However, the performance of additional

heat exchanger and particle separation subsystems would also need to be assessed. For the cases considered here, the particle mass loading at the inlet stream is the dominant parameter controlling whether the SVR primarily heats the particle or gas phase. Investigation of the influence of the two-phase flow direction revealed that alternative flow directions result in significantly different particle, gas and wall temperature distributions through the receiver, which, in turn, influences the thermal efficiency. It was found that the flow configuration of the SEVR – in which the two-phase flow proceeds from the rear to front of the receiver in the direction opposite to the incoming concentrated solar radiation – tends to increase the thermal efficiency of the receiver. This is due to the majority of particle/gas heating occurring in the front of the receiver near to the aperture, so that the temperature distribution in the rear of the receiver is on average lower and thermal losses are lower. Also, for the sensible heating of inert particles, it was found that the optimal length of the SVR is controlled by the balance between increased solar energy absorption and increased heat losses through the receiver wall, so that modelling is required to optimise the receiver on a case-by-case basis. However, for reacting particles, there is also potential to configure the receiver length such that particles achieve a given reaction temperature for a given residence time, so that the extent of chemical conversion can be optimised. More details of the findings from the numerical thermal performance investigation can be found in Section §3.4. This study of the sensitivity of thermal performance to the key input and geometric parameters of particle/gas mass flow rates, two-phase flow direction, particle size and receiver length provides the new understanding that is required to further develop the SVR technology in a range of configurations for potential deployment at larger scale. However, further work is needed to better identify the techno-economic potential of the various options with which to employ the SVR within an industrial system.

A fast-response, non-intrusive, inline, optical method for the measurement of particle residence time distributions within a SVR has been developed. This method is based on the injection of a pulse of monodisperse particles into the SVR operating with steady-state vortex flow of gas and allows for the assessment of the influence of particle size on the particle RTD within the vessel, which has not previously been implemented. This method was used to assess the influence of key dimensionless parameters on the particle residence time behaviour within a receiver of SEVR configuration. It was found that the particle residence time behaviour can be configured to generate various alternative characteristics, depending primarily on the Froude number of the two-phase vortex flow. The SEVR can be configured to enhance the recirculation of large particles, relative to small particles, by operating in the low Froude number *Froude-Stokes* regime ($Fr_{cyl} < 4$) and orienting the receiver with negative tilt angle (two-phase flow proceeds in the direction against gravity). Within this regime, the outlet Stokes number was found to have a controlling influence on particle residence time, such that the particle residence time increases with Sk_{out}. Operation in the *Froude-Stokes* regime is potentially beneficial to the processing of polydisperse particles and, therefore, has potential advantages for

application to a range of current industrial processes that also process particles with a wide range of sizes. Alternatively, the SEVR can be configured to feature uniform residence times that are not significantly influenced by Stokes number, by operating in the high Froude number *cyclonic* regime ($Fr_{cyl} > 4$). This is potentially beneficial to processes that require all particles to be processed with uniform residence time, so that they have uniform product quality. The calcination of alumina is one example of this type of process. Taken together, this highlights the flexibility of SVR technology in being able to operate within a range of alternative regimes for various applications, although further work is required to better understand the influence of these various regimes on the thermal performance of the device.

Further demonstration of the flexibility of SVR technology is provided by the assessment of the influence of a range of tilt angles of the SEVR on the particle RTD within the receiver. It was found that the influence of the receiver tilt angle on the particle residence time is weak for small particles. This implies that it is preferable to operate tower-mounted systems (i.e. with downward facing receiver tilt angles) with small particles whose outlet Stokes number is approximately (or smaller than) unity. Furthermore, preliminary projections of the performance of a scaled up SEVR, based on the dimensionless analysis of the device's operation at laboratory-scale, found that this same weak influence of tilt angle on particle residence time can be expected for a SEVR scaled up to a nominal size of 50 MW and operating with particles of approximately 200 µm (assuming constant particle density). This preliminary assessment suggests that the device has strong potential for application as a tower-mounted solar receiver that can operate flexibly with a range of tilt angles, so that in a CST system, optimal heliostat field layouts could be sought without limitations imposed by any required receiver tilt angles. In addition, a key challenge to the implementation of industrial scale CST technologies is their response to the natural variations of the solar resource over hourly, daily and yearly time periods. It has been shown here that SVRs have potential to respond to this variation in solar resource by tuning the particle residence time. More details of the findings from the systematic study of particle residence times in the SEVR configuration can be found in Section §4.4. This study provides the first experimental characterisation of particle residence times within a SVR and new understanding of the influence of key dimensionless parameters.

Finally, a first-of-a-kind experimental investigation demonstrated that alumina can be calcined with concentrated solar radiation in a small-scale SVR. It was found that the extent to which aluminium hydroxide was converted to aluminium oxide in the SVR increases with the solar radiative power input, hence also with the temperature of the SVR, up to a maximum of 95.8% for the present investigation and selected laboratory-scale SVR configuration. The reactor temperature was found to have the strongest influence on the extent of chemical conversion, while an increase in the nominal residence time was found to have only a secondary influence of increasing the conversion. Additional details of the key findings from this experimental investigation can be found in Section §5.3. Potential

improvements in the alumina product quality (particle pore diameter and specific surface area) were also identified, relative to the quality of alumina produced with the conventional industrial Bayer process. That is, the mean pore diameter and specific surface area of the solar-generated alumina with the greatest chemical conversion were found to be 5.8 nm and 132.7 $m^2 g^{-1}$, respectively, which are higher values than are typical for industrial smelter grade alumina. This suggests that concentrated solar thermal processing can be used to improve the quality of alumina over existing fossil fuel-based processes though a combination of a high heating rate and avoided contamination by combustion products. Preliminary projections of the performance of the solar calcination process with a scaled up SVR, based on dimensionless analysis of the operation of the device at laboratory-scale, suggest that complete conversion of the gibbsite particles to smelter grade alumina could be achieved with the possibility also of lower reactor temperatures and improved efficiency relative to that of the present laboratory-scale investigation. This suggests that the use of a refractory-lined steel SVR vessel for this solar-driven process has the potential to avoid the discharge of 165 kg-CO_2 per tonne-alumina of combustion-derived emissions for the calcination stage of the conventional Bayer process, at least during those periods when the solar resource is available. However, further work is needed to better understand the economic feasibility of such a process, together with the technical feasibility of performing the alumina calcination process with a whole CST system over longer periods.

6.2 Recommendations for future work

The further development of vortex-based solar particle receiver-reactor technology will require investigations into the following areas.

- Assessment of the influence of higher regimes of particle loading (within the four-way coupling regime) on the aerodynamics and heat transfer mechanisms of the two-phase vortex flow will be useful for the validation of heat transfer models and will provide important understanding of the requirements to ensure stability of the vortex flow for a range of receiver scales. This is because the heat transfer modelling of the thermal performance in the present thesis identified potential benefits of higher particle loading ($\dot{m}_p/\dot{m}_{air} > 2$, $\phi > 2 \times 10^{-4}$) to the thermal efficiency of the device. However, the data available for the performance of such a device in this four-way coupling regime are limited. Furthermore, both the residence time and solar calcination investigations were limited to operation with low particle loading within the one and two-way coupling regimes $\dot{m}_p/\dot{m}_{air} < 2$, $\phi < 2 \times 10^{-4}$), so that the new understanding of the particle residence time behaviour and alumina calcination performance is limited to these lower regimes of particle loading. These higher loading assessments may require in situ measurements of particle/gas temperature and particle concentration, together

with the extension of the present RTD measurement technique to enable the tracer pulse response to be recorded during steady-state operation in high mass loading regimes.

- Experimental visualisation of the two-phase gas-particle vortex flow field within SVRs will provide a deeper understanding of the sensitivity of particle trajectories within the device to the gaseous flow field. Chapter 4 infers particle trajectories within the SEVR based on a combination of particle residence time measurements, analysis of dimensionless parameters and CFD modelling, without directly measuring the particle motion within the device. Experimental methods, such as particle image velocimetry, are required to directly track particle flows within SVRs as well as to provide data for model validation.
- Investigation into the impact of a range of particle residence time distributions on the thermal performance of a SVR will provide useful information as to the required tuning of the RTD to achieve certain performance targets for the device (e.g. a given particle outlet temperature, or a given reaction extent). Chapter 4 presents the first direct measurements of particle RTD in such an entrained flow solar particle receiver, from which a compartment model has been developed to describe the residence this time behaviour for the range of operating conditions assessed in the present thesis. This compartment model is a useful design tool that could be incorporated into simplified receiver heat transfer models (such as that presented in Chapter 3) to assess the influence of realistic particle RTDs on the thermal performance of the receiver. Furthermore, such a simplified heat transfer model that incorporates a compartment model for residence time behaviour could be combined with kinetic data of the alumina calcination reaction to develop models that predict the solar alumina calcination process performance in SVRs under a range of alternative operating conditions and receiver tilt angles.
- The work presented in the main chapters of this thesis considers idealised spherical and monodisperse particles that enable assessments to be made about the influence of particle size on the performance of SVRs. However, particles of non-spherical shape and of polydisperse size distribution are also a common occurrence in many industrial and natural processes. Anisotropic particles translate, orient and rotate in turbulent flows in a way that is different to and much more complex than spherical particles (Voth & Soldati 2017). In a SVR, such particles will have a different response to the vortex gas flow field and will likely exhibit different particle residence time characteristics, compared to spherical particles. Therefore, future work can potentially assess the thermal performance and particle residence time performance of SVRs that operate with anisotropic and polydisperse particles.
- It is recommended that future work assesses the potential for windowless operation of a SVR, which may require that the receiver operates with negative pressure (relative to ambient)

to minimise particle egress. This could potentially be achieved with the use of a vacuum pump downstream of the receiver outlet port. It would be useful for future assessments to characterise the extent to which particles egress or air ingresses through the aperture with a systematic assessment of a range of operating and geometric parameters. Such an investigation could be extended to provide new understanding of the influence of windowless receiver operation on the particle RTDs within the receiver, together with new understanding of the impact of windowless operation on the solar calcination of alumina process.

- Understanding the impact of long term SVR operation on the particle properties will also be important for the potential scale up of such a device. That is, how does continuous cycling through the vortex flow of an SVR in a high flux concentrated solar radiation environment impact a particle in terms of its optical properties and its attrition? Particle comminution will likely be inevitable with such a continuous process, and so the impact of the resulting fines on the receiver and CST system will need to be investigated. Furthermore, abrasion of the receiver walls by the two-phase vortex flow should also be investigated.

Bibliography

Allal, KM, Dolignier, JC & Martin, G 1998, 'Determination of the residence time distribution of solid particles by a photometric method', *Chemical Engineering Research & Design*, vol. 76, no. 5, pp. 643–648. DOI: 10.1205/026387698525171.

Alonso, E & Romero, M 2015, 'Review of experimental investigation on directly irradiated particles solar reactors', *Renewable and Sustainable Energy Reviews*, vol. 41, pp. 53–67. DOI: 10.1016/j.rser.2014.08.027.

Amaral, SS, Carvalho, J de, Costa, M & Pinheiro, C 2015, 'An Overview of Particulate Matter Measurement Instruments', *Atmosphere*, vol. 6, pp. 1327–1345. DOI: 10.3390/atmos6091327.

Amsbeck, L, Buck, R, Ebert, M, Gobereit, B, Hertel, J, Jensch, A, Rheinländer, J, Trebing, D & Uhlig, R 2018, 'First tests of a centrifugal particle receiver with a 1m^2 aperture', *AIP Conference Proceedings*, vol. 2033. AIP Publishing, p. 040004. DOI: 10.1063/1.5067040.

ANSYS Inc. 2012, *ANSYS/FLUENT Release Version 14.5*, Report.

Bai, F, Zhang, Y, Zhang, X, Wang, F, Wang, Y & Wang, Z 2014, 'Thermal performance of a quartz tube solid particle air receiver', *Proceedings of the Solarpaces 2013 International Conference*, vol. 49, pp. 284–294. DOI: 10.1016/j.egypro.2014.03.031.

Beér, JM & Chigier, NA 1972, *Combustion aerodynamics*, Fuel and Energy Science Series, Applied Science Publishers Ltd., London.

Behar, O, Khellaf, A & Mohammedi, K 2013, 'A review of studies on central receiver solar thermal power plants', *Renewable & Sustainable Energy Reviews*, vol. 23, pp. 12–39. DOI: 10.1016/j.rser.2013.02.017.

Benoit, H, López, IP, Gauthier, D, Sans, J-L & Flamant, G 2015, 'On-sun demonstration of a 750ºC heat transfer fluid for concentrating solar systems: dense particle suspension in tube', *Solar Energy*, vol. 118, pp. 622–633. DOI: 10.1016/j.solener.2015.06.007.

Besarati, S & Goswami, D 2017, 'Supercritical CO_2 and other advanced power cycles for concentrating solar thermal (CST) systems', *Advances in Concentrating Solar Thermal Research and Technology*. Elsevier, pp. 157–178. DOI: 10.1016/B978-0-08-100516-3.00008-3.

Boer, J de 1958, 'The shapes of capillaries', *The structure and properties of porous materials*, pp. 68–94.

Boumaza, A, Favaro, L, Ledion, J, Sattonnay, G, Brubach, JB, Berthet, P, Huntz, AM, Roy, P & Tetot, R 2009, 'Transition alumina phases induced by heat treatment of boehmite: An X-ray diffraction and infrared spectroscopy study', *Journal of Solid State Chemistry*, vol. 182, no. 5, pp. 1171–1176. DOI: 10.1016/j.jssc.2009.02.006.

Buffham, BA & Mason, G 1993, 'Holdup and dispersion: tracer residence times, moments and inventory measurements', *Chemical Engineering Science*, vol. 48, no. 23, pp. 3879–3887. DOI: 10.1016/0009-2509(93)80366-X.

Buschman, AJ & Pittman, CM 1961, *Configuration Factors for Exchange of Radiant Energy Between Axisymmetrical Sections of Cylinders, Cones, and Hemispheres and Their Bases*, Report Technical Note D-944, NASA Langley Research Center.

Cañadas, L, Salvador, L & Ollero, P 1990, 'Radiative heat-transfer model in the interior of a pulverized coal furnace', *Industrial & Engineering Chemistry Research*, vol. 29, no. 4, pp. 669–675. DOI: 10.1021/ie00100a028.

Cai, RR, Zhang, YG, Li, QH & Meng, AH 2014, 'Experimental characterizing the residence time distribution of large spherical objects immersed in a fluidized bed', *Powder Technology*, vol. 254, pp. 22–29. DOI: 10.1016/j.powtec.2013.12.050.

Chase, MW 1998, 'NIST-JANAF Thermochemical Tables Fourth Edition, Part I, Al-Co', *Journal of Physical and Chemical Reference Data, Monograph 9*. DOI: 10.18434/T42S31.

Chen, H, Chen, Y, Hsieh, H-T & Siegel, N 2007, 'Computational Fluid Dynamics Modeling of Gas-Particle Flow Within a Solid-Particle Solar Receiver', *Journal of Solar Energy Engineering*, vol. 129, no. 2, p. 160. DOI: 10.1115/1.2716418.

Chigier, N & Beér, JM 1964, 'Velocity and static-pressure distributions in swirling air jets issuing from annular and divergent nozzles', *Journal of basic Engineering*, vol. 86, no. 4, pp. 788–796. DOI: 10.1115/1.3655954.

Chinnici, A, Arjomandi, M, Tian, ZF, Lu, Z & Nathan, GJ 2015, 'A Novel Solar Expanding-Vortex Particle Reactor: Influence of Vortex Structure on Particle Residence Times and Trajectories', *Solar Energy*, vol. 122, pp. 58–75. DOI: 10.1016/j.solener.2015.08.017.

Chinnici, A, Arjomandi, M, Tian, ZF & Nathan, GJ 2016, 'A Novel Solar Expanding-Vortex Particle Reactor: Experimental and Numerical Investigation of the Iso-thermal Flow Field and Particle Deposition', *Solar Energy*, vol. 133, pp. 451–464. DOI: 10.1016/j.solener.2016.04.006.

Chinnici, A, Xue, Y, Lau, TCW, Arjomandi, M & Nathan, GJ 2017, 'Experimental and numerical investigation of the flow characteristics within a Solar Expanding-Vortex Particle Receiver-Reactor', *Solar Energy*, vol. 141, pp. 25–37. DOI: 10.1016/j.solener.2016.11.020.

Clausing, A 1983, 'Convective losses from cavity solar receivers—comparisons between analytical predictions and experimental results', *Journal of Solar Energy Engineering*, vol. 105, no. 1, pp. 29–33. DOI: 10.1115/1.3266342.

Cortés, C & Gil, A 2007, 'Modeling the gas and particle flow inside cyclone separators', *Progress in Energy and Combustion Science*, vol. 33, no. 5, pp. 409–452. DOI: 10.1016/j.pecs.2007.02.001.

Danckwerts, PV 1953, 'Continuous flow systems: Distribution of residence times', *Chemical Engineering Science*, vol. 2, no. 1, pp. 1–13. DOI: 10.1016/0009-2509(53)80001-1.

Das, SK & Green, JAS 2010, 'Aluminum Industry and Climate Change-Assessment and Responses', *Jom*, vol. 62, no. 2, pp. 27–31. DOI: 10.1007/s11837-010-0027-5.

Derksen, JJ, Sundaresan, S & Akker, HEA van den 2006, 'Simulation of mass-loading effects in gas-solid cyclone separators', *Powder Technology*, vol. 163, no. 1-2, pp. 59–68. DOI: 10.1016/j.powtec.2006.01.006.

Ebert, M, Amsbeck, L, Buck, R, Rheinländer, J, Schlögl-Knothe, B, Schmitz, S, Sibum, M, Stadler, H & Uhlig, R 2018, 'First On-Sun Tests of a Centrifugal Particle Receiver System', *ASME 2018 12th International Conference on Energy Sustainability collocated with the ASME 2018 Power Conference and the ASME 2018 Nuclear Forum*, American Society of Mechanical Engineers, V001T11A002–V001T11A002. DOI: 10.1115/ES2018-7166.

Eglinton, T, Hinkley, J, Beath, A & Dell'Amico, M 2013, 'Potential Applications of Concentrated Solar Thermal Technologies in the Australian Minerals Processing and Extractive Metallurgical Industry', *Jom*, vol. 65, no. 12, pp. 1710–1720. DOI: 10.1007/s11837-013-0707-z.

Elghobashi, S 1994, 'On predicting particle-laden turbulent flows', *Applied Scientific Research*, vol. 52, no. 4, pp. 309–329. DOI: 10.1007/BF00936835.

Essadki, AH, Gourich, B, Vial, C & Delmas, H 2011, 'Residence time distribution measurements in an external-loop airlift reactor: Study of the hydrodynamics of the liquid circulation induced by the hydrogen bubbles', *Chemical Engineering Science*, vol. 66, no. 14, pp. 3125–3132. DOI: 10.1016/j.ces.2011.02.063.

Evans, G, Houf, W, Greif, R & Crowe, C 1987, 'Gas-Particle Flow within a High-Temperature Solar Cavity Receiver Including Radiation Heat-Transfer', *Journal of Solar Energy Engineering-Transactions of the Asme*, vol. 109, no. 2, pp. 134–142. DOI: 10.1115/1.3268190.

van Eyk, PJ, Ashman, PJ & Nathan, GJ 2016, 'Effect of High-Flux Solar Irradiation on the Gasification of Coal in a Hybrid Entrained-Flow Reactor', *Energy & Fuels*, vol. 30, no. 6, pp. 5138–5147. DOI: 10.1021/acs.energyfuels.6b00342.

Favaro, L, Boumaza, A, Roy, P, Lédion, J, Sattonnay, G, Brubach, J, Huntz, A & Tétot, R 2010, 'Experimental and ab initio infrared study of χ-, κ-and α-aluminas formed from gibbsite', *Journal of Solid State Chemistry*, vol. 183, no. 4, pp. 901–908. DOI: 10.1016/j.jssc.2010.02.010.

Feingold, A 1978, 'A new look at radiation configuration factors between disks', *Journal of Heat Transfer*, vol. 100, no. 4, pp. 742–744. DOI: 10.1115/1.3450893.

Flamant, G, Hernandez, D, Bonet, C & Traverse, J-P 1980, 'Experimental aspects of the thermochemical conversion of solar energy; Decarbonation of $CaCO_3$ ', *Solar Energy*, vol. 24, no. 4, pp. 385–395. DOI: 10.1016/0038-092x(80)90301-1.

Flamant, G, Gauthier, D, Benoit, H, Sans, J-L, Garcia, R, Boissière, B, Ansart, R & Hemati, M 2013, 'Dense suspension of solid particles as a new heat transfer fluid for concentrated solar thermal plants: On-sun proof of concept', *Chemical Engineering Science*, vol. 102, pp. 567–576. DOI: 10.1016/j.ces.2013.08.051.

Flamant, G, Gauthier, D, Benoit, H, Sans, JL, Boissière, B, Ansart, R & Hemati, M 2014, 'A New Heat Transfer Fluid for Concentrating Solar Systems: Particle Flow in Tubes', *Energy Procedia*, vol. 49, pp. 617–626. DOI: 10.1016/j.egypro.2014.03.067.

Fogler, HS 2006, *Elements of chemical reaction engineering*, 4th ed. Prentice Hall PTR, Upper Saddle River, NJ.

Gan, BK, Madsen, IC & Hockridge, JG 2009, 'In situ X-ray diffraction of the transformation of gibbsite to α-alumina through calcination: effect of particle size and heating rate', *Journal of Applied Crystallography*, vol. 42, no. 4, pp. 697–705. DOI: 10.1107/s0021889809021232.

Gao, Y, Vanarase, A, Muzzio, F & Ierapetritou, M 2011, 'Characterizing continuous powder mixing using residence time distribution', *Chemical Engineering Science*, vol. 66, no. 3, pp. 417–425. DOI: 10.1016/j.ces.2010.10.045.

Gao, Y, Muzzio, FJ & Ierapetritou, MG 2012, 'A review of the Residence Time Distribution (RTD) applications in solid unit operations', *Powder Technology*, vol. 228, pp. 416–423. DOI: 10.1016/j.powtec.2012.05.060.

Gokon, N, Takahashi, S, Yamamoto, H & Kodama, T 2009, 'New Solar Water-Splitting Reactor With Ferrite Particles in an Internally Circulating Fluidized Bed', *Journal of Solar Energy Engineering-Transactions of the Asme*, vol. 131, no. 1, p. 011007. DOI: 10.1115/1.3027511.

Guío-Pérez, DC, Pröll, T, Wassermann, J & Hofbauer, H 2013, 'Design of an inductance measurement system for determination of particle residence time in a dual circulating fluidized bed cold flow model', *Industrial and Engineering Chemistry Research*, vol. 52, no. 31, pp. 10732–10740. DOI: 10.1021/ie400211h.

Gupta, AK, Lilley, DG & Syred, N 1984, *Swirl flows*, Abacus Press, Tunbridge Wells, Kent.

Hamilton, DC & Morgan, WR 1952, *Radiant-interchange Configuration Factors*, Report 2836 (Technical Note), National Advisory Committee for Aeronautics.

Harris, AT, Davidson, JF & Thorpe, RB 2002, 'A novel method for measuring the residence time distribution in short time scale particulate systems', *Chemical Engineering Journal*, vol. 89, no. 1-3, pp. 127–142. DOI: 10.1016/S1385-8947(02)00004-9.

Harris, AT, Davidson, JF & Thorpe, RB 2003, 'Particle residence time distributions in circulating fluidised beds', *Chemical Engineering Science*, vol. 58, no. 11, pp. 2181–2202. DOI: 10.1016/s0009-2509(03)00082-4.

Haueter, P, Moeller, S, Palumbo, R & Steinfeld, A 1999, 'The production of zinc by thermal dissociation of zinc oxide—solar chemical reactor design', *Solar Energy*, vol. 67, no. 1-3, pp. 161–167. DOI: 10.1016/S0038-092X(00)00037-2.

Haugen, NEL & Mitchell, RE 2015, 'Modeling radiation in particle clouds: on the importance of inter-particle radiation for pulverized solid fuel combustion', *Heat and Mass Transfer*, vol. 51, no. 7, pp. 991–999. DOI: 10.1007/s00231-014-1472-4.

Hermann, WA 2006, 'Quantifying global exergy resources', *Energy*, vol. 31, no. 12, pp. 1685–1702. DOI: 10.1016/j.energy.2005.09.006.

Hilsenrath, J 1955, *Tables of thermal properties of gases: comprising tables of thermodynamic and transport properties of air, argon, carbon dioxide, carbon monoxide, hydrogen, nitrogen, oxygen, and steam*, US Dept. of Commerce, National Bureau of Standards.

Hirsch, D & Steinfeld, A 2004a, 'Radiative transfer in a solar chemical reactor for the co-production of hydrogen and carbon by thermal decomposition of methane', *Chemical Engineering Science*, vol. 59, no. 24, pp. 5771–5778. DOI: 10.1016/j.ces.2004.06.022.

Hirsch, D & Steinfeld, A 2004b, 'Solar hydrogen production by thermal decomposition of natural gas using a vortex-flow reactor', *International Journal of Hydrogen Energy*, vol. 29, no. 1, pp. 47–55. DOI: 10.1016/S0360-3199(03)00048-X.

Ho, CK 2016, 'A review of high-temperature particle receivers for concentrating solar power', *Applied Thermal Engineering*, vol. 109, pp. 958–969. DOI: 10.1016/j.applthermaleng.2016.04.103.

Ho, CK 2017, 'Advances in central receivers for concentrating solar applications', *Solar Energy*, vol. 152, pp. 38–56. DOI: 10.1016/j.solener.2017.03.048.

Ho, CK & Iverson, BD 2014, 'Review of high-temperature central receiver designs for concentrating solar power', *Renewable & Sustainable Energy Reviews*, vol. 29, pp. 835–846. DOI: 10.1016/j.rser.2013.08.099.

Ho, CK, Christian, J, Gill, D, Moya, A, Jeter, S, Abdel-Khalik, S, Sadowski, D, Siegel, N, Al-Ansary, H, Amsbeck, L, Gobereit, B & Buck, R 2014, 'Technology advancements for next generation falling particle receivers', *Proceedings of the Solarpaces 2013 International Conference*, vol. 49, pp. 398–407. DOI: 10.1016/j.egypro.2014.03.043.

Ho, CK, Christian, JM, Yellowhair, J, Siegel, N, Jeter, S, Golob, M, Abdel-Khalik, SI, Nguyen, C & Al-Ansary, H 2016, 'On-sun testing of an advanced falling particle receiver system', *AIP Conference Proceedings*, vol. 1734. AIP Publishing, p. 030022. DOI: 10.1063/1.4949074.

Ho, CK, Christian, JM, Romano, D, Yellowhair, J, Siegel, N, Savoldi, L & Zanino, R 2017, 'Characterization of Particle Flow in a Free-Falling Solar Particle Receiver', *Journal of Solar Energy Engineering-Transactions of the Asme*, vol. 139, no. 2, p. 021011. DOI: 10.1115/1.4035258.

Ho, CK, Christian, JM, Yellowhair, JE, Armijo, K, Kolb, WJ, Jeter, S, Golob, M & Nguyen, C 2019, 'On-Sun Performance Evaluation of Alternative High-Temperature Falling Particle Receiver Designs', *Journal of Solar Energy Engineering-Transactions of the Asme*, vol. 141, no. 1, p. 011009. DOI: 10.1115/1.4041100.

Hoffmann, AC & Stein, LE 2007, *Gas Cyclones and Swirl Tubes: Principles, Design, and Operation*, Springer, Berlin. DOI: 10.1007/978-3-540-74696-6.

Holman, JP 2010, *Heat transfer*, 10th ed. McGraw Hill Higher Education, Sydney.

Hottel, HC & Cohen, ES 1958, 'Radiant heat exchange in a gas-filled enclosure: Allowance for nonuniformity of gas temperature', *AIChE Journal*, vol. 4, no. 1, pp. 3–14. DOI: 10.1002/aic.690040103.

Hottel, HC & Sarofim, AF 1967, *Radiative transfer*, McGraw-Hill, New York.

Howell, JR, Siegel, R & Mengüç, MP 2011, *Thermal radiation heat transfer*, 5th. CRC press/Taylor & Francis, Boca Raton.

Hruby, J, Steeper, R, Evans, G & Crowe, C 1988, 'An experimental and numerical study of flow and convective heat transfer in a freely falling curtain of particles', *Journal of fluids engineering*, vol. 110, no. 2, pp. 172–181. DOI: 10.1115/1.3243531.

Hyland, MM, Gillespie, AR & Metson, JB 1997, 'Predicting moisture content on smelter grade alumina from measurement of the water isotherm', *Light Metals 1997*, pp. 113–117.

Imhof, A 1991, 'The cyclone reactor—an atmospheric open solar reactor', *Solar Energy Materials*, vol. 24, no. 1-4, pp. 733–741. DOI: 10.1016/0165-1633(91)90106-U.

Ingram-Jones, VJ, Slade, RCT, Davies, TW, Southern, JC & Salvador, S 1996, 'Dehydroxylation sequences of gibbsite and boehmite: Study of differences between soak and flash calcination and of particle-size effects', *Journal of Materials Chemistry*, vol. 6, no. 1, pp. 73–79. DOI: 10.1016/0165-1633(91)90106-U.

IAI – International Aluminium Institute 2019, *Statistics*, Web Page, URL: http://www.world-aluminium.org/statistics/ (visited on Jan. 9, 2019).

IEA – International Energy Agency 2011, *Solar Energy Perspectives*, OECD Publishing, Paris. DOI: 10.1787/9789264124585-en.

IEA – International Energy Agency 2015, *Technology Roadmap Solar Thermal Electricity*, IEA Technology Roadmaps, OECD Publishing, Paris. DOI: 10.1787/9789264238824-en.

IEA – International Energy Agency 2017, *Energy Technology Perspectives 2017: Catalysing Energy Technology Transformations*, OECD Publishing, Paris. DOI: 10.1787/energy_tech-2017-en.

IEA – International Energy Agency 2018a, *Low-Carbon Transition in the Cement Industry*, IEA Technology Roadmaps, OECD Publishing, Paris. DOI: 10.1787/9789264300248-en.

IEA – International Energy Agency 2018b, *World Energy Outlook 2018*, OECD Publishing, Paris. DOI: 10.1787/weo-2018-en.

Jafarian, M, Arjomandi, M & Nathan, GJ 2012, 'A hybrid solar and chemical looping combustion system for solar thermal energy storage', *Applied Energy*. DOI: 10.1016/j.apenergy.2012.10.033.

Jafarian, M, Arjomandi, M & Nathan, GJ 2013, 'The influence of high intensity solar radiation on the temperature and reduction of an oxygen carrier particle in hybrid chemical looping combustion', *Chemical Engineering Science*, vol. 95, pp. 331–342. DOI: 10.1016/j.ces.2013.03.007.

Jamel, MS, Abd Rahman, A & Shamsuddin, AH 2013, 'Advances in the integration of solar thermal energy with conventional and non-conventional power plants', *Renewable & Sustainable Energy Reviews*, vol. 20, pp. 71–81. DOI: 10.1016/j.rser.2012.10.027.

Jenkins, B & Bertrand, C 2001, 'Improvements in the Design and Operation of Alumina Flash Calciners', *IFRF Combustion Journal*.

Jenkins, B & Moles, F 1981, 'Modeling of Heat-Transfer from a Large Enclosed Flame in a Rotary Kiln', *Transactions of the Institution of Chemical Engineers*, vol. 59, no. 1, pp. 17–25.

Kang, SK, Kwon, TW & Kim, SD 1989, 'Hydrodynamic Characteristics of Cyclone Reactors', *Powder Technology*, vol. 58, no. 3, pp. 211–220. DOI: 10.1016/0032-5910(89)80116-0.

Kasule, JS, Turton, R, Bhattacharyya, D & Zitney, SE 2012, 'Mathematical modeling of a single-stage, downward-firing, entrained-flow gasifier', *Industrial and Engineering Chemistry Research*, vol. 51, no. 18, pp. 6429–6440. DOI: 10.1021/ie202121h.

Kehlenbeck, R, Yates, J, Felize, R, Hofbauer, H & Rauch, R 2002, 'Particle Residence Time and Particle Mixing in a Scaled Internal Circulating Fluidized Bed', *Industrial & Engineering Chemistry Research*, vol. 41, no. 11, pp. 2637–2645. DOI: 10.1021/ie010513u.

Kermeli, K, ter Weer, P-H, Crijns-Graus, W & Worrell, E 2015, 'Energy efficiency improvement and GHG abatement in the global production of primary aluminium', *Energy Efficiency*, vol. 8, no. 4, pp. 629–666. DOI: 10.1007/s12053-014-9301-7.

Khayyat, A, Knott, R, Nguyen, C, Golob, M, Abdel-Khalik, S, Jeter, S & Al-Ansary, H 2015, 'Measurement of Particulate Flow in Discrete Structure Particle Heating Receivers', *ASME 2015 9th International Conference on Energy Sustainability collocated with the ASME 2015 Power Conference, the ASME 2015 13th International Conference on Fuel Cell Science, Engineering and Technology, and the ASME 2015 Nuclear Forum*, American Society of Mechanical Engineers, V001T05A020–V001T05A020. DOI: 10.1115/ES2015-49510.

Kieviet, FGF & Kerkhof, PP 1995, 'Measurements of particle residence time distributions in a co-current spray dryer', *Drying Technology*, vol. 13, no. 5-7, pp. 1241–3937. DOI: 10.1080/07373939508917019.

Klein, HH, Karni, J, Ben-Zvi, R & Bertocchi, R 2007, 'Heat transfer in a directly irradiated solar receiver/reactor for solid–gas reactions', *Solar Energy*, vol. 81, no. 10, pp. 1227–1239. DOI: 10.1016/j.solener.2007.01.004.

Klett, C & Perander, L 2015, 'Alumina Calcination: A Mature Technology Under Review from Supplier Perspective', *Light Metals*, pp. 79–84. DOI: 10.1002/9781119093435.ch15.

Kodama, T & Gokon, N 2007, 'Thermochemical cycles for high-temperature solar hydrogen production', *Chemical Reviews*, vol. 107, no. 10, pp. 4048–77. DOI: 10.1021/cr050188a.

Kodama, T, Enomoto, SI, Hatamachi, T & Gokon, N 2008, 'Application of an internally circulating fluidized bed for windowed solar chemical reactor with direct irradiation of reacting particles', *Journal of Solar Energy Engineering*, vol. 130, no. 1, p. 014504. DOI: 10.1115/1.2807213.

Kodama, T, Gokon, N, Enomoto, S, Itoh, S & Hatamachi, T 2010, 'Coal Coke Gasification in a Windowed Solar Chemical Reactor for Beam-Down Optics', *Journal of Solar Energy Engineering-Transactions of the Asme*, vol. 132, no. 4, p. 041004. DOI: 10.1115/1.4002081.

Kodama, T, Gokon, N, Matsubara, K, Yoshida, K, Koikari, S, Nagase, Y & Nakamura, K 2014, 'Flux measurement of a new beam-down solar concentrating system in Miyazaki for demonstration of thermochemical water splitting reactors', *Proceedings of the Solarpaces 2013 International Conference*, vol. 49, pp. 1990–1998. DOI: 10.1016/j.egypro.2014.03.211.

Kodama, T, Bellan, S, Gokon, N & Cho, HS 2017a, 'Particle reactors for solar thermochemical processes', *Solar Energy*, vol. 156, pp. 113–132. DOI: 10.1016/j.solener.2017.05.084.

Kodama, T, Gokon, N, Cho, HS, Matsubara, K, Kaneko, H, Senuma, K, Itoh, S & Yokota, S-n 2017b, 'Particles fluidized bed receiver/reactor tests with quartz sand particles using a 100-kWth beam-down solar concentrating system at Miyazaki', *AIP Conference Proceedings*, vol. 1850. AIP Publishing, p. 100012. DOI: 10.1063/1.4984469.

Kogure, T 2004, 'Dehydration Sequence of Gibbsite by Electron-Beam Irradiation in a TEM', *Journal of the American Ceramic Society*, vol. 82, no. 3, pp. 716–720. DOI: 10.1111/j.1151-2916.1999.tb01822.x.

Kräupl, S & Steinfeld, A 2001, 'Experimental investigation of a vortex-flow solar chemical reactor for the combined ZnO-reduction and CH4-reforming', *Journal of Solar Energy Engineering, Transactions of the ASME*, vol. 123, no. 3, pp. 237–243. DOI: 10.1115/1.1384569.

Lapp, J, Davidson, J & Lipiński, W 2012, 'Efficiency of two-step solar thermochemical non-stoichiometric redox cycles with heat recovery', *Energy*, vol. 37, no. 1, pp. 591–600. DOI: 10.1016/j.energy.2011.10.045.

Lau, TCW & Nathan, GJ 2014, 'Influence of Stokes number on the velocity and concentration distributions in particle-laden jets', *Journal of Fluid Mechanics*, vol. 757, pp. 432–457. DOI: 10.1017/jfm.2014.496.

Lau, TCW & Nathan, GJ 2016, 'The effect of Stokes number on particle velocity and concentration distributions in a well-characterised, turbulent, co-flowing two-phase jet', *Journal of Fluid Mechanics*, vol. 809, pp. 72–110. DOI: 10.1017/jfm.2016.666.

Lede, J, Li, HZ, Soulignac, F & Villermaux, J 1987, 'Measurement of solid particle residence time in a cyclone reactor: A comparison of four methods', *Chemical Engineering and Processing: Process Intensification*, vol. 22, no. 4, pp. 215–222. DOI: 10.1016/0255-2701(87)85004-3.

Lee, KL, Chinnici, A, Jafarian, M, Arjomandi, M, Dally, B & Nathan, G 2018, 'Experimental investigation of the effects of wind speed and yaw angle on heat losses from a heated cavity', *Solar Energy*, vol. 165, pp. 178–188. DOI: 10.1016/j.solener.2018.03.023.

Lee, T, Lim, S, Shin, S, Sadowski, DL, Abdel-Khalik, SI, Jeter, SM & Al-Ansary, H 2015, 'Numerical simulation of particulate flow in interconnected porous media for central particle-heating receiver applications', *Solar Energy*, vol. 113, pp. 14–24. DOI: 10.1016/j.solener.2014.12.017.

Leibfried, U & Ortjohann, J 1995, 'Convective Heat-Loss from Upward and Downward-Facing Cavity Solar Receivers - Measurements and Calculations', *Journal of Solar Energy Engineering-Transactions of the Asme*, vol. 117, no. 2, pp. 75–84. DOI: 10.1115/1.2870873.

Leuenberger, H & Person, R 1954, *Compilation of radiation shape factors for cylindrical assemblies*, Report 56-A-144, ASME.

Levenspiel, O 1999, *Chemical reaction engineering*, 3rd ed. Wiley, New York.

Li, L, Coventry, J, Bader, R, Pye, J & Lipiński, W 2016, 'Optics of solar central receiver systems: a review', *Optics Express*, vol. 24, no. 14, A985–A1007. DOI: 10.1364/OE.24.00A985.

Li, SH, Yang, S, Yang, HR, Zhang, H, Liu, Q, Lu, JF & Yue, GX 2008, 'Particle holdup and average residence time in the cyclone of a CFB boiler', *Chemical Engineering & Technology*, vol. 31, no. 2, pp. 224–230. DOI: 10.1002/ceat.200700264.

Lichty, P, Perkins, C, Woodruff, B, Bingham, C & Weimer, A 2010, 'Rapid High Temperature Solar Thermal Biomass Gasification in a Prototype Cavity Reactor', *Journal of Solar Energy Engineering-Transactions of the Asme*, vol. 132, no. 1, p. 011012. DOI: 10.1115/1.4000356.

Lovegrove, K, Edwards, S, Jacobson, N, Jordan, J, Petersheim, J, Rutowitz, J, Saddler, H, Watt, M & Wyder, J 2015, *Renewable energy options for Australian industrial gas users*, Report ITP/A0142, Australian Renewable Energy Agency.

Maag, G, Lipiński, W & Steinfeld, A 2009a, 'Particle-gas reacting flow under concentrated solar irradiation', *International Journal of Heat and Mass Transfer*, vol. 52, no. 21-22, pp. 4997–5004. DOI: 10.1016/j.ijheatmasstransfer.2009.02.049.

Maag, G, Zanganeh, G & Steinfeld, A 2009b, 'Solar thermal cracking of methane in a particle-flow reactor for the co-production of hydrogen and carbon', *International Journal of Hydrogen Energy*, vol. 34, no. 18, pp. 7676–7685. DOI: 10.1016/j.ijhydene.2009.07.037.

Müller, F, Poživil, P, van Eyk, PJ, Villarrazo, A, Haueter, P, Wieckert, C, Nathan, GJ & Steinfeld, A 2017, 'A pressurized high-flux solar reactor for the efficient thermochemical gasification of carbonaceous feedstock', *Fuel*, vol. 193, pp. 432–443. DOI: 10.1016/j.fuel.2016.12.036.

Marchioli, C, Picciotto, M & Soldati, A 2006, 'Particle dispersion and wall-dependent turbulent flow scales: implications for local equilibrium models', *Journal of Turbulence*, vol. 7, no. 7. DOI: 10.1080/14685240600925171.

McLellan, BC, Corder, GD, Giurco, DP & Ishihara, KN 2012, 'Renewable energy in the minerals industry: a review of global potential', *Journal of Cleaner Production*, vol. 32, pp. 32–44. DOI: 10.1016/j.jclepro.2012.03.016.

Meier, A, Bonaldi, E, Cella, GM, Lipiński, W, Wuillemin, D & Palumbo, R 2004, 'Design and experimental investigation of a horizontal rotary reactor for the solar thermal production of lime', *Energy*, vol. 29, no. 5-6, pp. 811–821. DOI: 10.1016/S0360-5442(03)00187-7.

Meier, A, Bonaldi, E, Cella, GM, Lipiński, W & Wuillemin, D 2006, 'Solar chemical reactor technology for industrial production of lime', *Solar Energy*, vol. 80, no. 10, pp. 1355–1362. DOI: 10.1016/j.solener.2005.05.017.

Metson, J, Groutso, T, Hyland, M & Powell, S 2006, 'Evolution of microstructure and properties of SGA with calcination of Bayer Gibbsite', *Light Metals 2006, Vol 1: Alumina & Bauxite*, pp. 89–93.

Mikulcic, H, Vujanovic, M, Fidaros, DK, Priesching, P, Minic, I, Tatschl, R, Duic, N & Stefanovic, G 2012, 'The application of CFD modelling to support the reduction of CO_2 emissions in cement industry', *Energy(Oxford)*, vol. 45, no. 1, pp. 464–473. DOI: 10.1016/j.energy.2012.04.030.

Mills, P & Duduković, M 1989, 'Convolution and deconvolution of nonideal tracer response data with application to three-phase packed-beds', *Computers & Chemical Engineering*, vol. 13, no. 8, pp. 881–898. DOI: 10.1016/0098-1354(89)85062-8.

Mitsutani, K, Grace, JR & Lim, CJ 2005, 'Residence time distribution of particles in a continuous liquid–solid classifier', *Chemical Engineering Science*, vol. 60, no. 10, pp. 2703–2713. DOI: 10.1016/j.ces.2004.09.084.

Nathan, GJ, Kalt, PAM, Alwahabi, ZT, Dally, BB, Medwell, PR & Chan, QN 2012, 'Recent advances in the measurement of strongly radiating, turbulent reacting flows', *Progress in Energy and Combustion Science*, vol. 38, no. 1, pp. 41–61. DOI: 10.1016/j.pecs.2011.04.001.

Nathan, GJ, Battye, DL & Ashman, PJ 2013, 'Economic evaluation of a novel fuel-saver hybrid combining a solar receiver with a combustor for a solar power tower', *Applied Energy*, vol. 113, pp. 1235–1243. DOI: 10.1016/j.apenergy.2013.08.079.

Nathan, GJ, Dally, BB, Alwahabi, ZT, van Eyk, PJ, Jafarian, M & Ashman, PJ 2017a, 'Research challenges in combustion and gasification arising from emerging technologies employing directly irradiated concentrating solar thermal radiation', *Proceedings of the Combustion Institute*, vol. 36, no. 2, pp. 2055–2074. DOI: 10.1016/j.proci.2016.07.044.

Nathan, GJ, Jafarian, M, Dally, BB, Saw, WL, Ashman, PJ, Hu, E & Steinfeld, A 2017b, 'Solar thermal hybrids for combustion power plant: A growing opportunity', *Progress in Energy and Combustion Science*, vol. 64, pp. 4 –28. DOI: 10.1016/j.pecs.2017.08.002.

Nauman, EB 2008, 'Residence time theory', *Industrial & Engineering Chemistry Research*, vol. 47, no. 10, pp. 3752–3766. DOI: 10.1021/ie071635a.

Nikulshina, V, Halmann, M & Steinfeld, A 2009a, 'Coproduction of Syngas and Lime by Combined $CaCO_3$-Calcination and CH4-Reforming Using a Particle-Flow Reactor Driven by Concentrated Solar Radiation', *Energy & Fuels*, vol. 23, pp. 6207–6212. DOI: 10.1021/ef9007246.

Nikulshina, V, Gebald, C & Steinfeld, A 2009b, 'CO_2 capture from atmospheric air via consecutive CaO-carbonation and $CaCO_3$-calcination cycles in a fluidized-bed solar reactor', *Chemical Engineering Journal*, vol. 146, no. 2, pp. 244–248. DOI: 10.1016/j.cej.2008.06.005.

Olivier, JG, Janssens-Maenhout, G, Muntean, M & Peters, JA 2015, *Trends in global CO_2 emissions: 2015 report*, Report 1803, The Hague: PBL Netherlands Environmental Assessment Agency; Ispra: European Commission, Joint Research Centre.

Padilla, I, Lopez-Delgado, A, Lopez-Andres, S, Alvarez, M, Galindo, R & Vazquez-Vaamonde, AJ 2014, 'The application of thermal solar energy to high temperature processes: case study of the synthesis of alumina from boehmite', *The Scientific World Journal*, vol. 2014, p. 825745. DOI: 10.1155/2014/825745.

Perander, LM 2010, 'Evolution of nano- and microstructure during the calcination of Bayer gibbsite to produce alumina', PhD Thesis, The University of Auckland.

Perander, LM, Zujovic, ZD, Groutso, T, Hyland, MM, Smith, ME, O'Dell, LA & Metson, JB 2007, 'Characterization of metallurgical-grade aluminas and their precursors by 27Al NMR and XRD', *Canadian Journal of Chemistry*, vol. 85, no. 10, pp. 889–897. DOI: 10.1139/v07-106.

Perander, LM, Zujovic, ZD, Kemp, TF, Smith, ME & Metson, JB 2009, 'The Nature and Impacts of Fines in Smelter-Grade Alumina', *Jom*, vol. 61, no. 11, pp. 33–39. DOI: 10.1007/s11837-009-0164-x.

Perander, LM, Stam, MA, Hyland, MM & Metson, JB 2011, 'Towards Redefining the Alumina Specifications Sheet - The Case of HF Emissions', *Light Metals 2011*, pp. 285–290. DOI: 10.1007/978-3-319-48160-9_51.

Perkins, C & Weimer, AW 2009, 'Solar-thermal production of renewable hydrogen', *AIChE Journal*, vol. 55, no. 2, pp. 286–293. DOI: 10.1002/aic.11810.

Raahauge, BE 2015, 'Smelter Grade Alumina Quality in 40+ Year Perspective: Where to From Here?', *Light Metals*, pp. 73–78. DOI: 10.1007/978-3-319-48248-4_14.

Röger, M, Amsbeck, L, Gobereit, B & Buck, R 2011, 'Face-down solid particle receiver using recirculation', *Journal of Solar Energy Engineering*, vol. 133, no. 3, p. 031009. DOI: 10.1115/1.4004269.

Rouquerol, J, Rouquerol, F & Ganteaume, M 1975, 'Thermal decomposition of gibbsite under low pressures: I. Formation of the boehmitic phase', *Journal of Catalysis*, vol. 36, no. 1, pp. 99–110. DOI: 10.1016/0021-9517(75)90014-7.

Rowe, SC, Groehn, AJ, Palumbo, AW, Chubukov, BA, Clough, DE, Weimer, AW & Hischier, I 2015, 'Worst-case losses from a cylindrical calorimeter for solar simulator calibration', *Optics Express*, vol. 23, no. 19, A1309–A1322. DOI: 10.1364/OE.23.0A1309.

Sattler, C, Roeb, M, Agrafiotis, C & Thomey, D 2017, 'Solar hydrogen production via sulphur based thermochemical water-splitting', *Solar Energy*, vol. 156, pp. 30–47. DOI: 10.1016/j.solener.2017.05.060.

Saw, WL, Guo, PJ, van Eyk, PJ & Nathan, GJ 2017, 'Approaches to accommodate resource variability in the modelling of solar driven gasification processes for liquid fuels synthesis', *Solar Energy*, vol. 156, pp. 101–112. DOI: 10.1016/j.solener.2017.05.085.

Schmitz, M, Schwarzbozl, P, Buck, R & Pitz-Paal, R 2006, 'Assessment of the potential improvement due to multiple apertures in central receiver systems with secondary concentrators', *Solar Energy*, vol. 80, no. 1, pp. 111–120. DOI: 10.1016/j.solener.2005.02.012.

Schunk, LO, Haeberling, P, Wepf, S, Wuillemin, D, Meier, A & Steinfeld, A 2008, 'A receiver-reactor for the solar thermal dissociation of zinc oxide', *Journal of Solar Energy Engineering-Transactions of the Asme*, vol. 130, no. 2, p. 021009. DOI: 10.1115/1.2840576.

Shilapuram, V, Krishna, DJ & Ozalp, N 2011, 'Residence time distribution and flow field study of aero-shielded solar cyclone reactor for emission-free generation of hydrogen', *International Journal of Hydrogen Energy*, vol. 36, no. 21, pp. 13488–13500. DOI: 10.1016/j.ijhydene.2011.08.035.

Siegel, N, Kolb, G, Kim, K, Rangaswamy, V & Moujaes, S 2007, 'Solid Particle Receiver Flow Characerization Studies', *ASME 2007 Energy Sustainability Conference*, American Society of Mechanical Engineers, pp. 877–883. DOI: 10.1007/978-3-319-48248-4_14.

Siegel, N, Ho, CK, Khalsa, SS & Kolb, GJ 2010, 'Development and Evaluation of a Prototype Solid Particle Receiver: On-Sun Testing and Model Validation', *Journal of Solar Energy Engineering-Transactions of the Asme*, vol. 132, no. 2, p. 021008. DOI: 10.1115/1.4001146.

Siegel, N, Gross, M, Ho, C, Phan, T & Yuan, J 2014, 'Physical properties of solid particle thermal energy storage media for concentrating solar power applications', *Energy Procedia*, vol. 49, pp. 1015–1023. DOI: 10.1016/j.egypro.2014.03.109.

Siegel, N, Gross, MD & Coury, R 2015, 'The Development of Direct Absorption and Storage Media for Falling Particle Solar Central Receivers', *Journal of Solar Energy Engineering-Transactions of the Asme*, vol. 137, no. 4, p. 041003. DOI: 10.1115/1.4030069.

Sommerseth, C, Osen, KS, Rosenkilde, C, Meyer, AJ, Kristiansen, LT & Aarhaug, TA 2012, 'A Method for Comparing the HF Formation Potential of Aluminas with Different Water Contents', *Light Metals 2012*, pp. 827–832. DOI: 10.1007/978-3-319-48179-1_143.

Sparrow, EM & Jonsson, VK 1963, 'Radiant Emission Characteristics of Diffuse Conical Cavities', *Journal of the Optical Society of America*, vol. 53, no. 7, pp. 816–821. DOI: 10.1364/Josa.53.000816.

Stein, WH & Buck, R 2017, 'Advanced power cycles for concentrated solar power', *Solar Energy*, vol. 152, pp. 91–105. DOI: 10.1016/j.solener.2017.04.054.

Steinfeld, A 2005, 'Solar thermochemical production of hydrogen - a review', *Solar Energy*, vol. 78, no. 5, pp. 603–615. DOI: 10.1016/j.solener.2003.12.012.

Steinfeld, A & Palumbo, R 2001, 'Solar thermochemical process technology', *Encyclopedia of physical science and technology*, vol. 15, no. 1, pp. 237–56. DOI: 10.1016/B0-12-227410-5/00698-0.

Steinfeld, A, Imhof, A & Mischler, D 1992, 'Experimental Investigation of an Atmospheric-Open Cyclone Solar Reactor for Solid-Gas Thermochemical Reactions', *Journal of Solar Energy Engineering-Transactions of the Asme*, vol. 114, no. 3, pp. 171–174. DOI: 10.1115/1.2930001.

Steinfeld, A, Brack, M, Meier, A, Weidenkaff, A & Wuillemin, D 1998, 'A solar chemical reactor for co-production of zinc and synthesis gas', *Energy*, vol. 23, no. 10, pp. 803–814. DOI: 10.1016/S0360-5442(98)00026-7.

Syred, N 2006, 'A review of oscillation mechanisms and the role of the precessing vortex core (PVC) in swirl combustion systems', *Progress in Energy and Combustion Science*, vol. 32, no. 2, pp. 93–161. DOI: 10.1016/j.pecs.2005.10.002.

Szargut, JT 2003, 'Anthropogenic and natural exergy losses (exergy balance of the Earth's surface and atmosphere)', *Energy*, vol. 28, no. 11, pp. 1047–1054. DOI: 10.1016/S0360-5442(03)00089-6.

Szekely, J & Carr, R 1966, 'Heat transfer in a cyclone', *Chemical Engineering Science*, vol. 21, no. 12, pp. 1119–1132. DOI: 10.1016/0009-2509(66)85033-9.

Tan, TD & Chen, YT 2010, 'Review of study on solid particle solar receivers', *Renewable & Sustainable Energy Reviews*, vol. 14, no. 1, pp. 265–276. DOI: 10.1016/j.rser.2009.05.012.

Tescari, S, Neises, M, de Oliveira, L, Roeb, M, Sattler, C & Neveu, P 2013, 'Thermal model for the optimization of a solar rotary kiln to be used as high temperature thermochemical reactor', *Solar Energy*, vol. 95, pp. 279–289. DOI: 10.1016/j.solener.2013.06.021.

Tian, ZF, Nathan, GJ & Cao, Y 2015, 'Numerical modelling of flows in a solar–enhanced vortex gasifier: Part 1, comparison of turbulence models', *Progress in Computational Fluid Dynamics, an International Journal*, vol. 15, no. 2, pp. 114–122. DOI: 10.1504/PCFD.2015.068819.

Trachsel, F, Günther, A, Khan, S & Jensen, KF 2005, 'Measurement of residence time distribution in microfluidic systems', *Chemical Engineering Science*, vol. 60, no. 21, pp. 5729–5737. DOI: 10.1016/j.ces.2005.04.039.

Tregambi, C, Chirone, R, Montagnaro, F, Salatino, P & Solimene, R 2016, 'Heat transfer in directly irradiated fluidized beds', *Solar Energy*, vol. 129, pp. 85–100. DOI: 10.1016/j.solener.2016.01.057.

Viitanen, P 1997, 'Experiences on fast fourier transform as a deconvolution technique in determination of process equipment residence time distribution', *Applied Radiation and Isotopes*, vol. 48, no. 7, pp. 893–898. DOI: 10.1016/S0969-8043(97)00029-8.

Voth, GA & Soldati, A 2017, 'Anisotropic Particles in Turbulence', *Annual Review of Fluid Mechanics*, vol. 49, no. 1, pp. 249–276. DOI: 10.1146/annurev-fluid-010816-060135.

Wang, FZ, Bai, FW, Wang, TJ, Li, Q & Wang, ZF 2016, 'Experimental study of a single quartz tube solid particle air receiver', *Solar Energy*, vol. 123, pp. 185–205. DOI: 10.1016/j.solener.2015.10.048.

Wang, HP, Xu, BG, Smith, P, Davies, M, DeSilva, L & Wingate, C 2006, 'Kinetic modelling of gibbsite dehydration/amorphization in the temperature range 823-923 K', *Journal of Physics and Chemistry of Solids*, vol. 67, no. 12, pp. 2567–2582. DOI: 10.1016/j.jpcs.2006.07.016.

Wefers, K & Misra, C 1987, *Oxides and hydroxides of aluminum*, Report 19 (Technical Paper), Alcoa.

Whittington, B & Ilievski, D 2004, 'Determination of the gibbsite dehydration reaction pathway at conditions relevant to Bayer refineries', *Chemical Engineering Journal*, vol. 98, no. 1-2, pp. 89–97. DOI: 10.1016/S1385-8947(03)00207-9.

Williams, F & Schmidt, H-W 2012, 'Flash- and CFB Calciners, History and Difficulties of Development of Two Calcination Technologies', *Light Metals*, pp. 135–140. DOI: 10.1002/9781118359259.ch24.

Wind, S, Jensen-Holm, C & Raahauge, BE 2010, 'Development of Particle Breakdown and Alumina Strength during Calcination', *Light Metals 2010*, pp. 17–24. DOI: 10.1007/978-3-319-48176-0_104.

Wind, S & Raahauge, BE 2013, 'Experience with commissioning new generation Gas Suspension Calciner', *Light Metals*, pp. 155–162. DOI: 10.1002/9781118663189.ch28.

Wu, S-Y, Xiao, L & Li, Y-R 2010, 'Convection heat loss from cavity receiver in parabolic dish solar thermal power system: A review', *Solar Energy*, vol. 84, no. 8. DOI: 10.1016/j.solener.2010.04.008.

Wu, W, Amsbeck, L, Buck, R, Uhlig, R & Ritz-Paal, R 2014, 'Proof of concept test of a centrifugal particle receiver', *Proceedings of the Solarpaces 2013 International Conference*, vol. 49, pp. 560–568. DOI: 10.1016/j.egypro.2014.03.060.

Wu, W, Trebing, D, Amsbeck, L, Buck, R & Pitz-Paal, R 2015, 'Prototype Testing of a Centrifugal Particle Receiver for High-Temperature Concentrating Solar Applications', *Journal of Solar Energy Engineering-Transactions of the Asme*, vol. 137, no. 4, p. 041011. DOI: 10.1115/1.4030657.

Yogev, A, Kribus, A, Epstein, M & Kogan, A 1998, 'Solar "tower reflector" systems: a new approach for high-temperature solar plants', *International Journal of Hydrogen Energy*, vol. 23, no. 4, pp. 239–245. DOI: 10.1016/S0360-3199(97)00059-1.

Yong, Y 1996, 'Mass flow measurement of bulk solids in pneumatic pipelines', *Measurement Science and Technology*, vol. 7, pp. 1687–1706. DOI: 10.1088/0957-0233/7/12/002.

Z'Graggen, A 2008, 'Solar Gasification of Carbonaceous Materials: Reactor Design, Modeling and Experimentation', PhD Thesis, ETH Zürich. DOI: 10.3929/ethz-a-005633392.

Z'Graggen, A & Steinfeld, A 2008a, 'A two-phase reactor model for the steam-gasification of carbonaceous materials under concentrated thermal radiation', *Chemical Engineering and Processing*, vol. 47, no. 4, pp. 655–662. DOI: 10.1016/j.cep.2006.12.003.

Z'Graggen, A & Steinfeld, A 2008b, 'Hydrogen production by steam-gasification of carbonaceous materials using concentrated solar energy — V. Reactor modeling, optimization, and scale-up', *International Journal of Hydrogen Energy*, vol. 33, no. 20, pp. 5484–5492. DOI: 10.1016/j.ijhydene.2008.07.047.

Z'Graggen, A & Steinfeld, A 2009, 'Heat and mass transfer analysis of a suspension of reacting particles subjected to concentrated solar radiation – Application to the steam-gasification of carbonaceous materials', *International Journal of Heat and Mass Transfer*, vol. 52, no. 1-2, pp. 385–395. DOI: 10.1016/j.ijheatmasstransfer.2008.05.023.

Z'Graggen, A, Haueter, P, Trommer, D, Romero, M, Jesus, JC de & Steinfeld, A 2006, 'Hydrogen production by steam-gasification of petroleum coke using concentrated solar power — II Reactor design, testing, and modeling', *International Journal of Hydrogen Energy*, vol. 31, no. 6, pp. 797–811. DOI: 10.1016/j.ijhydene.2005.06.011.

Z'Graggen, A, Haueter, P, Maag, G, Vidal, A, Romero, M & Steinfeld, A 2007, 'Hydrogen production by steam-gasification of petroleum coke using concentrated solar power — III. Reactor experimentation with slurry feeding', *International Journal of Hydrogen Energy*, vol. 32, no. 8, pp. 992–996. DOI: 10.1016/j.ijhydene.2006.10.001.

List of Figures

List of Tables

A

Journal Articles

The following journal articles are included here in their published version or their submitted manuscript version.

- **Davis, D,** Jafarian, M, Chinnici, A, Saw, WL & Nathan, GJ 2019, 'Thermal performance of vortex-based solar particle receivers for sensible heating', *Solar Energy*, vol. 177, pp. 163–177.
- **Davis, D,** Troiano, M, Chinnici, A, Saw, WL, Lau, T, Solimene, R, Salatino, P & Nathan, GJ 2019, 'Particle residence time distributions in a vortex-based solar particle receiver-reactor: an experimental, numerical and theoretical study', Manuscript submitted to *Chemical Engineering Science*.
- **Davis, D,** Troiano, M, Chinnici, A, Saw, WL, Lau, T, Solimene, R, Salatino, P & Nathan, GJ 2019, 'Particle residence time distributions in a vortex-based solar particle receiver-reactor: the influence of receiver tilt angle', Manuscript submitted to *Solar Energy*.
- **Davis, D,** Müller, F, Saw, WL, Steinfeld, A & Nathan, GJ 2017, 'Solar-driven alumina calcination for CO_2 mitigation and improved product quality', *Green Chemistry*, vol. 19, no. 13, pp. 2992–3005.

Solar Energy 177 (2019) 163–177

Contents lists available at ScienceDirect

Solar Energy

journal homepage: www.elsevier.com/locate/solener

Thermal performance of vortex-based solar particle receivers for sensible heating

Dominic Davis[a,b,*], Mehdi Jafarian[a,b], Alfonso Chinnici[a,b], Woei L. Saw[a,c], Graham J. Nathan[a,b]

[a] Centre for Energy Technology, The University of Adelaide, SA 5005, Australia
[b] School of Mechanical Engineering, The University of Adelaide, SA 5005, Australia
[c] School of Chemical Engineering, The University of Adelaide, SA 5005, Australia

ARTICLE INFO

Keywords:
Solar particle receiver
Solar vortex receiver
Concentrated solar thermal
CST
Heat transfer

ABSTRACT

We report a first-order assessment of a novel vortex-based solar particle receiver and the sensitivity of its thermal performance to a number of key operational parameters. This assessment is made with a one-dimensional numerical model developed here to adapt the zonal method to calculate heat and mass transport within the enclosure of the solar vortex receiver (SVR) and to incorporate radiative and convective heat transfer between the particle phase, the air phase and the receiver wall together with re-radiative and conductive loss from the receiver. This simplified one-dimensional model allows for the systematic assessment of first order trends of mass and energy balance within the SVR and is used here to advance understanding of the dominant mechanisms controlling its thermal performance. Sensitivity studies of the thermal performance of the SVR reveal that the receiver can be configured to operate as either an air-heater or a particle-heater, depending primarily on the particle mass loading. For the present SVR configuration, the critical value of mass loading, $\dot{m}_p/\dot{m}_{air} \approx 1$ was found to define the boundary, above which the device acts as a particle heater, and below which it acts as an air heater. Furthermore, an assessment of the two-phase flow direction found that a counter-flow (relative to the incident concentrated solar radiation) tends to result in a higher efficiency than a co-flow direction. The first order trends of the sensitivity of thermal performance of the SVR to the particle and air mass flow rates, particle size and receiver length were also assessed, finding that the ratio of receiver thermal input to heat capacity of the two-phase flow has a controlling influence on the thermal efficiency of the SVR, particularly with the front entry configuration. Overall receiver thermal efficiencies of up to 88% were predicted for the SVR operating with high mass flow rates of both particles and air, but it is expected that the thermal efficiency of the device for all operating conditions assessed here would increase with an increase in receiver scale from the laboratory-scale device considered here.

1. Introduction

New technologies are required to achieve operating temperatures up to and above 1000 °C with concentrated solar thermal (CST) energy. This is because solar receivers in current commercially available systems are limited to ~600 °C due to radiative flux limitations arising from the use of indirect irradiation and the temperature limitations of the heat transfer medium (Ho, 2016). Temperatures in the range 700–1000 °C are being sought to enable the use of new advanced power cycles for concentrating solar power (CSP), such as Brayton cycles with recuperation and combined bottoming cycles as well as supercritical-CO_2 cycles (Besarati and Goswami, 2017; Stein and Buck, 2017). Operating temperatures of a similar range and even higher are also required for the application of solar energy into high temperature thermochemical processes via process heat, such as alumina and lime calcination (Davis et al., 2017; Flamant et al., 1980; Steinfeld et al., 1992), the gasification of carbonaceous feedstocks (Lichty et al., 2010; Z'Graggen et al., 2006), metal reduction (Kräupl and Steinfeld, 2001; Lapp et al., 2012) and the production of solar hydrogen (Kodama and Gokon, 2007; Perkins and Weimer, 2009; Sattler et al., 2017; Steinfeld, 2005). Solid particles are a heat transfer medium which, due to their high surface area per unit mass and capacity for direct irradiation, offer the potential to achieve receiver exit temperatures of over 1000 °C together with a low-cost storage medium (Ho, 2016; Ho and Iverson, 2014; Tan and Chen, 2010; Wu et al., 2014). However, little is known of their thermal performance during transient operation over long periods, which requires models of sufficient accuracy to estimate energetic performance with first-order accuracy and numerical simplicity to

* Corresponding author at: School of Mechanical Engineering, The University of Adelaide, SA 5005, Australia.
E-mail address: dominic.davis@adelaide.edu.au (D. Davis).

https://doi.org/10.1016/j.solener.2018.10.086
Received 22 May 2018; Received in revised form 10 October 2018; Accepted 30 October 2018

Nomenclature

A	area [m^2]
c_p	constant pressure specific heat capacity [J/kg K]
D	diameter [m]
d_p	particle diameter [μm]
E_b	blackbody emissive power [W]
F	radiation shape factor
$\Delta\dot{H}$	rate of enthalpy change [W]
h	coefficient of heat transfer [W/m^2 K], specific enthalpy [J/kg]
J	radiosity [W/m^2]
k	thermal conductivity [W/m K]
L	total length of the receiver [m]
m_{1p}	mass of one particle [kg]
$\dot{m}$	mass flow rate [kg/s]
N_p	number of particles
$\dot{N}_p$	number flow rate of particles [1/s]
Nu	Nusselt number
n	number of axial discretisations
$\dot{Q}$	rate of heat transfer [W]
$\dot{Q}_s$	solar radiative power input [W]
$\dot{q}$	heat flux [W/m^2]
$\dot{q}_s$	solar radiative flux input [W/m^2]
r	radial coordinate [mm]
Re	Reynolds number
T	temperature [K]
U	velocity [m/s]
V	volume [m^3]
$\dot{V}$	volumetric flow rate [m^3/s]
z	axial coordinate [mm]
α	receiver cone angle [°], absorptivity
ε	emissivity
ε_{max}	maximum absolute difference between two consecutive iterations
κ	linear radiation extinction coefficient [1/m]
η_{th}	overall thermal efficiency [%]
ρ	density [kg/m^3]
σ	Stefan-Boltzmann constant
τ	residence time [s]
ϕ	particle to air volume fraction
$\chi_{air\text{-}p}$	energy absorption ratio

Subscripts

air	air phase
ap	aperture (fictive surface)
back	the back entry configuration
c	cavity
d-b	the down-beam face of an element (relative to the direction of the concentrated solar radiation input)
end	end wall
fr	front wall
front	the front entry configuration
i	a given element
j	a given element
i − 1	the element up-beam of a given element, *i*
i + 1	the element down-beam of a given element, *i*
in	inlet
measured	from experimental measurements
modelled	from with the present numerical model
nom	nominal
out	outlet
p	particle phase
r	receiver
u-b	the up-beam face of an element (relative to the direction of the concentrated solar radiation input)
w	receiver wall
∞	surroundings

Abbreviations

CFD	computational fluid dynamics
CSP	concentrating solar power
CST	concentrated solar thermal
SVR	solar vortex receiver

allow a model to be solved for half-hour time-steps for multiple years (Saw et al., 2017). The overall objective of the present investigation is therefore to develop a one-dimensional model of a particle receiver with first-order accuracy of energetic performance for potential application in system models within high temperature power and thermochemical process systems.

One class of solar particle receiver technologies that has received significant attention employs direct irradiation to heat particles that are transported by a carrier gas within a vortex flow in a cylindrical cavity, termed the solar vortex receiver (SVR). Vortex-based solar particle receiver-reactors have been used to experimentally demonstrate several solar thermochemical processes (Davis et al., 2017; Hirsch and Steinfeld, 2004b; Steinfeld et al., 1992; Z'Graggen et al., 2006). They have the advantage of highly efficient heat transfer to the particle phase due to direct irradiation, as demonstrated by a high chemical conversion with residence times on the order of seconds (Davis et al., 2017; Z'Graggen et al., 2006). A vortex-based solar particle receiver is one device that enables the heating of particles to temperatures of more than 1000 °C with CST, but can be configured in many alternative ways. A simple one-dimensional model is useful to allow a wide range of configurations to be assessed rapidly within a system during transient operation, which is necessary because transients have a first order impact on performance in solar thermal systems (Kueh et al., 2015). The optimal configuration of a solar thermal particle receiver cannot be determined in isolation from other components but must be calculated together with that of the pneumatic conveying system, thermal storage system and hybridisation system (Nathan et al., 2017a,b), because their thermal performances also vary with turn-down. Hence, determining the transient performance of the SVR within a system of complex components requires a model that is sufficiently simple to avoid excessive computational expense and sufficiently accurate to account for the dominant physical processes within them. However, no first order model of the SVR is presently available. The aim of the present investigation is therefore to meet this need for a first-order model of the SVR.

A large number of solar thermochemical investigations have been undertaken previously using a SVR in which the concentrated solar radiation enters through a transparent quartz window aligned normal to the axis of a cylindrical cavity, while a gas transporting particles is introduced tangentially at the window-end of the cavity and both the particles and gases emerge axially from the rear of the cavity (Davis et al., 2017; Hirsch and Steinfeld, 2004b; Müller et al., 2017; Z'Graggen et al., 2007; Z'Graggen et al., 2006). The residence time of a 5 kW reactor is on the order of seconds and has achieved temperatures over 1000 °C. However, these experimental demonstrations were each conducted with a single geometric configuration, so that no information is available about how the performance may vary with changes to the relative dimensions. In addition, an alternative configuration of the SVR

has recently been investigated with a view to mitigating a key challenge to the original configuration associated with particle deposition on the window. Chinnici et al. (2015) proposed that by introducing the vortex gas-particle flow at the opposite end of the receiver cavity to the aperture and altering the geometry of the cavity (the cone angle and aperture-to-cavity diameter ratio) the propensity for particles to be transported through the aperture, and toward the window, is significantly reduced. The efficacy of the aerodynamic mechanism that facilitates the reduction in transport through the aperture has been demonstrated through validated combination of experiments and computational fluid dynamic (CFD) modelling (Chinnici et al., 2015; Chinnici et al., 2016). However, no previous study of the influence on the thermal performance of the two-phase gas-particle flow direction (front entry or back entry) within the SVR is available in the literature. Since it is expensive and time-consuming to fabricate and experimentally compare the performance of multiple receiver geometries and configurations, simplified models, which enable timely comparison of the thermal performance of many different cases, are required.

Several models of the heat transfer within entrained flow solar particle receiver-reactors have been developed, spanning simple one-dimensional models to more complex three-dimensional CFD models. These are complementary because CFD models are generally too computationally expensive to be used to assess a large number of receiver configurations and operating cases. In contrast, a one-dimensional model of the particle receiver operation can provide powerful insights into the dominant mechanisms influencing the thermal performance, before narrowing down to a limited number of configurations that justify the use of more detailed and computationally-expensive CFD models. Previous examples of first order models include the assessment by van Eyk et al. (2016) of an entrained flow solar reactor for the gasification of coal. They adapted a long furnace model (Kasule et al., 2012) to incorporate high-flux solar radiation in a reactor with a one-dimensional axial flow of gas and coal particles. Such lower dimension models (Kasule et al., 2012; van Eyk et al., 2016) have proven useful for sensitivity studies of a large number of configurations but are not well suited to assess the influence of geometry on heat transfer in a relatively short reactor. In contrast, the zonal model has been used to assess relatively short devices in which radiative heat transfer is important. The method has been used to predict gas and refractory wall temperature profiles in a furnace (Hottel and Cohen, 1958), a rotary kiln (Jenkins and Moles, 1981) and, in a modified form, to investigate radiation exchange associated with the solid particle phase in the furnace of a coal boiler (Cañadas et al., 1990). In each of these cases, radiation is treated as non-directional, as is typical of combustion. Solar concentrators, however, provide highly directional concentrated solar radiation to the receiver-reactor. Therefore, the zonal method of analysis needs to be modified to incorporate high-flux directional solar radiation as the heat input to the enclosure, so that its influence on the two-phase gas-particle flow within the receiver and the receiver's enclosure walls can be assessed. The directionality of concentrated solar radiation can alternatively be modelled with the use of advanced Monte Carlo and finite volume modelling techniques, as has been developed for the steam gasification reaction of carbonaceous particles in the SVR (Z'Graggen and Steinfeld, 2008a,b; Z'Graggen and Steinfeld, 2009). These models have been validated at 5 kW laboratory-scale and have been used to conduct extensive sensitivity analyses of molar extent of reaction and thermal efficiency to key input parameters, such as solar thermal input, feedstock feed rates and particle size. Despite significant modelling efforts characterising the solar steam-gasification of carbonaceous feedstocks in the SVR, there is a need for less computationally-intensive models of the sensible heating of a range of particle sizes in such a vortex-based solar particle receiver, which can be used to assess the influence of receiver geometry on the distribution of temperature and modes of heat transfer, while incorporating the directionality of the concentrated solar radiation input.

To meet these needs, the overall objective of the present paper is to assess the first-order trends of mass and energy balance within the SVR with a one-dimensional heat transfer model of the device. Specifically, this paper aims to assess the trends in thermal performance of the SVR as a function of the particle/gas flow rates, particle loading and size, receiver geometry and flow direction. The SVR can be configured to heat either the particle phase or the gas phase as the primary energy carrier and useful heat can also be recovered from the other phase through a secondary heat exchanger. Therefore the overall thermal efficiency incorporating enthalpy changes of both the particle and air phases between the inlet and the outlet of the receiver are assessed here, together with the partitioning of solar energy absorption between the particle and air phases, and the air and particle temperature rise through the receiver.

2. Methodology

2.1. Model description and assumptions

The one-dimensional heat transfer model presented here adapts the zonal method of Hottel and Cohen (1958) and Hottel and Sarofim

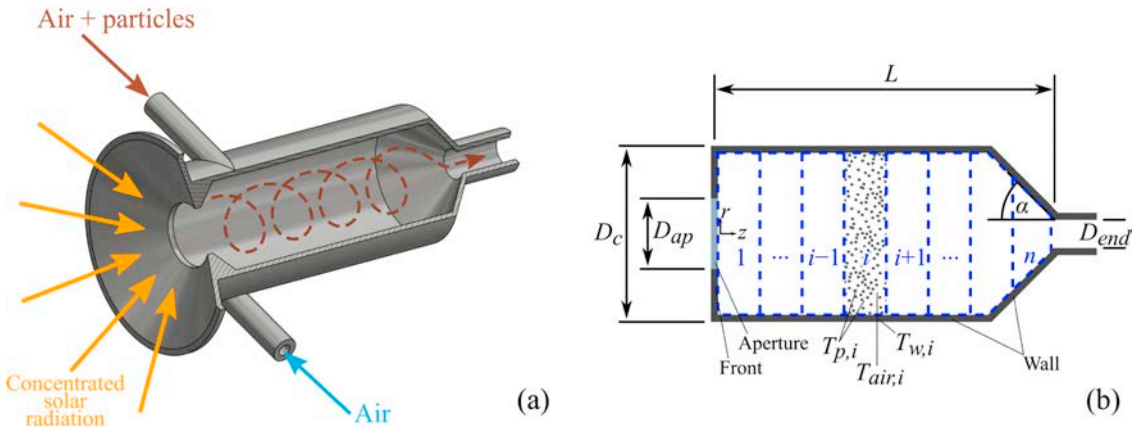

Fig. 1. Schematic diagrams of (a) the solar vortex receiver (SVR) showing concentrated solar radiation entering the receiver through the aperture, together with two tangential inlets for air and particles; and (b) the simplified model, showing the discretisation regime used in the present numerical model. The *n* cylindrical and conical volume elements are enclosed by *n* cylindrical and conical wall surface elements as well as by the additional surfaces of the aperture and the front wall. The temperature of the particle and air phases as well as the wall temperature of a given element, *i*, are also shown.

(1967) for application to the solar vortex receiver (SVR). This method requires that a simple one-dimensional flow pattern and particle distribution within the receiver cavity be known or assumed. The enclosure is then discretised into a number of volume zones (containing gas and particle phases) and surface zones that are small enough to be considered isothermal. A consideration of the energy balance for each of the zones (or elements) results in a set of simultaneous equations that can be solved to determine a one-dimensional distribution of particle, gas and wall temperatures within the receiver.

Fig. 1a presents a simplified schematic representation of the SVR first employed for the solar gasification of carbonaceous feedstocks (Z'Graggen et al., 2006). This shows that concentrated solar radiation enters the cylindrical receiver cavity through a circular aperture. The two-phase vortex flow of particles and air is established with two tangentially-oriented inlets located at the front of the receiver and the vortex flow proceeds to the rear, axially-oriented exit.

Fig. 1b presents the simplified SVR internal geometry and the discretisation regime for the present numerical model, considering only the internal volume of the cylindrical cavity. The receiver internal volume is discretised into n elements along the axial coordinate of the receiver, z, where each element, i, comprises a cylindrical or conical disk of air and particles in a two-phase combination. Each disk element, i, is bounded by a cylindrical or conical wall element. For an element, i, the width of the volume and surface zones is equal to L/n, while their diameter is equal to D_c for those in the cylindrical section of the receiver and $2(L - z)\tan\alpha + D_{end}$ in the conical section of the receiver. Within an element i, the particle phase is of a uniform temperature, $T_{p,i}$, as shown in Fig. 1b. Similarly, the air phase is $T_{air,i}$ and the wall is treated as isothermal at temperature $T_{w,i}$. The additional aperture, front and end surfaces are treated also as isothermal surfaces and included in the energy balance equations. While the receiver pictured in Fig. 1a has two tangential inlets, the one dimensional discretisation of the receiver (Fig. 1b) does not take into account the inlet conditions or distinguish between the two inlets. That is, the mass flowrate of particles and gas into the first discretised element ($i = 1$) models the total mass flow rate from the two tangential inlets of the practical receiver.

To incorporate the influence of the three-dimensional receiver geometry on the one-dimensional axial distribution of radiative heat transfer within the receiver, the present model calculates the radiative shape factors for the internal walls of the SVR as a function of the receiver geometry – D_{ap}, D_c, L, α and D_{end} shown in Fig. 1b. In addition to the n discretised cylindrical or conical wall surface elements, three additional surfaces are required to enclose the receiver cavity: the aperture surface (a disk), the front wall (an annulus surrounding the aperture disk) and the end wall (a disk). The shape factors between all discretised receiver walls, w_i, and the aperture, front and end walls are then calculated assuming diffuse radiation and using the reciprocity relation, to be:

$$F = \begin{bmatrix} F_{w_1-w_1} & F_{w_1-w_2} & \cdots & F_{w_1-ap} & F_{w_1-fr} & F_{w_1-end} \\ F_{w_2-w_1} & F_{w_2-w_2} & \cdots & F_{w_2-ap} & F_{w_2-fr} & F_{w_2-end} \\ \vdots & \vdots & \ddots & \vdots & \vdots & \vdots \\ F_{ap-w_1} & F_{ap-w_2} & \cdots & F_{ap-ap} & F_{ap-fr} & F_{ap-end} \\ F_{fr-w_1} & F_{fr-w_2} & \cdots & F_{fr-ap} & F_{fr-fr} & F_{fr-end} \\ F_{end-w_1} & F_{end-w_2} & \cdots & F_{end-ap} & F_{end-fr} & F_{end-end} \end{bmatrix}, \quad (1)$$

where $\sum_j^n F_{i-j} = 1$ for all i. For $i = w_1, \ldots w_n, fr, end$, the radiation shape factors F_{i-j} were calculated according to analytical equations for the equivalent geometry (Buschman and Pittman, 1961; Feingold, 1978; Hamilton and Morgan, 1952; Leuenberger and Person, 1954; Sparrow and Jonsson, 1963). Details of these calculations are provided in the Supplementary material.

The model is based on the following assumptions:

(1) The gas-particle flow proceeds in one direction only, along paths parallel to the receiver's axial axis (z-axis) with constant mass flow rates (plug flow). The residence time of particles, τ_p, in the receiver is therefore considered to be equal to the nominal air residence time, i.e. $\tau_p = \tau_{nom} = V_r/\dot{V}_{air}$ (where V_r is the total internal volume of the receiver and $\dot{V}_{air}$ is the volumetric flow rate of air corrected for temperature). The number of particles within the receiver at a given instant, N_p, is then calculated as follows:

$$N_p = \dot{N}_p \tau_p = \frac{\dot{m}_p}{m_{1p}} \tau_p, \quad (2)$$

where $\dot{N}_p$ is the number flow rate of particles into the receiver, $\dot{m}_p$ is the mass flow rate of the particle phase and m_{1p} is the mass of a single particle. Since the actual flow within the SVR is swirling, an alternative interpretation of this assumption is that the residence time is controlled by the axial component of the flow, or that the influence of the characteristic recirculation zone (Chinnici et al., 2017) is small. This assumption is expected to be reasonable for configurations with relatively low Swirl number, but the model will under-estimate both the residence time and the number density of particles within the receiver at larger Swirl numbers and will also assume the wrong axial flow direction within sub-volumes (such as along the axis), although the bulk flow direction remains correct. This limitation could be addressed in future versions of the model by adjusting the residence time and number density based on other input parameters, such as geometry and Stokes number. To modify the flow in the axial direction due to the recirculation zone would require a recirculation model to be developed. However, any of these additional improvements would also require additional data that are not yet available, so that they are not incorporated here.

(2) The particles assessed here are limited to $d_p < 100\,\mu m$, which is small enough to be transported in suspension and to follow closely the gas streamlines within the SVR. That is, the characteristic Stokes number of the two-phase flow is less than unity and the particles approach being flow tracers, providing justification to the assumption that $\tau_p = \tau_{nom}$. Such particle sizes are typical of suspension flow devices such as entrained flow gasifiers and flash calciners in the cement and alumina industry for which particles are conveyed pneumatically (Jenkins and Bertrand, 2001; Kasule et al., 2012). It can therefore additionally be assumed that the role of particle deposition onto the walls of the receiver is small. The particles are assumed to be spherical with a monodisperse size distribution for any given case.

(3) Particles are assumed to be uniformly distributed within each discretised volume element. Each volume element has an equal number of particles, such that $N_{p,i} = N_p/n$, where $N_{p,i}$ is the number of particle in a given element, i, and n is the number of volume elements into which the receiver internal volume is discretised. This one-dimensional simplification equates to an assumption that the dominant gradient in energy flux is axial, which is consistent with knowledge that the radiation is absorbed by the particles as it penetrates axially into the device. This could readily be extended in the future to account for radial gradients, but would require additional data that are not yet available. This assumption of a one-dimensional distribution of particles is expected to be reasonable for cases in which the two-phase flow is maintained in one- and two-way coupling regimes (Elghobashi, 1994), which corresponds to a particle to gas mass ratio, $\dot{m}_p/\dot{m}_{air} < 2$ for the present conditions. To make this distinction, the boundaries between the regimes is shown on the figures, where data in the four-way coupling regime is shown in dashed lines to provide insight into likely trends in this regime.

(4) The aperture was modelled as an opaque fictive surface of known radiosity, J_{ap}, that is equal in flux magnitude and direction to the incident concentrated solar radiative flux, following the modelling method of (Tescari et al., 2013). The directional distribution of

radiosity from the fictive aperture surface was weighted according to available experimental data for concentrated solar radiation entering a cylindrical cavity through a circular aperture, based on a 7 lamp solar simulator focussed at the aperture plane of the SVR. That is, for each geometrical receiver configuration assessed in this investigation, $F_{ap\text{-}j}$ was calculated with the use of a Monte Carlo ray tracer, *CUtrace*, which is freely available online at MATLAB Central (Rowe et al., 2015). It is further assumed that no mass transfer occurs through the aperture (no convective heat loss through the aperture) and that any thermal effects of the secondary concentrator are negligible. The method of treating the aperture as a fictive surface is justified by Tescari et al. (2013), who found no significant difference in the predicted temperature distributions of a laboratory-scale solar rotary kiln compared with those from a more computationally-intensive discrete ordinates method of radiation modelling. Note that the difference between the assumption of directional radiation from the fictive aperture surface and diffuse radiation (as with the internal discretised surface elements) is presented in Fig. 5 for the model validation. The assumption of directional radiation provides better validation of the model.

(5) Concentrated solar radiation emitted by the fictive aperture surface is absorbed either by the particles in suspension or by the receiver walls. The linear radiation extinction coefficient κ, is also used to model the rate at which the concentrated solar radiation intensity decreases along the axial coordinate of the receiver due to this absorption by the particle phase and the receiver walls. This is calculated as follows:

$$\kappa = \frac{\pi}{4} d_p^2 \varepsilon_p \frac{N_p}{V_r}, \tag{3}$$

where d_p is the particle size, and ε_p is the emissivity of the particle. The linear radiation extinction coefficient is used due to the one-dimensional discretisation of the receiver volume, so that the difference in solar radiative intensity between two axial locations is equal to the solar radiation absorbed by the particles and wall surface between the two locations, following van Eyk et al. (2016).

(6) Thermal radiation interchange between particles both within a given discretised volume and between volumes is assumed to be small relative to the incident concentrated solar radiation (Haugen and Mitchell, 2015). This is because for the present conditions the two-way coupling regime applies, that is, the SVR operates with particle mass loadings of $\dot{m}_p/\dot{m}_{air} < 2$, corresponding to particle-to-air volumetric loadings of $\phi = \dot{V}_p/\dot{V}_{air} < 2 \times 10^{-4}$, according to $\dot{m}_p/\dot{m}_{air} = (\dot{V}_p/\dot{V}_{air})(\rho_p/\rho_{air})$. Further support for this assumption can be found in the study by Jafarian et al. (2012) who found that convective cooling dominates over radiation heat transfer with a wall for individual particles of $d_p < 100\,\mu m$ within conditions relevant to the SVR. For these reasons and for the purpose of a simplified heat transfer model, inter-particle radiation is neglected in the present model, as was similarly assumed in the development of a one-dimensional model of an entrained-flow solar reactor for the gasification of coal (van Eyk et al., 2016).

(7) Thermal radiation heat transfer between the wall elements was calculated in one dimension using the radiosity method with shape factors calculated for the three-dimensional receiver geometry. The fictive aperture surface is considered as a black body absorber, whose radiosity matches the concentrated solar radiation receiver input. Its incident radiation from all other cavity wall elements is equal to the re-radiation losses of the receiver. The particle phase is assumed not to participate in the thermal radiation heat transfer between the internal walls because the low values of mass loading $\dot{m}_p/\dot{m}_{air} < 2$ (corresponding to volumetric loading, $\dot{V}_p/\dot{V}_{air} < 2 \times 10^{-4}$) are in the two-way coupling regime and because the intensity of thermal radiation from the walls is much lower than that entering through the aperture.

(8) Particle-to-wall radiative heat transfer is limited to within each element. The surface area of this emission is equal to the total surface area of particles within the element and all of this emission is intercepted by the wall surface of the element. This is an over estimate of the rate of radiative heat transfer between the particles and the wall of the element.

(9) Radiation emission and absorption by the particle phase, the receiver wall and the aperture are considered to be equal over all radiation wavelengths. Furthermore, both the particles and receiver walls are treated as grey bodies, for which Kirchhoff's identity holds, i.e. $\varepsilon = \alpha$. Their emissivities and absorptivities are here assumed to be constant and independent of temperature.

(10) The gas phase is transparent, so that it does not participate in radiation interactions.

(11) Each particle has a uniform temperature (i.e. there is no temperature gradient within any particle) as justified by the calculation of the Biot number for the particles directly irradiated by a concentrated source of thermal radiation following previous work (Jafarian et al., 2013; Maag et al., 2009). This calculation was made for the case of largest particle size and greatest radiative intensity of the present investigation.

(12) Although the simple flow field proceeding in one direction only does not consider the inlet conditions of a practical SVR, it is assumed that the SVR operates in a fully-turbulent regime, as was the case for the validation experiments (Davis et al., 2017;

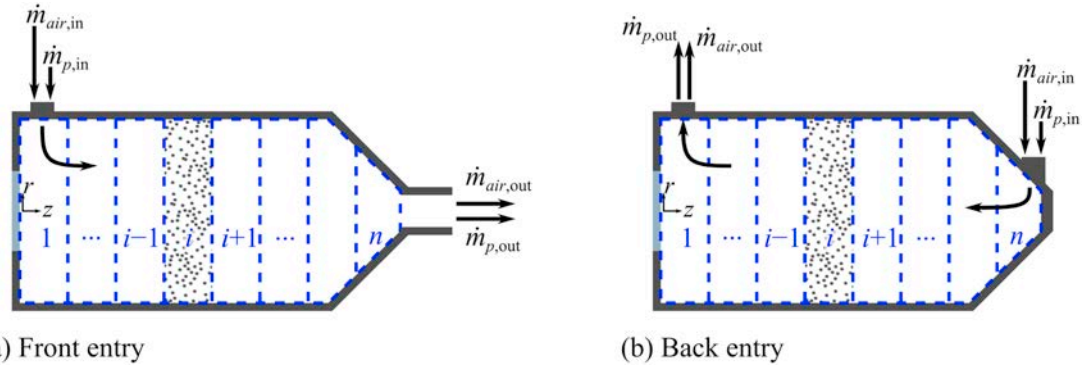

Fig. 2. Schematic diagram of the two one-dimensional flow configurations assessed with the present model, with (a) a front entry, in which the flow proceeds from the front to the rear of the receiver (elements 1 to *n*); and (b) a back entry configuration, in which the flow proceeds from the rear to the front of the receiver (elements *n* to 1).

Z'Graggen et al., 2006). Reynolds number will increase further with scale up.

It should be noted that these assumptions allow for the development of a simplified one-dimensional heat transfer model of the SVR for the identification of first order trends of mass and energy balance. Nevertheless, limitations to these assumptions exist particularly those of uniform distribution of particles and the neglect of inter-particle radiation, for cases of large volumetric loading. For this reason, model results presented for cases of mass loading, $\dot{m}_p/\dot{m}_{air} \geq 2$ (approximately corresponding to volumetric loading $\phi \geq 2 \times 10^{-4}$), are shown with dashed lines, indicating higher degree of uncertainty. The trends presented nevertheless provide a valuable insight into the thermal performance of the SVR.

2.2. Energy conservation equations

The energy conservation equation for the receiver cavity walls is formulated using the radiosity method, in which the net radiant energy absorbed by the wall of an element *i*, is balanced by heat lost to the air through convection and to the surroundings by conduction through the receiver walls. This equation can be written as follows:

$$\dot{Q}_{ap-w,i} + \dot{Q}_{w-w,i} + \dot{Q}_{p-w,i} - \dot{Q}_{w-air,i} - \dot{Q}_{w-\infty,i} = 0. \quad (4)$$

The energy conservation equations for the air and particle phases are formulated by accounting for the enthalpy change of mass transported across an element, *i*, due to various heat transfer mechanisms within the element, *i*. For the particle and air phases respectively, the energy balance can be written as follows:

$$\Delta\dot{H}_{p,i} = \dot{Q}_{ap-p,i} + \dot{Q}_{p-p,i} - \dot{Q}_{p-air,i} - \dot{Q}_{p-w,i}, \quad (5)$$

$$\Delta\dot{H}_{air,i} = \dot{Q}_{p-air,i} + \dot{Q}_{w-air,i}. \quad (6)$$

Fig. 2a presents the flow configuration for the case in which the two-phase air-particle flow proceeds from the front to the rear of the receiver (front entry). For this case, the enthalpy change across element *i* (with datum state, $h = 0$, at ambient temperature, T_∞) is quantified for the particle phase as follows:

$$\Delta\dot{H}_{p,i} = \dot{H}_{p,i} - \dot{H}_{p,i-1} = \dot{m}_p c_{p,p,i}(T_{p,i} - T_\infty) - \dot{m}_p c_{p,p,i-1}(T_{p,i-1} - T_\infty), \quad (7)$$

and for the air phase as follows:

$$\Delta\dot{H}_{air,i} = \dot{H}_{air,i} - \dot{H}_{air,i-1} = \dot{m}_{air} c_{p,air,i}(T_{air,i} - T_\infty) - \dot{m}_{air} c_{p,air,i-1}(T_{air,i-1} - T_\infty). \quad (8)$$

Fig. 2b presents the alternative case in which the two-phase air-particle flow proceeds from the rear to the front of the receiver (back entry). The enthalpy change across element *i* in this case is the difference in enthalpies from $i + 1$ to *i*.

The specific formulation of the heat transfer terms in Eqs. (4), (5) and (6) can be explained as follows. The equation

$$\dot{Q}_{ap-w,i} = A_{ap} F_{ap-w_i} J_{ap} e^{-\kappa_l z_l} \quad (9)$$

accounts for the solar radiative power emitted from the fictive aperture surface (which in reality enters through the aperture from the optical concentrator) that reaches the wall surface of element *i*. The imposed radiosity of the aperture surface, J_{ap}, is equivalent in flux magnitude and direction to concentrated solar radiation, such that $\dot{Q}_s = A_{ap} J_{ap}$ where, $\dot{Q}_s$ is the input solar energy to be modelled and A_{ap} is the receiver aperture area. The shape factor, F_{ap-w_i}, incorporates the directivity of the radiosity from the aperture along the one-dimensional discretisation of surface and volume elements (following assumption 4), while the exponential term accounts for the reduction in solar radiation intensity due to absorption up-beam of element *i* along the one-dimensional discretisation of the receiver. The radial component of the radiation path length in the exponential term of equation (9) was considered in the development of the model, however, it was found to have negligible impact on the temperature distributions calculated through the receiver, and therefore negligible impact on the trends presented here. To maintain the one-dimensionality of the present heat transfer model, the radial component is not included here.

The equation

$$\dot{Q}_{w-w,i} = \left[\sum_{j \neq i,ap}^{n} A_{w_i} F_{i-j} J_j - A_{w_i} J_i (1 - F_{i-i}) \right] \quad (10)$$

accounts for the net thermal radiation exchange between all wall elements, *j*, and the wall surface of element *i*, including the wall element itself and the end and front surfaces of the cavity, but not including the aperture radiosity (which is defined in Eq. (9)). Following assumption 7 the re-radiation losses of the receiver are calculated as $\dot{Q}_{w-ap} = \sum_i^n A_{w_i} F_{w_i-ap} J_i$.

The equation

$$\dot{Q}_{p-w,i} = N_{p,i} \pi d_p^2 h_{p-w,i} (T_{p,i} - T_{w,i}) \quad (11)$$

accounts for the thermal radiation interaction between the particles in element *i* and the wall surface of element *i*, following assumption 8, where the radiative heat transfer coefficient is defined as $h_{p-w,i} = \sigma \varepsilon_p (T_{p,i}^2 + T_{w,i}^2)(T_{p,i} + T_{w,i})$.

The equation

$$\dot{Q}_{w-air,i} = h_{w-air} A_{w,i} (T_{w,i} - T_{air,i}) \quad (12)$$

describes the heat lost from the cavity walls by forced convection to the vortex flow of air, where the convective heat transfer coefficient is calculated using the heat transfer correlation for cyclones: $Nu_{D_{in}} = 0.042 Re_{Din}^{0.8}$ (Szekely and Carr, 1966). Such a correlation was similarly used by Hirsch and Steinfeld (2004a) in their radiative transfer model of a vortex flow of methane in a cylindrical cavity and applies for vortex flow in the fully turbulent regime. Although the receiver inlet conditions are not directly considered in the model, the dimensions of the inlet are accounted for through the Nusselt and Reynolds numbers in the heat transfer correlations. These are calculated with an effective diameter, D_{in}, that gives an inlet velocity, $U_{in} = 20$ m/s, from each of two circular jets according to the explicit relationship: $D_{in} = [(2/\pi) \times (\dot{V}_{air,in}/U_{in})]^{1/2}$.

The equation

$$\dot{Q}_{w-\infty,i} = h_{w-\infty} A_{w,i} (T_{wi} - T_\infty) \quad (13)$$

accounts for the heat lost from the cavity walls by conduction through the wall to the surroundings. The overall heat transfer coefficient for heat lost to the surroundings is assumed to be uniform along the receiver, $h_{w-\infty} = 20\ \mathrm{W/m^2 K}$. While this is reasonable for the small-scale laboratory receiver chosen for validation, the conduction heat losses can be minimised by sufficient insulation and by upscaling toward commercial devices. Furthermore, conductive heat losses will not be uniform over the receiver, as surface sections near the focal plane of the concentrated solar radiation such as a secondary concentrator may require active cooling. It is expected that lower values of $h_{w-\infty}$ could be achieved with larger scale of SVR, resulting in relatively higher overall efficiency of the device. The sensitivity of thermal performance to the value of $h_{w-\infty}$ is provided in the Supplementary material.

The equation

$$\dot{Q}_{ap-p,i} = A_{ap} F_{ap-i_{u-b}} J_{ap} e^{-\kappa_l z_{iu-b}} - A_{ap} F_{ap-i_{d-b}} J_{ap} e^{-\kappa_l z_{id-b}} - A_{ap} F_{ap-w_i} J_{ap} e^{-\kappa_l z_l} \quad (14)$$

describes the amount of solar radiation absorbed by the particles in element, *i*. This is equal to the amount of radiation entering the up-beam face of the element, i_{u-b}, less the radiation absorbed by the wall of the element *i* and the radiation exiting the down-beam face of the element, i_{d-b}, as shown in Fig. 3. Radiation intensity from the aperture decreases along the axial direction of the receiver at a rate determined

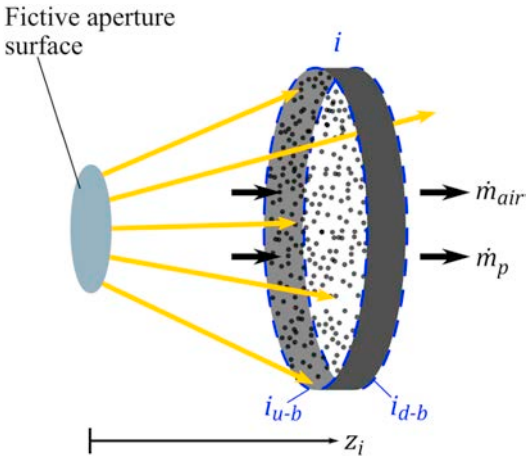

Fig. 3. Schematic representation of concentrated solar radiation emitted from the fictive aperture surface and either absorbed by the particles or the wall of a given element, *i*, or passing through to down-beam elements. Shown are the boundaries for the up-beam ($i_{u\text{-}b}$) and down-beam ($i_{d\text{-}b}$) faces of element *i*.

by the extinction coefficient, κ, which is a function of the number of particles in the elements up-beam of a given element and the total volume of the elements up-beam of a given element, *i*. Following the assumption that each element has an equal number of particles, $N_{p,i} = N_p/n$, the radiation intensity at any axial location, z_i, in the discretised receiver can be determined. This is used in Eqs. (9) and (14) to determine the rate of solar energy absorption by the receiver wall and the particle phase, and the spatial distribution of this absorption.

The equation

$$\dot{Q}_{p-air,i} = N_{p,i}\pi d_p^2 h_{p-air,i}(T_{p,i} - T_{air,i}) \tag{15}$$

accounts for the heat transferred to the air phase in each element by convection from the particle phase. It is assumed that convection heat transfer between particles and air occurs as forced convection over a sphere, where $h_{p\text{-}air,i} = (Nu \times k_{air,i})/d_p$, and $Nu = 2$ according to the empirical relation for no-slip velocity between the particle and the air (Jafarian et al., 2013). The area, over which the convective heat transfer occurs is equal to the sum of the particle surface area of the total number of particles in the element, *i*.

It should be noted that the heat transfer term for inter-particle radiation, $\dot{Q}_{p\text{-}p,i}$ in Eq. (5), is ignored here, following assumption 6.

2.3. Particle and air properties

The particles assessed in the present investigation are assumed to have similar properties to CARBO-HSP, a high temperature ceramic material that has been used previously in investigations of solar particle receivers (Siegel et al., 2014; Siegel et al., 2015). The particle density and emissivity, $\rho_p = 2000\,kg/m^3$ and $\varepsilon_p = 0.93$, are based on those of CARBO-HSP (Siegel et al., 2014). The temperature-dependent relation for the specific heat capacity, $c_{p,p}$, used here is based on that of aluminium oxide due to the wider range of temperatures for which $c_{p,p}$ data are available (Chase et al., 1998). These values of $c_{p,p}$ are nevertheless close to those of CARBO-HSP for the data that are available (Ho et al., 2017; Siegel et al., 2015). Following the assumption that the particle sizes investigated here are small enough to closely follow gas streamlines and thus $\tau_p = \tau_{nom}$, the particle sizes under consideration are limited to under 100 µm (Z'Graggen and Steinfeld, 2008a). For the present study, air was used as the transport gas conveying particles in suspension through the receiver. All thermophysical properties of the air phase and their temperature dependencies were provided by Hilsenrath (1955).

2.4. Solution technique

Fig. 4 presents a flow chart describing the solution algorithm used in the present numerical model to attain a steady-state solution to a given set of input parameters. The energy conservation equations (3), (4) and (5) were rearranged to obtain explicit equations for J_i, $T_{p,i}$ and $T_{air,i}$, for all discretised elements, $i = 1\ldots n$ (as well as for J_{ap}, J_{fr}, J_{end}). The resulting equations were then solved iteratively for each element and all cavity wall surfaces using a Gauss-Seidel technique with the use of MATLAB. With each iteration new values for $T_{p,i}$ and $T_{air,i}$ were calculated as well as new $T_{w,i}$ from J_i according to:

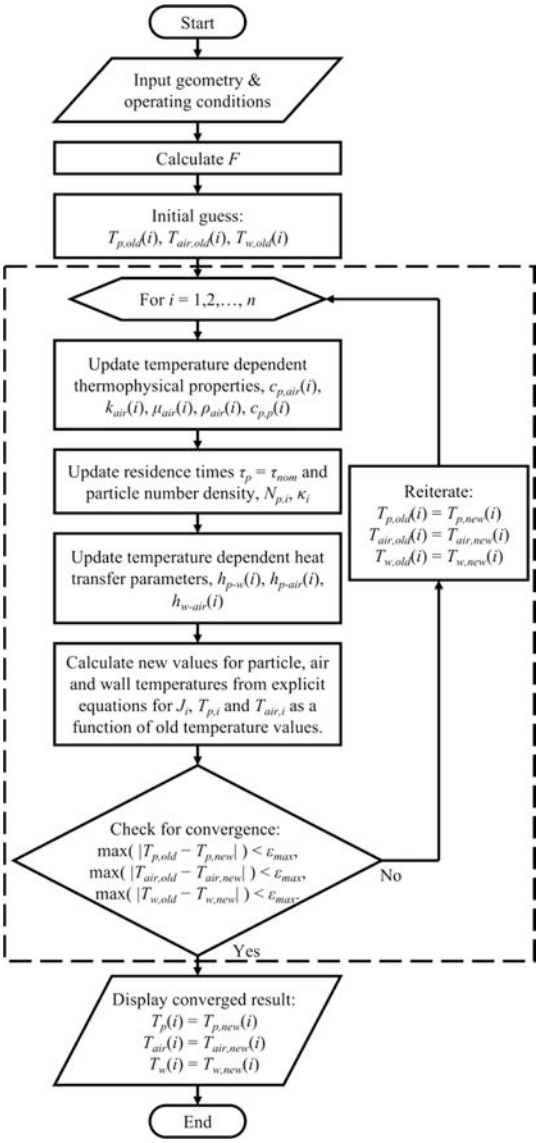

Fig. 4. Solution algorithm flow chart for the present numerical heat transfer model.

$$E_{b_i} = J_i + \frac{1-\varepsilon_w}{\varepsilon_w A_{w,i}}(\dot{Q}_{p-w,i} - \dot{Q}_{w-air,i} - \dot{Q}_{w-\infty,i}), \tag{16}$$

$$T_{w,i} = \sqrt[4]{\frac{E_{b_i}}{\sigma}}. \tag{17}$$

To ensure adequate convergence, iterations were terminated when the maximum absolute difference between two consecutive temperature values, ε_{max}, was $< 10^{-6}$. It was found that the solution of the energy balance equations and resulting temperature distributions was independent of the number of axial elements for $n = 500$ discretisations. This was number was used for each case assessed here.

2.5. Performance parameters

The thermal performance indicators of the SVR are the overall thermal efficiency, η_{th}, the energy absorption ratio, $\chi_{air\text{-}p}$, and the particle and air phase outlet temperatures, $T_{p,out}$ and $T_{air,out}$. These performance parameters are defined as follows:

- The overall thermal efficiency of the receiver accounts for the heat absorbed by both the particle and the air phase, which are both considered to be useful. The efficiency of downstream components of the system would need to be incorporated in a system model, which lies outside the scope of the present paper. Hence the efficiency of the receiver only is defined as follows:

$$\eta_{th} = \frac{\Delta\dot{H}_p + \Delta\dot{H}_{air}}{\dot{Q}_s} = \frac{\dot{m}_p \int c_{p,p} dT + \dot{m}_{air} \int c_{p,air} dT}{\dot{Q}_s}. \tag{18}$$

- The energy absorption ratio is the ratio of heat absorbed in the air phase through the receiver to the heat absorbed by the particle phase, defined as:

$$\chi_{air-p} = \frac{\Delta\dot{H}_{air}}{\Delta\dot{H}_p}. \tag{19}$$

- The particle and air outlet temperatures are defined as the steady state particle and air phase temperatures resulting from the steady-state solution in the last discretised receiver element ($i = n$), which is:

$$T_{p,out} = T_{p,n}, \tag{20}$$

$$T_{air,out} = T_{air,n}. \tag{21}$$

Note that for the case of the back entry flow direction (Fig. 2b) the outlet temperatures are the steady state solution temperature in the first receiver element ($i = 1$).

3. Model validation and reference case

The accuracy of the model was validated by comparison with experimental measurements for 16 separate cases of the solar sensible heating of air in the solar vortex reactor (SVR). Table 1 lists the geometric and operational conditions of the experimental measurements, which were used as the input parameters to the present heat transfer model. The overall conduction heat loss coefficient for the SVR used in the present validation cases, $h_{w,\infty}$, was previously reported to be variable along the receiver axial direction (Z'Graggen, 2008). Table 1 also presents the reference case geometric and operational conditions for the following sensitivity study, together with the range over which these values were varied from those of the reference case.

The model results for the validation cases are compared with temperature measurements taken in 8 locations: two air measurements with Al_2O_3-shielded thermocouples 20 mm inside (towards the central axis) from the inner wall of the SVR at axial locations $z = 52$ mm and 162 mm, and 6 wall measurements at axial locations $z = 50$ mm, 115 mm (with three angular locations) and 190 mm (with two angular locations). For the comparison, the wall temperature measurement at each axial location, z, was calculated as the average of all wall thermocouple readings at that axial location and corrected for the temperature gradient through the Inconel wall, such that the measurements represented internal wall temperatures.

Table 1
Geometric and operational input parameters to the present model for the reference 16 validation cases and the sensitivity study reference case together with the variation in input parameters for the following sensitivity study.

Input parameter	Validation case values	Reference case value	Sensitivity study variation
Geometric			
D_{ap} [m]	0.050	0.050	–
D_{ap}/D_c [–]	0.516	0.516	–
L/D_c [–]	2.547	2.55	1.00–4.00
α [°]	45	45	–
Operational			
Flow direction	Front entry	Front entry	Front/back entry
$\dot{q}_s$ [kW/m^2]	1086–2151	2000	–
$\dot{m}_{air}$ [kg/s]	$1.95–4.32 \times 10^{-4}$	4.00×10^{-4}	$1.41–11.31 \times 10^{-4}$
$\dot{m}_p/\dot{m}_{air}$ [–]	–	1	0.354–1.414 (and 2–5.657)
d_p [μm]	–	40	10–80
T_{in} [K]	290	300	–
$h_{w,\infty}$ [W/m^{2}K]	12–142	20	–
ε_w [–]	0.8	0.8	–

Fig. 5 compares measurements taken with the SVR for one experimental validation case and the prediction of the present numerical model with the two different assumptions of directional and diffuse radiation emitted by the fictive aperture surface (as outlined in assumption 4 in Section 2.1). It can be seen that the model with directional radiation assumption predicts a wall temperature over the range 459–1408 K with maximum temperature at $z = 97$ mm. It can also be seen that the model overestimates the measured wall temperature at measurement locations, $z = 115$ mm, and 190 mm, however the hottest part of the predicted wall temperature distribution is located near the middle of the receiver, as

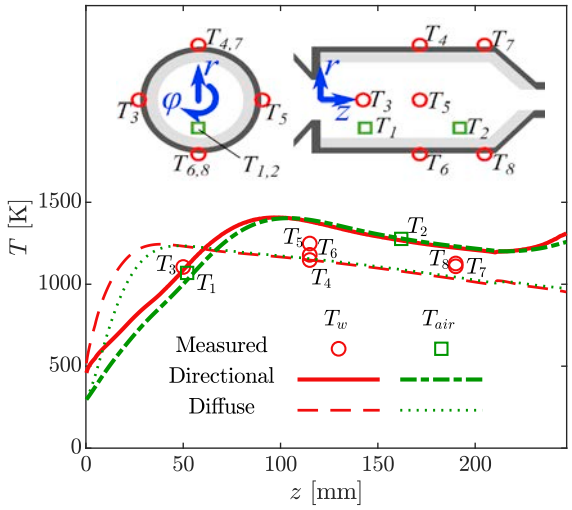

Fig. 5. A typical comparison between the measurements taken with the SVR and the numerical model calculated with the assumption of either directional or diffuse radiation from the fictive aperture surface. For this case, the solar radiative power input, $\dot{Q}_s = 2315.8$ kW, and mass flow rate of air, $\dot{m}_{air} = 2.59 \times 10^{-4}$ kg/s. Errors from all cases are shown in Table 2.

Table 2
Model comparison with experimental measurements from the 16 validation cases of the solar sensible heating of air in the SVR.

Measurement	Mean absolute relative error, $\lvert(T_{modelled} - T_{measured})\rvert/T_{measured}$	Minimum absolute relative error	Maximum absolute relative error	Standard deviation of absolute relative errors
$T_{w,z=50mm}$	9.0%	0.4%	16.5%	4.6%
$T_{w,z=115mm}$	25.9%	14.8%	48.2%	8.9%
$T_{w,z=190mm}$	17.0%	6.6%	27.4%	6.7%
$T_{air,z=52mm}$	17.0%	2.0%	37.2%	10.9%
$T_{air,z=162mm}$	5.4%	0.2%	14.1	4.5%

was similarly measured with the wall thermocouple measurements. Good agreement can also be seen between air temperature measurements at measurement locations, $z = 52$ mm, and 162 mm and the predicted temperature profile of air in the receiver with the directional radiation assumption. In this validation case (and each other validation case) the rear air thermocouple measurement was higher than the front measurement, which provides justification for the use of the directional radiation assumption. On the other hand, it can be seen for the diffuse radiation assumption that the model predicts the air to be of lower temperature at the rear measurement location compared to the front. Similarly, the hottest part of the wall temperature distribution is predicted to occur at the front of the receiver, which is not borne out in the temperature measurements made for each validation case.

A summary of the mean absolute relative error in the present model compared to 16 cases of experimental measurement of the solar sensible heating of air in the SVR is listed in Table 2. It can be seen that the standard deviation of the absolute relative errors between the model and experimental measurement varies over the range 4.5% and 10.9% for the data that are available. This is deemed to be sufficient for the present purposes. It should be noted that the mean errors presented in Table 2 are lower than those resulting from the model with the assumption of diffuse radiation from the aperture. No experimental measurements of particle temperatures within the SVR are available for the present validation.

4. Results & discussion

4.1. Reference case configuration performance

Fig. 6 presents the calculated dependence of the thermal performance of the SVR on the mass flow rate of air for a series of values of particle mass loading, as obtained from the present numerical model. Here, the reference case geometry is assessed ($D_{ap} = 0.050$ m, $D_{ap}/D_c = 0.516$, $L/D_c = 2.55$, $\alpha = 45^{\circ}$) with front entry flow direction and a constant solar thermal input $\dot{q}_s = 2000$ kW/m^2 ($\dot{Q}_s = 3.927$ kW), particle size $d_p = 40$ μm, and inlet temperature $T_{in} = 300$ K. Fig. 6a presents the dependence of η_{th} on $\dot{m}_{air}$ for nine different values of particle mass loading, $\dot{m}_p/\dot{m}_{air}$. For each value of $\dot{m}_{air}$ assessed here in the range 1.414–11.31 × 10^{-4} kg/s, $\dot{m}_p$ is varied to assess the particle mass loading, $\dot{m}_p/\dot{m}_{air}$, in the range 0.354–1.414 (together with $\dot{m}_p/\dot{m}_{air} = 2.000$–5.657 presented with dashed lines to represent a higher level of uncertainty as discussed in assumption 3 in Section 2.1). Lines of constant thermal input to total heat capacity of the two-phase flow, $\dot{Q}_s/(\dot{m}_p c_{p,p} + \dot{m}_{air} c_{p,air})$, are also plotted on Fig. 6a. It can be seen that a decrease in this ratio, $\dot{Q}_s/(\dot{m}_p c_{p,p} + \dot{m}_{air} c_{p,air})$, has the effect of increasing η_{th}, which is consistent with expectation because increasing mass flow rates at a constant energy input will decrease the temperature rise of the two-phase flow by an energy balance. This in turn results in lower thermal losses and a higher efficiency. Furthermore, for a given $\dot{Q}_s/(\dot{m}_p c_{p,p} + \dot{m}_{air} c_{p,air})$, there is a negligible change in η_{th}, for the range of mass loading values considered here. This indicates that, although the particle and air phases undergo heating by different mechanisms at different rates, heat transfer to and between the particle and air phases is fast enough for the performance of the SVR to be most strongly correlated with the total heat capacity of the particle and air throughput rather than the relative mass of each stream. It can also be seen that η_{th} increases both with $\dot{m}_p/\dot{m}_{air}$ for all values of $\dot{m}_{air}$ and with $\dot{m}_{air}$ for all values of $\dot{m}_p/\dot{m}_{air}$. This is because in both cases the input heat is absorbed by a greater mass flow rate of either particles or air, resulting in lower temperatures through the receiver and, in turn, lower thermal losses. It should also be noted that the modest values of thermal efficiency reported here are consistent with the small thermal scale of

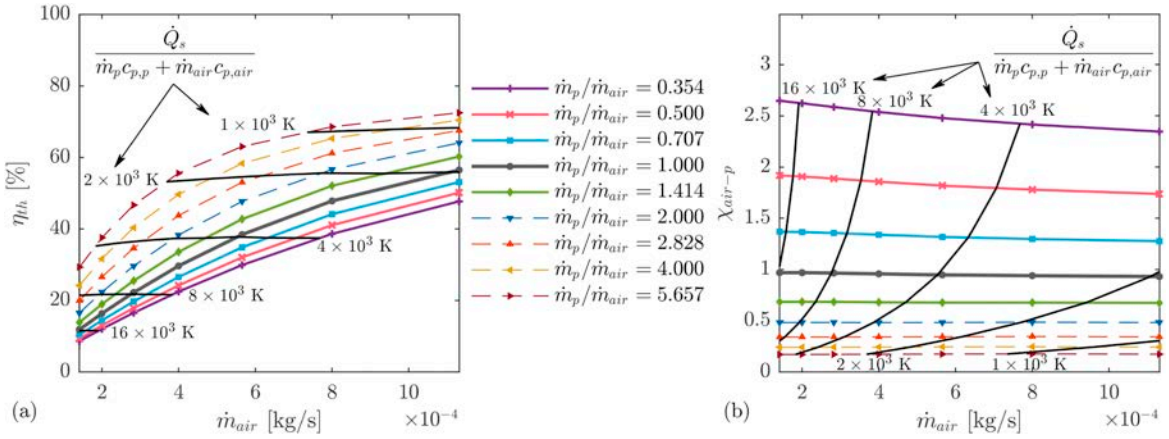

Fig. 6. Assessment of the operation of the SVR with reference case geometry ($D_{ap} = 0.050$ m, $D_{ap}/D_c = 0.516$, $L/D_c = 2.55$, $\alpha = 45^{\circ}$), and for a constant solar thermal input, $\dot{q}_s = 2000$ kW/m^2 ($\dot{Q}_s = 3.927$ kW), $d_p = 40$ μm, $T_{in} = 300$ K, for varying mass flow rates of the particle and air phases. Presented are (a) the receiver thermal efficiency, η_{th}, with lines of constant ratio of thermal input to total heat capacity of the two-phase flow, $\dot{Q}_s/(\dot{m}_p c_{p,p} + \dot{m}_{air} c_{p,air})$; and (b) the energy absorption ratio, $\chi_{air\text{-}p}$, also with lines of constant ratio of thermal input to total heat capacity of the two-phase flow; as a function of mass flow rate of air, $\dot{m}_{air}$, for nine different values of mass loading, $\dot{m}_p/\dot{m}_{air}$. The trends for $\dot{m}_p/\dot{m}_{air} \geq 2$, are presented with dashed lines due to higher levels of uncertainty as noted in assumption 3.

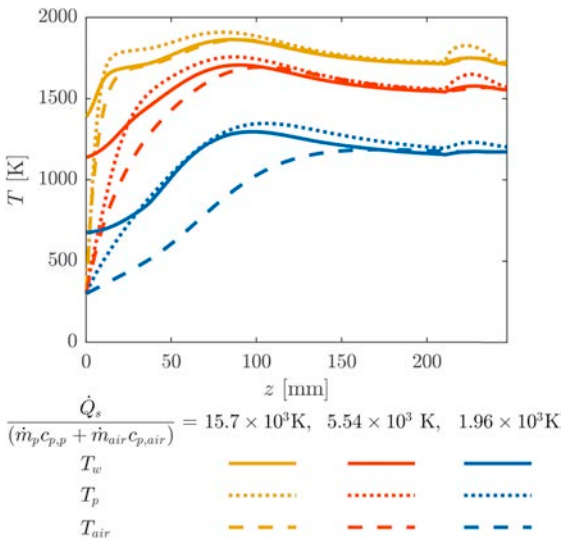

Fig. 7. Calculated axial temperature distributions of the receiver wall, T_w, the particle phase, T_p, and the air phase, T_{air}, for a constant solar thermal input, $\dot{q}_s = 2000$ kW/m^2 ($\dot{Q}_s = 3.927$ kW), a mass loading $\dot{m}_p/\dot{m}_{air} = 1$, and three different ratios of thermal input to total heat capacity of the two-phase flow, $\dot{Q}_s/(\dot{m}_p c_{p,p} + \dot{m}_{air} c_{p,air})$. Geometry and operational conditions of the reference case were used: front entry configuration with $D_{ap} = 0.050$ m, $D_{ap}/D_c = 0.516$, $L/D_c = 2.55$, $\alpha = 45°$, $d_p = 40$ μm, $T_{in} = 300$ K. These distributions are generated from the solution of the energy balance equations for each of the 500 discretised elements along the receiver's axial coordinate, z.

the experiment (Davis et al., 2017; Z'Graggen et al., 2006) and that an increase in this efficiency is expected with an increase in thermal scale.

Fig. 6b presents the dependence of $\chi_{air\text{-}p}$ on $\dot{m}_{air}$ for nine different values of $\dot{m}_p/\dot{m}_{air}$. Lines of constant thermal input to total heat capacity of the two-phase flow, $\dot{Q}_s/(\dot{m}_p c_{p,p} + \dot{m}_{air} c_{p,air})$, are also plotted. It can be seen that the dominant variable influencing $\chi_{air\text{-}p}$ is the particle mass loading, with the fraction of absorbed solar energy that is partitioned with the particle phase increasing with $\dot{m}_p/\dot{m}_{air}$ for constant $\dot{Q}_s/(\dot{m}_p c_{p,p} + \dot{m}_{air} c_{p,air})$. It is significant that for a mass loading of $\dot{m}_p/\dot{m}_{air} = 1$, $\chi_{air\text{-}p}$ is approximately equal to 1 for the cases considered here. This means that the incident solar energy is transferred in approximately equal proportions to the two phases. That is, for $\dot{m}_p/\dot{m}_{air} \leq 1$, the receiver acts as an air heater, while for $\dot{m}_p/\dot{m}_{air} > 1$, it acts as a particle heater. In addition, to achieve efficient operation, the recovery of energy from both streams needs to be considered.

Further insight into the trends presented above can be gained by assessing the temperature distributions within the SVR for certain cases. Fig. 7 presents the calculated axial temperature distributions of the receiver wall, T_w, the particle phase, T_p, and the air phase, T_{air}, for a constant solar thermal input, $\dot{q}_s = 2000$ kW/m^2 ($\dot{Q}_s = 3.927$ kW), a mass loading $\dot{m}_p/\dot{m}_{air} = 1$, and three different ratios of thermal input to total heat capacity of the two-phase flow, $\dot{Q}_s/(\dot{m}_p c_{p,p} + \dot{m}_{air} c_{p,air})$. These three values of $\dot{Q}_s/(\dot{m}_p c_{p,p} + \dot{m}_{air} c_{p,air}) = 15.7$, 5.54 and 1.96×10^3 K, correspond to particle and air mass flow rates of $\dot{m}_p = \dot{m}_{air} = 1.414$, 4.000 and 11.31×10^{-4} kg/s, respectively. It can be seen that the temperatures within the receiver decrease at each axial location with a decrease in $\dot{Q}_s/(\dot{m}_p c_{p,p} + \dot{m}_{air} c_{p,air})$, consistent with the trend presented in Fig. 6a of increasing η_{th} with a reduction in temperature. The model predicts nominal residence time for these cases of $\tau_{nom} = 2.42$, 1.00 and 0.55 s, respectively (calculated as $\tau_{nom} = V_r/\dot{V}_{air}$, where $\dot{V}_{air}$ is evaluated at mean air phase temperature). The reduction in τ_{nom} with an increase in $\dot{m}_{air}$ corresponds to a decrease in the temperatures of the particles, air and walls. It can be seen for the highest case of $\dot{Q}_s/(\dot{m}_p c_{p,p} + \dot{m}_{air} c_{p,air})$ both the particle and air phases undergo the majority of their temperature rise within the front 25 mm of the receiver. The two phases reach maximum temperatures of $T_p = 1909$ K and $T_{air} = 1862$ K at axial coordinate $z = 81$ mm and 89 mm, respectively, and then cool with further distance to reach $T_{p,out} = 1714$ K and $T_{air,out} = 1725$ K. The cooling is attributed to heat loss through the walls. In contrast, the rate of heating is lower for the cases of lower $\dot{Q}_s/(\dot{m}_p c_{p,p} + \dot{m}_{air} c_{p,air})$, so that the peak temperatures occur further toward the rear of the receiver. It is also evident that for each case, the particle phase is heated at a faster rate than the air phase in the front sections of the receiver and also reaches a higher peak temperature. This indicates that heat is absorbed by the particle phase and then transferred to the air phase. However, in the rear section of the receiver the particle and air phases approach equilibrium, tending towards the same temperature. The overall thermal efficiency for the conditions presented in Fig. 7 with $\dot{Q}_s/(\dot{m}_p c_{p,p} + \dot{m}_{air} c_{p,air}) = 15.7$, 5.54 and 1.96×10^3 K are $\eta_{th} = 11.9\%$, 29.6% and 56.5%, respectively. This trend is consistent with that of the wall temperature. A lower wall temperature reduces both the re-radiation losses from the wall through the aperture and the rate of conduction heat loss through the receiver wall. It should be noted, that the small rise in temperature at $z > 210$ mm for each of the temperature distributions is caused by the change in shape of the receiver. The conical section receives a larger proportion of radiation from the aperture than the adjacent cylindrical section due to the directional nature of the radiation and the comparatively larger radiative shape factors. In addition, the calculated particle number density increases in the conical section due to the smaller cross-sectional area. This results in a relatively greater proportion of solar radiation absorption in the conical section, leading to a higher particle temperature.

4.2. Influence of flow direction

Fig. 8a presents the calculated axial distributions of the temperatures of the receiver wall, the particle phase and the air phase for the front entry and back entry flow directions (shown in Fig. 2) with the reference conditions (Table 1). For the front entry flow direction, the two-phase flow enters at $z = 0$ mm and exits at $z = 247$ mm; and vice versa for the back entry flow direction. It can be seen that, for the front entry flow direction, the particle phase undergoes rapid heating to a maximum temperature, $T_p = 1757$ K at $z = 87$ mm, which then decreases slightly to an exit value of $T_{p,out} = 1571$ K. The air phase undergoes less rapid heating than the particle phase to reach a maximum temperature, $T_{air} = 1694$ K at $z = 104$ mm, which then also decreases slightly to an exit value of $T_{air,out} = 1566$ K. The difference in temperature between the air and particle phases in the front half of the chamber, $z = 0$–140 mm, is due to the greater rate of radiative heating to the particle phase, than that of cooling by convection to the air phase. However, for $z > 140$ mm, the temperatures of both phases approach that of the wall, indicating low rates of heat transfer due to near equilibrium.

It can be also seen from Fig. 8a that, in contrast to the front entry case, for the back entry flow direction, the particle and air phases are heated at similar rates from $z = 247$–210 m. The particle phase reaches a maximum temperature, $T_p = 1749$ K at $z = 61$ mm and exits with $T_{p,out} = 1717$ K, while the air phase reaches a maximum temperature, $T_{air} = 1664$ K at $z = 61$ mm and exits with $T_{air,out} = 1588$ K. While the peak temperatures of the respective phases are similar for the two configurations, the exit temperatures are higher for the back entry than the front entry. In addition, the two phases are not in equilibrium at the exit for the rear entry case, while they are for the front entry case. The η_{th} for the front and back entry flow configurations are 29.6% and 31.9%, respectively. This increase in efficiency for the back entry flow configuration can be attributed to the higher particle exit temperature because the particle phase undergoes greater heating in the front sections of the receiver than the air phase, and thus has higher temperature at the exit. It should be noted that while the back entry flow case may

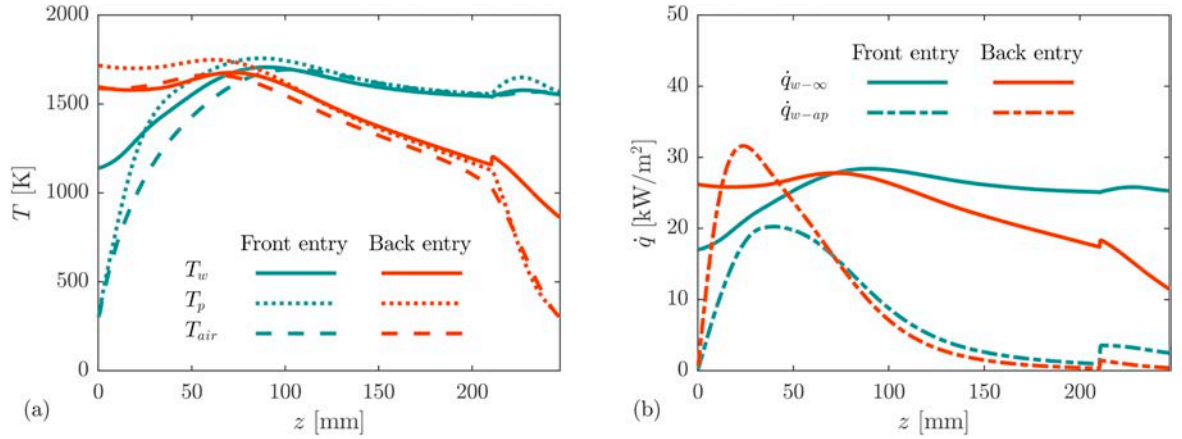

Fig. 8. Calculated axial distributions of (a) the temperatures of the receiver wall, T_w, the particle phase, T_p, and the air phase, T_{air}; and (b) the thermal losses via conduction through the wall, $\dot{q}_{w-\infty}$, and re-radiation through the aperture, $\dot{q}_{w-ap}$; for the front entry and back entry flow configurations with reference case geometry and operational conditions: $D_{ap} = 0.050$ m, $D_{ap}/D_c = 0.516$, $L/D_c = 2.55$, $\alpha = 45^\circ$, $\dot{q}_s = 2000$ kW/m^2 ($\dot{Q}_s = 3.927$ kW), $\dot{m}_p/\dot{m}_{air} = 1$, $\dot{m}_p = \dot{m}_{air} = 4.000 \times 10^{-4}$ kg/s, $d_p = 40$ μm, $T_{in} = 300$ K.

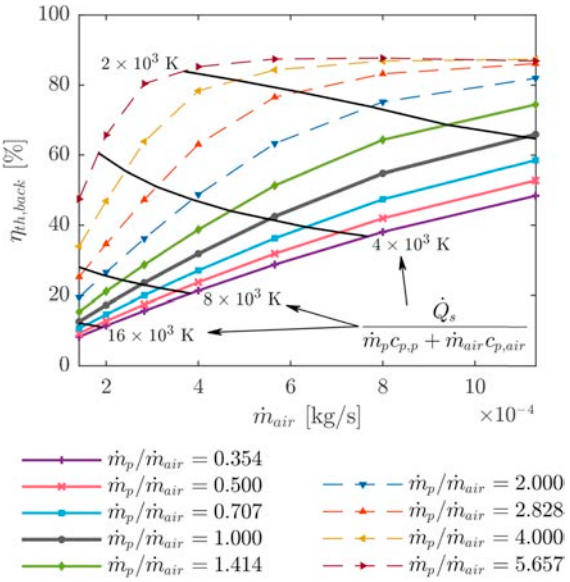

Fig. 9. The thermal efficiency of the SVR with back entry flow configuration, $\eta_{th,back}$, with lines of constant ratio of thermal input to total heat capacity of the two-phase flow, $\dot{Q}_s/(\dot{m}_p c_{p,p} + \dot{m}_{air} c_{p,air})$, as a function of mass flow rate of air, $\dot{m}_{air}$, for nine different values of mass loading, $\dot{m}_p/\dot{m}_{air}$. Assessments are made for the reference case geometry ($D_{ap} = 0.050$ m, $D_{ap}/D_c = 0.516$, $L/D_c = 2.55$, $\alpha = 45^\circ$), and for a constant solar thermal input, $\dot{q}_s = 2000$ kW/m^2 ($\dot{Q}_s = 3.927$ kW), $d_p = 40$ μm, $T_{in} = 300$ K, for varying mass flow rates of the particle and air phases. The trends for $\dot{m}_p/\dot{m}_{air} \geq 2$, are presented with dashed lines due to higher levels of uncertainty as noted in assumption 3.

have favourable efficiency, it can also be seen that the particle phase has a shorter residence time at elevated temperature (above 1500 K, say). For the back entry case, the particle phase has temperature greater than 1500 K only at axial locations $z = 0$–121 mm, whereas, for the front entry case the particle phase has temperature greater than 1500 K at axial locations $z = 34$–247 mm. The greater residence time at a given elevated temperature for the front entry configuration may be beneficial for the application of the SVR to reacting particles, which require minimum residence time at a given temperature for adequate chemical conversion. However, it is not an advantage for the heating of inert particles.

Fig. 8b presents the calculated axial distributions of the thermal losses via conduction through the wall, $\dot{q}_{w-\infty}$, and re-radiation through the aperture, $\dot{q}_{w-ap}$, for the front entry and back entry flow directions. It can be seen that the biggest component of heat loss for both the front and back entry configurations is by conduction through the receiver wall. The calculated values for conduction heat loss integrated over the internal surface area of the receiver are 51% and 47% of the solar thermal input for the front and back entry configurations, respectively. The distributions of these heat losses in Fig. 8b show that conduction heat loss is greater at the back of the receiver for the front entry configuration, while it is greater at the front of the receiver for the back entry flow configuration, as is expected from the axial distributions of receiver wall temperature presented in Fig. 8a. It can also be seen that the majority of re-radiation losses from the receiver wall through the aperture originate from the front sections of the receiver wall, due to the radiative shape factors, while most of the re-radiation from the back sections of the receiver wall intersect with the internal surface of the receiver rather than the aperture. As a consequence, it can be seen that re-radiation losses calculated with the present model are controlled by wall temperatures in the front section of the receiver. Here, the front entry configuration has reduced re-radiation losses compared with the back entry configuration, calculated to be 15% and 18% of the solar thermal input, respectively. The extent of thermal loss by re-radiation is significantly lower than that by conduction for the present case, which is consistent with the small size of the reactor. However, the present model assumes a constant, conservative conduction heat loss coefficient value ($h_{w-\infty} = 20$ W/m^{2}K), which could be minimised with the application of sufficient insulation and also with an increase in thermal scale, in which case re-radiation heat loss would become relatively more important.

Fig. 9 presents the dependence on particle and air phase mass flow rates of thermal efficiency of the SVR with the back entry flow configuration as calculated with the present numerical model. Here, the reference case geometry is assessed ($D_{ap} = 0.050$ m, $D_{ap}/D_c = 0.516$, $L/D_c = 2.55$, $\alpha = 45^\circ$) with a constant solar thermal input $\dot{q}_s = 2000$ kW/m^2 ($\dot{Q}_s = 3.927$ kW), particle size $d_p = 40$ μm, and inlet temperature $T_{in} = 300$ K. It can be seen that, as for the front entry flow configuration (Fig. 6a), η_{th} increases asymptotically with increasing $\dot{m}_{air}$, for all values of $\dot{m}_p/\dot{m}_{air}$ (noting that trends for $\dot{m}_p/\dot{m}_{air} \geq 2$ are presented with dashed lines due to the higher level of uncertainty as discussed in

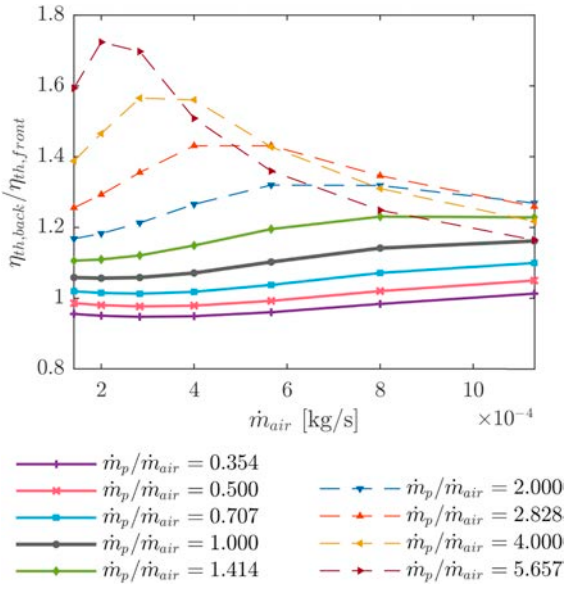

Fig. 10. The ratio of the thermal efficiency of the SVR with back entry configuration relative to the front entry configuration, $\eta_{th,back}/\eta_{th,front}$, as a function of mass flow rate of air, $\dot{m}_{air}$, for nine different values of mass loading, $\dot{m}_p/\dot{m}_{air}$. Assessments are made for the reference case geometry (D_{ap} = 0.050 m, D_{ap}/D_c = 0.516, L/D_c = 2.55, α = 45°), and for a constant solar thermal input, $\dot{q}_s$ = 2000 kW/m^2 ($\dot{Q}_s$ = 3.927 kW), d_p = 40 μm, T_{in} = 300 K, for varying mass flow rates of the particle and air phases. The trends for $\dot{m}_p/\dot{m}_{air} \geq 2$, are presented with dashed lines due to higher levels of uncertainty as noted in assumption 3.

assumption 3 in Section 2.1). The thermal efficiency tends towards a maximum of 88% for the highest particle loading considered here, $\dot{m}_p/\dot{m}_{air}$ = 5.657. In addition, the efficiency increases with $\dot{m}_p/\dot{m}_{air}$, so that the device is most efficient with high particle loadings. It can also be seen that, similar to the front entry flow configuration, a decrease in the ratio $\dot{Q}_s/(\dot{m}_p c_{p,p} + \dot{m}_{air} c_{p,air})$ has the effect of increasing η_{th}. However, Fig. 9a shows here that at constant $\dot{Q}_s/(\dot{m}_p c_{p,p} + \dot{m}_{air} c_{p,air})$ it is beneficial to the thermal efficiency for the SVR to be operated with higher particle loading. This implies that efficiency is dominated by the heat transfer between the incoming concentrated solar radiation and the particles, which directly absorb the radiation before leaving from the front section of the receiver where the concentrated solar radiation is most intense.

Fig. 10 presents the ratio of the receiver thermal efficiency for the back entry configuration relative to the front entry case, $\eta_{th,back}/\eta_{th,front}$, as a function of $\dot{m}_{air}$ for nine different values of $\dot{m}_p/\dot{m}_{air}$ (noting that trends for $\dot{m}_p/\dot{m}_{air} \geq 2$ are presented with dashed lines due to the higher level of uncertainty). It can be seen that the back entry flow configuration has a higher thermal efficiency for the majority of cases, although it has a lower thermal efficiency for the cases with sufficiently low particle loading $\dot{m}_p/\dot{m}_{air}$ = 0.354 and $\dot{m}_{air} \leq 8.000 \times 10^{-4}$ kg/s, and for $\dot{m}_p/\dot{m}_{air}$ = 0.500 and $\dot{m}_{air} \leq 5.657 \times 10^{-4}$ kg/s. This is consistent with general understanding of the difference between co-flow and counter-flow heat exchangers. The counter-flow arrangement achieves a higher outlet temperature, resulting in a greater thermal efficiency, despite the trade-off between an increase in radiation losses through the aperture. In contrast, for the low mass loading cases, the heat exchange is dominated by heat transfer from the walls to the air, so that the front entry configuration results in a counter-flow arrangement relative to the high temperature rear section of the chamber (Fig. 8). It can be seen that, for the cases of $\dot{m}_{air} \leq 2.828 \times 10^{-4}$ kg/s considered here, $\eta_{th,back}/\eta_{th,front}$ increases with particle loading, such that a maximum value of $\eta_{th,back}/\eta_{th,front}$ = 1.72 occurs for $\dot{m}_p/\dot{m}_{air}$ = 5.657, with $\dot{m}_{air} = 2.000 \times 10^{-4}$ kg/s. However, for higher $\dot{m}_{air}$ it can be seen that there is a critical mass loading, above which $\eta_{th,back}/\eta_{th,front}$ decreases. For $\dot{m}_{air} = 4.000 \times 10^{-4}$ kg/s this value is $\dot{m}_p/\dot{m}_{air}$ = 4.000, and for $\dot{m}_{air} = 5.657 \times 10^{-4}$ kg/s this value is $\dot{m}_p/\dot{m}_{air}$ = 2.828.

4.3. Influence of particle size

Fig. 11 presents the calculated axial distributions of the temperatures of the receiver wall, the particle phase and the air phase for two particle sizes, d_p = 40 and 80 μm, with reference case geometry, front entry configuration and $\dot{m}_p = \dot{m}_{air} = 4.000 \times 10^{-4}$ kg/s. It can be seen that a decrease in the particle size increases the rate at which the particle phase absorbs concentrated solar radiation in the front section of the receiver, as expected. For example, within the first 50 mm of the receiver the 80 μm sized particle phase heats to 1446 K, while the 40 μm size particle phase heats to 1633 K. This is consistent with the proportionality relationship between radiation extinction coefficient and particle size for a given mass of particles, which can be described as: $\kappa \propto d_p^{-1}$. The greater attenuation of concentrated solar radiation in the front part of the receiver by the smaller particles results in higher temperature and resulting higher wall temperature. However, the influence is small as the two-phase flow proceeds to the rear of the receiver, where the temperature of the particle and air phases approach equilibrium. For $z > 211$ mm the particle phase (and the air to a lesser extent) undergoes heating for both d_p = 40 and 80 μm. This is due to relatively larger radiation shape factors from the aperture to the conical section of the receiver as well as increased concentration of particles. In addition, the 80 μm particles undergo greater heating and thus leave with higher temperature than the 40 μm particles. This is because the solar radiation penetrates further into the receiver for the larger particles, such that its intensity is greater in the conical section of the receiver than for the smaller particle size. However, the net effect of increasing the particle size is to translate the temperature distribution toward the back of the cavity, which will lower radiative losses through the aperture.

Fig. 12 presents the influence of particle sizes in the range 10–80 μm on the thermal performance of the front entry configuration of the SVR, for the reference geometry and operating conditions (Table 1). Fig. 12a presents the dependence of η_{th} on d_p for four different values of $\dot{m}_p/\dot{m}_{air}$

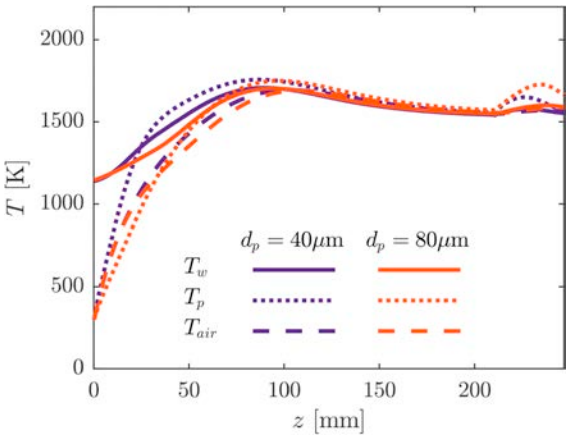

Fig. 11. Calculated axial temperature distributions of the receiver wall, T_w, the particle phase, T_p, and the air phase, T_{air}, for the SVR with front entry flow configuration and two different values of particle size, d_p = 40 and 80 μm. Geometry and operational conditions of the reference case were used: D_{ap} = 0.050 m, D_{ap}/D_c = 0.516, L/D_c = 2.55, α = 45°, $\dot{q}_s$ = 2000 kW/m^2 ($\dot{Q}_s$ = 3.927 kW), $\dot{m}_p/\dot{m}_{air}$ = 1, $\dot{m}_p = \dot{m}_{air} = 4.000 \times 10^{-4}$ kg/s, d_p = 40 μm, T_{in} = 300 K.

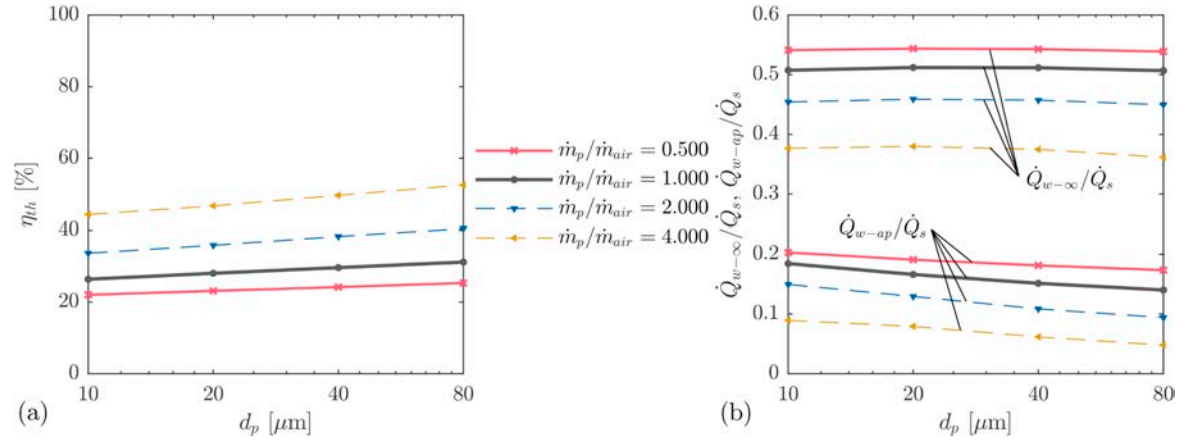

Fig. 12. The dependence on particle diameter, d_p, of the performance of the SVR with reference case geometry ($D_{ap} = 0.050$ m, $D_{ap}/D_c = 0.516$, $L/D_c = 2.55$, $\alpha = 45^{\circ}$), for a constant solar thermal input, $\dot{q}_s = 2000$ kW/m^2 ($\dot{Q}_s = 3.927$ kW), $\dot{m}_{air} = 4.000 \times 10^{-4}$ kg/s and for four different values of mass loading, $\dot{m}_p/\dot{m}_{air}$, with $T_{in} = 300$ K. Presented are (a) the receiver thermal efficiency, η_{th}; and (b) the relative thermal losses, $\dot{Q}_{w\text{-}\infty}/\dot{Q}_s$ and $\dot{Q}_{w\text{-}ap}/\dot{Q}_s$. The trends for $\dot{m}_p/\dot{m}_{air} \geq 2$, are presented with dashed lines due to higher levels of uncertainty as noted in assumption 3.

spanning 0.5–4.0 (noting that trends for $\dot{m}_p/\dot{m}_{air} \geq 2$ are presented with dashed lines due to the higher level of uncertainty). It can be seen that increasing the particle size causes a significant increase in the overall thermal efficiency of the process. Specifically, for $\dot{m}_p/\dot{m}_{air} = 1.000$ an increase in particle size from 10 μm to 80 μm results in a 18.2% improvement in thermal efficiency from 26.4% to 31.2%. This is consistent with the temperature distributions presented in Fig. 11, which imply a lower radiation loss through the aperture for the larger particles, whose temperatures peak further from the aperture.

Fig. 12b presents the dependence of the relative thermal losses by conduction, $\dot{Q}_{w\text{-}\infty}/\dot{Q}_s$, and re-radiation, $\dot{Q}_{w\text{-}ap}/\dot{Q}_s$, on d_p for four different values of $\dot{m}_p/\dot{m}_{air}$. It can be seen that, for the four particle mass loadings considered here, the particle size has the most significant influence on the re-radiation loss, $\dot{Q}_{w\text{-}ap}/\dot{Q}_s$, which reduces with increasing d_p as identified previously. This is due to the slower initial temperature rise as larger particles are introduced into the receiver and the resulting shift of the temperature profiles downstream to the rear of the receiver, where the receiver wall has smaller radiation shape factor with the aperture. It can also be seen that particle size has less of an influence on $\dot{Q}_{w\text{-}\infty}/\dot{Q}_s$.

4.4. Influence of receiver length

Fig. 13 presents the axial distributions of temperature of the particle and air phases, together with that of the receiver wall for three receivers of varying length, $L/D_c = 1.0$, 2.5 and 4.0 (where the front entry flow configuration is used and other geometries are those of the reference case). It can be seen that, for each case, the particle phase is heated rapidly in the front sections of the receiver where the incident concentrated solar radiation is most intense. This, in turn, causes the air phase to also heat rapidly. The rate of heating reduces with axial distance. For the case of shortest length, $L/D_c = 1.0$, it can be seen that the particle and air phases reach maximum temperatures towards the rear of the receiver; $T_{p,\max} = 2191$ K at $z/L = 0.77$ and $T_{air,\max} = 1955$ K at $z/L = 0.85$. Further down-beam (relative to the direction of the concentrated solar radiation input), their temperatures decrease only slightly before exiting with temperatures, $T_{p,out} = 1944$ K and $T_{air,out} = 1936$ K. The corresponding thermal efficiency is, $\eta_{th} = 39.5\%$. In comparison, the position of peak temperature is relatively further upstream for receivers with a greater length, $L/D_c = 2.5$ and 4.0, providing more distance for cooling to a progressively lower exit temperature ($T_{p,\max} = 1764$ K at $z/L = 0.36$ for $L/D_c = 2.5$ and $T_{p,\max} = 1681$ K at $z/L = 0.22$ for $L/D_c = 4.0$). This means that increasing the cavity length above an optimal has a net effect of increasing heat losses. It can also be observed that, for both $L/D_c = 2.5$ and 4.0, the particle and air phase tend towards equilibrium with the wall in the rear half of the cavity, which is a source of heat loss via

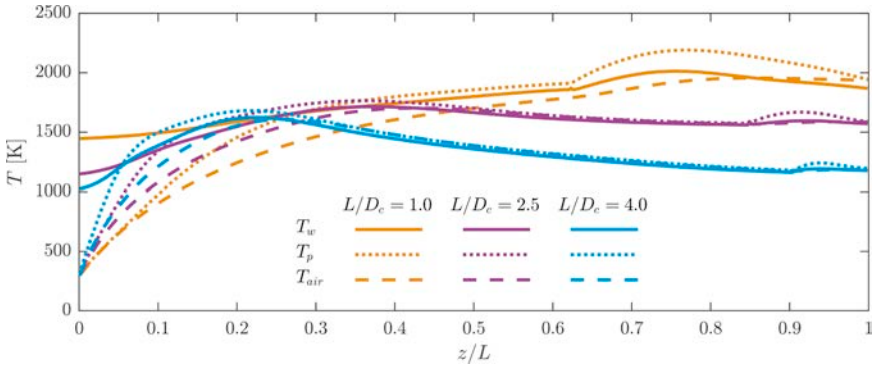

Fig. 13. Calculated axial temperature distributions of the receiver wall, T_w, the particle phase, T_p, and the air phase, T_{air}, in the SVR with front entry configuration and three different values of length to diameter ratio, L/D_c. Other geometry and operational conditions of the reference case were used: $D_{ap} = 0.050$ m, $D_{ap}/D_c = 0.516$, $\alpha = 45^{\circ}$, $\dot{q}_s = 2000$ kW/m^2 ($\dot{Q}_s = 3.927$ kW), $\dot{m}_p/\dot{m}_{air} = 1$, $\dot{m}_p = \dot{m}_{air} = 4.000 \times 10^{-4}$ kg/s, $d_p = 40$ μm, $T_{in} = 300$ K.

conduction and re-radiation. The extent of this heat loss increases with length of the receiver. This is borne out by the values of overall thermal efficiency for the processes: η_{th} = 30.1% and 20.0% for the receivers with L/D_c = 2.5 and 4.0, respectively. However, it should be noted that the residence time of the two-phase flow at elevated temperature increases with the length of the SVR. The model therefore provides a means to optimise residence time and conduction heat losses to suit the process. Additional assessments (in the supplementary information) confirm that $T_{p,out}$ and $T_{air,out}$ decrease with increasing receiver length for all values of $\dot{m}_p/\dot{m}_{air}$ considered here. This has the effect of a concurrent decrease in η_{th} with increasing receiver length.

5. Conclusions

The first order numerical model developed here to assess the fundamental aspects of heat transfer within a vortex-based solar particle receiver has been found to yield good qualitative and reasonable quantitative agreement with the available experimental data of operation of the device at laboratory-scale under solar simulated conditions. The first order assessment of the sensitivity of thermal performance of the solar vortex receiver to key geometric and operational parameters revealed the following:

- The particle mass loading of the two-phase flow was found to be important in defining whether the receiver acts primarily as an air-heater or a particle heater. For the case analysed here in which there is no particle recirculation, a critical value of $\dot{m}_p/\dot{m}_{air} \approx 1$ was found to define the boundary, above which the device acts as a particle heater, and below which it acts as an air heater. However, the critical value may increase for configurations with significant flow recirculation. To maximise the overall efficiency of a system, it will be necessary to consider the recovery of enthalpy from both the particle and air streams.
- The direction of the flow of particles relative to that of the concentrated solar radiation was found to have an important influence on the efficiency. A counter-flow direction tends to increase the efficiency relative to the co-flow direction for high mass loadings, consistent with known trends in other counter-flow heat exchangers. This configuration leads to higher exit temperature, primarily due to reduced conduction losses and particle heating directly before leaving from the front section of the receiver, where the concentrated solar radiation is most intense.
- The ratio of receiver thermal input to heat capacity of the two-phase flow controls the thermal efficiency of the SVR with front entry configuration. This is because the incident solar energy is absorbed by greater mass flow rates, resulting in lower temperatures and reduced thermal losses. However, for the back entry flow configuration and a given ratio of thermal input to total heat capacity of the two-phase flow, efficiency increases with the mass loadings because efficiency is dominated by the heat transfer between the incoming concentrated solar radiation and the particles in the counter-flow arrangement.
- The distribution of temperatures of the particles and walls within the device was found to have an important secondary influence on the radiation losses. A translation of the peak wall temperature toward the back was found to reduce radiation losses through the aperture and so increase thermal efficiency. This explains why operation with larger particles, which absorb radiation less efficiently and allow the incident concentrated solar radiation to penetrate further into the receiver, thereby shifting peak temperatures towards the rear of the receiver, results in higher efficiency.
- The optimal cavity length is controlled by the balance between increased solar energy absorption and increased conductive losses through the wall. Hence, modelling is needed to optimise the configuration on a case-by-case basis.

Acknowledgements

We gratefully acknowledge the financial support of the Australian Solar Thermal Research Initiative (ASTRI), a project supported by the Australian Government, through the Australian Renewable Energy Agency (ARENA). Dominic is also grateful for additional assistance in the form of an Australian Government Research Training Program Scholarship.

Appendix A. Supplementary material

Supplementary data to this article can be found online at https://doi.org/10.1016/j.solener.2018.10.086.

References

Besarati, S., Goswami, D., 2017. Supercritical CO 2 and other advanced power cycles for concentrating solar thermal (CST) systems. In: Advances in Concentrating Solar Thermal Research and Technology. Elsevier, pp. 157–178.
Buschman, A.J., Pittman, C.M., 1961. Configuration Factors for Exchange of Radiant Energy Between Axisymmetrical Sections of Cylinders, Cones, and Hemispheres and Their Bases. NASA Langley Research Center.
Cañadas, L., Salvador, L., Ollero, P., 1990. Radiative heat-transfer model in the interior of a pulverized coal furnace. Ind. Eng. Chem. Res. 29 (4), 669–675.
Chase, M.W., 1998. NIST-JANAF thermochemical tables fourth edition, Part I, Al-Co. J. Phys. Chem. Reference Data, Monograph 9.
Chinnici, A., Arjomandi, M., Tian, Z.F., Lu, Z., Nathan, G.J., 2015. A novel solar expanding-vortex particle reactor: influence of vortex structure on particle residence times and trajectories. Sol. Energy 122, 58–75.
Chinnici, A., Arjomandi, M., Tian, Z.F., Nathan, G.J., 2016. A novel solar expanding-vortex particle reactor: experimental and numerical investigation of the iso-thermal flow field and particle deposition. Sol. Energy 133, 451–464.
Chinnici, A., Xue, Y., Lau, T.C.W., Arjomandi, M., Nathan, G.J., 2017. Experimental and numerical investigation of the flow characteristics within a Solar Expanding-Vortex Particle Receiver-Reactor. Sol. Energy 141, 25–37.
Davis, D., Müller, F., Saw, W.L., Steinfeld, A., Nathan, G.J., 2017. Solar-driven alumina calcination for CO_2 mitigation and improved product quality. Green Chem. 19 (13), 2992–3005.
Elghobashi, S., 1994. On predicting particle-laden turbulent flows. Appl. Sci. Res. 52 (4), 309–329.
Feingold, A., 1978. A new look at radiation configuration factors between disks. J. Heat Transfer 100 (4), 742–744.
Flamant, G., Hernandez, D., Bonet, C., Traverse, J.-P., 1980. Experimental aspects of the thermochemical conversion of solar energy; Decarbonation of CaCO3. Sol. Energy 24 (4), 385–395.
Hamilton, D.C., Morgan, W.R., 1952. Radiant-interchange Configuration Factors. National Advisory Committee for Aeronautics.
Haugen, N.E.L., Mitchell, R.E., 2015. Modeling radiation in particle clouds: on the importance of inter-particle radiation for pulverized solid fuel combustion. Heat Mass Transf. 51 (7), 991–999.
Hilsenrath, J., 1955. Tables of Thermal Properties of Gases: Comprising Tables of Thermodynamic and Transport Properties of Air, Argon, Carbon Dioxide, Carbon Monoxide, Hydrogen, Nitrogen, Oxygen, and Steam. US Dept. of Commerce, National Bureau of Standards.
Hirsch, D., Steinfeld, A., 2004a. Radiative transfer in a solar chemical reactor for the co-production of hydrogen and carbon by thermal decomposition of methane. Chem. Eng. Sci. 59 (24), 5771–5778.
Hirsch, D., Steinfeld, A., 2004b. Solar hydrogen production by thermal decomposition of natural gas using a vortex-flow reactor. Int. J. Hydrogen Energy 29 (1), 47–55.
Ho, C.K., 2016. A review of high-temperature particle receivers for concentrating solar power. Appl. Therm. Eng. 109, 958–969.
Ho, C.K., Christian, J.M., Romano, D., Yellowhair, J., Siegel, N., Savoldi, L., Zanino, R., 2017. Characterization of particle flow in a free-falling solar particle receiver. J. Sol. Energy Eng. 139 (2), 021011.
Ho, C.K., Iverson, B.D., 2014. Review of high-temperature central receiver designs for concentrating solar power. Renew. Sustain. Energy Rev. 29, 835–846.
Hottel, H.C., Cohen, E.S., 1958. Radiant heat exchange in a gas-filled enclosure: allowance for nonuniformity of gas temperature. AIChE J. 4 (1), 3–14.
Hottel, H.C., Sarofim, A.F., 1967. Radiative Transfer. McGraw-Hill.
Jafarian, M., Arjomandi, M., Nathan, G.J., 2012. A hybrid solar and chemical looping combustion system for solar thermal energy storage. Appl. Energy.
Jafarian, M., Arjomandi, M., Nathan, G.J., 2013. The influence of high intensity solar radiation on the temperature and reduction of an oxygen carrier particle in hybrid chemical looping combustion. Chem. Eng. Sci. 95, 331–342.
Jenkins, B., Bertrand, C., 2001. Improvements in the design and operation of alumina flash calciners. IFRF Combust. J.
Jenkins, B., Moles, F., 1981. Modelling of heat transfer from a large enclosed flame in a rotary kiln. Trans. Instit. Chem. Eng. 59, 17–25.
Kasule, J.S., Turton, R., Bhattacharyya, D., Zitney, S.E., 2012. Mathematical modeling of a single-stage, downward-firing, entrained-flow gasifier. Ind. Eng. Chem. Res. 51 (18), 6429–6440.

Kodama, T., Gokon, N., 2007. Thermochemical cycles for high-temperature solar hydrogen production. Chem. Rev. 107 (10), 4048–4077.
Kräupl, S., Steinfeld, A., 2001. Experimental investigation of a vortex-flow solar chemical reactor for the combined ZnO-reduction and CH4-reforming. J. Sol. Energy Eng., Trans. ASME 123 (3), 237–243.
Kueh, K.C.Y., Nathan, G.J., Saw, W.L., 2015. Storage capacities required for a solar thermal plant to avoid unscheduled reductions in output. Sol. Energy 118, 209–221.
Lapp, J., Davidson, J., Lipiński, W., 2012. Efficiency of two-step solar thermochemical non-stoichiometric redox cycles with heat recovery. Energy 37 (1), 591–600.
Leuenberger, H., Person, R.A., 1954. Compilation of Radiation Shape Factors for Cylindrical Assemblies. Electro Metallurgical Co., Niagara Falls, NY.
Lichty, P., Perkins, C., Woodruff, B., Bingham, C., Weimer, A., 2010. Rapid high temperature solar thermal biomass gasification in a prototype cavity reactor. J. Sol. Energy Eng. 132 (1), 011012.
Maag, G., Lipiński, W., Steinfeld, A., 2009. Particle-gas reacting flow under concentrated solar irradiation. Int. J. Heat Mass Trans. 52 (21–22), 4997–5004.
Müller, F., Poživil, P., van Eyk, P.J., Villarrazo, A., Haueter, P., Wieckert, C., Nathan, G.J., Steinfeld, A., 2017. A pressurized high-flux solar reactor for the efficient thermochemical gasification of carbonaceous feedstock. Fuel 193, 432–443.
Nathan, G.J., Dally, B.B., Alwahabi, Z.T., van Eyk, P.J., Jafarian, M., Ashman, P.J., 2017a. Research challenges in combustion and gasification arising from emerging technologies employing directly irradiated concentrating solar thermal radiation. Proc. Combust. Inst. 36 (2), 2055–2074.
Nathan, G.J., Jafarian, M., Dally, B.B., Saw, W.L., Ashman, P.J., Hu, E., Steinfeld, A., 2017b. Solar thermal hybrids for combustion power plant: A growing opportunity. Progr. Energy Combust. Sci.
Perkins, C., Weimer, A.W., 2009. Solar-thermal production of renewable hydrogen. AIChE J. 55 (2), 286–293.
Rowe, S.C., Groehn, A.J., Palumbo, A.W., Chubukov, B.A., Clough, D.E., Weimer, A.W., Hischier, I., 2015. Worst-case losses from a cylindrical calorimeter for solar simulator calibration. Opt. Express 23 (19), A1309–A1322.
Sattler, C., Roeb, M., Agrafiotis, C., Thomey, D., 2017. Solar hydrogen production via sulphur based thermochemical water-splitting. Sol. Energy 156, 30–47.
Saw, W.L., Guo, P., van Eyk, P.J., Nathan, G.J., 2017. Approaches to accommodate resource variability in the modelling of solar driven gasification processes for liquid fuels synthesis. Sol. Energy 156, 101–112.
Siegel, N., Gross, M., Ho, C., Phan, T., Yuan, J., 2014. Physical properties of solid particle thermal energy storage media for concentrating solar power applications. Energy Proceed 49, 1015–1023.
Siegel, N.P., Gross, M.D., Coury, R., 2015. The development of direct absorption and storage media for falling particle solar central receivers. J. Sol. Energy Eng. 137 (4), 041003.
Sparrow, E.M., Jonsson, V.K., 1963. Radiant Emission Characteristics of Diffuse Conical Cavities. J. Opt. Soc. Am. 53 (7), 816–821.
Stein, W., Buck, R., 2017. Advanced power cycles for concentrated solar power. Sol. Energy 152, 91–105.
Steinfeld, A., 2005. Solar thermochemical production of hydrogen - a review. Sol. Energy 78 (5), 603–615.
Steinfeld, A., Imhof, A., Mischler, D., 1992. Experimental investigation of an atmospheric-open cyclone solar reactor for solid-gas thermochemical reactions. J. Sol. Energy-T ASME 114 (3), 171–174.
Szekely, J., Carr, R., 1966. Heat transfer in a cyclone. Chem. Eng. Sci. 21 (12), 1119–1132.
Tan, T.D., Chen, Y.T., 2010. Review of study on solid particle solar receivers. Renew. Sustain. Energy Rev. 14 (1), 265–276.
Tescari, S., Neises, M., de Oliveira, L., Roeb, M., Sattler, C., Neveu, P., 2013. Thermal model for the optimization of a solar rotary kiln to be used as high temperature thermochemical reactor. Sol. Energy 95, 279–289.
van Eyk, P.J., Ashman, P.J., Nathan, G.J., 2016. Effect of high-flux solar irradiation on the gasification of coal in a hybrid entrained-flow reactor. Energy Fuel 30 (6), 5138–5147.
Wu, W., Amsbeck, L., Buck, R., Uhlig, R., Ritz-Paal, R., 2014. Proof of concept test of a centrifugal particle receiver. In: Proceedings of the Solarpaces 2013 International Conference, vol. 49, pp. 560–568.
Z'Graggen, A., 2008. Solar Gasification of Carbonaceous Materials: Reactor Design, Modeling and Experimentation. ETH.
Z'Graggen, A., Haueter, P., Maag, G., Vidal, A., Romero, M., Steinfeld, A., 2007. Hydrogen production by steam-gasification of petroleum coke using concentrated solar power — III. Reactor experimentation with slurry feeding. Int. J. Hydrogen Energy 32 (8), 992–996.
Z'Graggen, A., Haueter, P., Trommer, D., Romero, M., de Jesus, J.C., Steinfeld, A., 2006. Hydrogen production by steam-gasification of petroleum coke using concentrated solar power — II Reactor design, testing, and modeling. Int. J. Hydrogen Energy 31 (6), 797–811.
Z'Graggen, A., Steinfeld, A., 2008a. Hydrogen production by steam-gasification of carbonaceous materials using concentrated solar energy — V. Reactor modeling, optimization, and scale-up. Int. J. Hydrogen Energy 33 (20), 5484–5492.
Z'Graggen, A., Steinfeld, A., 2008b. A two-phase reactor model for the steam-gasification of carbonaceous materials under concentrated thermal radiation. Chem. Eng. Process. 47 (4), 655–662.
Z'Graggen, A., Steinfeld, A., 2009. Heat and mass transfer analysis of a suspension of reacting particles subjected to concentrated solar radiation – Application to the steam-gasification of carbonaceous materials. Int. J. Heat Mass Trans. 52 (1–2), 385–395.

Title

Particle residence time distributions in a vortex-based solar particle receiver-reactor: an experimental, numerical and theoretical study

Authors

Dominic Davis[a,b,*], Maurizio Troiano[d], Alfonso Chinnici[a,b], Woei L. Saw[a,c], Timothy Lau[a,b], Roberto Solimene[e], Piero Salatino[d], Graham J. Nathan[a,b]

[a]Centre for Energy Technology, The University of Adelaide, South Australia 5005, Australia.

[b]School of Mechanical Engineering, The University of Adelaide, South Australia 5005, Australia.

[c]School of Chemical Engineering, The University of Adelaide, South Australia 5005, Australia.

[d]Dipartimento di Ingegneria Chimica, dei Materiali e della Produzione Industriale, Università degli Studi di Napoli Federico II, Piazzale V. Tecchio 80, 80125 Napoli, Italy.

[e]Istituto di Ricerche sulla Combustione, Consiglio Nazionale delle Ricerche, Piazzale V. Tecchio 80, 80125 Napoli, Italy.

Abstract

We report a joint experimental, numerical and theoretical study of particle residence times in a novel vortex-based particulate vessel, the Solar Expanding Vortex Receiver-Reactor (SEVR). The tracer pulse response method is used to measure the particle residence time distribution (RTD) within a laboratory-scale SEVR, where the particle phase itself is used as the tracer. The operating parameters of particle size, gas volumetric flow rate and inlet velocity were systematically varied to assess their influence on the particle RTD and to determine the mechanisms controlling the behaviour of the two-phase flow in the SEVR. Two regimes of particle behaviour are identified, characterised by both the Stokes (*Sk*) and Froude (*Fr*) numbers. In the low Froude number regime ($Fr < 4$), the Stokes number of the two-phase flow at the radially-oriented receiver outlet has a controlling influence on the particle residence time. That is, an increase in *Sk* increases particle residence time. In this regime large particles have a longer residence time than smaller particles, as is desirable for the efficient processing of polydisperse particles. In the high Froude number regime ($Fr > 4$), the Stokes number has a weaker influence on the residence time than it does in the low *Fr* regime. In this regime the residence time decreases with higher *Fr*. It was also found that the particle RTD in the SEVR can be described by a compartment model that consists of a small plug flow reactor followed by a series of two interconnected continuously-stirred tank reactors (CSTRs). The two particle behaviour regimes are then accounted for by the degree of back-mixing between the two CSTRs, the low *Fr* regime having significant back-mixing and the high *Fr* regime having negligible. The wide variation in particle RTD characteristics across the two regimes of operation suggests a high level of flexibility of operation of the SEVR technology, which is advantageous in facilitating control in response to the natural variability of the solar resource.

Keywords: Particle, residence time, RTD, solar particle receiver, solar vortex receiver, CST.

1 Introduction

The residence time distribution (RTD) of particles is widely used to characterise the performance of thermo-chemical particle reactors. The RTD of particles describes the probability distribution of the residence times of particles within a vessel for a given set of operational conditions, which is difficult to predict a priori without experimental data due to complexity of two-phase gas-particle flows. This is particularly the case in strongly recirculating flows such as those in swirling turbulent systems, owing to their non-linear behaviour (Allal et al., 1998; Lede et al., 1987; Li et al., 2008). One such swirling particulate device is a vortex-based solar particle receiver-reactor, in which particles are conveyed by a vortex flow of gas through the irradiation zone from a solar concentrator. This two-phase gas-particle flow is confined within a cylindrical cavity in a device that has been demonstrated with several solar thermochemical applications at laboratory-scale (Davis et al., 2017; Steinfeld et al., 1992; Z'Graggen et al., 2006). Knowledge of the particle RTD within a vessel is needed because most particulate vessels do not conform well to the classical idealisation of either a well-stirred reactor, with uniform properties through the vessel, or a plug-flow reactor, in which all fluid and particles have the same residence time, (Danckwerts, 1995; Nauman, 2008). Furthermore, the behaviour of particles is likely to be different from that of the transporting gas (Lede et al., 1987), particularly for cases where the Stokes number of the gas-particle flow is greater than unity (Chinnici et al., 2015). The overall objective of the present paper is, therefore, to support the development of vortex-based solar particle receiver-reactors by providing both new experimental data and understanding of the particle RTD within them.

Vortex-based solar particle receiver-reactors, typically referred to as Solar Vortex Receivers (SVRs), have been demonstrated experimentally at laboratory-scale for the thermal decomposition of natural gas (Hirsch and Steinfeld, 2004), the steam-gasification of carbonaceous feedstocks (Z'Graggen et al., 2006) and the calcination of alumina (Davis et al., 2017). Each of these investigations was conducted with a configuration in which the concentrated solar radiation is introduced into a cylindrical cavity through an aperture sealed by a transparent quartz window to directly irradiate a suspension of reacting particles in a vortex flow of gas. The vortex gas-particle flow proceeds through the cavity and exits with elevated temperature reported of order 1000°C. This device has the advantage of highly efficient heat transfer to the particle phase due to direct irradiation, as demonstrated by the high values of chemical conversion reported for residence times on the order of seconds. However, no previous direct measurements of particle residence time within it have been reported. In the absence of measured data, previous assessments have relied on the nominal particle residence time, based on the ratio of receiver internal volume to gas volumetric flow rate ($\tau_{nom} = V_r/\dot{V}_{gas}$). This value can be corrected for the dependence of density on temperature, and for the influence of chemical reactions on temperature and species. However, both the gas and particle phase residence times in a vortex flow configuration can differ significantly from this nominal residence time. Shilapuram et al. (2011) found that, for a solar cyclone reactor, the mean residence times of both particle and gas phases is significantly greater than the nominal value and that the particles exhibit a wide distribution of residence times that depend on the operating conditions. Therefore, it is desirable to characterise not only the mean residence time, $\overline{\tau_p}$, but also the full function of the RTD. The normalised variance, $\sigma_p^2 = \sigma_{p,t}^2/\overline{\tau_p}^2$, of the distribution has been

[*] Corresponding author: Dominic Davis, dominic.davis@adelaide.edu.au

recommended by Buffham and Mason (1993) to be the single best measure of the extent of spreading of the RTD and has been adopted elsewhere (Gao et al., 2011). Furthermore, various thresholds have also been adopted to characterise the particle RTD, such as the time required for a given fraction of particles (e.g. 90% of the inlet stream) to exit the vessel. For this reason, we aim to characterise the full function of the distribution of particle residence times in a SVR for a series of operating conditions.

An alternative configuration of SVR has recently been developed, with a view to capitalising on the high energy conversion efficiency of the original device developed by Z'Graggen et al. (2006), while also mitigating some of its limitations. The new configuration reduces the transport of particles through the aperture (Chinnici et al., 2015; Chinnici et al., 2016) and also generates a RTD that increases with the particle size for particles larger than a critical value characterised by the Stokes number (Chinnici et al., 2015). This is desirable because large particles require longer residence time for heating and reaction than small ones. The new configuration, termed the Solar Expanding-Vortex Particle Receiver-Reactor (SEVR), has a conical inlet section at the opposite end of the cylindrical cavity to the aperture and a radial outlet at the aperture end of the cavity (Chinnici et al., 2015). The different orientation of the outlet (radial) to that of the flow (tangential) is important to inhibit the exit of larger particles from the chamber due to their greater inertia. These proposed mechanisms have been partially validated by an experimental investigation into the flow field (Chinnici et al., 2016), but no direct assessments of particle RTD are available for either the SVR of the SEVR. Hence, a further aim of the present investigation is to assess the influence of the controlling parameters of particle size, gas flow rate and inlet velocity on the particle RTD within the SEVR.

The influence of receiver orientation on the performance of SVRs is also of interest because the alignment of gravity relative to the axis of the SVR will influence both its optical and thermal performance. For example, Chinnici et al. (2015) proposed that a vertical orientation helps to recirculate particles to the base of the conical section where velocity is greatest to facilitate their recirculation. While the significance of the orientation on the optical performance of the solar concentrator is beyond the scope of the present assessment, we do note that both conventional tower-mounted configurations (Ho and Iverson, 2014) and beam-down solar concentrating systems are under development (Kodama et al., 2014; Yogev et al., 1998), together with many variations between these two extremes. In addition, no experimental measurements are available of the influence of orientation on residence time within any configuration of SVR. Hence, we also aim to assess the role of alignment relative to gravity of the SEVR on the particle RTD.

Methods with which to measure particle residence time within a vessel have advanced from those measuring only a mean value (Lede et al., 1987; Li et al., 2008; Szekely and Carr, 1966) to those measuring the full distribution of residence times in micro-detail. Particle RTDs are typically measured by detecting the concentration with time of tracer particles using techniques such as phosphorescence (Harris et al., 2002), colour (Kieviet and Kerkhof, 1995), ferromagnetism (Guío-Pérez et al., 2013), chemically-doping (Kang et al., 1989), difference in electrical permittivity (Cai et al., 2014) and size (Mitsutani et al., 2005). However, methods requiring the off-line detection of the tracer (Kang et al., 1989; Kehlenbeck et al., 2002; Kieviet and Kerkhof, 1995; Mitsutani et al., 2005) have temporal resolution on the order of 10^{-2} – 10^{0} Hz, which is insufficient for the SVR, whose residence time is on the order of seconds. Optical measurement of particles offer a fast response, inline and non-intrusive method of tracer detection that can be based on light emission, scattering or extinction (Amaral et al., 2015). Phosphorescent tracers were employed by Harris et al. (2002) to measure the particle RTD in the riser of a circulating fluidised bed, but this method requires correction for the time-decay of phosphorescence. Lede et al. (1987) and Allal et al. (1998) used a combination of a light source and photoelectric sensors to measure the outlet pulse-response of particles injected into a cyclone reactor and a vertical tube reactor, respectively by measuring the extinction of light due to particles passing an illuminated zone at the reactor outlet. Such a method is suitable for operation in dilute particle volume fraction regimes so that the injection of particles has negligible impact on the steady-state gas flow (Elghobashi, 1994). The assessment by Lede et al. (1987) measured single particles and thus only reported mean residence times, while Allal et al. (1998) measured particle RTDs with particles whose properties were not monodisperse, making it impossible to isolate the effect of particle diameter from that of turbulence on the RTD. However, specialised particles with monodisperse properties are now available (Lau and Nathan, 2016), which offers the possibility of developing the light extinction method to isolate the influence of particle size on the RTD within a vessel. For this reason, a further aim of the paper is to develop a method to measure the particle RTD using inlet and outlet optical extinction measurements of a pulse of monodisperse particles introduced to the inlet of the device.

Simple flow models of reactors typically assume either a uniform residence time in a plug flow reactor, PFR, or perfect mixing of the flow in a continuously-stirred tank reactor, CSTR, (Danckwerts, 1995; Nauman, 2008), although real receiver-reactors deviate from these ideal flows. Hence it has become common to use the compartment modelling approach to model a real device as the sum of ideal flow reactors (PFRs and CSTRs) by comparison with measured RTDs. This analytical approach advances understanding of the device and provides a useful design tool (Gao et al., 2012), having been applied to circulating fluidised beds (Guío-Pérez et al., 2013; Kehlenbeck et al., 2002) and a liquid-solid classifier (Mitsutani et al., 2005). They are also useful for fault-finding, such as identifying stagnancy and bypassing (Nauman, 2008). Stagnancy is associated with a region of the flow with a much longer residence time than average and can be identified by a long tail in the RTD, while bypassing is associated with a region of much shorter residence time and can be identified by a sharp peak much shorter than the mean (Levenspiel, 1999; Nauman, 2008). A further aim of the present investigation is, therefore, to seek to decompose the measured particle RTDs of the SEVR into a combination of ideal reactors.

In summary, the aim of the present investigation is to determine the influence of the controlling parameters on the particle RTD within the Solar Expanding Vortex Receiver by systematic and independent variation of particle size, inlet velocity and gas volumetric flow rate during the steady-state operation of a laboratory-scale SEVR. To enable this, we aim to develop a pulse response method of particle RTD measurement using inlet and outlet optical extinction measurements. The present investigation has been undertaken with gravity aligned in the same direction as the axis as the simplest configuration, while alternative orientations of gravity at various angles to the axis will be reported separately. More specifically, we aim to identify the influence of key non-dimensional parameters on the mechanisms controlling particle behaviour within the SEVR and the resulting influence on measured particle residence times. Additionally, this paper aims to assess the similarities of vortex-based solar particle receivers to the operation of common ideal reactors with a view to relating this to the large-scale dynamics of the device.

2 Methodology

The particle residence time distribution within the Solar Expanding Vortex Receiver (SEVR) was measured by injecting a short pulse of particles, the concentration of which was directly measured at the inlet to and outlet from the SEVR cavity following the well-established tracer pulse response method described by Levenspiel (1999) and Fogler (2006). Here, the particle phase acts both as the tracer and the medium being traced, as the pulse of particles is injected into an empty vessel. This is considered valid because the SEVR operates with a very small particle inventory inside the vessel. That is, the particle-to-air volume fraction is $< 10^{-4}$, so that the particle phase has negligible effect on the flow field of the gas phase, as has been the case in previous assessments of vortex-based solar

particle receiver operation. The recorded concentration of the pulse of particles can therefore be considered to be representative of the particle behaviour for steady state operation of the SEVR with small particle hold-up and limited two-way coupling between particle and gas phases (Elghobashi, 1994).

The inlet and outlet concentration of particles was measured with time-resolved laser extinction measurements. This is a non-disruptive tracer measurement technique, based on the attenuation of a monochromatic electromagnetic wave transmitted through the particulate medium and is applicable to the measurement of dilute phase gas-solid flows (Yong, 1996). Furthermore, the SEVR cavity had well-defined, closed boundary conditions, as the flow in the inlet and outlet tubes was fast compared to mean flow velocities within the chamber and could therefore be assumed to be plug flow.

For a particulate system operating at steady state, the outlet concentration of particles is said to be the convolution of the inlet concentration with the residence time distribution (RTD). The convolution integral introduced by Danckwerts (1995) is:

$$o(t) = i(t) * E(t) = \int_0^t i(t-t')E(t')dt', \qquad (1)$$

where $i(t)$ and $o(t)$ are the inlet and outlet particle concentration measurements with time, and $E(t)$ is the residence time distribution of particles within the receiver (or the exit age distribution, following Danckwerts, 1995). For the case in which the injection pulse approaches a perfect Dirac delta function, the recorded outlet concentration of particles is a direct measure of the particle RTD, $E(t)$. However, since the injection pulse is rarely a true delta function, it is necessary to deconvolve Equation (1) to determine $E(t)$ (Gao et al., 2012), as has been done previously (Essadki et al., 2011; Trachsel et al., 2005). For the present investigation, this was accomplished by converting the recorded signals to the Fourier domain with a fast Fourier transform (Viitanen, 1997), and using a regularisation factor to solve the ill-posed problem in the frequency domain (Mills and Duduković, 1989). The present analysis of RTD ignores any influence of particle deposition onto the walls of the vessel. This was justified on the basis of observations that any deposition onto the walls was small.

Due to the stochastic distribution of particles as a discrete phase within the two-phase gas-particle flow, the extinction signal fluctuates with time. These fluctuations were reduced by averaging the $E(t)$ calculated from 12 repeated measurements, each normalised by the area bounded by the distribution, giving $\int_0^\infty E(t)dt = 1$. This number was found to result in a profile that converged closely to that from 40 repeated measurements, particularly for the measurement of mean particle residence time, which was found to be independent of the number of averaged repetitions for 12 or more repetitions.

2.1 Experimental arrangement

Figure 1 presents the experimental arrangement used to determine the particle RTD within the SEVR cavity. The particle feeding subsystem consisted of two air lines connected in parallel. Prior to each measurement, 0.3 g of particles was loaded into the particle basket connected to the secondary feeder air line with the valve closed. Steady state vortex flow conditions within the cavity were then established by introducing equal amounts of compressed air (with flow rate controlled by electronic mass flow controllers) to the two tangential inlets, through the primary feeder air line and the second tangential inlet. To inject a pulse of particles, the valve connected to the particle basket was opened such that air flowed through both feeder air lines without disrupting the total amount of air injected into the receiver cavity. The increase in total inlet mass flow rate due to the injection of a pulse of particles is estimated to be a maximum of 22% for the maximum duration of 0.5 s. It can therefore be assumed that the vortex flow closely approximates a steady state condition for the duration of measurement (60 s).

Extinction measurements were carried out with the use of a 4.5 mW, 635 nm collimated laser diode (*Thorlabs* CPS635S) and a photodetector (*Thorlabs* DET36A/M). The laser and photodetector were mounted perpendicular to the centre axis of the inlet and outlet tubes, as shown in Figure 1, so that the translation of particles through the beam causes an attenuation in the signal. Laser light levels were recorded with the photodetector with a sampling frequency of 10 kHz and for a total time of 60 seconds for each measurement repetition. The inlet/outlet concentration measurements were corrected for the flow time, $t_{correction}$, between the true inlet/outlet and the measurement position, $L_{correction}$, by assuming plug flow ($t_{correction} = L_{correction}A_{in/out} / \dot{V}_{air}$).

For the experiments reported here, the receiver cavity of SEVR configuration was oriented vertically with the inlet and conical section at the bottom, such that the axis of the cavity is aligned with gravity. This corresponds to the simplest flow configuration, since it avoids a gravity bias that may cause particles to settle on the wall, whilst also being relevant to the 'beam down' configuration. Other orientations will be considered in future work.

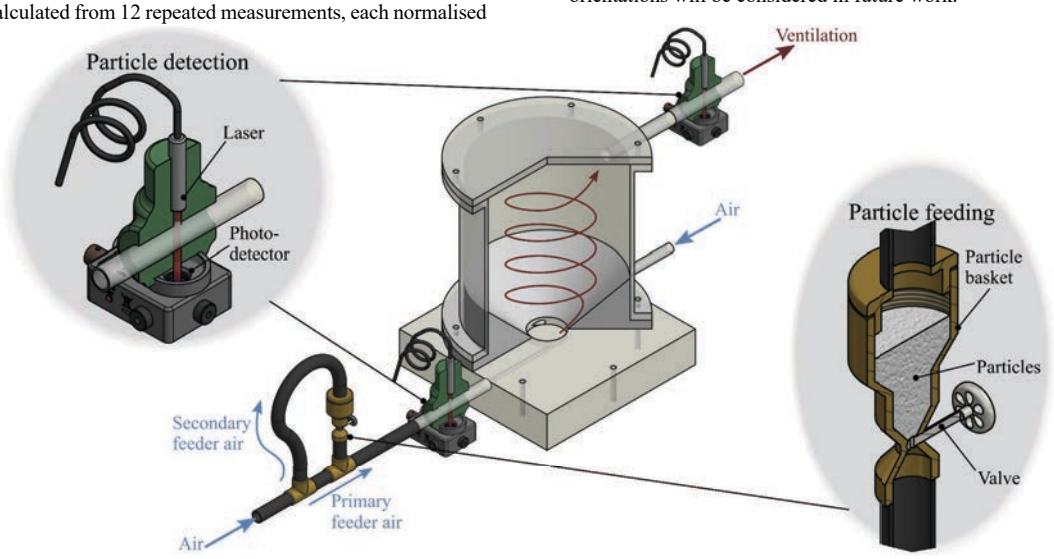

Figure 1: Experimental arrangement used to determine the residence time distribution of particles within a vortex-based solar particle receiver vessel. Shown are the particle feeding and detection subsystems, as well as the receiver cavity which features two tangentially-oriented inlets and a single radially-oriented outlet.

Figure 2, together with Table 1a, presents the geometry of the receiver, which was fabricated from acrylic and ABS plastics. This configuration maintains geometric similarity with that used in previous investigations of the SEVR (Chinnici et al., 2015; Chinnici et al., 2016). The following analysis refers to a cylindrical coordinate system as shown in Figure 2 with an origin at the centre of the base disc so that gravity acts in the negative z direction. Also shown are the zones in the receiver, at which key non-dimensional parameters are evaluated.

Table 1b presents the range of operational parameters that were varied in the present work, namely the air volumetric flow rate, air inlet velocity and particle size. To isolate the influence of particle size on the RTD, spherical polymer particles (ρ_p = 1200 kg/m^3) with a narrow size distribution were used, following Lau and Nathan (2016). Figure 3 presents the particle size distributions, whose mean values are $\bar{d}_p$ = 80, 40 and 20 µm.

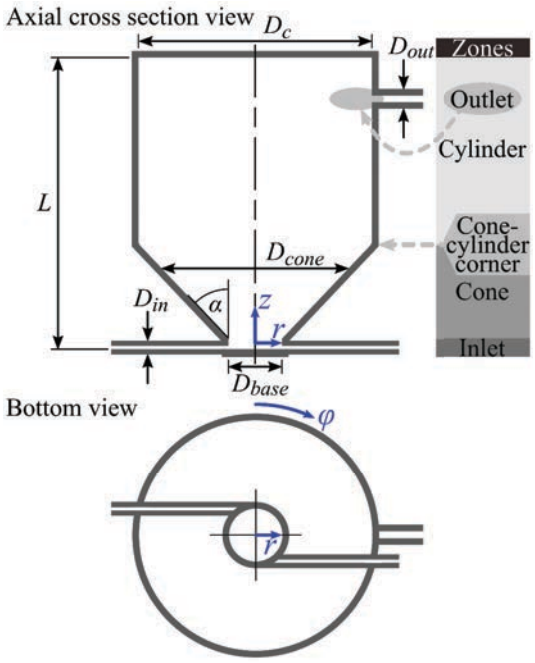

Figure 2: Schematic diagram of the SEVR showing the cylindrical coordinate system (r,φ,z) with origin at the centre of the base disc, together with key geometric dimensions, two inlets and one outlet. Also shown are the zones in the receiver, at which key non-dimensional parameters are evaluated.

Table 1: (a) Values of the key dimensions of the SEVR; and (b) the range of input parameters systematically varied in the current investigation.

(a)	
D_c	190 mm
L	237.5 mm
D_{base}	47.5 mm
D_{cone}	Min: 47.5 mm, max: 190 mm
α	50°
D_{in}	5, 6 and 7.5 mm
D_{out}	11 mm
(b)	
d_p	20, 40, 80 µm
$\dot{V}_{air}$	60 – 150 slpm
U_{in}	16.2 – 51.8 m/s

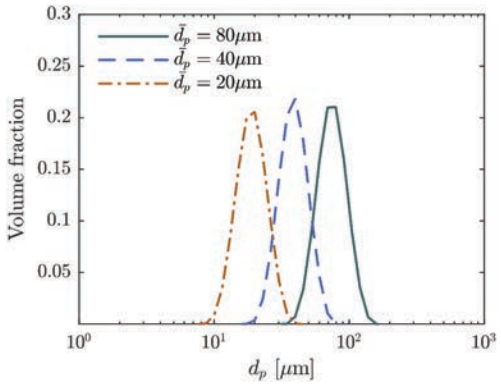

Figure 3: Particle size distributions of the spherical polymer particles used to measure the particle RTD in the SEVR.

2.2 Characterisation of the residence time distribution

The particle RTDs measured here, $E(t)$, are reported in terms of probability density functions, which can be characterised by the mean particle residence time, $\bar{\tau}_p$, the 90th percentile particle residence time, $\tau_{p,90}$, and the normalised variance, $\sigma_p^2 = \sigma_{p,t}^2/\bar{\tau}_p^2$. These parameters are calculated as follows:

$$\bar{\tau}_p = \int_0^\infty tE(t)dt, \tag{2}$$

$$\int_0^{\tau_{p,90}} E(t)dt = 0.90, \tag{3}$$

$$\sigma_{p,t}^2 = \int_0^\infty \left(t - \bar{\tau}_p\right)^2 E(t)dt. \tag{4}$$

The statistical parameters in Equations (2), (3) and (4) were calculated from curves fitted to the experimental $E(t)$ curves, with coefficient of determination values, $R^2 > 0.97$, following Buffham and Mason (1993), to mitigate the effect of measurement noise at large t.

To compare experimental RTD curves with theoretical models, it is useful to derive the normalised expression of $E(t)$ as:

$$E(\theta) = \bar{\tau}_p E(t), \tag{5}$$

where $\theta = t/\bar{\tau}_p$ is the dimensionless time term. These dimensionless terms are used in the application of generalised ideal reactor compartment models (PFRs and CSTRs) to the experimentally measured RTDs of the present investigation.

2.3 CFD modelling of the vortex-based solar particle receiver operation

To complement the analysis of the experimental measurements of particle RTDs in the SEVR a three-dimensional computational fluid dynamics (CFD) model was used to calculate numerical estimates of key velocity and length scales of the two-phase vortex flow within the SEVR. The model builds on previous work in which the model was validated against measurements of the gas flow field and particle deposition onto a window through the aperture (Chinnici et al., 2016; Chinnici et al., 2017). Further validation is required here because of slight differences to the geometric configuration and inflow conditions of the present investigation.

The commercial CFD code ANSYS/FLUENT 17.2 was again used to simulate the turbulent fluid flows and to track the particles in the SEVR, using the Reynolds-Averaged Navier-Stokes (RANS) approach. The operating conditions, working fluid and receiver geometry were the same as those of the experimental procedure. The 3-D geometry was built in Gambit and a non-uniform unstructured (tetrahedral) grid was generated with ANSYS/Meshing 17.2. A total

of ~2.5 million cells were employed for all configurations tested. The mesh independence was checked on a coarser mesh (1 million cells) and a finer mesh (4 million cells). The mesh quality was checked to ensure suitability based on aspect ratio, orthogonality, skewness, and expansion factor, according to Tian et al. (2015).

The RNG k-ε model (with swirl factor) was selected as the turbulence closure model, this being a validated model for the prediction of the vortex structure within SEVR configurations similar to those investigated here (Chinnici et al., 2015; Chinnici et al., 2016; Chinnici et al., 2017), while also being a preferred closure model for the flows within a vortex device (Syred, 2006). The Discrete Phase Model (DPM) was implemented to calculate the fluid flow fields, particle trajectories and residence time distributions, following previous work (Chinnici et al., 2015; Chinnici et al., 2016; Shilapuram et al., 2011).

For each operational case being simulated, the surface injection option in Fluent was used to inject monodisperse spherical particles with diameters d_p = 20, 40 or 80 µm into the modelled domain with a constant volume fraction of 2×10^{-5} corresponding to an inlet particle mass loading of 0.033. The circular tangential inlet was used as the injection surface that has a constant mesh density, which lead to a constant number of particle parcel injection points. The dispersion of the particles due to turbulence in the continuous gas phase was calculated using a stochastic tracking model with a discrete random walk that includes the effects of instantaneous turbulent velocity fluctuations on particle trajectories. Each injected particle parcel was tracked by the solver 20 times. The values of the Integral Time Scale parameter of the particle dispersion model used here, which is proportional to the particle dispersion rate (Marchioli et al., 2006), were calculated based on the average calculated values of k and ε within the receiver (ANSYS Inc., 2012). The effect of gravity (acting in the negative z-direction) was included in the simulations. All the simulations were performed with 32 cores on the Phoenix supercomputer facilities of The University of Adelaide. The CPU-time required to achieve the desired convergence (when all the residuals reached 1×10^{-6}) was ~100 CPU-hr.

The model was validated previously against measurements of the gas flow field for similar configurations (Chinnici et al., 2016; Chinnici et al., 2017), while additional validation from the present measurements is reported below. Table 2 presents a comparison between the experimentally-measured and numerically-modelled particle RTDs in terms of their mean and 90th percentile particle residence times, $\bar{\tau}_p$ and $\tau_{p,90}$, for four validation cases. The operational details of these validation cases include air volumetric flow rates of $\dot{V}_{air}$ = 104 and 140 slpm and two particle sizes d_p = 20 and 80 µm. These values of $\dot{V}_{air}$ generate inlet velocities of U_{in} = 30.7 and 41.3 m/s and nominal residence times $\tau_{nom} = V_r/\dot{V}_{air}$ = 3.2, and 2.4 s (with constant inlet diameter, D_{in} = 6 mm). The model yields an average error of 12% for $\bar{\tau}_p$ and 14% for $\tau_{p,90}$, when compared to the equivalent experimental measurements. It is therefore reasonable for the CFD model to be used in the present investigation to estimate key length and velocity scales used in calculating the Stokes and Froude numbers. Additionally, the validation of the CFD model is reasonable enough for it to be used for qualitative assessments of particle trajectories within the SEVR, to complement analysis of the experimental results and compartment modelling.

Figure 4 presents the axial, u_z, tangential, u_φ, and radial, u_r, components of the calculated mean air velocity profiles, normalised by the inlet velocity, U_{in}, at four axial cross-sections through the receiver for a value of $\dot{V}_{air}$ = 104 slpm and D_{in} = 6 mm, as calculated with the CFD model. It can be seen that the SEVR generates a well-defined vortex structure, as has been reported for the SEVR device previously (Chinnici et al., 2015; Chinnici et al., 2016). Key features of the vortex flow are that the vortex intensity is inversely proportional to the distance from the inlet. That is, there is a high swirl intensity in the conical section of the receiver, which transitions to a relatively low swirl intensity in the upper cylindrical part of the receiver. Furthermore, it should be noted that a reversed flow is generated in the core region of the vortex. Further details of the gas flow field generated within the SEVR can be found in previous publications (Chinnici et al., 2015; Chinnici et al., 2016; Chinnici et al., 2017).

Table 2: Comparison of the experimentally measured and numerically simulated values of $\bar{\tau}_p$ and $\tau_{p,90}$, for four different operational cases and for a fixed inlet jet diameter (D_{in} = 6 mm).

Validation Case	Operational details				Experimental result		Numerical result		Absolute relative difference	
	$\dot{V}_{air}$ [slpm]	d_p [µm]	U_{in} [m/s]	τ_{nom} [s]	$\bar{\tau}_p$ [s]	$\tau_{p,90}$ [s]	$\bar{\tau}_p$ [s]	$\tau_{p,90}$ [s]	$\bar{\tau}_p$	$\tau_{p,90}$
1	140	80	41.3	2.4	2.23	4.35	2.40	4.93	7.6%	13.3%
2	104	80	30.7	3.2	5.83	13.34	7.00	16.10	20.1%	20.7%
3	140	20	41.3	2.4	1.72	3.56	2.00	4.15	16.3%	16.6%
4	104	20	30.7	3.2	3.19	6.77	3.05	6.41	4.4%	5.3%

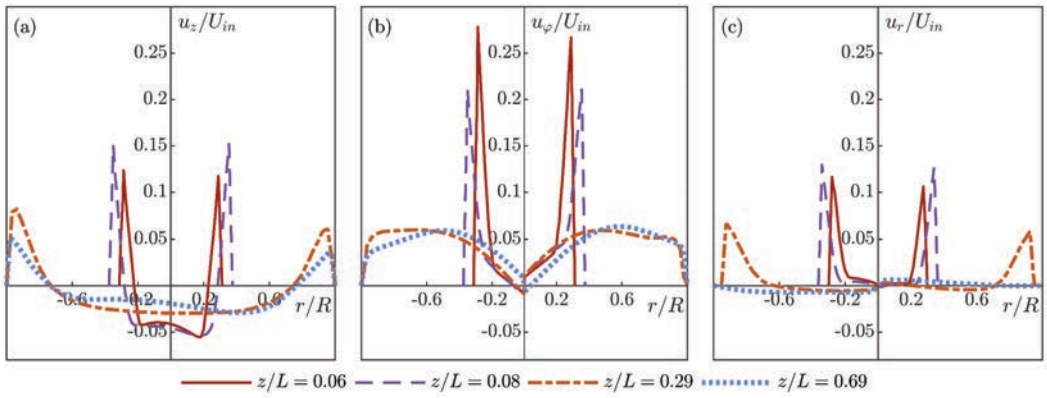

Figure 4: Mean air velocity profiles, as calculated with CFD, of the (a) axial, u_z, (b) tangential, u_φ, and (c) radial, u_r, components, normalised by the inlet velocity, U_{in}, at four axial cross-sections through the receiver for values of $\dot{V}_{air}$ = 104 slpm and D_{in} = 6 mm.

2.4 Key non-dimensional parameters

The key non-dimensional parameters influencing the isothermal multi-phase flow within the solar vortex receiver are the Reynolds number, *Re*, the Stokes number, *Sk*, and the Froude number, *Fr*. The air flow rates have been chosen to ensure that the inlet jet (with constant inlet jet diameter) is always in the turbulent regime ($Re_{in} = \rho_{air} U_{in} D_{in} / \mu_{air} > 8000$). This ensures relevance to industrial scale operation of the device. However, the Stokes and Froude numbers are systematically varied.

The Stokes number, which characterises how closely a particle will follow the gas streamlines through the receiver, is calculated for a given particle size at a given zone in the chamber as follows:

$$Sk = \frac{\rho_p d_p^2 U_f}{18 \mu_{air} D_f}, \tag{6}$$

where ρ_p is the particle density, d_p is the particle diameter, μ_{air} is the air dynamic viscosity, U_f is the characteristic fluid velocity scale of the flow at a given zone in the chamber and D_f is the characteristic fluid length scale of the flow at a given zone in the chamber. These zones (shown in Figure 2) are the inlet flow, the conical and the cylindrical sections of the receiver, the corner at the cone-cylinder intersection, and the outlet flow, of which the corresponding U_f and D_f values are presented in Table 3. The characteristic velocities within the receiver are taken to be the maximum tangential velocity of the air flow field in the *z*/*L* plane, as calculated with CFD (and shown in Figure 4b), while the characteristic length scales are taken to be the receiver diameter at the relevant *z*/*L* plane. For the Stokes number evaluated at the receiver outlet, the nominal outlet velocity was used, while the characteristic length scale was taken to be two times the outlet diameter. The outlet flow, at which point the vortex flow contracts to exit the receiver, features a range of velocity and length scales. However, for simplicity an average length scale of $2D_{out}$ is used to evaluate the Stokes number at the outlet, based on estimates of the gas flow field with the CFD model. Likewise, the flow tends towards the nominal outlet velocity, $U_{out} = \dot{V}_{air}/A_{out}$, so this is the single value used to evaluate Sk_{out}. Although the exact calculated values of Sk_{out} will differ from those of the actual flow, the residence time trends presented as a function of Sk_{out} are expected to be reliable.

The Froude number characterises the relative importance of the inertial centrifugal force ($F_{cent} = m_p U_\varphi^2 / R$) acting on a particle due to the circular motion of the two-phase vortex flow compared to that of the external gravitational field ($F_g = m_p g$). The Froude number is calculated at a given zone in the chamber as the ratio of these two forces, according to:

$$Fr = \frac{U_\varphi^2}{gR}, \tag{7}$$

where g is the standard acceleration due to gravity, U_φ is the characteristic tangential velocity of the flow at a given zone in the chamber and R is the characteristic radius of the circular motion of the two-phase flow at a given zone in the chamber. The zones (shown in Figure 2), for which the Froude number is evaluated, are the conical and the cylindrical sections of the receiver, together with the corner at the cone-cylinder intersection. The values of U_φ and R used in each of these zones are presented in Table 3. For simplicity, the Froude numbers presented here are considered to be independent of particle size. This is because U_φ is estimated from the air flow field only without accounting for the slip between the particles and the air phase. This implies that the Froude numbers overestimate slightly the influence of inertial forces because the tangential velocity of the particles will be less than that of the air phase. This overestimate is greatest for larger particles, due to their greater amount of slip, and is estimated from CFD to be approximately $u_{p,\varphi} \approx 0.8 u_\varphi$. That is, *Fr* is over-estimated by up to 36% by ignoring the slip velocity in Equation (7). Nevertheless, the relative trends in *Fr* are expected to be reliable.

3 Results

3.1 Measurements of the particle RTD

Figure 5 presents four measured particle RTDs within the SEVR for particle diameter d_p = 80 µm and inlet velocities in the range U_{in} = 25.4 – 41.3 m/s with constant inlet diameter, D_{in} = 6 mm, so that $U_{in} = \dot{V}_{air} / (2 \times (\pi/4) \times D_{in}^2)$. The corresponding nominal air residence times are in the range $\tau_{nom} = V_r / \dot{V}_{air}$ = 2.4 – 3.9 s. The distributions have been smoothed for clarity with a moving point average spanning 0.125 s of measured data. Each RTD curve can be described qualitatively to rise quickly to a maximum within 2 seconds of residence time and then to decrease more slowly. For each case also, a significant proportion of particles have a residence time much longer than the peak value. That is, the distributions are positively skewed. The slope of the initial increase to a maximum $E(t)$ value increases with U_{in} (and lower τ_{nom}), while the length of the tail of the distribution increases with lower U_{in} (and higher τ_{nom}), suggesting significant particle recirculation within the SEVR, particularly for lower flow rates and inlet velocities. It can additionally be noted that the U_{in} has a similar influence on the particle RTD in the SEVR to that of the superficial gas velocity in the riser of a square cross-section fluidised bed, whose particle RTDs bear a resemblance to those of the SEVR (Harris et al., 2003).

Table 3: The characteristic velocity and length scales used to evaluate the Stokes and Froude numbers in various zones of the receiver in the present study. The location of these zones within the receiver are shown in Figure 2.

Zone	***Sk***		***Fr***	
	Velocity, U_f	**Length, D_f**	**Velocity, U_φ**	**Length, R_{zone}**
Inlet (z/L = 0 – 0.04)	$U_{in} = \dot{V}_{air}/2A_{in}$	D_{base}	-	-
Cone (z/L = 0.04 – 0.29)	$u_{\varphi,max}$ in z/L plane (estimated with CFD)	D_{cone}	$u_{\varphi,max}$ in z/L plane (estimated with CFD)	$D_{cone}/2$
Cone-cylinder corner (z/L = 0.29)	$u_{\varphi,max}$ in z/L plane (estimated with CFD)	D_c	$u_{\varphi,max}$ in z/L plane (estimated with CFD)	$D_c/2$
Cylinder (z/L = 0.29 – 1)	$u_{\varphi,max}$ in z/L plane (estimated with CFD)	D_c	$u_{\varphi,max}$ in z/L plane (estimated with CFD)	$D_c/2$
Outlet (z/L = 0.85)	$U_{out} = \dot{V}_{air}/A_{out}$	$2D_{out}$	-	-

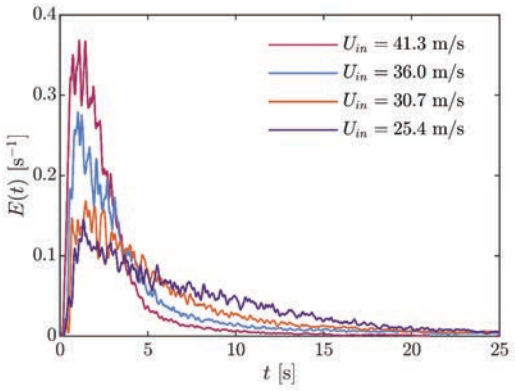

Figure 5: Measured particle RTDs in the SEVR for particle diameter d_p = 80 µm and inlet velocities in the range U_{in} = 25.4 – 41.3 m/s with constant inlet diameter, D_{in} = 6 mm, so that $U_{in} = \dot{V}_{air} / (2 \times (\pi/4) \times D_{in}^2)$. The corresponding nominal air residence times are in the range $\tau_{nom} = V_r/\dot{V}_{air}$ = 2.4 – 3.9 s. The distributions have been smoothed for clarity with a moving point average spanning 0.125 s of measured data.

Figure 6 presents the measured particle RTDs in the SEVR for three values of outlet Stokes number, Sk_{out}, and two values of inlet velocity U_{in} = 30.7 and 41.3 m/s, each for the case of a constant inlet diameter, D_{in} = 6 mm. It can be seen that, for a given inlet velocity, the values of Sk_{out} scale with d_p^2 (here, d_p = 20, 40 and 80 µm), while, for a given particle size, Sk_{out} scales with U_{in}, according to Equation (6) and Table 3. For U_{in} = 30.7 m/s (Figure 6a) it can be seen that an increase in Sk_{out} causes both a shift in the RTD to longer residence times and a broadening of the distribution. Quantitatively, the increase in Sk_{out} from 1.21 to 19.44 results in an increase in $\bar{\tau_p}$ from 2.59 to 6.46 s and an increase in $\tau_{p,90}$ from 5.50 to 15.17 s.

Figure 6b presents the case with higher inlet velocity (U_{in} = 41.3 m/s). It can be seen that the particle residence times are, on average, shorter than the lower velocity case (Figure 6a) and also that Sk_{out} has a weaker effect on the RTD. That is, the RTDs measured with the three values of d_p are more similar to each other for U_{in} = 41.3 m/s than is the case for U_{in} = 30.7 m/s. More specifically, an increase in Sk_{out} from 1.64 to 26.16 only increases $\bar{\tau_p}$ from 1.75 to 2.21 s and $\tau_{p,90}$ from 3.52 to 4.21 s.

Table 4 presents the Stokes and Froude numbers of the two-phase flow within the SEVR, as calculated with the length and velocity scales presented in Table 3, for three particle diameters, d_p = 20, 40 and 80 µm, and the two values of inlet velocity presented in Figure 6, U_{in} = 30.7 and 41.3 m/s. These are all evaluated in the five zones of the receiver: the inlet, the cone, the corner at the cone-cylinder intersection, the cylinder section and the receiver outlet (shown in Figure 2). It can be seen for U_{in} = 30.7 m/s (Table 4a), that the Stokes numbers for d_p = 20 µm are < 1 through the conical and cylindrical sections of the receiver, indicating that the particles approach being flow-tracers. In contrast, for d_p = 80 µm, Sk_{cone} > 1 in the lower regions of the cone but Sk_{cyl} < 1 in the cylindrical section. This implies that the larger particles will be preferentially distributed toward the wall in the cone but will become more uniformly distributed in the cylindrical section. At the receiver outlet, the larger particles have Sk_{out} >> 1 so that they tend not to follow the fluid through the strong gradients associated with the radial exit, but rather to be preferentially retained within the receiver. In contrast, the small particles with lower Sk_{out} will be more likely to leave with the fluid. This highlights the importance of the outlet Stokes number in controlling the particle residence time, as is shown in Figure 6a and has previously been hypothesised by Chinnici et al. (2015).

It can also be seen, for the case of U_{in} = 30.7 m/s (Table 4a), that the Froude number of the vortex flow decreases from Fr_{cone} = 299.5 in the conical section of the receiver to Fr_{corner} = 3.6 and Fr_{cyl} = 3.8 at the cone-cylinder corner and in the cylindrical section of the receiver, respectively. This indicates that the flow transitions from being highly dominated by the inertial centrifugal force as the vortex is introduced at the bottom of the cone to a flow regime in which the external gravitational field plays a more significant role as the flow undergoes an expansion through the cone. This expansion causes the air tangential velocity at the cone-cylinder corner and in the cylindrical section to be relatively low (~2 m/s) and implies that the SEVR operates with relatively low swirl compared with other swirl devices such as a cyclone particle separator (Hoffmann and Stein, 2007).

Table 4b shows that, for U_{in} = 41.3 m/s, particles exhibit higher Stokes numbers than those of the lower velocity case. However, despite the increase in Stokes numbers through the receiver for each of the particle sizes, the increase in U_{in} from 30.7 to 41.3 m/s causes each of the RTDs presented in Figure 6b to be shifted to shorter residence times, as compared with those presented in Figure 6a. Furthermore, for constant U_{in} = 41.3 m/s, the increase in Sk_{out} from 1.64 to 26.16 – an increase by the same factor as that shown in Figure 6a – has a significantly weaker influence on the residence time to that of the lower velocity case. This case of higher inlet velocity corresponds to increased Froude numbers at the cone-cylinder corner and in the cylinder, Fr_{corner} = 6.6 and Fr_{cyl} = 6.9. The increase by a factor of 1.8 relative to the lower velocity case indicates a significantly increased importance of the centrifugal inertial force in the cylindrical section of the receiver relative to that of external gravitational field. These results show that residence time depends in a complex way not only on Stokes number, which scales non-linearly with d_p^2, but also on Froude number, which scales non-linearly with U_{in}^2.

Figure 7 presents three statistical measures of the particle RTDs for each of the conditions shown in Table 1b with a constant inlet diameter, D_{in} = 6 mm. It can be seen from Figure 7a, which presents $\bar{\tau_p}$ as a function of Fr_{cyl} and U_{in}, that increasing Fr_{cyl} causes a monotonic decrease in $\bar{\tau_p}$ for all d_p. For $U_{in} \leq$ 30.7 m/s, it can be seen that the 80 µm sized particles have mean residence time significantly longer than that of the 40 µm sized particles, $\bar{\tau}_{p,80\mu m}/\bar{\tau}_{p,40\mu m} \sim 2$. However, as Fr_{cyl} increases, the values of $\bar{\tau_p}$ for all d_p converge to a value $\bar{\tau_p} \sim 2$ s with Fr_{cyl} = 6.9 and U_{in} = 41.3 m/s. This shows that there are two regimes of two-phase flow present in the SEVR, as mentioned previously. In one regime, the particle residence time of larger particles is significantly longer than that of smaller particles, while in the other, particle size has less of an influence on particle residence time.

More insight into the explanation of the two regimes of operation can be found from Figure 7b, which presents $\bar{\tau_p}$ as a function of Sk_{out}, with lines of constant Fr_{cyl}. It can be seen that, for Fr_{cyl} < 4, an increase in Sk_{out} causes an increase in $\bar{\tau_p}$. This effect has been discussed previously and is attributed to the greater inertia of large particles with high Sk_{out} having a greater likelihood of being retained within the chamber and not exiting through the radially-oriented outlet. However, an additional mechanism is apparent here, such that, as the Froude number of the vortex flow increases, the influence of Sk_{out} on $\bar{\tau_p}$ becomes weaker. This highlights the importance of the external gravitational field in influencing the particle residence for the selected orientation.

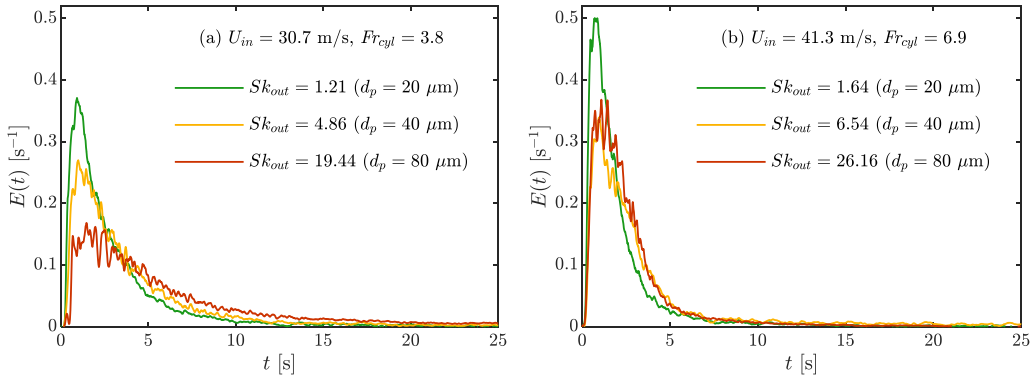

Figure 6: Measured particle RTDs in the SEVR for three values of Sk_{out} (three particle diameters, d_p = 20, 40 and 80 μm), with constant inlet diameter, D_{in} = 6 mm, and two values of inlet velocity and Froude number: (a) U_{in} = 30.7 m/s, Fr_{cyl} = 3.8; and (b) U_{in} = 41.3 m/s, Fr_{cyl} = 6.9. The values of Sk_{out} and Fr_{cyl} scale with U_{in} and U_{in}^2, respectively, according to Equations (6) and (7) and Table 3. The distributions have been smoothed for clarity with a moving point average spanning 0.125 s of measured data.

Table 4: The Stokes and Froude numbers of the two-phase flow evaluated at various zones within the SEVR for three particle diameters, d_p = 20, 40 and 80 μm and two values of inlet velocity: (a) U_{in} = 30.7 m/s; and (b) U_{in} = 41.3 m/s.

(a) U_{in} = 30.7 m/s				
Zone	***Sk***			***Fr***
	d_p = 20 μm	**d_p = 40 μm**	**d_p = 80 μm**	
Inlet (at z/L = 0.02)	0.95	3.78	15.13	-
Cone (at z/L = 0.06)	0.21	0.85	3.40	299.5
Corner (at z/L = 0.29)	0.01	0.06	0.23	3.6
Cylinder (at z/L = 0.69)	0.01	0.06	0.23	3.8
Outlet (at z/L = 0.85)	1.21	4.86	19.44	-
(b) U_{in} = 41.3 m/s				
Zone	***Sk***			***Fr***
	d_p = 20 μm	**d_p = 40 μm**	**d_p = 80 μm**	
Inlet (at z/L = 0.02)	1.27	5.09	20.36	-
Cone (at z/L = 0.06)	0.29	1.14	4.58	542.8
Corner (at z/L = 0.29)	0.02	0.08	0.30	6.6
Cylinder (at z/L = 0.69)	0.02	0.08	0.31	6.9
Outlet (at z/L = 0.85)	1.64	6.54	26.16	-

In the low Froude number regime (Fr_{cyl} < 4), the significantly longer $\overline{\tau_p}$ of larger particles (high Sk_{out}) can be explained by the expansion of the vortex flow through the cone of the SEVR, which results in the particles losing a significant fraction of their kinetic energy as they reach the cone-cylinder corner and the cylindrical section of the receiver. The relatively low Froude number of the flow also implies that particles are not entirely distributed close to the wall of the receiver, but that they can also be entrained into the central reversed flow zone and recirculated to the bottom of the cone. That is, for the receiver orientation considered here, gravity serves to recirculate larger particles into the most intense part of the vortex flow. This recirculation mechanism augments the trend for larger particles to be preferentially retained within the receiver and have longer residence time than smaller particles, which follow gas streamlines more closely. This is termed here the *Froude-Stokes* regime of SEVR operation, characterised by low Froude numbers and a strong influence of Sk_{out} on particle residence time.

As Fr_{cyl} increases, it is apparent from Figure 7b that the influence of Sk_{out} in increasing $\overline{\tau_p}$ becomes weaker. This can be explained by the increasing importance of the inertial centrifugal force (both at the cone-cylinder corner and in the cylindrical section) acting to maintain particles in vortex suspension flow preferentially distributed near to the walls of the cylindrical chamber. In this case, Fr_{cyl} scales with U_{in}^2, such that an increase in U_{in} from 20.0 to 41.3 m/s causes an increase in the strength of the centrifugal inertial force relative to that of gravity by a factor of 4.2. Therefore, although the larger particles are less likely to exit the radial outlet than the smaller particles due to their higher Sk_{out}, they are also less likely to enter the central reversed flow zone. This serves to decrease the mean residence time of all particle sizes within the receiver as a relatively smaller amount of particle recirculation is observed, with particles (of all sizes considered here) being retained near to the walls, and thus near to the SEVR outlet. This regime of SEVR operation, characterised by high Froude numbers and a weak influence of Sk_{out} on particle residence time, is termed here the *cyclonic* regime because particles tend to be centrifuged near to the wall of the receiver, as is the case in particle cyclones.

Figure 7c presents $\tau_{p,90}$ as a function of Fr_{cyl} and U_{in}, from which it can be seen that $\tau_{p,90}$ follows a similar trend to that of $\overline{\tau_p}$. It can be seen that, in the *Froude-Stokes* regime with Fr_{cyl} < 4, $\tau_{p,90}$ is greater for larger particle sizes, with a maximum of $\tau_{p,90}$ = 20.8 s (compared with $\overline{\tau_p}$ = 9.7 s) for d_p = 80 μm and Fr_{cyl} = 1.6. That 10% of particles have residence more than twice as long as the mean residence time highlights the significant recirculation of large particles in this low Froude number regime of operation. With increasing Fr_{cyl}, the values of $\tau_{p,90}$ for each d_p converge to ~ 4 s, corroborating the finding that in the *cyclonic* regime of operation, Sk_{out} has a weaker influence on the behaviour of particles within the SEVR.

Figure 7d presents the dependence of σ_p^2 on Fr_{cyl} and U_{in}. For d_p = 80 μm, the σ_p^2 values are relatively consistent in the range 0.43 – 0.62. These values indicate that the mixing pattern of larger particles within the SEVR is intermediate between those of an ideal continuously-stirred tank reactor (CSTR), for which σ_p^2 = 1, and an ideal plug flow reactor (PFR), for which σ_p^2 = 0 (Fogler, 2006; Levenspiel, 1999). In addition, over the range of values of Fr_{cyl}

presented, there is a slight decrease in σ_p^2 with increasing Fr_{cyl}, which can be described as a slight trend towards more uniform plug flow with increasing Fr_{cyl}. The larger values of σ_p^2 in the range 0.77 – 0.90, for d_p = 80 µm and 3.8 ≤ Fr_{cyl} ≤ 5.2, can be attributed to the longer tails of the measured RTD for these cases (relatively longer $\tau_{p,90}$ in Figure 7c), which increase the variance of the distribution relative to the mean. For d_p = 40 µm a more significant decrease in σ_p^2 with increasing Fr_{cyl} is visible, indicating that the mixing pattern shifts from close to perfectly mixed with Fr_{cyl} = 1.63 and σ_p^2 = 0.86 to a more uniform flow with Fr_{cyl} = 6.9 and σ_p^2 = 0.46. A similar reduction in the extent of mixing is visible for d_p = 20 µm. Therefore, it can be said that, as the operation of the device moves from the *Froude-Stokes* regime towards the *cyclonic* regime with increasing Fr_{cyl}, there is a reduction in σ_p^2 and, hence, a reduction in the extent of mixing in the SEVR. This is consistent with findings that the *Froude-Stokes* regime is characterised by large-scale particle recirculation within the receiver, while the *cyclonic* regime features minimal particle recirculation limited to the cylindrical section of the receiver.

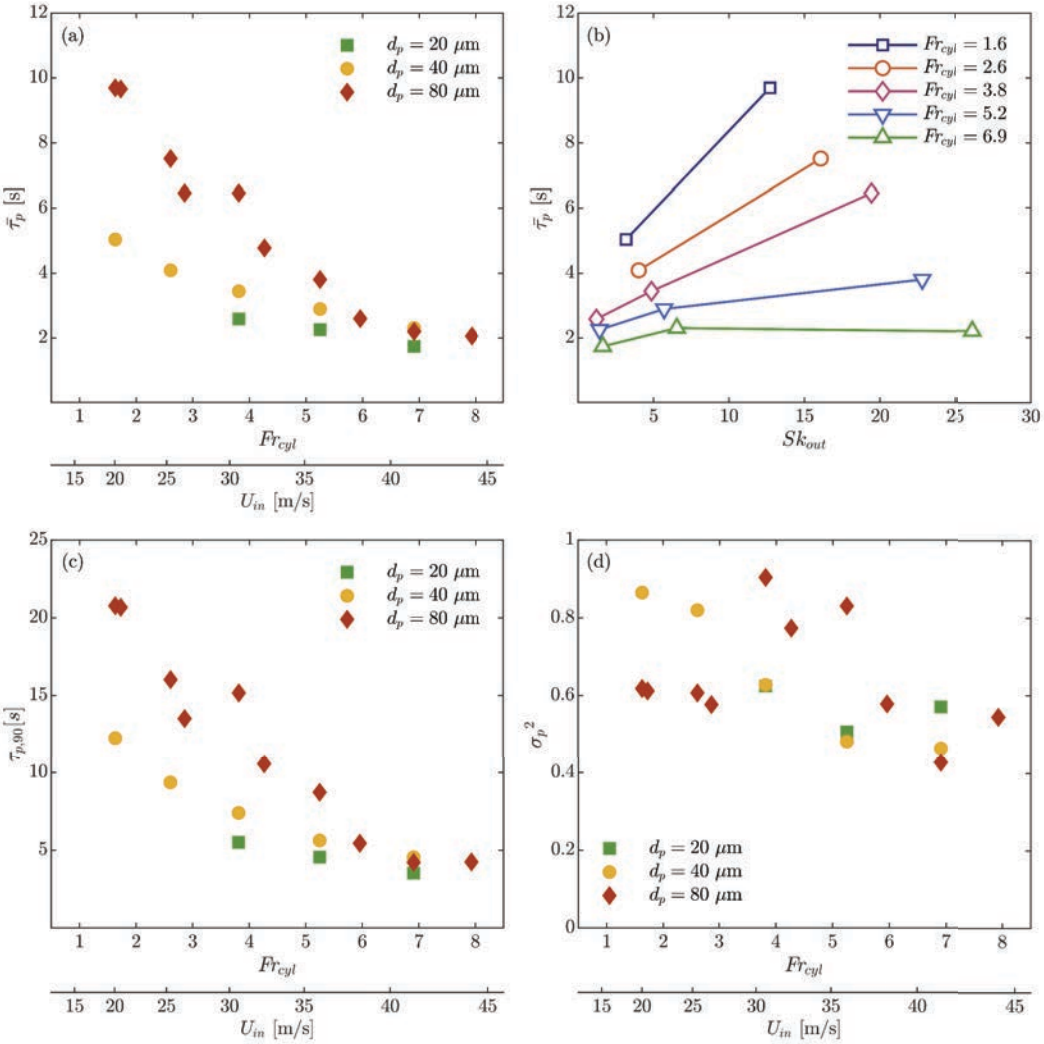

Figure 7: The statistical measures of the particle RTDs for three different particle diameters, d_p = 20, 40 and 80 µm, and inlet velocities in the range U_{in} = 20.0 – 44.2 m/s with constant inlet diameter, D_{in} = 6 mm, so that $U_{in} = \dot{V}_{air} / (2 \times (\pi/4) \times D_{in}^2)$. Presented are: (a) the mean particle residence time, $\bar{\tau}_p$, as a function of Fr_{cyl} and U_{in}; (b) the mean particle residence time, $\bar{\tau}_p$, as a function of Stokes numbers evaluated at the outlet, Sk_{out}, with lines of constant Fr_{cyl}; (c) the 90th percentile particle residence time, $\tau_{p,90}$, as a function of Fr_{cyl} and U_{in}; and (d) the normalised variance, σ_p^2, as a function of Fr_{cyl} and U_{in}.

Figure 8 presents $\bar{\tau_p}$ as a function of Fr_{cyl}, for one particle diameter, d_p = 80 µm, and three different values of inlet diameter, D_{in} = 5, 6 and 7.5 mm. It can be seen that, similarly to the trend for D_{in} = 6 mm, $\bar{\tau_p}$ decreases monotonically with increasing Fr_{cyl} for both D_{in} = 5 and 7.5 mm. This is consistent with the previous deduction that, as Fr_{cyl} increases, the two-phase flow within the SEVR moves towards a *cyclonic* regime of operation with shorter residence times. It can also be seen that, for a given value of Fr_{cyl}, an increase in D_{in} causes a decrease in $\bar{\tau_p}$. This is attributed to the higher air volumetric flow rate required to generate a given value of Fr_{cyl} with the larger D_{in}. That is, as D_{in} increases, velocities within the receiver decrease. The effect of increasing volumetric flow rate of air to decrease the nominal residence time is well known, according to $\tau_{nom} = V_r/\dot{V}_{air}$. Indeed, in this case, the higher volumetric flow rates of air, which transports particles through the receiver, serves also to decrease the measured particle residence time, as well as the nominal value.

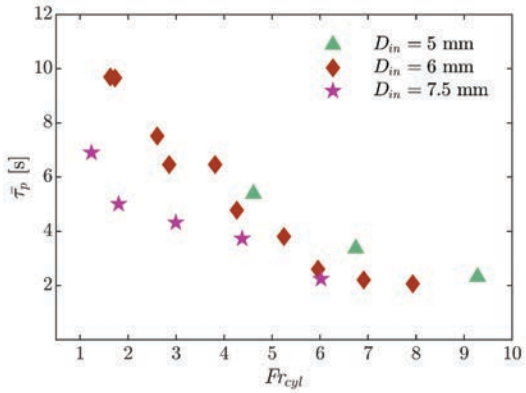

Figure 8: The mean particle residence time, $\bar{\tau_p}$, as a function of Fr_{cyl}, for one particle diameter, d_p = 80 µm, and three different values of inlet diameter, D_{in} = 5, 6 and 7.5 mm.

3.2 Compartment model analysis

Figure 9 presents the dimensionless particle RTDs, $E(\theta)$, for two different particle sizes, d_p = 20 and 80 µm, and two values of Fr_{cyl} (with constant D_{in} = 6 mm). These Froude numbers are chosen because they represent the *Froude-Stokes* and the *cyclonic* regimes identified above (the low and high Froude number regimes, respectively). Also shown in Figure 9 are the analytical RTDs derived from the compartment modelling approach of Levenspiel (1999) to describe the experimental RTDs. In each of the experimental distributions, $E(\theta)$ remains at zero for short dimensionless times, δ, defined as the ratio of the time for which the pulse response is zero to the mean particle residence time. After this delay time, $E(\theta)$ increases rapidly to a maximum value, and then decreases at a slower rate to zero, as described above.

Figure 9a presents the dimensionless particle RTDs for d_p = 80 µm and Fr_{cyl} = 2.6 and 6.9, corresponding to the two different particle behaviour regimes. For the *Froude-Stokes* regime (Fr_{cyl} = 2.6), $E(\theta)$ is well described by a step increase to a maximum after a short delay, δ, followed by an exponential decay. This corresponds to the RTD of two ideal reactors in series, in which the first is a small PFR of residence time δ and the second is a CSTR. The resulting analytical equation of $E(\theta)$ for the *Froude-Stokes* regime can be expressed as:

$$E(\theta)|_{Froude\text{-}Stokes} = \frac{1}{1-\delta} e^{\left(-\frac{\theta-\delta}{1-\delta}\right)} u(\theta-\delta), \qquad (8)$$

where $u(\theta-\delta)$ is the Heaviside function. This function, $E(\theta)|_{Froude\text{-}Stokes}$, is presented in Figure 9a.

Conversely, for the *cyclonic* regime (Fr_{cyl} = 6.9), the rate of increase that follows the similar initial dimensionless delay δ is lower, as is the peak, with a broader dimensionless RTD, which is also non-symmetrical. The tanks-in-series model can be used to describe this behaviour (Levenspiel, 1999), where the experimental curves are modelled with two tanks of different volume connected in series following an initial delay. The analytical equation of $E(\theta)$ for the *cyclonic* regime can therefore be expressed as:

$$E(\theta)|_{Cyclonic} = \frac{1+\varepsilon}{(\varepsilon-1)(1-\delta)}\left[e^{-\frac{(\theta-\delta)(1+\varepsilon)}{\varepsilon(1-\delta)}} - e^{-\frac{(\theta-\delta)(1+\varepsilon)}{(1-\delta)}}\right] u(\theta-\delta), \qquad (9)$$

where ε represents the ratio of the space-times of the two tanks and $u(\theta-\delta)$ is the Heaviside function. This function, $E(\theta)|_{Cyclonic}$, is also presented in Figure 9a. It is noteworthy that, as $\varepsilon \to 0$, Equation (9) collapses to Equation (8), demonstrating that the two regimes of operation are closely related and have potential to be combined into a unified compartment model to describe both regimes. As a whole, the particle RTDs in the SEVR deviate slightly from the perfectly-mixed flow pattern, as also confirmed by the values of σ_p^2 plotted in Figure 7d.

Figure 9b presents dimensionless particle RTDs for d_p = 20 µm and Fr_{cyl} = 3.8 and 6.9, also corresponding to the *Froude-Stokes* and *cyclonic* particle behaviour regimes, respectively. As for the larger particles, the experimental RTDs for the *Froude-Stokes* regime (Fr_{cyl} = 3.8) can be described by a small PFR (represented by the delay δ) connected in series with a CSTR (Equation 8), as illustrated in Figure 9b. For the *cyclonic* regime (Fr_{cyl} = 6.9) the reactor can be schematized similarly to the case with larger particle size, as two CSTRs in series with a delay (Equation 9). Altogether, Figure 9 highlights that the same analytical compartment model can be used to describe $E(\theta)$ for both particle sizes, suggesting that for a given particle behaviour regime, the same mixing pattern characterises the particle RTD behaviour of particles of all sizes. Further to this result, the ideal reactor schemes applied here to the two regimes of operation and described by Equations (8) and (9) were also found to hold for the experimentally measured particle RTDs with alternative inlet diameters, D_{in} = 5 and 7.5 mm, and the fixed particle size d_p = 80 µm, as presented in Figure 8.

Figure 10 presents the schematic representation of the unified compartment model describing the particle RTD behaviour of the SEVR in both the *Froude-Stokes* and the *cyclonic* regimes of operation (the low and high Froude number regimes, respectively). This compartment model is composed of a PFR followed by two CSTRs in series with a degree of back-mixing between them. For the *Froude-Stokes* regime, after the short delay (represented by the PFR), the back-mixing between the two CSTRs is active, so that the particle mixing behaviour of the two CSTRs can be considered the same as a single CSTR (Fogler, 2006), as is consistent with Equation (8). For the *cyclonic* regime, the same schematic is used to represent the SEVR. However, in this case only a small or negligible extent of back-mixing occurs between the two CSTRs, so that two independent mixing volumes are established. The volumetric ratio of the two CSTRs establishes the relative proportioning of residence time spent in each zone, as is consistent with Equation (9).

Table 5 presents 15 cases for which the particle RTDs were measured, together with the corresponding values of the parameters δ and ε used in Equations (8) and (9) for the compartment modelling of the two identified regimes of operation. Also shown is the coefficient of determination, R^2, between the experimental and analytical RTDs. It can be seen that δ varies between 0.055 and 0.13, which means that the ratio between the space-time of the PFR component and the total reactor space-time ranges between 5.5 and 13%. This small delay is likely due to the time needed for the particles to fulfil the reactor inventory. It is likely that in a practical reactor vessel, even in mixed flow conditions, some dispersion will occur also, resulting in a delay in the pulse response. Furthermore, for a given D_{in}, δ decreases with an increase in U_{in}, indicating that with higher inlet velocities the time to fulfil the reactor inventory reduces. The value of ε is equal to zero for all D_{in} and d_p in the *Froude-Stokes* (low Froude number) regime and then increases with U_{in} in the *cyclonic* (high Froude number) regime. Given that the

SEVR comprises a conical and a cylindrical section, the finding that $\varepsilon = 0$ for the *Froude-Stokes* regime indicates that the two sub-volumes behave as a single mixing volume in this regime. This is consistent with the deduction that, in the *Froude-Stokes* regime, particles (particularly those with large Sk_{out}) are recirculated via the central reversed flow zone that spans both the cylindrical and conical sections of the device. The transition to the *cyclonic* regime, and higher values of ε is analogous to a reduction in the extent of particle recirculation through the entire SEVR device. Values of ε up to and above 5 highlight that particles spend less time in the conical zone of the SEVR, being quickly entrained into the cylindrical zone, where the majority of the particles' residence time is spent.

The coefficient of determination values in the range $R^2 = 0.95 - 0.99$ (Table 5) demonstrate good agreement between the experimental and analytical dimensionless RTDs. The lowest values of R^2 are predominantly for the cases with lower U_{in} and can be attributed to the presence of small peaks before the primary peak. This could be related to wall-related interactions, such as adhesion/re-entrainment. However, the area bounded by these peaks is always less than 1% of the total area bounded by the RTD curve, so that these effects are small here.

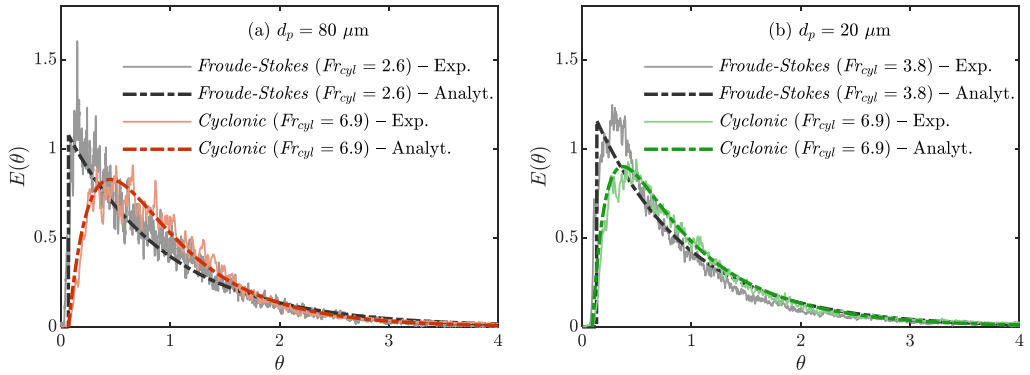

Figure 9: The experimentally measured dimensionless particle RTDs and functions of their corresponding analytical compartment models. Presented are distributions representing the *Froude-Stokes* and the *cyclonic* regimes (the low and high Froude number regimes, respectively) for particle sizes (a) d_p = 80 µm; and (b) d_p = 20 µm. The functions of the analytical distributions shown here are given in Equations (8) and (9), respectively.

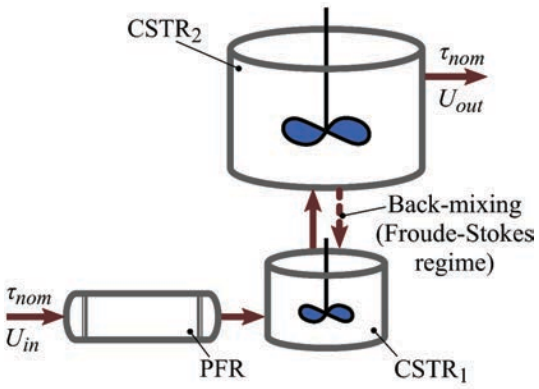

Figure 10: Schematic representation of the unified compartment model describing the particle RTD behaviour of the SEVR in both the *Froude-Stokes* and the *cyclonic* regimes (the low and high Froude number regimes, respectively) as a combination of an ideal plug flow reactor (PFR) and continuously-stirred tank reactors (CSTRs).

Table 5: The operational details and corresponding parameters used in Equations (8) and (9) to describe the measured particle RTDs with analytical compartment models, together with the coefficient of determination between experimental and analytical RTDs.

D_{in} [mm]	d_p [µm]	Fr_{cyl}	U_{in} [m/s]	Particle behaviour regime	δ	ε	R^2
6	80	2.6	25.4	*Froude-Stokes*	0.085	0	0.96
		5.2	36.0	Transitional	0.080	0.1	0.96
		6.9	41.3	*Cyclonic*	0.070	3	0.98
		7.9	44.2	*Cyclonic*	0.070	5.5	0.98
6	20	3.8	30.7	*Froude-Stokes*	0.13	0	0.95
		5.2	36.0	*Cyclonic*	0.094	6	0.99
		6.9	41.3	*Cyclonic*	0.094	6	0.99
5	80	3.2	30.6	*Froude-Stokes*	0.076	0	0.96
		4.4	35.7	Transitional	0.071	0.01	0.95
		6.0	41.6	Transitional	0.070	0.12	0.96
		6.7	44.1	*Cyclonic*	0.070	6.5	0.96
7.5	80	3.0	25.3	*Froude-Stokes*	0.11	0	0.95
		4.4	30.6	Transitional	0.10	0	0.95
		6.0	35.8	Transitional	0.080	0.02	0.96
		8.1	41.5	*Cyclonic*	0.055	6.5	0.96

4 Discussion of key findings

Table 6 summarises the key features of the two regimes of particle behaviour identified in the present investigation, incorporating the experimental, numerical and compartment modelling analyses. Additionally, Figure 11 presents simplified representations of the behaviour of the SEVR deduced from the experimental and numerical analyses, including the three-dimensional flow-field within the SEVR (Figure 11a) and the predominant particle trajectories of operation in the *Froude-Stokes* and *cyclonic* regimes (Figure 11b and Figure 11c, respectively). It can be seen from Figure 11a that a key feature of the air flow field other than the main outer vortex flow is the central reversed flow zone. The response of the particles to the flow depends on their Stokes number, while the Froude number has an additional influence on the trajectories of particles within the SEVR device.

It can be seen from Table 6 that the boundary of the *Froude-Stokes* regime identified here is $Fr_{cyl} < 4$. In this behaviour regime small particles are preferentially distributed in regions of maximum tangential velocity through the receiver. As larger particles enter the receiver, they are directed toward the wall by their inertia, but then also become more uniformly distributed through the cylindrical section of the receiver. At the radial outlet, the larger particles are less likely than smaller particles to follow the strong flow gradients and, as a result, have longer residence time than small particles ($\bar{\tau}_{p,LP} > \bar{\tau}_{p,SP}$). It has however also been deduced that due to the low Froude number at the cone-cylinder corner and in the cylindrical section of the receiver, particles have a significant likelihood of entering the central reverse flow zone of the SEVR to be recirculated in the direction augmented by gravity into the most intense part of the vortex flow. For this reason, experiments show that the lower the Froude number, Fr_{cyl}, the greater the influence of the Stokes number, Sk_{out}, in increasing the particle residence time, τ_p. These predominant particle trajectories of small particle following gas streamlines and large particles undergoing recirculation via the central reversed flow zone are illustrated in Figure 11b. It is worth noting that this mechanism provides validation to that proposed by Chinnici et al. (2015) in a previous numerical investigation of a SEVR configuration similar to that investigated here. However, the role of gravity in recirculating large particles in the low Froude number regime has been identified here. In terms of compartment models, the experimental particle RTDs can be closely described by a small plug flow reactor in series with two CSTRs with back-mixing so that the mixing behaviour of the two CSTRs can be considered to be that of a single larger CSTR. This back-mixing accounts for the recirculation phenomena that is characteristic of the low Froude number particle behaviour regime and occurs predominantly with larger particles.

Table 6: Summary of the key features of the two particle behaviour regimes for the SEVR in a vertical orientation, including details from experimental, numerical and theoretical analyses

Regime	Boundary	Experimental findings	Compartment model descriptions	Key features
Froude-Stokes (low Froude number)	$Fr_{cyl} < 4$	• Particles with large Sk_{out} preferentially retained within SEVR, longer τ_p • Lower inertial centrifugal force allows particles to enter central recirculation zone. • Gravitational field in vertical orientation augments particle recirculation mostly for larger particles, which have longer residence time.	• A small plug flow reactor in series with 2 CSTRs that have back-mixing.	• $\bar{\tau}_{p,LP} > \bar{\tau}_{p,SP}$ • $\tau_{p90,LP} >> \tau_{p90,SP}$
Cyclonic (high Froude number)	$Fr_{cyl} > 4$	• Sk_{out} has weak influence on τ_p. • Particles less likely to enter central recirculation zone due to large centrifugal inertial force.	• A small plug flow reactor in series with 2 CSTRs that have negligible back-mixing.	• $\bar{\tau}_{p,LP} \sim \bar{\tau}_{p,SP}$ • $\tau_{p90,LP} \sim \tau_{p90,SP}$

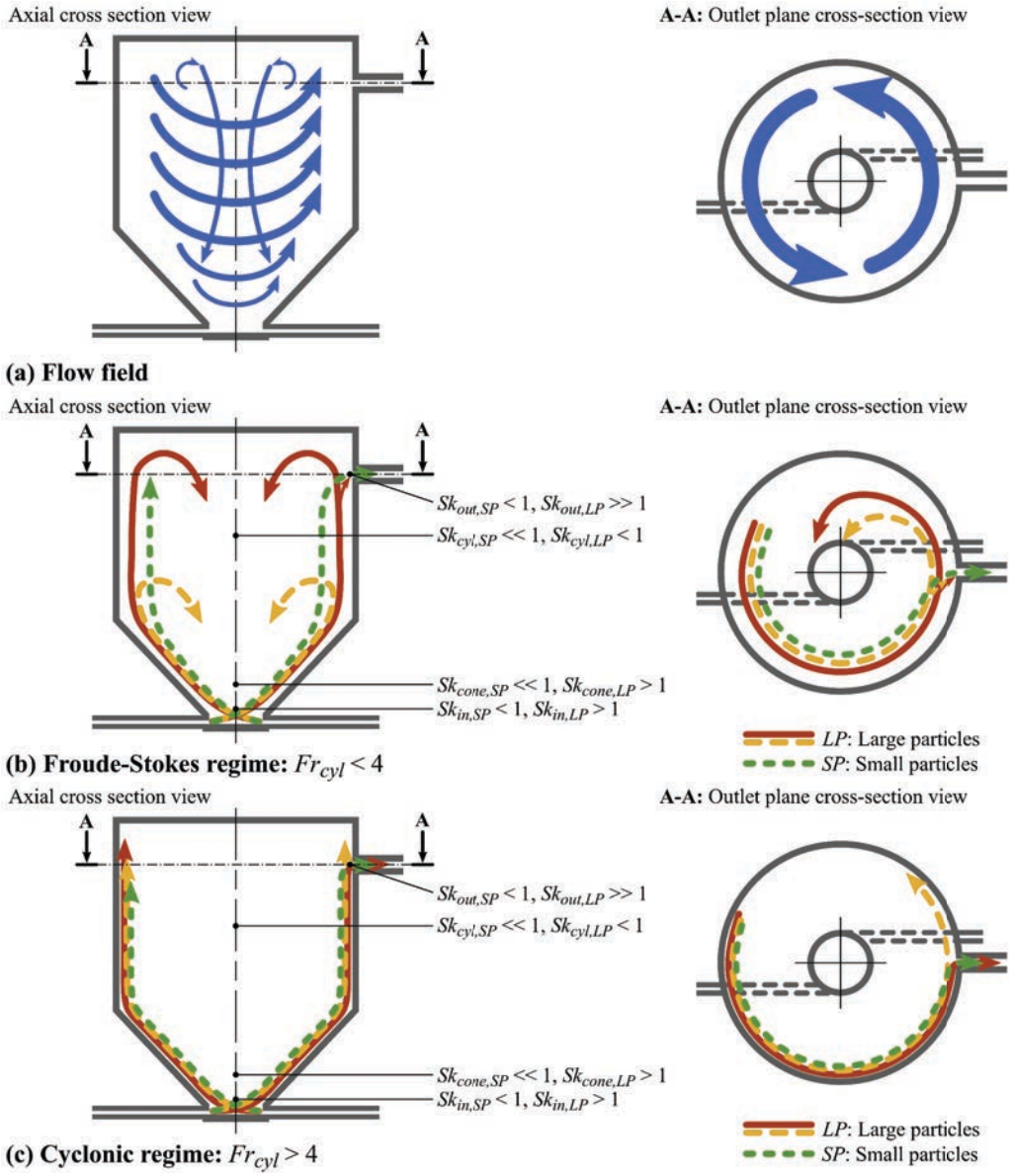

Figure 11: Simplified representations of the behaviour of the SEVR deduced from the experimental and numerical analyses, including (a) the three-dimensional flow-field within the SEVR; (b) the predominant particle trajectories of the *Froude-Stokes* regime; and (c) the predominant particle trajectories of the *cyclonic* regime. The trajectories of large (*LP*, red/yellow), and small (*SP*, green) particles are shown in axial and radial components through the receiver (left), and tangential and radial components at the exit plane $z/L = 0.85$ (right).

The higher Froude number regime has not been identified previously for this device, for which $Fr_{cyl} > 4$ (Table 6). This regime is characterised by a higher centrifugal inertial force acting on the particles (relative to the gravitational force) that distributes particles of all sizes near to the wall and prohibits particles from entering the central reversed flow zone as illustrated in Figure 11c. While Sk_{out} still has influence on the likelihood of particles leaving the receiver, the larger particles that are retained continue to circulate near to the wall of the receiver and therefore also near to the outlet. These large particles are more likely to exit the radially-oriented outlet than to enter the central reversed flow zone, thereby having shorter mean residence time than for the lower Froude number regime. This has the overall effect of significantly reducing the mean residence time of larger particles relative to those in the low Froude number regime, while also reducing the residence time of smaller particles to a lesser extent. The same compartment model configuration of a small plug flow reactor in series with two CSTRs applies to the experimentally measured RTDs of this high Froude number regime. Furthermore, for this case, only a small or negligible amount of back-mixing between the two CSTRs is required to closely describe the receiver operation. It should be emphasised that Figure 11b and c are a simplified representation of the most probable particle trajectories within the SEVR, although some particles will behave differently.

It is also instructive to compare the present device with a cyclone particle separator, for which the *Stokes-Froude* regime is typically not observed. The separation factor of a cyclone, which is analogous to the present definition of the Froude number, is typically greater

than 5 and often greater than 1000 (Cortés and Gil, 2007; Hoffmann and Stein, 2007). This gives further support for the deduction that the critical value separating the two regimes is $Fr_{cyl} \approx 4$. Nevertheless, it should be noted that the transition between the two regimes occurs over a range of Froude numbers around this critical value. Furthermore, the magnitude of the deduced critical value will be sensitive to the magnitude of the characteristic length and velocity scales, which have been estimated with a CFD model.

The wide variation in particle RTD characteristics across the two regimes of operation, as influenced by inlet velocity, air volumetric flow rate and particle size, suggests a high level of flexibility of operation of the SEVR technology. Typically, the time required to thermally process a particle will depend on its size. Therefore, the *Froude-Stokes* regime of operation, in which $\bar{\tau}_{p,LP} > \bar{\tau}_{p,SP}$, has potential for use in processing polydisperse groups of particles. The *Froude-Stokes* regime is also potentially advantageous to reactions in which the solid particles are destroyed (e.g. the solar gasification of solid fuel). This is because it is desirable that a large particle is preferentially retained within the reactor until it has completely reacted. As the particle reacts its size/density will reduce so that the particle becomes more likely to exit the reactor. Alternatively, for processes that require a uniform product quality (e.g. the calcination of alumina), particles should be processed with uniform residence time. The more uniform particle RTDs that were identified to be characteristic of the *cyclonic* regime of operation may be more suitable for such an application of the SEVR. Finally, for a SEVR operating in either particle behaviour regime, the residence time could potentially be altered by changing U_{in}, $\dot{V}_{air}$, which is advantageous in facilitating control in response to the natural variability of the solar resource.

5 Conclusions

A method for directly measuring the residence time distribution of the particle phase has been demonstrated in a laboratory-scale vortex-based solar particle receiver-reactor. The systematic assessment of the influence of particle size, inlet velocity, and air volumetric flow rate on the particle RTD has revealed two regimes of particle behaviour, a low Froude number regime, where Stokes number is also important, and a high Froude number regime, dominated by centrifugal inertial forces in a similar manner to cyclonic separators.

In the low Froude number regime of operation, termed the *Froude-Stokes* regime, the characteristic Froude number of the vortex within the cylindrical section of the receiver is less than four, i.e. $Fr_{cyl} < 4$. The characteristics of this regime of operation are:

- the Stokes number of the two-phase flow at the outlet from the device has the greatest influence on the residence time of particles. Increasing Stokes number increases the residence time of particles due to their greater inertia, particularly in the vicinity of the radially-oriented outlet, making them more likely to be recirculated within the vessel.
- the low Froude number implies that gravity is also important, which, for the vertical orientation, increases the likelihood that particles will be returned to the base of the vessel with the central reversed flow zone of the vortex.

Within the above regime, for a vertical orientation, both mechanisms work synergistically to preferentially increase the residence time of larger particles, relative to smaller particles.

The high Froude number regime of operation, termed the *cyclonic* regime, occurs for $Fr_{cyl} > 4$ and is characterised by the greater centrifugal inertial force acting on the particles. The characteristics of this regime of operation are:

- the centrifugal inertial force acting on the particles due to their tangential velocity is large enough to preferentially distribute particles near to the wall of the receiver. This keeps them out of the central reversed flow zone generated by the vortex.
- the close proximity of the particles to the outer wall means that particles are more likely to exit the receiver and have shorter residence time than if they are recirculated through the central reversed flow zone.

It was also found that, in both regimes of operation, an increase in the inlet diameter of the SEVR causes a decrease in residence time for a given value of Froude number. This is because the Froude number scales with velocity, so that increasing the diameter requires an increase in volumetric flow rate to maintain the Froude number, which decreases the nominal residence time of the transporting air phase.

It was also found that the particle residence time behaviour within the SEVR can be well described with a compartment model consisting of a small plug flow reactor followed by a series of two interconnected CSTRs. For operation in the *Froude-Stokes* regime (low Froude number) the experimentally observed particle recirculation phenomenon is accounted for with back-mixing between the two CSTRs. For the *cyclonic* regime of operation (high Froude number) back-mixing between the CSTRs is negligible. Deviations from ideal reactor behaviour in terms of bypass and stagnation were very limited under the range of operating conditions investigated here.

Nomenclature

A	Area [m^2].
D	Diameter (a characteristic length scale) [m]
d_p	Particle diameter [μm].
$E(t)$	The residence time (or exit age) probability distribution function [1/s].
$E(\theta)$	The dimensionless residence time distribution.
F	Force [N].
Fr	Froude number.
g	Acceleration due to gravity [m/s^2].
$i(t)$	Inlet concentration of tracer at a time, t.
L	Length [mm].
m	Mass [kg].
$o(t)$	Outlet concentration of tracer at a time, t.
r	Radial coordinate [mm].
R	Radius of the receiver at a given cross-section [m].
R^2	Coefficient of determination.
Re	Reynolds number.
Sk	Stokes number.
t	Time [s].
U	Velocity (a characteristic velocity scale) [m/s].
u	Component of total velocity, U [m/s]

$u(\theta-\delta)$	The Heaviside unit step function, with dimensionless time delay δ.
V	Volume [m^3].
$\dot{V}$	Volumetric flow rate [m^3/s, slpm].
z	Axial coordinate [mm].
α	Receiver cone angle [°].
δ	Dimensionless time delay.
ε	Volume ratio of the two CSTRs of the compartment model.
θ	Dimensionless time, $\theta = t/\overline{\tau_p}$.
μ	Dynamic viscosity [kg/ms].
ρ	Density [kg/m^3].
σ_p^2	Normalised variance, $\sigma_p^2 = \sigma_{p,t}^2/\overline{\tau_p}^2$.
$\sigma_{p,t}^2$	Calculated variance of $E(t)$ [s^2].
τ	Residence time [s].
τ_{nom}	Nominal residence time, $\tau_{nom} = V_r/\dot{V}_{gas}$ [s].
$\overline{\tau_p}$	Mean particle residence time [s].
$\tau_{p,90}$	90th percentile particle residence time [s].
φ	Angular coordinate [°].
Subscripts	
air	Air phase.
base	Receiver base.
c	Receiver internal cavity.
cent	Centrifugal inertial
correction	Correction for distance between true in/outlet and measurement location.
cone	Receiver cone section.
corner	Corner at the receiver cone-cylinder intersection.
cyl	Receiver cylindrical section.
f	Fluid.
g	Gravitational
gas	Gas input to a device.
in	Inlet.
LP	Large particles.
max	Maximum value along the radial axis.
nom	Nominal.
out	Outlet.
p	Part`icle phase.
r	Receiver.
	Radial component.
SP	Small particles
z	Axial component.
φ	Tangential component.
Abbreviations	
CFD	Computational fluid dynamics.
CST	Concentrated solar thermal.
CSTR	Continuously-stirred tank reactor.
PFR	Plug flow reactor.
RTD	Residence time distribution.
SEVR	Solar expanding vortex receiver-reactor.
SVR	Solar vortex receiver-reactor.

Acknowledgements

We gratefully acknowledge the financial support of the Australian Solar Thermal Research Initiative (ASTRI), a project supported by the Australian Government, through the Australian Renewable Energy Agency (ARENA). Dominic is also grateful for additional assistance in the form of an Australian Government Research Training Program Scholarship.

References

Allal, K.M., Dolignier, J.C., Martin, G., 1998. Determination of the residence time distribution of solid particles by a photometric method. Chemical Engineering Research & Design 76, 643-648.

Amaral, S.S., de Carvalho, J., Costa, M., Pinheiro, C., 2015. An Overview of Particulate Matter Measurement Instruments. Atmosphere 6, 1327-1345.

ANSYS Inc., 2012. ANSYS/FLUENT Release Version 14.5.

Buffham, B.A., Mason, G., 1993. Holdup and dispersion: tracer residence times, moments and inventory measurements. Chemical Engineering Science 48, 3879-3887.

Cai, R.R., Zhang, Y.G., Li, Q.H., Meng, A.H., 2014. Experimental characterizing the residence time distribution of large spherical objects immersed in a fluidized bed. Powder Technology 254, 22-29.

Chinnici, A., Arjomandi, M., Tian, Z.F., Lu, Z., Nathan, G.J., 2015. A Novel Solar Expanding-Vortex Particle Reactor: Influence of Vortex Structure on Particle Residence Times and Trajectories. Solar Energy 122, 58-75.

Chinnici, A., Arjomandi, M., Tian, Z.F., Nathan, G.J., 2016. A Novel Solar Expanding-Vortex Particle Reactor: Experimental and Numerical Investigation of the Iso-thermal Flow Field and Particle Deposition. Solar Energy 133, 451-464.

Chinnici, A., Xue, Y., Lau, T.C.W., Arjomandi, M., Nathan, G.J., 2017. Experimental and numerical investigation of the flow characteristics within a Solar Expanding-Vortex Particle Receiver-Reactor. Solar Energy 141, 25-37.

Cortés, C., Gil, A., 2007. Modeling the gas and particle flow inside cyclone separators. Progress in Energy and Combustion Science 33, 409-452.

Danckwerts, P.V., 1995. Continuous flow systems. Distribution of residence times. Chemical Engineering Science 50, 3855.

Davis, D., Müller, F., Saw, W.L., Steinfeld, A., Nathan, G.J., 2017. Solar-driven alumina calcination for CO_2 mitigation and improved product quality. Green Chemistry 19, 2992-3005.

Elghobashi, S., 1994. On predicting particle-laden turbulent flows. Applied Scientific Research 52, 309-329.

Essadki, A.H., Gourich, B., Vial, C., Delmas, H., 2011. Residence time distribution measurements in an external-loop airlift reactor: Study of the hydrodynamics of the liquid circulation induced by the hydrogen bubbles. Chemical Engineering Science 66, 3125-3132.

Fogler, H.S., 2006. Elements of chemical reaction engineering, 4th ed. ed. Prentice Hall PTR, Upper Saddle River, NJ.

Gao, Y., Muzzio, F.J., Ierapetritou, M.G., 2012. A review of the Residence Time Distribution (RTD) applications in solid unit operations. Powder Technology 228, 416-423.

Gao, Y., Vanarase, A., Muzzio, F., Ierapetritou, M., 2011. Characterizing continuous powder mixing using residence time distribution. Chemical Engineering Science 66, 417-425.

Guío-Pérez, D.C., Pröll, T., Wassermann, J., Hofbauer, H., 2013. Design of an inductance measurement system for determination of particle residence time in a dual circulating fluidized bed cold flow model. Industrial and Engineering Chemistry Research 52, 10732-10740.

Harris, A.T., Davidson, J.F., Thorpe, R.B., 2002. A novel method for measuring the residence time distribution in short time scale particulate systems. Chemical Engineering Journal 89, 127-142.

Harris, A.T., Davidson, J.F., Thorpe, R.B., 2003. Particle residence time distributions in circulating fluidised beds. Chemical Engineering Science 58, 2181-2202.

Hirsch, D., Steinfeld, A., 2004. Solar hydrogen production by thermal decomposition of natural gas using a vortex-flow reactor. International Journal of Hydrogen Energy 29, 47-55.

Ho, C.K., Iverson, B.D., 2014. Review of high-temperature central receiver designs for concentrating solar power. Renewable & Sustainable Energy Reviews 29, 835-846.

Hoffmann, A.C., Stein, L.E., 2007. Gas Cyclones and Swirl Tubes: Principles, Design, and Operation. Berlin, Heidelberg: Springer, Berlin.

Kang, S.K., Kwon, T.W., Kim, S.D., 1989. Hydrodynamic Characteristics of Cyclone Reactors. Powder Technology 58, 211-220.

Kehlenbeck, R., Yates, J., Felize, R., Hofbauer, H., Rauch, R., 2002. Particle Residence Time and Particle Mixing in a Scaled Internal Circulating Fluidized Bed. Industrial & Engineering Chemistry Research 41, 2637-2645.

Kieviet, F.G.F., Kerkhof, P.P., 1995. Measurements of particle residence time distributions in a co-current spray dryer. Drying Technology 13, 1241-3937.

Kodama, T., Gokon, N., Matsubara, K., Yoshida, K., Koikari, S., Nagase, Y., Nakamura, K., 2014. Flux measurement of a new beam-down solar concentrating system in Miyazaki for demonstration of thermochemical water splitting reactors. Proceedings of the Solarpaces 2013 International Conference 49, 1990-1998.

Lau, T.C.W., Nathan, G.J., 2016. The effect of Stokes number on particle velocity and concentration distributions in a well-characterised, turbulent, co-flowing two-phase jet. Journal of fluid mechanics 809, 72-110.

Lede, J., Li, H.Z., Soulignac, F., Villermaux, J., 1987. Measurement of solid particle residence time in a cyclone reactor: A comparison of four methods. Chemical Engineering and Processing: Process Intensification 22, 215-222.

Levenspiel, O., 1999. Chemical reaction engineering, 3rd ed. ed. Wiley, New York.

Li, S.H., Yang, S., Yang, H.R., Zhang, H., Liu, Q., Lu, J.F., Yue, G.X., 2008. Particle Holdup and Average Residence Time in the Cyclone of a CFB Boiler. Chemical Engineering & Technology 31, 224-230.

Marchioli, C., Picciotto, M., Soldati, A., 2006. Particle dispersion and wall-dependent turbulent flow scales: implications for local equilibrium models. Journal of Turbulence 7.

Mills, P., Duduković, M., 1989. Convolution and deconvolution of nonideal tracer response data with application to three-phase packed-beds. Computers & chemical engineering 13, 881-898.

Mitsutani, K., Grace, J.R., Lim, C.J., 2005. Residence time distribution of particles in a continuous liquid–solid classifier. Chemical Engineering Science 60, 2703-2713.

Nauman, E.B., 2008. Residence time theory. Industrial & Engineering Chemistry Research 47, 3752-3766.

Shilapuram, V., Krishna, D.J., Ozalp, N., 2011. Residence time distribution and flow field study of aero-shielded solar cyclone reactor for emission-free generation of hydrogen. International Journal of Hydrogen Energy 36, 13488-13500.

Steinfeld, A., Imhof, A., Mischler, D., 1992. Experimental Investigation of an Atmospheric-Open Cyclone Solar Reactor for Solid-Gas Thermochemical Reactions. Journal of Solar Energy Engineering-Transactions of the Asme 114, 171-174.

Syred, N., 2006. A review of oscillation mechanisms and the role of the precessing vortex core (PVC) in swirl combustion systems. Progress in Energy and Combustion Science 32, 93-161.

Szekely, J., Carr, R., 1966. Heat transfer in a cyclone. Chemical Engineering Science 21, 1119-1132.

Tian, Z.F., Nathan, G.J., Cao, Y., 2015. Numerical modelling of flows in a solar–enhanced vortex gasifier: Part 1, comparison of turbulence models. Progress in Computational Fluid Dynamics, an International Journal 15, 114-122.

Trachsel, F., Günther, A., Khan, S., Jensen, K.F., 2005. Measurement of residence time distribution in microfluidic systems. Chemical Engineering Science 60, 5729-5737.

Viitanen, P., 1997. Experiences on fast fourier transform as a deconvolution technique in determination of process equipment residence time distribution. Applied Radiation and Isotopes 48, 893-898.

Yogev, A., Kribus, A., Epstein, M., Kogan, A., 1998. Solar "tower reflector" systems: a new approach for high-temperature solar plants. International Journal of Hydrogen Energy 23, 239-245.

Yong, Y., 1996. Mass flow measurement of bulk solids in pneumatic pipelines. Measurement Science and Technology 7, 1687-1706.

Z'Graggen, A., Haueter, P., Trommer, D., Romero, M., de Jesus, J.C., Steinfeld, A., 2006. Hydrogen production by steam-gasification of petroleum coke using concentrated solar power — II Reactor design, testing, and modeling. International Journal of Hydrogen Energy 31, 797-811.

Title

Particle residence time distributions in a vortex-based solar particle receiver-reactor: the influence of receiver tilt angle

Authors

Dominic Davis[a,b,*], Maurizio Troiano[d], Alfonso Chinnici[a,b], Woei L. Saw[a,c], Timothy Lau[a,b], Roberto Solimene[e], Piero Salatino[d], Graham J. Nathan[a,b]

[a]Centre for Energy Technology, The University of Adelaide, South Australia 5005, Australia.

[b]School of Mechanical Engineering, The University of Adelaide, South Australia 5005, Australia.

[c]School of Chemical Engineering and Advanced Materials, The University of Adelaide, South Australia 5005, Australia.

[d]Dipartimento di Ingegneria Chimica, dei Materiali e della Produzione Industriale, Università degli Studi di Napoli Federico II, Piazzale V. Tecchio 80, 80125 Napoli, Italy.

[e]Istituto di Ricerche sulla Combustione, Consiglio Nazionale delle Ricerche, Piazzale V. Tecchio 80, 80125 Napoli, Italy.

Abstract

We present the first experimental assessment of the influence of receiver tilt angle on the particle residence time distribution (RTD) of a two-phase solar particle receiver. The tracer pulse response method is used to measure the particle RTD within a laboratory-scale vortex-based solar particle receiver, with the particle phase itself used as the tracer. The experimental parameters of particle size, transporting gas inlet velocity and a range of receiver tilt angles – spanning 180° from vertically upward to downward facing – were systematically varied to determine the influence of key controlling parameters on the particle RTD within the receiver. It was found that the Stokes number of the two-phase flow evaluated at the receiver outlet, Sk_{out}, has a controlling influence on the residence time and that the influence of the receiver tilt angle is significant for large particles ($Sk_{out} > 10$) but weak for small particles ($Sk_{out} \sim 1$). This implies that it is preferable to operate tower-mounted systems (i.e. with downward facing receiver tilt angles) with $Sk_{out} \sim 1$. Furthermore, a preliminary scale-up assessment suggests that the influence of tilt angle on the residence time of particles 200 µm and smaller will be insignificant for a nominal 50 MW-scale receiver, which will provide flexibility in the design of industrial-scale devices. Finally, the residence time behaviour for the range of tilt angles assessed can be well described by an analytical compartment model consisting of a small plug flow reactor, followed by two continuously-stirred tank reactors in parallel with a second plug flow reactor.

Keywords: solar particle receiver, vortex flow, residence time, RTD, tilt angle, CST.

1 Introduction

Understanding the influence of the receiver tilt angle on the performance of solar cavity receivers is a necessary component in the development of optimal concentrating solar thermal (CST) systems. This is because the receiver tilt angle relative to gravity has a bearing, not only on the heat and mass transport within the receiver itself, but also on the layout of the heliostat field and the height of the tower on which the receiver is mounted (Behar et al., 2013; Ho, 2017; Ho and Iverson, 2014; Li et al., 2016). While many investigations of the influence of receiver tilt angle on the thermal performance have been performed for single-phase gas cavity receivers, particularly with respect to their convective losses (Clausing, 1983; Lee et al., 2018; Leibfried and Ortjohann, 1995; Wu et al., 2010), this is not true for two-phase devices that employ a gas-particle suspension flow within the cavity. In such solar particle receivers the particle mass transport has potential to be strongly influenced by the direction of gravity. One measure of this particle mass transport performance of a solar particle receiver is the particle residence time distribution (RTD) within the receiver, which describes the probability distribution of residence times a particle spends within the receiver for a given set of operational conditions (Danckwerts, 1995; Fogler, 2006; Levenspiel, 1999). However, no data is presently available as to the influence of the cavity tilt angle of a suspension flow solar particle receiver on its particle RTD. Furthermore, as an alternative to the tower-mounted systems, beam-down receivers are also under development (Kodama et al., 2014; Yogev et al., 1998), for which the receiver will be oriented upwards, together with many variations between the two extremes of beam-up and beam-down. Hence, the objective of the present investigation is to support the further development of suspension flow solar particle cavity receivers by providing first-of-a-kind measurements of the influence of a wide range of receiver tilt angles on the RTD of particles within the cavity.

The vortex-based solar particle receiver-reactor, typically referred to as the Solar Vortex Receiver (SVR), is a particle receiver concept in which the alignment of gravity relative to the direction of particle mass transport is important. In this class of receiver, particles are conveyed by a vortex flow of gas through a zone of direct, concentrated solar radiation within a cylindrical cavity with a circular aperture at one end (Chinnici et al., 2015; Steinfeld et al., 1992; Z'Graggen et al., 2006). SVRs have been demonstrated experimentally at laboratory-scale for a number of different solar thermochemical particle reactions, in which the concentrated solar radiation is typically introduced into the cavity through an aperture sealed by a transparent quartz window (Hirsch and Steinfeld, 2004; Kräupl and Steinfeld, 2001; Z'Graggen et al., 2006). These devices achieve highly efficient heat transfer to the particle phase due to direct irradiation as demonstrated by the high values of chemical conversion reported for residence times on the order of seconds (Davis et al., 2017; Müller et al., 2017; Z'Graggen et al., 2006). In addition, SVRs also have the potential to operate without a window, so that the cavity is open to the aperture (Chinnici et al., 2015; Steinfeld et al., 1992). Whether the SVR operates atmospherically-open or as a closed system with a window, detailed data for both cases is required, including RTD measurements in a closed system. However, all previous thermochemical assessments of SVRs have been performed with the cylindrical cavity oriented horizontally so that gravity acts normal to the central axis. This introduces some potential differences to tower-mounted cavities in which the axis of the receiver is likely to be directed with a downward tilt to align it with the heliostat array. Hence there is a need to investigate the effect of orientation on particle residence time.

A new type of SVR, termed the Solar Expanding Vortex Receiver (SEVR), has recently been developed with a view to capitalising on the high energy conversion efficiency of previous prototypes whilst also mitigating some of their limitations (Chinnici et al., 2015). These limitations of the SVR design concept have been identified as

* Corresponding author: Dominic Davis, dominic.davis@adelaide.edu.au

a particle residence time distribution that is approximately independent of the particle size, and a tendency of particles to egress through the aperture and deposit onto the sealing window or be lost to the environment (Chinnici et al., 2015). The SEVR prototype reverses the axial flow direction relative to the aperture to reduce particle flow through the aperture by an order of magnitude, and also features a radially-oriented outlet that helps to recirculate larger particles to the base of the receiver where velocity is greatest to increase their residence time. Chinnici et al. (2015) also identified some potential advantages of a vertical orientation of the SEVR in further augmenting the retention of large particles within the receiver to increase their residence time relative to small particles, notwithstanding other advantages of the tower-mounted receiver orientation. Recent experimental measurements have confirmed the potential of the device to increase the residence time of large particles relative to smaller ones for the vertical orientation relevant to beam-down solar concentrating systems (Davis et al., 2019). This is a potential benefit to processing polydisperse particles, of which larger particles require a longer residence time to undergo a given extent of heating or reaction than smaller particles. However, no experimental measurements of the influence of the orientation on residence time have been reported previously for any type of SVR. Hence, we aim to assess the role of alignment relative to gravity of the SEVR in influencing the particle RTD.

Previous work has found that the SEVR can be configured to operate in two different flow regimes: The *Froude-Stokes* regime and the *cyclonic* regime (Chinnici et al., 2015; Davis et al., 2019). In the *Froude-Stokes* regime, the residence time of larger particles can be increased due to their higher inertia that inhibits them from leaving the receiver, which can also be augmented by gravity for certain orientations (Chinnici et al., 2015; Davis et al., 2019). This applies where a characteristic Froude number of the two-phase gas-particle flow is below a threshold value. In the *cyclonic* regime the particle behaviour is somewhat analogous to that in a cyclone, so that particles are centrifuged toward the wall of the receiver when the characteristic Froude number is above a certain threshold (Davis et al., 2019). In this regime, the residence time is relatively independent of particle size and is shorter than for the *Froude-Stokes* regime due to the reduced significance of recirculation (Davis et al., 2019). However, these two regimes have only been reported for the vertical orientation, so that there is a need to expand this understanding for other orientations. Hence an additional aim of the present paper is to expand understanding of the two regimes of operation for the SEVR with a range of tilt angles other than vertical.

In summary, the overall objective of this work is to provide new understanding of the influence of receiver tilt angle on the residence time distributions of particles within a solar particle receiver. Specifically, this paper aims to assess how the alignment of the central axis of the SEVR relative to gravity affects the RTD of particles with large and small inertia, for operation within the low and high Froude number regimes. It has become common to use a compartment modelling approach to model a real device as the sum of ideal flow reactors by comparison with measured RTDs. This analytical approach advances understanding of the device and provides a useful design tool. Hence, we also aim to describe the influence of receiver tilt angle on the residence time behaviour of particles in the SEVR with a compartment model. Finally, we aim to project the particle residence time characteristics of a scaled-up SEVR by providing a preliminary scaling analysis of the particle RTD measurements from a laboratory-scale SEVR. The measurements presented here are for the SEVR operating with isothermal room temperature conditions because of the need to understand the isothermal particle residence time behaviour before assessing the effects of temperature and buoyancy.

2 Methodology

2.1 Experimental technique

The particle residence time distribution within the Solar Expanding Vortex Receiver (SEVR) was measured for various orientations relative to the direction gravity with the tracer pulse response method described by Levenspiel (1999) and Fogler (2006) and illustrated in Figure 1. The experimental technique follows that described previously by Davis et al. (2019) with the key features reported here. This technique injected a short pulse of particles into the cavity of the SEVR, so that the particle phase acts both as the tracer and the medium being traced. The particles were injected into an empty vessel while maintaining a steady-state flow of gas. As the particle pulse concentration measurement at the inlet approaches a perfect Dirac delta function, the recorded outlet concentration of particles approaches being a direct measure of the particle RTD, $E(t)$.

Before each measurement, 0.3 g of particles was loaded into the particle basket connected to the secondary feeder air line with the valve closed. Steady-state vortex flow conditions were then established with equal amount of compressed air introduced into the two tangential inlets. The particle pulse was then injected by opening the valve to introduce the particles into the air lines without disrupting significantly the total amount of air injected into the receiver cavity. The temporal concentration of particles was measured directly throughout this process at the inlet to, and outlet from, the SEVR with time-resolved laser extinction measurements. This was performed with a laser and photodetector, both mounted perpendicularly to the inlet and outlet tubes, through which the particles were transported (Figure 1). The passage of particles through the inlet and outlet tubes attenuates the laser and this attenuation scales with the particle number density for particles of uniform diameter. The particle RTD, $E(t)$, for a given case, was then obtained by deconvolving the inlet and outlet particle concentration measurements. A series of average $E(t)$ distributions were then obtained from 12 repeated measurements to reduce the influence of fluctuations generated by the turbulent swirling processes, as well as the discrete nature of the particles being measured. Each of the distributions used in the average was normalised by the area bounded by the distribution, so that $\int_0^\infty E(t)dt = 1$. To identify the number of repetitions required in calculating the average $E(t)$, 40 repetitions of one operational case were conducted. The statistical parameters, the mean particle residence time, the 90th percentile particle residence time and the normalised variance of the distribution were calculated from the distributions averaged from an increasing number of repetitions. It was found that 12 repetitions were required to obtain values of the parameters that converged closely to those from 40 repeated measurements. In calculating the parameters from an increasing number of repetitions greater than 12, the maximum deviation from the statistical parameters calculated from 40 repetitions was found to be 1.2%. The $E(t)$ distributions presented here therefore approach the converged probability distribution functions of particle residence times within the SEVR and it can be said that the statistical parameters characterising the RTDs presented here have an approximate relative error of 1.2%. These experiments were conducted with isothermal flow conditions and with particles and gas at room temperature.

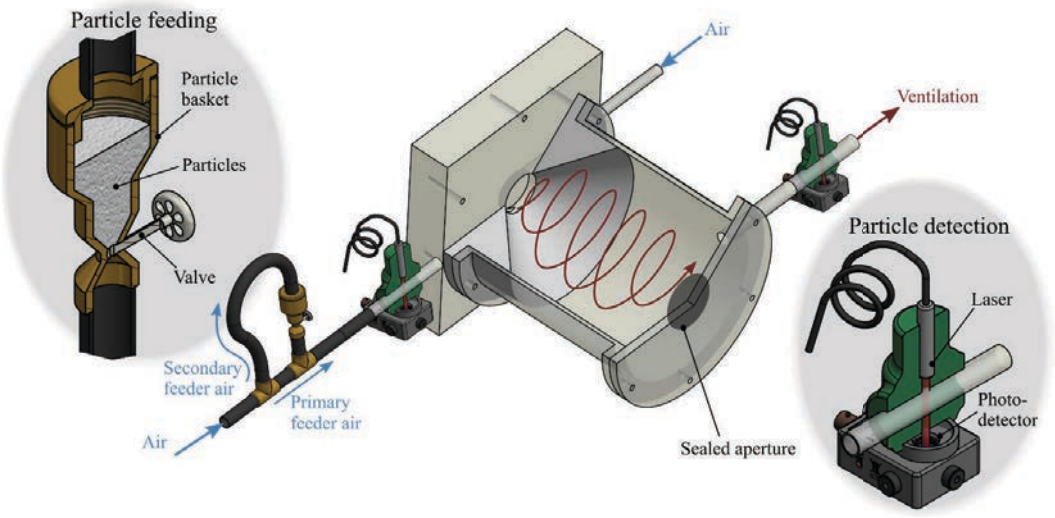

Figure 1: The experimental arrangement used to measure the residence time distribution of particles within a vortex-based solar particle receiver vessel for a range of receiver tilt angles. Shown are the particle feeding and detection subsystems, together with the receiver cavity comprising two tangentially-oriented inlets, a single radially-oriented outlet and a sealed aperture. The device is shown here with a receiver oriented approximately horizontally.

2.2 Measurement cases

Table 1a, together with Figure 2, presents the geometry of the present receiver configuration, which maintains geometric similarity with that of previous particle RTD measurements in the SEVR (Davis et al., 2019). The receiver features two circular inlets of diameter D_{in} = 6 mm, and a single radially-oriented outlet of diameter, D_{out} = 11 mm. The two-phase flow is introduced at the base end of the conical section, so that receiver cross-section increases through the conical section and is then constant in the cylindrical section, as the vortex flow proceeds towards the outlet. The following analysis refers to a cylindrical coordinate system, (r, φ, z), as shown in Figure 2 with an origin at the centre of the base disc. We define the receiver tilt angle, ψ (shown in Figure 2), as the angle between the central axis of the receiver and the horizontal, with downward-facing angles considered as positive, following previous work (Leibfried and Ortjohann, 1995; Wu et al., 2010). This implies that positive tilt angles ($\psi > 0°$) are relevant to tower-mounted solar receiver configurations, while a tilt angle of $\psi = -90°$ is relevant to a receiver with beam-down solar concentrating system.

Table 1b presents the range of operational parameters that were varied in the present investigation. The particle RTD was measured for seven receiver tilt angles in the range $\psi = -90°$ to $+90°$. It can be seen that this change of receiver orientation is made with the radially-oriented outlet positioned on the side of the receiver to avoid gravity bias. For each value of ψ the particle RTD was measured for two particle sizes, d_p = 20 and 80 µm, and two values of air volumetric flow rate, $\dot{V}_{air}$ = 104 and 122 slpm, generating two values of inlet velocity, U_{in} = 30.7 and 36.0 m/s, due to the constant inlet diameter. These values of U_{in} were chosen because they generate the two different particle behaviour regimes identified by our previous measurement of the particle RTD in the SEVR for a single vertical orientation (Davis et al., 2019). A value of U_{in} = 30.7 m/s lies within the *Froude-Stokes* regime of operation, while a value of U_{in} = 36.0 m/s lies within the *cyclonic* regime of operation. It should also be noted that these velocities are sufficient for ensuring particles are retained in suspension, while not being so high as to require excessive fan power or to cause excessive erosion in a scaled-up receiver.

The particle sizes, d_p = 20 and 80 µm, were chosen as the two extremes of particle size assessed previously. Particles of these sizes are recirculated within the receiver to different extents in the *Froude-Stokes* regime having different residence times, but behave similarly with similar residence time in the *cyclonic* regime. The particles used here are spherical polymer particles (ρ_p = 1200 kg/m^3) that have a monodisperse size distribution, which allows for the influence of particle size on the particle RTD to be isolated. The particle size distributions have been reported previously (Davis et al., 2019; Lau and Nathan, 2016). However, it should be noted that these polymer particles are not suitable for use in on-sun operation of a solar receiver. Nevertheless, the measured residence time characteristics of the present particles can be related to those of particles that are commonly used in solar receivers (e.g. ceramic particles of alternative sizes) by matching the relevant dimensionless numbers (outlined in section 2.3).

Table 1: (a) Values of the key dimensions of the SEVR; and (b) the range of variation of the independent parameters systematically varied in the current investigation.

(a)	
D_c	190 mm
L	237.5 mm
D_{base}	47.5 mm
D_{cone}	47.5 – 190 mm
α	50°
D_{in}	6 mm
D_{out}	11 mm
(b)	
ψ	−90° to +90°
d_p	20, 80 µm
$\dot{V}_{air}$	104, 122 slpm
U_{in}	30.7, 36.0 m/s

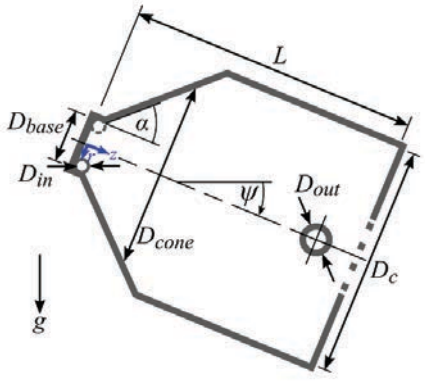

Figure 2: Schematic diagram of the SEVR showing the cylindrical coordinate system (r, φ, z), with origin at the centre of the base disc and the symbols that define the geometric configuration. The φ axis is defined as the right handed angle about the z axis. The values of each geometric parameter are shown in Table 1. Gravity acts downwards as shown by g.

2.3 Key dimensionless parameters.

The Stokes number is defined as the ratio of the characteristic time-scale of a particle to the characteristic time-scale of a fluid eddy. In the present case, the Stokes number can be evaluated to characterise how closely a particle will follow the gas streamlines through the various zones of the receiver. It has been found previously, that the Stokes number of the two-phase flow at the outlet of the SEVR (Sk_{out}) best characterises the likelihood of particles leaving the SEVR and therefore has a controlling influence on the particle residence time (Davis et al., 2019). This Stokes number is defined as follows:

$$Sk_{out} = \frac{\rho_p d_p^2 U_{out}}{18\mu_{air}(2D_{out})}, \quad (1)$$

where ρ_p is the particle density, d_p is the particle diameter, μ_{air} is the air dynamic viscosity, U_{out} is the nominal outlet velocity of the receiver ($U_{out} = \dot{V}_{air}/A_{out}$) and $D_{out,}$ is the outlet diameter. Here, U_{out} is used as the characteristic fluid velocity scale, and twice the outlet diameter, $2D_{out}$, is used as the characteristic fluid length scale of the flow at the outlet from the receiver. This is based on estimates of the velocity and length scales of the outlet flow with a computational fluid dynamics model of the SEVR (Chinnici et al., 2015; Chinnici et al., 2016). The trends in the measured distributions presented as a function of Sk_{out} are therefore reasonable even though turbulent flows necessarily comprise a range of velocity and length scales whose values depend on the geometric configuration. The values of the characteristic length and velocity scales used to evaluate Sk_{out} are presented in Table 2.

The Froude number, for a particle within a vortex flow, is defined as the ratio of the centrifugal inertial force acting on the particle due to its circular (vortex) motion, to that of the external gravitational field. The Froude number specifically evaluated for the flow within the cylindrical section of the receiver (Fr_{cyl}) has been found previously to characterise whether the SEVR operates within the *Froude-Stokes* or *cyclonic* regimes of operation (Davis et al., 2019). A critical value of this parameter, $Fr_{cyl} = 4$, was found to delineate the transition between the two regimes. The Froude number of the flow in the cylindrical section of the receiver is evaluated as:

$$Fr_{cyl} = \frac{u_{\varphi,max}^2}{g\,{D_c}/{2}}, \quad (2)$$

where, $u_{\varphi,max}$ is the maximum tangential velocity of the air flow field in the cylindrical section of the receiver, g is the standard acceleration due to gravity, and D_c is the cylinder diameter. Here, $u_{\varphi,max}$ is used as the characteristic tangential fluid velocity scale of the circular (vortex) flow, and $D_c/2$, is used as the characteristic radius of the circular flow, the values of which are presented in Table 2. These definitions of Sk_{out} and Fr_{cyl} follow Davis et al. (2019).

Table 2 presents the values of the key dimensionless parameters, Sk_{out} and Fr_{cyl}, for operation in the *Froude-Stokes* and *cyclonic* regimes. These parameters are generated with the two values of inlet velocity and two particle sizes used in the present investigation. It can be seen that the lower velocity, $U_{in} = 30.7$ m/s, results in $Fr_{cyl} = 3.8 < 4$ so that the operation of the SEVR is within the *Froude-Stokes* regimes, while the higher velocity case resulting in $Fr_{cyl} = 5.2 > 4$ corresponds to the *cyclonic* regime of operation.

Table 2: The operational details of the *Froude-Stokes* and *cyclonic* regimes of operation investigated here, generated with the two values of inlet velocity, U_{in}. The characteristic velocity and length scales, and values of the key dimensionless parameters, Sk_{out} and Fr_{cyl}, for each regime are also presented.

	Froude-Stokes	***Cyclonic***
U_{in} [m/s]	30.7	36.0
U_{out} [m/s] [a]	18.2	21.4
$2D_{out}$ [m] [b]	0.022	
$u_{\varphi,max}$ [m/s] [c]	1.9	2.2
$D_c/2$ [m] [d]	0.095	
Sk_{out} for $d_p = 20$ µm	1.2	1.4
Sk_{out} for $d_p = 80$ µm	19.4	22.8
Fr_{cyl}	3.8	5.2

[a] Characteristic velocity scale for the Sk_{out}.
[b] Characteristic length scale for Sk_{out}.
[c] Characteristic tangential velocity scale for Fr_{cyl}.
[d] Characteristic radius of circular motion for Fr_{cyl}.

2.4 Characterisation of the residence time distribution

The three statistical measures used to characterise the particle RTDs, $E(t)$, are the mean particle residence time, $\overline{\tau_p}$, the 90th percentile particle residence time, $\tau_{p,90}$, and the normalised variance, $\sigma_p^2 = \sigma_{p,t}^2/\overline{\tau_p}^2$. These parameters are calculated with the following equations:

$$\overline{\tau_p} = \int_0^\infty tE(t)dt, \quad (3)$$

$$\int_0^{\tau_{p,90}} E(t)dt = 0.90, \quad (4)$$

$$\sigma_{p,t}^2 = \int_0^\infty \left(t - \overline{\tau_p}\right)^2 E(t)dt. \quad (5)$$

The $E(t)$ values used in Equations (3), (4) and (5) were generated by fitting curves to match the experimental $E(t)$ data that achieve a coefficient of determination, $R^2 > 0.97$. This avoids any significant influence of measurement noise, particularly for $t > 20$ s, and follows the recommendation of Buffham and Mason (1993).

A dimensionless form of the particle RTD, $E(\theta)$, is used to compare the experimental distributions with those of ideal reactors (e.g. plug flow reactors, continuously-stirred tank reactors). The dimensionless expression of $E(t)$ is derived as follows:

$$E(\theta) = \overline{\tau_p}E(t), \quad (6)$$

where $\theta = t/\overline{\tau_p}$, which is a dimensionless time.

3 Results & discussion

3.1 Measurements of the particle RTD

Figure 3 presents the measured particle RTDs within the SEVR for seven receiver tilt angles in the range $\psi = -90°$ to $+90°$, for two outlet Stokes numbers (Sk_{out} = 19.4 and 1.2), a single inlet velocity U_{in} = 30.7 m/s and constant inlet diameter D_{in} = 6 mm, generating a nominal residence time τ_{nom} = 3.2 s, where $U_{in} = \dot{V}_{air} / (2 \times (\pi/4) \times D_{in}^2)$ and $\tau_{nom} = V_r/\dot{V}_{air}$. The distributions have been smoothed for clarity with a moving point average spanning 0.125 s of measured data.

Figure 3a and b present the RTDs measured for Sk_{out} = 19.4, and d_p = 80 µm. This shows that increasing ψ shifts the RTDs to shorter residence times. It can be seen that, for the negative tilt angles (Figure 3a) in which the two-phase flow proceeds upwards against gravity, the length of the tail of the RTD is longest for $\psi = -90°$, indicating that this orientation results in the most particle recirculation within the SEVR. It can also be seen that, as the tilt angle is increased to $\psi = -60°$ and $-30°$, the peak in the RTD becomes more prominent and shifts to shorter residence times. However, the tails of the two distributions are still prominent, indicating continued particle recirculation within the SEVR for residence times up to ~10 s. Figure 3b presents RTDs measured for the SEVR with a horizontal orientation, as well as with positive tilt angles (noting that the scale of the abscissa in Figure 3b is increased relative to Figure 3a). Here, the peak in the RTD increases with ψ and the distributions feature small or negligible tails, such that, for the three positive tilt angles, 90% of particles have a residence time of less than 2.5 s. Therefore, for beam-down receiver tilt angles ($\psi < 0°$), the RTDs depend strongly on the angle, while for tower-mounted receiver tilt angles ($\psi > 0°$), the RTDs are less influenced by the angle. From a reactor design perspective, increasing the receiver tilt angle causes the RTD to change from that resembling a mixed flow reactor to that resembling a plug flow reactor. This in turn indicates that the broad RTDs measured for negative receiver tilt angles favour particle recirculation and potentially enhanced heat transfer in a practical solar receiver, while the positive receiver tilt angles favour reduced recirculation and uniform particle residence times.

Figure 3c and d present the measured RTDs for Sk_{out} = 1.2 and d_p = 20 µm. This shows that the RTD is not significantly affected by the receiver orientation for the majority of tilt angles assessed, $\psi \geq -60°$, and is shifted to slightly longer residence times for $\psi = -90°$. It can be seen (Figure 3c) that the RTD is broadest with longest residence times for $\psi = -90°$. With an increase in tilt angle to $\psi = -60°$ there is a reduction in residence time with a more prominent peak in the distribution. This is a similar trend to that shown for Sk_{out} = 19.4 (Figure 3a). However, further increases in ψ (Figure 3c and d) do not result in significant changes to the measured RTD. That is, the RTDs for $\psi = -60°$ to $+90°$ are similar to each other and do not exhibit significant differences in measured residence time. Comparing the RTDs measured with positive ψ for Sk_{out} = 1.2 (Figure 3d) with those measured for Sk_{out} = 19.4 (Figure 3b) it can be seen that, for each ψ, the RTDs are shifted to longer residence times with a reduction in Sk_{out} (e.g. by smaller particle size). This indicates that, for the tower-mounted orientation ($\psi > 0°$) over the range of conditions assessed here, particle residence times decrease with an increase in Sk_{out}. Taken together, it is hypothesised from Figure 3 that particles with outlet Stokes number ~ 1 are less influenced by the receiver tilt angle than are particles with an outlet Stokes number >> 1. However, to draw further conclusions, additional data are required for operation with a wider range of Stokes numbers.

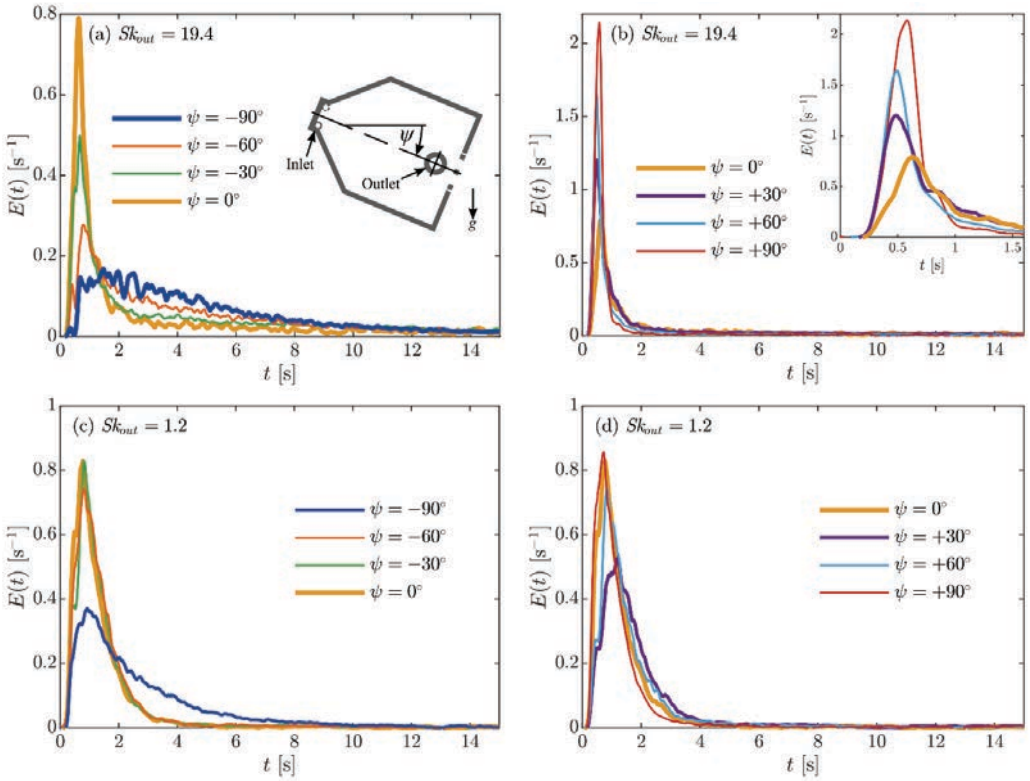

Figure 3: Measured particle RTDs in the SEVR for seven receiver tilt angles in the range $\psi = -90°$ to $+90°$, with inlet velocity U_{in} = 30.7 m/s and constant inlet diameter D_{in} = 6 mm, generating a nominal residence time τ_{nom} = 3.2 s, where $U_{in} = \dot{V}_{air} / (2 \times (\pi/4) \times D_{in}^2)$ and $\tau_{nom} = V_r/\dot{V}_{air}$. Presented are the distributions for two outlet Stokes numbers (a, b) Sk_{out} = 19.4 (particle diameter d_p = 80 µm); and (c, d) Sk_{out} = 1.2 (particle diameter d_p = 20 µm). The inset in (b) presents the same RTDs with time axis in the range, t = 0 – 1.6 s. The distributions have been smoothed for clarity with a moving point average spanning 0.125 s of measured data.

Figure 4 presents three statistical measures of the particle RTDs, the mean particle residence time, $\bar{\tau}_p$, the 90th percentile particle residence time, $\tau_{p,90}$, and the normalised variance, σ_p^2, as a function of ψ, for each of the conditions shown in Table 1b. It can be seen from Figure 4a that the dependence of $\bar{\tau}_p$ on ψ is stronger for the larger particle size, d_p = 80 µm, than for d_p = 20 µm. Specifically, the $\bar{\tau}_p$ for d_p = 20 µm decreases with an increase from ψ = −90º to −60°, but then remains almost constant with a further increase in ψ. This implies that the alignment of gravity with the axis of the SEVR does not play a significant role for this particle size, due to their smaller inertia. That is, their residence time is controlled by their response to the vortex flow field, rather than their response to changes in the direction of gravity. In contrast, the $\bar{\tau}_p$ for d_p = 80 µm decreases to a significant extent with an increase from ψ = −90º to +90°, indicating that the alignment of gravity does play a role for these larger particles. This can be attributed to a reduction in the component of gravitational force resisting axial motion in the positive z direction as the tilt angle increases from ψ = −90º to 0°, and, additionally, the increase in the component of gravitational force augmenting axial motion as the tilt angle increases from ψ = 0º to +90°. Importantly, for ψ greater than approximately +30°, gravity augments the axial motion in the positive z direction towards the outlet to such an extent that the $\bar{\tau}_p$ is less than that of the smaller particles. That is, due to their weaker response to the vortex flow field, the change in the direction of gravity with a change in ψ has a significant influence on the residence time of d_p = 80 µm particles. This highlights the sensitivity of the particle residence times to the orientation of the receiver for particles of size d_p = 80 µm, which undergo a greater reduction in mean residence time with increasing tilt angle than do the particles of size d_p = 20 µm.

Figure 4a also shows that a negative receiver tilt angle (ψ < 0°), i.e. when gravity resists axial motion in the positive z direction, enhances recirculation of particles by gravity towards the base of the conical section of the receiver. This trend is strong for the d_p = 80 µm particles and weak for the d_p = 20 µm particles. The smaller particles exhibit a weaker increase in $\bar{\tau}_p$ and recirculation with decreasing ψ for U_{in} = 36.0 m/s and only exhibit longer residence time for the vertical ψ = −90º orientation with the lower velocity case, U_{in} = 30.7 m/s. The difference in $\bar{\tau}_p$ between the two particle sizes increases with lower U_{in}, as is characteristic of the *Froude-Stokes* regime, which was previously reported for the single tilt angle of ψ = −90º (Davis et al., 2019). It is noteworthy that this trend persists also for the alternative negative tilt angles of ψ = −60º and −30º. Although the two values of U_{in} assessed here differ by only 17%, the increase from U_{in} = 30.7 to 36.0 m/s results in $\bar{\tau}_p$ decreases for d_p = 80 µm of 41%, 33% and 34% for ψ = −90º, −60º and −30º, respectively. However, for d_p = 20 µm, there is no noticeable influence of U_{in} on the $\bar{\tau}_p$ for any ψ, which can potentially be attributed to the small difference in U_{in} assessed. Previous work reported that the value of $\bar{\tau}_p$ for d_p = 20 µm and ψ = −90º decreases by 32% for a 34% increase from U_{in} = 30.7 to 41.3 m/s (Davis et al., 2019). It can therefore be expected that for the negative receiver tilt angles, higher values of U_{in} would decrease the values of $\bar{\tau}_p$ for both particle sizes, but also that the difference between the values of $\bar{\tau}_p$ of both particle sizes would also decrease, as is characteristic of the *Froude-Stokes* regime (Davis et al., 2019). Overall, the SEVR configuration selected here has the potential to operate with a particle residence time that increases with particle size for a range of negative receiver tilt angles. This is a potential benefit to the processing of polydisperse particles, because larger particles need a longer residence time to undergo a given extent of heating or reaction than smaller particles.

Figure 4b shows that $\tau_{p,90}$ is strongly dependent on ψ for d_p = 80 µm, while it is almost independent of ψ for d_p = 20 µm, which is consistent with the trend of $\bar{\tau}_p$. The greatest $\tau_{p,90}$ values were measured for d_p = 80 µm, U_{in} = 30.7 m/s and ψ = −90º, −60º and −30º ($\tau_{p,90}$ = 15.2, 14.7 and 14.2 s, respectively). This indicates that, for these conditions, gravity enhances the recirculation of large particles towards the base of the conical section of the SEVR so that they are re-entrained by the most intense part of the vortex flow. The values of $\tau_{p,90}$ for d_p = 80 µm, decreases with ψ to a minimum at ψ = +90º with values of $\tau_{p,90}$ = 0.85 and 0.79 s for U_{in} = 30.7 and 36.0 m/s, respectively. These values are only a factor of 1.4 greater than their respective mean residence times, indicating that there is little particle recirculation of larger particles within the SEVR, for positive tilt angles. The values $\tau_{p,90}$ for d_p = 20 µm are relatively consistent in the range 1.7 to 3.0 s for $\psi \geq$ −60º, indicating that the alignment of gravity relative to the axis of the receiver has no significant effect on the extent to which 20 µm particles recirculate within the SEVR, in contrast to the effect of receiver tilt angle on the larger 80 µm particles.

Figure 4c presents the dependence of σ_p^2 on ψ. It can be seen that, for the conditions assessed, the normalised variance and mixing behaviour of the SEVR varies between that of a well-stirred reactor (for which σ_p^2 = 1) and that of a plug flow reactor (for which σ_p^2 = 0), following Danckwerts (1995), Levenspiel (1999) and Fogler (2006). The normalised variance increases from σ_p^2 = 0.90 with ψ = −90º to a maximum of σ_p^2 = 1.23 with ψ = 0º for d_p = 80 µm and U_{in} = 30.7 m/s, which correspond to the cases in Figure 4a and b featuring longest residence time and greatest extent of particle recirculation. This indicates that the large-scale recirculation for particles of this size within the SEVR with $\psi \leq$ 0º is close to the mixing behaviour of an ideal continuously-stirred tank reactor (CSTR). It should be noted that, for d_p = 80 µm, U_{in} = 30.7 m/s, and the two tilt angles, ψ = −30º and 0°, the normalised variance values are σ_p^2 > 1, which indicates a slight departure from an ideal reactor, as also indicated by the highly skewed RTDs for these cases (as shown in Figure 3a and b). This can be attributed to a departure from the steady recirculation that occurs when particles return to the most intense region of the vortex for the negative tilt angles, $\psi \leq$ −60º. In contrast, the particles that fall to the bottom of the cylinder for ψ = −30º and 0° undergo unsteady recirculation by the less intense region of the vortex flow, resulting in a less uniform RTD with σ_p^2 > 1. For d_p = 80 µm and positive tilt angles, an increase in ψ causes a decrease in σ_p^2 to a minimum of 0.10 with ψ = +90º and both U_{in}, indicating that the flow pattern of d_p = 80 µm particles approaches a plug flow. This is also evident from the RTDs plotted in Figure 3a and b. In contrast, for the smaller particles, d_p = 20 µm, and both U_{in}, the value of σ_p^2 decreases from a maximum at ψ = −90º of σ_p^2 = 0.62 and 0.51 for U_{in} = 30.7 and 36.0 m/s, respectively, but is then relatively consistent around ~0.32 ± 0.10 for $\psi \geq$ −30º, for both U_{in}. This indicates that for these conditions there is not significant variation of the particle residence time, which is a potential benefit to processes that require uniform residence time for all particles (e.g. for uniform product quality in the calcination of alumina process). Taken together, the trends presented in Figure 4c suggest that the mixing behaviour of 20 µm particles is significantly less influenced by the receiver tilt angle than are the larger 80 µm particles, which varies between the extremes of well-stirred and plug flow mixing behaviours.

Figure 5 presents the mean residence time of the measured particle RTDs, $\bar{\tau}_p$, as a function of Sk_{out}, for five values of receiver tilt angle in the range, ψ = −90° to +90°, and for two Froude numbers evaluated in the cylindrical section of the receiver, Fr_{cyl} = 3.8 and 5.3 (generated with U_{in} = 30.7 and 36.0 m/s, respectively). These two values of Fr_{cyl} correspond to the *Froude-Stokes* and *cyclonic* regimes of particle behaviour within the SEVR. The data for ψ = −60° and +60° are not presented in Figure 5 for clarity.

For the negative tilt angles, ψ = −90° and −30°, it can be seen that the particle residence time is controlled by both the particle inertia at the receiver outlet (Sk_{out}) and the influence of gravity. That is, for both Fr_{cyl} = 3.8 (Figure 5a) and Fr_{cyl} = 5.2 (Figure 5b), $\bar{\tau}_p$ increases with Sk_{out}, due to the increased inertia of a particle at the radially-oriented outlet that inhibits it from leaving the receiver. For the *Froude-Stokes* regime, this increase is more pronounced because, in addition to the effect of increased inertia, gravity plays a greater role in resisting the axial motion in the positive z direction and recirculating the particles to the bottom of the receiver. This results in significantly longer residence time. For the *cyclonic* regime, the inertial centrifugal force is of greater importance in influencing

particle motion and retaining particles in suspension flow near to the receiver outlet. This implies that, for beam-down receiver tilt angles ($\psi < 0°$), the features of the *Froude-Stokes* and *cyclonic* regimes of operation are the same as those reported previously for $\psi = -90°$ (Davis et al., 2019); namely a preferential increase in residence time for larger (and more dense) particles in the *Froude-Stokes* regime, and a less pronounced increase in residence time in the *cyclonic* regime.

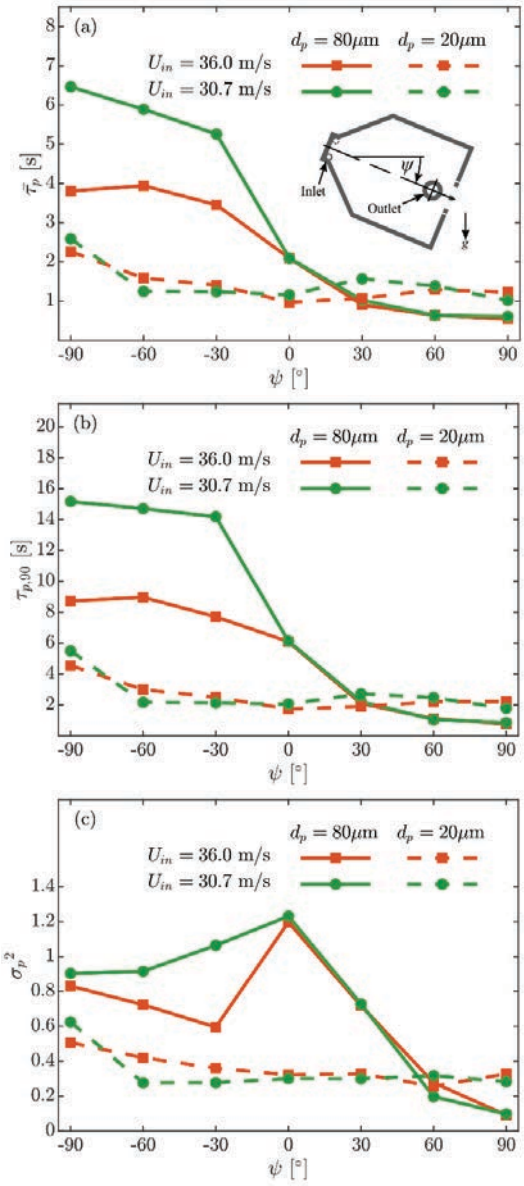

Figure 4: The statistical measures of the particle RTDs measured for seven receiver tilt angles in the range $\psi = -90°$ to $+90°$, and for two particle diameters, $d_p = 20$ and 80 µm, two inlet velocities $U_{in} = 30.7$ and 36.0 m/s with constant inlet diameter, $D_{in} = 6$ mm. The two inlet velocities generate nominal residence times $\tau_{nom} = 3.2$ and 2.7 s according to $\tau_{nom} = V_r/\dot{V}_{air}$ and $\dot{V}_{air} = U_{in} \times [2 \times (\pi/4) \times D_{in}^2]$. Presented are: (a) the mean particle residence time, $\bar{\tau}_p$, as a function of ψ; (b) the 90th percentile particle residence time, $\tau_{p,90}$, as a function of ψ; and (c) the normalised variance, σ_p^2, as a function of ψ. The data for $\psi = -90°$ have been reported previously in (Davis et al., 2019).

In contrast, for the positive receiver tilt angles $\psi \geq 0°$, the effect of both ψ and Fr_{cyl} is relatively weak, with approximately equal values of $\bar{\tau}_p$ at the same Sk_{out} for both regimes. That is, for $\psi \geq 0°$ and the conditions assessed in the present study, the *Froude-Stokes* and *cyclonic* regimes of operation cannot be distinguished, which may indicate that the device is inertia dominated. Furthermore, both regimes exhibit a residence time trend that decreases with Sk_{out} for $\psi > 0°$, which is a feature not identified in previous work (Davis et al., 2019). That is, for both $Fr_{cyl} = 3.8$ and 5.3, $\bar{\tau}_p$ decreases with increasing Sk_{out}, for the cases where the outlet is below the inlet. This is because at low Sk_{out}, particles exhibit a strong response to the flow, such that they are entrained within the vortical flow for a longer duration than particles with large Sk_{out}, which have a more direct path to the exit due to the effect of gravity. It should also be noted that for the case of a horizontal receiver tilt angle ($\psi = 0°$), there is a weak increase in $\bar{\tau}_p$ with Sk_{out}, for both $Fr_{cyl} = 3.8$ and 5.3. For $\psi = 0°$, there is no component of gravity acting in the axial direction, so that the increase in $\bar{\tau}_p$ can be attributed only to the increased inertia of the particles. This indicates that the particle residence time characteristics of vortex-based solar particle receivers operated in a horizontal orientation for laboratory testing with a solar simulator will potentially exhibit different residence time characteristics to those of solar particle receivers with beam-up or beam-down orientations in CST systems.

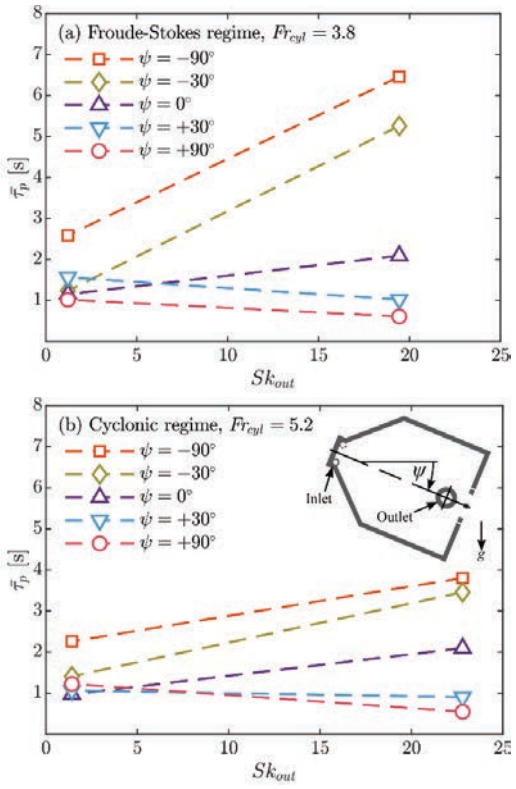

Figure 5: The mean particle residence time, $\bar{\tau}_p$, as a function of Sk_{out}, for five values of receiver tilt angle in the range, $\psi = -90°$ to $+90°$, and for (a) the *Froude-Stokes* regime of operation with $Fr_{cyl} = 3.8$ (generated with $U_{in} = 30.7$ m/s); and (b) the *cyclonic* regime of operation with $Fr_{cyl} = 5.2$ (generated with $U_{in} = 36.0$ m/s).

3.2 Compartment model analysis

Figure 6 presents the dimensionless particle RTDs, $E(\theta)$, measured for the smaller particle size, $d_p = 20$ µm, for $U_{in} = 30.7$ m/s and for the receiver tilt angles $\psi = -60°$, $-30°$, $0°$ and $+90°$. The dimensionless RTDs for the range of receiver tilt angles considered can be described similarly to those presented previously for $\psi = -90°$ (Davis et al., 2019). That is, $E(\theta)$ remains at zero for short dimensionless times, δ_1, defined as the ratio of the time for which

the pulse response is zero to the mean particle residence time, after which $E(\theta)$ increases rapidly to a maximum value, and then decreases at a slower rate to zero. It can also be seen that, for ψ = −30° and 0° (Figure 6b and c), small peaks were detected in the RTD before the primary peak. This can be attributed to wall-related interactions, such as adhesion/re-entrainment, that are prevalent for these cases with tilt angle close to the horizontal. However, the area bounded by these peaks is always less than 5% of the total area bounded by the RTD, so that these effects are small here.

The compartment model describing the experimental residence time behaviour presented in Figure 6, has been proposed previously for ψ = −90° and both d_p = 20 and 80 µm. The compartment model consists of a very small plug flow reactor (PFR) in series with two continuously-stirred tank reactors (CSTRs). For the case of low velocities and Froude numbers (*Froude-Stokes* regime) there is back mixing between the two CSTRs causing them to behave as a single CSTR, while for higher velocities and Froude numbers (*cyclonic* regime) there is no back-mixing. Figure 6 presents the analytical RTDs corresponding to this configuration of compartment model as applied to the alternative values of ψ in the present study. It can be seen from the comparison between the experimental and analytical dimensionless RTDs that this same configuration of compartment model describes the residence time behaviour of the smaller particles, d_p = 20 µm, and all alternative receiver tilt angles, ψ > −90°, assessed here.

The analytical equation of the dimensionless RTDs presented in Figure 6 can be expressed as follows:

$$E(\theta) = \frac{1+\varepsilon}{(\varepsilon-1)(1-\delta_1)}\left[e^{-\frac{(\theta-\delta_1)(1+\varepsilon)}{\varepsilon(1-\delta_1)}} - e^{-\frac{(\theta-\delta_1)(1+\varepsilon)}{(1-\delta_1)}}\right]u(\theta-\delta_1), \quad (7)$$

where ε represents the ratio of the space-times of the two CSTRs and $u(\theta - \delta)$ is the Heaviside function. This analytical equation corresponds to the above mentioned configuration of compartment model and applies for operation in both the *Froude-Stokes* and *cyclonic* regimes. For the *Froude-Stokes* regime, $\varepsilon \rightarrow 0$ so that $E(\theta)$ tends towards that describing a PFR in series with a single CSTR, while for operation in the *cyclonic* regime, $E(\theta)$ describes a PFR in series with two CSTRs. The constant compartment model configuration for all ψ and d_p = 20 µm implies that the behaviour of smaller particles within the SEVR is not significantly affected by the receiver tilt angle. While not pictured in Figure 6, the same equation and mixing patterns were found to apply for the higher inlet velocity case, U_{in} = 36.0 m/s.

The values of the parameters used in Equation (7) to describe the dimensionless RTDs for d_p = 20 µm and all ψ are listed in Table 3. The values were determined by fitting the analytical RTD described by Equation (7) to the experimentally measured dimensionless RTDs, with a coefficient of determination R^2 always higher than 0.94. It can be seen that, for both U_{in}, ε is in the range 1.01 to 3, suggesting that for the present range of velocities, there is not a significant distinction in the amount of recirculation through the receiver. Also, for the smaller particle size, d_p = 20 µm and all tilt angles except ψ = +60°, the value of δ_1 decreases to a small extent with U_{in}, indicating that the higher velocity causes the particles to fill the reactor inventory more rapidly. The small increase in δ_1 for ψ = +60° can be attributed to experimental error.

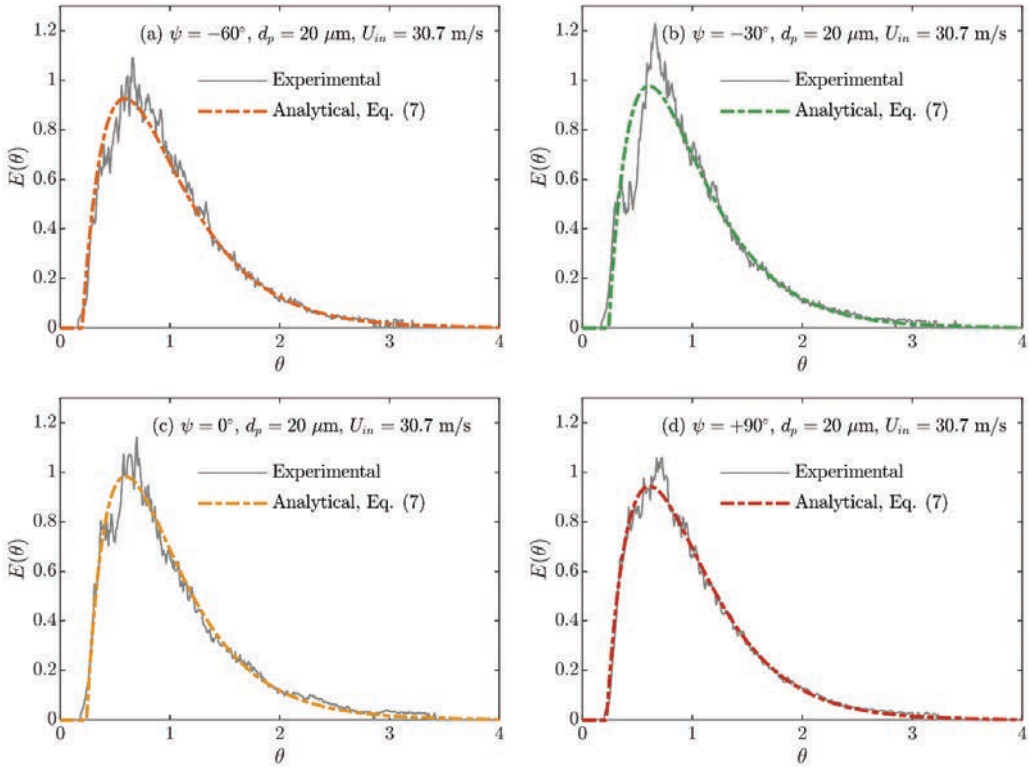

Figure 6: The experimentally measured dimensionless particle RTDs and functions of their corresponding analytical compartment models for U_{in} = 30.7 m/s, d_p = 20 µm and the receiver tilt angles: (a) ψ = −60°; (b) ψ = −30°; (c) ψ = 0°; and (d) ψ = +90°. The function of the analytical distributions shown here is given in Equation (7) while the values of the equation parameters are listed in Table 3.

Figure 7 presents the dimensionless particle RTDs, $E(\theta)$, measured for the larger particle size, d_p = 80 µm, for U_{in} = 30.7 m/s and for the receiver tilt angles ψ = −60°, −30°, 0° and +90°. It can be seen that the measured dimensionless RTDs deviate significantly from the previously developed compartment model described by Equation (7), due to the prominence of a peak in the measured distributions at dimensionless time, $\theta \approx 0.1 - 0.2$. This peak is visible for ψ = −60°, −30° and 0° (Figure 7a, b and c) and appears at a significantly shorter dimensionless time than the than the peak in the dimensionless RTDs for d_p = 20 µm (Figure 6). This type of peak in the distribution is associated with a pathway through the reactor alternative to the well-mixed CSTR path identified previously. Aerodynamically, the alternative path is associated with a different flow regime, such that larger particles follow a different path to the flow, resulting in less particle recirculation and shorter mean residence times. Analytically, such an alternative path can be approximated by a PFR (Levenspiel, 1999).

To account for the deviations from the compartment model described above that occur for d_p = 80 µm and $\psi > -90°$, a modified compartment model configuration is proposed here. This modified compartment model consists of a small PFR (as previously) followed by two parallel branches, one containing the two CSTRs in series (as previously) and the other branch containing a PFR. The analytical equation to describe the modified compartment model of small PFR followed by a CSTR and PFR in parallel can be expressed as follows:

$$\begin{aligned} E(\theta) &= \frac{\beta}{\theta_{\mathrm{CSTR}}} e^{-\frac{\theta-\delta_1}{\theta_{CSTR}}} u(\theta-\delta_1) \\ &+ (1-\beta)\frac{1}{\delta_2}\left(\frac{\theta-\delta_1}{\delta_2}\right)^{N-1}\frac{N^N}{(N-1)!}e^{-\frac{(\theta-\delta_1)N}{\delta_2}}u(\theta-\delta_1), \end{aligned} \quad (8)$$

where β is the fraction of particles taking the path to the CSTR, $(1-\beta)$ is the fraction of particles taking the path to the PFR (with dimensionless space-time equal to δ_2) and θ_{CSTR} is the dimensionless space-time of the CSTR. It should be noted that the two CSTRs in series from the compartment model describing d_p = 20 µm is here modelled as a single CSTR for simplicity. Also the PFR on the parallel branch (with $(1-\beta)$ fraction of particles) is modelled as N CSTRs in series, where N is the number of CSTRs that best approximates the residence time of the parallel PFR component of the compartment model (Fogler, 2006). The compartment model expressed by Equation (8) describes the residence time behaviour for d_p = 80 µm, U_{in} = 30.7 m/s and all alternative receiver tilt angles $\psi > -90°$, as can be seen from the analytical dimensionless RTDs also presented in Figure 7.

The values of the parameters used in Equation (8) to describe the dimensionless RTDs for d_p = 80 µm are listed in Table 3. These values were also determined by fitting the analytical RTD described by Equation (8) to the experimentally measured dimensionless RTDs, with a coefficient of determination R^2 always higher than 0.94. It can be seen from Table 3 that β decreases so that the relative proportioning of two-phase flow to the PFR branch increases with both U_{in} and the tilt angle from ψ= −60° to +90°. This implies that the fraction of large particles that bypass the recirculation (i.e. to take the PFR branch) increases with the tilt angle. The significance of the bypass is greatest for ψ = +90° (Figure 7d), where all of the particles tend towards a plug flow response. This deduction is also consistent with the values of the normalised variance presented in Figure 4c and with the values β = 0 and N = 17 for d_p = 80 µm and ψ = +90° (Table 3). The analytical distribution in Figure 7d is almost symmetrical about θ = 1 as is the case for an ideal PFR. Furthermore, for N CSTRs in series, the RTD can be assumed to be representative of a plug flow reactor for $N \geq 10$ (Levenspiel, 1999). While not pictured in Figure 7, the modified compartment model and Equation (8) were also found to apply for the higher inlet velocity case, U_{in} = 36.0 m/s and d_p = 80 µm for each value of ψ.

Figure 8 presents a schematic representation of the unified compartment model describing the particle RTD behaviour of the SEVR for the range of receiver tilt angles assessed here and for U_{in} = 30.7 and 36.0 m/s, and d_p = 20 and 80 µm. For each case, the values of the parameters used in Equations (7) and (8) are listed in Table 3. The influence of receiver tilt angle on the residence time behaviour of the SEVR in the present study can be described with this compartment model as follows:

- For all ψ, d_p and U_{in} (assessed here), the flow passes through the small PFR_1, which represents the time taken for particles to fulfil the reactor inventory. The space-time of the PFR_1 component, δ_1, generally decreases with U_{in}.
- For ψ = −90° and both d_p = 20 and 80 µm, β = 1, so that the residence time behaviour of particles of both sizes is represented by particles taking only the CSTR path to pass through the receiver undergoing significant extents of particle recirculation (Equation 7). In the low velocity, *Froude-Stokes* regime there is back-mixing between $CSTR_1$ and $CSTR_2$ so that they behave as a single CSTR, while for the higher velocity, *cyclonic* regime, the back-mixing is negligible.
- For all $\psi \geq -90°$ and d_p = 20 µm, β = 1, so that the residence time behaviour of smaller particles is represented by particles taking only the CSTR branch and the extent of their recirculation is not significantly influenced by the receiver tilt angle (Equation 7).
- For ψ = −60°, −30°, 0°, +30°, +60° and d_p = 80 µm, $\beta \neq 1$, so that the residence time behaviour of larger particles is represented by some fraction of particles taking the shorter parallel PFR_2 branch (Equation 8). The fraction of particles taking the PFR_2 branch increases with both ψ and U_{in}. Furthermore, the behaviour of the PFR_2 branch tends towards that of an ideal PFR with increasing ψ, as N increases from 3 to 11 for an increase from ψ = −60° to +60°.
- For ψ = +90° and d_p = 80 µm, β = 0, so that the residence time behaviour of larger particles is represented by particles taking only the PFR_2 branch and the particle RTD is representative of a purely plug flow reactor (Equation 8).

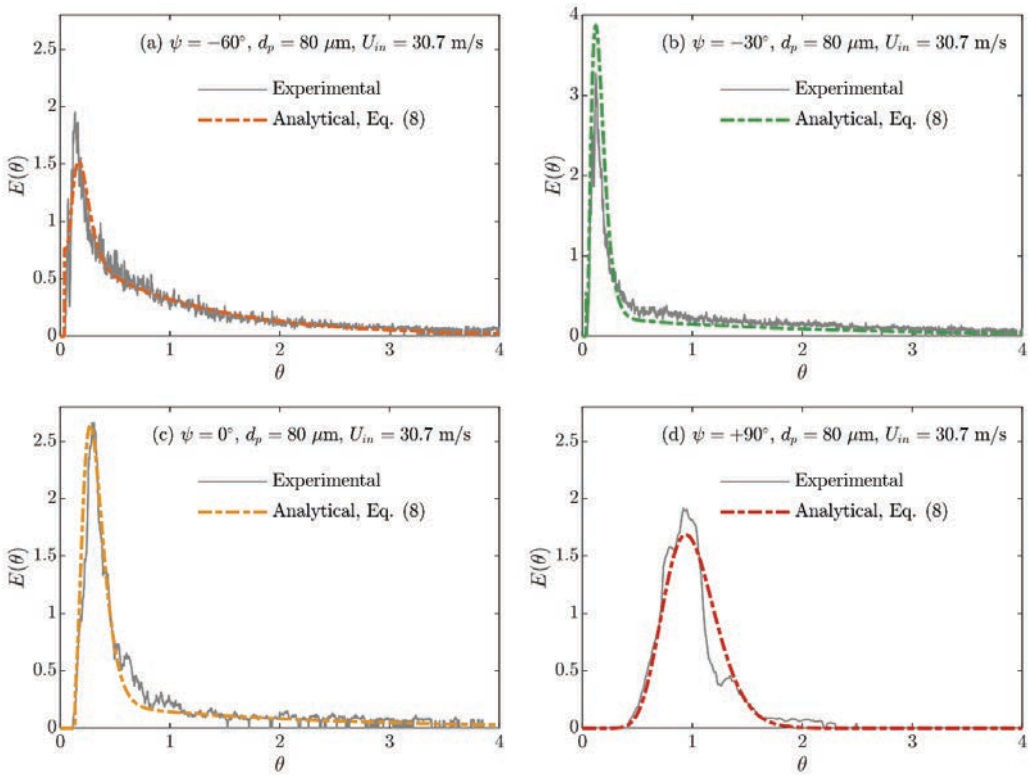

Figure 7: The experimentally measured dimensionless particle RTDs and functions of their corresponding analytical compartment models for U_{in} = 30.7 m/s, d_p = 80 μm and the receiver tilt angles: (a) $\psi = -60°$; (b) $\psi = -30°$; (c) $\psi = 0°$; and (d) $\psi = +90°$. The function of the analytical distributions shown here is given in Equation (8) while the values of the equation parameters are listed in Table 3.

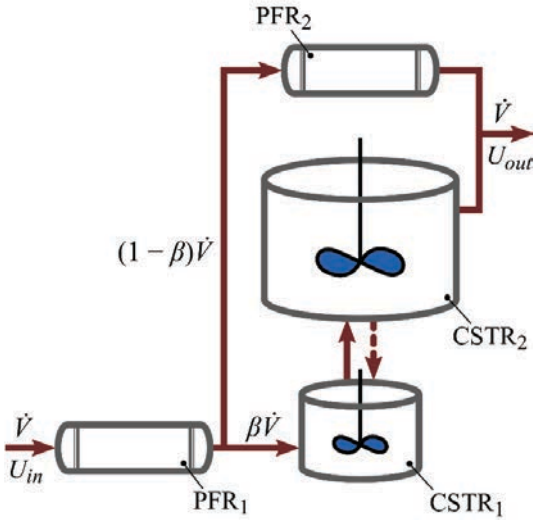

Figure 8: Schematic representation of the unified compartment model describing the particle RTD behaviours of the SEVR for the seven receiver tilt angles assessed here, $\psi = -90°$, $-60°$, $-30°$, $0°$, $+30°$, $+60°$ and $+90°$, and for U_{in} = 30.7 and 36.0 m/s, and d_p = 20 and 80 μm. For each operational case, the relative proportioning, β, between the CSTR branch (CSTR$_1$ + CSTR$_2$) and the parallel PFR$_2$ branch is listed in Table 3, together with the values of the additional parameters used to describe the analytical dimensionless RTDs with Equations (7) and (8).

Table 3: The operational details and corresponding values of the parameters used in Equations (7) and (8) to describe the measured particle RTDs with analytical compartment models.

ψ [°]	d_p [µm]	Fr_{cyl}	U_{in} [m/s]	δ_1	ε	δ_2	N	β
−90	80	3.8	30.7	0.09	0	-	-	1
		5.2	36.0	0.08	0.1	-	-	1
	20	3.8	30.7	0.13	0	-	-	1
		5.2	36.0	0.094	6	-	-	1
−60	80	3.8	30.7	0.05	-	0.17	4	0.84
		5.2	36.0	0.08	-	0.18	4	0.89
	20	3.8	30.7	0.25	3	-	-	1
		5.2	36.0	0.2	1.5	-	-	1
−30	80	3.8	30.7	0.04	-	0.12	3	0.47
		5.2	36.0	0.06	-	0.17	3	0.64
	20	3.8	30.7	0.24	1.6	-	-	1
		5.2	36.0	0.21	1.6	-	-	1
0	80	3.8	30.7	0.21	-	0.21	4	0.42
		5.2	36.0	0.18	-	0.18	4	0.48
	20	3.8	30.7	0.24	1.9	-	-	1
		5.2	36.0	0.24	2	-	-	1
+30	80	3.8	30.7	0.25	-	0.35	3	0.20
		5.2	36.0	0.22	-	0.35	4	0.26
	20	3.8	30.7	0.23	1.01	-	-	1
		5.2	36.0	0.22	2.55	-	-	1
+60	80	3.8	30.7	0.26	-	0.55	10	0.18
		5.2	36.0	0.16	-	0.63	11	0.26
	20	3.8	30.7	0.24	1.1	-	-	1
		5.2	36.0	0.26	1.1	-	-	1
+90	80	3.8	30.7	0	-	1	17	0
		5.2	36.0	0	-	1	17	0
	20	3.8	30.7	0.22	1.01	-	-	1
		5.2	36.0	0.15	1.01	-	-	1

3.3 Preliminary scaling analysis

A preliminary scaling analysis is presented here with the goal of providing insights into the mechanisms controlling the particle residence time behaviour of a nominal industrial scale SEVR. Table 4 presents the nominal thermal scale of the present laboratory-scale SEVR device, $\dot{Q}_s = 5$ kW, compared with that of a SEVR scaled up to a nominal industrial scale of $\dot{Q}_s = 50$ MW. The preliminary sizing of the nominal industrial device has been determined by assuming constant solar thermal heat flux, so that the aperture area scales linearly with the thermal input ($A_{ap} \propto \dot{Q}_s$) and by assuming geometric similarity, so that all receiver dimensions scale with the square root of the thermal input ($D_c \propto \dot{Q}_s^{1/2}$). By further assuming that the SEVR is scaled with constant inlet velocity and constant efficiency (i.e. that mass flow rates scale linearly with thermal input, $\dot{m}_p$, $\dot{m}_{air} \propto \dot{Q}_s$), it can be seen from Table 4 that the nominal residence time of the scaled-up receiver is two orders of magnitude longer than that of the laboratory-scale receiver (with a four order of magnitude increase in thermal scale). The choice of constant velocity scaling is reasonable for flow with particles in suspension because velocity cannot be reduced significantly without resulting in particles no longer being carried in suspension and also cannot be increased significantly without resulting in both excessive fan power requirements and excessive erosion. It should be noted that this preliminary scaling analysis is intended to provide insight into the controlling mechanisms at larger scale, rather than providing a guide to the design of a scaled-up SEVR, which is a complex process that requires data at larger scale.

It can also be seen from the preliminary scaling analysis presented in Table 4 that particles of the same size in the scaled industrial receiver have lower values of both Fr_{cyl} and Sk_{out} by two orders of magnitude because dimensions of the receiver scale with the square root of thermal input, D_c, $D_{out} \propto \dot{Q}_s^{1/2}$. That is, this scaled-up SEVR would operate with relatively low Froude number and therefore the *Froude-Stokes* regime of operation would be more likely. Furthermore, for this scaling, the particle size is an order of magnitude larger to achieve the equivalent *Froude-Stokes* behaviour. That is, a particle size of $d_p = 200$ µm would have the same $Sk_{out} \sim 1$ in the larger device as the $d_p = 20$ µm particles in the laboratory-scale device, although the nominal residence time is two orders of magnitude greater. This implies that the influence of the tilt angle of the scaled-up SEVR on the residence time of particles will be insignificant for particles $d_p < 200$ µm, indicating that the particle residence time characteristics of a tower-mounted SEVR using particles of this size will be constant, regardless of the required tilt angle for a given heliostat field layout. This potentially provides flexibility for incorporation of the scaled-up SEVR into CST systems with a range of tilt angles and is significant because many current industrial processes operate with particles of approximately this size. It should also be noted that alternative commonly used materials for particles in solar thermal receivers (e.g. ceramic particles) will likely have different density to the polymer particles used in the present study. This implies that the dimensionless Stokes numbers of alternative particles (with alternative size and density) will need to be compared to gain insight into the likely residence time characteristics of alternative particles in a scaled-up SEVR.

The influence of higher operating temperatures on the particle residence time characteristics of a scaled-up SEVR can be estimated by also assuming constant velocity scaling and geometric similarity. Under these assumptions, the largest impact of increasing operating temperatures would be the change in gas-phase properties, most notable, the gas density and viscosity. For example, an operating temperature of 1000 K would reduce air density, and hence mass flow rate, in the scaled-up SEVR by a factor of 3.3 relative to room temperature (300 K). Although this will decrease the gas-phase mass flow rate, the effect on the particle RTD is expected to be minimal. The particle residence time is expected to be more significantly influenced by the gas-phase velocity, which is a function of the gas volumetric flow rate, rather than the mass flow rate. However, the increase in operating temperatures will typically increase gas-phase viscosity, which in turn will decrease the characteristic Stokes number, Sk_{out} (because $Sk_{out} \propto \mu_{air}^{-1}$ with constant U_{in}, ρ_p, d_p and geometry). For instance, an increase in operating temperatures from

300 K to 1000 K will decrease Sk_{out} by a factor of 2.3. The impact of this decrease in Sk_{out} is difficult to predict in general, because the influence of Stokes number is typically non-linear, such that a factor of 2.3 is expected to influence the two-phase flow only where $Sk_{out} \sim 1$ (Lau and Nathan, 2014; Lau and Nathan, 2016). That is, for cases where $Sk_{out} >> 1$ the effect of higher operating temperatures is expected to be small, while for cases where $Sk_{out} \sim 1$, the reduction in Sk_{out} with higher operating temperatures will result in the particle-phase RTD more closely matching the gas-phase residence time. In summary, a change in operating temperature is only expected to significantly influence the particle RTD characteristics for cases where $Sk_{out} \sim 1$. However, experimental data are required to truly assess the impact of temperature on the particle residence time within the SEVR.

Table 4: Comparison of key operational and dimensionless parameters of the Solar Expanding Vortex Receiver (SEVR) at the present laboratory-scale with the equivalent values from a preliminary scaling analysis of the receiver at a nominal industrial scale. The preliminary scaling analysis assumes constant inlet velocity, volumetric loading and heat flux through the aperture, as well as geometric similarity of the SEVR.

	SEVR at laboratory-scale		**SEVR scaled to industrial-scale**	
$\dot{Q}_s$ [kW]	5		50×10^3	
D_c [m][a]	0.19		19	
U_{in} [m/s][b]	30.7	36.0	30.7	36.0
τ_{nom} [s][c]	3.2	2.7	320	270
Fr_{cyl}[d]	3.8	5.3	0.038	0.053
Sk_{out} for $d_p = 20$ µm[e, f]	1.2	1.4	0.012	0.014
Sk_{out} for $d_p = 80$ µm[e, f]	19.4	22.8	0.194	0.228
Sk_{out} for $d_p = 200$ µm[e, f]	~120	~140	~1.2	~1.4
Sk_{out} for $d_p = 800$ µm[e, f]	~1940	~2280	~19.4	~22.8

[a] $D_c \propto \dot{Q}_s^{1/2}$;
[b] Constant velocity scaling;
[c] $(V_r/\dot{V}_{air}) \propto (\dot{Q}_s^{3/2}/\dot{Q}_s)$, $\tau_{nom} \propto \dot{Q}_s^{1/2}$;
[d] $Fr_{cyl} \propto \dot{Q}_s^{-1/2}$;
[e] $Sk_{out} \propto \dot{Q}_s^{-1/2}$, $(Sk_{out} \propto d_p^2)$;
[f] Constant particle density scaling.

4 Conclusions

The systematic variation of receiver tilt angle with two inlet velocities, and two particles sizes has revealed that alignment of the central axis of the SEVR relative to gravity has a significant influence on the particle RTD for large particles ($Sk_{out} > 10$), while it is relatively weak for small particles ($Sk_{out} \sim 1$). This implies that it may be preferable to operate a tower-mounted SEVR ($\psi > 0°$) with $Sk_{out} \sim 1$, so that the receiver's particle residence time characteristics are independent of the tilt angle and the range of possible heliostat field and central tower system configurations.

It was found that the residence time of higher Stokes number particles relative to those of order unity is increased by upward facing receiver orientations (i.e. with negative tilt angles, $\psi < 0°$) due to their increased inertia at the radially-oriented outlet and the influence of gravity in recirculating particles to the bottom of the receiver. For these upward facing orientations and the conditions assessed here, the increase in particle residence time with higher Stokes numbers is strong for operation in the low Froude number *Froude-Stokes* regime, while the increase is weaker for operation in the higher Froude number *cyclonic* regime, due to the greater importance of the inertial centrifugal force in retaining particles in suspension flow near to the receiver outlet. It was further found that, for downward facing receiver orientation (i.e. positive tilt angles, $\psi > 0°$), the particle residence time decreases with increasing Stokes number, which can be attributed to the weaker response to the vortex flow of particles with higher Stokes number. These higher Stokes number particles therefore, have a more direct path to the exit due to the effect of gravity, than smaller particles which are entrained within the vortical flow for a longer duration. This effect was found to occur for both Froude numbers assessed, so that for $\psi > 0°$, residence time trend of the high and low Froude number regimes is the same.

From a reactor design point of view, it was found that, for the largest particles assessed ($d_p = 80$ µm), increasing the tilt angle of the device switches between well-stirred mixing conditions to plug flow particle RTD characteristics, as the normalised variance of the particle RTD for larger particles tends towards zero. The mixing behaviour of the smallest particles assessed ($d_p = 20$ µm) were found to have intermediate mixing behaviour between well-stirred and a plug flow, which is independent of the tilt angle. A compartment model was found to describe this behaviour, consisting of a small PFR followed by two parallel branches, one containing two CSTRs in series and the other containing a PFR. The smaller particle residence time behaviour is described exclusively with the first PFR and the CSTR branch of the compartment model. The proportioning of the larger particles between the two parallel branches is dependent on the tilt angle, such that negative tilt angles favour the CSTR and undergo significant recirculation and long residence times, and positive tilt angles favour the PFR with shorter residence times. This compartment model provides an indication of the particle residence time behaviour in the present laboratory-scale SEVR and is a useful design tool. However additional validation of the model over a wider range of conditions and scales is required.

A preliminary scaling analysis of the present receiver configuration scaled to a nominal industrial scale of 50 MW has shown that particles of size 200 µm and smaller would have residence time behaviour similar to the smallest particles considered in the present experimental assessment with $Sk_{out} \sim 1$. That is, the influence of receiver tilt angle on the residence time of particle with $d_p < 200$ µm would be small, which indicates flexibility for incorporation of the scaled-up SEVR into CST systems. Although the design of a scaled-up receiver is a complex process requiring further data of operation at larger scale.

Nomenclature

A	Area [m^2].
D	Diameter (a characteristic length scale) [m]
d_p	Particle diameter [μm].
$E(t)$	The residence time (or exit age) probability distribution function [1/s].
$E(\theta)$	The dimensionless residence time distribution.
Fr	Froude number.
g	Acceleration due to gravity [m/s^2].
L	Length [mm].
$\dot{m}$	Mass flow rate [kg/s].
N	Number of CSTRs in series used to model a PFR. $N \geq 10$ representative of PFR.
$\dot{Q}_s$	Nominal thermal input to receiver [W].
r	Radial coordinate [mm].
R^2	Coefficient of determination.
Sk	Stokes number.
t	Time [s].
U	Velocity (a characteristic velocity scale) [m/s].
u	Component of total velocity, U [m/s]
$u(\theta-\delta)$	The Heaviside unit step function, with dimensionless time delay δ.
V	Volume [m^3].
$\dot{V}$	Volumetric flow rate [m^3/s, slpm].
z	Axial coordinate [mm].
α	Receiver cone angle [°].
β	Fraction of particles taking compartment modelling CSTR branch.
δ_1, δ_2	Dimensionless space-time of the compartment modelling plug flow reactors, PFR_1, PFR_2.
ε	Volume ratio of the two CSTRs of the compartment model.
θ	Dimensionless time, $\theta = t/\overline{\tau_p}$.
θ_{CSTR}	Dimensionless space-time of the compartment modelling CSTR component.
μ	Dynamic viscosity [kg/ms].
ρ	Density [kg/m^3].
σ_p^2	Normalised variance, $\sigma_p^2 = \sigma_{p,t}^2/\overline{\tau_p}^2$.
$\sigma_{p,t}^2$	Calculated variance of $E(t)$ [s^2].
τ	Residence time [s].
τ_{nom}	Nominal residence time, $\tau_{nom} = V_r/\dot{V}_{gas}$ [s].
$\overline{\tau_p}$	Mean particle residence time [s].
$\tau_{p,90}$	90th percentile particle residence time [s].
φ	Angular coordinate [°].
ψ	Receiver tilt angle (horizontal: $\psi = 0°$; down facing: $\psi > 0°$, upward facing: $\psi < 0°$) [°].
Subscripts	
air	Air phase.
ap	Aperture.
base	Receiver base.
c	Receiver internal cavity.
cone	Receiver cone section.
cyl	Receiver cylindrical section.
in	Inlet.
max	Maximum value along the radial axis.
nom	Nominal.
out	Outlet.
p	Particle phase.
r	Receiver.
φ	Tangential component.
Abbreviations	
CST	Concentrated solar thermal.
CSTR	Continuously-stirred tank reactor.
PFR	Plug flow reactor.
RTD	Residence time distribution.
SEVR	Solar expanding vortex receiver-reactor.
SVR	Solar vortex receiver-reactor.

Acknowledgements

We gratefully acknowledge the financial support of the Australian Solar Thermal Research Initiative (ASTRI), a project supported by the Australian Government, through the Australian Renewable Energy Agency (ARENA). Dominic is also grateful for additional assistance in the form of an Australian Government Research Training Program Scholarship. We have no conflict of interest to disclose.

References

Behar, O., Khellaf, A., Mohammedi, K., 2013. A review of studies on central receiver solar thermal power plants. Renewable & Sustainable Energy Reviews 23, 12-39.

Buffham, B.A., Mason, G., 1993. Holdup and dispersion: tracer residence times, moments and inventory measurements. Chem Eng Sci 48(23), 3879-3887.

Chinnici, A., Arjomandi, M., Tian, Z.F., Lu, Z., Nathan, G.J., 2015. A Novel Solar Expanding-Vortex Particle Reactor: Influence of Vortex

Structure on Particle Residence Times and Trajectories. Solar Energy 122, 58-75.

Chinnici, A., Arjomandi, M., Tian, Z.F., Nathan, G.J., 2016. A Novel Solar Expanding-Vortex Particle Reactor: Experimental and Numerical Investigation of the Iso-thermal Flow Field and Particle Deposition. Solar Energy 133, 451-464.

Clausing, A., 1983. Convective losses from cavity solar receivers—comparisons between analytical predictions and experimental results. Journal of Solar Energy Engineering 105(1), 29-33.

Danckwerts, P.V., 1995. Continuous flow systems. Distribution of residence times. Chem Eng Sci 50(24), 3855.

Davis, D., Muller, F., Saw, W.L., Steinfeld, A., Nathan, G.J., 2017. Solar-driven alumina calcination for CO_2 mitigation and improved product quality. Green Chemistry 19(13), 2992-3005.

Davis, D., Troiano, M., Chinnici, A., Saw, W.L., Lau, T.C.W., Solimene, R., Salatino, P., Nathan, G.J., 2019. Particle residence time distributions in a vortex-based solar particle receiver-reactor: an experimental, numerical and theoretical study. Manuscript submitted for publication.

Fogler, H.S., 2006. Elements of chemical reaction engineering, 4th ed. ed. Prentice Hall PTR, Upper Saddle River, NJ.

Hirsch, D., Steinfeld, A., 2004. Solar hydrogen production by thermal decomposition of natural gas using a vortex-flow reactor. Int J Hydrogen Energ 29(1), 47-55.

Ho, C.K., 2017. Advances in central receivers for concentrating solar applications. Solar Energy 152, 38-56.

Ho, C.K., Iverson, B.D., 2014. Review of high-temperature central receiver designs for concentrating solar power. Renewable & Sustainable Energy Reviews 29, 835-846.

Kodama, T., Gokon, N., Matsubara, K., Yoshida, K., Koikari, S., Nagase, Y., Nakamura, K., 2014. Flux measurement of a new beam-down solar concentrating system in Miyazaki for demonstration of thermochemical water splitting reactors. Proceedings of the Solarpaces 2013 International Conference 49, 1990-1998.

Kräupl, S., Steinfeld, A., 2001. Experimental investigation of a vortex-flow solar chemical reactor for the combined ZnO-reduction and CH4-reforming. Journal of Solar Energy Engineering, Transactions of the ASME 123(3), 237-243.

Lau, T.C.W., Nathan, G.J., 2014. Influence of Stokes number on the velocity and concentration distributions in particle-laden jets. Journal of Fluid Mechanics 757, 432-457.

Lau, T.C.W., Nathan, G.J., 2016. The effect of Stokes number on particle velocity and concentration distributions in a well-characterised, turbulent, co-flowing two-phase jet. Journal of Fluid Mechanics 809, 72-110.

Lee, K.L., Chinnici, A., Jafarian, M., Arjomandi, M., Dally, B., Nathan, G., 2018. Experimental investigation of the effects of wind speed and yaw angle on heat losses from a heated cavity. Solar Energy 165, 178-188.

Leibfried, U., Ortjohann, J., 1995. Convective Heat-Loss from Upward and Downward-Facing Cavity Solar Receivers - Measurements and Calculations. J Sol Energ-T Asme 117(2), 75-84.

Levenspiel, O., 1999. Chemical reaction engineering, 3rd ed. ed. Wiley, New York.

Li, L., Coventry, J., Bader, R., Pye, J., Lipiński, W., 2016. Optics of solar central receiver systems: a review. Optics Express 24(14), A985-A1007.

Müller, F., Poživil, P., van Eyk, P.J., Villarrazo, A., Haueter, P., Wieckert, C., Nathan, G.J., Steinfeld, A., 2017. A pressurized high-flux solar reactor for the efficient thermochemical gasification of carbonaceous feedstock. Fuel 193, 432-443.

Steinfeld, A., Imhof, A., Mischler, D., 1992. Experimental Investigation of an Atmospheric-Open Cyclone Solar Reactor for Solid-Gas Thermochemical Reactions. J Sol Energ-T Asme 114(3), 171-174.

Wu, S.-Y., Xiao, L., Li, Y.-R., 2010. Convection heat loss from cavity receiver in parabolic dish solar thermal power system: A review. Solar Energy 84(8).

Yogev, A., Kribus, A., Epstein, M., Kogan, A., 1998. Solar "tower reflector" systems: a new approach for high-temperature solar plants. Int J Hydrogen Energ 23(4), 239-245.

Z'Graggen, A., Haueter, P., Trommer, D., Romero, M., de Jesus, J.C., Steinfeld, A., 2006. Hydrogen production by steam-gasification of petroleum coke using concentrated solar power — II Reactor design, testing, and modeling. Int J Hydrogen Energ 31(6), 797-811.

Green Chemistry

PAPER

Cite this: *Green Chem.*, 2017, **19**, 2992

Solar-driven alumina calcination for CO_2 mitigation and improved product quality†

Dominic Davis, ‡[a] Fabian Müller, ‡[b] Woei L. Saw, [c] Aldo Steinfeld *[b] and Graham J. Nathan *[a]

Received 24th February 2017,
Accepted 10th May 2017

DOI: 10.1039/c7gc00585g

rsc.li/greenchem

We report on the first-of-a-kind experimental demonstration of the calcination of alumina with concentrated solar thermal (CST) radiation at radiative fluxes up to 2190 suns using a 5 kW novel solar transport reactor. Aluminium hydroxide was calcined at nominal reactor temperatures over the range 1160–1550 K to yield chemical conversions of up to 95.8% for nominal residence times of approximately 3 s. Solar energy conversion efficiencies of up to 20.4% were achieved. The mean pore diameter and specific surface area of the solar-generated alumina with the greatest chemical conversion were 5.8 nm and 132.7 $m^2\ g^{-1}$, respectively, which are higher values than are typical for industrial alumina production. In addition, the product is dominated by the γ-phase, which is desirable for the downstream processing to aluminium. This suggests that CST can improve the quality of alumina over existing fossil fuel based processes though a combination of a high heating rate and avoided contamination by combustion products. Furthermore, the solar-driven process has the potential to avoid the discharge of combustion-derived CO_2 emissions for the calcination stage of the conventional Bayer process, which is typically 165 kg-CO_2 per tonne-alumina.

1 Introduction

The use of concentrated solar thermal energy (CST) for high-temperature thermal processing of minerals has the potential to reduce reliance on fossil fuels and hence also to reduce greenhouse gas (GHG) emissions.[1,2] The calcination stage of alumina refining with the Bayer process is potentially well suited to the application of CST because it is a highly endothermic process that proceeds at ~1273 K, which is readily achievable with solar tower technology. In addition, the calcination process is not sensitive to some ingress of air, which raises the possibility that direct irradiation of particles may be achievable without the need for a window to completely seal a solar reactor. However, the technical feasibility of this process is yet to be evaluated experimentally. The overall objective of this investigation is therefore to assess and demonstrate the technical feasibility of alumina calcination with direct irradiation *via* CST.

Alumina is an intermediate product in the production of aluminium and is also a product in its own right. Alumina refining accounts for approximately 27% of the primary energy used in aluminium production, over 90% of which is provided by the combustion of fossil fuels.[3] A total of 115.2 million tonnes of alumina was produced globally in 2015 at an average energy intensity of 11.9 GJ per tonne-alumina, representing a significant contribution to GHG emissions.[4] Calcination is the last step of the Bayer process, which heats the hydrated alumina (aluminium hydroxide or gibbsite, $Al(OH)_3$) from the precipitation stage, to drive off the water of hydration and form anhydrous alumina (aluminium oxide, Al_2O_3). It is an energy-intensive process, which has historically been conducted with the use of fossil fuels and a rotary-kiln.[5] However, since the oil crisis of the 1970s, with the resulting increase in the cost of fuels, stationary calciners (circulating fluidised bed, gas suspension and fluid-flash calciners) have been favoured over rotary-kilns due to their significantly reduced fuel consumption.[6,7] The process heat requirements of modern industrial calciners and estimated resulting CO_2 emissions (calculated from the combustion of methane) are now approximately 3 GJ per tonne-alumina and 165 kg-CO_2 per tonne-alumina product, respectively, for which the predominant fuel is natural gas.[8,9] Today, the increasing cost of fuels continues to be a driver for technological development of more fuel

[a]*School of Mechanical Engineering, Centre for Energy Technology, The University of Adelaide, South Australia 5005, Australia. E-mail: graham.nathan@adelaide.edu.au*
[b]*Department of Mechanical and Process Engineering, ETH Zürich, 8092 Zürich, Switzerland. E-mail: aldo.steinfeld@ethz.ch*
[c]*School of Chemical Engineering, Centre for Energy Technology, The University of Adelaide, South Australia 5005, Australia*

†Electronic supplementary information (ESI) available. See DOI: 10.1039/c7gc00585g

‡The first two authors have contributed equally to this work.

efficient alumina calciner technology.[10] With the price of natural gas forecast to increase in some locations such as Australia,[9] and with the global need to reduce GHG emissions, there is strong incentive to seek alternative energy sources such as CST for process heat.[11] This provides the motivation for the present investigation.

The calcination of alumina is a thermal decomposition chemical reaction, which proceeds endothermically according to the following reaction:

$$2Al(OH)_3 \rightarrow \alpha\text{-}Al_2O_3 + 3H_2O, \Delta\bar{h}^{\circ}_{calcination} = +185.2\ kJ\,mol^{-1}. \quad (1)$$

Modern plants typically process alumina (generally in the gibbsite form) within flash calciners using particles of ~100 μm in diameter transported in a gas suspension through the reactor with residence times on the order of a few seconds. A solar reactor that processes powders of similar size to a flash calciner is the solar vortex transport reactor. This employs a vortex flow to transport particles in suspension through an irradiation zone where they undergo high heating rates to drive a thermochemical reaction. Direct solar irradiation of such a suspension of reacting particles is an efficient means of heat transfer to the reactants.[12–15] Furthermore, the temperature at which alumina calcination takes place in the Bayer process, 1273–1373 K, is readily achievable in current commercially available solar tower concentrators[11] and is significantly less than the 1750 K that has been achieved previously in the solar vortex transport reactor used for solar gasification.[16] The potential for alumina to be calcined with CST has been assessed with a packed bed of boehmite (an aluminium oxyhydroxide) in a crucible positioned at the focal plane of a Fresnel concentrator by Padilla *et al.*[17] They reported 75% conversion after 10 minutes of exposure to solar radiation concentrated to 2644 suns and full conversion with exposure time of 90 minutes.[17] However to date, no assessments have been reported for the calcination of gibbsite in a practical reactor under conditions relevant to flash calcination. The industrial gibbsite calcination process shares similarities with the calcination of limestone, which takes place at ~1150 K and has previously been demonstrated with the application of CST.[18–21] This demonstration has been performed with direct irradiation in a cavity-receiver transporting a flow of entrained particles,[18] which suggests that it may also be suitable for alumina calcination. It is also noteworthy that the alumina calcination process is sensitive to the gas-phase composition, which is one reason that natural gas is a preferred fuel for alumina production.[22,23] The application of CST to the calcination process has the potential to further improve product quality by eliminating the possibility of contamination with combustion products and by reducing the significance of back-reactions from the presence of H_2O, which is a product of combustion. While these reasons suggest that the alumina calcination process is potentially well suited to solar processing, its technical feasibility cannot be determined by implication. Due to the complex, coupled nature of the process, it is necessary to assess this experimentally with a prototype solar reactor.

When gibbsite is calcined, the solid reactant evolves through various intermediate materials, including the monohydrated aluminium oxyhydroxide and several transition phases of alumina before the final, thermodynamically stable α-alumina is formed at temperatures in the range 1375–1450 K.[23,24] Both the type of intermediate transition aluminas that are formed and their relative presence in the alumina product depend particularly on the heating rate, particle size and the presence of water vapour in the reaction atmosphere.[25] Studies have previously proposed the gibbsite reaction pathways according to these parameters,[23,24,26] the consensus of which is as follows:

(a) Fine gibbsite particles (<10 μm) decompose *via* χ-Al_2O_3, an amorphous alumina, followed by κ-Al_2O_3 before reaching the final α-Al_2O_3 phase;

(b) Coarse gibbsite particles (>100 μm) decompose *via* the intermediate aluminium oxyhydroxide, boehmite (AlO(OH)). Upon further heating this progressively decomposes to γ-, δ-, and θ-Al_2O_3, before reaching the α-Al_2O_3 phase; and

(c) Gibbsite which undergoes the high heating rates of flash calcination (4700–15 000 K s^{-1}) thermally decomposes initially to the amorphous χ-Al_2O_3 as in pathway (a) before crossing over to pathway (b) and progressively forming γ-, δ-, θ-Al_2O_3, and finally the α-Al_2O_3 phase.

The formation of the intermediate species, boehmite, occurs in the range 380–575 K and is favoured by rapid heating of coarse gibbsite particles, such that there is a high local water vapour pressure within the large gibbsite particles.[23] For the case where the gibbsite particles are small enough for the water of hydration to be released without the increase of internal pressure, boehmite does not evolve.[23] Its formation is also favoured by high water vapour pressures in the transport air, as is typical of combustion gases in alumina refinery calciners.[24,27] On the basis that the use of CST will avoid the presence of H_2O as a combustion product, it can be deduced that the substitution of combustion with CST will inhibit the formation of boehmite. This would be beneficial because boehmite contains structural hydroxyls that degrade product quality for alumina smelting. The transition aluminas are characterised by their large internal porosity and resulting large surface area. They are thus useful for smelting and as catalysts. In contrast, the highly ordered and stable crystalline structure of the α-alumina phase makes it suitable for use in abrasives, refractories and ceramics.[26] The present investigation focusses on the refining of alumina for the purpose of smelting to produce primary aluminium. A study conducted by Whittington & Ilievski[24] suggests that the majority of refinery-prepared smelter grade aluminas (SGAs) reacts *via* χ-Al_2O_3 (pathway c) to feature large proportions of the γ-Al_2O_3 phase. The phase composition of numerous SGAs has previously been determined with quantitative X-ray diffraction (XRD) analysis to reveal that the product from stationary calciners comprises 60–90% γ-Al_2O_3 content while that from rotary-kiln calciners comprises 60–70% γ-Al_2O_3 content.[24] This was corroborated by

Wind & Raahauge,[28] who reported that in an industrial gas suspension calcination system only 3–8% boehmite content was found in the pre-calcination stages, and by Perander *et al.*,[29] who found that refinery-produced SGA was dominated by the γ-Al_2O_3 phase. On this basis it can be anticipated that the high heating rates inherent with solar processing will favour reaction pathway (c) to form predominantly γ-Al_2O_3. However, there is a need to assess the validity of this deduction by experiment.

The fraction of residual water in the alumina product is another important measure of product quality. This is because residual water has the propensity to drive the adverse formation of hydrogen fluoride gas during the downstream aluminium smelting process.[30] It is important that alumina is calcined to a sufficient extent for the residual water content to be in the range 0.69–0.95 wt%.[31] Alumina water content can be present in both a chemically-bound state (as in the case of aluminium hydroxides, $Al(OH)_3$ and AlO(OH)) and in a physically-adsorbed state. It has been found that both types of moisture in alumina contribute to hydrogen fluoride formation in the downstream smelting process although the physically-adsorbed moisture is more easily removed from alumina at low temperatures below 473 K, while chemically-bound moisture requires higher temperatures. The present investigation at laboratory-scale features a single pass of gibbsite particles through the solar reactor. There is thus a need to determine the maximum extent of conversion (minimum moisture content) that can be achieved with a single pass. There is also a further need to assess the partitioning of any residual water within the alumina product into these two types.

Two crucial measures of alumina product quality are its mean pore size and specific surface area (SSA). This is because, for the subsequent smelting process, the alumina serves not only as the feedstock but also as the material with which hydrogen fluoride (and other fluorine compounds) from smelter gases are removed (*via* a dry-scrubbing process).[28] The SSA and mean pore size are the primary indicators of the adsorption capacity of alumina, so that product quality is enhanced both by a larger SSA and a larger mean pore size.[32] Specifically, the subsequent process of aluminium smelting requires that the characteristic pore diameter of the alumina be an order of magnitude larger than the hydrogen fluoride molecule (having a van der Waals diameter of 0.36 nm).[32] This is to ensure high adsorption of the hydrogen fluoride in the dry-scrubbing process used in aluminium production. Previous investigations have determined that, during the calcination of gibbsite through the transition alumina, the SSA of the material increases rapidly to a maximum (>300 $m^2\ g^{-1}$) at about 673 K, due to its microporous structure (average pore size <2 nm). With higher temperatures, the extent of calcination increases, causing the average pore size to increase and the SSA to decrease and generate a mesoporous structure. Hence the final α-alumina has the lowest SSA of the various alumina phases,[6,7,23,33] and there is a trade-off between the desire to obtain both a low residual water content and a high SSA.[29,34] It has been proposed, however, that under rapid heating, such as tends to occur with flash calcination, the structural rearrangement of the gibbsite calcination sequence can be decoupled from the water removal.[33] The high heating rates possible with directly irradiated CST therefore offer the potential to produce alumina with both favourable residual moisture content and favourable microstructural properties. There is thus a need to confirm whether or not this potential benefit can be realised in practice through testing with a small scale solar reactor.

To meet these needs, the primary aim of this paper is to provide an insight into whether or not the solar-driven calcination of alumina is technically feasible. Specifically, the present investigation aims to obtain detailed understanding of the influence of key experimental parameters on the extent to which alumina may be calcined in a solar vortex transport reactor. It particularly aims to assess the influence of particle residence time and reactor temperature on the alumina product quality and to relate the performance of a laboratory-scale reactor to a full-scale device. It also aims to assess the impact of solar processing on the alumina moisture content and the alumina microstructure (mean pore size and specific surface area), which are primary measures of product quality, and to deduce the transition alumina reaction pathway.

2 Experimental methodology

2.1 Solar reactor

The solar vortex transport reactor is shown schematically in Fig. 1. This configuration was developed previously for the gasification of petroleum coke[16] and the cracking of natural gas.[35] It consists of a 200 mm-long, 100 mm-diameter ceramic lined cylindrical cavity-receiver, enclosed by a 210 mm-long, 120 mm-diameter Inconel 601 shell and a water-cooled aluminium frustum with a 3 mm-thick transparent fused quartz window. The flow of transport air and suspended $Al(OH)_3$ particles is confined to the cavity-receiver and is directly exposed to concentrated solar radiation entering through a 50 mm-diameter aperture, with an apparent absorptivity estimated to exceed 93%.[36] The window is cooled and protected from particle deposition by two injected air flows: one entering radially through a circular gap directed over the internal face of the window (with flow rate 2–4 $L_n\ min^{-1}$), and a second through four tangential nozzles on the frustum (with flow rate 1–2 $L_n\ min^{-1}$). The combination of the two purge flows suppresses the migration of particles into the frustum region. The vortex transport gas flow of synthetic air was generated by two tangentially arranged nozzles at the top (2–7 $L_n\ min^{-1}$ air flow) and the bottom (2–7 $L_n\ min^{-1}$ air flow) of the cavity and 30 mm behind the aperture. The particles were fed to the reactor through the tangential nozzle at the top of the cavity.

2.2 Reactants

Aluminium hydroxide particles in the gibbsite form with a purity of 99% were used as the reactant. Fig. 2 presents the particle size distribution of the $Al(OH)_3$, whose mean was

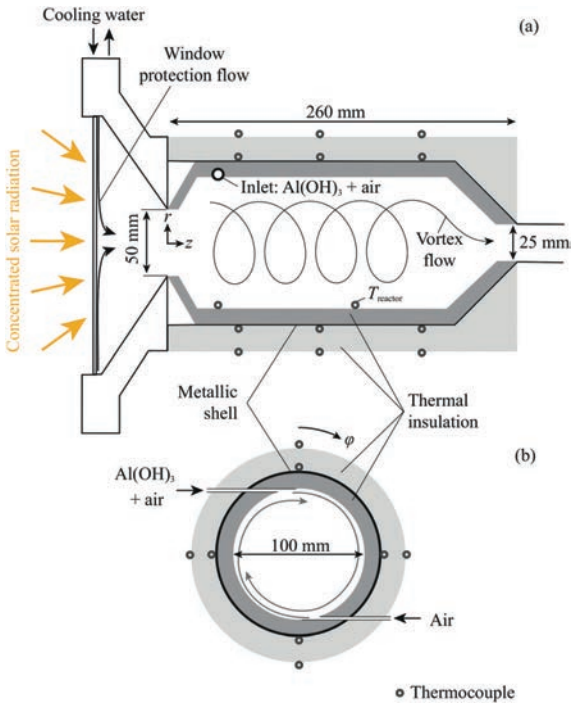

Fig. 1 Schematic diagram of (a) the axial cross section; and (b) the front view of the solar vortex transport reactor.

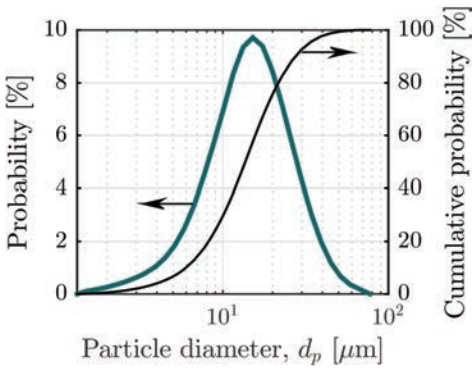

Fig. 2 Size distribution of the reactant gibbsite particles fed to the reactor.

15.5 μm as determined with laser scattering (HORIBA LA-950). The SSA of the particles was found to be 1.3 m^2 g^{-1}, determined with Brunauer–Emmett–Teller method (BET, Belsorpmax). Particles were entrained and fed using a fluidised bed feeder designed to operate over the range 1–2 g min^{-1}. Two streams of air were used to control the feeding of the $Al(OH)_3$ particles, one entering through a sintered plate at the bottom of the feeder fluidising the particles, and a second flow passing through a horizontal 5 mm-diameter carrier tube, which is aligned approximately 30 mm below the top of the static particle bed. A 1 mm hole in the upper surface of the carrier tube was used to entrain particles into the carrier tube air flow. The gibbsite mass feed rate was monitored online with weight scales (Kern FKB).

2.3 Experimental arrangement

The experimental arrangement is shown in Fig. 3. Measurements were performed with the High-Flux Solar Simulator of ETH Zurich, which comprises an array of 7 high-pressure Xenon arcs, each close-coupled with truncated ellipsoidal specular reflectors. This provides an external source of intense thermal radiation – mostly in the visible and IR spectra – that closely approximates the heat transfer characteristics of highly concentrating solar optical systems. The solar radiative input power, $\dot{Q}_s$, was measured optically with a Lambertian target and a calibrated CCD camera. $\dot{Q}_s$ was varied over the range 2.1–4.3 kW, which corresponds to mean solar concentration ratios, C, through the aperture in the range 1070–2190 suns (1 sun = 1 kW m^{-2}). Temperatures were measured with type-K thermocouples at locations shown in Fig. 1. A reference nominal reactor temperature, $T_{reactor}$, was measured with an Al_2O_3-shielded thermocouple located within the cavity as shown in Fig. 1. The nominal wall temperature, T_{wall}, was calculated as the average of seven thermocouples located on the outside of the Inconel shell (r = 61 mm),

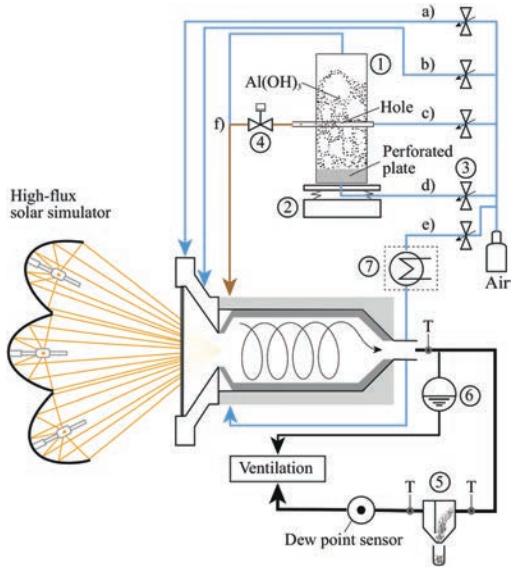

Fig. 3 Experimental arrangement used to calcine alumina with the high-flux simulated solar radiation: (T) thermocouples, (1) fluidised bed feeder, (2) weight scales, (3) mass flow controllers, (4) piston valve, (5) settling chamber (with particle collection), (6) hydrostatic over pressure system, (7) optional steam generator unit, (a) radial window purge air, (b) tangential window purge air, (c) carrier air, (d) fluidising air, (e) 2nd tangential reactor inlet (no particles), (f) fluidising air exhaust connects to other gas flows.

covered with insulation, at various z–φ locations: (50 mm, 0°); (115 mm, 0°; 90°; 180°; 270°); (190 mm, 0°; 180°). The total transport air normal flow rate, $\dot{V}_{air,n}$, was controlled with electronic flow controllers (Bronkhorst HI-TEC). Dry synthetic air was used as the transport air with normal flow rates, $\dot{V}_{air,n}$, in the range 12.0–20.0 L_n min^{-1}. Additionally, the gibbsite particle nominal residence time, τ, within the reactor was calculated from the cavity volume, V, and the total volumetric flow rate of transport air and gas product, $\dot{V}_{air}$ ($\dot{V}_{air,n}$ corrected for reactor temperature). The $\dot{V}_{air}$ input of the present investigation led to τ = 1.38–3.40 s. The similar value of nominal residence time in the present experimental facility to that of an industrial device despite three orders of magnitude smaller volume is attributed in part to much smaller ratio of the diameter of the inlet pipe to that of the reactor and, in part, to different methods of determining residence time. The Stokes number of the particles was calculated to be, Sk = 0.19, where:[37]

$$\mathrm{Sk} = \frac{\rho_p {d_p}^2 U_{in}}{18 \mu D_c}. \quad (2)$$

Since Sk ≪ 1, it is reasonable to assume that the residence time of the particles is equal to that of the gas. The $Al(OH)_3$ particles were fed to the reactor with constant feeder conditions at ambient temperature and at mass flow rates, $\dot{m}_{Al(OH)_3}$, in the range 0.55–2.53 g min^{-1}. The particle to air volume fraction, ϕ, was controlled over the range 0.35×10^{-5}–1.66×10^{-5} with changes to either $\dot{V}_{air}$ or $\dot{m}_{Al(OH)_3}$, and is defined as:

$$\phi = \frac{\dot{V}_{Al(OH)_3}}{\dot{V}_{air}}. \quad (3)$$

The product particles were collected in a settling chamber downstream from the reactor. The water vapor concentration in the outlet air, $\dot{m}_{H_2O}$, was measured online, downstream from the settling chamber, with a dew point sensor (Vaisala DMT346). Additionally, for one experimental run the water vapour partial pressure in the reactor was controlled by adding steam to the air flow of the second tangential inlet with an electric steam generator (Bronkhorst F- 201C). The steam was injected with a mass flow rate of $\dot{m}_{steam}$ = 1.17 g min^{-1} corresponding to a vapour partial pressure of 68.6 mbar. Measurements were taken at approximately steady-state and isothermal (to within 26 K) conditions, which follows a period of pre-heating to the desired temperature. Operating parameters were averaged over the duration of reactant particle feeding. A summary of the operating conditions of the 19 nominally steady-state experimental runs is provided in Table 1.

2.4 Product characterisation

Representative samples were taken from the collected particles in the settling chamber for post-experimental analyses of the following parameters: the loss on ignition (LoI) determined from the relative mass change during thermogravimetric analysis (TGA, Netzsch STA 409 CD); the particle morphology imaged by scanning electron microscopy (SEM, Philips XL30); the phases present in the sample by X-ray diffraction data (XRD, Rigaku MiniFlex 600 diffractometer), and the product microstructure, which was in turn evaluated by measurement of both SSA with the Brunauer–Emmett–Teller method (BET, Belsorp-max) and pore size distribution with the Barrett–Joyner–Halenda method (BJH, Belsorp-max).

Fig. 4 presents the relative mass changes for the reactant $Al(OH)_3$ and for a representative solar-processed sample collected from the settling chamber as a function of the TGA reference temperature, T_{TGA}. This shows that the $Al(OH)_3$ begins to decompose at about 500 K, following which the mass loss increases to a maximum of 34.6 wt% corresponding to the complete conversion of $Al(OH)_3$ to Al_2O_3. Fig. 4 also shows that a small quantity of adsorbed moisture from the cooled, solar-processed alumina sample is released during its re-heating from ambient temperature to 423 K. The mass of this process can be quantified by the mass "Loss on Ignition" (LoI) in the

Table 1 Summary of operational conditions for the 19 nominally steady-state experimental runs

#	$\dot{Q}_s$ [W]	$\dot{V}_{air,n}$ [L_n min^{-1}]	$\dot{m}_{steam}$ [g min^{-1}]	$\dot{m}_{Al(OH)_3}$ [g min^{-1}]	$T_{reactor}$ [K]	T_{wall} [K]	ϕ [—]	τ [s]
1	2285	20.03	—	1.12	1259	1114	0.57×10^{-5}	1.74
2	2108	20.03	—	0.73	1213	1020	0.40×10^{-5}	1.91
3	3642	20.03	—	0.95	1479	1246	0.43×10^{-5}	1.56
4	2132	20.03	—	0.84	1226	934	0.51×10^{-5}	2.08
5	2316	12.03	—	1.35	1258	1122	1.13×10^{-5}	2.81
6	2117	12.03	—	1.39	1161	928	1.40×10^{-5}	3.40
7	3773	12.03	—	1.45	1454	1272	1.07×10^{-5}	2.47
8	2291	20.03	—	2.07	1230	1106	1.06×10^{-5}	1.72
9	2211	20.03	—	1.33	1216	977	0.77×10^{-5}	1.97
10	4224	20.03	—	1.98	1421	1258	0.89×10^{-5}	1.51
11	3730	12.03	—	2.32	1480	1311	1.66×10^{-5}	2.33
12	3383	17.03	—	1.26	1414	1227	0.68×10^{-5}	1.84
13	3492	12.03	—	1.75	1408	1219	1.35×10^{-5}	2.55
14	4262	19.85	—	2.53	1551	1371	1.05×10^{-5}	1.38
15	3766	16.03	—	1.06	1456	1254	0.60×10^{-5}	1.92
16	2362	16.03	—	1.14	1208	1051	0.76×10^{-5}	2.29
17	2198	16.03	—	0.55	1179	943	0.41×10^{-5}	2.58
18	3965	20.03	—	1.35	1459	1284	0.59×10^{-5}	1.50
19	3832	20.03	1.17	0.85	1439	1262	0.35×10^{-5}	1.43

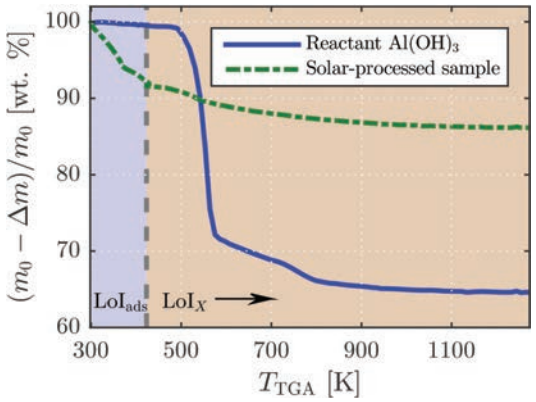

Fig. 4 Relative mass change of the reactant $Al(OH)_3$ and a representative solar-processed alumina as a function of the reference TGA temperature, T_{TGA}, during a dynamic TGA run between 298 K and 1273 K in synthetic air. The temperature ranges used in the present study for determining LoI_{ads} and LoI_X are indicated.

temperature range: 298–423 K, denoted here as LoI_{ads}. The further mass loss of the solar-processed alumina from its heating to higher temperatures corresponds to the mass percentage of unreacted $Al(OH)_3$ in the solar-processed alumina. The LoI over this second range, 423–1273 K is denoted as LoI_X, and is used in the present investigation to calculate the overall molar conversion of $Al(OH)_3$ to Al_2O_3, X, according to:

$$X = \frac{2n_{Al_2O_3}}{n_{Al(OH)_3} + 2n_{Al_2O_3}}, \quad (4)$$

where, $n_{Al_2O_3}$ and $n_{Al(OH)_3}$ are the molar quantities of alumina product and unreacted $Al(OH)_3$ in the solar-processed alumina (as determined from LoI_X). The ISO standard for reporting alumina moisture content is by the LoI_{1273}, evaluated over the temperature range 573–1273 K.[30,34,38] However, it has been shown that the reactant $Al(OH)_3$ begins to decompose at temperatures below 573 K, which means that the LoI_{1273} underestimates the amount of unreacted $Al(OH)_3$. This provides justification for the use of LoI_{ads} and LoI_X in the present investigation. Errors in the TGA measurements result from the large SSA of transition aluminas and their reactivity with moisture in the air. This error affects measurement of the LoI_{ads} most significantly, but also affects the measurement of chemical conversion, X. The relative errors in LoI_{ads} and X were determined to be ±3.3% and ±18.7%, respectively, based on repetitions of TGA tests and the maximum deviation from the mean result.

3 Results & discussion

3.1 Steady-state operation

The operational conditions for the 19 nominally steady-state experimental runs listed in Table 1 resulted in $T_{reactor}$ = 1161–1551 K and T_{wall} = 928–1371 K.§ The solar energy conversion efficiency, η, of the solar calcination process is defined to account for the energy required for the endothermic calcination process, as well as the sensible heating of the reaction products and the transport air, as follows:

$$\eta = \frac{\Delta\dot{H}}{\dot{Q}_s} = \frac{\dot{H}^{T_R}_{products} - \dot{H}^{\circ}_{reactant} + \Delta\dot{H}_{air}}{\dot{Q}_s}. \quad (5)$$

Here the sensible heat of the transport air is included in the useful energy because an industrial flash calcination process recovers the majority of such sensible heat through downstream heat exchangers, which are also used to pre-heat the particles. That is, the present solar reactor needs to both heat and react the particles, while they enter an industrial reactor hot. The performance indicators, X and η were measured to be in the range X = 84.8–95.8% and η = 8.8–20.4%, respectively. In terms of product quality parameters, the measured values of loss on ignition of adsorbed moisture were LoI_{ads} = 5.9–14.1%, the measured values of SSA were found to be in the range 132.7–226.6 $m^2\ g^{-1}$ and the mean pore size was measured to be in the range d_{pore} = 2.54–5.75 nm.

Fig. 5 presents the outputs from a typical experimental run (#9). Plotted are the temporal variations of $\dot{Q}_s$, $T_{reactor}$, T_{wall}, $\dot{m}_{Al(OH)_3}$, and $\dot{m}_{H_2O}$. When the desired T_{wall} was reached and steady temperatures were measured, the particle feeding was

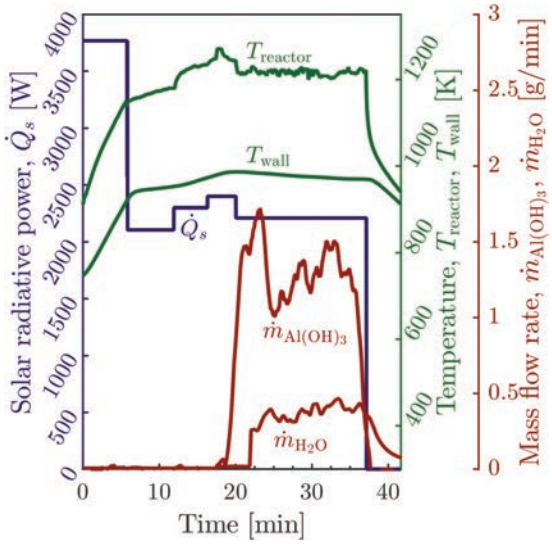

Fig. 5 Temporal variations of solar radiative power input, $\dot{Q}_s$, reactor temperatures, $T_{reactor}$ and T_{wall}, particle mass feed rate, $\dot{m}_{Al(OH)_3}$, and mass flow rate of evolved water within the outlet stream, $\dot{m}_{H_2O}$, during a representative solar experimental run (#9).

§ X, η and XRD results are presented as functions of T_{wall} rather than $T_{reactor}$ due to the greater number of thermocouples contributing to the mean measurement and the lesser influence of direct irradiation on the thermocouple reading.

turned on. The period, 21–35 min, is considered to be nominally steady-state.

3.2 Extent of calcination and efficiency

Fig. 6a presents the dependence of X on T_{wall} for all experimental runs with four different values of $\dot{V}_{air,n}$. It is evident that the reactor temperature has a controlling influence on the extent of conversion, so that an increase in T_{wall} results in greater X. It can also be seen that a maximum chemical conversion of 95.8% was obtained for T_{wall} = 1371 K. Despite this temperature being within the range typical of industrial flash calciners (1273–1373 K),[11] the conversion was below 100%. This can be attributed both to the much smaller scale of the reactor in the present study relative to industrial-scale calciners and to the additional stages in industrial calcination systems, incorporating both particle preheating stages and a holding vessel, which together reduce the temperature rise and/or residence time required for full conversion. Fig. 6b presents the dependence of X on τ for three T_{wall}. This shows that X is increased by an increase in τ, although the influence is relatively weak in comparison with that of T_{wall}. The trend of increasing X with longer τ is also consistent with well-established understanding of the alumina calcination reaction.[23,24] The slightly stronger influence of T_{wall} than that of τ is further evident from results of experimental run 14 with T_{wall} = 1371 K, which featured the greatest X despite having the shortest τ = 1.38 s.

Fig. 7 presents the dependence of η on $\dot{V}_{air}$ (corrected for reactor temperature), for four different values of T_{wall}. A maximum energy efficiency of 20.4% was achieved for this reactor. It can be seen that η increases with a reduction in T_{wall} because both the conduction and re-radiation losses depend on the reactor wall temperature. It can also be seen that, for a given value of T_{wall}, η increases with an increase in $\dot{V}_{air}$. This implies that an increase in the flow rate of air and particles causes a greater fraction of the radiation to be absorbed by the reactant and transport air than by the walls, which increases the ratio of useful heat to losses. The values of η for this reactor are low relative to industrial-scale reactors but are comparable with those from other laboratory-scale reactors.[16,20] This is because the ratio of internal surface area to internal volume of the reactor decreases with an increase in scale, causing a greater fraction of energy to be absorbed by the reactants and transport air relative to the walls of the reactor, which increases efficiency consistent with the results from Fig. 7. In addition, large scale industrial reactors are designed with heat integration and heat recovery systems to minimise heat losses and maximise efficiency.

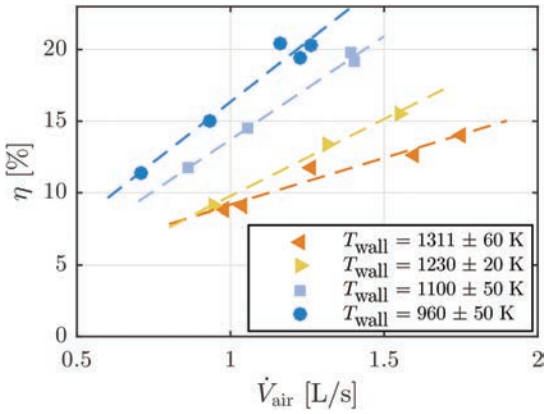

Fig. 7 The energy efficiency, η (defined in eqn (5)), of the present solar calcination reactor as a function of the volumetric flow rate of transport air, $\dot{V}_{air}$, for four different wall temperatures, T_{wall}. See Table 1 for details.

3.3 Product quality: residual moisture

Fig. 8 presents the LoI_{ads} as a function of ϕ for four different values of T_{wall}. It can be seen that, for each value of T_{wall}, the

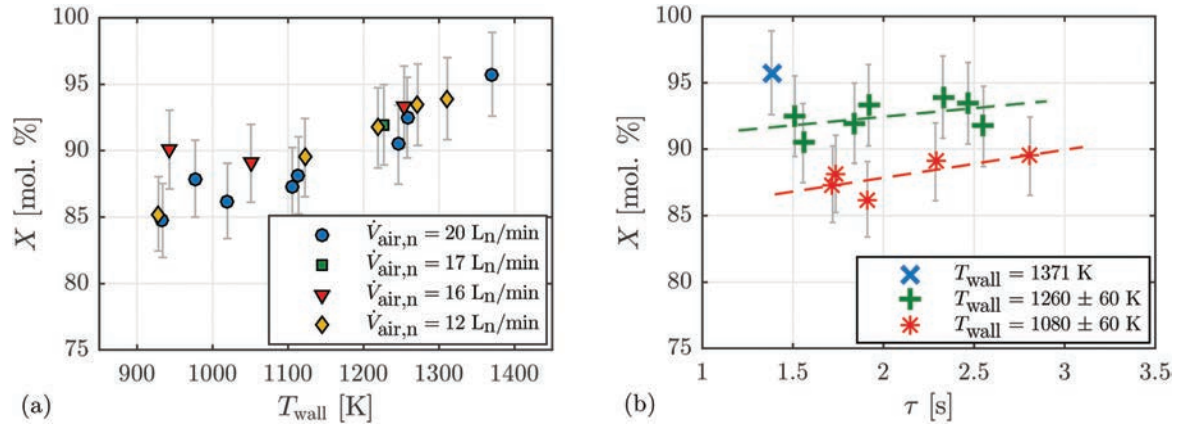

Fig. 6 The extent of chemical conversion, X, as a function of (a) the average characteristic wall temperature, T_{wall}, for four different air normal flow rates, $\dot{V}_{air,n}$, and for experimental runs 1 to 17; and (b) the nominal particle residence time, τ, for three different average characteristic wall temperatures, T_{wall}. Also shown are the linear lines of best fit for the data points in the two temperature ranges.

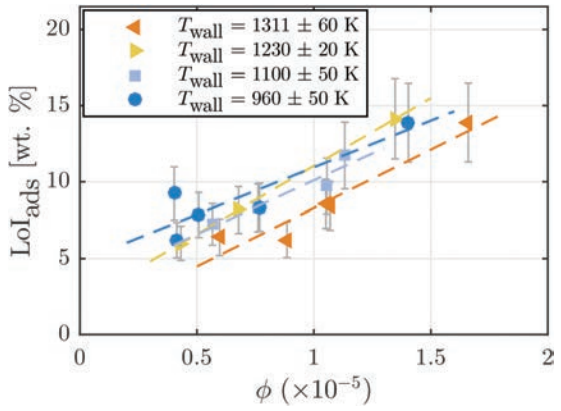

Fig. 8 Mass percentage of adsorbed moisture, LoI_{ads}, in the product from the solar reactor as a function of the particle to air volume fraction, ϕ (defined in eqn (3)), for four different wall temperatures, T_{wall}, for experimental runs 1 to 17.

Table 2 The influence of addition of steam to the transport air on the mass percentage of adsorbed moisture, LoI_{ads}, extent of chemical conversion, X, and energy efficiency, η, based on experimental runs 18 and 19

$\dot{m}_{steam}/\dot{m}_{air}$	#	LoI_{ads}	X	η
[—]		[wt%]	[mol%]	[%]
0	18	5.91	94.5	14.0
0.045	19	7.99	94.0	14.2

LoI_{ads} increases with ϕ. This can be explained by the increase in the concentration of water vapour, the gas-phase product of the reaction, due to an increase in volumetric loading of particles. That is, an increase in the partial pressure of water vapour in the reactor increases the resistance to the release of water into the gas phase. It can also be seen that T_{wall} has a second order influence on the LoI_{ads}, so that the highest T_{wall} = 1311 ± 60 K resulted in the lowest values of LoI_{ads}.

Table 2 presents the influence of the addition of steam ($\dot{m}_{steam}$ = 1.17 g min^{-1}) to the transport air flow on LoI_{ads}, X, and η, with all other operating conditions maintained nominally constant. It can be seen that the additional steam input, resulting in a water vapour partial pressure of 68.6 mbar, has a significant influence on the amount of surface moisture adsorbed by the alumina product, consistent with the trends in Fig. 8. More specifically, the LoI_{ads} was found to increase from 5.91% (run #18) to 7.99% (run #19). This can be explained by the increase in the partial pressure of water vapour in the transport air, which inhibits the diffusion of chemically-released water vapour into the gas phase. It also favours an increase in the readsorption of water vapour onto the surface of the alumina particle. For reference, the partial pressure of water vapour generated by the complete combustion of methane with 10% excess air is calculated to be 176.7 mbar, which is more than twice the 68.6 mbar used in the present experiment. Because methane is the dominant component of natural gas, which is the most common fuel used for industrial flash calciners, this implies that removing H_2O from combustion by solar calcination has the potential to provide a significant benefit to product quality by reducing the partial pressure of the gas-phase moisture. It can also be noted from Table 2, that the increase of the partial pressure of water vapour has no significant influence on X or η for the present conditions.

3.4 Product quality: alumina microstructure

Fig. 9 presents SEM micrographs of the solid alumina product from experimental runs (a) #4 (T_{wall} = 934 K), (b) #11 (T_{wall} = 1311 K), (c) #14 (T_{wall} = 1371 K), and (d) #19 (T_{wall} = 1262 K). It is clear that slit-shaped pores have formed in the particles, whose width increases with the value of T_{wall}. From previous work, this can be deduced to result from the calcination reaction mechanism, in which the structural hydroxyls (–OH) that hold gibbsite layers together are released rapidly as water during the calcination process, causing the gibbsite layers to split and form slit-shaped pores.[6,39]

Fig. 10 presents the mean pore diameter, d_{pore}, and the total specific pore volume, V_{pore}, of the solar processed alumina as a function of X. It can be seen that both d_{pore} and V_{pore} increase with an increase in X, consistent with both the SEM micrographs (Fig. 9) and the previous assessments for non-solar calcination by Perander *et al.*[6] For X = 95.8%, d_{pore} reaches up to 5.8 nm for run 14. It can also be seen from a comparison with reported mean pore sizes of typical SGAs produced with industrial flash calciners (presented as the open symbols in Fig. 10),[28,32,34] the solar process generates larger values of d_{pore} for a given value of X than does the conventional process. Extrapolation suggests that d_{pore} will continue to increase with X, so that solar-processed alumina has potential to achieve a larger mean pore size than the majority of conventionally-processed aluminas, noting the exception for two SGAs with pore size larger than 8 nm. It should also be recalled that the solar-processed alumina has been calcined with residence times in the order of a few seconds. This contrasts the industrial process, which also includes both a preheating stage and a holding vessel to provide additional residence time for pore growth. That is, the solar process generates a higher product quality by this measure than does the conventional processing, indicating potential to improve hydrogen fluoride adsorption capacity in the downstream dry-scrubbing process.

Fig. 11 presents the measured values of SSA for the solar-produced alumina as a function of X. The figure shows that SSA is nearly constant (mostly in the range 168–190 m^2 g^{-1}) for lower values of X in the range 85–92%, but then decreases with further increases in X to the minimum of 132.7 m^2 g^{-1} for X = 95.8%. The present values of SSA are significantly greater than previously reported values of SGA produced industrially, as shown in Fig. 11.[28] Nevertheless, more data are required before a reliable comparison with the industrial data can be made, owing to the different values of X for the experi-

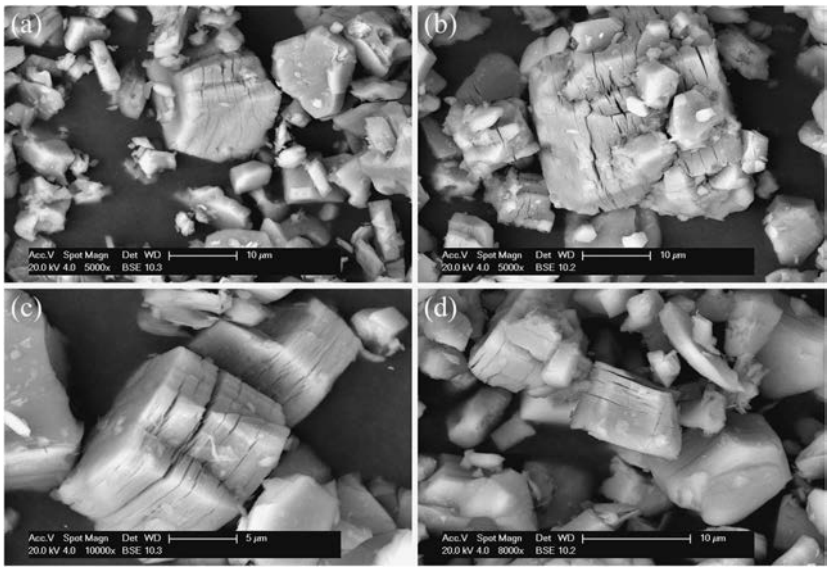

Fig. 9 SEM micrographs of solar-processed alumina obtained from experimental runs (a) #4 (T_{wall} = 934 K), (b) #11 (T_{wall} = 1311 K), (c) #14 (T_{wall} = 1371 K), and (d) #19 (T_{wall} = 1262 K) at 5000, 5000, 10 000, and 8000 magnification, respectively.

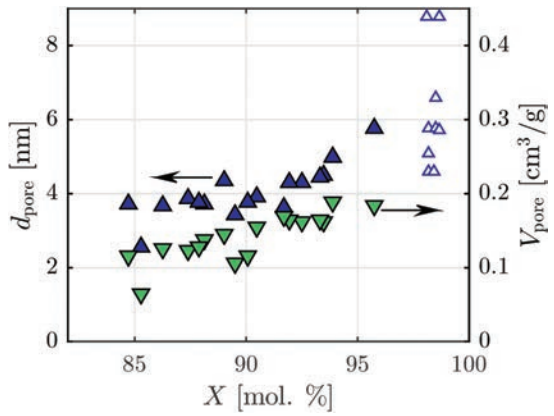

Fig. 10 Mean pore diameter, d_{pore}, and total specific pore volume, V_{pore}, of the solar-produced aluminas as a function of the extent of chemical conversion, X, for experimental runs 1 to 17. Also shown with open symbols are the typical mean pore diameter of nine SGAs produced with industrial calciners as reported in the literature.[28,32,34]

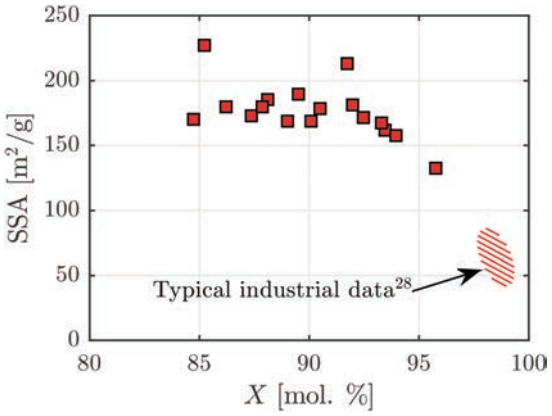

Fig. 11 Specific surface area, SSA, of the present solar-produced aluminas as a function of the extent of chemical conversion, X, for experimental runs 1 to 17. Also shown is the typical X and SSA product quality properties of SGA calcined in an industrial gas suspension calciner.[28]

mental and industrial data, which is associated with the difference in scale of the facilities.

3.5 Product quality: X-ray diffraction analysis

Fig. 12 presents a series of XRD spectra of alumina powder samples produced with different values of T_{wall}, but at constant $\dot{V}_{air,n}$ = 20 L_n min^{-1} (ϕ = 0.40 × 10^{-5}–1.06 × 10^{-5}). For the case with T_{wall} = 934 K, the presence of unconverted reactant can be seen from the discrete diffraction peaks corresponding to gibbsite, notably from the two peaks of greatest intensity at 2θ = 18.3° and 20.3°. For higher values of T_{wall} the discrete diffraction peaks of gibbsite reduce in intensity and are replaced by the more diffuse diffraction peaks of the transition alumina. The presence of some residual gibbsite in the alumina samples, which each combine many alumina particles, indicates that a fraction of the particles did not reach sufficient temperature for long enough to convert all of the original gibbsite. Given the wide size distribution of the particles, it is likely that the residual gibbsite is preferentially partitioned in the larger particles, which require the longest residence time for

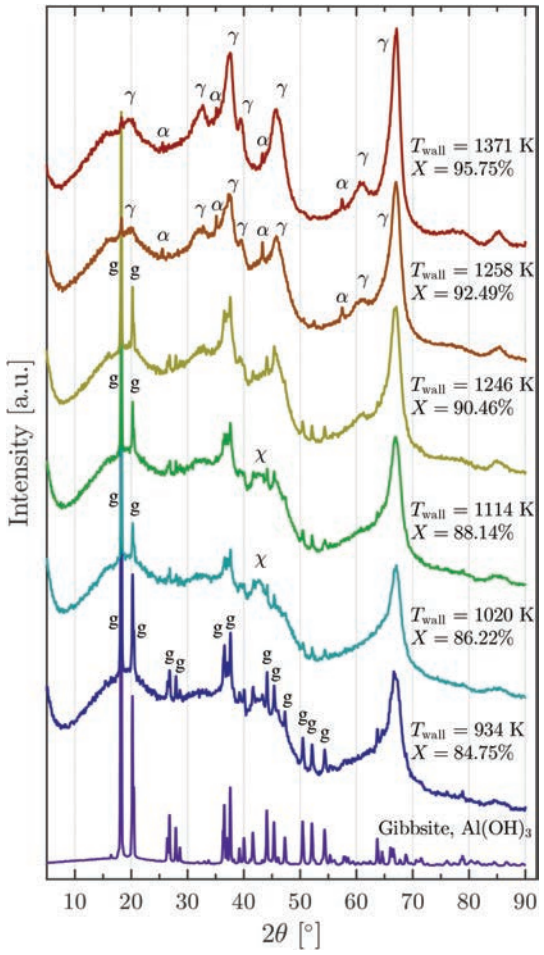

Fig. 12 X-ray diffractograms of gibbsite and solar-processed alumina samples produced with a series of reactor temperatures (experimental runs 4, 2, 1, 3, 10 and 14) with a constant normal flow rate of transport air ($\dot{V}_{air,n}$ = 20 L_n min^{-1}). The reference raw gibbsite X-ray diffractogram is also shown at 1/14th the intensity. Annotations show where the diffraction peaks correspond to reported diffraction peaks of gibbsite (g), χ-Al_2O_3, γ-Al_2O_3 and α-Al_2O_3 (COD PDF Card No. 1011081, 2015530 & 1000017).

complete conversion. However, further work will be required to verify this. For T_{wall} = 1020 K and 1114 K a broad diffuse peak at 2θ = 42.8° can be seen, which corresponds to the χ-Al_2O_3 phase.[23,24,40] For T_{wall} = 1258 K and 1371 K the χ-Al_2O_3 peak is not present and the dominant diffuse diffraction peaks occur at 2θ = 19.4°, 31.9°, 37.6°, 39.3°, 45.7°, 60.6°, and 66.7° corresponding to γ-Al_2O_3. This is corroborated by an additional analysis of the samples by Fourier Transform Infrared Spectroscopy (not shown), which found that the spectra from the solar-processed alumina samples are characterised by a broad distribution without sharp peaks. This is consistent with the alumina having a complex disordered structure, which is typical of χ-Al_2O_3 and γ-Al_2O_3.[41,42] It should also be noted that the XRD results from the two cases with the highest T_{wall} feature small discrete peaks corresponding to α-Al_2O_3 (2θ = 25.6°, 35.1°, 43.3°, and 57.5°), indicating that the particles reached the temperature at which α-Al_2O_3 forms (1375–1450 K). Although it is difficult to quantify the relative presence of the transition aluminas due to their diffuse diffraction peaks,[6,29] it is clear that γ-Al_2O_3 is the predominant phase produced during solar calcination, while small amounts of the α-Al_2O_3 phase were also observed. This is consistent with published results from refinery-produced aluminas, in which the dominant alumina phase is also γ-Al_2O_3, while α-Al_2O_3 makes up 2–9% (see Table 3).[31] Taken together, these results imply that high temperature solar calcination favours the reaction pathway of χ- to γ- to α-Al_2O_3 (pathway c[23,24,26]).

Fig. 13 presents XRD spectra of solar-processed alumina samples produced with a range of values of T_{wall} for $\dot{V}_{air,n}$ = 12 L_n min^{-1} (ϕ in the range 1.07×10^{-5}–1.66×10^{-5}). As for Fig. 12, the samples produced at lower temperatures have discrete diffraction peaks corresponding to gibbsite, which also implies the presence of unreacted gibbsite. The general trend is that the intensity of these peaks decreases with an increase in both T_{wall} and X. The exception to this is the alumina sample processed with T_{wall} = 1219 K, which exhibits gibbsite diffraction peaks with lower intensity than those of the two alumina samples processed with higher temperature. It should also be noted from Fig. 13 that the only clearly visible discrete diffraction peaks of gibbsite for the cases with low T_{wall} are those at 2θ angles of 18.3° and 20.3°. In contrast, numerous discrete gibbsite peaks are visible for the alumina samples produced with low values of T_{wall} and larger values of $\dot{V}_{air,n}$ (Fig. 12). The evolution of χ-Al_2O_3 at T_{wall} = 928 K and T_{wall} = 1122 K and the subsequent evolution of γ-Al_2O_3 is evident for both the lower and higher values $\dot{V}_{air,n}$ = 12 L_n min^{-1} and $\dot{V}_{air,n}$ = 20 L_n min^{-1}. However, diffraction peaks corresponding to the intermediate aluminium oxyhydroxide, boehmite, are also visible in the XRD traces of Fig. 13. The diffraction peaks at 2θ values of 14.5° and 28.2° also correspond to boehmite and are particularly evident from the samples calcined with T_{wall} = 1219 K and 1311 K. For the sample calcined at T_{wall} = 1311 K, the species that can be observed are unreacted gibbsite, boehmite and, most predominantly, γ-Al_2O_3. This indicates that, under these conditions, the calcination reaction follows both the χ- to γ- to α-Al_2O_3 pathway (pathway c as in Fig. 12) and the boehmite to γ- to α-Al_2O_3 pathway (pathway b[23,24,26]). The same particle size distribution was used throughout the present investigation, suggesting that the boehmite formation is attributable to the increased concentration of water vapour in the immediate presence of the reacting gibbsite particles due to the lower value of $\dot{V}_{air,n}$, which can be deduced to increase ϕ.

3.6 Projection to a 50 MW solar vortex transport reactor and comparison of the product quality with the conventional process

Table 3a presents the ratio of internal surface area to internal volume of the reactor, A_S/V, the thermal input of solar radi-

Table 3 (a) Comparison of key operational parameters of the solar vortex transport reactor (SVR) at present laboratory-scale and the equivalent values for a reactor at industrial scale, as scaled with constant inlet velocity and thermal efficiency. (b) Comparison of product quality parameters of solar-calcined alumina for the case with the highest extent of conversion (run #14), together with typical properties of Smelter Grade Alumina (SGA) produced with industrial flash calciners as reported in the literature[24,28,29,31–34]

	SVR at laboratory-scale	SVR scaled to industrial-scale
(a) Operational parameter comparison		
$\dot{Q}_s$	5 kW	50 MW
A_S/V	31.9 m^{-1}	0.319 m^{-1}
τ	1.38 s	138 s

	Solar-processed alumina (run #14)	Ref. 24, 29 and 33	Ref. 28	Ref. 31	Ref. 32	Ref. 34
(b) Product quality comparison						
LoI_{1273}	1.20 wt%		0.7–0.8 wt%	0.69–0.95 wt%	0.3–1.5 wt%	0.72–1.05 wt%
α-Al_2O_3 content	Small amounts		3–6 wt%	2–9 wt%	2–20 wt%	3.9–8.1 wt%
Gibbsite content	Small amounts		<0.1 wt%	<0.1 wt%		0.56–2.65 wt%
Dominant alumina phase	γ-Al_2O_3	γ-Al_2O_3			γ-Al_2O_3	
SSA	132.7 m^2 g^{-1}		73–81 m^2 g^{-1}	72–80 m^2 g^{-1}	68–80 m^2 g^{-1}	68.1–76.1 m^2 g^{-1}
d_{pore}	5.8 nm		6.6–8.8 nm		4.6–5.8 nm	5.7–11.2 nm

ation, $\dot{Q}_s$, and the nominal particle residence time, τ, for the case of greatest conversion in the present investigation. Predicted values for the 50 MW industrial scale are also shown, where the scale up procedure assumes constant C, constant ϕ, constant input velocity, geometric similarity and constant η (*i.e.* that $\dot{m}_{Al(OH)_3}$ scales linearly with thermal input). The resulting scale up proportionality relationships are $A_S/V \propto \dot{Q}_s^{-1/2}$ and $\tau \propto \dot{Q}_s^{1/2}$. The assumption of constant input velocity is reasonable because the minimum velocity is set by the need to transport particles, while higher values are undesirable to avoid erosion. The assumption of constant efficiency is conservative because the 100-fold reduction in A_S/V with the increase in scale will result in a significant reduction in relative heat losses.[43] Table 3a shows that, with these assumptions, the constant-velocity scale up results in a 100-fold increase in τ. Even though this represents an over-estimate of the increase in residence time because the scale-up process would also increase the relative diameter of the inlet gas stream, this is more than offset by the addition of the pre-heater and the holding vessel in the industrial process. That is, scale-up can be expected to increase X and/or reduce the value of $T_{reactor}$ relative to the present laboratory-scale investigation.

Table 3b presents the parameters used to characterise the product quality for the present alumina product with greatest X (run #14), together with typical properties of SGA produced in industrial flash calciners as reported in the literature.[24,28,29,31–34] This shows that the minimum LoI_{1273} of 1.20% achieved in the present investigation is somewhat higher than the typical value of alumina produced in industrial flash calciners. However, given that extent of conversion increases with τ, it can be deduced that the LoI_{1273} would decrease to <1% with scale up of the solar reactor, which would comply with industrial requirements.[28] Furthermore, the additional incorporation of the preheating stages and holding vessels employed in current industrial processes, which provide sufficient residence time to achieve both a high conversion and a high surface area, can be expected to allow the solar reactor to be operated at lower temperature.[28] It can also be seen that the dominant alumina phase of the present solar product is γ-Al_2O_3 with small amounts of α-Al_2O_3, which is

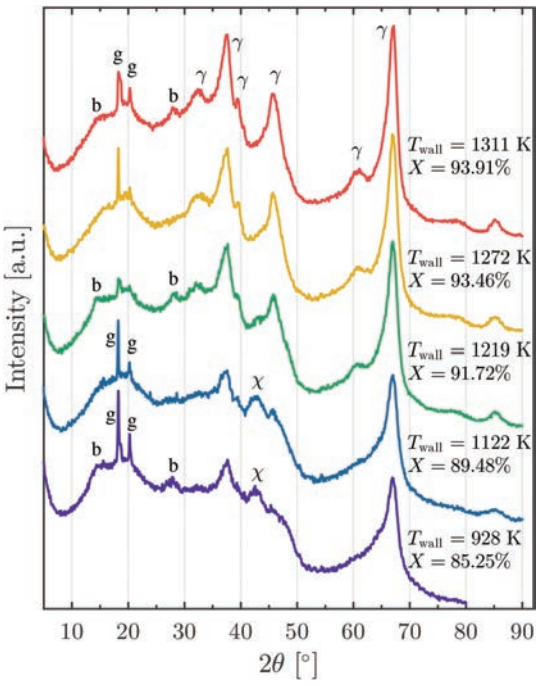

Fig. 13 X-ray diffractograms of solar-processed alumina samples produced with a series of reactor temperatures (experimental runs 6, 5, 13, 7 and 11), with a constant normal flow rate of transport air ($\dot{V}_{air,n}$ = 12 L_n min^{-1}). Annotations show where the diffraction peaks correspond to reported diffraction peaks of gibbsite (g), boehmite (b), χ-Al_2O_3 and γ-Al_2O_3 (COD PDF Card No. 1011081, 9009155 & 2015530).

consistent with that found in industrial processes. However, traces of gibbsite were also found from the XRD in the present samples of calcined solar alumina, which implies a poorer quality than is required for SGA. On the other hand, the SSA of the solar-processed alumina was found to be much higher than typical for SGA, which is consistent with the small scale, since SSA is expected to decrease with an increase in conversion. Of particular note is that the mean pore size of the solar-calcined alumina is in the upper range of industrially-produced alumina. This represents a benefit from solar calcination of alumina over conventional combustion-driven calcination.

4 Conclusions

The first-of-a-kind demonstration of the thermochemical calcination of alumina with concentrated solar thermal radiation has been undertaken with a solar vortex transport reactor. This shows that it is technically possible to calcine alumina without combustion and its concomitant CO_2 emissions, at least during those periods when the solar resource is available. The extent of chemical conversion from aluminium hydroxide to aluminium oxide was found to increase with the solar radiative power input, and hence also with the reactor temperature, to a value of up to 95.8% in this small laboratory reactor (4.3 kW of solar radiative power and an average reactor wall temperature of 1371 K). The reactor temperature was found to be the dominant experimental variable controlling the extent of solar calcination. It was also found that an increase in the nominal particle residence time has a secondary influence, also increasing the extent of conversion. Solar energy conversion efficiencies of up to 20.4% were measured for this small scale reactor, on the basis that both the sensible and chemical heat are included as the useful heat, which is consistent with the high level of heat recovery from industrial processes. A higher reactor temperature results in a drop in efficiency, due to greater re-radiation and conduction losses. It is expected, however, that the extent of calcination and energy efficiency will increase with the scale up of a solar vortex transport reactor, allowing for lower reactor temperatures due to the longer particle residence time and relatively lower heat losses associated with larger scale reactors.

Product quality assessments of the solar-calcined alumina provide strong evidence that solar calcination can result in improved quality alumina, relative to conventional industrially-calcined alumina. The addition of steam (to a water vapour partial pressure of 68.6 mbar) to the reactor transport gas flow resulted in an increase in the amount of adsorbed moisture (from 5.91% to 7.99%). This implies that the use of solar calcination, which avoids the production of steam by combustion, can reduce the amount of surface-adsorbed moisture in the alumina product (which is deleterious to alumina smelting). Consistent with this, the amount of moisture adsorbed by the alumina surface also depends on the particle to air volume fraction. This is because an increase in the partial pressure of water vapour, resulting from an increase in particle to air volume fraction, was found to inhibit diffusion of the water vapour into the transporting air phase.

The alumina microstructure analysis provided further evidence of the improved product quality from solar calcined alumina. The conditions producing a conversion of 95.8% were associated with a specific surface area of 132.7 $m^2\ g^{-1}$ and critically, a mean pore diameter of 5.8 nm. The mean pore size of the solar-produced alumina was found to increase with the extent of conversion and can be expected to increase further with scale-up. The solar-produced aluminas of the present investigation are characterised by a relatively large specific surface area and mesoporous structure (with large pore sizes), which is desirable for increased hydrogen fluoride adsorption required for the downstream dry-scrubbing process in aluminium smelting.

The X-ray diffraction analysis revealed that the alumina produced with concentrated solar thermal energy is typically characterised by a high fraction of γ-Al_2O_3 phase and a low fraction of α-Al_2O_3. This is consistent with published results from refinery-produced aluminas. Furthermore, the transition pathway was found to be consistent with that associated with high heating rates.[23,24,26] That is, the gibbsite is deduced to primarily decompose *via* the amorphous χ-alumina before reaching γ-alumina (pathway c of ref. 23, 24 and 26). Significantly, the cases with highest particle volume fraction ($\phi > 10^{-5}$), which are associated with greatest partial pressure of water vapour from the calcination reaction, were found to exhibit some decomposition of the gibbsite *via* boehmite before reaching γ-alumina and higher order transition aluminas.

Nomenclature

A_S	Reactor internal surface area [m^2]
C	Solar concentration ratio (1 sun = 1 kW m^{-2})
D_c	Reactor cavity internal diameter [m]
d_p	Mean particle diameter [μm]
d_{pore}	Mean pore diameter [nm]
$\Delta\dot{H}$	Rate of enthalpy change of a species [W]
$\Delta\bar{h}°$	Standard enthalpy of reaction [kJ mol^{-1}]
LoI	Loss on ignition [wt%]
m	Mass of a species/sample [g]
$\dot{m}$	Mass flow rate of a species [g min^{-1}]
n	Number of moles of a species [mol]
$\dot{Q}_s$	Solar radiative power input [W]
r	Radial coordinate [mm]
Sk	Stokes number
T	Temperature [K]
U_{in}	Transport air inlet velocity [m s^{-1}]
V	Reactor internal volume [m^3]
V_{pore}	Total specific pore volume [$cm^3\ g^{-1}$]
$\dot{V}$	Total gas volumetric flow rate
X	Chemical conversion [mol%]
z	Horizontal coordinate [mm]
η	Solar energy conversion efficiency [%]
θ	XRD incident angle [°]

μ	Dynamic viscosity [kg m^{-1} s^{-1}]
ρ	Density [kg m^{-3}]
τ	Nominal particle residence time [s]
ϕ	Particle to air volume fraction
φ	Angular coordinate [°]

Subscripts

1273	Over the temperature range 573–1273 K
ads	Of adsorbed moisture, evaluated over the range 298–423 K
air	Of air (making up the transport gas flow)
$Al(OH)_3$	Of aluminium hydroxide (gibbsite) feed particles
Al_2O_3	Of aluminium oxide (alumina) produced
calcination	Of the calcination reaction
H_2O	Of evolved water vapour
n	At normal conditions (273 K, 1 atm)
p	Of the particle
products	Of the reaction products
reactant	Of the reactant
reactor	Of the reactor cavity
steam	Of additional steam (into the transport gas flow)
TGA	Reference TGA temperature
wall	Of the reactor wall
X	Over the range for determining *X*, evaluated over the range 423–1273 K

Superscripts

T_R	Evaluated at reactor cavity temperature
o	Evaluated at standard conditions

Abbreviations

BET	Brunauer–Emmett–Teller
BJH	Barrett–Joyner–Halenda
CCD	Charge-coupled device
CST	Concentrated solar thermal
GHG	Greenhouse gas
ISO	International Organization for Standardization
SEM	Scanning electron microscope
SGA	Smelter grade alumina
SSA	Specific surface area
TGA	Thermogravimetric analysis
XRD	X-ray diffraction

Acknowledgements

We gratefully acknowledge the financial support by the Swiss State Secretariat for Education, Research and Innovation (Grant No. 16.0183) and the European Union's Horizon 2020 research and innovation programme (Project INSHIP – Grant No. 731287). This program has been supported by the Australian Government through the Australian Renewable Energy Agency (ARENA) program (Grant 1-USO034), and by the Australian Research Council (Grant DP150102230). The views expressed herein are not necessarily the views of the Australian Government, and the Australian Government does not accept responsibility for any information or advice contained herein. We are also grateful for the provision of an Australian Government Research Training Program Scholarship.

References

1 B. C. McLellan, G. D. Corder, D. P. Giurco and K. N. Ishihara, *J. Cleaner Prod.*, 2012, **32**, 32–44.
2 J. G. J. Olivier, G. Janssens-Maenhout, M. Muntean and J. A. H. W. Peters, *Trends in global CO_2 emissions: 2015 report*, PBL Netherlands Environmental Assessment Agency, The Hague, European Commission, Joint Research Centre, Ispra, 2015.
3 The International Aluminium Institute, Statistics, http://www.world-aluminium.org/statistics/, (accessed 4 December, 2016).
4 K. Kermeli, P.-H. ter Weer, W. Crijns-Graus and E. Worrell, *Energy Effic.*, 2015, **8**, 629–666.
5 F. Williams and H.-W. Schmidt, *Light Met.*, 2012, 135–140.
6 L. M. Perander, Z. D. Zujovic, T. F. Kemp, M. E. Smith and J. B. Metson, *JOM*, 2009, **61**, 33–39.
7 B. E. Raahauge, *Light Met.*, 2015, 73–78.
8 B. Jenkins and C. Bertrand, *IFRF Combustion J.*, 2001, 200110.
9 K. Lovegrove, S. Edwards, N. Jacobson, J. Jordan, J. Petersheim, J. Rutowitz, H. Saddler, M. Watt and J. Wyder, Renewable energy options for Australian industrial gas users, Report ITP/A0142, Australian Renewable Energy Agency, 2015.
10 C. Klett and L. Perander, *Light Met.*, 2015, 79–84.
11 T. Eglinton, J. Hinkley, A. Beath and M. Dell'Amico, *JOM*, 2013, **65**, 1710–1720.
12 D. Hirsch and A. Steinfeld, *Chem. Eng. Sci.*, 2004, **59**, 5771–5778.
13 R. Bertocchi, *Trans. ASME: J. Sol. Energy Eng.*, 2002, **124**, 230–236.
14 L. A. Dombrovsky, W. Lipiński and A. Steinfeld, *J. Quant. Spectrosc. Radiat. Transfer*, 2007, **103**, 601–610.
15 D. Mischler and A. Steinfeld, *J. Heat Transfer*, 1995, **117**, 346–354.
16 A. Z'Graggen, P. Haueter, D. Trommer, M. Romero, J. C. de Jesus and A. Steinfeld, *Int. J. Hydrogen Energy*, 2006, **31**, 797–811.
17 I. Padilla, A. Lopez-Delgado, S. Lopez-Andres, M. Alvarez, R. Galindo and A. J. Vazquez-Vaamonde, *Sci. World J.*, 2014, **2014**, 825745.
18 A. Steinfeld, A. Imhof and D. Mischler, *Trans. ASME: J. Sol. Energy Eng.*, 1992, **114**, 171–174.
19 A. Meier, E. Bonaldi, G. M. Cella, W. Lipiński and D. Wuillemin, *Sol. Energy*, 2006, **80**, 1355–1362.
20 V. Nikulshina, M. Halmann and A. Steinfeld, *Energy Fuels*, 2009, **23**, 6207–6212.
21 G. Flamant, D. Hernandez, C. Bonet and J.-P. Traverse, *Sol. Energy*, 1980, **24**, 385–395.
22 H. P. Wang, B. G. Xu, P. Smith, M. Davies, L. DeSilva and C. Wingate, *J. Phys. Chem. Solids*, 2006, **67**, 2567–2582.

23 K. Wefers and C. Misra, Oxides and hydroxides of aluminum, Report 19, Alcoa, 1987.
24 B. Whittington and D. Ilievski, *Chem. Eng. J.*, 2004, **98**, 89–97.
25 B. K. Gan, I. C. Madsen and J. G. Hockridge, *J. Appl. Crystallogr.*, 2009, **42**, 697–705.
26 V. J. Ingram-Jones, R. C. T. Slade, T. W. Davies, J. C. Southern and S. Salvador, *J. Mater. Chem.*, 1996, **6**, 73–79.
27 J. Rouquerol, F. Rouquerol and M. Ganteaume, *J. Catal.*, 1975, **36**, 99–110.
28 S. Wind and B. E. Raahauge, *Light Met.*, 2013, 155–162.
29 L. M. Perander, Z. D. Zujovic, T. Groutso, M. M. Hyland, M. E. Smith, L. A. O'Dell and J. B. Metson, *Can. J. Chem.*, 2007, **85**, 889–897.
30 C. Sommerseth, K. S. Osen, C. Rosenkilde, A. J. Meyer, L. T. Kristiansen and T. A. Aarhaug, *Light Met.*, 2012, 827–832.
31 S. Wind, C. Jensen-Holm and B. E. Raahauge, *Light Met.*, 2010, 757–764.
32 L. M. Perander, PhD thesis, The University of Auckland, 2010.
33 J. Metson, T. Groutso, M. Hyland and S. Powell, *Light Met.*, 2006, 89–93.
34 L. M. Perander, M. A. Stam, M. M. Hyland and J. B. Metson, *Light Met.*, 2011, 285–290.
35 G. Maag, G. Zanganeh and A. Steinfeld, *Int. J. Hydrogen Energy*, 2009, **34**, 7676–7685.
36 J. R. Howell, R. Siegel and M. P. Mengüç, *Thermal radiation heat transfer*, CRC press, 5th edn, 2011.
37 J. J. Derksen, S. Sundaresan and H. E. A. van den Akker, *Powder Technol.*, 2006, **163**, 59–68.
38 M. M. Hyland, A. R. Gillespie and J. B. Metson, *Light Met.*, 1997, 113–117.
39 J. de Boer, *The structure and properties of porous materials*, 1958, pp. 68–94.
40 T. Kogure, *J. Am. Ceram. Soc.*, 2004, **82**, 716–720.
41 A. Boumaza, L. Favaro, J. Ledion, G. Sattonnay, J. B. Brubach, P. Berthet, A. M. Huntz, P. Roy and R. Tetot, *J. Solid State Chem.*, 2009, **182**, 1171–1176.
42 L. Favaro, A. Boumaza, P. Roy, J. Lédion, G. Sattonnay, J. Brubach, A. Huntz and R. Tétot, *J. Solid State Chem.*, 2010, **183**, 901–908.
43 A. Z'Graggen and A. Steinfeld, *Int. J. Hydrogen Energy*, 2008, **33**, 5484–5492.

B

Supplementary information to the thermal performance modelling

B.1 Radiation shape factor calculations

The receiver cavity is discretised into a number of volume zones (containing gas and particle phases) and surface zones that are small enough to be considered isothermal in the present numerical model. Figure B.1 illustrates these surfaces, which include the fictive aperture disc, the front wall, the end disc and n annular (cylindrical and conical) wall elements. The heat transfer model requires that the radiation shape factors between each of these surfaces is known. That is, each element in the following matrix needs to be calculated:

$$\boldsymbol{F} = \begin{bmatrix} F_{\mathrm{w}_1-\mathrm{w}_1} & F_{\mathrm{w}_1-\mathrm{w}_2} & \cdots & F_{\mathrm{w}_1-\mathrm{ap}} & F_{\mathrm{w}_1-\mathrm{fr}} & F_{\mathrm{w}_1-\mathrm{end}} \\ F_{\mathrm{w}_2-\mathrm{w}_1} & F_{\mathrm{w}_2-\mathrm{w}_2} & \cdots & F_{\mathrm{w}_2-\mathrm{ap}} & F_{\mathrm{w}_2-\mathrm{fr}} & F_{\mathrm{w}_2-\mathrm{end}} \\ \vdots & \vdots & \ddots & \vdots & \vdots & \vdots \\ F_{\mathrm{ap}-\mathrm{w}_1} & F_{\mathrm{ap}-\mathrm{w}_2} & \cdots & F_{\mathrm{ap}-\mathrm{ap}} & F_{\mathrm{ap}-\mathrm{fr}} & F_{\mathrm{ap}-\mathrm{end}} \\ F_{\mathrm{fr}-\mathrm{w}_1} & F_{\mathrm{fr}-\mathrm{w}_2} & \cdots & F_{\mathrm{fr}-\mathrm{ap}} & F_{\mathrm{fr}-\mathrm{fr}} & F_{\mathrm{fr}-\mathrm{end}} \\ F_{\mathrm{end}-\mathrm{w}_1} & F_{\mathrm{end}-\mathrm{w}_2} & \cdots & F_{\mathrm{end}-\mathrm{ap}} & F_{\mathrm{end}-\mathrm{fr}} & F_{\mathrm{end}-\mathrm{end}} \end{bmatrix}, \tag{B.1}$$

For the present numerical model, the calculation of $\boldsymbol{F}$ has been programmed with Matlab, such that any cylindrical cavity with conical section can be considered. That is, $\boldsymbol{F}$ can be calculated for any values of total length, cavity diameter, aperture diameter, end diameter, cone angle and number of axial discretisations. The following sections outline the calculation method of each F_{i-j} and the geometric shape factor relations used. The calculation of shape factors follows the diffuse gray surface model, and the reciprocal rule and summation rule are also used; $A_i F_{i-j} = A_j F_{j-i}$ and $F_{i-(j+k)} = F_{i-j} + F_{i-k}$.

Note that in the present numerical model, the radiation shape factors from the aperture are weighted to account for the directivity of concentrated solar radiation. Here, however, the shape factors are calculated for a diffusely radiating fictive aperture surface.

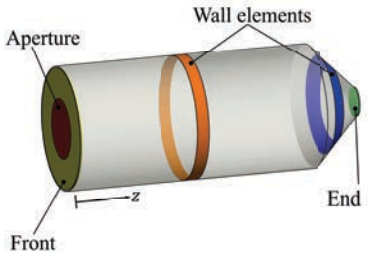

Figure B.1: Illustration of the receiver cavity surfaces, for which the radiation shape factors are calculated.

B.1.1 Shape factors from the aperture

$F_{\mathrm{ap-ap}}$

- The aperture is considered as a flat disc, therefore:

$$F_{\mathrm{ap-ap}} = 0. \tag{B.2}$$

$F_{\mathrm{ap-fr}}$

- The front wall is a flat annulus in the same plane as the aperture disc, therefore:

$$F_{\mathrm{ap-fr}} = 0. \tag{B.3}$$

$F_{\mathrm{ap-w}_i}$

- The shape factor from the aperture to a wall element w_i (Figure B.2) is calculated as the radiation reaching a disc covering the up-beam face of element i, minus the radiation reaching a disc covering the down-beam face.
- Here, up/down-beam refers to the beam direction of the incident concentrated solar radiation entering the receiver cavity through the aperture.
- The shape factors are then calculated using the relation for a *disc to a parallel coaxial disc of unequal radius* (Hamilton & Morgan 1952; Leuenberger & Person 1954; Feingold 1978), as follows:

$$F_{\mathrm{ap-w}_i} = F_{\mathrm{ap}-i_{\mathrm{u\text{-}b}}} - F_{\mathrm{ap}-i_{\mathrm{d\text{-}b}}}, \tag{B.4}$$

where:

$$F_{\mathrm{ap}-i_{\mathrm{u\text{-}b}}} = \frac{1}{2}\left[X_{i_{\mathrm{u\text{-}b}}} - \sqrt{X_{i_{\mathrm{u\text{-}b}}}^2 - 4\left(\frac{r_{i_{\mathrm{u\text{-}b}}}}{r_{\mathrm{ap}}}\right)^2}\right], \tag{B.5}$$

$$F_{ap-i_{\mathrm{d\text{-}b}}} = \frac{1}{2}\left[X_{i_{\mathrm{d\text{-}b}}} - \sqrt{X_{i_{\mathrm{d\text{-}b}}}^2 - 4\left(\frac{r_{i_{\mathrm{d\text{-}b}}}}{r_{ap}}\right)^2}\right], \tag{B.6}$$

and:

$$X_{i_{\mathrm{u\text{-}b}}} = 1 + \frac{1 + (r_{i_{\mathrm{u\text{-}b}}}/z_{i_{\mathrm{u\text{-}b}}})^2}{(r_{\mathrm{ap}}/z_{i_{\mathrm{u\text{-}b}}})^2}, \qquad X_{i_{\mathrm{d\text{-}b}}} = 1 + \frac{1 + (r_{i_{\mathrm{d\text{-}b}}}/z_{i_{\mathrm{d\text{-}b}}})^2}{(r_{\mathrm{ap}}/z_{i_{\mathrm{d\text{-}b}}})^2}.$$

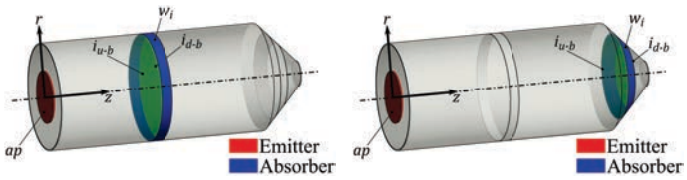

Figure B.2: Illustration of the surfaces used to calculate $F_{\mathrm{ap}-\mathrm{w}_i}$, showing the emitting aperture and the absorbing cylindrical and conical wall elements.

$F_{\mathrm{ap}-\mathrm{end}}$

- Similarly, the shape factor from the aperture to the end wall (Figure B.3) is calculated using the relation for a *disc to a parallel coaxial disc of unequal radius* (Hamilton & Morgan 1952; Leuenberger & Person 1954; Feingold 1978), as follows:

$$F_{\mathrm{ap}-\mathrm{end}} = \frac{1}{2}\left[X_{\mathrm{end}} - \sqrt{X_{\mathrm{end}}^2 - 4\left(\frac{r_{\mathrm{end}}}{r_{\mathrm{ap}}}\right)^2}\right], \tag{B.7}$$

where:

$$X_{\mathrm{end}} = 1 + \frac{1 + (r_{\mathrm{end}}/z_{\mathrm{end}})^2}{(r_{\mathrm{ap}}/z_{\mathrm{end}})^2}.$$

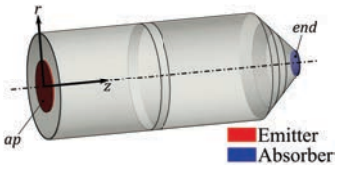

Figure B.3: Illustration of the surfaces used to calculate $F_{\mathrm{ap}-\mathrm{end}}$, showing the emitting aperture and the absorbing end wall.

B.1.2 Shape factors from the end wall

$F_{\mathrm{end}-\mathrm{end}}$

- The end wall is treated as a flat disc, so:

$$F_{\mathrm{end}-\mathrm{end}} = 0. \tag{B.8}$$

$F_{\mathrm{end}-\mathrm{ap}}$

- To calculate $F_{\mathrm{end}-\mathrm{ap}}$ the reciprocal rule is used:

$$F_{\mathrm{end}-\mathrm{ap}} = \frac{A_{\mathrm{ap}}}{A_{\mathrm{end}}} F_{\mathrm{ap}-\mathrm{end}}. \tag{B.9}$$

$F_{\text{end}-\text{fr}}$

- The relation for a *disc to a parallel coaxial disc of unequal radius* (Hamilton & Morgan 1952; Leuenberger & Person 1954; Feingold 1978) is used to calculate shape factors from the end wall to the front wall (Figure B.4).
- Specifically, $F_{\text{end}-\text{fr}}$ is calculated with the summation rule to be equal to the shape factor from the end wall to a disc of same outer radius as the front wall, minus the amount of radiation reaching the smaller aperture disc. That is:

$$F_{\text{end}-\text{fr}} = F_{\text{end}-\text{front disc}} - F_{\text{end}-\text{ap}}, \tag{B.10}$$

where:

$$F_{\text{end}-\text{front disc}} = \frac{1}{2}\left[X_{\text{fr}} - \sqrt{X_{\text{fr}}^2 - 4\left(\frac{r_{\text{fr}}}{r_{\text{end}}}\right)^2}\right], \tag{B.11}$$

and:

$$X_{\text{fr}} = 1 + \frac{1 + (r_{\text{fr}}/z_{\text{end}})^2}{(r_{\text{end}}/z_{\text{end}})^2},$$

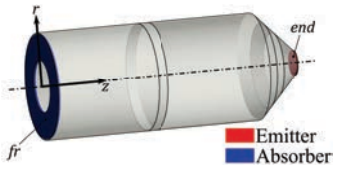

Figure B.4: Illustration of the surfaces used to calculate $F_{\text{end}-\text{fr}}$, showing the emitting end wall and the absorbing front wall.

$F_{\text{end}-\text{w}i}$

- Shape factors from the end wall to the receiver wall elements are calculated similarly to the previous section for shape factors from the aperture:

$$F_{\text{end}-\text{w}_i} = F_{\text{end}-i_{\text{d-b}}} - F_{\text{end}-i_{\text{u-b}}}, \tag{B.12}$$

where $F_{\text{end}-i_{\text{d-b}}}$ and $F_{\text{end}-i_{\text{u-b}}}$ are the shape factors from the end wall disc to discs covering the down-beam and up-beam faces of the receiver wall element, respectively (as shown in Figure B.5)

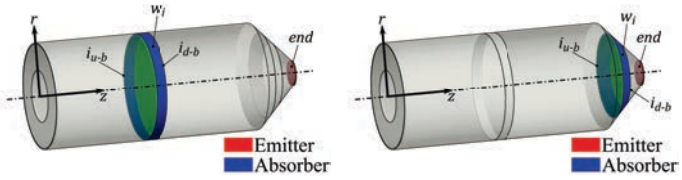

Figure B.5: Illustration of the surfaces used to calculate $F_{\text{end}-\text{w}_i}$, showing the emitting end wall and the absorbing cylindrical and conical wall elements.

B.1.3 Shape factors from the receiver wall elements

$F_{\mathrm{w}i-\mathrm{ap}}$ & $F_{\mathrm{w}i-\mathrm{end}}$

- Radiation shape factors from the receiver wall elements to the aperture and end wall surfaces are calculated with the reciprocal rule:

$$F_{\mathrm{w}i-\mathrm{ap}} = \frac{A_{\mathrm{ap}}}{A_{\mathrm{w}_i}} F_{\mathrm{ap}-\mathrm{w}_i}, \tag{B.13}$$

$$F_{\mathrm{w}i-\mathrm{end}} = \frac{A_{\mathrm{end}}}{A_{\mathrm{w}_i}} F_{\mathrm{end}-\mathrm{w}_i}. \tag{B.14}$$

$F_{\mathrm{w}_i-\mathrm{w}_i}$

- The radiation shape factors between the discretised cylindrical and conical wall elements are divided into four types of calculation:
  1. cylindrical wall section to itself (Figure B.6),
  2. cylindrical wall section to other wall element (Figure B.7),
  3. conical wall section to itself (Figure B.8), and
  4. conical wall section to other wall element (Figure B.9).
- The first type of shape factor (Figure B.6) is calculated using the relation for the *interior surface of a cylinder to itself* (Buschman & Pittman 1961), which is:

$$F_{\mathrm{w}_i-\mathrm{w}_i} = 1 + \frac{\Delta z}{2r_i} - \sqrt{1 + \frac{\Delta z^2}{4r_i^2}} \tag{B.15}$$

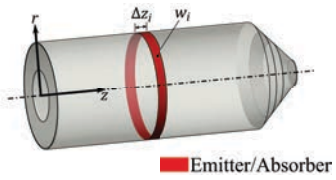

Figure B.6: Illustration of the wall element surface used to calculate $F_{\mathrm{w}_i-\mathrm{w}_i}$ for cylindrical wall elements, which absorbs some of the radiation it emits.

- The second type of shape factor (Figure B.7) is calculated using the relation for the *interior surface of a cylinder to a coaxial disc perpendicular to the axis of the cylinder* (Buschman & Pittman 1961).
- The shape factor from a cylindrical wall element to another wall element (cylindrical or conical) is the difference between shape factors to the discs covering the down-beam and up-beam faces of the element, calculated as:

$$F_{\mathrm{w}i-\mathrm{w}j} = F_{\mathrm{w}i-j_{\mathrm{u\text{-}b}}} - F_{\mathrm{w}i-j_{\mathrm{d\text{-}b}}}, \tag{B.16}$$

where:

$$F_{\mathrm{w}i-j_{\mathrm{u\text{-}b}}} = \frac{1}{4R_{\mathrm{u\text{-}b}}(L_{2,\mathrm{u\text{-}b}} - L_{1,\mathrm{u\text{-}b}})} \times \left[(X_{1,\mathrm{u\text{-}b}} - X_{2,\mathrm{u\text{-}b}}) - \sqrt{X_{1,\mathrm{u\text{-}b}}^2 - 4R_{\mathrm{u\text{-}b}}^2} + \sqrt{X_{2,\mathrm{u\text{-}b}}^2 - 4R_{\mathrm{u\text{-}b}}^2}\right], \tag{B.17}$$

$$F_{\mathrm{w}i-j_{\mathrm{d\text{-}b}}} = \frac{1}{4R_{\mathrm{d\text{-}b}}(L_{2,\mathrm{d\text{-}b}} - L_{1,\mathrm{d\text{-}b}})} \times \left[(X_{1,\mathrm{d\text{-}b}} - X_{2,\mathrm{d\text{-}b}}) - \sqrt{X_{1,\mathrm{d\text{-}b}}^2 - 4R_{\mathrm{d\text{-}b}}^2} + \sqrt{X_{2,\mathrm{d\text{-}b}}^2 - 4R_{\mathrm{d\text{-}b}}^2}\right], \tag{B.18}$$

and:

$$R_{\mathrm{u\text{-}b}} = \frac{r_{\mathrm{w}i}}{r_{j_{\mathrm{u\text{-}b}}}} \qquad L_{1,\mathrm{u\text{-}b}} = \frac{z_{j_{\mathrm{u\text{-}b}}} - z_{i_{\mathrm{d\text{-}b}}}}{r_{j_{\mathrm{u\text{-}b}}}} \qquad L_{2,\mathrm{u\text{-}b}} = \frac{z_{j_{\mathrm{u\text{-}b}}} - z_{i_{\mathrm{u\text{-}b}}}}{r_{j_{\mathrm{u\text{-}b}}}}$$

$$X_{1,\mathrm{u\text{-}b}} = L_{1,\mathrm{u\text{-}b}}^2 + R_{\mathrm{u\text{-}b}}^2 + 1 \qquad X_{2,\mathrm{u\text{-}b}} = L_{2,\mathrm{u\text{-}b}}^2 + R_{\mathrm{u\text{-}b}}^2 + 1$$

$$R_{\mathrm{d\text{-}b}} = \frac{r_{\mathrm{w}i}}{r_{j_{\mathrm{d\text{-}b}}}} \qquad L_{1,\mathrm{d\text{-}b}} = \frac{z_{j_{\mathrm{d\text{-}b}}} - z_{i_{\mathrm{d\text{-}b}}}}{r_{j_{\mathrm{d\text{-}b}}}} \qquad L_{2,\mathrm{d\text{-}b}} = \frac{z_{j_{\mathrm{d\text{-}b}}} - z_{i_{\mathrm{u\text{-}b}}}}{r_{j_{\mathrm{d\text{-}b}}}}$$

$$X_{1,\mathrm{d\text{-}b}} = L_{1,\mathrm{d\text{-}b}}^2 + R_{\mathrm{d\text{-}b}}^2 + 1 \qquad X_{2,\mathrm{d\text{-}b}} = L_{2,\mathrm{d\text{-}b}}^2 + R_{\mathrm{d\text{-}b}}^2 + 1.$$

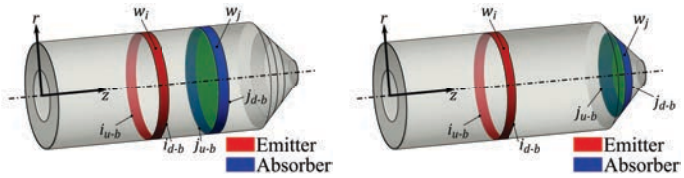

Figure B.7: Illustration of the surfaces used to calculate $F_{\mathrm{w}i-\mathrm{w}j}$ for a cylindrical emitting wall element and both cylindrical and conical absorbing wall elements.

- The third type of shape factor (Figure B.8) is calculated using the relation for the *interior of a frustum of a circular cone to itself* (Sparrow & Jonsson 1963), which is:

$$F_{\mathrm{w}i-\mathrm{w}i} = 1 + \frac{\left(1 - \frac{\xi_{i_{\mathrm{d\text{-}b}}}}{\xi_{i_{\mathrm{u\text{-}b}}}}\right)\cos^2\alpha - \sqrt{\left(\frac{\xi_{i_{\mathrm{d\text{-}b}}}}{\xi_{i_{\mathrm{u\text{-}b}}}} + 1\right)^2 - 4\left(\frac{\xi_{i_{\mathrm{d\text{-}b}}}}{\xi_{i_{\mathrm{u\text{-}b}}}}\right)\cos^2\alpha}}{\left(1 + \frac{\xi_{i_{\mathrm{d\text{-}b}}}}{\xi_{i_{\mathrm{u\text{-}b}}}}\right)\sin\alpha}, \tag{B.19}$$

where α is the cone angle and $\xi_{i_{\mathrm{d\text{-}b}}}$ and $\xi_{i_{\mathrm{u\text{-}b}}}$ are coordinates along the cone slant from the cone vertex to the down-beam and up-beam faces of conical wall element w_i, respectively.

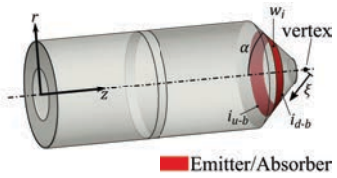

Figure B.8: Illustration of the wall element surface used to calculate $F_{\mathrm{w}i-\mathrm{w}i}$ for conical wall elements, which absorbs some of the radiation it emits.

- The fourth type of shape factor (Figure B.9) is calculated using the relation for a *finite frustum of a circular cone to a separated finite frustum of the same circular cone* (Buschman & Pittman 1961), which is:

$$\begin{aligned} F_{\mathrm{w}_i-\mathrm{w}_j} =& \frac{1}{2(L_3-L_2)(2-L_2-L_3)}\times \\ & \Big\{(L_3-L_1)\sqrt{(L_3-L_1)^2\csc^2\alpha+4(1-L_1)(1-L_3)} \\ & -(L_2-L_1)\sqrt{(L_2-L_1)^2\csc^2\alpha+4(1-L_1)(1-L_2)} \\ & -L_3\sqrt{L_3^2\csc^2\alpha+4(1-L_3)} \\ & +L_2\sqrt{L_2^2\csc^2\alpha+4(1-L_2)} \\ & +2L_1(L_3-L_2)\cos\alpha\cot\alpha\Big\}, \end{aligned} \tag{B.20}$$

  where:

$$L_1=\frac{z_{j_{\text{d-b}}}-z_{j_{\text{u-b}}}}{z_{\text{vertex}}-z_{j_{\text{u-b}}}} \qquad L_2=\frac{z_{i_{\text{u-b}}}-z_{j_{\text{u-b}}}}{z_{\text{vertex}}-z_{j_{\text{u-b}}}} \qquad L_3=\frac{z_{i_{\text{d-b}}}-z_{j_{\text{u-b}}}}{z_{\text{vertex}}-z_{j_{\text{u-b}}}}$$

- Note that Equation (B.20) is only valid for $z_i > z_j$. Therefore, the reciprocal rule is used for all other conical wall elements: $F_{\mathrm{w}j-\mathrm{w}i} = (A_{\mathrm{w}i}/A_{\mathrm{w}j})F_{\mathrm{w}i-\mathrm{w}j}$.

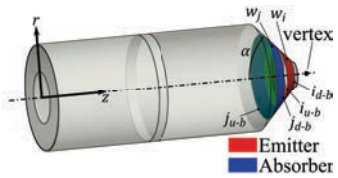

Figure B.9: Illustration of the surfaces used to calculate $F_{\mathrm{w}_i-\mathrm{w}_j}$ for a conical emitting wall element and a conical absorbing wall element.

$F_{\mathrm{w}_i-\mathrm{fr}}$

- To calculate the shape factors from the cylindrical and conical wall elements to the front wall, the summation rule is used again, where:

$$F_{\mathrm{w}_i-\mathrm{fr}} = F_{\mathrm{w}_i-\text{front disc}} - F_{\mathrm{w}_i-\mathrm{ap}}. \tag{B.21}$$

- Using the reciprocal rule, $F_{\mathrm{w}_i-\text{front disc}}$ is calculated from $F_{\text{front disc}-\mathrm{w}_i}$, for which the relation for a *disc to parallel coaxial disc of unequal radius* (Hamilton & Morgan 1952; Leuenberger & Person 1954; Feingold 1978) is used.
- It is shown schematically in Figure B.10 and is calculated as follows:

$$F_{\text{front disc}-\mathrm{w}_i} = F_{\text{front disc}-i_{\text{u-b}}} - F_{\text{front disc}-i_{\text{d-b}}}, \tag{B.22}$$

  where:

$$F_{\text{front disc}-i_{\text{u-b}}} = \frac{1}{2}\left[X_{i_{\text{u-b}}} - \sqrt{X_{i_{\text{u-b}}}^2 - 4\left(\frac{r_{i_{\text{u-b}}}}{r_{\text{front disc}}}\right)^2}\right], \tag{B.23}$$

$$F_{\text{front disc}-i_{\text{d-b}}} = \frac{1}{2}\left[X_{i_{\text{d-b}}} - \sqrt{X_{i_{\text{d-b}}}^2 - 4\left(\frac{r_{i_{\text{d-b}}}}{r_{\text{front disc}}}\right)^2}\right], \tag{B.24}$$

and:

$$X_{i_{\text{u-b}}} = 1 + \frac{1 + (r_{i_{\text{u-b}}}/z_{i_{\text{u-b}}})^2}{(r_{\text{front disc}}/z_{i_{\text{u-b}}})^2}, \qquad X_{i_{\text{d-b}}} = 1 + \frac{1 + (r_{i_{\text{d-b}}}/z_{i_{\text{d-b}}})^2}{(r_{\text{front disc}}/z_{i_{\text{d-b}}})^2}.$$

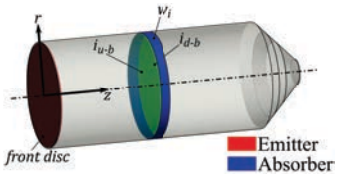

Figure B.10: Illustration of the surfaces used to calculate $F_{\text{front disc}-\text{w}_j}$ showing an emitting disc and absorbing wall element.

B.1.4 Shape factors from the front wall

$F_{\text{fr}-\text{fr}}$

- The front wall is considered as a flat annulus, therefore:

$$F_{\text{fr}-\text{fr}} = 0. \tag{B.25}$$

$F_{\text{fr}-\text{ap}}$

- The front wall is in the same plane as the aperture disc, therefore:

$$F_{\text{fr}-\text{ap}} = 0. \tag{B.26}$$

$F_{\text{fr}-\text{w}_i}$

- Following the calculations of the previous sections, the shape factors from the front wall to the discretised wall elements are calculated with the reciprocal rule, as follows:

$$F_{\text{fr}-\text{w}_i} = \frac{A_{\text{w}_i}}{A_{\text{fr}}} F_{\text{w}_i-\text{fr}}. \tag{B.27}$$

$F_{\text{fr}-\text{end}}$

- Similarly, the reciprocal rule is used for the shape factor to the end wall:

$$F_{\text{fr}-\text{end}} = \frac{A_{\text{end}}}{A_{\text{fr}}} F_{\text{end}-\text{fr}}. \tag{B.28}$$

B.2 Additional sensitivity studies

B.2.1 Sensitivity to receiver length

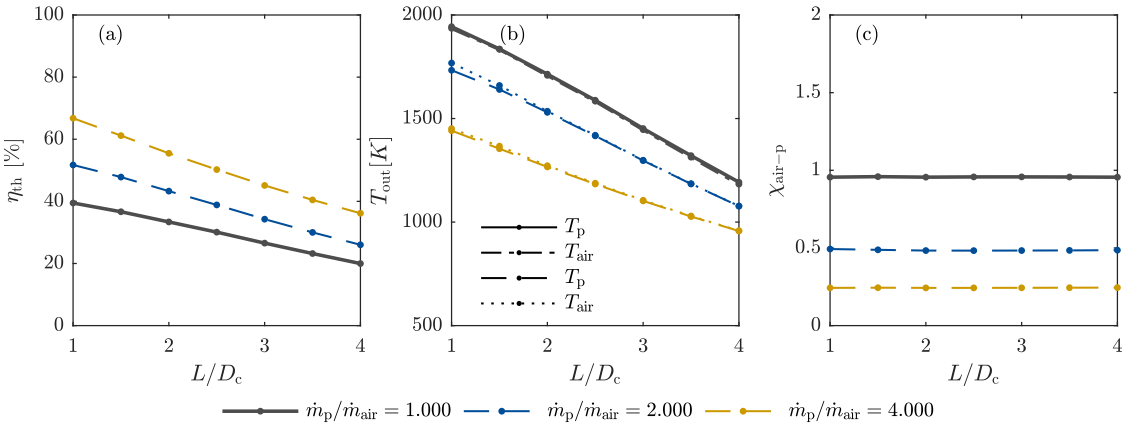

Figure B.11: Assessment of the operation of the SVR with varying length to diameter ratio, L/D_c, other reference case geometries, (D_{ap} = 0.050 m, D_{ap}/D_c = 0.516, α = 45°) and solar thermal input, $\dot{q}_s$ = 2000 kW m^{-2} ($\dot{Q}_s$ = 3.927 kW), $\dot{m}_{air}$ = 4.000 × 10^{-4} kg/s, T_{in} = 300 K and 3 different values of mass loading. Presented are **(a)** the receiver thermal efficiency, η_{th}; **(b)** the particle and air outlet temperatures, $T_{p,out}$ and $T_{air,out}$; and **(c)** the energy absorption ratio, χ_{air-p}, as a function of length to diameter ratio, L/D_c, for three different values of mass loading, $\dot{m}_p/\dot{m}_{air}$.

B.2.2 Sensitivity to input temperature

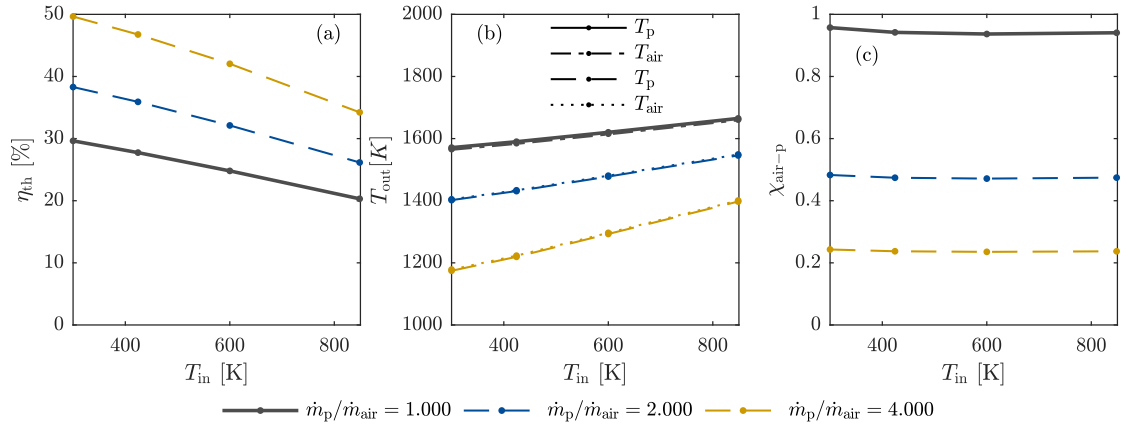

Figure B.12: Assessment of the operation of the SVR with varying inlet temperature of the particle and air phase, T_{in}, with reference case geometry (D_{ap} = 0.050 m, D_{ap}/D_c = 0.516, L/D_c = 2.55 α = 45°) and solar thermal input, $\dot{q}_s$ = 2000 kW m^{-2} ($\dot{Q}_s$ = 3.927 kW), $\dot{m}_{air}$ = 4.000 × 10^{-4} kg/s, and three different values of mass loading, $\dot{m}_p/\dot{m}_{air}$. Presented are **(a)** the receiver thermal efficiency, η_{th}; **(b)** the particle and air outlet temperatures, $T_{p,out}$ and $T_{air,out}$; and **(c)** the energy absorption ratio, χ_{air-p}, as a function of particle and air inlet temperature, T_{in}, for three different values of mass loading, $\dot{m}_p/\dot{m}_{air}$.

B.2.3 Sensitivity to overall conduction heat loss coefficient

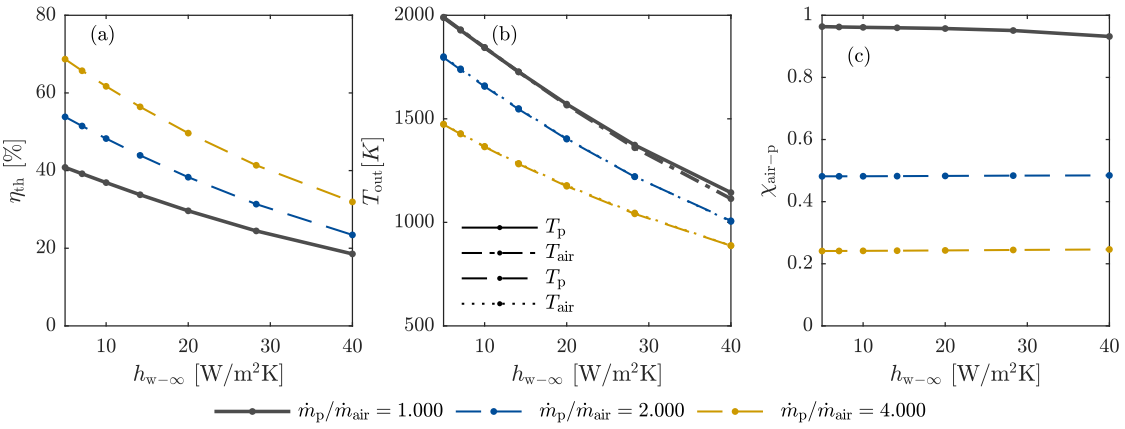

Figure B.13: Assessment of the operation of the SVR with varying overall conduction heat loss coefficient, $h_{w-\infty}$, with reference case geometry (D_{ap} = 0.050 m, D_{ap}/D_c = 0.516, L/D_c = 2.55 α = 45º) and solar thermal input, $\dot{q}_s$ = 2000 kW m^{-2} ($\dot{Q}_s$ = 3.927 kW), $\dot{m}_{air}$ = 4.000 × 10^{-4} kg/s, and three different values of mass loading, $\dot{m}_p/\dot{m}_{air}$. Presented are **(a)** the receiver thermal efficiency, η_{th}; **(b)** the particle and air outlet temperatures, $T_{p,out}$ and $T_{air,out}$; and **(c)** the energy absorption ratio, χ_{air-p}, as a function of overall conduction heat loss coefficient, $h_{w-\infty}$, for three different values of mass loading, $\dot{m}_p/\dot{m}_{air}$.

B.2.4 Sensitivity to emissivities

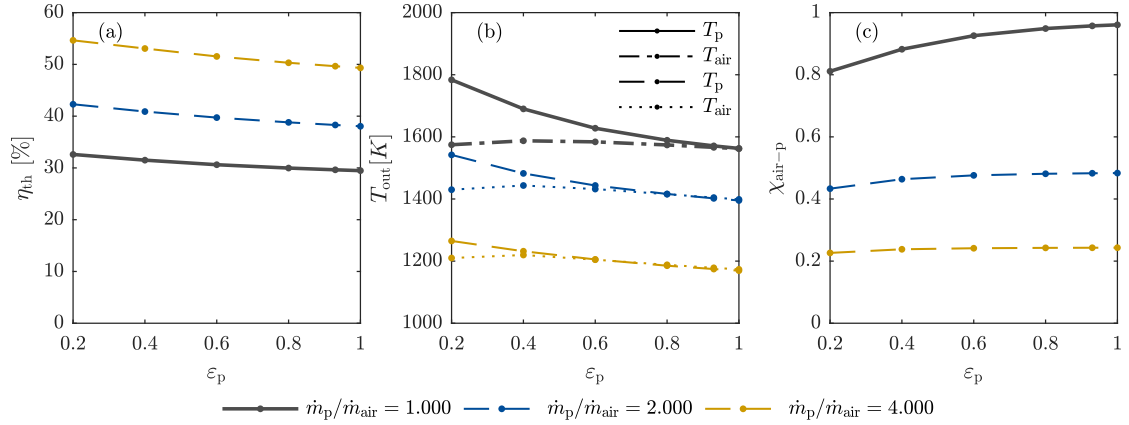

Figure B.14: Assessment of the operation of the SVR with varying particle emissivity, ε_p, with reference case geometry (D_{ap} = 0.050 m, D_{ap}/D_c = 0.516, L/D_c = 2.55 α = 45°) and solar thermal input, $\dot{q}_s$ = 2000 kW m^{-2} ($\dot{Q}_s$ = 3.927 kW), $\dot{m}_{air}$ = 4.000 × 10^{-4} kg/s, and three different values of mass loading, $\dot{m}_p/\dot{m}_{air}$. Presented are **(a)** the receiver thermal efficiency, η_{th}; **(b)** the particle and air outlet temperatures, $T_{p,out}$ and $T_{air,out}$; and **(c)** the energy absorption ratio, χ_{air-p}, as a function of particle emissivity, ε_p, for three different values of mass loading, $\dot{m}_p/\dot{m}_{air}$.

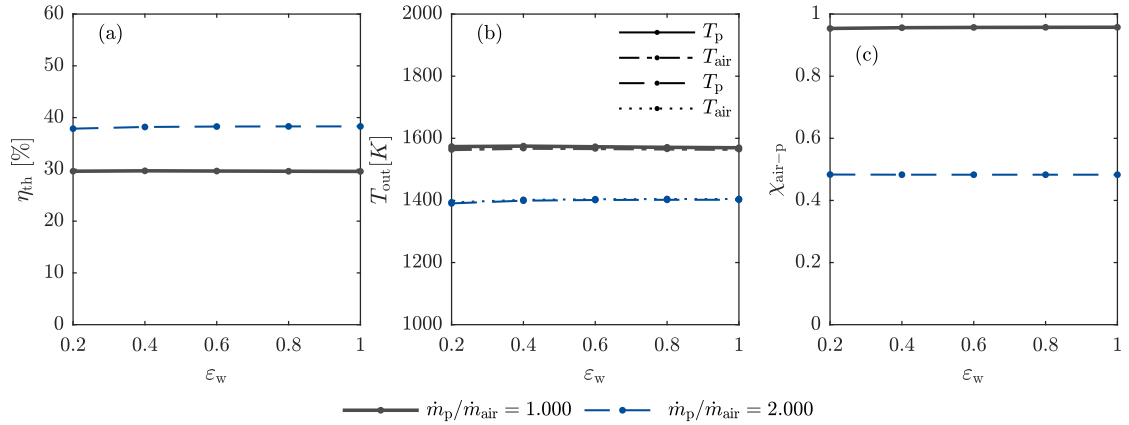

Figure B.15: Assessment of the operation of the SVR with varying particle emissivity, ε_p, with reference case geometry (D_{ap} = 0.050 m, D_{ap}/D_c = 0.516, L/D_c = 2.55 α = 45°) and solar thermal input, $\dot{q}_s$ = 2000 kW m^{-2} ($\dot{Q}_s$ = 3.927 kW), $\dot{m}_{air}$ = 4.000 × 10^{-4} kg/s, and two different values of mass loading, $\dot{m}_p/\dot{m}_{air}$. Presented are **(a)** the receiver thermal efficiency, η_{th}; **(b)** the particle and air outlet temperatures, $T_{p,out}$ and $T_{air,out}$; and **(c)** the energy absorption ratio, χ_{air-p}, as a function of particle emissivity, ε_w, for two different values of mass loading, $\dot{m}_p/\dot{m}_{air}$.

C

Supplementary information to the solar calcination of alumina

Table C.1: Summary of operational conditions and the measurements taken during the 19 nominally steady-state solar calcination of alumina experimental runs.

#	$\dot{Q}_s$ [W]	$\dot{V}_{air,n}$ [L_n min^{-1}]	$\dot{m}_{trans}$ [g min^{-1}]	$\dot{m}_{steam}$ [g min^{-1}]	$\dot{m}_{Al(OH)_3}$ [g min^{-1}]	$T_{reactor}$ [K]	T_{wall} [K]	ϕ [-]	τ_{nom} [s]	X [mol.%]	η_{th} [%]	LoI_{ads} [wt.%]	LoI_{573}[a] [wt.%]	LoI_{1273}[b] [wt.%]	SSA [m^2 g^{-1}]	d_{pore} [nm]
1	2285	20.03	25.88	-	1.12	1259	1114	0.57×10^{-5}	1.74	88.1	19.8	7.23	9.76	2.96	184.8	3.71
2	2108	20.03	25.88	-	0.73	1213	1020	0.40×10^{-5}	1.91	86.2	20.4	9.25	11.96	3.47	179.2	3.69
3	3642	20.03	25.88	-	0.95	1479	1246	0.43×10^{-5}	1.56	90.5	15.6	6.00	8.32	2.20	178.4	3.94
4	2132	20.03	25.88	-	0.84	1226	934	0.51×10^{-5}	2.08	84.8	20.4	7.84	11.54	3.20	170.1	3.71
5	2316	12.03	15.54	-	1.35	1258	1122	1.13×10^{-5}	2.81	89.4	11.7	11.72	13.65	2.74	189.5	3.45
6	2117	12.03	15.54	-	1.39	1161	928	1.40×10^{-5}	3.40	85.3	11.4	13.88	16.67	3.46	226.6	2.54
7	3773	12.03	15.54	-	1.45	1454	1272	1.07×10^{-5}	2.47	93.5	8.8	8.42	9.68	1.81	162.1	4.52
8	2291	20.03	25.88	-	2.07	1230	1106	1.06×10^{-5}	1.72	87.4	19.1	9.74	12.22	3.19	172.3	3.87
9	2211	20.03	25.88	-	1.33	1216	977	0.77×10^{-5}	1.97	87.9	19.5	8.35	10.74	3.14	180.5	3.78
10	4224	20.03	25.88	-	1.98	1421	1258	0.89×10^{-5}	1.51	92.4	12.7	6.22	7.64	2.17	170.9	4.30
11	3730	12.03	15.54	-	2.32	1480	1311	1.66×10^{-5}	2.33	93.9	9.1	13.89	14.98	1.60	157.0	5.01
12	3383	17.03	22.00	-	1.26	1414	1227	0.68×10^{-5}	1.84	92.0	13.4	8.16	9.85	2.06	180.6	4.32
13	3492	12.03	15.54	-	1.75	1408	1219	1.35×10^{-5}	2.55	91.7	9.1	14.14	15.50	2.25	213.7	3.63
14	4262	19.85	25.65	-	2.53	1551	1371	1.05×10^{-5}	1.38	95.8	14.1	8.56	9.38	1.20	132.7	5.75
15	3766	16.03	20.71	-	1.06	1456	1254	0.60×10^{-5}	1.92	93.3	11.8	6.40	7.72	1.88	167.4	4.47
16	2362	16.03	20.71	-	1.14	1208	1051	0.76×10^{-5}	2.29	89.1	14.5	8.30	10.37	2.96	168.5	4.36
17	2198	16.03	20.71	-	0.55	1179	943	0.41×10^{-5}	2.58	90.1	15.0	6.20	7.91	2.98	168.7	3.78
18	3965	20.03	25.88	-	1.35	1459	1284	0.59×10^{-5}	1.50	94.5	14.0	5.91	6.875	1.67	135.9	4.93
19	3832	20.03	25.88	1.17	0.85	1439	1262	0.35×10^{-5}	1.43	94.0	14.2	7.99	9.10	1.75	164.3	4.58

[a] Evaluated over the T_{TGA} range 298 – 573 K.
[b] Evaluated over the T_{TGA} range 573 – 1273 K.